Modelling Buckling and Post-buckling Behaviours of Corrugated Paperboard Structures

A thesis

submitted in fulfilment

of the requirements for the degree

of

Doctor of Philosophy in Engineering

at

The University of Waikato

by

CELIA SWEE LI KUEH

THE UNIVERSITY OF
WAIKATO
Te Whare Wānanga o Waikato

2012

Abstract

The buckling and post-buckling behaviours of corrugated paperboard packaging structures are the focus of this study. The motivations for this study are to improve understanding of post-buckling behaviour to better predict packaging performance and investigate reasons for the discrepancy between experimental and predicted results reported in literature.

The research questions posed consider how post-buckling behaviour of corrugated paperboard panels are affected by varying in-plane boundary conditions and using multi-term out-of-plane displacement functions in analytical Galerkin's method models with symmetric and / or anti-symmetric geometric imperfections. The panels of varying in-plane boundary conditions and geometric imperfections were also modelled by the Finite Element (FE) method. The material properties of corrugated paperboard obtained by different methods were compared, involving materials testing methods (edge compression, four-point bending and sonic vibration frequency tests) and equivalent single-layered and detailed geometric material models. Comparisons between experimental and predicted panel buckling results consider what boundary conditions best resemble experimental conditions and which displacement modes are dominant.

Difference of in-plane boundary conditions were not the likely source of discrepancy between post-buckling behaviour in models and experiments. Instead, shortcomings in the equivalent single-layered material models used were thought to be the most significant source of discrepancy in the post-buckling results.

The number of modes in the displacement function of the analytical Galerkin's models influences the post-buckling results. A nine-term symmetric mode model with fundamental geometric imperfection had an increased panel central deflection of 16% at a load ratio of 1.8 times the

critical load, compared to the single-term solution. Interactions between symmetric and anti-symmetric displacement modes were observed only for panels with both symmetric and anti-symmetric geometric imperfections, thought to be due to changes in the in-plane stress distribution.

Equivalent single-layered material models for corrugated paperboard did not give sufficient agreement in effective in-plane elastic moduli compared with materials tests indicating this modelling approach is inadequate for predicting the post-buckling behaviour. Detailed geometric or alternative homogenisation material models for corrugated paperboard accounting for changes in humidity, viscoelastic and plastic behaviour, and transverse shear deformation should be considered for future studies.

The equivalent single-layered analytical Galerkin's models, and equivalent and detailed geometric FE models show that the in-plane boundary conditions case for which loaded edges are subjected to uniform displacement and unloaded edges are free of constraints, had the least disagreement with the panel buckling experiments in this study. Possible sources of the discrepancy were investigated, involving panel imperfection and material properties. The fundamental displacement mode was most dominant in the experimental results, but only four non-zero modes were given by fitting panel deflections into a Fourier series using the collocation method, due to limited deflection measurement points. The least squares method for estimating the experimental critical load had slightly better agreement than Southwell's method in comparisons with analytical and FE model predictions, but caused difficulties with convergence in some cases. The in-plane and flexural material properties from the frequency testing of corrugated paperboard were scaled to consider their impact on the analytical post-buckling model results. Calibration of the material properties from frequency tests to suit prediction of post-buckling behaviour may be possible if it can be justified in further experiments.

Acknowledgments

Firstly, I wish to thank Prof. Sinniah Ilanko and Dr. Mike Duke of the University of Waikato, and Dr. Namasivayam Navaranjan of Scion Research for their supervision of my research.

I wish to acknowledge and thank Professor David Kennedy and Dr. Carol Featherston at Cardiff University, School of Engineering, for permitting the use of their VICONOPT corrugated paperboard model results for comparisons in my research. My grateful acknowledgments are also given to Professor Jim Woodhouse of Cambridge University for allowing the use of his frequency test vibration model in Matlab.

The financial support of my research by Scion Research and the University of Waikato is gratefully acknowledged.

Thanks to my fellow students and staff at the University of Waikato School of Engineering and Scion Research for their help in providing resources and interest in my research.

Finally, I wish to express my appreciation for my family and friends who have continued to support and encourage me through this time.

Table of Contents

List of Figures

List of Tables

1 Introduction

1.1 Background

Corrugated paperboard boxes are a common and cost-effective way to store or transport goods. Most boxes are overdesigned to avoid packaging failure, since their functional performance is sensitive to environmental conditions and raw material variations. This is because the price to pay for incorrectly loaded boxes could be costly or irreparable damage to their contents. This illustrates the need to gain a better understanding of paperboard failure, so that such occurrences can be prevented.

The subject of this research is on modelling the buckling of corrugated paperboard packaging, a mode of failure which occurs in compression loading of paperboard packaging. Post-buckling behaviour of the paperboard panels at loads beyond the critical buckling load is also modelled. The study was carried out in collaboration with the Crown Research Institute SCION in Rotorua.

Computer modelling of the buckling phenomena has a useful application in determining the performance of corrugated paperboard; a conventional packaging material used for transporting produce and manufactured goods.

Corrugated paperboard consists of facing (linerboard) layers and a corrugated core (fluted medium), as shown in Figure 1-1. The corrugated paperboard layers can be made from standard virgin (kraft) wood pulp or recycled paper fibres. The term grammage refers to the mass (in grams) per unit area of paper or paperboard. The principal material directions for corrugated paperboard are *x* - the machine-direction (MD) along which the paperboard was manufactured and paper fibres become aligned, y - the cross-direction (CD) parallel to the corrugated fluting and *z* - the out-of plane direction.

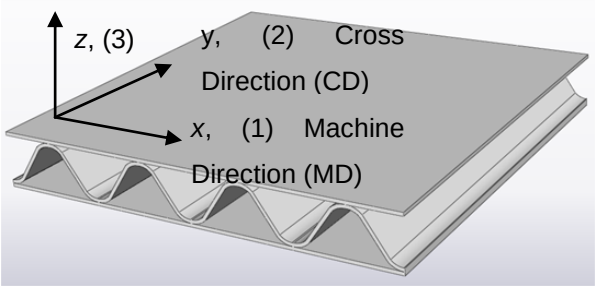

Figure 1-1: Corrugated paperboard principal directions.

Corrugated paperboard has been manufactured in a variety of thicknesses, corrugation profiles and number of walls of sandwiched facings and core layers. The corrugation profile determines the rigidity of the paperboard and is classified in terms of the corrugation height and take-up factor - the ratio of the length of the core material used compared to the length of the facing. The C-flute is the most commonly used profile, with a take-up factor of about 1.45.

The production of single wall corrugated paperboard involves the corrugated core, formed by a preheated and presteamed sheet passing through corrugating rollers, being glued to a liner termed the single facer, before gluing of a second liner termed the double backer to the other side of the core. The starch based adhesive is applied to the core flute tips by glue applicator rollers and pressure rollers secure the glue seams between core and facings.

Box blanks are cut from corrugated paperboard sheets according to design, having flaps and possible features such as perforations and holes. The blanks are converted to boxes by being creased along fold lines and glued.

The primary functions of packaging are to contain and protect the packaged goods from distribution hazards in handling, storage and transportation.

The contents of packages risk of being damaged in static loads from lateral crushing and compression in stacking during storage or in-transit. Additionally, packaging may encounter impact and dynamic vibration loads

due to vertical and horizontal acceleration, and humidity and temperature differences in handling and transportation.

Compressive loads can lead to short-term elastic and or long term non-linear viscoelastic creep buckling behaviour in corrugated paperboard structures. Long-term cyclic loading from vibration in transport can also cause buckling at a load below the critical buckling load.

Elastic buckling can be defined as failure that occurs when a compressive load on a structure reaches a critical value such that there is a sudden decrease in the structure's out-of- plane stiffness resulting in large out-of-plane deformations. Elastic buckling is seen in compressed boxes as panel bulging that initiates from the corners, while, inelastic buckling occurs with minimal bulging and uniform crushing of the loaded edges (Urbanik & Frank, 2006).

In the design of corrugated paperboard packaging, compression strength refers to the load that can be supported up to failure, which may exceed the critical buckling load. A commonly referred to formula to predict the compression strength of boxes proposed by McKee, Gander, & Wachuta (1963) and further developed by other researchers since, make use of empirical data from the testing of paperboard and packaging geometry. These include tests for edge compression strength in CD and flexural stiffness in planar directions on paperboard samples.

Urbanik & Frank (2006) found that the post-buckling box panel strength prediction formula by Urbanik & Saliklis (2003) applied to data sets for single-wall box compression from multiple literature sources, gave an average estimated error of within ±8.5% of the actual box compression strength. The variations in the input data of the models from variability in the test methods or the raw materials were cited as possible sources of error. The error between the experimental and modelled behaviour of the corrugated paperboard boxes often means boxes tend to be overdesigned.

The methods that have been used for the modelling buckling of corrugated paperboard include analytical and numerical techniques. The material definitions used have involved detailed models of the corrugated paperboard structure or equivalent models for corrugated paperboard. Material testing of corrugated paperboard is necessary either on constituent layers or the whole corrugated paperboard structure, to obtain input data for the models.

The modelling of corrugated paperboard material is complex due to raw material variability since it is biologically derived, has a composite structure, has a non-linear stress-strain relationship and is sensitive to changes in humidity. The corrugated paperboard material is more conveniently modelled as an equivalent orthotropic single lamina than with detailed paperboard layers. However, the complete definition of corrugated paperboard material properties as a whole remains a challenge.

Further study into modelling corrugated paperboard packaging buckling behaviour therefore would be justified to improve the understanding of the phenomena and its prediction, given its importance in measuring the packaging's performance. The detrimental effects of loads leading to buckling, on the condition of packaging and consequently of packaged goods, are motivations for this study of the deformation behaviour of corrugated paperboard in buckling. Post-buckling behaviour is modelled in this study since the effect of plate curvature in increasing stiffness and hence allowing further loads to be sustained beyond the critical buckling load till failure, should be taken into account.

As a result of improved understanding of buckling of corrugated paperboard packaging, subsequent optimisation of packaging would be beneficial to the corrugated paperboard packaging industry.

1.2 Objectives

The main objective of this work is to improve the understanding of the post-buckling behaviour of corrugated paperboard packaging, so that conditions leading to such failure can be predicted and thus avoided.

Analytical and numerical computer models for buckling of corrugated paperboard panels were developed in this work. The corrugated paperboard panels can be considered as side walls of a box packaging structure. The analytical Galerkin's method and Finite Element (FE) models predict the critical load and failure of paperboard panels at 50% and 90% constant relative humidity. Material properties of paperboard from testing are used as input data and the models are compared with experimental buckling results.

The sub-objectives of the study include investigations into reasons for the discrepancy between modelled and experimental buckling and post-buckling results of corrugated paperboard panels. The categories dealt with include the effect of differences in modelled in-plane boundary conditions compared to experimental conditions and the effect of including multi-term out-of-plane displacement shape functions in the analytical buckling model. The material constants of corrugated paperboard obtained by different tests and theories relevant to the buckling models are compared. The analysis of experimental buckling panel data is also explored in the comparisons with predicted results.

1.3 Literature Review

In examining the performance of corrugated paperboard packaging, buckling behaviour is a key concern. The problem of buckling of corrugated paperboard due to static compression loads has been addressed in previous studies, using various analytical and numerical approaches such as the Finite Element (FE) method, and experimental work on panels and boxes. Loading conditions such as long-term creep and cyclic loading and changes in humidity are also complicating factors in the issue of buckling,

which are not dealt with in this study. The methods to determine material properties of paperboards, analytical and FE models for buckling are briefly highlighted.

Previous literature modelling buckling of corrugated paperboard structures has continued to show a difference in modelled and experimental buckling behaviour (Biancolini, Brutti, & Porziani, 2009a; Nordstrand, 2004a). This may be attributed to the complexity of modelling corrugated paperboard, due to the composite structure with layered geometry, as shown in Figure 1-1, and sensitivity of material properties to environmental changes, and factors such as imprecise experimental boundary conditions in buckling tests.

1.3.1 Buckling

For the solution of the buckling problem of corrugated paperboard, orthotropic plate theory is often used. The constitutive equation for an anisotropic laminate plate element in bending is given by (Weaver, 2008):

$$\begin{Bmatrix} \boldsymbol{N} \\ \boldsymbol{M} \end{Bmatrix} = \begin{bmatrix} \boldsymbol{A} & \boldsymbol{B} \\ \boldsymbol{B} & \boldsymbol{D}^{*} \end{bmatrix} \begin{Bmatrix} \boldsymbol{\varepsilon}^{0} \\ \boldsymbol{\kappa} \end{Bmatrix}$$

Equation 1-1

Where $\boldsymbol{N}$ is in-plane loading resultant vector, $\boldsymbol{M}$ the bending moment vector, $\boldsymbol{\varepsilon}^0$ the strain at $z = 0$ the reference plate surface, $\boldsymbol{\kappa}$ the curvature and $\boldsymbol{A}$, $\boldsymbol{B}$, $\boldsymbol{D}^*$ are the in-plane, coupling, flexural stiffness matrices respectively.

For materials with symmetry about the middle plate surface, which corrugated paperboard is commonly assumed to be, $\boldsymbol{B}$ is zero and no coupling of in-plane loads with bending moments and shear or twisting.

The constitutive relations for orthotropic materials reduced to the following (Jones, 1975):

$$\begin{Bmatrix} N_x \\ N_y \\ N_{xy} \end{Bmatrix} = \begin{bmatrix} A_{11} & A_{12} & 0 \\ A_{12} & A_{22} & 0 \\ 0 & 0 & A_{66} \end{bmatrix} \begin{Bmatrix} \varepsilon_x^0 \\ \varepsilon_y^0 \\ \varepsilon_{xy}^0 \end{Bmatrix}$$

Equation 1-2

$$\begin{Bmatrix} M_x \\ M_y \\ M_{xy} \end{Bmatrix} = \begin{bmatrix} D_{11}^* & D_{12}^* & 0 \\ D_{12}^* & D_{22}^* & 0 \\ 0 & 0 & D_{66}^* \end{bmatrix} \begin{Bmatrix} \kappa_x \\ \kappa_y \\ \kappa_{xy} \end{Bmatrix}$$

Equation 1-3

Corrugated paperboard may be considered as a thin plate, however Von Kármán plate assumptions and large deflection theory is used as in (Nordstrand, 2004a) because deflections can be greater than the plate thickness. Plane stress conditions are assumed and transverse shear and normal strains neglected.

The strains are given in terms of displacements from the reference surface *u*, *v,* and *w* in the *x*, *y*, *z* directions (Jones, 1975)

$$\varepsilon_x^0 = \frac{\partial u}{\partial x} + \frac{1}{2}\left(\frac{\partial w}{\partial x}\right)^2$$

$$\varepsilon_y^0 = \frac{\partial v}{\partial y} + \frac{1}{2}\left(\frac{\partial w}{\partial y}\right)^2$$

$$\varepsilon_{xy}^0 = \frac{\partial u}{\partial y} + \frac{\partial v}{\partial x} + \frac{\partial w}{\partial x}\frac{\partial w}{\partial y}$$

Equation 1-4

and curvatures given by (Jones, 1975)

$$\kappa_x = -\frac{\partial^2 w}{\partial x^2}$$

$$\kappa_x = -\frac{\partial^2 w}{\partial y^2}$$

$$\kappa_{xy} = -2\frac{\partial^2 w}{\partial x \partial y}$$

Equation 1-5

The solution of the plate buckling problem involves finding a deflection shape function which solves the governing differential equation static equilibrium equation of the plate under loading.

The static equilibrium equation of an imperfect orthotropic plate with in-plane loading in term of deflection w, initial imperfection w_0, and Airy's stress function F (Weaver, 2008):

$$D_{11}^{*}\frac{\partial^4(w-w_0)}{\partial x^4}+2(D_{12}^{*}+2D_{66}^{*})\frac{\partial^4(w-w_0)}{\partial x^2y^2}+D_{22}^{*}\frac{\partial^4(w-w_0)}{\partial y^4}$$
$$=\frac{\partial^2(w-w_0)}{\partial x^2}\frac{\partial^2F}{\partial y^2}+\frac{\partial^2(w-w_0)}{\partial y^2}\frac{\partial^2F}{\partial x^2}-2\frac{\partial^2(w-w_0)}{\partial x\partial y}\frac{\partial^2F}{\partial x\partial y}$$

Equation 1-6

The resultant loads are given by stress function derivatives (Weaver, 2008):

$$N_x=-\frac{\partial^2F}{\partial y^2},N_y=-\frac{\partial^2F}{\partial x^2},N_{xy}=\frac{\partial^2F}{\partial x\partial y}$$

Equation 1-7

Additionally for post-buckling problems, the compatibility condition between in-plane strains and out-of-plane displacement is satisfied.

$$\frac{\partial^2\varepsilon_x}{\partial y^2}-\frac{\partial^2\varepsilon_{xy}}{\partial x\partial y}+\frac{\partial^2\varepsilon_y}{\partial x^2}=\left(\frac{\partial^2w}{\partial x\,\partial y}\right)^2-\frac{\partial^2w}{\partial x^2}\frac{\partial^2w}{\partial y^2}-\left[\left(\frac{\partial^2w_o}{\partial x\,\partial y}\right)^2-\frac{\partial^2w_o}{\partial x^2}\frac{\partial^2w_o}{\partial y^2}\right]$$

Equation 1-8

The compatibility equation is rewritten in terms of the effective elastic material constants for corrugated paperboard below (Nordstrand, 2004a):

$$\frac{1}{h}\left(\frac{1}{E_{22}^{*}}\frac{\partial^4F}{\partial x^4}+\left(\frac{1}{G_{12}^{*}}-\frac{2v_{12}^{*}}{E_{11}^{*}}\right)\frac{\partial^4F}{\partial x^2\partial y^2}+\frac{1}{E_{11}^{*}}\frac{\partial^4F}{\partial y^4}\right)$$
$$=\left(\frac{\partial^2w}{\partial x\,\partial y}\right)^2-\frac{\partial^2w}{\partial x^2}\frac{\partial^2w}{\partial y^2}-\left[\left(\frac{\partial^2w_o}{\partial x\,\partial y}\right)^2-\frac{\partial^2w_o}{\partial x^2}\frac{\partial^2w_o}{\partial y^2}\right]$$

Equation 1-9

Solutions of buckling problems can be obtained by analytical methods and numerical methods. Among the numerical methods, the Finite Element Method is a common choice (Biancolini & Brutti, 2003; Daxner, Flatscher, & Rammerstorfer, 2007; Nordstrand, 1995; Pommier & Poustis, 1989). Examples of analytical methods include the semi-energy method (Marguerre, 1937; Nordstrand, 2004a; Rhodes & Harvey, 1977), approximate energy methods such as the Rayleigh-Ritz based on minimising strain energy with respect to displacements (Nyman & Gustafsson, 1999) or Galerkin's method which minimises error in the approximate solution of the equilibrium equation with respect to the deflection function coefficients (Ilanko, 2002).

The theoretical critical load solution for a corrugated paperboard panel of width *a* and length *b* with an in-plane loading intensity N_y is given by (Hahn, de Ruvo, Westerlind, & Carlsson, 1992):

$$N_{crit} = \pi^2 \left[\frac{b^2 D_{11}}{a^4} + \frac{2(D_{12} + 2D_{66})}{a^2} + \frac{D_{22}}{b^2} \right]$$

Equation 1-10

1.3.1.1 Failure Load

The failure or collapse load which is the maximum load sustained in compression. In the presence of initial imperfections that increase with loading, the collapse load is more easily obtained from tests than the critical load for plates. It has been reported that the collapse load is not sensitive to panel imperfection (Hahn, Carlsson, & Westerlind, 1992). This may be due to the fact that at very high loadings above the classical critical loads, the load-deflection curve is insensitive to initial imperfections. Failure in corrugated paperboard commonly occurs in the facings or core by material failure in compression when the material exceeds its elastic limit. Crushing in compression without buckling occurs if the material failure load is below the critical load. The crushing failure mode could be caused by localised buckling of the corrugated structure.

McKee's box collapse load model for corrugated paperboard treats a box as an assembly of panels with simply supported conditions (McKee et al., 1963). The McKee box compression strength *BCT* equation is given in terms of edge compression strength of corrugated paperboard *ECT*, flexural stiffness of corrugated paperboard in machine and cross directions D_{11} and D_{22}, box perimeter *Z*, and empirical constants k_1 and k_2 which are 2.028 and 0.746 respectively (McKee et al., 1963):

$$BCT = k_1 \, ECT^{k_2} \sqrt{D_{11} D_{22}}^{(1-k_2)} Z^{(2k_2-1)}$$

Equation 1-11

The empirical collapse load for uniformly compressed corrugated panel of width *a* is given by with two empirical parameters *c* and *d*, critical load per unit width N_{crit} and edge compression strength of the paperboard *ECT* (McKee et al., 1963)*:*

$$P_{collapse} = a\left[c {N_{crit}}^{(1-d)} ECT^{d}\right]$$

Equation 1-12

1.3.1.2 Failure criteria

The Tsai-Wu failure criterion for plane stress developed by Tsai & Wu (1971) is the most used criterion for determining material failure in facings of corrugated paperboard since it accounts for difference in material behaviour in tension and compression. Material failure occurs when the left side of the equation below exceeds one:

$$F_1\sigma_{11} + F_2\sigma_{22} + F_{11}{\sigma_{11}}^2 + F_{22}{\sigma_{22}}^2 + F_{66}{\tau_{12}}^2 + 2F_{12}\sigma_{11}\sigma_{22} = 1$$

Equation 1-13

Where $F_1 = \frac{1}{\sigma_{x,t}} + \frac{1}{\sigma_{x,c}}$, $F_2 = \frac{1}{\sigma_{y,t}} + \frac{1}{\sigma_{y,c}}$, $F_{11} = -\frac{1}{\sigma_{x,t}\,\sigma_{x,c}}$, $F_{22} = -\frac{1}{\sigma_{y,t}\,\sigma_{y,c}}$, $F_{66} = \frac{1}{T^2}$, for paper $F_{12} = f\sqrt{F_{11}F_{22}}$, $f = -0.36$, $T = \beta\sqrt{\sigma_{x,c}\,\sigma_{y,c}}$

$\sigma_{x,t}$ = Tensile strength in MD

$\sigma_{x,c}$ = Compressive strength in MD

$\sigma_{y,t}$= Tensile strength in CD

$\sigma_{y,c}$= Compressive strength in MD

T = Shear strength

β = constant relating compressive strengths in MD and CD to shear strength

In the work of (Beldie, Sandberg, & Sandberg, 2001; Haj-Ali, Choi, Wei, Popil, & Schaepe, 2009; Nyman & Gustafsson, 2000b) using the Tsai-Wu failure criteria for paperboard, the value of the shear strength constant in the equation above of $\beta = 0.78$ is used based on maximum strain theory. However, the shear strength definition for paper in the work of (Biancolini, Brutti, & Porziani, 2009b) uses an empirical relation between shear strength and compressive strengths in MD and CD where $\beta = 1$. Nyman & Gustafsson (2000b) used a combined analysis of failure stress in the collapse of corrugated paperboard cylinders, with failure criteria based on material and structural local buckling failure.

The Tsai-Wu criterion was used to determine whether the elastic limit was reached in box compression tests by Viguié et al. (2011; 2010) using Digital Image Stereocorrelation to study surface stress and strain fields on two box panels.

1.3.1.3 Buckling tests

Test fixtures for past studies on buckling in corrugated paperboard panels are aimed at reproducing the behaviour of a panel of a box (Hahn, Carlsson et al., 1992; Hahn, de Ruvo et al., 1992; Nordstrand, 2004a). The loading considered is uniform compression on the horizontal edges (Hahn, Carlsson et al., 1992; Hahn, de Ruvo et al., 1992; Nordstrand, 2004a). The horizontal loading edges of the panels are simply-supported, to correspond to the box's horizontal edge condition. Score lines and flaps in boxes lead to reduced bending stiffness along the folds and rotations are allowed (Peterson & Schimmelpfenning, 1982). The vertical edges are

also simply supported and are allowed free in-plane normal displacement (Hahn, Carlsson et al., 1992; Hahn, de Ruvo et al., 1992; Nordstrand, 2004a).

In the tests by Hahn, Carlsson et al. (1992) the test fixture has continuous slotted rollers on loading edges, and four discrete slotted rollers on unloaded edges. The single rollers were used to avoid stress concentration as with discrete junctions although a slightly larger critical may result (Hahn, Carlsson et al., 1992). Comparisons of a flat and grooved loading platen configuration showed the grooved configuration exhibited hysteresis in the loading and unloading cycle due to friction, and had a larger critical load and uncertainty in fitting into a non-linear post-buckling model. The crosshead speed loading rate was 10 mm/min and the out-of-plane displacement measurement was made at the panel centre with a digital displacement gauge.

The panel test fixture in Hahn, de Ruvo et al. (1992) was similar except cut-open ball bearings were used on the unloaded edges and initial imperfection amplitude w_0 was obtained from radius of curvature estimates from measurement of deflection w at five points along panel width at half the panel length.

The test fixture used by Allansson & Svärd (2001) has simply supported edges conditions with discrete slotted rollers on loaded edges, and knife edge supports on unloaded edges. The in-plane and out-of-plane displacements were measured by Digital speckle photography.

The test fixture used by Nordstrand (2004a) has sectioned slotted rollers supported by needle bearings and in grooves along the loaded edges, and knife edge supports on the unloaded edges. Displacements were measured at the panel centre with a displacement gauge.

The assumption that the edges of the panel are simply-supported may not accurately represent the behaviour of a whole box. This is because there could be some resistance to rotation at the corners of the box, which

needs to be quantified in experiments. In particular, the presence of rotational stiffness along the loaded edges of the panel would have a significant effect on its buckling and post-buckling behaviour.

1.3.1.4 Critical load determination

Theoretically, the critical load of a plate can be determined from the load-deflection plot of the perfectly flat plate, at the load where a sudden increase in the plate deflection occurs (refer to Figure 1-2). For plates with initial imperfection present, the critical buckling load is not obvious from the post-buckling load-deflection plot. This is because curvature in the post-buckling plot, due to the deflection increasing with applied load even below the critical load, makes it difficult to determine the value of the critical load.

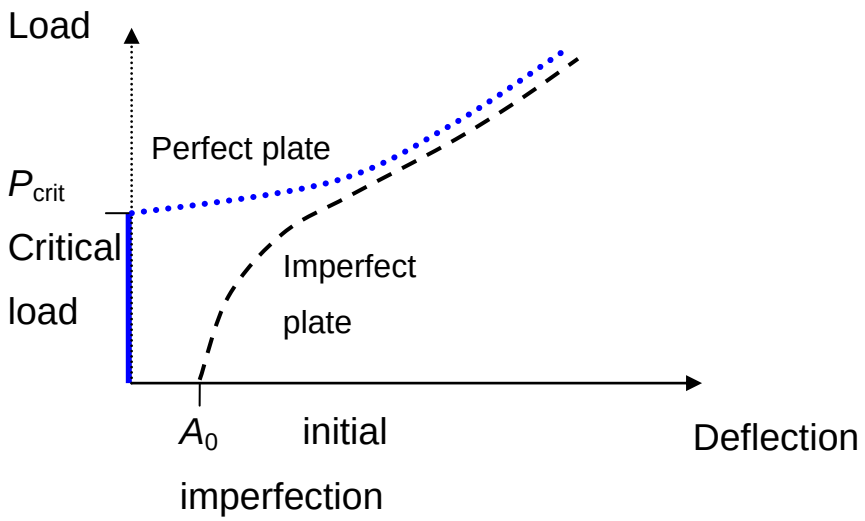

Figure 1-2: Post-buckling load-deflection plots for a perfectly flat plate and a plate with initial imperfection.

Several methods are in use for determining the critical load from buckling experiments on plates, where imperfections could be present.

The method proposed by Southwell (1932) for centrally loaded, simply-supported columns involves obtaining load *P* and mid-span displacement *d* at small deflections below the elastic limit and critical load P_{crit}. The *P*-*d* curve if approximated by a rectangular hyperbola, with asymptotes of the

axis of zero deflection and horizontal line through critical load, and passing through the origin, could be plotted as a straight line relationship of *d* / *P* plotted against *d*:

$$d/P = d/P_{crit} + d_o/P_{crit}$$

Equation 1-14

The slope of the equation above gives the inverse of P_{crit} and horizontal axis intercept can then be used to find the initial deflection d_0.

Limitations of the method are: the deflections must not be too large or very small nor exceed the elastic limit of the material; ratio *d*/*P* can be indeterminate if load and deflection are small; the method suits only elastic stability problems; the load-deflection curve must be a rectangular hyperbola; the deflection shape and imperfection is given by a Fourier series function and the first mode must be dominant in the deflection; no eccentricity in loading is allowed and rotations must be small.

Although the Southwell method has successfully been applied to flexural and lateral-torsional buckling of beams which are linear buckling analysis problems (Zirakian, 2010), the authors Hahn, Carlsson et al. (1992), Mandal & Calladine (2002), and Spencer & Walker (1975) consider the method to be inadequate for plates and shells. The reasons being lack of Southwell plot line straightness due to low-load and high load non-linearities and inestimable plate critical load at low loads because of stable post-buckling behaviour.

However, the portion of the Southwell plot between the regions non-linearity for plate buckling may possibly be used as a first estimate of critical load. The low-load non-linearity in the plot could be expected to introduce errors in determining initial imperfections. These ideas will be considered in the chapter on experimental work for buckling of a corrugated paperboard panel.

Alternative methods to the Southwell method proposed by Spencer & Walker (1975) are linearisation of the data and graphical and numerical approaches for small plate imperfection and changing boundary conditions

Post-buckling equations for plates with critical load, initial imperfection and a post-buckling parameter are also used in (Biancolini et al., 2009a; Hahn, Carlsson et al., 1992; Nordstrand, 2004a; Spencer & Walker, 1975). The Three Point and Least Square techniques for estimating the critical load and initial imperfection from post-buckling data are described in (Fok, 1984). A non-linear regression is used to fit data to the post-buckling equation in (Hahn, Carlsson et al., 1992; Nordstrand, 2004a).

1.3.2 Material Properties of Corrugated Paperboard

Paper is a planar network of wood cellulose fibres bonded together. The material behaviour of corrugated paperboard can be considered at the level of the corrugated paperboard structure as a whole and also the local behaviour of the paperboard layers. The materials testing methods that are used for corrugated paperboard and previous studies modelling corrugated paperboard material behaviour are presented.

1.3.2.1 Paperboard materials testing

The material behaviour of paperboard layers and corrugated paperboard at a macroscopic level is often treated as orthotropic because of the tendency of paper fibres to be aligned along the direction of manufacture the machine direction (MD). The cross direction (CD) is the planar direction perpendicular to MD. Hydrogen bonding between fibres is predominant in the cross-direction. The compressive behaviour of paperboard is of more concern as its stiffness and strength is less in compression than tension. Compression testing of paperboard and corrugated paperboard in the MD is not straightforward because of its tendency to buckle. Åslund & Isaksson (2010) suggest including the mechanism of fibre buckling when modelling macroscopic compressive behaviour of networks.

Allaoui, Aboura, & Benzeggagh (2009) studied the effect of relative humidity on mechanical properties of corrugated paperboard and its components. At 90% relative humidity (RH), Young's modulus of the components reduced up to 50% in CD compared to the 50% RH condition. The increase in moisture content in the material means the weakening of bonds between cellulose fibres, affecting the mechanical behaviour and failure load of the material significantly in the CD.

The following discussion is focused of materials testing methods of corrugated paperboard. The testing of paperboard layers is also crucial for detailed modelling of corrugated paperboard based on its geometry and constitution, but discussion on this will be limited.

Paperboard component testing

There are test standards for measuring in-plane properties of paperboard components to be used for facing and corrugated layers in tension and compression.

There are several methods for compression testing of paperboard components. The short span compression test (SCT) developed by the Swedish Pulp and Paper Research Institute and Lorentzen & Wettre (Markstrom, 2005) has advantages over other methods such as the Crush Linear Test (CLT), Ring Crush Test (RCT), and Corrugated Crush Test (CCT). These test methods are shown in Figure 1-3. The SCT sample is a paper strip compressed between clamps with a short free length and low slenderness ratio that prevents buckling.

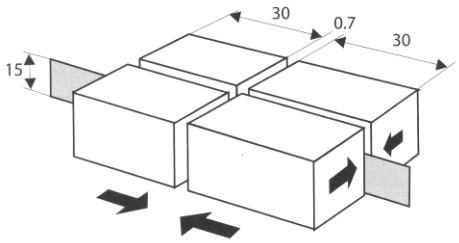

(a) Short span compression test (SCT)

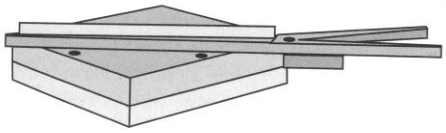

(b) Crush Linear Test (CLT)

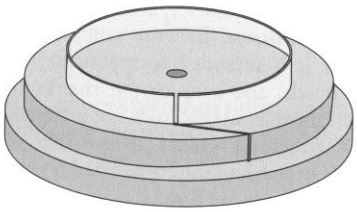

(c) Ring Crush Test (RCT)

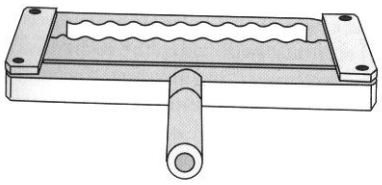

(d) Corrugated Crush Test (CCT)

Figure 1-3: Compression test methods for paperboard (Markstrom, 2005, p.32, 33).

The experimental characterisation of paper by Biancolini, Brutti, & Porziani (2009b) specifies five elastic constants: Young's modulus in MD E_{11} and CD E_{22}, shear modulus G_{12}, and Poisson's ratios v_{12} and v_{21}; and five strength constants: tensile and compressive strength in MD and CD and shear strength. Biancolini et al. (2009b) obtained the Young's modulus from tensile tests in MD, CD and computed shear modulus and Poisson's ratios from the Young's modulus of the MD, CD and 45°-direction tensile tests:

$$G_{12} = \left(\frac{2\,\nu_{12}}{E_{11}} - \frac{1}{E_{11}} - \frac{1}{E_{22}} + \frac{4}{E_{45°}}\right)^{-1}$$

Equation 1-15

$$\nu_{12} = 0.293\sqrt{E_{22}/E_{11}}$$

Equation 1-16

$$\nu_{21} = \nu_{12}\,E_{22}/E_{11}$$

Equation 1-17

Biancolini et al. (2009b) obtained tensile strengths in MD $\sigma_{11,\,t}$ and in CD $\sigma_{22,\,t}$ from the ultimate stress from tensile MD and CD tests, while SCT and

RCT tests were used to obtain compression strengths in MD $\sigma_{11,\,c}$ and CD $\sigma_{22,\,c}$ respectively. The shear strength was computed by an empirical relation (Biancolini et al., 2009b):

$$\tau_{12} = \sqrt{\sigma_{11,c}\,\sigma_{22,c}}$$

Equation 1-18

Alternative testing devices have been developed to overcome the tendency for buckling in compression testing of paperboard such as the Vacuum Compression Apparatus (VCA) designed by Forest Products Laboratory (FPL) of the US Department of Agriculture and built by Isthmus Engineering of Madison, Wisconsin (refer to Figure 1-4). The air-conditioned apparatus allows samples to be laterally supported under vacuum on a spaced grid of slender, vertical, square rods ends held in a flexible elastomer on a rigid base. Stress and strain measurements can be made in tension and compression, as well as dimensional stability and creep performance measurements at varying relative humidity.

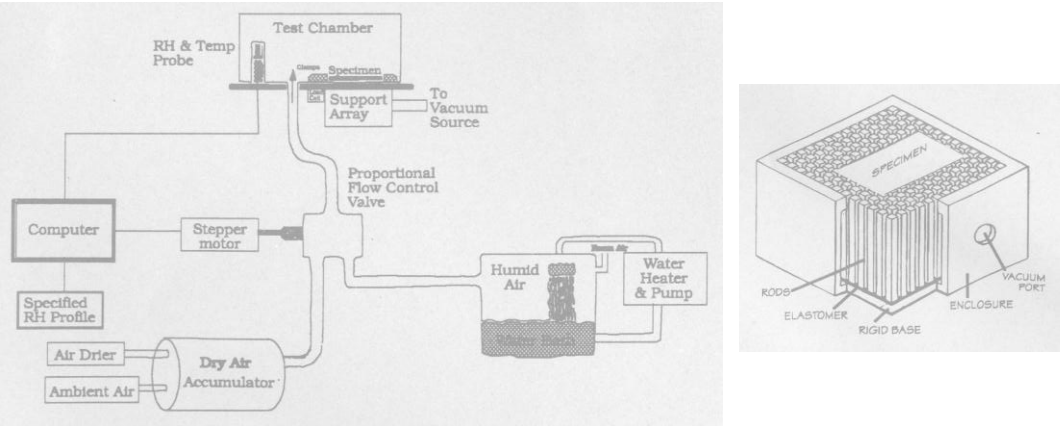

(a) VCA testing system

(b) VCA specimen support

Figure 1-4: Vacuum Compression Apparatus VCA 1000 (Chalmers).

The VCA test method was used to measure the in-plane material properties of paperboard components of the corrugated paperboard materials used in this study, which were reported in (Ilmonen, 2007).

Corrugated paperboard testing

For consideration of buckling performance of corrugated paperboard, the in-plane strength and stiffness as well as bending and flexural rigidities are important. There are test standards for corrugated paperboard in edge compression in CD and bending in MD and CD. Alternative methods for obtaining shear and twisting stiffness and Poisson's ratios such as the anti-clastic twist and sonic vibration tests are also presented in the following section.

Edge compression tests

Short column edge compression tests on corrugated paperboard are carried out in CD. Several edge compression standards exist with different specimen shapes (refer to Figure 1-5). The specimens are short to reduce the likelihood of failure by buckling. To reduce stress concentration at loaded edges and prevent edge failure, some standards specify a smaller cross-section at mid length of the specimen such as in the FPL circular router-necked-down method proposed in (Koning, 1986); while the Technical Association of Pulp and Paper Industry (TAPPI) standard T-811 has the loaded edges dipped in molten paraffin wax for reinforcement. The paraffin wax reinforced specimens are reconditioned after waxing which is considered time consuming and laborious by Koning (1986).

The TAPPI edge compression test was used to obtain elastic stiffness in CD of the corrugated paperboard materials in this study.

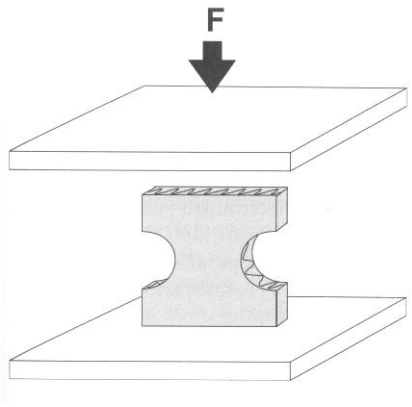

(a) Edge compression test

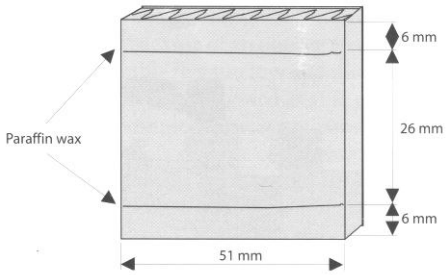

(b) Edge compression test specimen according to TAPPI method

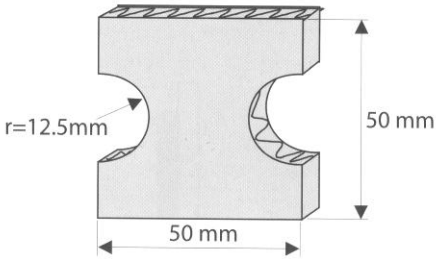

(c) Necked-down edge compression test specimen according to FPL method

Figure 1-5: Edge compression test method for corrugated paperboard (Markstrom, 2005, p. 17, 19, 21).

Bending tests

The flexural stiffness of corrugated paperboard can be obtained by several loading methods including two-, three- and four-point bending summarised in (Fellers & Carlsson, 2002). The four-point bending method has the advantage of giving bending stiffness results that are independent of the specimen bending span length because of the uniform bending moment and absence of shear forces in the central portion of the specimen (refer to Figure 1-6) (Steadman, 2002). Pommier & Poustis (1989) used bending stiffness D_{11} and D_{22} from four-point bending test in Finite Element box models to predict box compression strength.

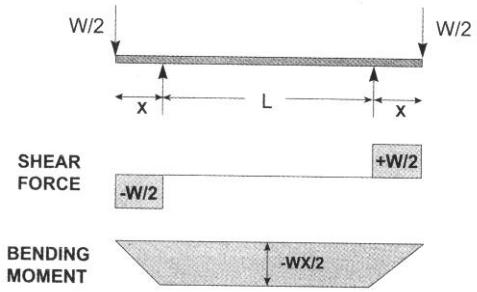

(a) Shear force and bending moment diagrams for four-point bending test

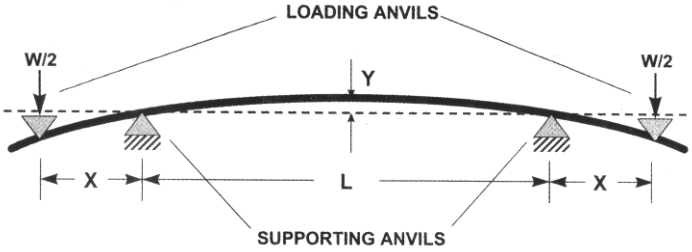

(b) Four-point beam loading method to obtain bending stiffness according to TAPPI T 820

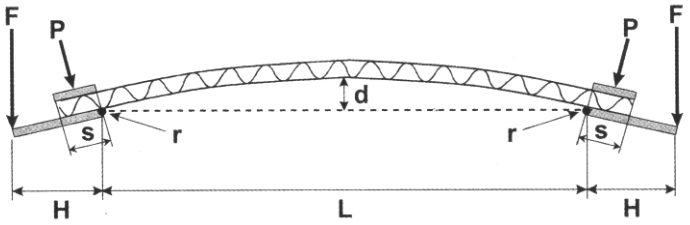

(c) Four-point beam loading method to obtain bending stiffness according to TAPPI T 836

Figure 1-6: Four-point bending test (Mark, Borch, & Habeger, 2001, p.627, 629).

The TAPPI standard T-820, a four-point bending method with the specimen supported by a pair of anvils, loaded by a nested second pair of anvils and deflection measured at midspan, was used to obtain bending stiffness of in MD and CD for the corrugated paperboard materials in this study. An estimate of the in-plane stiffness of the corrugated paperboard was also calculated from the bending stiffness results using orthotropic plate theory. A more advanced method of measuring four-point bending stiffness is described in the TAPPI standard T-836 where the specimen clamped at its ends and bent by rotating the clamps.

Anti-clastic test

The flexural stiffnesses D_{12} and D_{66} for corrugated paperboard can be obtained by the anti-clastic test developed by Pommier & Poustis (1989) (refer to Figure 1-7(a)), where a square plate is loaded at a pair of diagonally opposite corners and simply-supported at the other corners. The method is also used in (Carlsson, Nordstrand, & Westerlind, 2001) to obtain twisting stiffness D_{66}.

Block shear test

The shear loading of corrugated paperboard can also be conducted by the block shear test (refer to Figure 1-7(b)), where the face sheets are bonded to rigid metal platens and loaded in shear (Carlsson et al., 2001). Single- or double-lap shear tests by (Lu & Zhu, 2001) were used to measure transverse shear moduli G_{23} and G_{13}. Carlsson et al. (2001) compares the single-lap block shear and three-point bending test for obtaining shear stiffnesses and notes the deformation of face sheets is much restricted by the adhesion in the block shear test. According to the experiments by Nordstrand & Carlsson (1997), three-point bending gives transverse shear moduli that is lower by a factor of two, though more realistic, compared to block shear tests, attributed to deformation of facings and denting at supports.

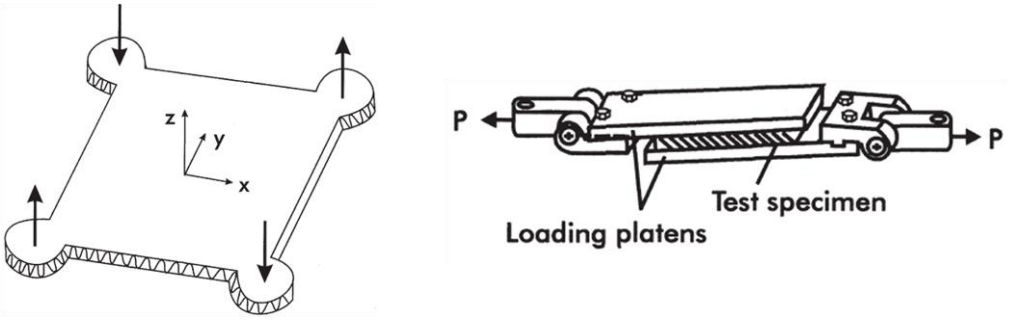

(a) Anti-clastic test (b) Block shear test

Figure 1-7: Anti-clastic and block shear tests (Carlsson et al., 2001, p. 260, 261).

Ultrasonic method

The use of the ultrasonic method for predicting the edge compression strength of corrugated paperboard was described in (Sandstrom & Titus, 1995). The velocity of an ultrasonic pulse and a constant from Poisson's ratio of the material is used to calculate a tensile stiffness index (TSI) in MD and CD (Sandstrom & Titus, 1995). The correlation of paperboard components' TSI with compression strength from RCT, SCT and CCT methods and bending stiffness of corrugated paperboard was found but requires extensive testing for correlation (Sandstrom & Titus, 1995). A cross machine profile of the compression strength along CD is possible with the ultrasonic method and useful for process control and manufacturing optimisation such as pulp refining levels, line pressure and drying (Sandstrom & Titus, 1995).

According to McIntyre & Woodhouse (1988), disadvantages in using the ultrasonics tests are that it is difficult to achieve strong transmission of ultrasound for some materials and the microstructure of composite materials could disperse sound waves with short wavelengths of the order used in ultrasonic tests.

Sonic vibration tests

Low frequency sonic vibration tests developed by McIntyre & Woodhouse (1988) can be performed to estimate the elastic properties of orthotropic plates from free-boundary condition vibration modes. The plate samples are supported by soft foam blocks along nodal points to preserve the free boundary condition. A powder or small particles such as tea leaves can be used to show nodal lines of the vibration modes. The lowest frequencies corresponding to modes for twisting and bending in MD and CD and the mass and geometry of the sample are input into a vibration model to obtain elastic constants such as the in-plane elastic and shear modulus, flexural stiffnesses and Poisson's ratios.

The sonic vibration method described in (Sato, Hutchings, & Woodhouse, 2008) was used to obtain elastic properties of the corrugated paperboard materials in the study from frequencies of free boundary condition vibration modes.

Lu & Zhu (2001) obtained elastic properties of corrugated paperboard from sonic vibration tests as well as lateral compression, three-point bending and shear tests and Finite Element predictions. Sato et al. (2008) compared elastic moduli of corrugated paperboard in MD and CD from sonic vibration, tensile and ultrasonic tests. The sonic vibration method gives MD elastic moduli values that are higher than the static tensile tests but are lower than the ultrasonic test (Sato et al., 2008). The CD elastic moduli of the sonic vibration and ultrasonic tests are more similar and higher than the static tensile test (Sato et al., 2008).

There are difficulties in relating static tests to vibration properties due to creep behaviour in a polymeric material such as paper (McIntyre & Woodhouse, 1988). Paper exhibits viscoelastic behaviour hence elastic properties are frequency dependent (Sato et al., 2008). Stress relaxation is prevented at higher frequencies thus a higher elastic modulus is apparent (Sato et al., 2008). The frequency dependence of the elastic modulus is more pronounced along CD because of amorphous polymeric behaviour in deforming links between paper fibres (Sato et al., 2008).

1.3.2.2 Theoretical material models of corrugated paperboard

The material models that are available for modelling corrugated paperboard are discussed in this section. There are approximate models which consider the composite structure as an equivalent plate or a layered sandwich with an equivalent solid core. More complex modelling approaches include unit cell analytical or Finite Element homogenisation model approaches to define effective material constants; and detailed geometric models in analytical or Finite Element models.

Equivalent plate model

The manufacturing of paper and corrugated paperboard results in material orientations that allow equivalent orthotropic models to be used to approximate its material properties. The method of elastic equivalence simplifies modelling of a sandwich plate structure by replacing it with an equivalent orthotropic plate of constant thickness with the same stiffness properties (Luo, Suhling, Considine, & Laufenberg, 1992). Analytical solutions then use orthotropic plate theory such as von Karman's large deflection theory to obtain out-of-plane displacements in the buckling of plates.

The equivalent plate model is a convenient and less computationally intensive approach compared to alternative models accounting for detailed geometry of the sandwich structure. Luo et al. (1992) summarise some provisions for its use for sandwich plates such as a small ratio of the plate dimensions to the sandwich's periodic structure, uniform distribution of rigidities and their independence of load and boundary conditions, and perfect bonding between the structure's constituents.

According to Daxner, Pahr, & Rammerstorfer (2008) material models of corrugated paperboard which have effective stiffness from shell theory should be limited to global buckling and post-buckling prediction and cannot account for material nonlinearity, local buckling and failure mechanisms. Discontinuity in the sandwich structure means that actual stresses are not comparable with those from the equivalent plate model (Luo et al., 1992).

The equivalent lamina model in (Hahn, Carlsson et al., 1992) treats corrugated paperboard as an effective homogeneous orthotropic plate but bending stiffness is specified independent of effective in-plane elastic modulus. The bending stiffnesses in MD, D_{11} and in CD, D_{22} are measured from four-point bending tests on corrugated paperboard. The elastic modulus in CD, E_{22} was obtained from short column compression tests on corrugated paperboard. The tests were conducted at a cross head speed

of 10 mm/min. The in-plane Poisson's ratios v_{12} and v_{21} and shear modulus G_{12} for paper are calculated from the measured in-plane moduli of paper E_{11} and E_{22}, and the bending stiffnesses D_{12} and D_{66} for corrugated paperboard are calculated using the measured bending stiffnesses D_{11} and D_{22} in (Hahn, Carlsson et al., 1992) using orthotropic plate theory and empirical relations from (Baum, Brennan, & Habeger, 1981):

$$(\nu_{12}\,\nu_{21})^{\frac{1}{2}} \approx 0.293$$

$$G_{12} \approx 0.387\sqrt{E_{11}\,E_{22}}$$

$$D_{12} \approx 0.293\sqrt{D_{11}\,D_{22}}$$

$$D_{66} \approx 0.354\sqrt{D_{11}\,D_{22}}$$

Equation 1-19

The MD elastic modulus was not measured and was not used in the calculation of the buckling load of a corrugated paperboard panel in (Hahn, Carlsson et al., 1992). Only the bending stiffnesses D_{11}, D_{22}, D_{12} and D_{66} and the panel width *a* and height *b* are used to calculate the critical buckling load of the panel treated as an effective homogeneous orthotropic plate.

Classical laminate plate theory is often used in analytical calculations of equivalent properties of the corrugated paperboard using material data and geometry of its constituent layers as in (Carlsson et al., 2001; Nordstrand, 2004a). The transverse shear is not included in the material model in (Nordstrand, 2004a).

The material modelling approach used by Carlsson et al.(2001) and Nordstrand (2004a) are applied to the analytical corrugated paperboard panel models in the current study.

The formulae for the equivalent elastic moduli along MD E^*_{11} and CD E^*_{22}, the in-plane shear modulus G^*_{12} and Poisson's ratio v^*_{12} from (Nordstrand,

2004a) are presented in chapter 2, equations 2-1 to 2-5. The formulae use the corrugated paperboard geometry, take-up factor of the corrugated core α and thicknesses of the facings and core and the in-plane elastic moduli and Poisson's ratio of the facings and core.

The flexural stiffness D_{11}, D_{12}, D_{22}, D_{66} in (Nordstrand, 2004a) are calculated using the material properties of the facings and core layers using the approach in (Carlsson et al., 2001). The formulae for bending stiffnesses from (Carlsson et al., 2001) are presented in chapter 4, equations 4-3 to 4-6.

Bending stiffness

The "bending stiffness" (also referred to as flexural rigidity) of a beam is experimentally given by the ratio of the applied bending moment divided by the curvature and specimen width, and is dependent on the elastic modulus *E* and second moment of area *I* of the section. For orthotropic plates, the in-plane Poisson's ratios v_{12} and v_{21} also influence the bending stiffness. The bending stiffnesses (plate rigidity terms) of an orthotropic plate is given by Luo et al. (1992):

$$D_{11} = \frac{E_{11} I_{yy}}{1 - \nu_{12}\nu_{21}}$$

$$D_{22} = \frac{E_{22} I_{xx}}{1 - \nu_{12}\nu_{21}}$$

$$D_{12} = \nu_{21} D_{11} = \nu_{12} D_{22}$$

$$D_{66} = G_{12} I$$

Equation 1-20

where second moment of area I about MD I_{xx} and CD axes I_{yy},

$I = I_{xx} = I_{yy} = \frac{h^3}{12}$ for a single layered plate of unit width and thickness *h*.

The bending stiffness of corrugated paperboard is given by the sum of the contributions of the facings and medium. The bending stiffness of

corrugated paperboard is mainly due to overall board thickness and the properties of facings but the corrugated medium also has an influence. For the corrugated paperboard medium, $I_{xx} \neq I_{yy}$ as the cross-section is discontinuous and the moment of inertia is not easily defined in MD. Therefore, there could be more than one solution for the last two equations in Equation 1-20. Luo et al. (1992) suggests finding an average solution from the two possible solutions for the torsional rigidities D_{12}, and D_{66}.

Several models for determining the bending stiffness of corrugated paperboard have been developed. Luo et al. (1992) compared analytical bending stiffness models for corrugated paperboard, with the corrugated profile represented by different shapes. The equations for bending stiffness D_{11}, D_{22}, D_{12}, and D_{66} for an equivalent plate representing corrugated paperboard in (Luo et al., 1992) use the geometry and material properties of the paperboard components as input. The methods considered for representing the shape of the corrugated medium were sinusoidal, arc-and-tangent and semi elliptical models (Luo et al., 1992). The approximate sinusoidal model was the simplest and fairly accurate for obtaining the second moment of area of the medium.

Peterson (1980, 1983) considered the contribution of the corrugated medium to bending stiffness of corrugated paperboard in MD and CD, with the medium approximated as a sinusoidal shape. Peterson (1980) used numerical integration to obtain the second moment of area of the medium in CD, and defined the second moment of area per unit width of the medium in MD as $t_m^3/12$, where t_m is the thickness of the medium.

Urbanik (2001) developed a model of corrugated paperboard with fluting geometry considered as connected curved arc and tangent straight sections to obtain edge compression strength and bending stiffness.

Urbanik (2001) also predicted average stress-strain properties of component materials from corrugated paperboard edge compression

strength and bending stiffness. Then, Urbanik (2001) set out a method to optimise flute profile by predicting change in performance in modifying non-dimensional parameters that define the flute geometry.

The relations between in-plane and bending stiffness of corrugated paperboard do not conform to the orthotropic plate theory with the bending stiffness being higher than what the in-plane stiffness would suggest.

However, the absence of other methods to measure the in-plane stiffness of corrugated paperboard in MD has led the author to consider estimating the in-plane stiffness from the bending stiffness result. The in-plane stiffness values obtained are compared with values from other means such as calculations based on the properties of paperboard components.

Layered sandwich model

The equivalent plate models from the previous section replaced the whole sandwich structure with an equivalent single layer model. A layered sandwich model only replaces the core structure with an effective core layer distinct from the facings. A layered sandwich was used to simplify the material model of corrugated paperboard in the study by Nordstrand (1995) of the post-buckling strength of structural core sandwich panels. The facings and core are treated as layers in a sandwich structure and effective properties of the core are defined.

The effective core in-plane moduli in MD $E^*_{11,c}$ and in CD $E^*_{22,c}$ are approximated below (Carlsson et al., 2001; Nordstrand, 1995):

$$E^*_{11,c} \approx 0$$

$$E^*_{22,c} = \alpha S_{2,c}/h_c = \alpha E_{22,c} t_c/h_c$$

Equation 1-21

Where α = take-up factor, $S_{2,c}$ = tensile stiffness of the core material in CD, h_c= core height, $E_{22,c}$ = elastic modulus of the core material in CD, t_c = thickness of the core material (refer to Figure 1-8).

The effective Poisson's ratio $\nu_{12,c}^{*}$ and in-plane shear modulus $G_{12,c}^{*}$ of the core are approximately zero (Carlsson et al., 2001), but are given small values as in (Nordstrand, 1995; Paetow & Göttsching, 1990).

The effective transverse shear moduli of the core can be calculated from transverse shear stiffness measurements on the corrugated paperboard.

Nordstrand, Carlsson, & Allen (1994) proposed an analytical method to evaluate the effective transverse shear stiffness of sandwich plates with core structures, which was used along with three-point bending and block shear experiments and geometric Finite Element models in (Nordstrand & Carlsson, 1997).

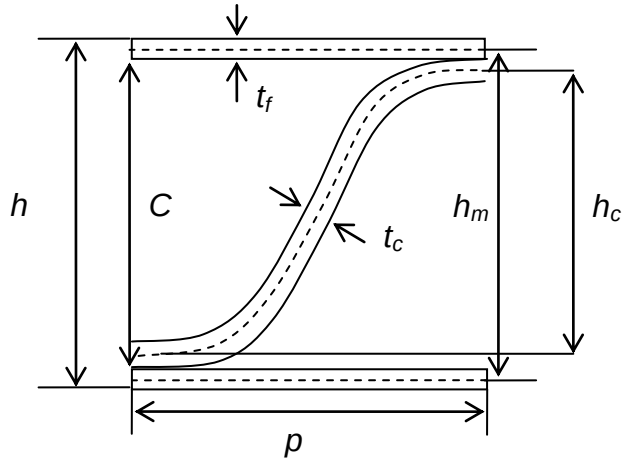

Figure 1-8: A half wavelength profile of a corrugated core sandwich

The effective transverse shear moduli of the corrugated core $G_{i3,c}^{*}$ is given by Nordstrand & Carlsson (1997):

$$G_{i3,c}^{*} = \frac{c}{h} G_{i3,a}\,, \qquad i = 1,2$$

Equation 1-22

Where $G_{i3,\,a}$ = Average transverse shear moduli of the sandwich structure, c = corrugated core height, h = total sandwich thickness (refer to Figure 1-8).

The transverse shear modulus of the sandwich structure $G_{23,\,a}$ is given by Nordstrand et al. (1994) assuming deformation of the core only:

$$G_{23,a} = \frac{h_m\, t_c}{pS} G_{12,c}$$

Equation 1-23

Where h_m = distance between facing mid-planes, p = half of the corrugation wavelength, S = arc length of the centre line of half a corrugation wave between crest and trough, $G_{12,\ c}$ = in-plane shear modulus of the corrugated layer (refer to Figure 1-8).

The expression for transverse shear modulus $G_{13,\ a}$ of the sandwich structure is given below in terms of a dimensionless coefficient Γ that depends on core geometry and flexibility of the joint between the facing and core, and the elastic modulus of the core material $E_{11,\ c}$ (Nordstrand et al., 1994):

$$G_{13,a} = \Gamma E_{11,c}$$

Equation 1-24

For plates, the $E_{11,\ c}$ in the equation above is replaced by $E_{11,\ c}$ / (1- $v_{12,\ c}{}^2$), where $v_{12,\ c}$ is the Poisson's ratio of the core material.

The dimensionless shear modulus coefficients Γ for semicircular, trapezoidal, sinusoidal and triangular core shapes given by an analytical curved beam theory and Finite Element method are reported in (Carlsson et al., 2001; Nordstrand et al., 1994). The value of Γ = 0.00275 is reported for a sinusoidal core shape.

The properties of the facing layers are also defined in the layered sandwich model. The in-plane elastic moduli of the facings $E_{11,f}$ and $E_{22,f}$ and in-plane Poisson's ratio $\nu_{12,f}$ are measured, while the in-plane shear modulus is calculated by the empirical relation reported by Baum et al. (1981):

$$G_{12} \approx 0.387\sqrt{E_{11}\, E_{22}}$$

Equation 1-25

The definition of the transverse shear moduli and Poisson's ratio of the facings are less certain. The transverse Poisson's ratios are given the value of 0.01 as in (Paetow & Göttsching, 1990), while the transverse shear moduli G_{13} is defined as ten times smaller than G_{23} according to Nordstrand et al. (1994) and Nordstrand & Carlsson (1997).

Patel, Nordstrand, & Carlsson (1997a, 1997b) created Finite Element models of corrugated paperboard cylindrical columns under combined stress (axial compression and torque) to consider global buckling and failure of the cylinder, using layered shell elements with equivalent homogeneous properties given to core.

The simplified layered sandwich model with a solid core of effective stiffness equivalent to a corrugated core was also considered by Allansson & Svärd (2001) and Armentani, Caputo, & Esposito (2006) in addition to detailed geometry models used in their Finite Element models of corrugate paperboard buckling.

Armentani et al. (2006) modelled the paperboard layers as orthotropic, homogeneous, linear elastic with material properties estimated from in-plane properties of paper as in (Allansson & Svärd, 2001).

The in-plane elastic moduli E_{11} and E_{22} of the layers are measured and used in the calculation of the out-of-plane elastic modulus as in (Persson, 1991):

$$E_{33} = E_{11}/200,$$

Equation 1-26

and the shear moduli using the relations of (Baum et al., 1981; Mann, Baum, & Habeger, 1980):

$$G_{12} = 0.387\sqrt{E_{11}E_{22}}$$

$$G_{13} = E_{11}/55$$

$$G_{23} = E_{22}/35$$

Equation 1-27

Allansson & Svärd (2001) also used alternative values of the transverse shear moduli from (Nordstrand, 1995) and adjusted values to fit the load vs. out-of-plane displacement buckling data.

The solid core model of the corrugated core in (Armentani et al., 2006) were given material properties as in (Nordstrand, 1995). The solid core properties in (Allansson & Svärd, 2001) also follow Equation 1-21 from (Nordstrand, 1995). $E_{11,c}^{*}$ is set at a low value of 5 MPa and $G_{12,c}^{*}$ is set at 0.1% of $E_{22,c}^{*}$. The values of the transverse shear moduli, the out-of-plane elastic modulus and Poisson's ratios of the core are as in (Nordstrand, 1995).

Unit cell homogenisation models

Several homogenisation approaches for sandwich structures such as corrugated paperboards exist. The preceding two material models homogenised the corrugated paperboard structure into a single- or multi-layered equivalent orthotropic plate. The methods presented in this section use a unit cell of the periodic structure modelled analytically or with Finite Elements to determine material properties in the ***A***, ***B***, ***D*** * matrices of the constitutive equation of an anisotropic plate, shown in Equation 1-1.

The homogenisation approaches replace a sandwich structure that has periodic microstructure with a quasi-homogeneous material having constitutive equations and material properties that result in equivalent mechanical behaviour on a macroscopic scale (Hohe & Becker, 2002).

Hohe & Becker (2002) reviewed homogenisation schemes and material models which give effective stress-strain relations for sandwich structures with large-scale two-dimensional cellular cores. The approaches

presented use the concept of the representative volume element (RVE), where the constitutive model and material properties of a repeating structural cell are determined on a mesoscopic level. The conditions for mechanical equivalence are that the stress distribution and strain states are equivalent for a representative volume element and a volume element with an effective medium. Three homogenisation approaches were discussed in (Hohe & Becker, 2002). The approaches can be implemented analytically or numerically with Finite Element model.

Firstly, the most common approach described in (Hohe & Becker, 2002) termed the 'surface average based approach' involves the redistribution of stress components on external surfaces of the representative volume element. A constitutive equation for the effective medium is found, then both the RVE and volume element with the effective mediums are deformed by independent reference strain states. Traction vectors on the surfaces of the volume elements are found and the material properties of the effective medium chosen to satisfy equivalence conditions.

Secondly, the 'volume average based approach' given in (Hohe & Becker, 2002) uses the equivalence of average strain energy density for the representative and effective medium volume elements, and a volume integral for the strain equivalence condition. Similarly, a constitutive model for the effective medium is found and the volume elements are deformed by independent reference strain states satisfying the strain equivalence condition. The effective material properties are then chosen to satisfy average strain energy density equivalence for the volume elements. This approach is used for effectively non-orthotropic structures as it accounts for possible stress couples at structural intersections of the RVE leading to rotations which contribute to the total strain energy.

Thirdly, the 'two-scale expansion of mechanical fields' approach explained in (Hohe & Becker, 2002) is a mathematical homogenisation method involving power series expansion of the displacement and stress fields. Local spatial vectors for points in a RVE in a local coordinate system are

related with global spatial vectors by small quantity *e* in the order of the ratio of the characteristic length of periodic structure to the plate length. Displacement and stress fields are expanded into power series with respect to *e.* Strain and stress distributions also represented by power series because of the kinematic equation, are substituted in the linear elastic constitutive equation, resulting in an independent equation for each power of *e.* Effective displacements are linearly related to the displacement deviation by an unknown tensor and the relation used in a term of the constitutive equation power series expansion. A volume average integral of the constitutive equation power series term with respect to the RVE gives the effective elasticity tensor. As with the surface and volume average based approaches, independent reference strain states are applied to the RVE, and local strain distributions used to compute the unknown tensor and evaluate the effective elasticity tensor.

These homogenisation methods have not been used in the current study, but have been popular in recent studies modelling corrugated paperboard. Examples of homogenisation models used for corrugated sandwich structures are briefly highlighted.

A periodic numerical homogenisation method described in (Buannic, Cartraud, & Quesnel, 2003), based on the asymptotic expansion method, uses Finite Element modelling of a unit cell and accounts for transverse shear stiffness, with consideration given to several corrugated core sandwich shapes.

In the work of Biancolini & Brutti (2003), (Biancolini, Brutti, Mottola, & Porziani (2005) Biancolini et al. (2009a) and Biancolini, Brutti, & Porziani (2010) modelling buckling of corrugated paperboard packaging, an equivalent corrugated paperboard element is obtained from a numerical homogenisation approach detailed in (Biancolini, 2005), equating strain energies of Finite Element detailed and equivalent models. In (Biancolini & Brutti, 2003), virtual tests on FE models of corrugated paperboard with

detailed paperboard geometry, were used to determine equivalent in-plane and out-of-plane elastic constants.

The work of Abbès & Guo (2010), Aboura, Talbi, Allaoui, & Benzeggagh (2004) and Talbi, Batti, Ayad, & Guo (2009) uses an analytical homogenisation method for corrugated paperboard, involving numerical integration of local ***A***, ***B***, ***D*** matrices over a unit cell to obtain global ***A***, ***B***, ***D*** matrices of a homogeneous plate implemented in Finite Element models. The analytical point wise lamination approach on a unit cell of corrugated paperboard in (Aboura et al., 2004) was validated with tensile, shear and three-point bending tests. The analytical homogenisation method in (Talbi et al., 2009) includes transverse shear and torsion behaviour. Abbès & Guo (2010) developed an analytical homogenisation model for torsion of orthotropic sandwich plates, where plate torsion is decomposed into two beam torsion problems with rigidities calculated analytically or numerically.

In a homogenisation model by Isaksson, Krusper, & Gradin (2007), corrugated paperboard is divided into thin virtual layers with unique effective elastic moduli that are assembled for analysis of the corrugated paperboard as a continuous structure with equivalent mechanical properties. Shear correction factors, found from equilibrium of stress fields, to account for through thickness variation of transverse shear strain for corrugated paperboard, was shown to improve modelling of corrugated paperboard plate bending behaviour (Isaksson et al., 2007).

The work of Daxner et al. (2007) and Daxner et al., 2007; Flatscher, Daxner, Pahr, & Rammerstorfer (2011) optimising corrugated paperboard design under local and global buckling constraints uses the homogenisation method explained in *(Pahr & Rammerstorfer, 2006).* Effective mechanical behaviour of corrugated paperboard are predicted using a geometrically representative unit cell in Finite Elements having periodicity boundary conditions, applied with six unit load cases: two in-plane compression loads, one of in-plane shear, two of bending moments, and one of twist. Forces, moments, displacement and curvature at master

nodes of the unit cell, obtained from FE results, are related to resultant forces and moments, and reference surface strains and curvatures, with a generalised periodicity tensor in the effective constitutive law, used to compute homogenised ***A***, ***B***, ***D*** stiffness matrices.

Detailed geometric models

The previously discussed homogenisation models are alternatives to modelling sandwich structures with geometric details. However, detailed geometric models of sandwich structures typically in Finite Elements are often used to benchmark the validity of homogenised models and compared with experimental results such as in (Aboura et al., 2004; Allansson & Svärd, 2001; Armentani et al., 2006; Biancolini & Brutti, 2003; Biancolini et al., 2005; Biancolini et al., 2009a, 2010; Lu, Chen, & Zhu, 2001; Nordstrand & Carlsson, 1997; Pommier & Poustis, 1990).

There could be some variations in the Finite Element geometric models of corrugated paperboard such as the types of elements used, modelling details of the facing and core interface and approximations of the corrugation geometry. The material properties of the facings and core materials are defined separately.

In the Finite Element detailed geometric shell models of corrugated paperboard in three-point bending by Nordstrand & Carlsson (1997), the core and facings were separated by a distance of half the thickness of the facing and the core, and constraint equations applied to rigidly connect degrees of freedom of nodes at the core and facing interface.

Detailed Finite Element shell models of corrugated paperboard in four-point bending, pure twisting and edge compression were used to obtain material behaviour and correlated with analogous experiments in (Gilchrist, Suhling, & Urbanik, 1999). Four-node quadrilateral shear flexible shell (S4R5) elements allowing for transverse shear were used. The facing and core interface was modelled as perfectly bonded glue lines by node

sharing and by beam-like multi-point constraint connections. The models allowed for geometric and elastic-plastic material non-linearity.

Allansson & Svärd (2001) used a detailed Finite Element shell model in addition to simplified layered model of corrugated paperboard for panel buckling analyses. The shape of the corrugation profile used was a slightly modified sine function with point contact between facings and the core, without offsetting the middle surfaces of the interfacing elements.

The Finite Element buckling analyses on edge compressed corrugated paperboard panels by Rahman & Abubakr (2004) considering the role of the adhesive the properties on failure, used shell elements for the facings core and three-layered shell elements along the glue lines.

Popil, Schaepe, Haj-Ali, Wei, & Choi (2006) also created non-linear Finite Element models of corrugated paperboard in edge compression tests with an adhesive layer and fused but hinged elements at facing and core interfaces to consider the effect on compression strength.

Haj-Ali, Choi, Wei, Popil, & Schaepe (2009) modelled the edge compression test of corrugated paperboards by detailed Finite Element models with 8-node reduced integration quadratic shell (S8R) element and non-linear material properties given to the facings and core. A sine function was used to approximate the core profile with full bonding at facing and core interfaces.

In the detailed Finite Element model of corrugated paperboard panels and boxes in buckling by Biancolini et al. (2010), the corrugation shape is modelled accurately by dividing a single wavelength into eight segments and connecting the facings and core by rigid elements.

These edge compression test models in (Haj-Ali et al., 2009) allow for failure of the paperboard layers though not of the bonding between the core and the facings of the corrugated paperboard. The FE simulations from (Haj-Ali et al., 2009) show failure regions occur between flutings and along the joints between the core and the facing. Imperfect bonding at the

core-facing interfaces caused by defects in manufacturing such as intermittent glue application or glue line skip would have the effect of reducing its bending stiffness and compression strength (Schaepe, 2000).

The computational cost in using detailed geometric Finite Element models is however a reason for the preference of homogenisation methods in modelling corrugated paperboard over detailed geometry models. Detailed geometric Finite Elements models of materials testing on corrugated paperboard have been used for comparison with experimental results in the current study.

1.3.3 Analytical Models - Buckling Panel

1.3.3.1 Analytical methods

The analytical techniques that have been used for modelling buckling and post-buckling problems of plate and shells made of corrugated paperboard and for isotropic materials are presented below. The analytical techniques discussed include the semi-energy, the Rayleigh-Ritz, the Galerkin's and the exact strip methods.

Semi-energy method

The semi-energy method developed by Marguerre (1937, 1947) for post-buckling of a simply-supported isotropic plate in compression uses the von Kármán compatibility condition between in-plane strains and therefore in-plane stress with the out-of-plane deflection. The method uses an Airy stress function in the definition of the in-plane stress and the total potential energy of the plate which is minimised to obtain the magnitude of coefficients in the deflection function. The semi-energy method has been used for post-buckling models of mild steel plates (Rhodes, Harvey, & Fok, 1975), thin-walled beam sections (Rhodes & Harvey, 1975), composite panels (Banks, Harvey, & Rhodes, 1978), and corrugated paperboard panels (Nordstrand, 2004a).

The post-buckling model for a corrugated paperboard panel with geometric imperfection in (Nordstrand, 2004a) uses effective homogenised properties of the corrugated core. The deflection shape function used in (Nordstrand, 2004a) is a one-term cosine function along the loading direction and a polynomial along the unloaded direction. A 15-20% difference between experimentally estimated and analytically predicted buckling loads was reported and attributed to transverse shear deformation. The difference in the analytical and experimental load-displacement curves was claimed to be a result of non-linear high stress paper behaviour and local buckling of the facings. The cause of differences between predicted and experimental results deserves further investigation.

Energy method

The Rayleigh-Ritz approximate energy method for the solution of eigenvalue problems, such as the buckling of plates, uses the principle of minimisation of total potential energy due to strain energy of the plate and potential energy of loads. The critical stress is approximated by choosing the form of the deflection function *w.* The potential energy is minimised with respect to unknown coefficients of the plate deflection function.

The Rayleigh-Ritz method is used by Nyman & Gustafsson (1999, 2000a) for modelling local buckling of corrugated paperboard facings under combinations of in-plane loading. In (Nyman & Gustafsson, 1999) the corrugated paperboard facings between corrugation glue lines are modelled as infinite orthotropic plates on parallel simple supports with applied in-plane stress. Transverse shear strain is considered by a higher order analytical shape function using Reddy shear deformation theory. Accounting for transverse shear deformation reduces the buckling coefficient for the uniaxial and in-plane shear load cases but increases it for the pure bending cases.

Equilibrium method

The Galerkin's method is an approximate method for the solution of eigenvalue and boundary value problems which uses the governing partial differential equation for equilibrium. The von Kármán compatibility condition between in-plane strains and stresses and deflection is also met in the solution of the problem. Appropriate boundary conditions are applied to solve the equilibrium equation, determining the coefficients of the deflection function. An iterative scheme such as Newton-Raphson is used for solution of the system of non-linear equations given by the product of the equilibrium equation and a weighting function of the same form as the deflection function. The Galerkin's method is employed in the isotropic plate vibration and buckling models in (Hui & Leissa, 1983; Ilanko, 2002; Ilanko & Dickinson, 1991).

Exact strip method

The approximate analytical approach based on the exact strip method (DSM) and Wittrick-Williams algorithm (Williams & Wittrick, 1969; Wittrick, 1968; Wittrick & Williams, 1971, 1973) is suited for eigenvalue analysis of prismatic plate structures with longitudinally invariant loading. This method is the basis of the specialist software VICONOPT in FORTRAN 77 for eigenvalue analysis and design optimisation (Williams, Kennedy, Butler, & Anderson, 1991).

The use of analytical solutions of the governing differential equations results in a transcendental eigenvalue problem where the structure's stiffness matrix consists of transcendental non-linear functions of the load factor or frequency. The Wittrick-Williams algorithm is used to solve the eigenvalue problem with iterations using trial eigenvalues and calculating the number of eigenvalues exceeded between zero and the trial value. Exact solutions for isotropic and orthotropic plates with simply supported ends and without shear loading are obtained by the approach, assuming end conditions of the structure are such that modes vary sinusoidally along the longitudinal direction. For cases of shear loading and anisotropic

plates, Lagrangian multipliers are used in minimising the total energy of the panel to approximate panel end conditions.

The approach has been applied to aerospace and lightweight repetitive structures. Recent developments in the method include local post-buckling analysis and design optimisation for post-buckling (Kennedy, Fischer, & Featherston, 2007). The method has potential to be used for analysis of corrugated paperboard and some buckling results obtained using VICONOPT for panels used in this study are used for comparison. However, the detailed analysis done by the author does not include this approach.

1.3.3.2 Effect of in-plane boundary conditions on post-buckling

One of the potential sources of discrepancy in the model and experimental results of Nordstrand (2004a) is the panels' in-plane boundary conditions. The buckling experiment and semi-energy analytical model by Nordstrand (2004a), involved a simply supported corrugated paperboard panel, uniformly compressed along the loaded edges (Figure 1-9 (b)), with free in-plane normal movement along unloaded edges (Figure 1-9 (c)) and in-plane free tangential movement (shear free) along all four edges.

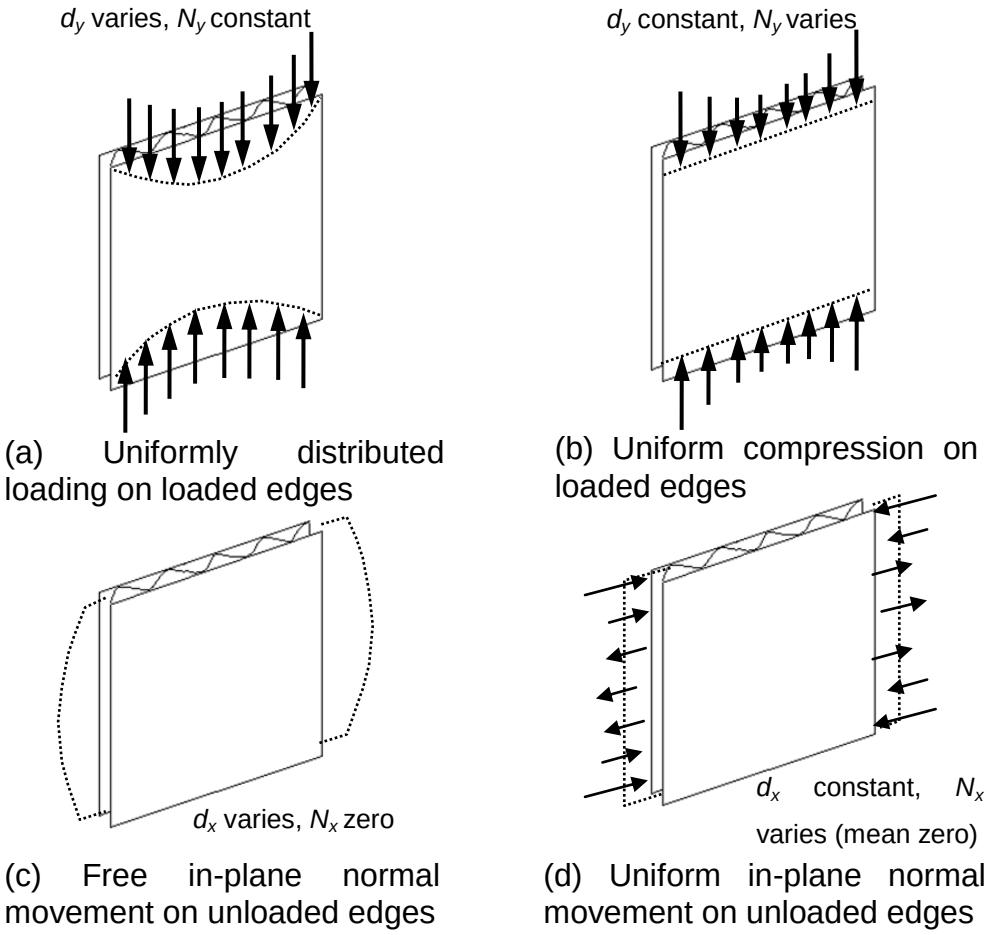

(a) Uniformly distributed loading on loaded edges

(b) Uniform compression on loaded edges

(c) Free in-plane normal movement on unloaded edges

(d) Uniform in-plane normal movement on unloaded edges

Figure 1-9: Loading cases and in-plane boundary conditions of unloaded edges of a panel.

The impact of different boundary conditions on the post-buckling of plates was shown in semi-energy analytical models and experiments of (Banks et al., 1978; Rhodes & Harvey, 1977; Rhodes et al., 1975).

The boundary conditions modelled by Rhodes et al. (1975) were simply supported uniformly compressed plates with different boundary conditions on unloaded edges. The experimental rig used in the study had roller-bearing supports on loading edges with uniform compression (Figure 1-9 (b)) or eccentric load. The unloaded edges were simply supported (by knife edge supports) (Figure 1-9 (d)) or free edges (Figure 1-9 (c)). The slightly larger theoretical deflection compared to the experimental values was attributed to friction in the test rig.

The boundary conditions considered in (Banks et al., 1978) were simply-supported and uniform loading on loaded edges (Figure 1-9(a)) and free in-plane (Figure 1-9 (c)) or uniform in-plane movement (Figure 1-9 (d)) and shear free on unloaded edges. For the free in-plane unloaded edges condition, the maximum stress due to membrane and bending stress moves from the panel centre towards the unloaded edges as the deflection shape flattens at the centre (Banks et al., 1978).

For the straight unloaded edges condition, the maximum transverse bending stress is at the panel centre, and the panel is more stiff with smaller deflections and stresses at the unloaded edges (Banks et al., 1978).

Rhodes & Harvey (1977) studied simply supported panels with uniform (Figure 1-9 (b)) or linearly varying compression on loaded edges and combinations of clamped, simply supported or free unloaded edges. The boundary conditions of the unloaded edges producing least deflections and stresses at given load was the fixed-fixed, followed by fixed-simply supported, simply supported-simply supported, fixed-free and simply supported-free boundary conditions (Rhodes & Harvey, 1977). Deflections were larger and failure load less for central loading type compared to uniform compression for the simply supported–free unloaded edge condition.

The Galerkin's method is used in the post-buckling analytical models of corrugated paperboard in this study. The motive for using Galerkin's method was the goal of obtaining a multi-term displacement solution to the post-buckling problem. Other methods based on potential energy considerations such as the Rayleigh-Ritz method could also have been used to achieve this goal. Combinations of the loading type and in-plane boundary conditions on the unloaded edges are modelled to compare with the experimental post-buckling plot of Nordstrand (2004a). In this way, difference in boundary conditions was examined as a possible source of discrepancy for previous analytical results.

The models draw on the previous work on imperfect, simply supported isotropic plates (Hui & Leissa, 1983; Ilanko, 2002; Ilanko & Dickinson, 1991). The in-plane boundary conditions of case 1 in (Ilanko & Dickinson, 1991) were uniform static load distribution and free movement normally on the loaded edges, free movement normally on remaining edges and free tangential movement (shear free) on all four edges. The in-plane boundary conditions of the case described in (Hui & Leissa, 1983; Ilanko, 2002) were uniform compression along loaded edges and constant normal in-plane movement and free tangential movement (shear free) along all edges.

The method used by Ilanko & Dickinson (1991) is a single term Galerkin's solution, where the in-plane component of the Airy stress function is an analogous summation series product of characteristic beam vibration functions in the planar directions, to enforce in-plane boundary conditions. This analogy between the stress function formulation of a plane stress problem and out-of-plane plate bending problem is explained in (Bassily & Dickinson, 1977). The boundary condition used in the first analytical model in the current study makes use of orthogonality between an in-plane free edge and an out-of-plane clamped edge (refer to Figure 1-10).

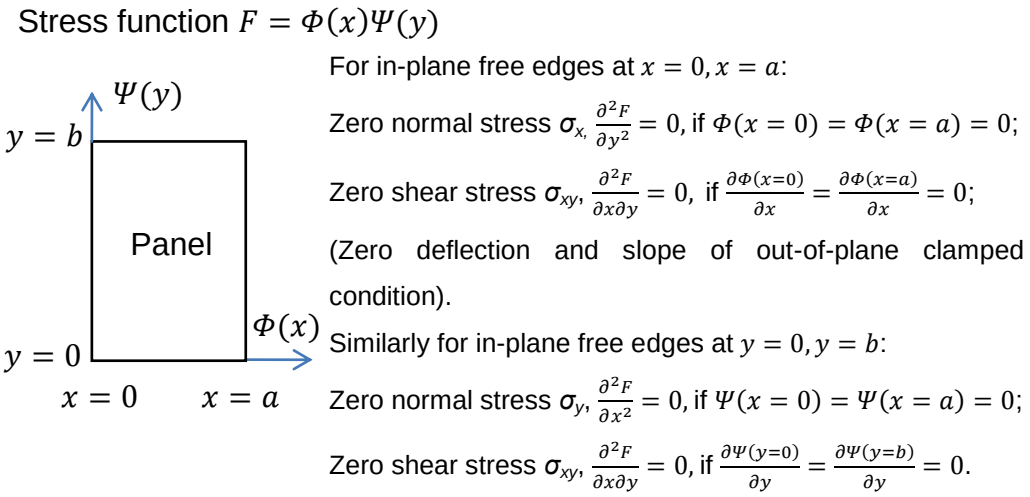

Figure 1-10: Orthogonality between in-plane free boundary condition and out-of-plane clamped boundary condition.

1.3.3.3 Effect of initial imperfections on post-buckling

For plates with geometric imperfection, the buckling load is less easily identified from the post-buckling load-deflection curve than for the perfect plate. In the experiments by Banks et al. (1978) and Rhodes et al. (1975) the magnitudes of initial geometric imperfections in the plates were unknown and the magnitudes of imperfection for the theoretical results were chosen to match the experimental load-deflection curves. The determination of the critical load and imperfection of plates in experiments is problematic as previously discussed.

The initial imperfections reduce plate load carrying capacity resulting in larger deflections and stresses near the critical load, with the effect being most significant for imperfections similar to the local buckling mode (Banks et al., 1978; Rhodes et al., 1975). The effect of imperfections on plate deflections reduces above the critical load, with the deflections approaching those of a perfect plate (Rhodes et al., 1975).

On a positive aspect of the effect of geometric imperfections, the studies by Hui (1984, 1986) on thin-walled columns proposed that beneficial geometric imperfections modes could be used to improve their energy absorption. For a short, angled thin-walled column, a symmetric deflection mode, clamped along the joint of two plates, resulted in higher energy absorption compared to an anti-symmetric mode, simply-supported along the joint of the two plates (Hui, 1984). For a thin-walled box column, introducing initial imperfection of as many half-waves as possible would increase its energy absorption and post-buckling stiffness (Hui, 1986). The beneficial geometric imperfection would be useful up to formation of the first fold.

Previous investigations of the interactions between fundamental and higher deflection modes have been reported for thin-walled columns as cited in (Hui, 1984) but not for the post-buckling of corrugated paperboard plates in particular.

1.3.3.4 Multi-term out-of-plane displacement function

For a post-buckling load range beyond twice the critical load, buckling form may change from the initial buckling mode shape and therefore more terms in the deflection function are needed to account for these changes (Rhodes & Harvey, 1977). The semi-energy models by Rhodes & Harvey (1977) and Nordstrand (2004a) use polynomials in the defection function which describe the buckled form with a good accuracy with few terms.

A two-term solution by the semi-energy method in the post-buckling regime was presented by Banks et al. (1978). More recent developments have included a multi-term semi-energy finite strip method by Assaee & Ovesy (2007) for post-buckling analysis of composite plates, which was found to be as effective as the full energy finite strip method.

The analytical Galerkin's models for corrugated paperboard panels in the current study includes a multi-term Fourier series deflection function, which builds on the isotropic models of Hui & Leissa (1983) Ilanko & Dickinson (1991) and Ilanko (2002).

1.3.4 Finite Element Models

The Finite Element Method is one of the most used numerical methods with a wide range of analysis capabilities. An overview of FE modelling tools applicable to corrugated paperboard was given in (Jiménez-Caballero, Conde, García, & Liarte, 2009). Although the present study is focused on buckling and post-buckling of corrugated paperboard at constant humidity levels, other key areas of research on corrugated paperboard that use Finite Element models include analyses of moisture diffusion (Rahman, Urbanik, & Mahamid, 2002; Rahman, Urbanik, & Mahamid, 2003), creep or hygroscopic viscoelastic behaviour (Bronkhorst & Riedemann, 1994; Navaranjan & Johnson, 2006; Navaranjan, Paltakari, & Ilmonen, 2008) and dynamic loading and vibration (Bernad, Laspalas, González, Liarte, & Jiménez, 2010). Past work in numerical modelling of

buckling and post-buckling of corrugated paperboard panels and boxes are reviewed in this section.

1.3.4.1 Finite Element panel models

Finite Element local buckling models for corrugated paperboard panels in cross direction edge compression by Johnson & Urbanik (1989; 1987), consider facing and core components as long rectangular paper plates in elastic buckling, neglecting curvature in the corrugation profile. Both fixed and simply supported edge restraints with no lateral movement along the glue lines are modelled. The actual edge restraint conditions of the facing and core interfaces are believed to be elastic, in between simply supported and fixed. The non-linear stress-strain orthotropic material model for paper from (Johnson & Urbanik, 1984) is applied in the buckling equations. The non-linear material behaviour of paper characterised by Urbanik (1982) is given below:

$$\sigma = c_1 \tanh\left(\frac{c_2}{c_1}\varepsilon\right)$$

Equation 1-28

Where c_1 is the horizontal asymptote of stress-strain curve as strain increases and c_2 the initial slope of stress-strain curve.

The local buckling Finite Element theory used in (Johnson & Urbanik, 1987) was extended to modelling machine direction compression strength corrugated fibreboard in (Urbanik, 1996a). The model of machine direction compression strength of paperboard showed facing sections between corrugation lines could be treated as short wide columns elastically restrained (between simply supported and fixed conditions) at their ends by the corrugated core. The buckling model in (Urbanik, 1996a) used nonlinear material stress-strain relations for paper, and paper compression strength, in-plane stiffness and bending stiffness.

Compared to experimental strength data, the buckling load predicted from the model in (Urbanik, 1996a) had an average discrepancy of 8%, being

accurate for low basis weight materials but conservative for high basis weight materials. With empirical correction for material crush and structural buckling failure interactions, the MD failure loads predicted had an average discrepancy of 5.4% compared to the experimental strength, being conservative for low basis weight linerboards.

Urbanik & Saliklis (2002, 2003) generated post-buckling data for corrugated panels using Finite Elements to validate the post-buckling formula proposed in (Urbanik, 1996b) for compression strength, accounting for elastic and inelastic post-buckling, non-linear material behaviour and with empirical correction of the panel stiffness.

The parametric Finite Element study of corrugated paperboard panels by Nordstrand (1995), using an equivalent layered sandwich material model, investigates how the buckling and failure loads are affected by the transverse shear stiffness of the core, initial out-of-plane imperfections, asymmetry in corrugated paperboard components, panel slenderness ratio (side length to thickness), and eccentric loading. According to the results of Nordstrand (1995) transverse shear stiffness and initial imperfections (unless the amplitudes of imperfections are larger than the panel thickness), have a minor effect on the failure load. Corrugated paperboard asymmetry, panel slenderness ratio and loading eccentricity have significant effect on failure load.

Allansson & Svärd (2001) conducted experiments and Finite Element post-buckling analyses of corrugated paperboard panels in compression, with detailed geometric and simplified effective solid core material models. The paper layers of the detailed model were treated as orthotropic, homogeneous, linear elastic, with material properties estimated from measured in-plane properties of paper according to Equation 1-26 and Equation 1-27. The solid core of the simplified model was given material properties from (Nordstrand, 1995). The Finite Element post-buckling analysis was conducted using Newton-Raphson iteration increments with automatic stabilisation damping to avoid problems with convergence. The

post-buckling load-displacement curves compare well between the model and experimental results but the initial stiffness is overestimated. Failure load prediction error compared to the experimental value was within 5.8% and 3.2% for the detailed and simplified models respectively, considering structural failure, and within 2.8 % and 16.3% for the detailed and simplified models respectively, considering material failure.

Armentani et al.(2006) conducted local and global buckling Finite Element analyses on single- and double-walled, 0.4 m square, simply-supported corrugated paperboard panels with in-plane compression. A quarter panel model was used, assuming symmetry conditions. Detailed geometric models with isoparametric four-node shell elements and simplified models with solid cores of effective stiffness and eight-node layered shell elements were used. Double walled panels with equal width and height fluting with eight different values of fluting phase shift, and one panel of different flute width and height were modelled. Different combinations of facing stiffness and thickness ratio were also considered. The single-walled panel model post-buckling results were compared with the experimental results of Allansson & Svärd (2001), showing agreement in the load-centre out-of-plane displacement curves except for low loads prior to buckling. The larger experimental displacements prior to buckling are thought to be due to panel imperfections or local perturbations decreasing initial stiffness.

Talbi et al. (2009) obtained Finite Element model buckling results for the corrugated paperboard panel from (Nordstrand, 2004b), simply-supported and uniformly compressed in CD, using the homogenised element developed by analytical homogenisation and detailed geometric models. The critical load prediction from the homogenised model had discrepancies of 4% and 11% with the analytical and experimental value from (Nordstrand, 2004b). The detailed geometric model critical load was within 1% and 8% of the analytical and experimental value of (Nordstrand, 2004b).

Biancolini et al. (2009a) investigated variations in initial imperfection, paperboard composition and thickness, and their influence on buckling behaviour with Finite Element (FE) quarter models of the panel dimensions in (Nordstrand, 2004a). The models use detailed geometric and homogenised corrugated paperboard models, modelled with four-node isoparametric large-displacement shell elements, and rigid elements connecting the facings and core of the detailed model. The load was applied at an external node that is linked to nodes of the loaded edge by rigid elements. The detailed model of the panel had good agreement of the post-buckling curve of load-out-of-plane displacement at the panel centre, but the simplified model did not.

Finite Element detailed unit cell models were used by Daxner et al. (2007) and Flatscher et al. (2011) to optimise corrugated paperboard design for minimum mass per unit area by modifying geometric parameters under constraints of effective bending stiffness in CD for global buckling and critical buckling strength for local buckling. The paper material was given orthotropic behaviour and modelled using eight-node, bi-quadratic, reduced integration, shell elements. The corrugations were modelled as a sinusoidal shape, and perfect bonding enforced by kinematic coupling applied at sharing nodes of core and facing interfaces but with the facing elements offset from their reference surface. The effective bending stiffness in CD was predicted by an analytical calculation based on width-specific area, second moments of area and elastic moduli of paperboard components. Kinematic boundary conditions were used to predict effective mechanical behaviour corrugated paperboard design by modelling representative geometric unit cell of one full flute wave with periodicity boundary conditions. The unit cell length in CD was optimised to obtain local buckling patterns of the infinite corrugated paperboard strip and the critical load in CD. The optimised corrugated paperboard design compared to the reference configuration had an increased overall paperboard thickness, reduction in corrugation wavelength and component layer thicknesses, and steeper corrugation profile. The improved corrugated

paperboard was designed to exhibit simultaneous local buckling of facings and core under in-plane compression in CD. Localisation of buckling patterns leading to fold formation and global bending was also investigated by a post-buckling analysis of a corrugated paperboard strip in (Flatscher et al., 2011).

1.3.4.2 Finite Element box models

The compression strength of boxes have been predicted by numerical models of the box as an assembly of simply-supported plates, accounting for the facings and core properties of corrugated paperboard (Bennett, 1977; Pommier & Poustis, 1989; Pommier, Poustis, Fourcade, & Morlier, 1991). Pommier & Poustis (1989) validates the models results with the McKee box compression strength formula for boxes of the same box perimeter with different paperboard profiles and material. The McKee formula uses bending stiffness D_{11} and D_{22} from a four-point bending test and shear bending stiffness D_{12} and D_{66} from an anticlastic test.

A study of statically compressed paperboard packaging in (Beldie et al., 2001), a material not dissimilar to corrugated paperboard, was conducted with FE modelling and experiments on panels, package segments - upper, middle and lower, and whole packages. Failure occurs near corners with the maximum stress moving from the panel centre to corners as panel deflects. The study highlighted the point that stiffness reductions in the upper and lower portion of packaging were due to horizontal creases at the corners. An orthotropic, elastic-plastic laminate shell model material was used, including geometric imperfection. Some discrepancy of experimental and predicted load-deformation results was attributed to creases along the box edges being modelled, as the plate is free to rotate instead of having rotational stiffness.

The Finite Element model predicting failure loads of corrugated paperboard boxes in compression by Nordstrand, Blackenfeldt, & Renman (2003), is a quarter model using two planes of symmetry, including a corner and half of two side panels. An effective layered sandwich model

with transverse shear moduli correction was used to model the corrugated paperboard material. The influence of creases along the top and bottom of panel on loading distribution was modelled by edge springs and also eccentricity moments to account for their effect on buckling modes. The crease stiffness properties were obtained from measurements on creases. The vertical edges at the box corner were connected in translational degrees of freedom and were permitted to rotate. The predictions of box failure load for B-flute and C-flute corrugated paperboard had an average discrepancy of 3% higher and 5% lower than the experimental values respectively.

In a study predicting compression strength of corrugated paperboard packaging by Biancolini & Brutti (2003), equivalent in-plane and out-of-plane elastic constants, determined from virtual tests on FE models of corrugated paperboard with detailed paperboard geometry, were assigned to single laminate FE model of an open box with flaps in uniform compression. The compression of the box was modelled using vertical translation constraints on the bottom edges of the box, and the top edges of the box were constrained in vertical translation to a master node where a point load was applied. According to Biancolini & Brutti (2003), the closure flaps of the box introduce clamped–like constraints on the edges of the vertical panels. The box compression strength prediction was 7.4% lower than the experimental value for high quality kraft corrugated paperboard.

A study by Biancolini et al. (2005) analyses buckling and post buckling of a quarter panel and an eighth of a box modelled in FE, with detailed corrugated paperboard geometry and accounting for creasing in fold lines. The box model has flaps and folding lines created by a geometrical mesh modification with a 45^{o} slope and coincident nodes from the mesh modification used as folding axes. Critical loads and load-displacement curves were obtained for panels and boxes with various geometry and materials to show their effect on compression stiffness. Localised stiffness

reduction at folds was apparent in differences in panels and boxes solutions.

Biancolini et al. (2010) validated the box models using the FE approach in (Biancolini et al., 2005) with box compression experimental results. The critical loads predicted by single equivalent lamina and detailed models were 8.38% above and 3.41% below the theoretical value for a simply supported panel. The failure loads of the FE models were slightly closer to experimental values than McKee formula predictions.

Box compression strength and stress distribution around holes in corrugated paperboard were also examined numerically in (Han & Park, 2007). This study optimised hand or vent hole design - shape and location, with FE models of rectangular tube boxes in uniform compression, supported with experimental results. The FE shell models' in-plane Young's Moduli in (Han & Park, 2007) were calculated using the moment of inertia and flexural stiffness of the corrugated paperboard.

The current study is concerned with modelling the buckling and post-buckling behaviour of a corrugated paperboard panel. In the Finite Element models of the work, the equivalent plate model and detailed geometry material models of corrugated paperboard are used. The literature shows that the modelling of box structures using Finite Elements is a developing area of research where further improvements in accuracy of predicting buckling and failure could be made.

1.4 Research Questions

This work aims to attain reasons for discrepancy and possible improvement of the correlation between the predicted and observed buckling problem for corrugated paperboard panels. The research questions put forward below investigate the themes of in-plane boundary conditions, multi-term analytical models, effective material properties, and experimental verification.

1.4.1 In-plane boundary conditions for corrugated paperboard panel

The literature showed differences in experimental and analytical semi-energy model results for buckling corrugated paperboard panels (Nordstrand, 2004a). The work of Banks et al. (1978) on composite plates show that the in-plane boundary conditions influences post-buckling behaviour. Therefore, the following question is posed:

What is the effect of different boundary conditions and loading conditions (i.e. uniformly distributed loading or uniform in-plane normal edge displacement, as in Figure 1-9) applied to the corrugated paperboard panel, on the critical buckling load and deflection response due to loading?

1.4.2 Multi-term analytical Galerkin's model

The analytical Galerkin's models of Ilanko (2002) on isotropic plates show that the post-buckling behaviour is affected by the number of terms in the displacement shape functions. The following questions are posed:

- How is the load vs. displacement post-buckling plot influenced by higher mode (multi-term) out-of-plane displacement shape functions?
- How is the post-buckling plot affected by symmetric and / or anti-symmetric modes of geometric imperfection in the panel and the out-of plane displacement function?

1.4.3 Effective material properties of corrugated paperboard

The input data and material models for corrugated paperboard material used in buckling models are reported to be influential on the post-buckling behaviour (Biancolini et al., 2005). Past work comparing models and materials testing experiments have involved homogenisation and detailed analytical and Finite Element models by Aboura et al. (2004), Biancolini (2005), Gilchrist et al. (1999) and Isaksson et al. (2007). There is still

discrepancy between homogenised buckling model and experimental results in the work by Talbi et al. (2009). The following questions are posed:

- How do corrugated paperboard material properties compare among the different materials testing methods?
- How do the material properties for an equivalent single layer orthotropic plate calculated using properties of constituent layers compare with those given by materials tests on corrugated paperboard?
- How do the corrugated paperboard properties obtained from materials tests compare with those from the Finite Element models of the tests with equivalent single-layered and detailed geometry?

1.4.4 Predicted and experimental results for corrugated paperboard panel

The experimental boundary conditions for the buckling tests on corrugated paperboard panels as in the work by Nordstrand (2004a) could be further investigated, since differences in boundary conditions may account for discrepancy with model results. The initial imperfection and comparison of panel displacement from the reference is only given at the panel centre. Additional displacement modes apart from the fundamental mode may be of significance if imperfections in the other modes are present. The following questions are posed:

- What boundary conditions most resemble the panel buckling test boundary conditions?
- Which panel out-of-plane displacement mode shapes are dominant in the test conditions?

1.4.5 Other Research Questions

As the research progressed, several other research questions emerged and these are described and discussed in the relevant chapters. For

example, the question of how to determine the initial imperfection from the post-buckling tests arose after the commencement of the experiments. An attempt to determine this through Southwell's plot method showed that the linearity of the plot was affected by the interaction between the bending and membrane stiffness of the plate. Thus the question on the best method to find the imperfection is addressed in Chapter 5.

1.5 Summary

This chapter introduced the background and rationale for undertaking research on modelling the buckling and post-buckling of corrugated paperboard structures. The review of literature discussed buckling theory and experimental methods, materials testing and models of corrugated paperboard, and analytical and Finite Element methods and relevant prior research. The next four chapters develop answers to the research questions posed in this chapter. The second chapter considers the effect of different in-plane boundary conditions of the buckling and post-buckling behaviour of the corrugated paperboard panel from Nordstrand (2004a). The third chapter presents multi-term analytical Galerkin's method post-buckling models, and considers the impact of the number of out-of-plane displacement modes included and symmetric and / or anti-symmetric geometric imperfections on the post-buckling behaviour of the panel from Nordstrand (2004a). The fourth chapter compares different methods for obtaining the effective material properties of corrugated paperboard used in the buckling tests in this study, including three materials testing methods and equivalent single-layered and detailed geometric material models. The fifth chapter compares the buckling and post-buckling results from the corrugated paperboard panel experiments conducted in this study and predicted from analytical Galerkin's method and FE models. The overall conclusions and recommendations of the research and a summary of these follow in the last chapter. The appendices which follow consist of the procedure used to include imperfection modes in the FE models and detailed, additional results from the main chapters on the analytical

Galerkin’s multi-term post-buckling models, determining properties of corrugated paperboard, and comparison of experimental and predicted post-buckling panel results.

2 Effect of in-plane boundary conditions on post-buckling behaviour of corrugated paperboard panels

2.1 Introduction

Single term analytical and numerical finite element models for buckling of a corrugated paperboard panel are presented in this chapter. The corrugated paperboard panel can be considered as one of the side walls of a box packaging structure.

The differences found between experimental and model results for a buckling corrugated paperboard panel by (Nordstrand, 2004a), leads to a consideration of whether the boundary conditions applied in the models actually resemble those in the buckling experiments.

The following research question is investigated:

- What is the effect of different boundary conditions and loading applied to the corrugated paperboard panel, on the critical buckling load and deflection response due to loading?

In an attempt to answer this question, analytical and finite element buckling models for a uniaxially compressed, simply supported corrugated paperboard panel, with different in-plane boundary conditions were created. Although change to the out-of- plane boundary condition would have a greater influence on the buckling behaviour, only different in-plane boundary conditions are considered. It was thought that while the previous experimental arrangements seemed reasonable for providing the assumed simply supported out-of-plane conditions, the in-plane conditions were less clear. The cases with combinations of loading and in-plane boundary conditions shown in Figure 2-1 were selected for study because case (A) is less constrained than the assumed experimental conditions of case (C), while case (B) is more constrained compared to case (C).

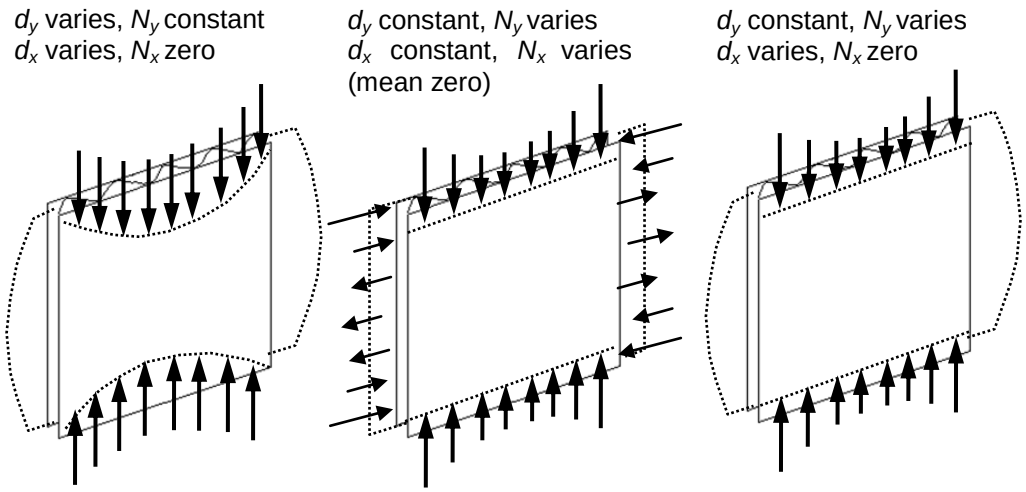

(A) Uniform load intensity and free in-plane movement on unloaded edges

(B) Uniform compression on loaded edges and uniform in-plane normal movement on unloaded edges

(C) Uniform compression on loaded edges and free in-plane movement on unloaded edges

Figure 2-1: Loading cases and in-plane boundary conditions of panels studied.

The in-plane boundary conditions modelled were:

Case (A)

i. uniform load intensity, N_y and free movement normally on loaded edges,

ii. free normal movement on unloaded edges, and

iii. free tangential movement (shear free) on all four edges, as in (Ilanko & Dickinson, 1991);

Case (B)

i. uniform normal displacement with average resultant load intensity, N_y along loaded edges,

ii. uniform normal movement along unloaded edges, and

iii. free tangential movement (shear free) along all edges, as in (Hui & Leissa, 1983; Ilanko, 2002);

Case (C)

i. uniform normal displacement with average resultant load intensity, N_y along the loaded edges,

ii. free normal movement along unloaded edges, and
iii. free tangential movement (shear free) along all edges as in (Nordstrand, 2004a).

The boundary condition case A is the same as case 1 in (Ilanko & Dickinson, 1991) for an imperfect, simply supported isotropic plate uniaxially compressed in-plane.

The boundary condition case B was described in (Hui & Leissa, 1983; Ilanko, 2002) for an imperfect, simply supported isotropic plate, biaxially loaded in-plane with uniform compression.

The boundary conditions of case C are described in (Nordstrand, 2004a), the referenced experimental buckling condition, a simply supported corrugated paperboard panel, uniformly compressed along the loaded edges, with free in-plane normal movement along unloaded edges.

Post-buckling behaviour is modelled since the effect of any initial geometric out-of-plane imperfection would be expected to result in increasing curvature with load, thus increasing the overall stiffness. Hence, allowing further loads to be sustained beyond the first critical load, needs to be taken into account. If no initial imperfection is present in the panel, there would be a sudden “instability” at critical load, with out-of-plane deflections increasing with further load that would converge towards those of an imperfect panel with increasing load.

2.2 Methods of Study

Post-buckling models of a simply supported corrugated paperboard panel with out-of-plane geometric imperfection, uniaxially compressed with different combinations of in-plane boundary conditions were created using analytical Galerkin’s method and numerical Finite Element Method (FEM) approaches. The analytical models were created using *MATLAB* software, while the FEM models were created using *Abaqus* software.

The experimental and analytical results from (T. Nordstrand, 2004) are used for comparison with the post-buckling models. Hence, the dimensions assigned to the corrugated paperboard panel from the reference were unchanged. The panel was of width, *a*, height, *b*, and thickness, *h*, shown in Table 2-1 (refer to Figure 2-2).

Table 2-1: Dimensions of buckling panel (Nordstrand, 2004a).

Panel geometry	
Width, *a* (m)	0.4
Height, *b* (m)	0.4
Thickness, *h* (mm)	4.02

The corrugated paperboard was of a single-wall structure and C-flute profile which is the most commonly used paperboard profile, with an estimated take-up factor, α (the length ratio between the corrugated layer and facings), of 1.45. The principal directions of the material shown in Figure 2-2 are *1* - the machine direction (MD) along *x*; *2* - the cross-direction (CD) along *y*; and *3* – the out-of-plane direction along *z*.

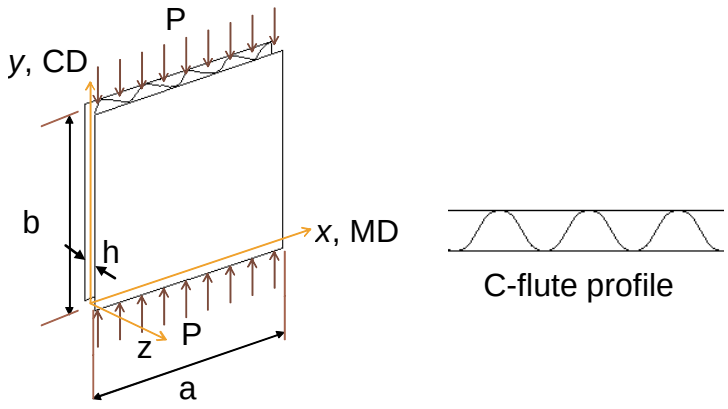

Figure 2-2: Corrugated paperboard panel uniaxially compressed.

2.2.1 Material model

The material models of corrugated paperboard used in the analytical and numerical methods are described in this section.

The geometry and material properties of the constituent layers of the paperboard from (T. Nordstrand, 2004) are used in material models for the different methods. However, there are differences in the material models of paperboard used for the analytical and FEM models. Both material models give overall equivalent properties for paperboard, to avoid modelling the detailed geometric structure of paperboard. The analytical and FEM material models have the same flexural stiffness but differ in their in-plane elastic properties. This is because the in-plane properties could be defined independently of the flexural stiffness in the analytical material model, while for the FEM orthotropic material definition used, the in-plane properties and flexural stiffness were interdependent.

The geometric parameters of the paperboard are shown in Figure 2-3. The paperboard consists of two outer layers - the single facer of thickness, $t_{f\,1}$, and double backer of thickness $t_{f\,2}$. The corrugated core or fluted medium is of thickness, t_c. The overall paperboard thickness is h, and the 'wavelength' of the corrugation profile is λ.

The corrugation profile can been approximated as a combination of circular arcs of inner radius, r, outer radius, r_1, and arc angle from vertical, θ; and tangential angled straight sections of length, L and glue joints of width, t_g, as in (Ilmonen, 2007).

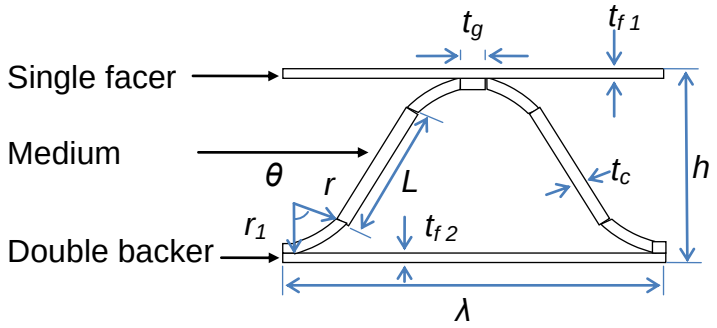

Figure 2-3: Geometric parameters of paperboard

The geometry of the corrugated paperboard is given in Table 2-2. The grammage (g/m^2), a measure of mass per unit area, of the layers is

indicated with the paperboard name in the order of single facer / medium / double backer.

Table 2-2: Paperboard geometry from (T. Nordstrand, 2004).

Geometric parameters	Paperboard 184.3/140.2/187.4
single facer thickness, $t_{f\,1}$ (mm)	0.268
double backer thickness, $t_{f\,2}$ (mm)	0.244
fluted medium thickness. t_c (mm)	0.217
take-up factor [2], α	1.45

[2] Estimated.

For the paperboard models, the room condition (23 °C, 50 % relative humidity) properties of the facings (averaged) and core layers from Table 1 of (Nordstrand, 2004a), were used in calculating the equivalent paperboard properties.

In the analytical models, the material is modelled as an orthotropic lamina with properties equivalent to the composite structured corrugated paperboard as in (T. Nordstrand, 2004). First-order shear deformation laminated plate theory was used to obtain equivalent material properties of the corrugated paperboard in directions MD and CD, assuming plane stress conditions for the problem as in (Nordstrand, 2004a) and (Carlsson et al., 2001). Thin plate theory is used in the analytical model neglecting transverse shear deformations as in (Nordstrand, 2004a).

The most important properties were the paperboard's overall equivalent Young's moduli E^*_{11} (Pa) and E^*_{22} (Pa), along MD and CD directions respectively, the in-plane shear modulus G^*_{12} (Pa) and Poisson's ratio v^*_{12}, shown in Table 2-3, calculated using the equations below from Equations (1) and (6) in the reference (Nordstrand, 2004a):

$$\bar{h} = 1 \Big/ \left[1 + \frac{\alpha \; t_{\mathrm{c}} \, E_{22,\mathrm{c}}}{2 \; t_f \; E_{22,\mathrm{f}}} \right]$$

Equation 2-1

$$E_{11}^{*} = 2\ t_f\ E_{11,\mathrm{f}}/h$$

Equation 2-2

$$E_{22}^{*} = \frac{2\ t_f\ E_{22,\mathrm{f}}}{h\ \bar{h}}$$

Equation 2-3

$$G_{12}^{*} = 2\ t_f\ G_{12,\mathrm{f}}/h$$

Equation 2-4

$$\nu_{12}^{*} = \bar{h}\ \nu_{12,\mathrm{f}}$$

Equation 2-5

where

t_f = average of facings' thicknesses (m)

$E_{11,\,\mathrm{f}}$ = average of facings' MD-direction Young Modulus (Pa)

$E_{22,\,\mathrm{f}}$ = average of facings' CD-direction Young Modulus (Pa)

$E_{22,\,\mathrm{c}}$ = medium layer's CD-direction Young Modulus (Pa)

$v_{12,\,\mathrm{f}}$ = average of facings' Poisson's ratio

Table 2-3: Calculated equivalent corrugated paperboard properties for analytical and FEM models.

Equivalent properties	Paperboard properties for analytical model	Paperboard properties for FEM model
E^{*}_{11} (MPa)	1023.36	2447.02
E^{*}_{22} (MPa)	483.81	910.09
G^{*}_{12} (MPa)	235.45	616.95
v^{*}_{12}	0.254	0.499

The in-plane Poisson's ratio $v_{21,\mathrm{f}}$ and in-plane shear modulus for the facings $G_{12,\mathrm{f}}$ (Pa) were based on empirical relationships for paper materials, between Poisson's ratios v_{12} and v_{21}, and G_{12} (Pa) with E_{11} (Pa) and E_{22} (Pa), shown below from Equations (6a) and (6b) of (Carlsson et al., 2001) respectively:

$$G_{12,f} = 0.387\sqrt{E_{11,\mathrm{f}}\, E_{22,\mathrm{f}}}$$

Equation 2-6

$$\nu_{21,\mathrm{f}} = 0.293^2/\nu_{12,\mathrm{f}}$$

Equation 2-7

A Poisson's ratio for the facings of $\nu_{12,\ \mathrm{f}}$ = 0.34 from Table 1 of (Nordstrand, 1995), for the paperboard in (Nordstrand, 2004a) was used in the calculations. The flexural stiffnesses D_{11} (N m), D_{12} (N m), D_{22} (N m) and D_{66} (N m) for Nordstrand's paperboard from Table 2 of (Nordstrand, 2004a), shown in Table 2-4, were also used in the analytical models.

Table 2-4: Flexural stiffnesses of paperboard in (Nordstrand, 2004a).

Flexural stiffnesses	
D_{11} (N.m)	14.6
D_{12} (N.m)	2.71
D_{22} (N.m)	5.43
D_{66} (N.m)	3.34

In the FEM *Abaqus* models, an elastic lamina material definition was also used for an equivalent single layer paperboard model. However, it should be noted that the equivalent properties $E^*_{11,}$ $E^*_{22,}$ G^*_{12} and ν^*_{12} used shown in Table 2-3 were calculated differently than for the analytical models.

The bending stiffnesses $D_{11,}$ $D_{22,}$ $D_{12,}$ and D_{66}, and the overall paperboard thickness h, given from (Nordstrand, 2004a) were used to obtain $E^*_{11,}$ $E^*_{22,}$ G^*_{12} and ν^*_{12}. The following relations for an orthotropic plate were used:

$$\nu_{21} = D_{12}/D_{11}$$

Equation 2-8

$$\nu_{12} = D_{12}/D_{22}$$

Equation 2-9

$$E_{11} = 12\, D_{11}(1 - \nu_{12}\, \nu_{21})/h^3$$

Equation 2-10

$$E_{22} = 12\ D_{22}(1 - \nu_{12}\ \nu_{21})/h^3$$

Equation 2-11

$$G_{12} = 12\ D_{66}/h^3$$

Equation 2-12

The transverse shear moduli G^*_{13} (Pa) and G^*_{23} (Pa) were assumed to be equal to G^*_{12}.

2.2.2 Analytical model

The analytical methods used to model three cases of in-plane boundary conditions mentioned in the introduction, for a simply supported, uniaxially compressed corrugated paperboard panel, with amplitude of initial imperfection, A_0, of 0.0008 m as in (Nordstrand, 2004a) are described in the following.

The buckling panels are modelled using the Galerkin method with a single-term double sine product for the out-of-plane static deflection function w (m) and initial out-of-plane imperfection, w_0 (m) below, where $A_{i,\ j}$ is the deflection amplitude and $A_{0i,j}$ is the initial imperfection amplitude. For the purpose of studying the effect of in-plane boundary conditions, single term solutions were generated. In the final analysis discussed in another chapter, mult-term solutions were generated.

$w = \sum_i \sum_j A_{i,j}\ sin\left(\frac{i\pi x}{a}\right) sin\left(\frac{j\pi y}{b}\right)$, i and j = 1

Equation 2-13

$w_0 = \sum_i \sum_j A_{0\ i,j}\ sin\left(\frac{i\pi x}{a}\right) sin\left(\frac{j\pi y}{b}\right)$, i and j = 1

Equation 2-14

Airy stress functions F (N m) for the three cases modelled were required to satisfy the compatibility condition between w, w_0 and F, for an orthotropic plate, shown in below as in Equation (10) of (Nordstrand, 2004a):

$$\frac{\boldsymbol{1}}{\boldsymbol{E_{22}^*}}\frac{\boldsymbol{\partial^4 F}}{\boldsymbol{\partial x^4}}+\left(\frac{\boldsymbol{1}}{\boldsymbol{G_{12}^*}}-\frac{\boldsymbol{2v_{12}^*}}{\boldsymbol{E_{11}^*}}\right)\frac{\boldsymbol{\partial^4 F}}{\boldsymbol{\partial x^2 \partial y^2}}+\frac{\boldsymbol{1}}{\boldsymbol{E_{11}^*}}\frac{\boldsymbol{\partial^4 F}}{\boldsymbol{\partial y^4}}$$
$$=\boldsymbol{h}\left(\frac{\boldsymbol{\partial^2 w}}{\boldsymbol{\partial x\,\partial y}}\right)^2-\frac{\boldsymbol{\partial^2 w}}{\boldsymbol{\partial x^2}}\frac{\boldsymbol{\partial^2 w}}{\boldsymbol{\partial y^2}}-\left[\left(\frac{\boldsymbol{\partial^2 w_o}}{\boldsymbol{\partial x\,\partial y}}\right)^2-\frac{\boldsymbol{\partial^2 w_o}}{\boldsymbol{\partial x^2}}\frac{\boldsymbol{\partial^2 w_o}}{\boldsymbol{\partial y^2}}\right]$$

Equation 2-15

Substitution of Equations (2-13) and (2-14) into the right side of Equation (2-15) gives:

$$\frac{\boldsymbol{1}}{\boldsymbol{E_{22}^*}}\frac{\boldsymbol{\partial^4 F}}{\boldsymbol{\partial x^4}}+\left(\frac{\boldsymbol{1}}{\boldsymbol{G_{12}^*}}-\frac{\boldsymbol{2v_{12}^*}}{\boldsymbol{E_{11}^*}}\right)\frac{\boldsymbol{\partial^4 F}}{\boldsymbol{\partial x^2 \partial y^2}}+\frac{\boldsymbol{1}}{\boldsymbol{E_{11}^*}}\frac{\boldsymbol{\partial^4 F}}{\boldsymbol{\partial y^4}}$$
$$=h\sum_i\sum_j\sum_k\sum_l\left(\frac{ijkl\pi^4}{a^2b^2}\right)\left(A_{i,j}\,A_{k,l}\right.$$
$$\left.-A_{0\,i,j}\,A_{0\,k,l}\right)\frac{1}{2}\left[cos\left(\frac{(i+k)\pi x}{a}\right)cos\left(\frac{(j-l)\pi y}{b}\right)\right.$$
$$\left.+cos\left(\frac{(i-k)\pi x}{a}\right)cos\left(\frac{(j+l)\pi y}{b}\right)\right]$$

Equation 2-16

The Airy stress functions, *F* used for the in-plane boundary condition cases A and B, are from Equations (4) and (5) in (Ilanko & Dickinson, 1991); and Equation (5) of (Ilanko, 2002) respectively. The in-plane boundary condition case C uses a combination of the Airy stress functions of case A and B along the *x*- and *y*-directions respectively.

The stress function *F* can be defined in terms of F_o the stress function due to in-plane displacement and F_z the stress function due to out-of-plane displacement.

$$F = F_o + F_z$$

Equation 2-17

F_o satisfies

$$\frac{1}{E_{22}^*}\frac{\partial^4 F_o}{\partial x^4}+\left(\frac{1}{G_{12}^*}-\frac{2v_{12}^*}{E_{11}^*}\right)\frac{\partial^4 F_o}{\partial x^2\partial y^2}+\frac{1}{E_{11}^*}\frac{\partial^4 F_o}{\partial y^4}=0,$$

Equation 2-18

while F_z satisfies Equation 2-16.

The in-plane boundary conditions for all three cases requires that on the unloaded panel edges, at $x = 0$ and $x = a$,

$$\frac{\partial^2 F}{\partial y^2} = \frac{\partial^2 F}{\partial x \partial y} = 0.$$

Equation 2-19

The above condition satisfies for case A, free normal and tangential movement boundary conditions (A) ii and iii, and for cases B and C, free tangential movement boundary condition (B) iii and (C) iii.

Similarly, for all three cases, on the loaded panel edges, at $y = 0$ and $y = b$,

$$\frac{\partial^2 F}{\partial x^2} = -N_y, \frac{\partial^2 F}{\partial x \partial y} = 0.$$

Equation 2-20

The above satisfies for case A, uniform load intensity, N_y and free normal and tangential movement boundary conditions (A) i and iii, and for cases B and C, average resultant load intensity, N_y and free tangential movement boundary conditions (B) i and iii, and (C) i and iii.

It follows that for all three cases, at $x = 0$ and $x = a$,

$$\frac{\partial^2 F_o}{\partial y^2} = \frac{\partial^2 F_o}{\partial x \partial y} = \frac{\partial^2 F_z}{\partial y^2} = \frac{\partial^2 F_z}{\partial x \partial y} = 0,$$

Equation 2-21

and at $y = 0$ and $y = b$,

$$\frac{\partial^2 F_o}{\partial x^2} = -N_y, \frac{\partial^2 F_o}{\partial x \partial y} = \frac{\partial^2 F_z}{\partial x^2}, \frac{\partial^2 F_z}{\partial x \partial y} = 0.$$

Equation 2-22

Therefore, the stress function due to in-plane displacement, F_o, below is used for all three cases.

$$\boldsymbol{F_o = -N_y x^2/2}$$

Equation 2-23

Conversely, the stress function due to out-of-plane displacement, F_z, is different among the cases. The analogy between the stress function

formulation of a plane stress problem and out-of-plane plate bending problem explained in (Bassily & Dickinson, 1977), is used to determine F_z for each case.

F_z is in the form a summation series product of characteristic beam functions along the planar *x*- and *y*-directions, to enforce the in-plane boundary conditions.

Case A makes use of the analogy between an in-plane free edge and an out-of-plane clamped edge to approximate the in-plane free edge boundary condition along all edges, boundary condition (A) ii.

The stress function due to out-of-plane displacement stress F_z for case A below is a series product of characteristic out-of-plane clamped-clamped beam functions along the *x* and *y* directions, φ_p (*x*) and ψ_q (*y*), with coefficients $\alpha_{p,q}$.

$F_z = \sum_p \sum_q \alpha_{p,q}\, \varphi_p(x)\psi_q(y)$, where p, q = 1, 2, 3, 4, 5.

Equation 2-24

$$\varphi_p(x) = cosh\left(\frac{\lambda_p x}{a}\right) - \frac{cosh(\lambda_p) - cos(\lambda_p)}{sinh(\lambda_p) - sin(\lambda_p)} sinh\left(\frac{\lambda_p x}{a}\right) - cos\left(\frac{\lambda_p x}{a}\right) + \frac{cosh(\lambda_p) - cos(\lambda_p)}{sinh(\lambda_p) - sin(\lambda_p)} sin\left(\frac{\lambda_p x}{a}\right)$$

Equation 2-25

$$\psi_q(y) = cosh\left(\frac{\lambda_q y}{b}\right) - \frac{cosh(\lambda_q) - cos(\lambda_q)}{sinh(\lambda_q) - sin(\lambda_q)} sinh\left(\frac{\lambda_q y}{b}\right) - cos\left(\frac{\lambda_q y}{b}\right) + \frac{cosh(\lambda_q) - cos(\lambda_q)}{sinh(\lambda_q) - sin(\lambda_q)} sin\left(\frac{\lambda_q y}{b}\right)$$

Equation 2-26

Clamped-clamped beam eigenvalues λ, shown in Table 2-5 from (Blevins, 1979) up to the fifth mode shape, were used in φ_p (*x*) and ψ_q (*y*) for case A.

Table 2-5: Clamped-clamped beam vibration eigenvalues used for case A.

Mode no.	Eigenvalue, λ_i	(cosh(λ)-cos(λ))/(sinh(λ)-sin(λ))
1	4.73004074	0.982502
2	7.85320462	1.000777
3	10.9956079	0.999966
4	14.1371655	1.000001
5	17.2787597	1

The coefficients $\alpha_{p,q}$ in the series for F_z were determined by solving the compatibility equation, Equation 2-15, using the Galerkin method, multiplying with a weighting function $\varphi_r(x)\,\psi_s(y)$, of the same form as the characteristic beam functions, where $r, s = 1, 2 \ldots 5$, and integrating twice with respect to x and y.

$$\int_{x=0}^{x=a}\int_{y=0}^{y=b}\left[\frac{1}{E_{22}^*}\frac{\partial^4 F_z}{\partial x^4}+\left(\frac{1}{G_{12}^*}-\frac{2\nu_{12}^*}{E_{11}^*}\right)\frac{\partial^4 F_z}{\partial x^2\partial y^2}+\frac{1}{E_{11}^*}\frac{\partial^4 F_z}{\partial y^4}\right]\varphi_r(x)\,\psi_s(y)\,dx\,dy$$

$$= h\int_{x=0}^{x=a}\int_{y=0}^{y=b}\left[\sum_i\sum_j\sum_k\sum_l\left(\frac{ijkl\pi^4}{a^2b^2}\left(A_{i,j}\,A_{k,l}-A_{0\,i,j}\,A_{0\,k,l}\right)\frac{1}{2}\left(\cos\left(\frac{(i+k)\pi x}{a}\right)\cos\left(\frac{(j-l)\pi y}{b}\right)+\cos\left(\frac{(i-k)\pi x}{a}\right)\cos\left(\frac{(j+l)\pi y}{b}\right)\right)\right)\right]\varphi_r(x)\,\psi_s(y)\,dx\,dy$$

Equation 2-27

Case B makes use of the analogy between an in-plane normally restrained edge and an out-of-plane sliding edge to exactly satisfy the constant normal in-plane movement along all edges, boundary conditions (B) i and ii.

For case B, the stress function due to out-of-plane displacement stress F_z below is a series of double cosine functions along the x- and y-directions as in (Hui & Leissa, 1983; Ilanko, 2002).

$F_z = \sum_p\sum_q \alpha_{p,q}\cos\left(\frac{p\pi x}{a}\right)\cos\left(\frac{q\pi y}{b}\right)$, where p, q = 0, 1, 2, 3, 4, 5.

Equation 2-28

Coefficients $\alpha_{p,q}$ of the series in F_z for case B were also found by solving the compatibility equation, Equation 2-16, using the Galerkin method, multiplying with a weighting function cos (r π x/a) cos (s π y/b), where r, s = 0, 1, 2, ... 5, and integrating twice with respect to x and y.

Case C has in-plane boundary conditions along the loaded edges like that of case B but its unloaded edges have boundary conditions like that of case A. Therefore, the stress function due to out-of-plane displacement, F_z, for case C is a combination of the functions used for case A and B. The in-plane boundary conditions (C) i, uniform normal displacement along the loaded edges, and (C) ii, free normal movement along unloaded edges are satisfied by the following:

$$F_z = \sum_p \sum_q \alpha_{p,q}\, \varphi_p(x) cos\left(\frac{q\pi y}{b}\right),$$

Equation 2-29

where p = 1, 2, 3, 4, 5, q = 0, 1, 2, 3, 4, 5, and $\varphi_p(x)$ is the same as that for case A, given in Equation 2-25, with the same λ_p used as in Table 2-5.

The coefficients $\alpha_{p,q}$ in the stress function were determined by solving the compatibility equation, Equation 2-15, using the Galerkin method, multiplying with a weighting function $\varphi_r(x)\, cos$(s π y/b), where r = 1, 2 … 5, s = 0, 1, 2, ... 5, and φ_r is the same form as in Equation 2-25, and integrating twice with respect to x and y.

Then, for all three cases, the static equilibrium equation for an orthotropic plate below, based on the Equation (6.12) of (Weaver, 2008) for anisotropic laminates, was satisfied for various values of the loading intensity, N_y.

$$D_{11}^* \frac{\partial^4 (w - w_0)}{\partial x^4} + 2(D_{12}^* + 2D_{66}^*) \frac{\partial^4 (w - w_0)}{\partial x^2 y^2} + D_{22}^* \frac{\partial^4 (w - w_0)}{\partial y^4} = \frac{\partial^2 w}{\partial x^2} \frac{\partial^2 F}{\partial y^2} + \frac{\partial^2 w}{\partial y^2} \frac{\partial^2 F}{\partial x^2} - 2 \frac{\partial^2 w}{\partial x \partial y} \frac{\partial^2 F}{\partial x \partial y}$$

Equation 2-30

The corrugated paperboard was assumed to have symmetric properties about the middle plane of the panel. Hence, twisting stiffness terms were neglected in the equilibrium equation (Weaver, 2008). The assumption of symmetry about the middle plane is applicable to global buckling but not localised buckling or failure prediction.

The relationship between load intensity, N_y and out-of-plane deflection, w, is obtained by solution of the equilibrium equation, again using the Galerkin method with a weighting function of sin ($m \pi x / a$) sin ($n \pi y / b$), where m, n = 1, for all cases.

$$\int_0^a \int_0^b \left[D_{11}^* \frac{\partial^4 (w - w_0)}{\partial x^4} + 2(D_{12}^* + 2D_{66}^*) \frac{\partial^4 (w - w_0)}{\partial x^2 y^2} + D_{22}^* \frac{\partial^4 (w - w_0)}{\partial y^4} - \left(\frac{\partial^2 w}{\partial x^2} \frac{\partial^2 F}{\partial y^2} + \frac{\partial^2 w}{\partial y^2} \frac{\partial^2 F}{\partial x^2} - 2 \frac{\partial^2 w}{\partial x \partial y} \frac{\partial^2 F}{\partial x \partial y} \right) \right] \sin\left(\frac{m\pi x}{a}\right) \sin\left(\frac{n\pi y}{ab}\right) dy\, dx = 0$$

Equation 2-31

The resulting non-linear cubic equation, in terms of the unknown deflection amplitude, $A_{i,j}$ is of the form in the following equation, where $a_{1\,i,\,j}$, $a_{2\,i,\,j}$, $a_{3\,i,\,j}$ are calculable constants. The cubic equations for all cases were solved iteratively using the Newton-Raphson method, for a given load intensity, N_y. The post-buckling plot of resultant load, P, against out-of-plane displacement, w, was then produced.

$$\left(\boldsymbol{A_{i,j} - A_{0\,i,j}}\right)\boldsymbol{a_{1\,i,j}} = \boldsymbol{A_{i,j}\, N_y a_{2\,i,j}} + \boldsymbol{A_{i,j}}\left(\boldsymbol{A_{i,j}}^2 - \boldsymbol{A_{0\,i,j}}^2\right)\boldsymbol{a_{3\,i,j}}$$

Equation 2-32

The critical loads of the panel of the mode with i term(s) in the x- direction and j term(s) in the y-direction in the displacement function, for all cases were also estimated from the Equation 2-32, by calculating the ratio $a_{1\,i,\,j}$ / $a_{2\,i,\,j}$, the terms associated with bending and the load intensity, N_y, while neglecting membrane stretching terms and initial imperfection, $A_{0\,i,\,j.}$ The

load intensity at buckling determined by this calculation is then multiplied with the panel width, *a*, to give the resultant critical load, P_{crit}.

2.2.3 Finite Element model

The FEM models created in *Abaqus* consider the same corrugated panel as in the analytical models, with in-plane boundary conditions cases A, B and C mentioned in the introduction.

Symmetry in the panel dimensions enabled simplification to a quarter model of the panel. The material definition of *elastic lamina* (SIMULIA, 2009e, 2009f) was used, with equivalent properties of the corrugated paperboard given previously in Table 2-3. The element type used was S8R5, an 8-node doubly curved thin shell, with reduced integration, using five degrees of freedom per node (SIMULIA, 2009l). The procedures used include the *linear perturbation, buckle* step to obtain buckling modes (SIMULIA, 2009h) and g*eneral, static Riks* steps to obtain post-buckling behaviour results (SIMULIA, 2009m). Convergence tests have been carried out for the *linear perturbation, buckle* and g*eneral, static Riks* steps.

The load at which material failure occurs was predicted in the post-buckle *general, static* step using the Tsai-Wu criterion (SIMULIA, 2009g, 2009j) assuming plane stress conditions as described in Equation (27) of (Nordstrand, 2004a). A Tsai-Wu failure index of one or above indicates material failure. The average tensile and compressive strengths in the *x*- and *y*-directions of the paperboard outer facing layers from the reference (Nordstrand, 2004a) listed in Table 2-6, were input into the FEM model's material failure stress definition. The shear strength was conservatively estimated to be half the compressive strength in the CD-direction. The shear strength estimate was conservative compared to the theoretical and empirical relation used between shear strength and compressive strengths in MD and CD in Equation 1-13 where $\beta = 0.78$ from (Beldie et al., 2001; Haj-Ali et al., 2009; Nyman & Gustafsson, 2000b) and $\beta = 1$ from (Biancolini et al., 2009b).

Table 2-6: Parameters for Tsai-Wu Failure criterion used in FEM model.

Failure stress parameters	
$\sigma_{x,c}$ compressive strength in MD-direction (MPa)	30.35
$\sigma_{x,t}$ tensile strength in MD-direction (MPa)	81.75
$\sigma_{y,c}$ compressive strength in CD-direction (MPa)	16.40
$\sigma_{y,t}$ tensile strength in CD-direction (MPa)	29.95
τ_{xy} shear strength [a] (MPa)	8.20
Cross-Product Term Coefficient	-0.36

[a] Estimated by $\tau_{xy} = \sigma_{y,c} / 2$

The modelled in-plane boundary conditions were case A, B, and C (refer to Figure 2-4 to Figure 2-6). The upper-left-quarter model of the panel was applied the following boundary conditions in all FEM model cases:

- zero out-of-plane *z*-displacement, U3 = 0, along top and left edges;
- *x*-symmetry, with zero *x*-displacement and rotations about *y* and *z*, XSYMM (U1 = UR2 = UR3 = 0), on the right edge;
- *y*-symmetry, with zero *y*-displacement and rotations about *x* and *z*, YSYMM (U2 = UR1 = UR3 = 0), on the bottom edge.

For case A, a uniform *shell edge load* (Nm^{-1}) was applied to the top panel edge (SIMULIA, 2009c). For case B, a uniform *y*-displacement U2 boundary condition was applied on the top edge of the panel (SIMULIA, 2009b). For case C, a constant *y*-displacement U2 of the top edge was enforced through a concentrated load (N) in the y-direction applied at a reference point at the top right corner (SIMULIA, 2009a). The reference point constrained the y-direction displacement U2 of the top edge with a *coupling* constraint (SIMULIA, 2009d). Unit values of the *shell edge load,* uniform *y*-displacement and concentrated force were applied in the buckling analyses for cases A, B and C respectively.

For case B the uniform in-plane normal movement boundary conditions along the left panel edge was enforced by a *coupling* constraint in the *x*-direction displacement U1, between the left edge and a reference point at the bottom left corner.

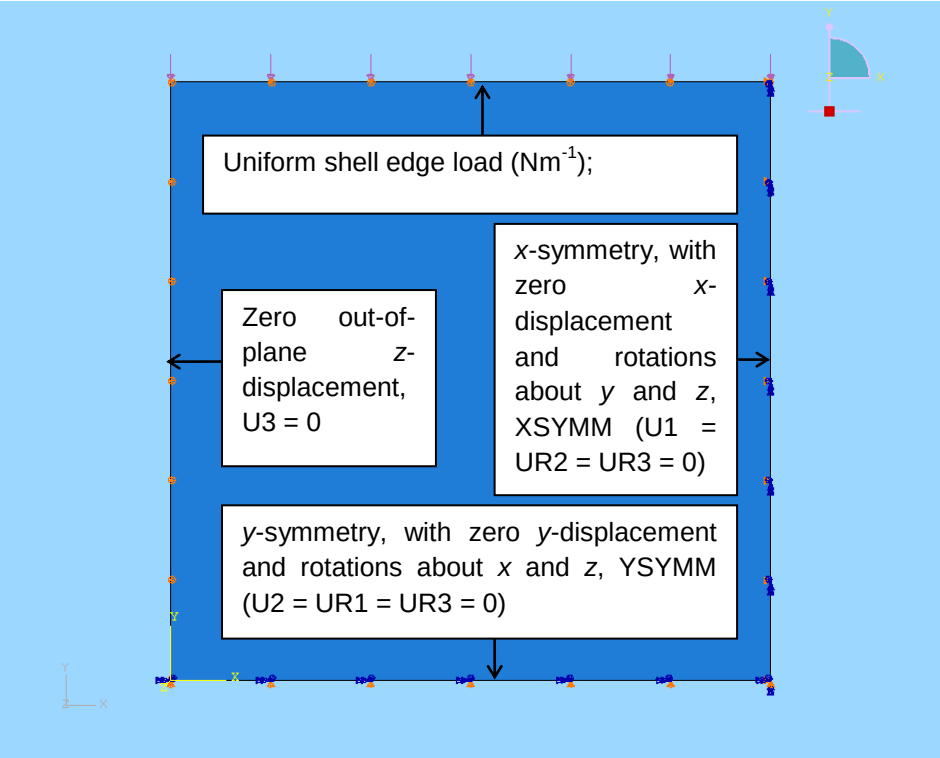

Figure 2-4: FEM In-plane boundary condition Case A.

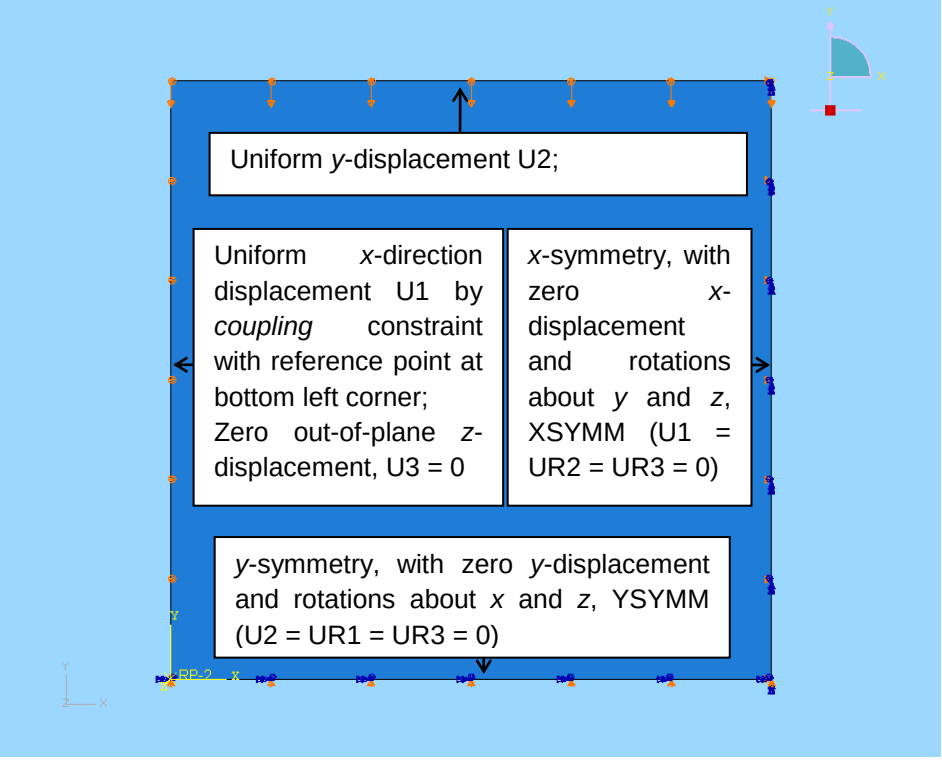

Figure 2-5: FEM In-plane boundary condition Case B.

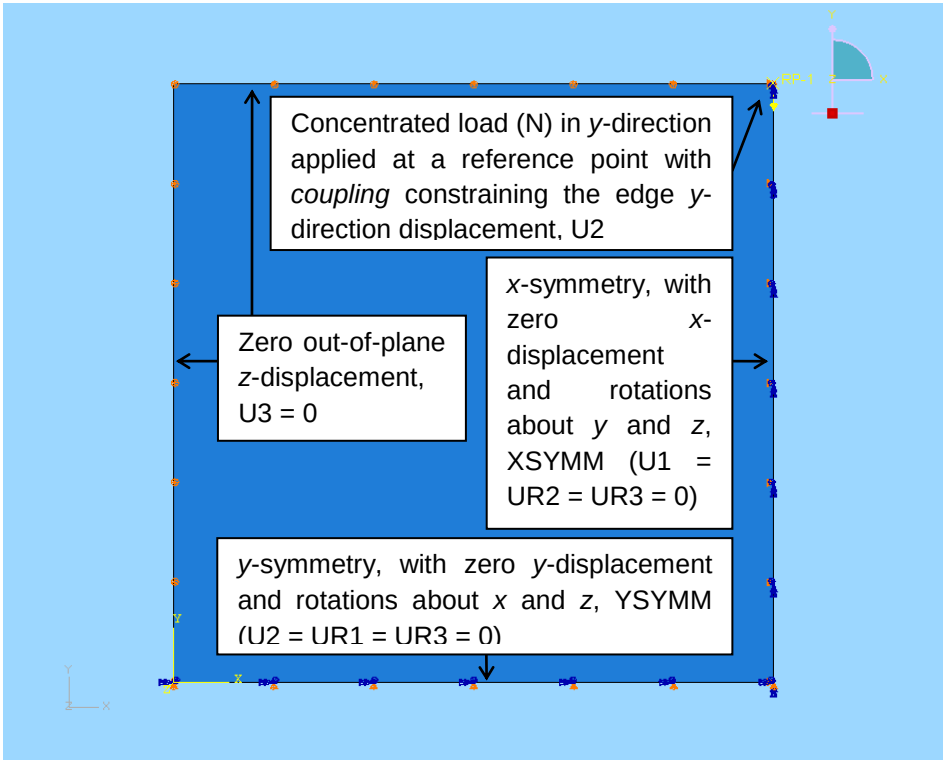

Figure 2-6: FEM In-plane boundary condition Case C.

The eigenvalues obtained in the buckling analyses were used to obtain the critical loads for the panel. The eigenvalue from case A was a factor of the uniform loading, which needed to be multiplied by the panel width to give the critical load. The eigenvalue of case B was a factor of the y-direction displacement applied to the top edge of the panel. For case B the eigenvalues from a prior buckle analysis was applied as a top edge in-plane *y*-displacement in a separate *general, static* analysis (SIMULIA, 2009k) on the panel, to obtain the critical load from a summation of reaction forces in the *y*-direction RF2 along the top edge. The eigenvalue for case C was a factor of the concentrated load applied for the case, which was multiplied by two to give the critical load.

For the post-buckling analyses of all cases modelled, a loading of about three times the first critical loading value found from the buckle analyses results, was applied. The average experimental initial imperfection amplitude A_0 from (Nordstrand, 2004a) of 0.0008 m or 0.2 *h*, where *h* is the corrugated paperboard thickness, was introduced to the panel geometry in the input file of the post-buckling analyses by defining the

displacement amplitude in the first buckling mode. This uses the scaled displacement output for the imperfection mode recorded from a prior buckling analysis and alters the panel geometry before the post-buckling analysis in the *general, static* step (SIMULIA, 2009i). An initial perturbation load or out-of-plane imperfection is necessary in the post-buckling procedure for the panel to deform in the buckling mode of interest.

2.3 Results and Discussion

The analytical and FEM model results for the different cases of in-plane boundary conditions considered for a uniaxially compressed simply supported corrugated paperboard panel are presented in this section.

2.3.1 Buckling critical load results

The analytical critical loads, P_{crit} calculated from the ratios of a_1 / a_2 of Equation 2-32 for cases A, B and C are presented in Table 2-7. The critical loads in Table 2-7 are presented in comparison to the experimental critical load 814 N of (Nordstrand, 2004a). The deflection amplitudes at buckling A_{crit}, from the analytical post-buckling results are also presented in Table 2-7 and compared with the experimental value from (Nordstrand, 2004a). The analytical results for case C from (Nordstrand, 2004a) are also listed for reference.

The analytical critical loads for cases A, B and C are similar to each other and compare well to the analytical result of 958 N in (Nordstrand, 2004a). The analytical critical loads are however higher than the experimental value by 17.64%.

The FEM critical loads from the *linear perturbation, buckle* analyses and deflection amplitudes at buckling from the *general, static Riks* analyses are also presented in Table 2-7.

Table 2-7: Critical loads and deflection of panel centre at buckling for analytical and FEM models of paperboard material from (Nordstrand, 2004a) with initial imperfection A_0 of 0.0008 m or 0.2 h.

Case	Model	Critical load, P_{crit} (N)	% Δ P_{crit}	Deflection amplitude at buckling, A_{crit}/h	% Δ A_{crit}
A	Analytical	957.60	17.64%	1.44	1.36%
B	Analytical	957.60	17.64%	1.09	-23.18%
C	Analytical	957.60	17.64%	1.38	-3.25%
A	FEM	948.68	16.55%	1.12	-20.96%
B	FEM	947.73	16.43%	0.83	-41.33%
C	FEM	948.66	16.54%	1.09	-23.51%
C	Analytical (Nordstrand, 2004a)	958.00	17.69%	1.12	-21.07%
C	Experiment (Nordstrand, 2004a)	814.00		1.42	

The FEM buckle results converged to a resultant critical load of 949 N for the in-plane boundary condition cases A and C, and 948 N for case B as shown in Figure 2-7.

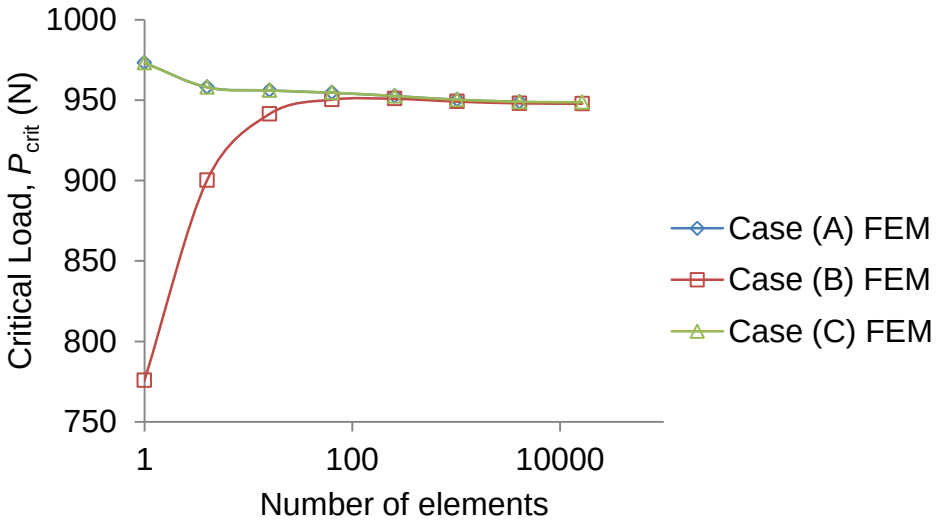

Figure 2-7: Convergence of critical load with mesh refinement for FEM models of paperboard panel.

The critical load convergence for cases A and C is from above, while case B converges from below. This difference could be due to the indirect extraction of the critical load for case B, from a summation of *y*-direction

reaction forces along the loaded edge in a static analysis with in-plane *y*-displacement applied along the edge.

The critical loads from the FEM models are slightly lower than the analytical critical loads, at about 16.4% to 16.6% above the experimental reference value. The differences in critical loads between the analytical and FEM models are likely due to the differences in the material models used.

The FEM model uses overall equivalent properties of corrugated paperboard calculated from the flexural properties of the material, defined in a single layered section without the detailed geometry of true corrugated paperboard. The analytical model also uses equivalent properties of corrugated paperboard but flexural and in-plane properties incorporated in the material model, account for some difference in behaviour of corrugated paperboard in the flexural and in-plane directions due to its geometry.

Both the classical plate theory used for the analytical models and the choice of thin shell elements in FEM models have meant transverse shear deformation in the panel was not accounted for. It is thought that allowance for transverse shear deformation would likely cause changes in the prediction of failure in the facings by local buckling.

The deflection amplitudes obtained from the post-buckling results in Table 2-7 show more variation among the cases modelled. The analytical case A shows the largest deflection amplitude at buckling among the cases at 1.4% higher than the experimental reference value. The analytical case B deflection amplitude at buckling is 23% below the experimental value. The analytical case C deflection amplitude at buckling is second closest at 3% below the experimental value.

The experimental result being referenced, with boundary conditions assumed to be like that of case C, had the largest deflection response of the results in the comparison. Therefore, the results of case A gave the best agreement with the experimental results because the case A had the

least constrained boundary conditions and the largest deflections for given load compared to cases B and C.

The FEM models for the cases A and C give similar deflection amplitudes at about 21% and 24% below the experimental value. The FEM model for case B gives the lowest deflection amplitudes at buckling, at 41% below the experimental value. The analytical results show generally larger deflections than the FEM results, with case A having deflection values closest to the experimental result.

2.3.2 Post-buckling results

The FEM post-buckling results for cases A, B and C were checked for convergence with mesh refinement shown in Figure 2-8 to Figure 2-10. The FEM post-buckling plot for case A converges from above, while cases B and C converge from below. This may be due to the difference in application of load in the different cases, since case A has a uniform loading intensity applied, while cases B and C have uniform displacement applied to the loaded edges.

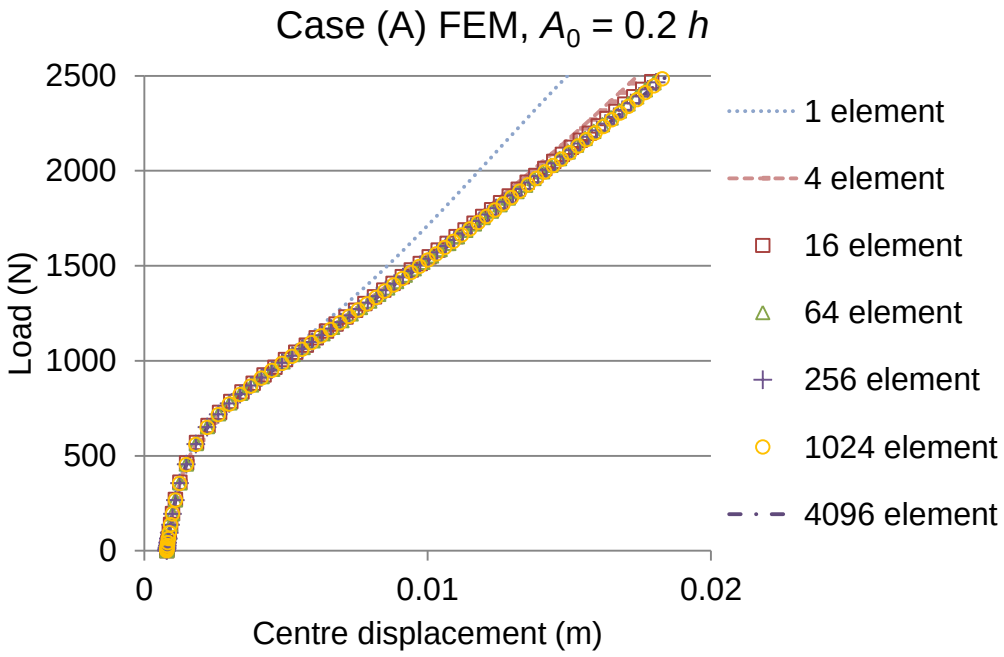

Figure 2-8: Convergence of FEM case A post-buckling plot with mesh refinement.

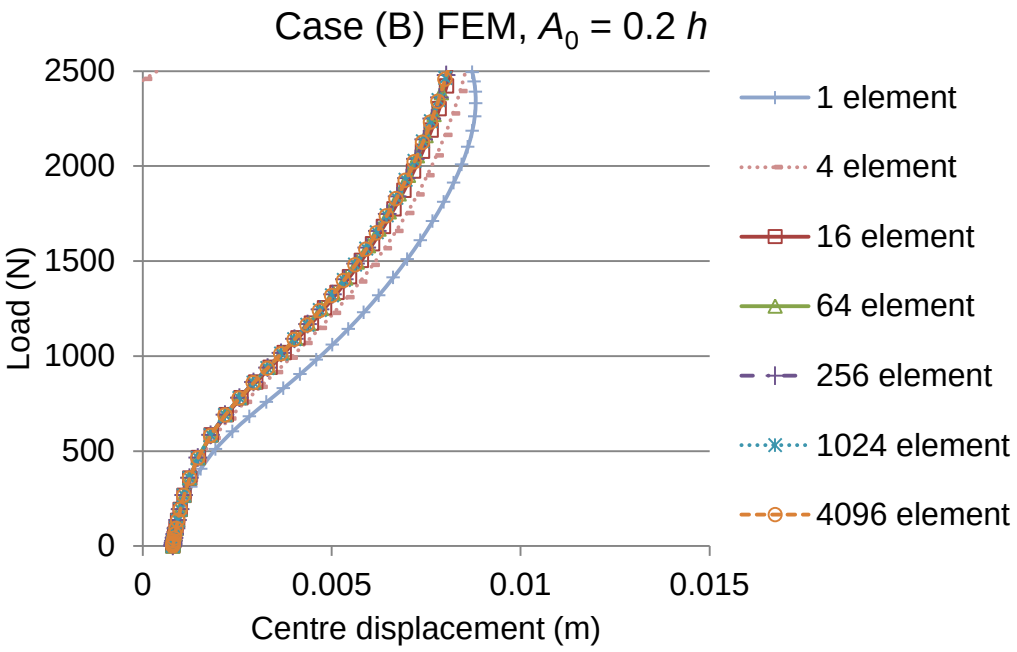

Figure 2-9: Convergence of FEM case B post-buckling plot with mesh refinement.

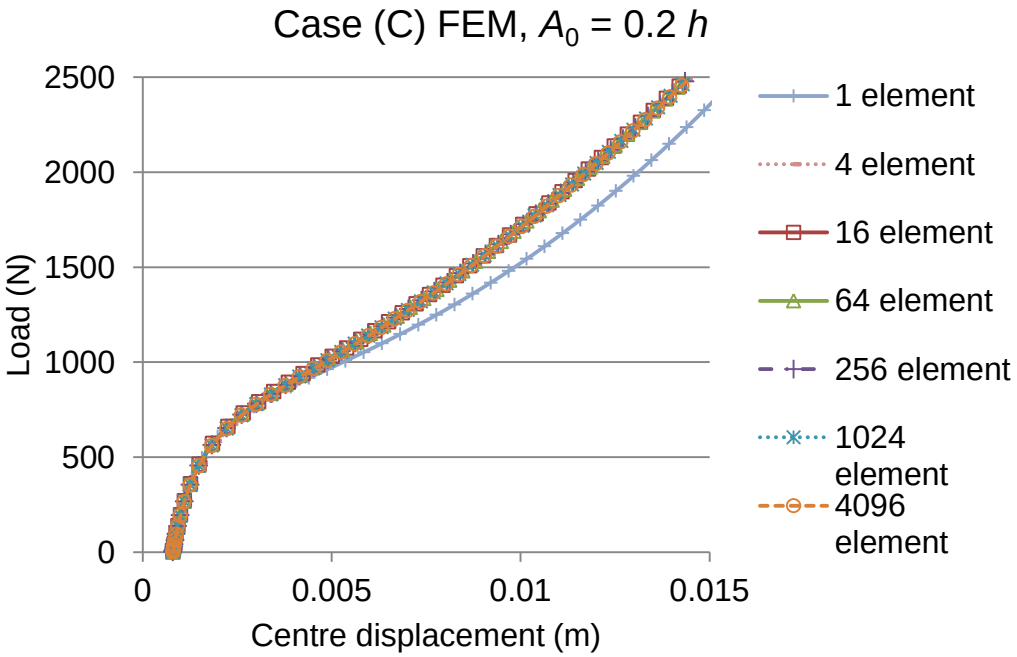

Figure 2-10: Convergence of FEM case C post-buckling plot with mesh refinement.

The analytical and FEM model post-buckling results for the corrugated paperboard panel are presented in Figure 2-11, as resultant applied load v. deflection amplitude plots.

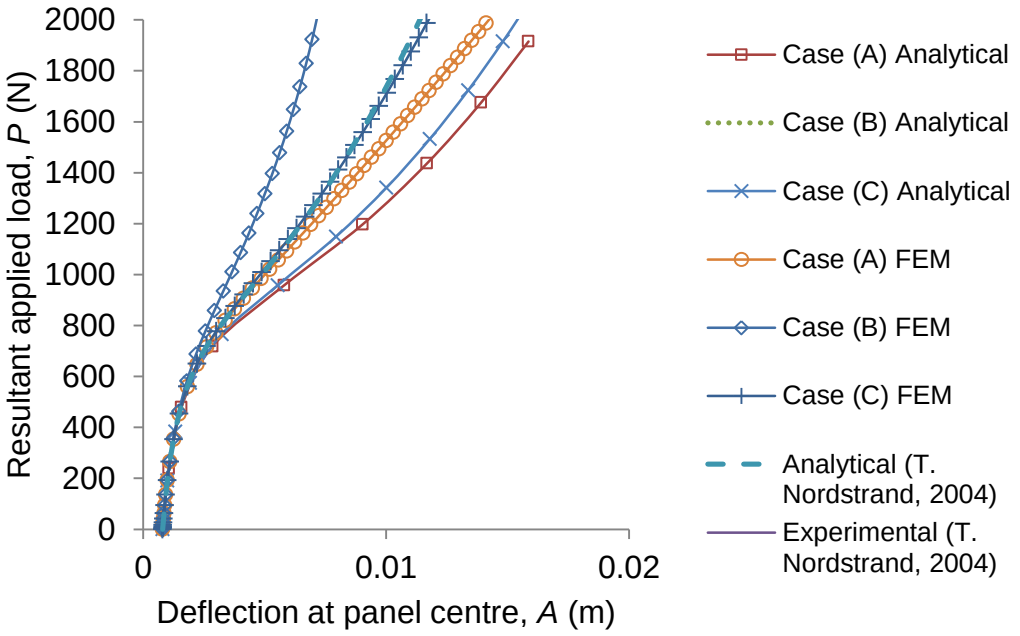

Figure 2-11: Post-buckling load v. deflection amplitude plots for analytical cases A and B, and FEM case A, B and C with analytical and experimental results of (Nordstrand, 2004a).

The post-buckling plots have the same initial panel centre displacement but the reference experimental plot of (Nordstrand, 2004a) shows comparatively larger deflections than all the analytical and numerical post-buckling plots with increasing load. The analytical cases generally show larger deflections than the FEM plots of the same panel in-plane boundary conditions.

The analytical case A plot shows the closest agreement with the experimental post-buckling plot (Nordstrand, 2004a). The case A panel in-plane boundary condition is the least constrained among the cases modelled with uniformly distributed loading along the loaded edges and free in-plane movement along the unloaded edges, so larger deflections than other cases are expected.

The analytical post-buckling plot for case B extends to the left side of the reference analytical plot from (Nordstrand, 2004a) beyond the critical load and remains close to the reference analytical plot.

The analytical post-buckling plot for case C is similar to the analytical plot of case A, but has slightly lower deflections. Case C has panel in-plane boundary conditions as described for the panel from (Nordstrand, 2004a).

The FEM analytical post-buckling plots are similar to each other up to a load of about 600 N. The FEM plot for case A extends to larger deflection amplitudes with higher loads. The case A FEM plot is closest among the FEM cases to the experimental plot (Nordstrand, 2004a).

The case B FEM plot shows the least deflection of all the plots. The panel in-plane-boundary condition for case B is the most constrained with all the panel edges moving uniformly in-plane.

The FEM plot for case C is similar to the reference analytical plot (Nordstrand, 2004a), which is expected since they model the same in-plane-boundary conditions of uniform displacement along the loaded edges and free in-plane movement along the unloaded edges.

The difference between the FEM and analytical post-buckling plots are likely due to the single-layered material model in FEM not accounting for corrugated paperboard having different material properties in flexural and in-plane directions.

The post-buckling plots for all the cases are presented again in Figure 2-12 in non-dimensional form, with deflection given in terms of the panel thickness, *h*, and the applied load as a ratio of the first critical load.

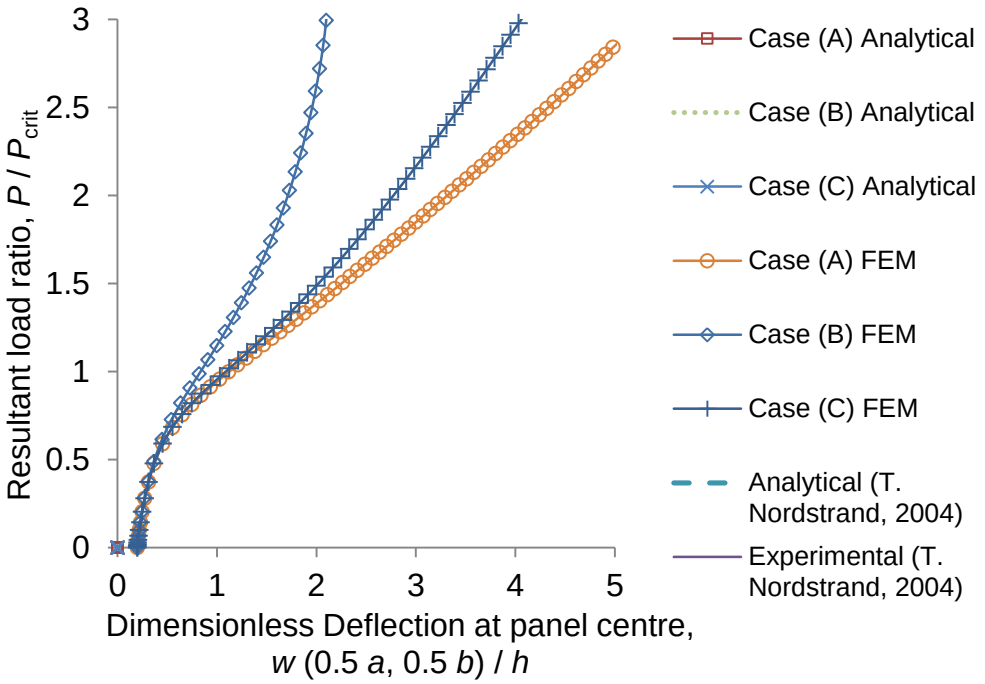

Figure 2-12: Dimensionless post-buckling plots for cases A, B and C.

A noticeable difference in the non-dimensional post-buckling plots is that the analytical and FEM plots of case A are shown as being closer to the experimental reference plot than in the dimensional plot. This is due to the difference in the buckling loads of the experimental and modelling plots. Otherwise, the order of the plots for the different cases modelled in relation to the reference plots remains the same.

The failure loads for the FEM models obtained from the *general, static* analyses using the Tsai-Wu failure criterion are presented in Table 2-8. The maximum Tsai-Wu failure index for the panels occurred at the upper left corners of the model, near the loaded and unloaded edges. The deflection amplitudes at the failure are also shown in Table 2-8.

The FEM failure loads do not compare well, being 95% for case A, 224% for case B and 158% for case C, above the reference experimental value of (Nordstrand, 2004a). The deflection amplitudes at failure for the FEM models for cases A and C were more similar, at about 53%and 57% above the reference experimental value respectively. The deflection at failure

load for case B was negative but of a similar magnitude as the reference analytical deflection.

Table 2-8: Failure loads and deflection amplitudes for FEM cases A, B and C.

Case	Model	Failure load (N)	% Difference failure load	Deflection amplitude at failure load (m)	% Difference failure deflection amplitude
(A)	FEM	2331.47	95.10%	0.0171	52.98%
(B)	FEM	3875.86	224.34%	-0.0069	-161.81%
(C)	FEM	3085.06	158.16%	0.0175	57.24%
(C)	Analytical (Nordstrand, 2004a)	1265.00	5.86%	0.0070	-37.20%
(C)	Experiment (Nordstrand, 2004a)	1195.00	0.00%	0.0112	0.00%

The failure loads of the FEM models vary between the cases because of the panel in-plane boundary conditions, with case A failing at lower loads than cases B and C. The case A boundary condition was least constrained in-plane, which resulted in large out-of-plane deflection and a lower failure load. The case B boundary condition was the most constrained in-plane of the cases, with the least out-of-plane deflections, which lead to a higher failure load. The case C boundary condition had deflection values in between cases A and B, and similarly a failure load between those of cases A and B.

The likely reason for the large difference in the FEM failure models and experimental results is that the strength values assigned in the failure stress definition of the single-layered equivalent corrugated paperboard FEM material model, only apply to the paperboard's outer facing layers. Improvements to the material modelling of the paperboard strength appears necessary if a FEM single layer model is to be used.

Based on the results for the critical loads of the analytical and FEM cases modelled, the effect of variation in in-plane boundary conditions does not

appear to cause a large difference between the cases. The post-buckling plots for both the analytical and FEM models however show the case A in-plane boundary condition has the closest agreement with the experimental plot. The experimental result of (Nordstrand, 2004a) was described as having the same the panel boundary condition as case C, which is a less constrained in-plane boundary condition than case A. The difference between analytical and experimental results could possibly be attributed to differences in-plane boundary conditions but this implies the loaded edges are not fully constrained to move at constant displacement. This may be possible if the loaded edges are damaged during the test and thus have a weak strip that allows normal displacements to vary in the in-plane normal directions. However, in such a case the out-of-plane boundary condition may also be more flexible than the assumed simply supported conditions.

It is possible that the panel boundary conditions for the experimental result have not been accurately described or strictly enforced by the experimental method in (Nordstrand, 2004a). The panel's out-of-plane boundary conditions have not been altered in the current models and the influence of variation in this on the post-buckling plot could also be considered.

However, the difference between the analytical and FEM post-buckling plots show the material model for the corrugated paperboard also has a large influence on the post-buckling results. The differences between corrugated paperboard and the material models used in the current analytical and FEM approaches, illustrated in Figure 2-13, could be likened to a truss being modelled as a composite beam section with facings and a homogenous core, and as a homogenous beam section of the same flexural stiffness respectively.

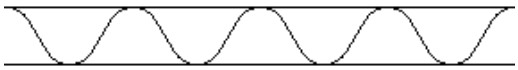

Corrugated paperboard profile

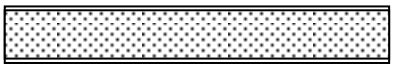

Analytical approach - Laminated orthotropic plate with homogenous core (Nordstrand, 2004a)

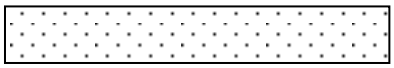

FEM approach - Equivalent homogenous orthotropic plate

Figure 2-13: Comparison of material models of corrugated paperboard in the analytical and FEM approaches.

The analytical approach used the material definition from (Nordstrand, 2004a), which has overall elastic in-plane constants calculated using the material properties of the layers in the corrugated paperboard and geometry of the corrugated paperboard profile. The calculation uses classical laminate theory for orthotropic plates, considering the corrugated paperboard as a laminated sandwich, with the corrugated core treated as a homogenous layer. The same flexural stiffness of corrugated paperboard as in (Nordstrand, 2004a) was used.

The material definition used for the FEM approach was a single layered homogenous shell section with overall elastic in-plane material constants calculated from flexural stiffness of the corrugated paperboard in (Nordstrand, 2004a) using orthotropic thin plate theory.

Therefore, the analytical material model has different stiffness for the in-plane membrane and the bending behaviours of the corrugated paperboard, which the FEM material model does not account for.

The study into the reasons for discrepancy between experimental buckling results and analytical results for a simply supported uniaxially compressed corrugated paperboard panel could consider the impact of a multi-term analytical solution compared to the single term results and changes in the

material modelling of the corrugated paperboard. The effects of variations in the out-of-plane boundary condition may also need to be considered, in order to determine what loading and boundary conditions applied to the corrugated paperboard panel, most resemble the experimental buckling panel boundary conditions.

2.4 Concluding remarks

2.4.1 Critical loads

Shortcomings in the material models of corrugated paperboard were the likely cause of the discrepancy between the critical loads of the analytical and Finite Element models and reference experimental values. Another possibility is some inaccuracies in the modelling of the experimental out-of-plane boundary conditions.

2.4.2 Post-buckling plots

Variation of in-plane boundary conditions could account for some difference between the reference experimental plot and the modelled post-buckling plots, but the material models used for corrugated paperboard have a more significant influence on the results.

2.5 Summary

The work presented was aimed at studying one of the potential reasons for the discrepancy between analytical and experimental results for the buckling problem of a simply supported uniaxially compressed corrugated paperboard panel. The focus was on the effect of the in-plane boundary conditions.

Analytical single-term Galerkin and numerical FEM approaches were taken to model slight variation of in-plane boundary conditions for the buckling problem, to study the effect of in-plane boundary conditions on the critical load and post-buckling behaviour. Three different combinations of in-plane boundary conditions were modelled: (A) uniform load intensity

with free normal in-plane movement and shear free on all edges; (B) uniform compression, with constant normal in-plane movement and shear free on all edges; and (C) uniform compression, free normal in-plane movement on unloaded edges, and shear free on all edges. The analytical approach included a novel application to corrugated paperboard of analogous out-of-plane clamped-clamped beam functions for the Airy stress function to approximately satisfy the in-plane free normal movement boundary conditions in cases A and C.

Comparison of critical loads from the analytical and numerical FEM results of cases A, B and C, to the results in (Nordstrand, 2004a), showed close agreement to the analytical value, but were 16% to 18% above the experimental value.

Post-buckling load v. deflection amplitude plots for the analytical models show case A had closest agreement with the experimental plot, followed by case C. The analytical plot for case B was closer to the reference analytical plot.

The case A FEM plot was closest among the FEM cases to the experimental plot (Nordstrand, 2004a). The FEM case B had the lowest panel deflections of the post-buckling plots. The FEM case C was more similar to the analytical plot in (Nordstrand, 2004a).

The difference between the reference experimental plot and the modelled post-buckling plots may be attributable to slight variation of in-plane boundary conditions, but the material models used for corrugated paperboard appear to have a more significant influence on the results.

Further work could be done to reduce the discrepancy by considering a multi-term analytical solution, material modelling of corrugated paperboard and changes to the out-of-plane boundary conditions to resemble experimental conditions. These will be presented in the following chapters.

3 Effect of multi-term out-of-plane displacement function and geometric imperfection on post-buckling of corrugated paperboard panels

3.1 Introduction

In the previous chapter, one possible reason for discrepancy between experimental buckling results and analytical results, namely the effect of different in-plane boundary conditions was considered. This chapter examines the impact of using multi-term displacement functions on panel post-buckling behaviour. The load vs. displacement response is known to be influenced by the initial out-plane geometric imperfection present in a panel, but the interaction between different modes of imperfection does not appear to have been studied well, even for isotropic plates and is therefore worthy of further study.

The following research questions are investigated:

- How is the load vs. displacement post-buckling plot influenced by higher mode (multi-term) out-of-plane displacement shape functions?
- How is the post-buckling plot affected by symmetric and / or anti-symmetric modes of geometric imperfection in the panel and the out-of plane displacement function?

The difference in displacement amplitudes for single-term, four-term (products of two terms in each coordinate direction) and nine-term (product of three terms in the x, y directions) results for the buckling of imperfect isotropic plates are found in Table 1 of (Ilanko, 2002).

The non-dimensional numerical results presented in (Ilanko, 2002), show four-term and nine-term displacement amplitudes for an initially perfectly

flat isotropic plate do not differ from the single term displacement at critical buckling load. However, with the same plate at four times the critical load, four-term and nine-term displacement amplitudes differ from the single term result by 5.5 % and 5.4% respectively.

When the plate has fundamental mode imperfection amplitude of plate thickness, at critical load, both four-term and nine-term displacement amplitudes differ from the single-term solution by 1.1%. At four times the critical load, the four-term and nine-term displacements differ from the single-term solution of the same imperfect plate by 4.7% and 4.7% respectively.

These show that the difference between multi-term and single-term solutions increase significantly with the load ratio particularly above the lowest critical load. The order of difference with a multi-term solution for the corrugated panel with slight imperfection modelled in the work could be estimated to be in the order of about 1% at the critical load and about 2.5% at twice the critical load. However, the previous study did not consider a mix of asymmetric and anti-symmetric terms as the imperfection applied was only in the fundamental symmetric mode.

3.2 Methods of Study

The methods used in addressing the research questions are presented in the following section. Multi-term forms of the analytical Galerkin's method buckling models for the in-plane boundary condition case A from Chapter 2, for the same paperboard panel from (Nordstrand, 2004a), were created using *MATLAB* software. The analytical equations and material property data shown in Chapter 2, sections 2.2.1 and 2.2.2 should be referred to for further details.

The Finite Element (FE) model of the paperboard panel from (Nordstrand, 2004a), created in *Abaqus,* for the in-plane boundary case A from Chapter 2 is also used, with the introduction of different geometric out-of-plane imperfections modes in the *general, static* post-buckling analysis. The

procedure for introducing geometric imperfections into the panel FE model is detailed in Appendix I.

The analytical model of the paperboard panel of Chapter 2 is extended with the inclusion of higher mode shapes in planar *x*- and *y*-directions in the out-of-plane displacement function, *w* (m) and initial out-of-plane imperfection, w_0 (m).

$$w = \sum_i \sum_j A_{i,j}\, sin\left(\frac{i\pi x}{a}\right) sin\left(\frac{j\pi y}{b}\right),$$

Equation 3-1

where $A_{i,\,j}$ is the deflection amplitude, i = 1 … i_{max}, j = 1 … j_{max}, i_{max} is the maximum value of i and j_{max} the maximum value of j.

$$w_0 = \sum_i \sum_j A_{0\,i,j}\, sin\left(\frac{i\pi x}{a}\right) sin\left(\frac{j\pi y}{b}\right),$$

Equation 3-2

where $A_{0\,i,\,j}$ is the initial imperfection amplitude, i = 1 … i_{max}, j = 1 … j_{max}.

The compatibility condition between Airy stress functions *F* (N m) and *w*, w_0 below, for an orthotropic plate is satisfied.

$$\frac{\boldsymbol{1}}{\boldsymbol{E_{22}^*}}\frac{\boldsymbol{\partial^4 F}}{\boldsymbol{\partial x^4}} + \left(\frac{\boldsymbol{1}}{\boldsymbol{G_{12}^*}} - \frac{\boldsymbol{2\nu_{12}^*}}{\boldsymbol{E_{11}^*}}\right)\frac{\boldsymbol{\partial^4 F}}{\boldsymbol{\partial x^2 \partial y^2}} + \frac{\boldsymbol{1}}{\boldsymbol{E_{11}^*}}\frac{\boldsymbol{\partial^4 F}}{\boldsymbol{\partial y^4}} = \boldsymbol{h}\left(\frac{\boldsymbol{\partial^2 w}}{\boldsymbol{\partial x\,\partial y}}\right)^2 - \frac{\boldsymbol{\partial^2 w}}{\boldsymbol{\partial x^2}}\frac{\boldsymbol{\partial^2 w}}{\boldsymbol{\partial y^2}} - \left[\left(\frac{\boldsymbol{\partial^2 w_o}}{\boldsymbol{\partial x\,\partial y}}\right)^2 - \frac{\boldsymbol{\partial^2 w_o}}{\boldsymbol{\partial x^2}}\frac{\boldsymbol{\partial^2 w_o}}{\boldsymbol{\partial y^2}}\right]$$

Equation 3-3

Substitution of Equations 3-1 and 3-2 into the right side of Equation 3-3 gives:

$$\frac{\mathbf{1}}{\boldsymbol{E_{22}^{*}}}\frac{\boldsymbol{\partial^4 F}}{\boldsymbol{\partial x^4}}+\left(\frac{\mathbf{1}}{\boldsymbol{G_{12}^{*}}}-\frac{\boldsymbol{2v_{12}^{*}}}{\boldsymbol{E_{11}^{*}}}\right)\frac{\boldsymbol{\partial^4 F}}{\boldsymbol{\partial x^2 \partial y^2}}+\frac{\mathbf{1}}{\boldsymbol{E_{11}^{*}}}\frac{\boldsymbol{\partial^4 F}}{\boldsymbol{\partial y^4}}$$
$$= h\sum_i\sum_j\sum_k\sum_l\left(\frac{ijkl\pi^4}{a^2b^2}\right)\left(A_{i,j}\,A_{k,l}\right.$$
$$\left.-A_{0\,i,j}\,A_{0\,k,l}\right)\frac{1}{2}\left[cos\left(\frac{(i+k)\pi x}{a}\right)cos\left(\frac{(j-l)\pi y}{b}\right)\right.$$
$$\left.+cos\left(\frac{(i-k)\pi x}{a}\right)cos\left(\frac{(j+l)\pi y}{b}\right)\right]$$

Equation 3-4

where i = 1 … i_{max}, j = 1 … j_{max}, k = 1 … i_{max}, l = 1 … j_{max}.

The same stress function F using characteristic clamped-clamped beam vibration deflection functions to model case A as in Chapter 2 is used,

$$F = F_o + F_z;$$

Equation 3-5

where F_o is the stress function due to in-plane displacement and F_z the stress function due to out-of-plane displacement.

$$\boldsymbol{F_o = -N_y\,x^2/2;}$$

Equation 3-6

$$F_z = \sum_i\sum_j\sum_k\sum_l\sum_p\sum_q \alpha_{p,q,i,j,k,l}\,\varphi_p(x)\psi_q(y),$$

Equation 3-7

where p, q = 1, 2, 3, 4, 5 and i = 1 … i_{max}, j = 1 … j_{max}, k = 1 … i_{max}, l = 1 … j_{max}.

$$\varphi_p(x) = cosh\left(\frac{\lambda_p x}{a}\right)-\frac{cosh(\lambda_p)-cos(\lambda_p)}{sinh(\lambda_p)-sin(\lambda_p)}sinh\left(\frac{\lambda_p x}{a}\right)-cos\left(\frac{\lambda_p x}{a}\right)$$
$$+\frac{cosh(\lambda_p)-cos(\lambda_p)}{sinh(\lambda_p)-sin(\lambda_p)}sin\left(\frac{\lambda_p x}{a}\right)$$

Equation 3-8

$$\psi_q(y) = cosh\left(\frac{\lambda_q y}{b}\right) - \frac{cosh(\lambda_q) - cos(\lambda_q)}{sinh(\lambda_q) - sin(\lambda_q)} sinh\left(\frac{\lambda_q y}{b}\right) - cos\left(\frac{\lambda_q y}{b}\right) + \frac{cosh(\lambda_q) - cos(\lambda_q)}{sinh(\lambda_q) - sin(\lambda_q)} sin\left(\frac{\lambda_q y}{b}\right)$$

Equation 3-9

The clamped-clamped beam eigenvalues in Chapter 2, Table 2-5 are used for λ_p and λ_q. The coefficients $\alpha_{p,q,i,j,k,l}$ in the series for F_z were determined by solving the compatibility equation, Equation 3-4, using the Galerkin's method, multiplying with a weighting function $\varphi_r(x)\ \psi_s(y)$, of the same form as the characteristic beam functions, where r, s = 1, 2 … 5, and integrating twice with respect to x and y.

The following equation results for each combination of r and s, giving a system of linear equations to determine $\alpha_{p,q,i,j,k,l}$

$$\int_{x=0}^{x=a}\int_{y=0}^{y=b}\sum_i\sum_j\sum_k\sum_l\left[\frac{1}{E_{22}^*}\sum_p\sum_q \alpha_{p,q,i,j,k,l}\frac{\partial^4\varphi_p(x)}{\partial x^4}\psi_q(y) + \left(\frac{1}{G_{12}^*} - \frac{2v_{12}^*}{E_{11}^*}\right)\sum_p\sum_q \alpha_{p,q,i,j,k,l}\frac{\partial^2\varphi_p(x)}{\partial x^2}\frac{\partial^2\psi_q(y)}{\partial y^2} + \frac{1}{E_{11}^*}\sum_p\sum_q \alpha_{p,q,i,j,k,l}\,\varphi_p(x)\frac{\partial^4\psi_q(y)}{\partial y^4}\right]\varphi_r(x)\,\psi_s(y)\,dx\,dy = h\int_{x=0}^{x=a}\int_{y=0}^{y=b}\sum_i\sum_j\sum_k\sum_l\left[\left(\frac{ijkl\pi^4}{a^2b^2}\right)(A_{i,j}\,A_{k,l} - A_{0\,i,j}\,A_{0\,k,l})\frac{1}{2}\left(cos\left(\frac{(i+k)\pi x}{a}\right)cos\left(\frac{(j-l)\pi y}{b}\right) + cos\left(\frac{(i-k)\pi x}{a}\right)cos\left(\frac{(j+l)\pi y}{b}\right)\right)\right]\varphi_r(x)\,\psi_s(y)\,dx\,dy$$

Equation 3-10

where p, q = 1, 2, 3, 4, 5 and i = 1 … i_{max}, j = 1 … j_{max}, k = 1 … i_{max}, l = 1 … j_{max}.

The static equilibrium equation for an orthotropic plate below is then satisfied for various values of the loading intensity, N_y

$$D_{11}^{*}\frac{\partial^4(w-w_0)}{\partial x^4}+2(D_{12}^{*}+2D_{66}^{*})\frac{\partial^4(w-w_0)}{\partial x^2y^2}+D_{22}^{*}\frac{\partial^4(w-w_0)}{\partial y^4}$$
$$=\frac{\partial^2 w}{\partial x^2}\frac{\partial^2 F}{\partial y^2}+\frac{\partial^2 w}{\partial y^2}\frac{\partial^2 F}{\partial x^2}-2\frac{\partial^2 w}{\partial x\partial y}\frac{\partial^2 F}{\partial x\partial y}$$

Equation 3-11

The solution of the equilibrium equation by the Galerkin's method with a weighting function of sin ($m\ \pi\ x\ /\ a$) sin ($n\ \pi\ y\ /\ b$), where m = 1 … i_{max}, n = 1 … j_{max}, results in the following equation for each combination of m and n:

$$f_{m,n}=\int_0^a\int_0^b\left[D_{11}^{*}\frac{\partial^4(w-w_0)}{\partial x^4}+2(D_{12}^{*}+2D_{66}^{*})\frac{\partial^4(w-w_0)}{\partial x^2y^2}+D_{22}^{*}\frac{\partial^4(w-w_0)}{\partial y^4}\right.$$
$$-\left(\frac{\partial^2 w}{\partial x^2}\frac{\partial^2 F}{\partial y^2}+\frac{\partial^2 w}{\partial y^2}\frac{\partial^2 F}{\partial x^2}\right.$$
$$\left.\left.-2\frac{\partial^2 w}{\partial x\partial y}\frac{\partial^2 F}{\partial x\partial y}\right)\right]\sin\left(\frac{m\pi x}{a}\right)\sin\left(\frac{n\pi y}{ab}\right)dy\,dx=0$$

Equation 3-12

The above function for each m and n combination gives a system of non-linear cubic equations, in terms of the unknown deflection amplitude, $A_{i,j,}$, solved iteratively using the Newton-Raphson method, for a given load intensity, N_y. Initial values are given for $A_{i,j}$, then iterations are made using the following linear system of equations until the error in $A_{i,j}$ and $f_{m,n}$ is zero within the specified tolerance.

$$\left[\frac{\partial f_{m,n}}{\partial A_{i,j}}\right]\{\Delta A_{i,j}\}=\{f_{m,n}\}$$

Equation 3-13

3.2.1 Single-term vs. Multi-term Post-buckling Analysis

For the multi-term analytical Galerkin's models, symmetric modes of w (i, j, k, l, m, n = 1, 3 …) are used to compare between multi-term and single-

term displacement function post-buckling solutions. The influence of the panel's initial geometric out-of-plane imperfection on the single- vs. multi-term post-buckling results is also considered.

Table 3-1: Symmetric out-of-plane displacement modes *i* and *j*, and first symmetric geometric imperfection modelled for single- vs. multi-term post-buckling comparison.

Symmetric Multi-term Case	First symmetric imperfection $A_{0\,1,1}$	Displacement modes in *x*-direction *i*	Displacement modes in *y*-direction *j*
1(i)	0.2 *h*	1	1
1(ii)	0.2 *h*	1, 3	1
1(iii)	0.2 *h*	1	1, 3
1(iv)	0.2 *h*	1, 3	1, 3
1(v)	0.2 *h*	1, 3, 5	1
1(vi)	0.2 *h*	1	1, 3, 5
1(vii)	0.2 *h*	1, 3, 5	1, 3
1(viii)	0.2 *h*	1, 3	1, 3, 5
1(ix)	0.2 *h*	1, 3, 5	1, 3, 5
2(i)	0.02 *h*	1	1
2(ii)	0.02 *h*	1, 3	1
2(iii)	0.02 *h*	1	1, 3
2(iv)	0.02 *h*	1, 3	1, 3
2(v)	0.02 *h*	1, 3, 5	1
2(vi)	0.02 *h*	1	1, 3, 5
2(vii)	0.02 *h*	1, 3, 5	1, 3
2(viii)	0.02 *h*	1, 3	1, 3, 5
2(ix)	0.02 *h*	1, 3, 5	1, 3, 5
3(i)	0.000025 *h*	1	1
3(ii)	0.000025 *h*	1, 3	1
3(iii)	0.000025 *h*	1	1, 3
3(iv)	0.000025 *h*	1, 3	1, 3
3(v)	0.000025 *h*	1, 3, 5	1
3(vi)	0.000025 *h*	1	1, 3, 5
3(vii)	0.000025 *h*	1, 3, 5	1, 3
3(viii)	0.000025 *h*	1, 3	1, 3, 5
3(ix)	0.000025 *h*	1, 3, 5	1, 3, 5

Table 3-1 lists the combinations of symmetric *x*- and *y*-direction modes of the out-of-plane displacement amplitude $A_{i,\,j}$ modelled and the first symmetric geometric imperfection amplitudes $A_{0\,1,\,1}$ relative to the panel thickness *h*. These cases have the first symmetric geometric imperfection

of 0.2 *h*, 0.02 *h* and 0.000025 *h*, and symmetric modes in *w* range from 1 to 5 in the *x*- and *y*-directions.

The out-of-plane displacement at the panel centre with increasing applied load will be compared for the symmetric multi-term analytical models. The displacement is presented non-dimensionally relative to the panel thickness, *h*, while the non-dimensional load is relative to the first critical load $P_{\text{crit } 1,1}$.

3.2.2 Geometric Imperfections in symmetric and anti-symmetric modes

The interactions between symmetric and anti-symmetric out-of-plane geometric imperfection and buckling modes are studied by comparison of panel displacement at loads corresponding to different buckling modes.

The multi-term analytical Galerkin's model above is used, this time including even modes (*i*, *j*, *k*, *l*, *m*, *n* ≥ 1, 2 …) also. Different combinations of symmetric and anti-symmetric geometric imperfections amplitude are modelled.

The imperfection modes modelled were the lowest symmetric and anti-symmetric buckling modes, since imperfection in these modes are thought to be critical to the post-buckling response.

The analytical model of the buckling panel included the imperfection modes and amplitudes listed in Table 3-2. The out of-plane displacement function has up to five terms in the *y*-direction (direction of loading) including anti-symmetric displacement modes. FE models of the panel with the same imperfections as in the analytical cases were also created for comparison.

Table 3-2: Symmetric / anti-symmetric modes of geometric imperfection modelled for multi-term post-buckling in *MATLAB*.

Symmetric / Anti-symmetric Imperfection Case	First symmetric imperfection $A_{0\,1,1}$	First anti-symmetric imperfection $A_{0\,1,2}$	Displacement modes in *x*-direction *i*	Displacement modes in *y*-direction *j*
4(i)	0.2 *h*	0	1	1, 2
4(ii)	0.2 *h*	0	1	1, 2, 3
4(iii)	0.2 *h*	0	1	1, 2, 3, 4
4(iv)	0.2 *h*	0	1	1, 2, 3, 4, 5
4(v)	0.2 *h*	0	1, 2	1, 2
4(vi)	0.2 *h*	0	1, 2, 3	1, 2, 3
4(vii)	0.2 *h*	0	1, 2, 3, 4	1, 2, 3, 4
4(viii)	0.2 *h*	0	1, 2, 3, 4, 5	1, 2, 3, 4, 5
5(i)	0	0.2 *h*	1	1, 2
5(ii)	0	0.2 *h*	1	1, 2, 3
5(iii)	0	0.2 *h*	1	1, 2, 3, 4
5(iv)	0	0.2 *h*	1	1, 2, 3, 4, 5
5(v)	0	0.2 *h*	1, 2	1, 2
5(vi)	0	0.2 *h*	1, 2, 3	1, 2, 3
5(vii)	0	0.2 *h*	1, 2, 3, 4	1, 2, 3, 4
5(viii)	0	0.2 *h*	1, 2, 3, 4, 5	1, 2, 3, 4, 5
6(i)	0.2 *h*	0.1 *h*	1	1, 2
6(ii)	0.2 *h*	0.1 *h*	1	1, 2, 3
6(iii)	0.2 *h*	0.1 *h*	1	1, 2, 3, 4
6(iv)	0.2 *h*	0.1 *h*	1	1, 2, 3, 4, 5
6(v)	0.2 *h*	0.1 *h*	1, 2	1, 2
6(vi)	0.2 *h*	0.1 *h*	1, 2, 3	1, 2, 3
6(vii)	0.2 *h*	0.1 *h*	1, 2, 3, 4	1, 2, 3, 4
6(viii)	0.2 *h*	0.1 *h*	1, 2, 3, 4, 5	1, 2, 3, 4, 5
7(i)	0.2 *h*	0.2 *h*	1, 2	1, 2
7(ii)	0.2 *h*	0.2 *h*	1, 2, 3	1, 2, 3
7(iii)	0.2 *h*	0.2 *h*	1, 2, 3, 4	1, 2, 3, 4
7(iv)	0.2 *h*	0.2 *h*	1, 2, 3, 4, 5	1, 2, 3, 4, 5

3.3 Results and Discussion

3.3.1 Single-term vs. multi-term post-buckling for symmetric fundamental imperfection mode

The dimensionless post-buckling plots of symmetric multi-term cases presented below show the panel centre out-of-plane displacement *w*(0.5 *a*,

0.5 *b*) relative to the panel thickness *h* with the applied resultant load relative to the first critical load P / P_{crit}.

Figure 3-1 shows post-buckling plots for the symmetric multi-term cases 1(i) to 1(ix) which have a geometric imperfection of 0.2 *h* in the first symmetric out-of-plane displacement mode. The panel centre displacements of cases 1(i) to 1(ix) for different number of modes in the out-of-plane displacement function *w*, are similar up to the first critical load, but differ for loads above this. The plots for cases with the same number of modes in the loading *y*-direction are similar.

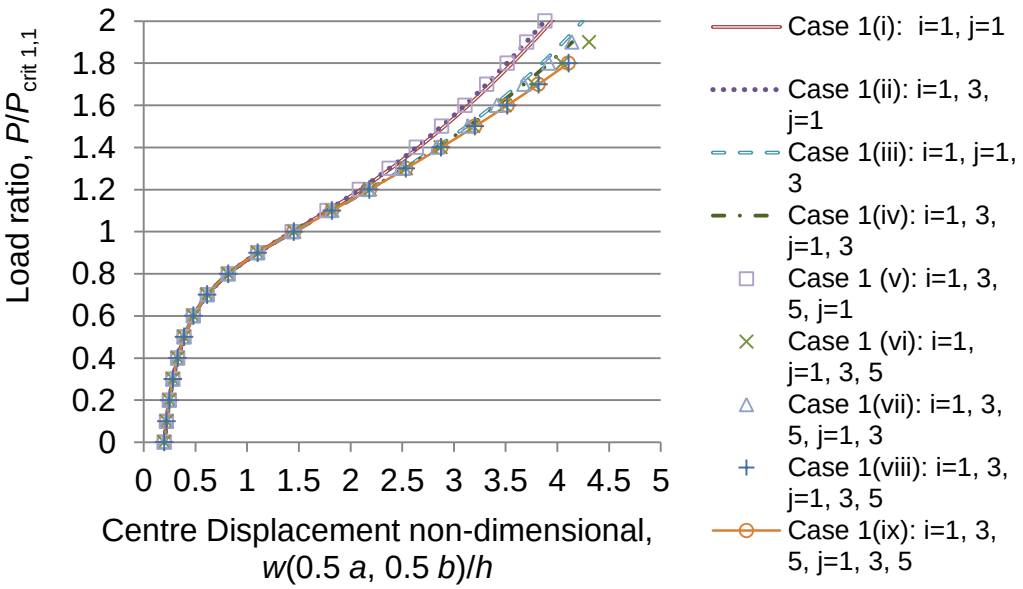

Figure 3-1: Post-buckling of paperboard panel from (Nordstrand, 2004a) with geometric imperfection, $A_{0\ 1,1}$ = 0.2 *h*, and multiple symmetric terms in the out-of-plane displacement function *w*.

The percentage differences in the panel centre out-of-plane displacement for these cases compared to the single-term case with the same imperfection are shown in Table II-1 in Appendix II.

Below the critical load, the multi-term cases 1(ii) to 1(ix) vary from the single-term displacement result up to about 1%, similar to what was found for the isotropic panel result of (Ilanko, 2002).

The displacements for the multi-term cases, above the first critical load, are larger than the single term results for the cases considered, except for cases 1(ii) and 1(v) which were smaller. These cases had only a single displacement mode in the loading *y*-direction.

The other cases generally show that if more modes are included in the out-of-plane displacement function *w*, particularly in the loading *y*-direction, the greater the difference in displacement relative to the single-term result. It is noted however, that case 1(viii) which has more displacement modes in the loading *y*-direction than the unloaded *x*-direction, had a slightly higher displacement for load ratios above 1.6, compared to case 1(ix) which has an equal number of modes in the *x*- and *y*-direction.

At a load ratio of 1.8, the four-term case 1(iv) and nine-term case 1(ix) panel centre displacements differ from the single-term value by 9.98% and 15.29% respectively. This was about four and seven times the hypothetical difference predicted based on the isotropic results from (Ilanko, 2002).

The value of *j*, the number of modes in the loading direction, causes more significant change to the post-buckling load-displacement relationship. The value of *i*, the number of modes in the direction transverse to loading, has less effect on the post-buckling relationship. However, it is necessary to have a sufficient number of modes in the transverse direction for accurate modelling of the stress distribution in the panel. The number of displacement modes required for accuracy in the post-buckling result would depend of the boundary conditions and the geometry or aspect ratio of the panel being modelled.

The most number of symmetric displacement modes attempted in this work was *i, j* = 1, 3, 5, 7, only for the imperfection amplitude of 0.2 *h*. The analysis was computationally costly and the panel centre displacement result had a level of agreement within 0.03% of the result of the case with *i, j* = 1, 3, 5, up to a load ratio of 1.8 times the critical load.

Two other imperfection amplitudes are given to the panel to investigate their influence on the multi-term post-buckling results.

Figure 3-2 shows the post-buckling plot for the panel of the same paperboard material with a smaller out-of-plane imperfection of 0.02 *h* cases 2(i) to 2(ix). There is again some difference in multi-term displacements compared to the single-term result that becomes noticeable above the first critical load.

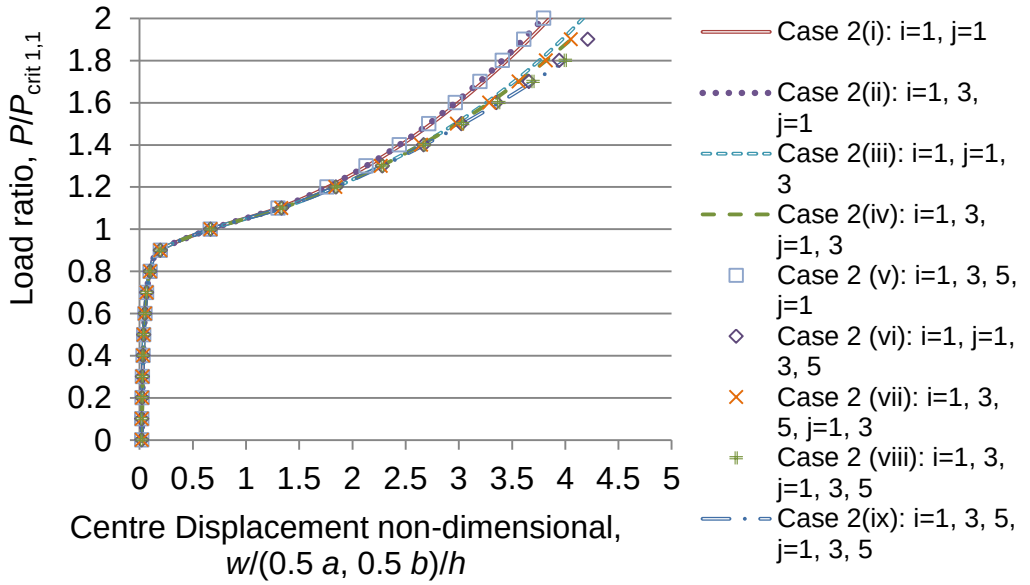

Figure 3-2: Post-buckling of paperboard panel from (Nordstrand, 2004a) with geometric imperfection, $A_{0\ 1,1}$ = 0.02 *h*, and multiple symmetric terms in the out-of-plane displacement function *w*.

Table II-2 in Appendix II compares the panel centre out-of-plane displacement between the single-term case 2(i) and cases 2(ii) to 2(ix). The magnitude of difference in the displacements is smaller and negative for cases 2(ii) and 2(v) which have one displacement mode in the loading *y*-direction, as with the previous imperfection amplitude. The differences in displacements for these multi-term cases compared to single-term results are similar to those in the previous imperfection amplitude but appear from above a higher load ratio of 0.8. This is expected since the initial panel imperfection is ten times smaller than those in cases 1(i) to 1(ix).

The displacements for the cases 2(ii) to 2(ix) differ from the single-term case 2(i) by up to 0.23% at the critical load. At a load ratio of 1.8, the four-term case 2(iv) and nine-term case 2(ix) have displacements 10.66% and 15.96% higher than case 2(i) respectively. Next, Figure 3-3 shows the post-buckling plot for the same panel with a relatively small out-of plane imperfection of 0.000025 *h* multi-term cases 3(i) to 3(ix). The plot shows near zero displacement, not varying among cases below critical load, then a sudden increase in displacement beyond the critical load.

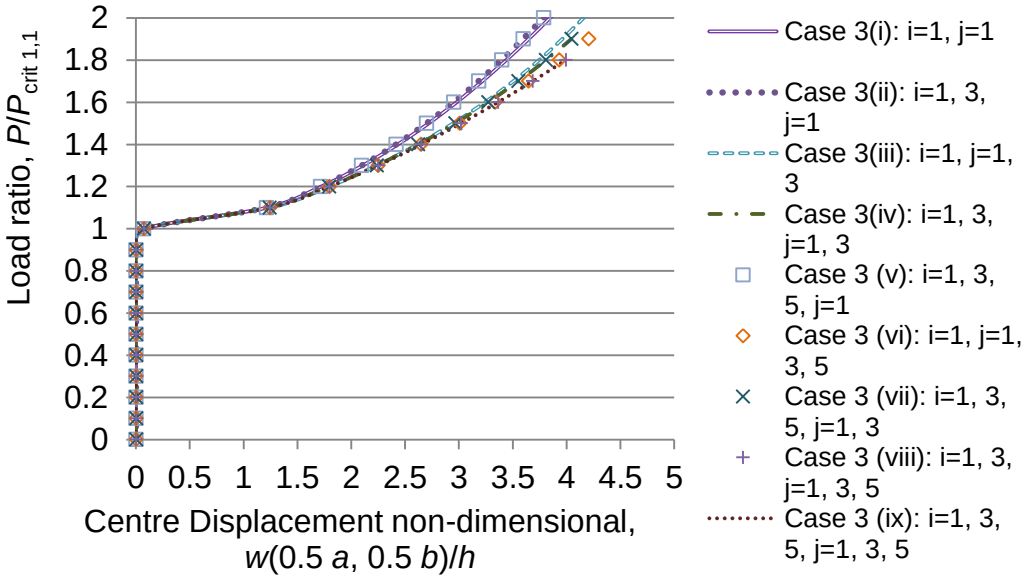

Figure 3-3: Post-buckling of paperboard panel from (Nordstrand, 2004a) with geometric imperfection, $A_{0\ 1,1}$ = 0.000025 *h*, and multiple symmetric terms in the out-of-plane displacement function *w*.

The percentage difference of centre displacements of these cases compared to the single term case 3(i) of the same imperfection are listed in Table II-3 in Appendix II. The difference at given load ratio are of similar magnitude to the previous cases 2(i) to 2(ix), when comparing cases with the same number of displacement modes.

As before, the cases with only a single displacement mode in the loading *y*-direction cases 3(ii) and 3(v) show a smaller and negative percentage difference. The displacements for the cases 3(ii) to 3(ix) differ from the single-term case 3(i) up to 2.23% at load ratio 1.1. At a load ratio of 1.8,

the four-term case 3(iv) and nine-term case 3(ix) have displacements 10.74% and 16.04% higher than case 3(i) respectively.

In Figure 3-4, the post-buckling plots of cases 1(i), 1(iv), 1(ix), cases 2 (i), 2(iv), 2(ix) and cases 3(i), 3(iv), 3(ix) are shown on the same graph. The plots of different initial imperfection but with the same number of out-of-plane displacement modes appear to converge towards each other with increasing load above the critical load before diverging above a load ratio of 1.4.

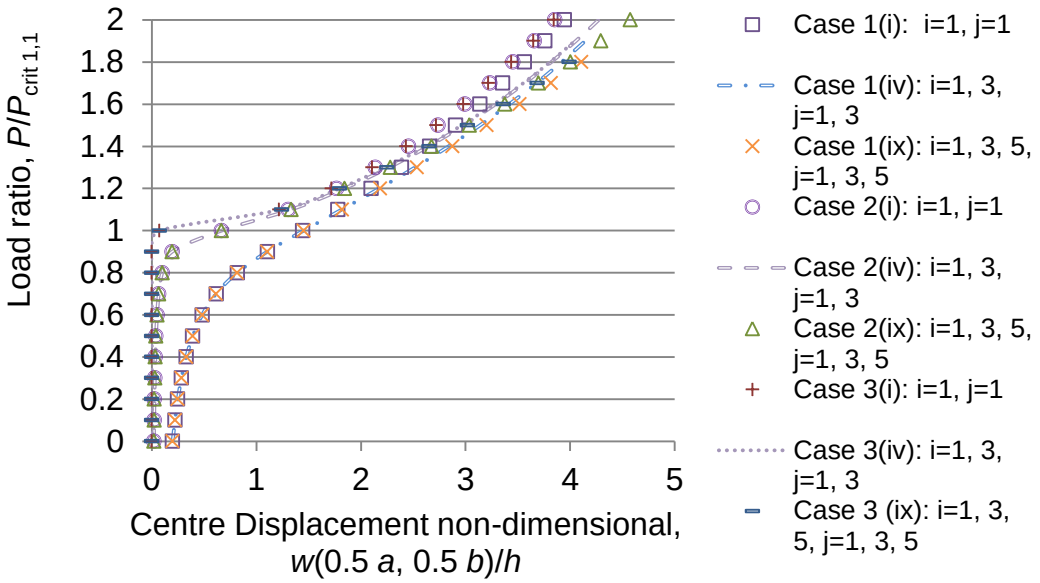

Figure 3-4: Post-buckling of paperboard panel from (Nordstrand, 2004a) with geometric imperfection and multiple symmetric terms in the out-of-plane displacement function *w*, cases 1(i), 1(iv), 1(ix) with $A_{0\,1,1}$ = 0.2 *h*, cases 2 (i), 2(iv), 2(ix) with $A_{0\,1,1}$ = 0.02 *h* and cases 3(i), 3(iv), 3(ix) with $A_{0\,1,1}$ = 0.000025 *h*.

The out-of-plane displacement and Tsai-Wu failure index contour plots for case 1(ix), the symmetric nine-term panel model with $A_{0\,1,1}$ = 0.2 *h* are shown in Figure 3-5, at failure load ratio 1.8 or load 1724 N. The peak out-of-plane displacement of 0.0165 m occurs in the panel centre and the peak Tsai-Wu failure index of 1.08 occurs in corner regions.

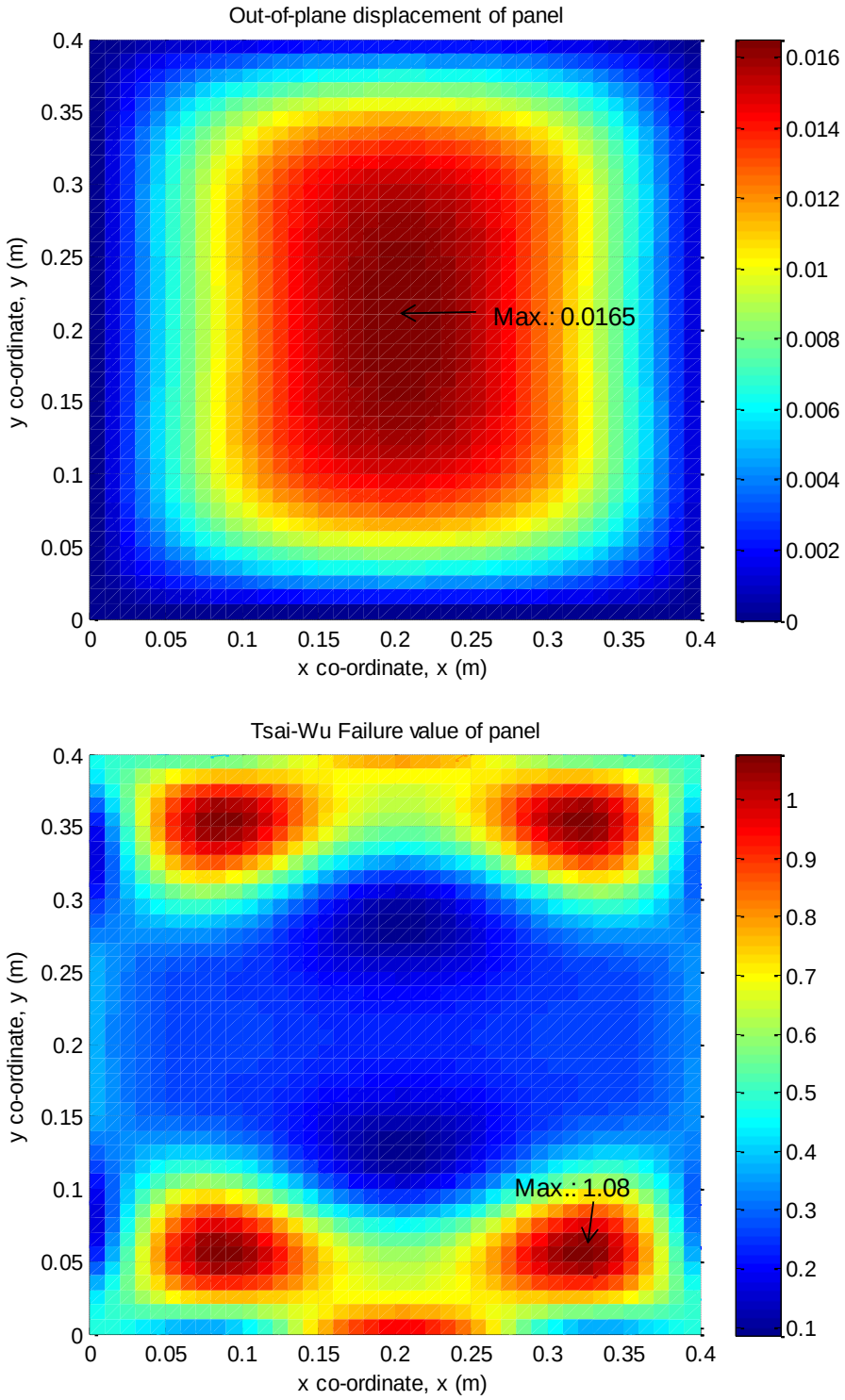

Figure 3-5: Out-of-plane displacement and Tsai-Wu failure index contour plots at the failure load ratio 1.8 or load 1724 N, for analytical symmetric multi-term model Case 1(ix), for paperboard panel from (Nordstrand, 2004a) with imperfection $A_{0\,1,1}$ = 0.2 *h*.

It was found that the Tsai-Wu failure index contour plots are influenced by the number of modes used in the panel's out-of-plane displacement function. This was supported by the difference in the Tsai-Wu contour plots among the cases of the same geometric imperfection but different number of out-of-plane displacement modes. Tsai-Wu contour plots for other cases were generated but are not presented in the thesis as failure analysis has not been carried out.

Figure II-1 and Figure II-2 in Appendix II show the out-of-plane displacement and Tsai-Wu failure index contour plots for cases 2(ix) and 3(ix), symmetric nine-term panel models with $A_{0\ 1,1}$ = 0.02 h and $A_{0\ 1,1}$ = 0.000025 h respectively, at failure load ratio 1.8 or load 1724 N. The contour plots for cases 2(ix) and 3(ix) are similar to case 1(ix), but lower peak value displacements of 0.016 m and Tsai-Wu failure index of 1.03 are reached.

3.3.2 Geometric imperfections with multi-term symmetric and anti-symmetric displacement modes

The previous section compared post-buckling results for cases with symmetric modes only in the multi-term displacement function. In this section, the effect of including anti-symmetric modes in the displacement function w for the same panel is considered. It was found that for panels with either symmetric or anti-symmetric only imperfection, including both symmetric and anti-symmetric modes in the displacement function has no effect on the results compared to when only modes of the same type as the imperfection are in the displacement function. If there are both symmetric and anti-symmetric imperfections present, the number of symmetric and anti-symmetric displacement modes included has an effect on the results due to interactions between the mode types.

3.3.2.1 Symmetric imperfection mode

First, the effect of anti-symmetric displacement modes on panels with symmetrical imperfection will be considered.

For symmetric / anti-symmetric cases 4(i), 4(ii), 4(iii) and 4(iv) the panel is given a symmetric imperfection $A_{0\ 1,\ 1} = 0.2\ h$ and the out-of-plane displacement function w has multiple symmetric and anti-symmetric modes only in the loading y-direction.

Figure 3-6 shows dimensionless post-buckling plots for the symmetric / anti-symmetric cases 4(i) to 4(iv) along with the symmetric multi-term cases 1(i), 1(iii) and 1(iv), which have the same imperfection but with only symmetric modes in w. The Finite Element (FE) post-buckling result for the same panel and imperfection amplitude is also plotted.

The cases 1(i) and 4(i), cases 1(iii), 4(ii) and 4(iii), and cases 1(vi) and 4(iv) have similar post-buckling plots since they differ in the inclusion of anti-symmetric displacement modes in cases 4, but have the same symmetric displacement modes. The FE plot is similar to the other plots up to a load ratio of 0.7, and then appears linear above this load ratio.

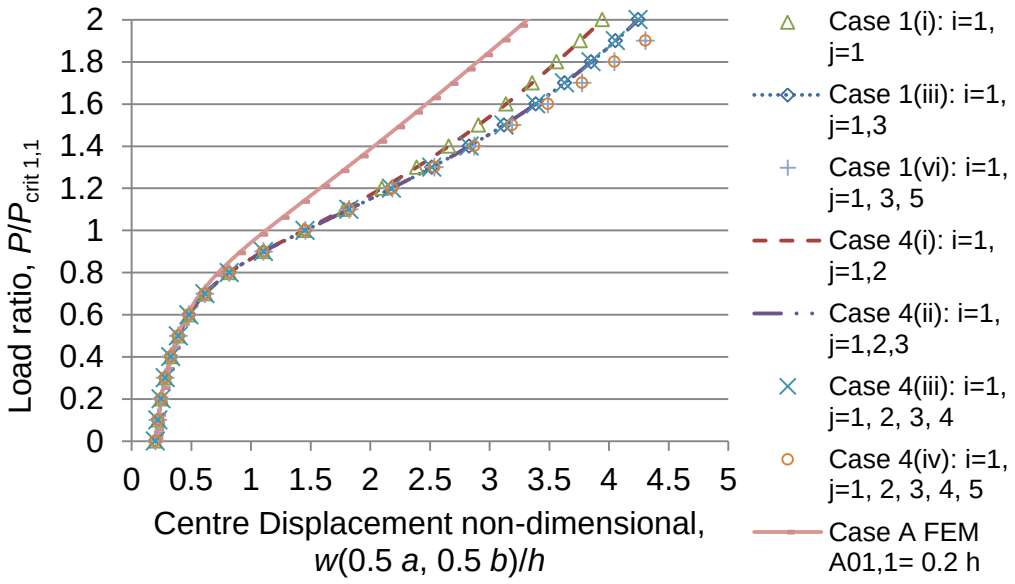

Figure 3-6: Post-buckling paperboard panel from (Nordstrand, 2004a) with geometric imperfection $A_{01,1} = 0.2\ h$, with multiple symmetric only or symmetric and anti-symmetric modes of out-of-plane displacement function w, $i = 1$ and j_{max} up to 5.

The out-of-plane displacement at the panel centre for these cases compared to case 1(i) are shown in Table II-4 in Appendix II. The centre displacement of cases 1(iii), 4(ii) and 4(iii) differ from case 1(i) by 0.85% at critical load and 8.11% at load ratio 1.8. Cases 1(vi) and 4(iv) differ from case 1(i) by 0.92% at critical load and 13.61% at load ratio 1.8. The FE panel centre displacement is generally lower than the analytical values, being less than case 1(i) by 21.94% at critical load and 18.67% at load ratio 1.8.

Figure 3-7 shows a similar plot comparing single-term case 1(i) with symmetric/anti-symmetric multi-term cases 4(v), 4(vi), 4(vii) and 4(viii), and symmetric multi-term cases 1(iv) and 1(ix), which have the same number of terms in the unloaded *x*- and loaded *y*-directions. Cases 1(i) and 4(v), cases 1(iv), 4(vi) and 4(vii), and cases 1(ix) and 4(viii) also have similar post-buckling plots since they only differ in the inclusion of anti-symmetric displacement modes in cases 4.

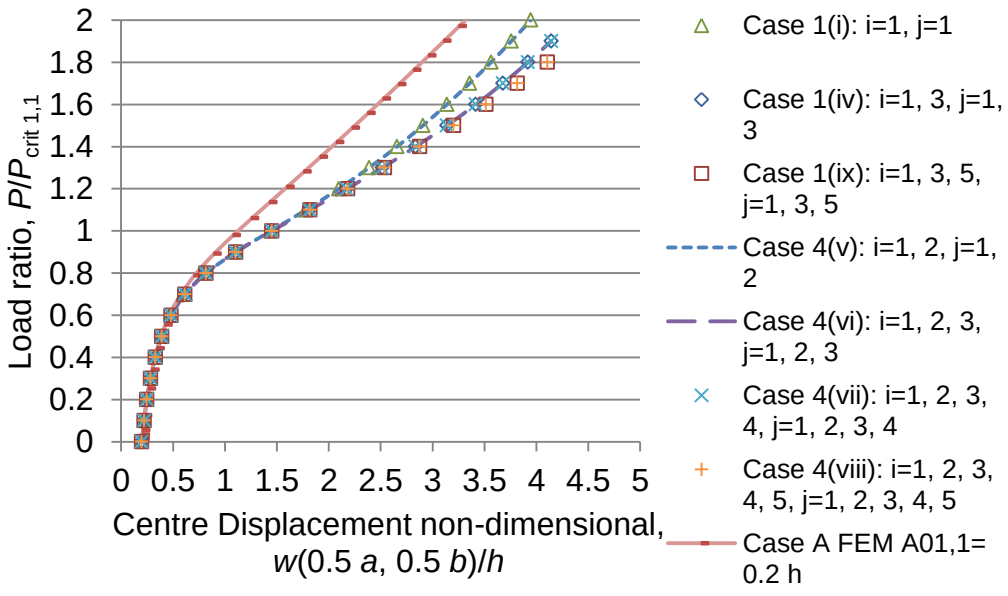

Figure 3-7: Post-buckling paperboard panel from (Nordstrand, 2004a) with geometric imperfection $A_{0\ 1,1}$ = 0.2 *h*, with the same number of symmetric only or symmetric and anti-symmetric modes of out-of-plane displacement function *w* in the unloaded *x*- and loaded *y*-directions.

The out-of-plane displacement at the panel centre for these cases compared to case 1(i) are shown in Table II-5 in Appendix II The centre displacement of cases 1(iv), 4(vi) and 4(vii) differ from case 1(i) by 0.63% at critical load and 9.98% at load ratio 1.8. Cases 1(ix) and 4(viii) differ from case 1(i) by 0.71% at critical load and 15.29% at load ratio 1.8.

The FE model is not limited to a specific number of displacement mode shapes, unlike with the analytical models, so some difference is expected. There is however a difference in the definition of the corrugated paperboard material in the FE model may account for the difference between FE and analytical results obtained. In the FE model, the material is modelled as orthotropic with elastic properties Young's moduli, shear modulus and Poisson's ratio calculated from flexural properties.

It is apparent that the central out-of-plane displacements are identical among cases 1 and 4, particularly for cases with the same symmetric displacement modes. However, the contributions of particular displacement modes to the panel out-of-plane displacement can be further examined.

Table II-6 in Appendix II shows the dimensionless out-of-plane displacement amplitudes at different load ratios, for the cases 1(i) and 4(i), cases 1(iii), 4(ii) and 4(iii), with symmetric only or symmetric and anti-symmetric displacement modes of i = 1 and j = 1 up to 4.

The amplitudes of the (1, 1) displacement mode for case 1(i) with i and j=1 and anti-symmetric case 4(i) with i = 1 and j = 1, 2 are the same. The nonzero displacement modes (1, 1) and (1, 3) above load ratio 0.6, for symmetric case 1(iii) and symmetric and anti-symmetric cases 4(ii) with i = 1 and j = 1 to 3, and symmetric and anti-symmetric case 4(iii) with i = 1 and j = 1 to 4, are also the same.

The dimensionless post-buckling results for cases 1(vi) and 4(iv), with symmetric only or symmetric and anti-symmetric displacement modes i = 1 and j = 1 to 5, are shown in Table II-7 in Appendix II. These show that only

the out-of-plane displacement modes (1, 1), (1, 3) above load ratio 0.6, and (1, 5) above critical load are nonzero.

Similarly, for cases with the same number of modes in the *x*- and *y*-directions, with *i* and j = 1 up to 5, comparisons of dimensionless out-of-plane displacement amplitudes at given load ratio are made between symmetric only or symmetric and anti-symmetric cases in Table II-8, Table II-9, Table II-10, Table II-11, Table II-12 and Table II-13 in Appendix II. It was found that only displacement modes (1, 1), (1, 3), (1, 5), (3, 1), (3, 3), (3, 5), (5, 1) and (5, 3) contribute to the panel displacement.

Table II-8 in Appendix II shows only mode (1, 1) is nonzero for symmetric case 1(i) with *i* and *j* = 1 and symmetric and anti-symmetric case 4(v) with *i* and *j* = 1, 2.

Table II-9 and Table II-10 in Appendix II show that for symmetric case 1(iv) and symmetric and anti-symmetric cases 4(vi) with *i* and *j* =1 to 3, and symmetric and anti-symmetric case 4(vii) with *i* and *j* = 1 to 4 the displacement modes (1, 1), (1, 3) above load ratio 0.6, (3, 1) above load ratio 0.7, and (3, 3) above critical load are nonzero.

Similarly, Table II-11, Table II-12 and Table II-13 in Appendix II show that displacement modes (1, 1), (1, 3) above load ratio 0.6, (1, 5) above critical load, (3, 1) above load ratio 0.7, (3, 3) above critical load, (3, 5) above load ratio 1.3, (5, 1) above load ratio 1.3, and (5, 3) above load ratio 1.5 are nonzero for symmetric case 1(ix) with *i* and *j* = 1 to 5, and symmetric and anti-symmetric case 4(viii) with *i* and *j* = 1 to 5.

These results show that in case 1 and 4, since the panel imperfection is symmetric, only the number of symmetric modes in the displacement function *w* is influential on the panel out-of-plane displacement. The anti-symmetric displacement modes included in cases 4(i) to 4(iv) do not contribute significantly to the panel displacement.

3.3.2.2 Anti-symmetric imperfection mode

Next, the effect of including symmetrical displacement modes for panels with anti-symmetrical imperfection is examined.

For symmetric / anti-symmetric cases 5(i) to 5(viii), the same panel is given an imperfection of the same amplitude 0.2 *h* but in an anti-symmetric mode $A_{0\,1,\,2}$.

Figure 3-8 shows the dimensionless post-buckling plots for cases 5(i) to 5(viii) and the FE plot for the same panel, with displacements taken at the location (*x*, *y*) = (0.5 *a*, 0.25 *b*). The analytical plots obtained are very similar, with cases 5(i), 5(ii), and 5(v), cases 5(iii) and 5(iv), and cases 5(vii) and 5(viii) having the same displacements since they have the same anti-symmetric displacement modes. However, the FE plot deviates from the other results from a load ratio of about 0.5.

Table II-14 in Appendix II compares the displacements of cases 5(ii) to 5(viii) and the FE model with those of case 5(i). The cases 5(i), 5(ii), and 5(v) have the same displacement, since they have a similar number of anti-symmetric displacement modes in the loaded *y*-direction. It is noted for case 5(v), the additional anti-symmetric displacement mode in the *x*-direction has not altered the displacement values from case 5(i).

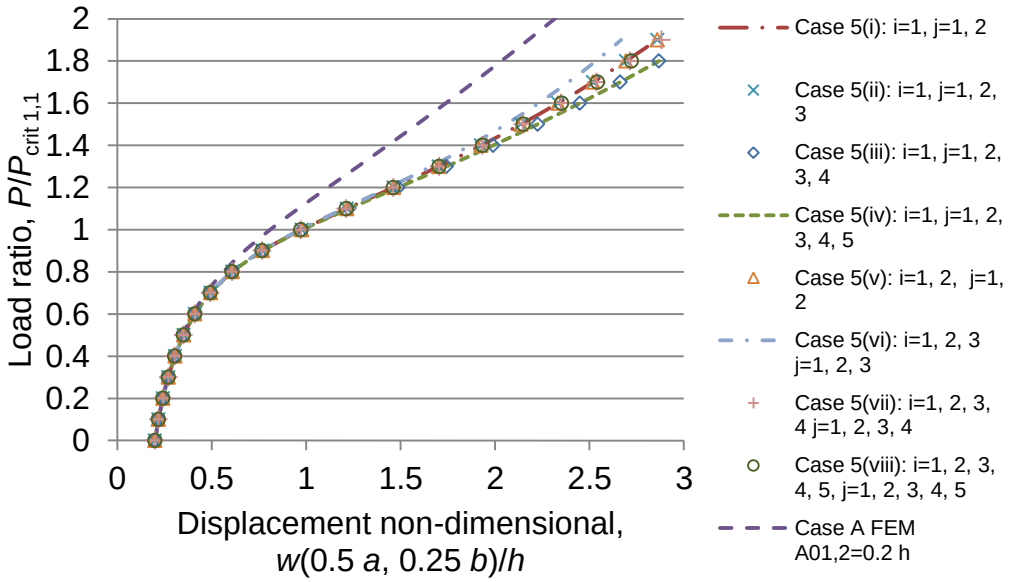

Figure 3-8: Post-buckling for paperboard panel from (Nordstrand, 2004a) with anti-symmetric geometric imperfection $A_{0\ 1,2}$ = 0.2 *h*, including symmetric and anti-symmetric out-of-plane displacement modes.

Cases 5(iii) and 5(iv) have the same displacements and the same number of anti-symmetric displacement modes in the *y*-direction. These cases differ from case 5(i) by 0.42% at the critical load and 6.49% at a load ratio of 1.8.

Case 5(vi) shows smaller displacements than case 5(i), differing by -0.84% at critical load and -5.91% at a load ratio of 1.8. This case has only one anti-symmetric term in each of the *x*- and *y*-directions.

Cases 5(vii) and 5(viii) have similar displacements up to a load ratio of 0.7, beyond which case 5(viii) has slightly higher displacements. These cases have the same number of anti-symmetric displacement modes in the *x*- and *y*-directions. Cases 5(vii) and 5(viii) differ from case 5(i) by -0.41% and -0.40% respectively at critical load and 0.80% and 1.08% respectively at a load ratio of 1.8.

The FE displacements for the panel with the same imperfection are comparatively smaller than the analytical cases. The FE result differs from case 5(i) by -17.07% at critical load and -24.52% at a load ratio of 1.8. The difference between the results predicted using the analytical and FE

models is much more significant than the differences due to effect of the imperfection amplitude and number of displacement modes among the analytical model cases. The major contributing factor to this discrepancy is that the material models, specifically, the in-plane elastic properties of corrugated paperboard, are defined differently in the two modelling method. Also, the accuracy in the solutions from the analytical models are limited by the number of panel displacement modes allowed, unlike the solution of the FE models.

Table II-15 in Appendix II shows the dimensionless out-of-plane displacement amplitudes at different load ratios, for cases 5(i) to 5(iv) with i = 1, j = 1 up to 5. Only modes (1, 2) and (1, 4) above load ratio 0.7 are nonzero.

Table II-16, Table II-17, Table II-18 and Table II-19 in Appendix II show dimensionless out-of-plane displacement amplitudes at different load ratios, for cases 5 (v) to 5(viii), with the same number of displacement modes in the x- and y-direction, i and j =1 up to 5. Only the displacement modes (1, 2), (1, 4), (3, 2), (3, 4), (5, 2) and (5, 4) contribute to the overall panel displacement.

The displacement amplitudes of case 5(v) with i and j = 1, 2, shown in Table II-16 in Appendix II are nonzero only for mode (1, 2). Case 5(vi) with i and j = 1, 2, 3 also has nonzero modes of (1, 2) and (3, 2) above load ratio 0.6.

Table II-17 in Appendix II shows that case 5(vii) with i and j = 1, 2, 3, 4, has nonzero modes of (1, 2), (1, 4) above load ratio 0.7, (3, 2) above load ratio 0.6 and (3, 4) above load ratio 1.2.

The displacement amplitudes for case 5(viii) with i and j = 1, 2, 3, 4, 5 in Table II-18 and Table II-19 in Appendix II are nonzero for modes (1, 2), (1, 4) above load ratio 0.8, (3, 2) above load ratio 0.6, (3, 4) above load ratio 1.2, (5, 2) above load ratio 1.2, and (5, 4) above load ratio 1.8.

These results confirm that anti-symmetric displacement amplitudes are the same among cases with the same number of contributing anti-symmetric displacement modes. The symmetric displacement modes contribute little to panel displacement in these cases since the initial panel imperfection was anti-symmetric.

From the observations above, it may be deduced that if initial imperfections are purely of the symmetric type the inclusion of anti-symmetric displacement modes has little influence on the post-buckling result and vice versa.

3.3.2.3 Mixed symmetric and anti-symmetric imperfection modes

Now, we consider the situation where the initial imperfection shape is mixed, both symmetric and anti-symmetric.

Symmetric imperfection mode and smaller magnitude anti-symmetric imperfection mode

The results for symmetric / anti-symmetric cases 6(i) to 6(viii) which have a combination of symmetric and anti-symmetric modes of panel imperfection $A_{0\,1,\,1} = 0.2\,h$ and $A_{0\,1,\,2} = 0.1\,h$ are presented below.

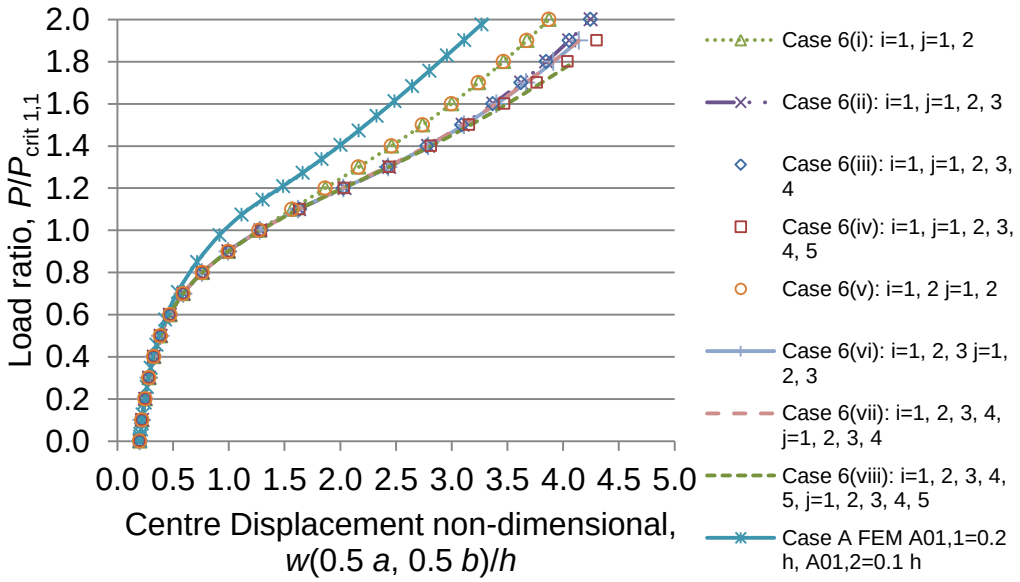

Figure 3-9: Post-buckling paperboard panel from (Nordstrand, 2004a) with symmetric and anti-symmetric geometric imperfection $A_{0\ 1,1} = 0.2\ h$, $A_{0\ 1,2} = 0.1\ h$ with symmetric and anti-symmetric modes of out-of-plane displacement function w.

Figure 3-9 shows the dimensionless post-buckling plots for cases 6(i) to 6(viii) and the FE plot for the same panel and initial imperfection. The plots are similar for cases 6(i) and 6(v), cases 6(ii) and 6(iii), cases 6(vi) and 6(vii), and cases 6(iv) and 6(viii). The displacements are generally larger with increasing number of out-of-plane displacement modes, particularly in the *y*-direction. The FE plot deviates from the other cases above a load ratio of 0.4.

Comparisons of the panel centre displacements for the analytical case 6(i) with cases 6(ii) to 6(viii) and the FE model of the panel of the same imperfection are made in Table II-20 in Appendix II.

Case 6(v) has the same displacements as Case 6(i), since they have the same symmetric displacement mode (1, 1).

Cases 6(ii) and 6(iii) have the same displacements up to a load ratio of 0.3 and have fairly similarly displacements at higher loads. These cases differ from case 6(i) by 0.91% and 1.35% at the critical load, and 11.07% and 11.01% at a load ratio of 1.8 respectively. These cases differ only in the inclusion of the mode (1,4) in case 6(iii).

Likewise, cases 6(vi) and 6(vii) have the same displacements up to a load ratio of 0.5, with similar displacements at higher loads. These cases differ from case 6(i) by 0.54% and 1% at the critical load, and 12.97% and 12.92% at a load ratio of 1.8 respectively. The cases differ in the inclusion of the fourth mode in *i* and *j* of the displacement function in case 6(vii).

Cases 6(iv) and 6(viii) are most similar to each other but differ in panel centre displacements values. These cases differ from case 6(i) by 1.51% and 1.15% at the critical load, and 16.69% and 18.41% at a load ratio of 1.8 respectively. Both these cases have five displacement modes in *y*-direction but case 6(iv) has only one displacement mode in the *x*-direction.

The FE displacements for the panel with the same imperfection are comparatively smaller than the analytical cases. The FE result differs from case 6(i) by -24.26% at critical load and -16.50% at a load ratio of 1.8.

Table II-21 in Appendix II shows the dimensionless displacement amplitudes at different load ratios for cases 6(i) to 6(iv) with $i = 1$ and $j = 1$ up to 5. All the displacement modes included in the cases shown in Table II-21 (1, 1), (1, 2), (1, 3) above load ratio 0.6, (1, 4) above load ratio 0.7, and (1, 5) above load ratio 0.9 are non-zero. The displacement amplitudes in the modes (i, j) = (1, 1) and (1, 2) are the same between the cases up to a load ratio of 0.6. At higher loads, the additional modes included in the displacement function have an influence on the contribution of the modes to the panel displacement.

The displacement mode amplitudes for case 6(v) with i and $j = 1, 2$ and case 6(vi) with i and $j = 1$ to 3, are shown in Table II-22 in Appendix II. Case 6(v) has the same nonzero displacement mode amplitudes as case 6(i), modes (1, 1) and (1, 2). Case 6(vi) has the nonzero displacement modes (1, 1), (1, 2), (1, 3) above load ratio 0.6, (3, 1) above load ratio 0.7, (3, 2) above load ratio 0.7, and (3, 3) above critical load.

Table II-23 in Appendix II shows the displacement mode amplitudes for case 6(vii) with i and $j = 1$ to 4. The modes (1, 1), (1, 2), (1, 3) above load

ratio 0.6, (1, 4) above load ratio 0.7, (3, 1) above load ratio 0.7, (3, 2) above load ratio 0.7, (3, 3) above load ratio 0.9, and (3, 4) above load ratio 1.1 are nonzero.

The displacement mode amplitudes for case 6(viii) with *i* and *j* = 1 to 5 are given in Table II-24 and Table II-25 in Appendix II. This case has the following nonzero displacement modes: (1, 1), (1, 2), (1, 3) above load ratio 0.6, (1, 4) above load ratio 0.6, (1, 5) above load ratio 0.9, (3, 1) above load ratio 0.7, (3, 2) above load ratio 0.7, (3, 3) above critical load, (3, 4) above load ratio 1.1, (3, 5) above load ratio 1.3, (5, 1) above load ratio 1.3, (5, 2) above load ratio 1.6, and (5, 3) above load ratio 1.5.

The inclusions of additional higher displacement modes in the different cases appear to influence the amplitudes of lower displacement modes with initial imperfection. However, the symmetric (1, 1) mode remains the dominant displacement mode for cases 6(i) to 6(viii).

Next, interactions between symmetric and anti-symmetric modes are examined by comparing cases 4(viii), 5(viii) and 6(viii) which have symmetric and / or anti-symmetric initial imperfection modes and displacement modes *i* and *j* = 1 to 5.

The amplitudes of the nonzero symmetric modes (1, 1), (1, 3), (1, 5), (3, 1), (3, 3), (5, 1), and (5, 3), in cases 6(viii) and 4(viii) are compared in Table 3-3. The percentage difference in amplitudes of cases 4(viii) and 6(viii) are calculated relative to that of case 4(viii).

The amplitude of mode (1, 1) is initially the same for cases 4(viii) and 6(viii), with the imperfection $A_{0\ 1,\ 1}$ = 0.2 *h*. With increasing load up to critical load, the case 6(viii) displacement mode amplitude becomes increasing lower compared to case 4(viii). At critical load, the mode (1, 1) displacement amplitude for case 6(viii) is 12% lower than case 4(viii). Beyond the critical load, the difference in mode (1, 1) amplitudes of the cases decreases down to 0.2% difference at failure load.

Table 3-3: Comparison of nonzero symmetric displacement modes of case 6(viii) with case 4(viii)[1].

Load ratio	Difference in displacement mode amplitudes of Case 6(viii) relative to case 4(viii)							
$P/P_{crit\ 1,1}$	$A_{1,1}/h$	$A_{1,3}/h$	$A_{1,5}/h$	$A_{3,1}/h$	$A_{3,3}/h$	$A_{3,5}/h$	$A_{5,1}/h$	$A_{5,3}/h$
0	0.00%							
0.1	-0.07%							
0.2	-0.18%							
0.3	-0.37%							
0.4	-0.68%							
0.5	-1.23%							
0.6	-2.22%	-26.20%						
0.7	-4.01%	-28.60%		75.35%				
0.8	-6.87%	-32.95%		50.82%				
0.9	-10.15%	-37.52%		27.08%				
1	-12.09%	-38.67%	118.12%	11.07%	0.69%			
1.1	-11.43%	-33.90%	43.46%	2.98%	-12.31%			
1.2	-8.09%	-23.01%	9.03%	-0.08%	-13.69%			
1.3	-4.54%	-12.39%	-1.34%	-0.67%	-9.45%	24.60%	12.48%	
1.4	-2.37%	-6.15%	-2.50%	-0.58%	-5.50%	5.10%	9.22%	
1.5	-1.23%	-3.05%	-1.80%	-0.39%	-3.07%	0.70%	6.51%	0.09%
1.6	-0.65%	-1.56%	-1.09%	-0.25%	-1.71%	-0.19%	4.47%	-0.13%
1.7	-0.35%	-0.82%	-0.64%	-0.15%	-0.98%	-0.29%	3.01%	-0.14%
1.8	-0.19%	-0.45%	-0.37%	-0.09%	-0.58%	-0.23%	1.99%	-0.12%

[1] The grey background indicates that for one or both cases the dimensionless displacement was zero within three decimal places.

The other nonzero modes in the table show a large percentage difference in amplitude between the cases up to critical load. However, the absolute values of these displacement modes are relatively small below the critical load. The displacement amplitudes of case 6(viii) for these modes become closer to those of case 4(viii) above the critical load.

The amplitudes of the nonzero anti-symmetric modes (1, 2), (1, 4), (3, 2), (3, 4), (5, 2), and (5, 4), in cases 5(viii) and 6(viii) are compared in Table 3-4. The percentage difference in amplitudes of cases 5(viii) and 6(viii) are calculated relative to that of case 5(viii). In the comparison of mode (1, 2), the amplitude for case 6(viii) was doubled to account for the initial amplitude of case 5(viii) being twice that of case 6(viii).

The amplitudes of anti-symmetric mode (1, 2) for case 6(viii) show increasing disagreement with those of case 5(viii) with increasing load. The other anti-symmetric modes for case 6(viii) shown in Table 3-4 are also very different from case 5(viii). These differences show that in case 6(viii) with both symmetric and anti-symmetric imperfection, the symmetric modes have influenced the anti-symmetric displacement mode amplitudes. This gives further confirmation that the symmetric displacement mode is dominant in case 6(viii), though this may be due to the amplitude of the initial imperfection with the symmetric (1, 1) being twice that of anti-symmetric mode (1, 2).

Table 3-4: Comparison of nonzero anti-symmetric displacement modes of case 6(viii) with case 5(viii)[2].

Load ratio	Difference in displacement mode amplitudes of Case 6(viii) relative to case 5(viii) normalised by initial values					
$P/P_{crit\,1,1}$	$A_{1,2}/h$	$A_{1,4}/h$	$A_{3,2}/h$	$A_{3,4}/h$	$A_{5,2}/h$	$A_{5,4}/h$
0	0.00%					
0.1	-0.01%					
0.2	-0.02%					
0.3	-0.06%					
0.4	-0.13%					
0.5	-0.30%					
0.6	-0.69%					
0.7	-1.65%		-48.99%			
0.8	-3.94%	10.92%	-47.65%			
0.9	-8.77%	9.42%	-49.03%			
1	-16.95%	-0.34%	-54.01%			
1.1	-28.86%	-15.25%	-60.93%			
1.2	-44.91%	-33.47%	-68.61%	111.20%		
1.3	-60.64%	-52.15%	-76.04%	27.79%		
1.4	-72.16%	-66.76%	-81.94%	-18.76%		
1.5	-79.92%	-76.85%	-86.25%	-45.97%		
1.6	-85.14%	-83.63%	-89.36%	-62.63%	-87.13%	
1.7	-88.73%	-88.20%	-91.62%	-73.29%	-89.29%	
1.8	-91.25%	-91.33%	-93.30%	-80.39%	-90.92%	

Equal magnitude symmetric and anti-symmetric imperfection modes

The comparison of the anti-symmetric mode displacements for cases 6(viii) and 5(viii) could be biased by the difference in the initial imperfection given to mode (1, 2) as the imperfection is still dominated by a symmetric mode. Therefore, analytical cases 7(i) to 7(iv) were modelled, where the same imperfection amplitude was given to modes (1, 1) and (1, 2), $A_{0\,1,1} = 0.2\,h$,

[2] The grey background indicates that for one or both cases the dimensionless displacement was zero within three decimal places.

$A_{0\ 1,2}$ = 0.2 *h*, with displacement modes *i* and *j* = 1 up to 5. The same panel and geometric imperfection was modelled with FEM.

The dimensionless post-buckling plots for cases 7(i) to 7(iv) using displacements at the panel centre are shown in Figure 3-10. The peak displacement of the panel centre occurs near the critical load. There is a gradual decrease in the centre displacement above the critical load, showing that the overall out-of-plane displacement shape is becoming more anti-symmetric. The central displacement decreases as the load increases past the critical load because the mode shape has changed to become dominated by a higher order mode with a small centre displacement.

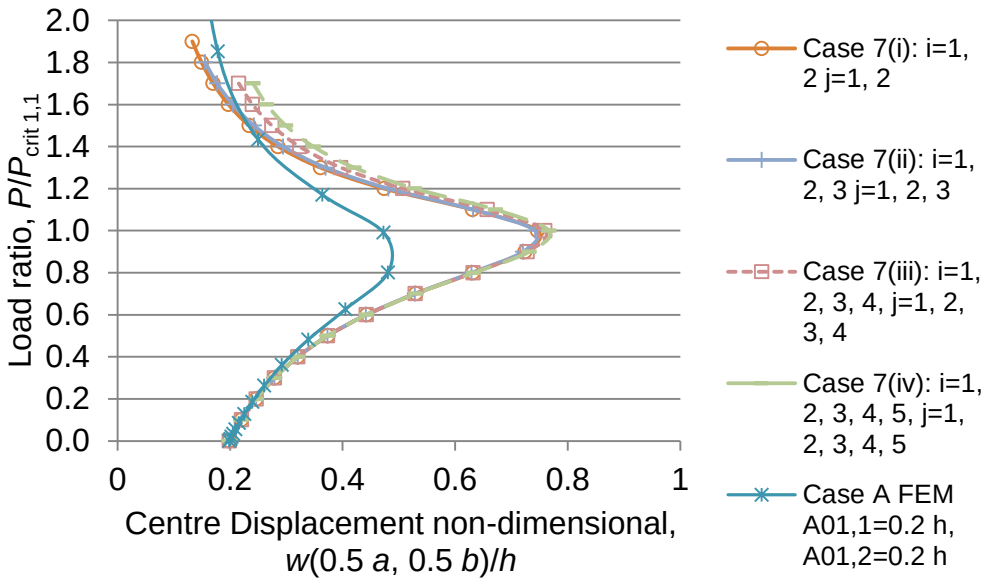

Figure 3-10: Post-buckling paperboard panel from (Nordstrand, 2004a) with symmetric and anti-symmetric geometric imperfection $A_{0\ 1,1}$ = 0.2 *h*, $A_{0\ 1,2}$ = 0.2 *h* with symmetric and anti-symmetric modes of out-of-plane displacement function *w*.

The analytical plots are similar to each other up to the critical load but deviate beyond critical load, the displacements being higher with increasing number of modes in the displacement function. The FE plot shows a similar trend of panel centre displacement increasing up to critical load and decreasing beyond critical load. The FE plot has generally lower displacements than the analytical plots from above a load ratio of 0.2, but

intersects the analytical plots of cases 7(i) and 7(ii) and has higher displacements than these cases above a load ratio of 1.5.

The panel centre displacements for cases 7(ii) to 7(iv) and the FEM model with the same geometric imperfection are compared with those of case 7(i) in Table II-28 in Appendix II. The difference between the analytical cases 7(ii), 7(iii), 7(iv) and the FEM model compared to case 7(i) is -0.50%, 1.78%, 2.75% and -37.44% respectively at critical load. At a load ratio of 1.7, the difference for cases 7(ii), 7(iii) and 7(iv) have increased to 4.03%, 26.68%, 41.65% respectively and 15.04% for the FEM model.

The amplitudes of the displacement modes at different load ratios for the analytical cases are also presented. Cases 7(i) and 7(ii) are shown in Table II-29, case 7(iii) in Table II-30, and case 7(iv) in Table II-31 and Table II-32 in Appendix II.

For case 7(i), only modes (1, 1) and (1, 2) are nonzero, while case 7(ii) additionally has nonzero modes of (1, 3) above critical load, (3, 1) above a load ratio of 0.5, (3, 2) above a load ratio of 0.6 and (3, 3) above a load ratio of 0.9.

Case 7(iii) shown in Table II-30 in Appendix II, has nonzero modes of (1, 1), (1, 2), (1, 3) above critical load, (1, 4) above a load ratio of 0.5, (3, 1) above a load ratio of 0.5, (3, 2) above a load ratio of 0.6 and (3, 3) above a load ratio of 0.9, and (3, 4) above a load ratio of 1.1.

Case 7(iv) shown in Table II-31 and Table II-32 in Appendix II, has nonzero modes of (1, 1), (1, 2), (1, 3) above critical load, (1, 4) above a load ratio of 0.5, (1, 5) above a load ratio of 0.7, (3, 1) above a load ratio of 0.5, (3, 2) above a load ratio of 0.6 and (3, 3) above a load ratio of 0.9, (3, 4) above a load ratio of 1.1, (3, 5) above a load ratio of 1.1, (5, 1) above a load ratio of 1.4, and (5, 2) above a load ratio of 1.2.

For cases 7(i) to 7(iv), it was found that the amplitudes of modes (1, 1) and (1, 2) were similar up to the critical load, with the amplitude of mode (1, 1)

being slightly higher than mode (1, 2). However, beyond critical load the symmetric (1, 1) displacement mode amplitude decreased, with a corresponding increase in the amplitude of the anti-symmetric displacement mode (1, 2). This trend could be due to a lower energy state for further deformation in the anti-symmetric mode compared to the symmetric mode, as the critical load for buckling in the anti-symmetric mode, which is only slightly higher than the first critical load, is approached. The FE result for this combination of imperfection modes confirms the out-of-plane displacement shape is eventually dominated by the anti-symmetric (1, 2) mode as the load increases.

3.3.2.4 Interaction of symmetric and anti-symmetric displacement modes

Next, we further investigate the interactions between symmetric and anti-symmetric displacement modes in influencing each other's displacement amplitudes. Comparison is made between the displacement mode amplitudes of case 7(iv) and those of cases 4(viii) and 5(viii) which had symmetric and anti-symmetric initial imperfections respectively.

Figure 3-11 compares the dimensionless displacement amplitudes of the fundamental $A(1,1)$ and anti-symmetric $A(1,2)$ modes with increasing load ratio for case 4(viii), case 5(viii) and case 7(iv). Case 4(viii) has only fundamental mode imperfection $A_0(1,1) = 0.2\,h$ and case 5(viii) only anti-symmetric imperfection mode $A_0(1,2) = 0.2\,h$, while case 7(iv) has both imperfection modes $A_0(1,1) = A_0(1,2) = 0.2\,h$.

The plots in Figure 3-11 clearly show that the case 7(iv) displacement modes $A(1,1)$ and $A(1,2)$ have the same magnitude initially and increase with load at similar rates up to the critical load. At loads above the critical load, the case 7(iv) $A(1,1)$ mode amplitude decreases gradually to its initial value, while the case 7(iv) $A(1,2)$ mode amplitude continues to increase.

The case 4(viii) $A(1,1)$ mode amplitude increases with load at a much higher rate than the case 7(iv) $A(1,1)$ mode up to the critical load, and continues to increase with load past the critical load.

The case 5(viii) $A(1,2)$ mode amplitudes increases with load at a similar but slightly higher rate than the case 7(iv) $A(1,2)$ mode, up to a load ratio of around 1.3, above which the $A(1,2)$ amplitudes for cases 5(viii) and 7(iv) become identical.

The differences in the amplitude of the $A(1,1)$ and $A(1,2)$ displacement modes from cases 4(viii), 5(viii) and 7(iv) show that there are interactions and interdependence between the symmetric and anti-symmetric mode amplitudes in the case 7(iv) with both symmetric and anti-symmetric imperfection.

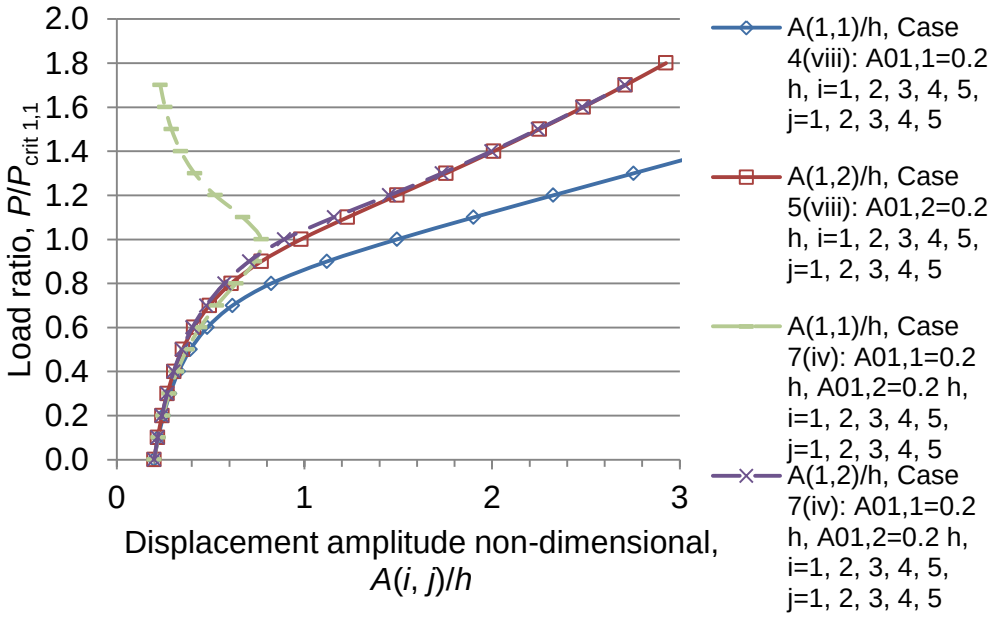

Figure 3-11: Comparison of displacement amplitudes of the fundamental $A(1,1)$ and the anti-symmetric $A(1,2)$ modes for case 4(viii) having imperfection $A_0(1,1) = 0.2\ h$ and case 5(viii) having imperfection $A_0(1,2) = 0.2\ h$, with case 7(iv) having imperfection modes $A_0(1,1) = A_0(1,2) = 0.2\ h$.

Table 3-5 compares the amplitudes of the symmetric displacement modes in case 7(iv) with those of case 4(viii).

Table 3-5: Comparison of nonzero symmetric displacement modes of case 7(iv) with case 4(viii)[3].

Load ratio	Difference in displacement mode amplitudes of Case 7(iv) relative to case 4(viii)						
$P/P_{crit\ 1,1}$	$A_{1,1}/h$	$A_{1,3}/h$	$A_{1,5}/h$	$A_{3,1}/h$	$A_{3,3}/h$	$A_{3,5}/h$	$A_{5,1}/h$
0	0.00%						
0.1	-0.28%						
0.2	-0.72%						
0.3	-1.43%						
0.4	-2.61%						
0.5	-4.60%						
0.6	-8.04%	-91.32%					
0.7	-13.83%	-91.84%		257.01%			
0.8	-22.74%	-95.00%		163.57%			
0.9	-34.40%	-100.31%		83.66%			
1	-48.43%	-106.71%	347.76%	29.59%	-0.15%		
1.1	-64.70%	-110.64%	131.43%	-9.38%	-49.50%		
1.2	-77.45%	-109.50%	16.90%	-38.69%	-76.37%		
1.3	-84.95%	-107.27%	-38.09%	-57.66%	-88.92%	101.90 %	
1.4	-89.29%	-105.57%	-64.42%	-69.50%	-94.75%	0.75%	-31.38%
1.5	-91.94%	-104.44%	-77.81%	-77.08%	-97.60%	-42.26%	-40.32%
1.6	-93.64%	-103.68%	-85.10%	-82.11%	-99.10%	-63.35%	-47.71%
1.7	-94.79%	-103.17%	-89.35%	-85.54%	-99.94%	-74.81%	-54.57%

The amplitude of mode (1, 1) for case 7(iv) is initially the same as case 4(viii), but with increasing load becomes lower in comparison. The other symmetric modes listed in Table 3-5 do not show good agreement between cases 7(iv) and 4(viii). For modes (1, 5), (3, 1), (3, 3), and (5, 1), the difference between the cases becomes increasingly more negative with increasing load. The difference in mode (1, 3) changes little. For mode (3, 5), the difference between the cases is initially large and

[3] The grey background indicates that for one or both cases the dimensionless displacement was zero within three decimal places.

negative but becomes positive and increasingly more negative above critical load.Table 3-6 compares the anti-symmetric displacement mode amplitudes of case 7(iv) with those of case 5(viii). The amplitude of mode (1, 2) of case 7(iv) is initially the same as case 5(viii), with their difference becoming increasingly more negative, as much as -9.08% at the critical load, before reducing down to -0.10% at the load ratio of 1.7.

Table 3-6: Comparison of nonzero anti-symmetric displacement modes of case 7(iv) with case 5(viii)[4].

Load ratio	Difference in displacement mode amplitudes of Case 7(iv) relative to case 5(viii)				
$P/P_{crit\ 1,1}$	$A_{1,2}/h$	$A_{1,4}/h$	$A_{3,2}/h$	$A_{3,4}/h$	$A_{5,2}/h$
0	0.00%				
0.1	-0.06%				
0.2	-0.17%				
0.3	-0.34%				
0.4	-0.62%				
0.5	-1.12%				
0.6	-1.99%		54.24%		
0.7	-3.49%		47.20%		
0.8	-5.81%	111.35%	34.31%		
0.9	-8.44%	78.61%	16.34%		
1	-9.08%	42.70%	0.27%		
1.1	-5.92%	16.89%	-5.27%		
1.2	-2.76%	6.10%	-3.79%	38.57%	-1.66%
1.3	-1.26%	2.60%	-2.09%	12.47%	-1.61%
1.4	-0.61%	1.33%	-1.15%	5.08%	-1.13%
1.5	-0.32%	0.79%	-0.67%	2.48%	-0.77%
1.6	-0.18%	0.52%	-0.41%	1.40%	-0.53%
1.7	-0.10%	0.37%	-0.26%	0.88%	-0.38%

[4] The grey background indicates that for one or both cases the dimensionless displacement was zero within three decimal places.

The amplitudes of modes (1, 4), (3, 2) and (5, 2) for case 7(iv) are initially larger than for case 5(viii) but the differences between the cases reduce with increasing load. The amplitude of mode (3, 4) for case 7(iv) is initially lower than for case 5(viii), with the difference becoming more negative up to the critical load. The difference for mode (3, 4) became positive at higher loads and reduced to 0.88% at the load ratio of 1.7.

From these comparisons, there appears to be more similarity between the anti-symmetric modes of cases 7(iv) and 5(viii), than in the symmetric modes of cases 7(iv) and 4(viii). The symmetric (1, 1) and anti-symmetric (1, 2) modes have similar amplitude up to the critical load, with the symmetric mode being the slightly larger of the two. The anti-symmetric displacement shape then becomes dominant just above the first critical load. This could be because the combination of similar amplitudes for the (1, 1) and (1, 2) modes gives an overall shape that more resembles the (1, 2) mode. The second critical load, with a (1, 2) buckling mode, also occurs at a load ratio of 1.14, which is the load when the large increase in the amplitude of the (1, 2) mode was found.

This leads to the conclusion that if both symmetric and anti-symmetric imperfection modes are present, the symmetric and anti-symmetric modes in the displacement function do not exist independently without having an influence on each other's amplitudes. The relative magnitudes of imperfection to the panel are also influential on which displacement mode type (symmetric or anti-symmetric) is dominant, as seen in the difference between the failure displacement modes obtained for cases 6(i) to 6(viii) and cases 7(i) to 7(iv).

The interactions between symmetric and anti-symmetric displacement modes when there are both symmetric and anti-symmetric imperfections in the panel could be explained by the relationship between in-plane stress and out-of-plane displacement. The in-plane stress distribution is different for when both symmetric and anti-symmetric modes contribute to the panel displacement than when only symmetric or anti-symmetric displacement

modes are present. The contributing symmetric and anti-symmetric displacements modes have an impact on the in-plane stress distribution and therefore each other's amplitudes.

Although, this work has been carried out at a particular panel aspect ratio, the interactions observed between symmetric and anti-symmetric modes when both symmetric and anti-symmetric imperfections are present, would be relevant for different panel aspect ratios. The dominance of a particular mode over another depends on the relative magnitudes of the imperfections present and the panel aspect ratio.

3.3.2.5 Out-of-plane displacement and Tsai-Wu index contour plots

Next, comparisons of out-of-plane displacement and Tsai-Wu contour plots are made for the analytical cases and FE models with different geometric imperfection.

Figure II-3 in Appendix II shows contour plots for case 4(viii), the analytical symmetric and anti-symmetric panel model with i and j =1 to 5, at failure load ratio 1.8 or load 1724 N. The plots are similar to those for case 1(ix) in Figure 3-5, which had the same initial imperfection but only symmetric out-of-plane displacement modes.

FE model contour plots of the panel with the same geometric imperfection are shown in Figure 3-12. The plots are for a higher load ratio of 2.70 or load 2564 N, and therefore show higher displacements and Tsai-Wu failure indices. The peak displacement and Tsai-Wu failure index being 0.0182 m and 1.0 respectively.

The overall displacement and Tsai-Wu failure index contours are similar among the analytical and finite element models. The highest Tsai-Wu failure indices are distributed nearer to the panel corners in the FE model than for the analytical model.

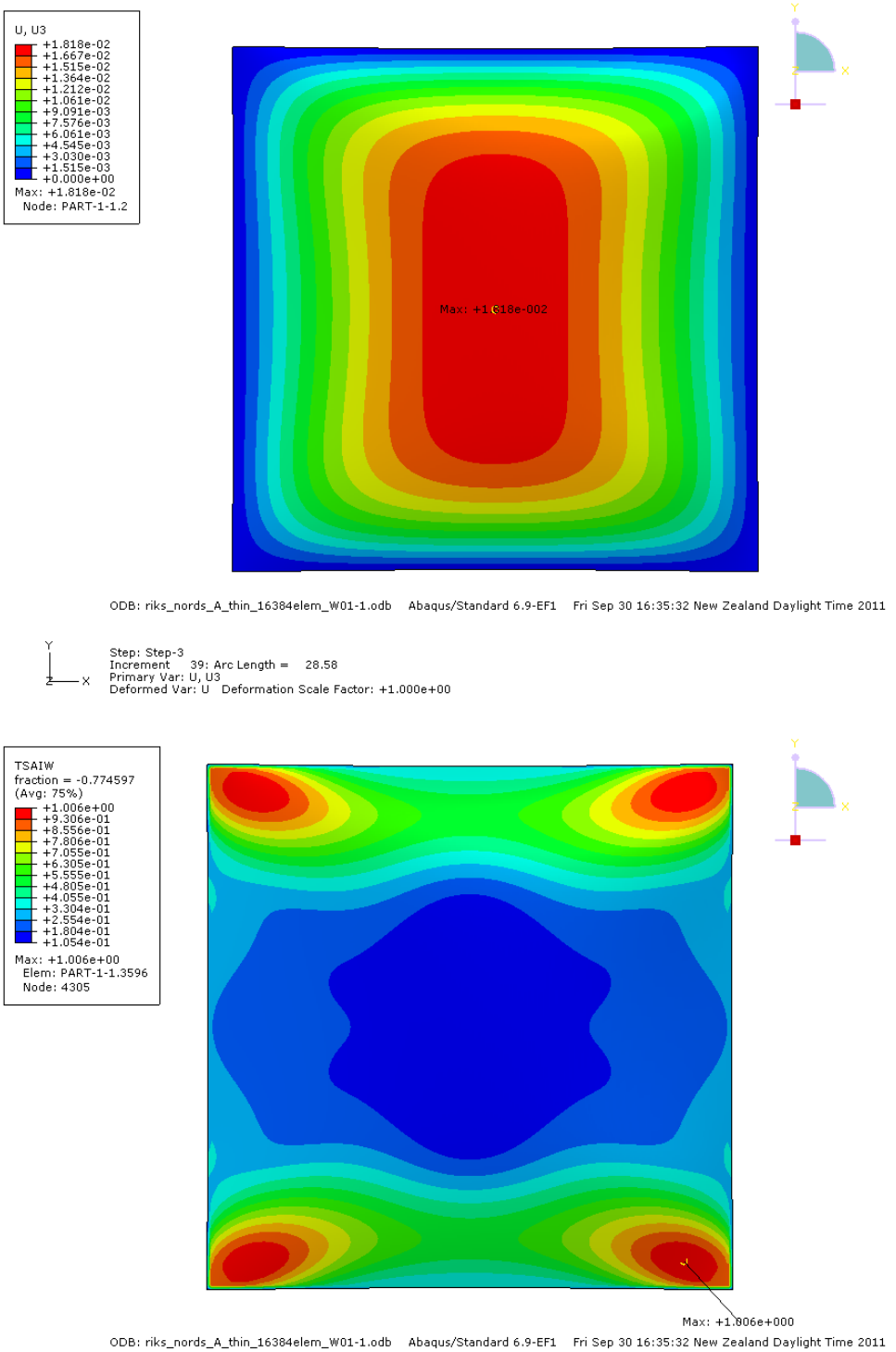

Figure 3-12: Out-of-plane displacement and Tsai-Wu failure index contour plot at the failure load ratio 2.70 or load 2564 N, for FE model of paperboard panel from (Nordstrand, 2004a) with imperfection $A_{0\,1,1}$ = 0.2 *h*.

This difference is due to the limited number of displacement modes allowed in the analytical model unlike the FE model. The number of displacement modes in the analytical model needs to be increased to improve accuracy of the failure index contour plot.

Contour plots for case 5(viii), the analytical model with *i* and *j* =1 to 5, and imperfection $A_{0\ 1,2}$ = 0.2 *h,* at load ratio 1.8 or load 1724 N are shown in Figure 3-13. The out-of-plane displacement contour plot shows the general (1, 2) anti-symmetric mode as expected, with a peak amplitude of 0.011 m. The analytical model Tsai-Wu failure indices are highest in the region near the centre of the bottom edge of the panel, with a peak of 1.22.

FE model contour plots of the same panel with imperfection $A_{0\ 1,\ 2}$ = 0.2 *h,* at load ratio 2.79 or load 2650 N, are shown in Figure 3-14. The peak displacement amplitude is 0.0132 m, while the peak Tsai-Wu failure index is 1.0.

The out-of-plane displacements for the FE model are slightly higher than the analytical model. The Tsai-Wu failure indices for the FE model have similar distribution as the analytical model when comparing regions with the same displacement direction. Areas of low failure index in the region of negative out-of-plane displacement and near the panel centre are seen in both the analytical and FE contour plots. The peak Tsai-Wu failure index values occur nearer the panel corners in the FE model. The difference in the peak location of the Tsai-Wu failure index in the analytical and FE models may be due to inaccuracy in the stress distribution obtained from the analytical model. There is inaccuracy in stresses from the analytical model because of the limited number of displacement modes allowed.

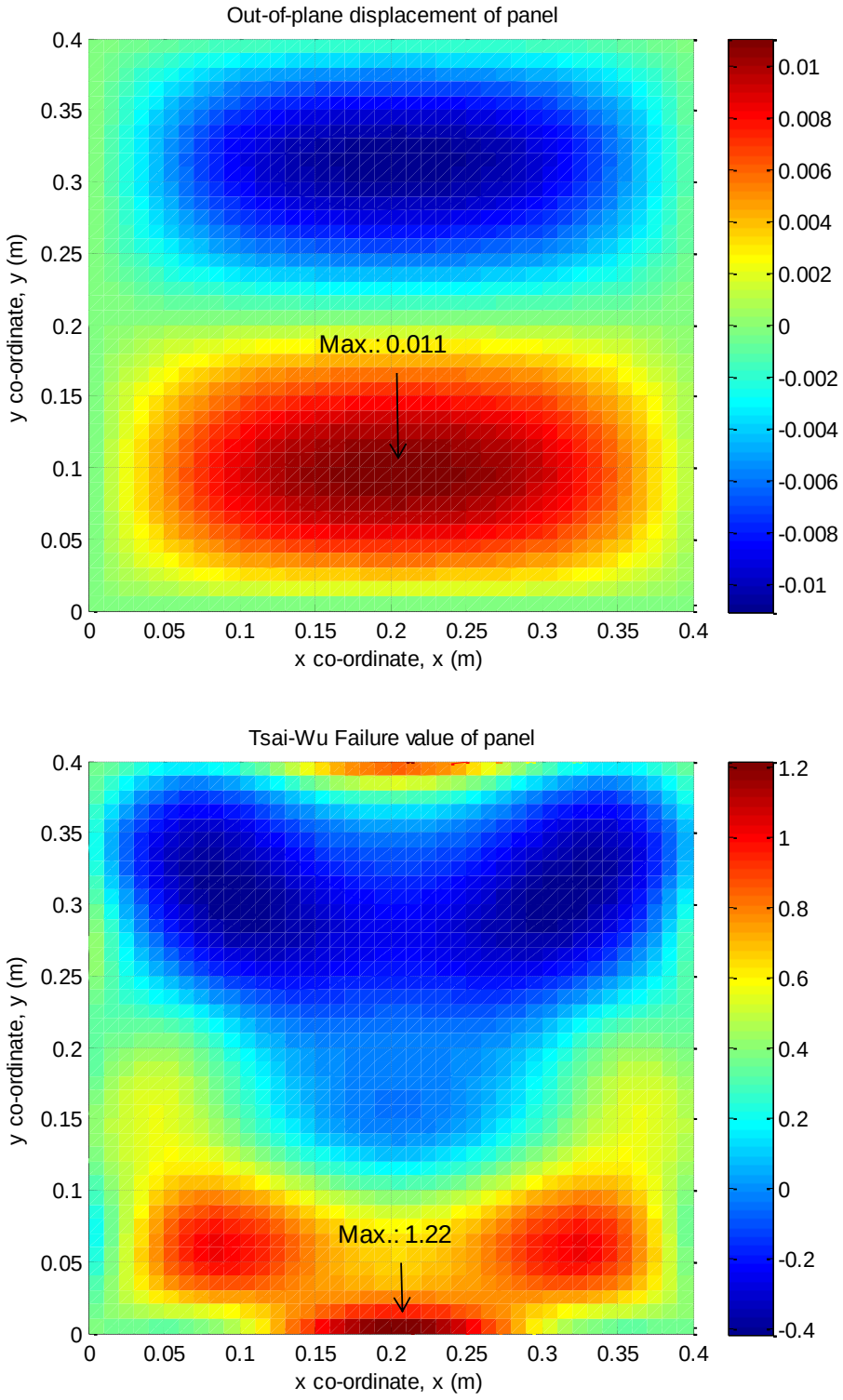

Figure 3-13: Out-of-plane displacement and Tsai-Wu failure index contour plots at the failure load ratio 1.8 or load 1724 N, for analytical symmetric and anti-symmetric multi-term model Case 5(viii), for paperboard panel from (Nordstrand, 2004a) with imperfection $A_{0\,1,2} = 0.2\,h$.

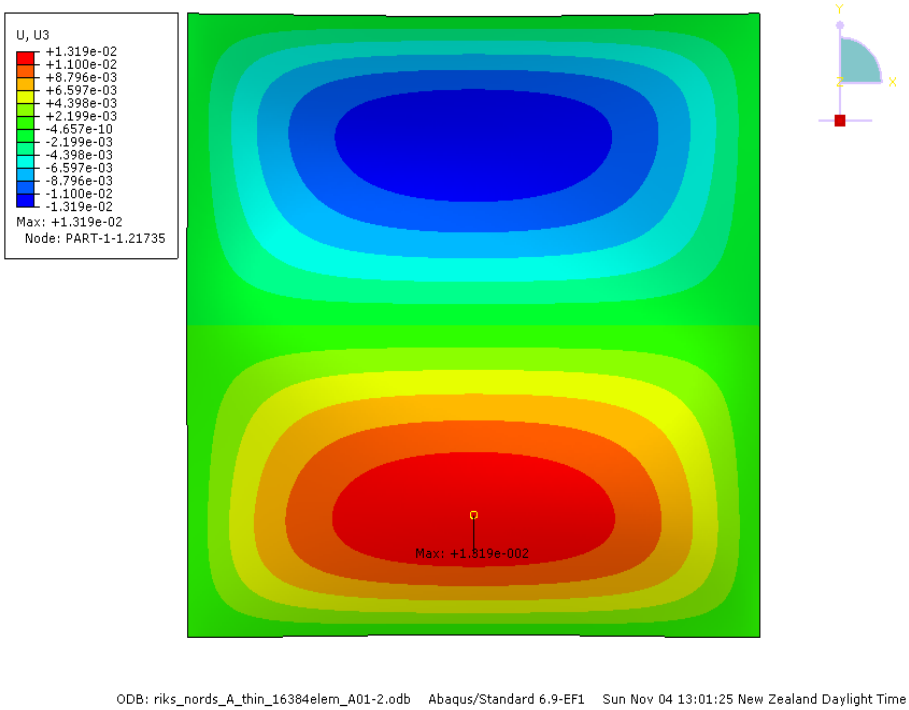

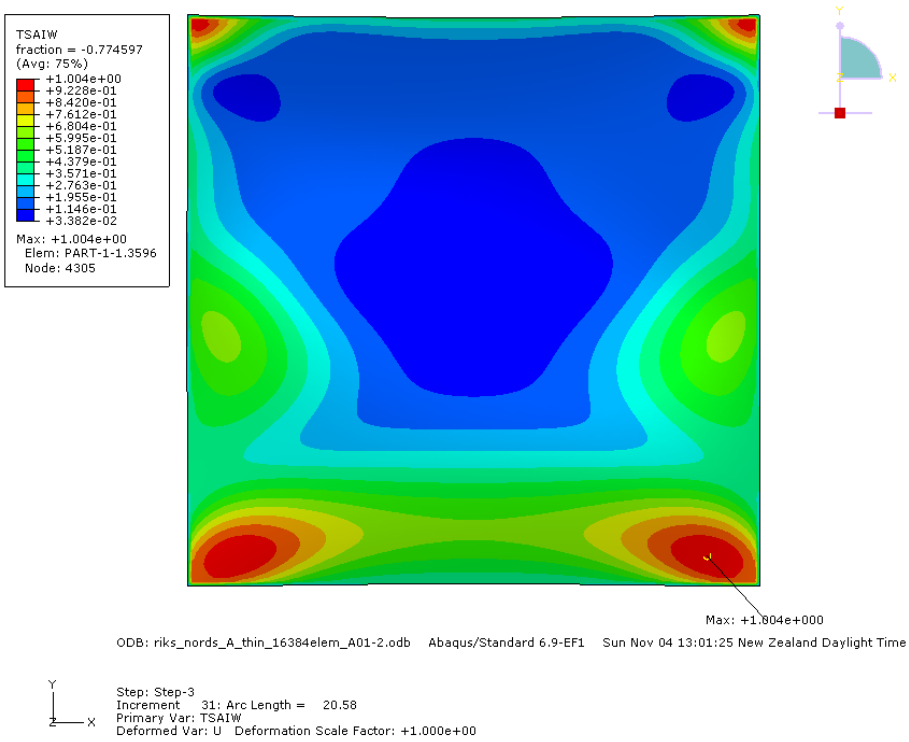

Figure 3-14: Out-of-plane displacement and Tsai-Wu failure index contour plot at the failure load ratio 2.79 or load 2650 N, for FE model of paperboard panel from (Nordstrand, 2004a) with imperfection $A_{0\,1,2}$ = 0.2 *h*.

The contour plots for the analytical case 6(viii) with i and j = 1 to 5 and panel imperfection $A_{0\ 1,1}$ = 0.2 h, $A_{0\ 1,2}$ = 0.1 h, at the failure load ratio of 1.8, or load 1724 N are shown in Figure 3-15.

The displacement plot appears almost like that of case 4(viii). However, the plot shows the maximum displacement of 0.0166 m occurs below the panel centre. The Tsai-Wu plot reveals some anti-symmetry about y-direction, in the higher failure indices of the lower half of the panel compared to the upper half of the panel. The peak Tsai-Wu failure index of 1.13 occurs in the lower corner regions of the panel.

FE model contour plots of the same panel and imperfection are given in Figure 3-16, though at a higher failure load ratio of 2.76 or load 2623 N. The peak displacement of 0.0187 m is off-centre, suggesting there is asymmetry in the panel displacement underlying the symmetric (1, 1) mode. The Tsai-Wu plot shows hints of asymmetry by the difference between the upper and lower halves in the regions near the vertical edges.

The anti-symmetry in the displacement and Tsai-Wu contour plots are due to the presence of both symmetric and anti-symmetric imperfection modes. The symmetric displacement mode is dominant at the load shown in Figure 3-15 and Figure 3-16.

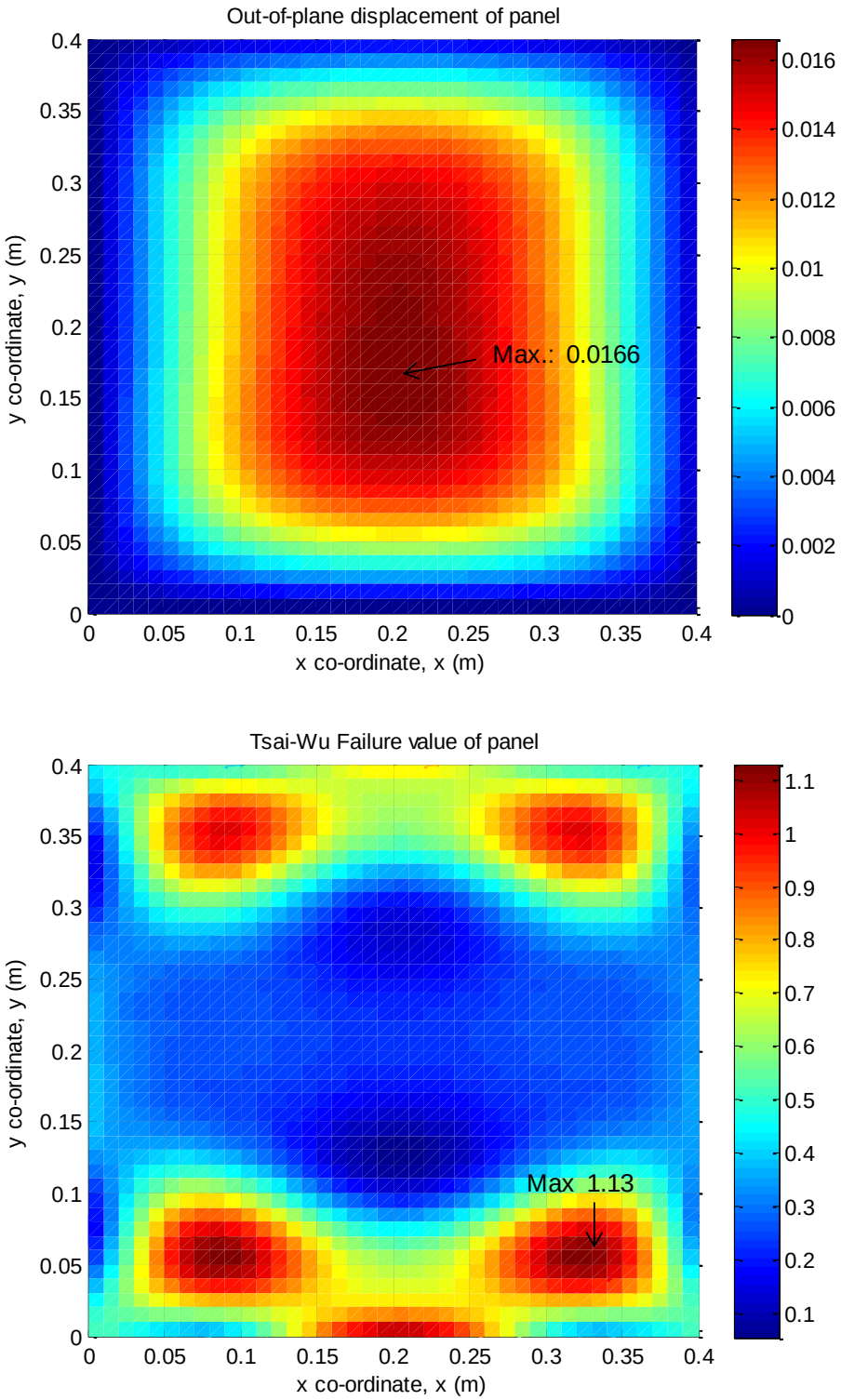

Figure 3-15: Out-of-plane displacement and Tsai-Wu failure index contour plots at the failure load ratio 1.8 or load 1724 N, for analytical multi-term model Case 6(viii), for paperboard panel from (Nordstrand, 2004a) with imperfection $A_{0\ 1,1} = 0.2\ h$, $A_{0\ 1,2} = 0.1\ h$.

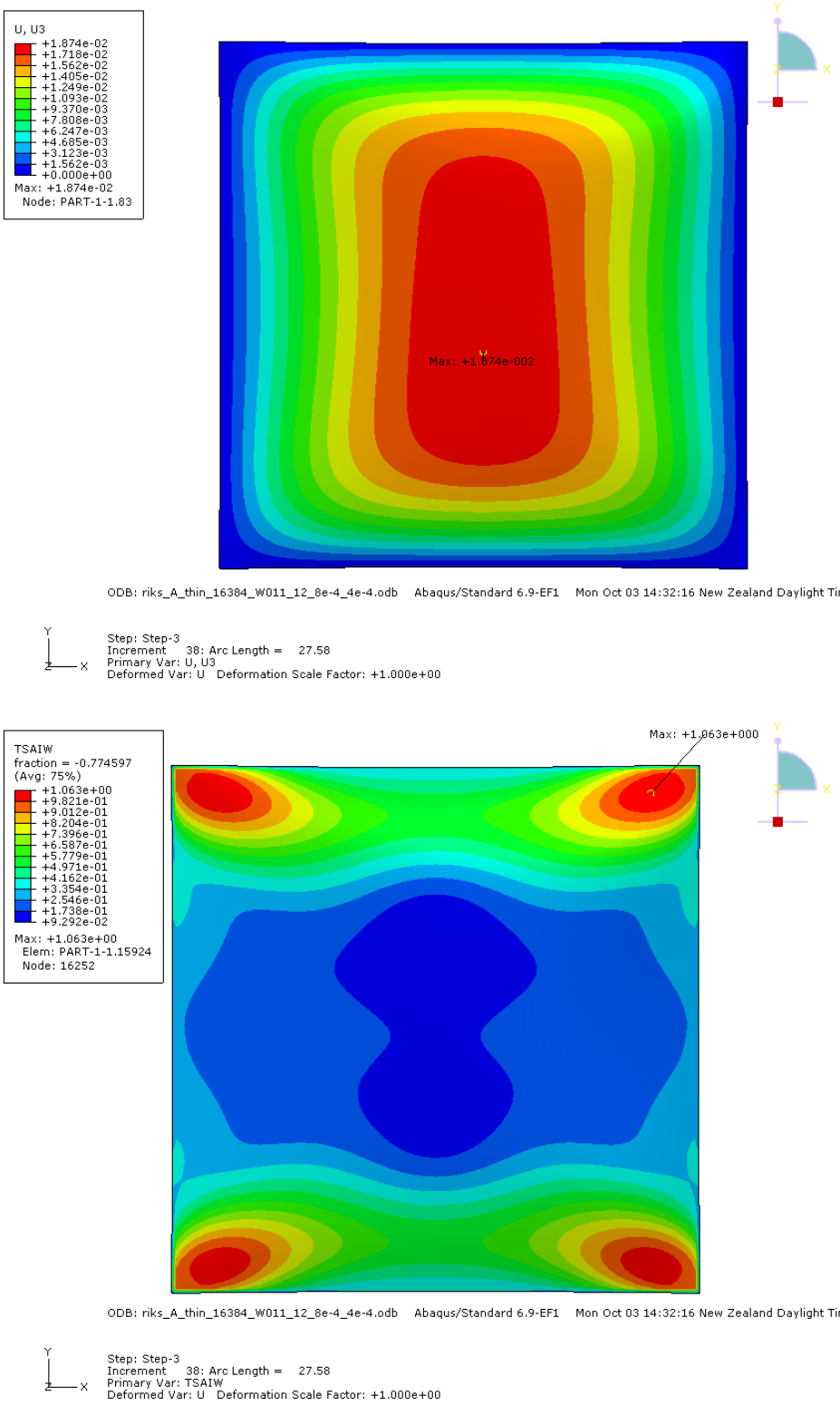

Figure 3-16: Out-of-plane displacement and Tsai-Wu failure index contour plot at the failure load ratio 2.76 or load 2623 N, for FE model of paperboard panel from (Nordstrand, 2004a) with imperfection $A_{0\ 1,1}$ = 0.2 *h*, $A_{0\ 1,2}$ = 0.01 *h*.

The contour plots for the analytical case 7(iv) with i and j = 1 to 5 and panel imperfection $A_{0\ 1,1}$ = 0.2 h, $A_{0\ 1,2}$ = 0.2 h, at the failure load ratio of 1.7, or load 1628 N are shown in Figure 3-17.

The displacement plot appears almost like that of case 5(viii) with an anti-symmetric imperfection mode. However, the displacement amplitude is greater in the lower half compared to the upper half of the panel, with a maximum displacement of 0.0108 m. The peak Tsai-Wu failure index of 1.02 occurs in the region near the centre of the bottom edge of the panel.

FE model contour plots of the same panel and imperfection are given in Figure 3-18, at a higher failure load ratio of 2.92 or load 2770 N. The out-of-plane displacements are given opposite directions to that of the analytical model. The peak displacement amplitude of 0.0142 m occurs in the lower half of the panel. The peak Tsai-Wu failure index of 1.1 occurs in the upper left corner of the panel.

The analytical and FE contour plots both show that the panel displacement is generally in the anti-symmetric (1, 2) with slightly different displacement amplitudes between the upper and lower halves of the panel. The difference in the displacement amplitudes in the upper and lower halves of the panel are due to the symmetric and anti-symmetric imperfections present. The combination of the symmetric and anti-symmetric displacement modes results in asymmetry in the displacement contour. The anti-symmetric mode is dominant for this case at the load shown in Figure 3-17 and Figure 3-18.

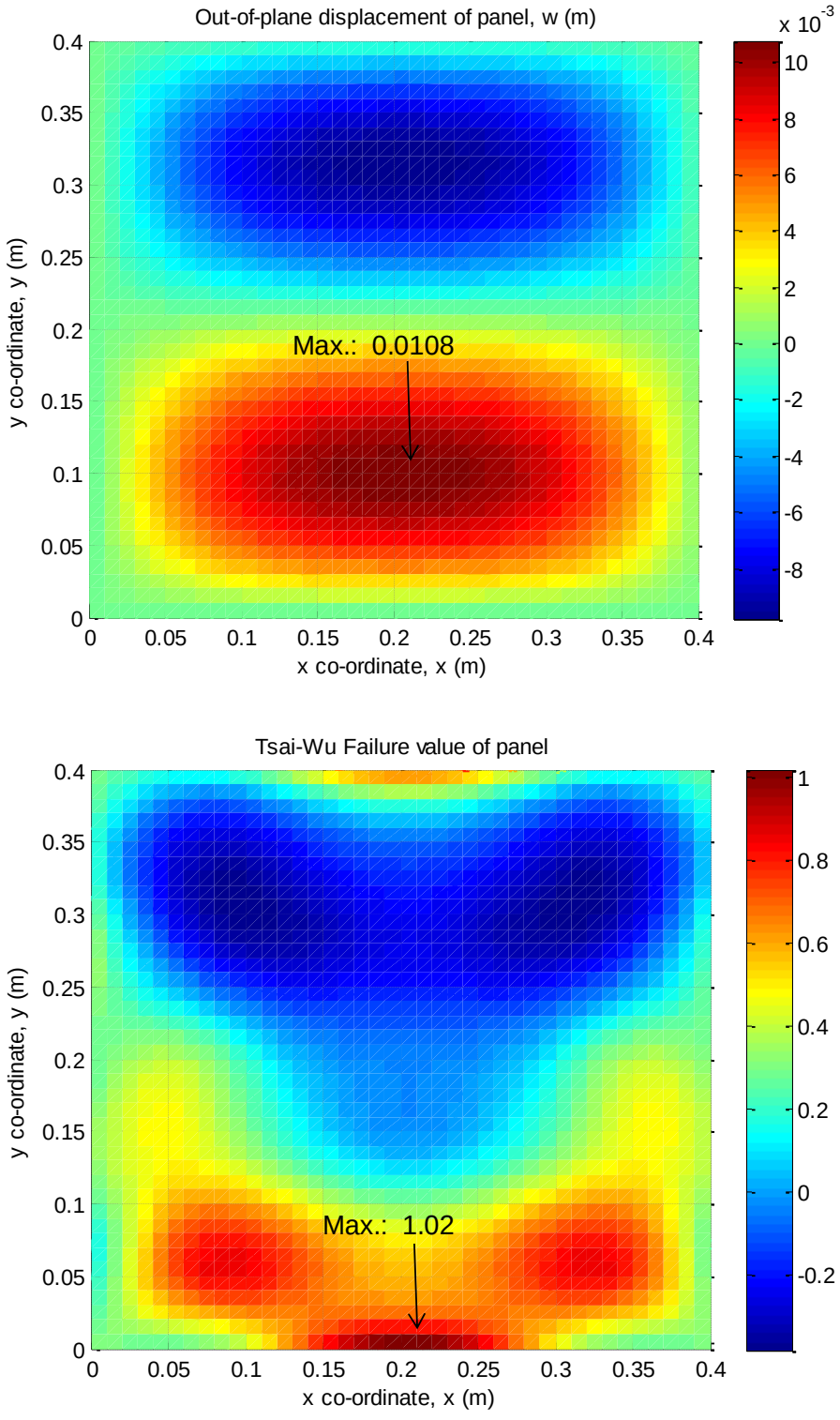

Figure 3-17: Out-of-plane displacement and Tsai-Wu failure index contour plots at the failure load ratio 1.7 or load 1628 N, for analytical multi-term model Case 7(iv), for paperboard panel from (Nordstrand, 2004a) with imperfection $A_{0\,1,1}$ = 0.2 *h*, $A_{0\,1,2}$ = 0.2 *h*.

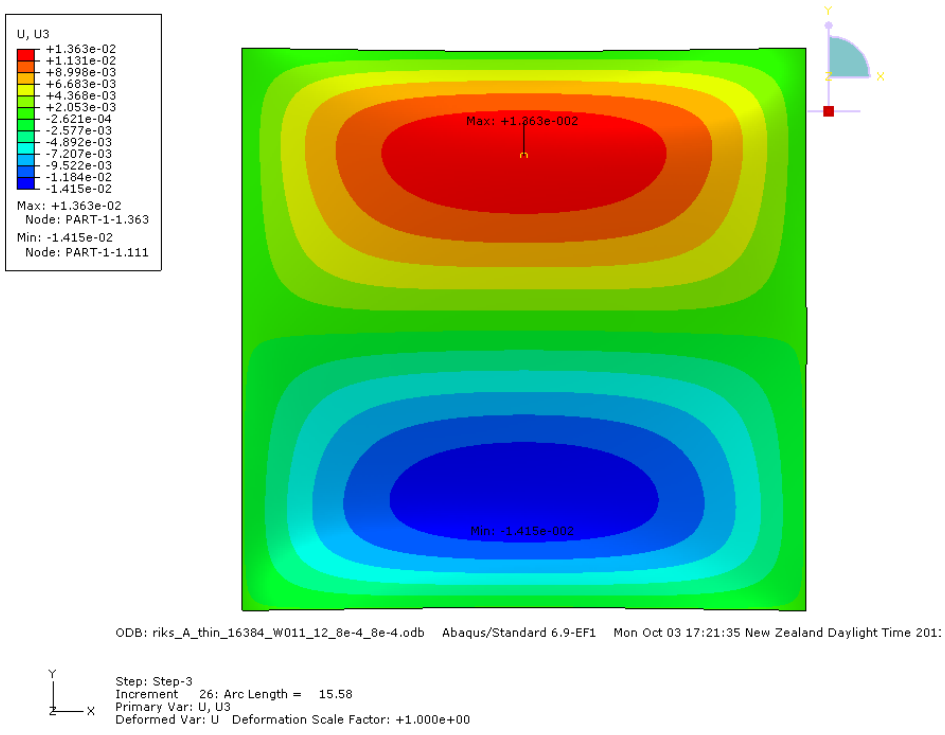

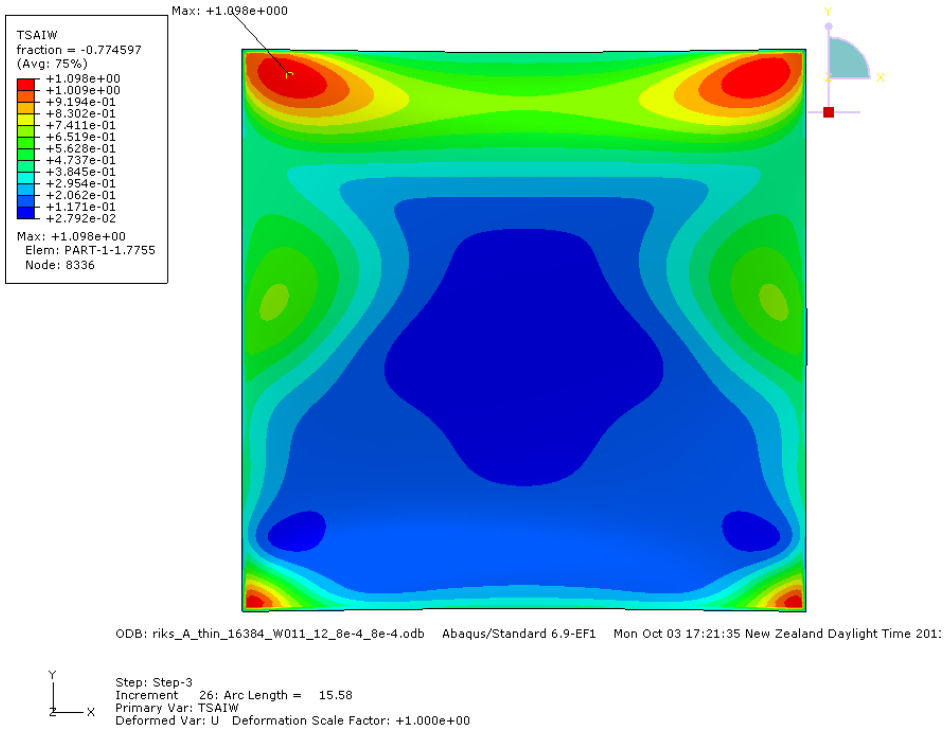

Figure 3-18: Out-of-plane displacement and Tsai-Wu failure index contour plot at the failure load ratio of 2.92 or load 2770 N, for FE model of paperboard panel from (Nordstrand, 2004a) with imperfection $A_{0\ 1,1} = 0.2\ h$, $A_{0\ 1,2} = 0.2\ h$.

3.3.2.6 Effect of higher imperfection modes

The previous sections considered the effect of including higher symmetric and anti-symmetric displacement modes for panels with symmetric and /or anti-symmetric imperfection. Now, we briefly consider how the presence of higher symmetric modes of imperfection in addition to the fundamental imperfection mode could influence the post-buckling plot for out-of-plane displacements at the panel centre.

The load vs. centre displacement plots for FE detailed geometry and simplified panel models and experiments in the work by (Armentani et al., 2006) showed deviation at low loads, with the models having higher initial structural stiffness. The apparent higher initial stiffness in the models was attributed to the load application by rigid coupling and the absence of local perturbations. This justified further investigation of the influence of imperfection modes on the post-buckling load vs. displacement plot.

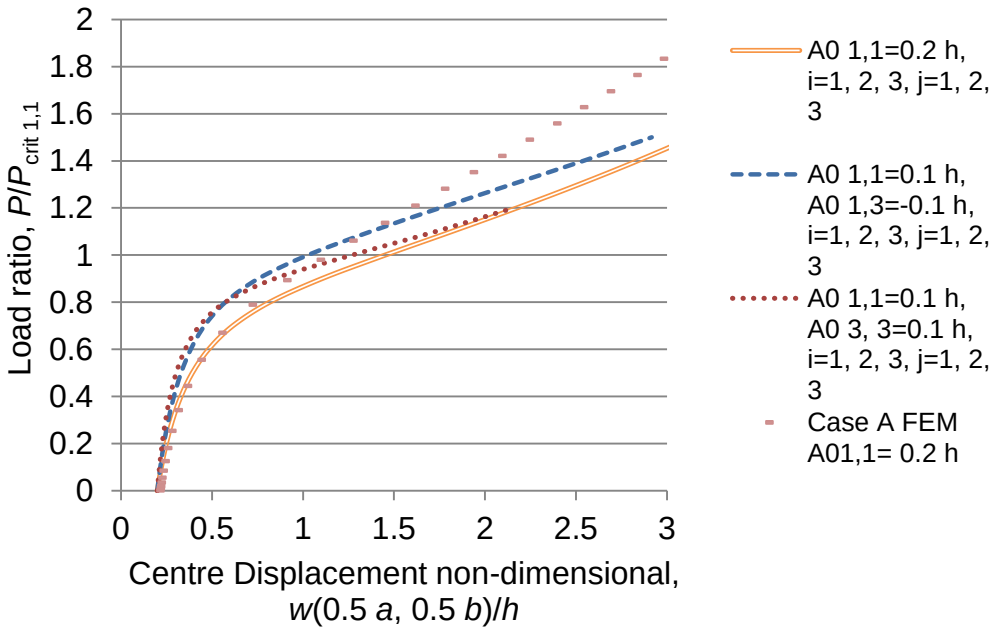

Figure 3-19: Comparison of dimensionless load vs. centre displacement for panel with boundary conditions of case A, central deflection 0.2 *h* with cases of higher symmetric imperfection modes $A_{0\,i,j}$ of equal amplitude to the fundamental mode.

Figure 3-19 shows dimensionless post-buckling plots of analytical and FE models of a panel with the in-plane boundary condition case A. The analytical models have nine terms in the out-of-plane displacement function *w* and different symmetric imperfection modes $A_{0\,1,\,1}$ = 0.2 *h; *$A_{0\,1,\,1}$ = 0.1 *h* and $A_{0\,1,\,3}$ = - 0.1 *h*; and $A_{0\,1,\,1}$ = 0.1 *h* and $A_{0\,3,\,3}$ = 0.1 *h*.

The panel centre displacement for the cases shown in Figure 3-19 are initially the same at 0.2 h. Below the critical load, the rates of increase in centre displacement with load are lower for the cases in Figure 3-19 with higher imperfection modes compared to the case with only the fundamental imperfection mode. The plots of the cases with higher imperfection modes approach those of the case with the fundamental imperfection mode at higher load ratios of about 1.2 for the case with $A_{0\,1,\,1}$ and $A_{0\,3,\,3}$ imperfection modes and at a load ratio 1.6 for the case with $A_{0\,1,\,1}$ and $A_{0\,1,\,3}$ imperfection modes.

This illustrates that the rate of increase in displacement with load in the range below the critical load is lower when higher imperfection modes of equal amplitude are present in addition to the fundamental imperfection mode. The lower initial imperfection of the fundamental mode causes the panel to behave more like a perfectly flat plate which has a post-buckling plot with small increase in displacement until the critical load is reached.

A further question follows of whether this trend holds when the fundamental initial imperfection mode is larger but the central deflection is as previous cases because of negating higher imperfection modes.

The cases previously considered have equal amplitudes of the fundamental and higher imperfection modes. Additional cases presented in Figure 3-20 have larger initial imperfection amplitude for the first mode relative to the higher modes, with a resulting lower central deflection due to the higher mode having an opposite sign. The imperfection modes for these cases are $A_{0\,1,1}$ = 0.3 *h* and $A_{0\,1,3}$ = 0.1 *h*; and $A_{0\,1,1}$ = 0.3 *h* and $A_{0\,3,3}$ = -0.1 *h*.

The post-buckling plots for these cases show larger displacements at a given load than the case with only fundamental imperfection mode $A_{0\,1,\,1}$ = 0.2 *h*. This contradicts the trend from earlier cases with equal amplitudes of the fundamental and higher imperfection modes. The case with $A_{0\,1,\,1}$ and $A_{0\,3,\,3}$ imperfection modes approaches the plot of the case with only fundamental imperfection mode at a load ratio of about 1.1. The case with $A_{0\,1,\,1}$ and $A_{0\,1,\,3}$ imperfection modes coincides with the fundamental mode case at a load ratio of 1.7.

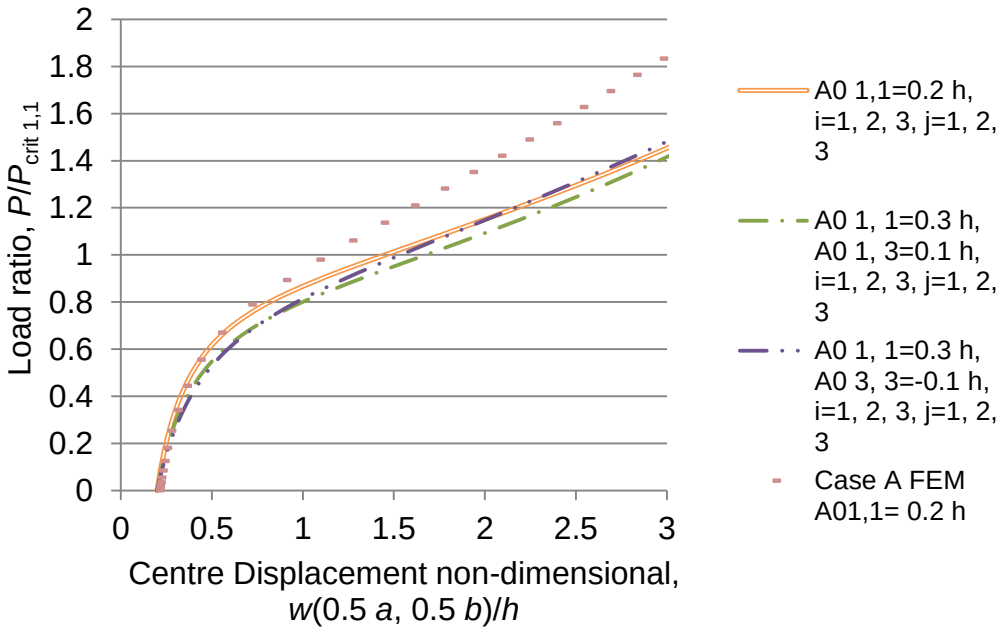

Figure 3-20: Comparison of dimensionless load vs. centre displacement for panel with boundary conditions of case A, central deflection 0.2 *h* with cases of higher symmetric imperfection modes $A_{0\,i,\,j}$ of lower amplitude and opposite sign to the fundamental mode.

Additive higher symmetric imperfection modes of similar magnitude as the fundamental mode are shown to decrease the panel centre out-of-plane displacement prior to the critical load compared to the plot for fundamental only imperfection. The inclusion of negating higher symmetric modes of opposite direction to the fundamental mode of larger magnitude has the opposite effect.

This makes it plausible for the lower apparent initial stiffness up to the first critical load (while the physical system is the same, the greater rate of growth of the fundamental mode imperfection makes it appear that the system is more flexible) in the experimental plot compared to modelled plots found in (Armentani et al., 2006) to be due to the presence of higher imperfection modes of a lower amplitude and opposite sign to the larger amplitude fundamental imperfection mode.

3.4 Concluding remarks

3.4.1 Single-term and multi-term displacement modes

A single-term solution may be inadequate particularly at loads significantly above the critical load. The more modes are included in the out-of-plane displacement function particularly in the loading *y*-direction, the greater the difference in panel deflection relative to the single-term result. For loading of up to 1.8 times the first critical load, it appears that including three terms in each direction of the displacement function gives results which have converged to within 16% higher than the single-term result.

For the case with (1, 1) symmetric imperfection of amplitude 0.2 *h*, there was convergence in the centre deflection in including up to the third symmetric term in both planar directions, with a 5.31% increase in centre deflection at a load ratio of 1.8 times the critical load compared to including up to the second symmetric term in both planar directions.

For the case with (1, 2) anti-symmetric imperfection of amplitude 0.2 *h*, there was a 6.71% increase at a load ratio of 1.8, in including four symmetric and anti-symmetric terms compared to three symmetric and anti-symmetric terms in both planar directions.

For the case with (1, 1) symmetric imperfection with an amplitude of 0.2 *h* and (1, 2) anti-symmetric imperfection with an amplitude of 0.1 *h*, there was a 5.49% increase at a load ratio 1.8, in including five symmetric and

anti-symmetric terms compared to four symmetric and anti-symmetric terms in both planar directions.

For the case with (1, 1) symmetric and (1, 2) anti-symmetric imperfection both with an amplitude of 0.2 *h*, there was a 15% increase at a load ratio 1.7, in including five symmetric and anti-symmetric terms compared to four symmetric and anti-symmetric terms in both planar directions.

The difference between single-term and multi-term post-buckling plots appears and increases at loads above a threshold load determined by the initial imperfection value. The smaller the imperfection, the higher the threshold load will be up to critical load.

3.4.2 Symmetric and/or anti-symmetric imperfection

Interactions between symmetric and anti-symmetric displacement modes in the presence of both symmetric and anti-symmetric panel imperfections are noted and are attributed to changes to the in-plane stress distribution. The relative imperfection magnitudes also determine the dominance of displacement mode types.

The direction of higher symmetric imperfections modes relative to the fundamental imperfection mode has an effect of decreasing or increasing out-of-plane displacements relative to the result for fundamental mode only imperfection at loads below the critical load. Higher imperfection modes opposing the larger amplitude fundamental imperfection mode direction have higher out-of-plane displacements due to the larger component of the fundamental imperfection mode. Additive higher imperfection modes of the same amplitude as the fundamental mode have lower out-of-plane displacements because of the presence of smaller magnitude of the fundamental imperfection mode.

3.5 Summary

This chapter considered the influence of including multi-term out-of-plane displacement shapes functions in the analytical panel model on the post-buckling plot.

Firstly, cases with symmetric initial imperfections of different amplitude and different number of symmetric modes in the displacement function were compared. Increasing the number of modes in the displacement function had the effect of producing larger out-of-plane panel displacements than the single-term solution at loads above a threshold load for which the multi-term solution displacements differ from the single-term solution. The threshold load is dependent on the magnitude of the initial geometric imperfection, where the smaller the imperfection magnitude the higher the value up to the first critical load. Also, the addition of displacement modes in the loading direction appears to increase the panel displacements more than modes in the unloaded direction. The difference between the multi-term and single-term displacements increases with load, particularly above critical load. The results showed for a symmetric displacement mode nine-term case, three modes in each planar direction, the out-of-plane panel displacement at a load ratio of 1.8 can differ to the single-term case by 16%. It can be concluded that a single-term solution is generally not adequate at loads above the critical load.

Secondly, the effect of including both symmetric and anti-symmetric modes in the displacement function was investigated by comparing panels with symmetric and / or anti-symmetric initial imperfection. The results show that for cases with either a symmetric or anti-symmetric imperfection, only the displacement modes of the same type as the imperfection contribute to the panel displacement. For the cases with both symmetric and anti-symmetric imperfection, the symmetric and anti-symmetric displacement modes present in the displacement function have an influence on each other's amplitudes because of their impact of the in-plane stress distribution. The relative magnitudes of initial imperfection

given to the symmetric and anti-symmetric modes also determine which mode type is dominant in the panel displacement. The influence of higher symmetric imperfection modes in addition to a fundamental imperfection mode was also considered in terms of the out-of-plane displacements at the plane centre. The direction of higher imperfection modes relative to the fundamental mode and the magnitude of the fundamental mode affect the apparent panel stiffness below the critical load, observed as higher or lower out-of-plane displacements. A small fundamental imperfection mode with additive higher imperfection modes causes the panel to appear stiffer, while a larger fundamental imperfection mode with opposing higher imperfection modes makes the panel appear more flexible, compared to a panel with only a fundamental imperfection mode.

4 Determination of effective material properties of corrugated paperboard

4.1 Introduction

The complexity of modelling corrugated paperboard material can be attributed to its composite structure, coupled with its time-dependent behaviour and sensitivity to changes in humidity. The corrugated paperboard material is more conveniently modelled as an equivalent orthotropic single lamina than with detailed paperboard layers. However, the material properties of corrugated paperboard as a whole cannot be easily obtained due to limitations in measurement methods. As can be seen from the results presented here, the significant variation in the predicted behaviour depending on the testing/theoretical model used suggests that further investigation is needed to obtain a satisfactory analytical model that can represent the in-plane and out-of-plane load-displacement characteristics as well as vibratory and buckling behaviour.

In this chapter, the overall effective material properties of corrugated paperboard obtained using orthotropic Kirchhoff plate theory, and from materials testing and Finite Element (FE) models are compared. The following research questions are investigated:

- How do material properties of corrugated paperboard compare among the different materials testing methods?
- How do the material properties for an equivalent single layer orthotropic plate calculated using properties of constituent layers compare with those given by materials tests on corrugated paperboard?
- How do the corrugated paperboard properties from materials tests compare with those from Finite Element models of the tests with equivalent single-layered and detailed geometry?

To answer these questions, some elastic material properties of corrugated paperboard have been obtained experimentally by edge compression, four-point bending and sonic vibration tests. The sonic vibration method described in (Lu & Zhu, 2001; Sato et al., 2008) uses Chladni-patterns formed by the free vibration modes of the sample to determine dynamic elastic properties of the corrugated paperboard. Theoretical equivalent orthotropic plate material properties based on properties of the constituent layers, properties obtained from the materials tests, and equivalent single-layered and detailed geometric FE models of the tests are presented.

4.2 Methods of Study

The theoretically calculated models, materials tests and Finite Element (FE) materials test models used for the comparison of overall material properties of corrugated paperboard are described below.

4.2.1 Materials and theoretical models

The materials provided by Scion Research were (Kraft) standard and recycled fibre corrugated paperboards for two different test conditions,: (a). 23 $^{\circ}$C, 50 % relative humidity; and (b). 23 $^{\circ}$C, 90 % relative humidity. Different theoretical paperboard models were used in the analytical models for buckling and post-buckling analysis in Chapters 2 and 3, and also for the equivalent single-layered FE models. The paperboard materials were the same as those used by (Ilmonen, 2007; Navaranjan, Dickson, Paltakari, & Ilmonen, 2012). Therefore, the paperboard geometry and constituent layers' property data from (Ilmonen, 2007) have been used in the theoretical calculations.

The corrugated paperboards tested were of a single-wall structure and C-flute profile. The principal directions of the material shown in Figure 4-1 are *1* - the machine direction (MD) along *x*; *2* - the cross-direction (CD) along *y*; and *3* – the out-of-plane direction along *z*.

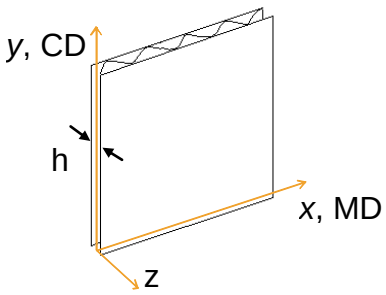

Figure 4-1: Corrugated paperboard principal directions.

The geometric parameters of the paperboard were shown previously in Figure 2-3. The paperboard consists of two outer layers - the single facer of thickness, $t_{f\,1}$, and double backer of thickness $t_{f\,2}$. The corrugated core or fluted medium is of thickness, t_c. The overall paperboard thickness is h, and the 'wavelength' of the corrugation profile is λ.

The corrugation profile has been approximated as a combination of circular arcs of inner radius, r, outer radius, r_1, and arc angle from vertical, θ; and tangential angled straight sections of length, L and glue joints of width, t_g, as in (Ilmonen, 2007).

The corrugation profile geometry from (Ilmonen, 2007, p. 58) for the tested corrugated paperboards are given in Table 4-1. The grammage (g/m^2), a measure of mass in grams per unit area, of the layers is indicated with the paperboard name in the order of single facer / medium / double backer.

The angled core length between corrugation arcs, L and take-up factor α, the ratio between the lengths of the corrugated layer and facings, in Table 4-1 were calculated using the following equations:

$$L = \frac{2\left[\frac{\lambda}{4} - \frac{t_g}{2} - \sin(\theta)\,(r + r_1)/2\right]}{\cos(\theta)}$$

Equation 4-1

$$\alpha = \left[4\,\frac{r + r_1}{2}\,\theta + 2\,L + 2\,t_g\right]/\lambda$$

Equation 4-2

Table 4-1: Paperboard geometry from (Ilmonen, 2007).

Geometric parameters	Kraft paperboard 205/160/205	Recycled paperboard 190/140/190
Overall thickness, h (mm)	4.23	4.23
single facer thickness, t_{f1} (mm)	0.229	0.253
double backer thickness, t_{f2} (mm)	0.222	0.253
fluted medium thickness. t_c (mm)	0.193	0.185
glue joint width, t_g (mm)	0.07	0.07
corrugation 'wavelength', λ (mm)	8	8
corrugation arc inner radius, r (mm)	1.47	1.47
corrugation arc outer radius, r_1 (mm)	1.663	1.655
corrugation arc angle from vertical, θ ($^\circ$)	60.41	59.73
core length between corrugation arcs [2], L (mm)	2.442	2.442
take-up factor [2], α	1.454	1.443

[2] Calculated based on data in (Ilmonen, 2007).

Overall equivalent properties were calculated from the material properties of the paperboards' component layers from Scion test data in (Ilmonen, 2007, pp. 68, 81) given in Table 4-2.

4.2.1.1 Analytical equivalent paperboard model

In the analytical models, the material is modelled as an orthotropic lamina with properties equivalent to the composite structured corrugated paperboard. First-order shear deformation laminated plate theory was used to obtain equivalent material properties of the corrugated paperboard in directions MD and CD, assuming plane stress conditions as in (Nordstrand, 2004a) and (Carlsson et al., 2001). The material models in the buckling and post-buckling analyses of this work use thin plate theory neglecting transverse shear.

Table 4-2: Corrugated board component properties from (Ilmonen, 2007, pp. 68, 81).

Corrugated board component properties	*Standard corrugated board*		*Recycled corrugated board*	
	50% RH	90%RH	50% RH	90%RH
single facer				
σ_{MD} or σ_{11} - Max. strength (MPa)	13.16	9.51	13.18	9.46
E_{MD} or E_{11} - Elastic Modulus (MPa)	6833	4779	4503	3424
v_{12} - Poisson's ratio	0.308	0.319	0.325	0.289
σ_{CD} or σ_{22} - Max. strength (MPa)	8.4	6.77	6.91	4.97
E_{CD} or E_{22} - Elastic Modulus (MPa)	2811	1894	1444	1281
medium				
σ_{MD} or σ_{11} - Max. strength (MPa)	12.35	9.89	14.76	9.07
E_{MD} or E_{11} - Elastic Modulus (MPa)	4999	3877	5407	4331
v_{12} - Poisson's ratio	0.293	0.304	0.371	0.391
σ_{CD} or σ_{22} - Max. strength (MPa)	8.58	5.71	7.55	4.9
E_{CD} or E_{22} - Elastic Modulus (MPa)	2741	1790	1686	1493
double backer				
σ_{MD} or σ_{11} - Max. strength (MPa)	15.54	12.03	13.18	9.46
E_{MD} or E_{11} - Elastic Modulus (MPa)	6398	4759	4503	3424
v_{12} - Poisson's ratio	0.196	0.279	0.325	0.289
σ_{CD} or σ_{22} - Max. strength (MPa)	8.4	7.51	6.91	4.97
E_{CD} or E_{22} - Elastic Modulus (MPa)	2784	1927	1444	1281

The paperboard's overall equivalent Young's moduli E^*_{11} (Pa) and E^*_{22} (Pa), along MD and CD directions respectively, the in-plane shear modulus G^*_{12} (Pa) and Poisson's ratio v^*_{12}, shown in Table 4-3, are calculated using Equations (1) and (6) in the reference (Nordstrand, 2004a) shown previously in Equations 2-1 to 2-5 of Chapter 2.

The in-plane Poisson's ratio $v_{21,f}$ and in-plane shear modulus for the facings $G_{12,f}$ (Pa) were based on empirical relationships for paper materials, between Poisson's ratios v_{12} and v_{21}, and G_{12} (Pa) with E_{11} (Pa) and E_{22} (Pa), from Equations (6a) and (6b) of (Carlsson et al., 2001)

(Carlsson et. al., 2001, p. 257) shown previously in Equations 2-6 and 2-7 of Chapter 2.

Table 4-3: Equivalent corrugated paperboard properties for analytical model.

Equivalent paperboard properties	*Standard corrugated board*		*Recycled corrugated board*	
	50% RH	90%RH	50% RH	90%RH
$\hbar$	0.621	0.632	0.619	0.619
E^*_{11} (MPa)	705.34	508.47	538.66	409.58
E^*_{22} (MPa)	480.07	322.42	279.10	247.43
G^*_{12} (MPa)	177.51	124.55	118.05	96.95
v^*_{12}	0.157	0.189	0.201	0.179

The flexural stiffnesses D_{11} (N m), D_{12} (N m), D_{22} (N m) and D_{66} (N m) of the Kraft and recycled paperboards shown in Table 4-4 were calculated using the equations below from (Carlsson et al., 2001) (Carlsson et. al., 2001, p. 266). The material properties of the facings and core layers are denoted using subscripts by 'f' and 'c' respectively:

$$D_{11} = t_f \left(h - t_f\right)^2 E_{11,\mathrm{f}} / \left[2\left(1 - \nu_{12,\mathrm{f}}\,\nu_{21,\mathrm{f}}\right)\right]$$

Equation 4-3

$$D_{12} = \nu_{12,\mathrm{f}}\, t_f \left(h - t_f\right)^2 E_{22,\mathrm{f}} / \left[2\left(1 - \nu_{12,\mathrm{f}}\,\nu_{21,\mathrm{f}}\right)\right]$$

Equation 4-4

$$D_{22} = \frac{t_f \left(h - t_f\right)^2 E_{22,\mathrm{f}}}{2\left(1 - \nu_{12,\mathrm{f}}\,\nu_{21,\mathrm{f}}\right)} + \frac{\alpha\, E_{22,\mathrm{c}}\, t_c}{12\,(h - 2\,t_f)}\, h^3\,(1 - 6\,t_f/h)$$

Equation 4-5

$$D_{66} = 0.387\, t_f \frac{\left(h - t_f\right)^2}{2} \sqrt{E_{11,\mathrm{f}}\, E_{22,\mathrm{f}}}$$

Equation 4-6

Table 4-4: Flexural stiffnesses of Scion paperboards.

Flexural stiffnesses	*Standard corrugated board*		*Recycled corrugated board*	
	50% RH	90%RH	50% RH	90%RH
D_{11} (N m)	13.1	9.4	9.9	7.5
D_{12} (N m)	1.4	1.1	1.0	0.8
D_{22} (N m)	6.4	4.3	3.6	3.2
D_{66} (N m)	3.0	2.1	2.0	1.6

4.2.1.2 Finite Element equivalent paperboard model

In the single-layered Finite Element paperboard models, an elastic lamina material definition was also used for an equivalent single layer paperboard model. However, the equivalent properties E^*_{11}, E^*_{22}, G^*_{12} and v^*_{12} shown in Table 4-5 were calculated differently for the Finite Element models. The in-plane material properties for the FE models are different to that of the analytical models because of the elastic lamina definition used. The elastic lamina definition enables the in-plane properties to be input, but the flexural properties are calculated by the software automatically, based on lamina theory. Therefore, the in-plane and flexural material properties of the FE model are interdependent, unlike that of the analytical model. The flexural properties of the FE model were kept the same as that of the analytical model, but its in-plane properties, to be input into the software, were calculated from the flexural properties.

Table 4-5: Equivalent corrugated paperboard properties for single-layered Finite Element model.

Equivalent paperboard properties	*Standard corrugated board*		*Recycled corrugated board*	
	50% RH	90%RH	50% RH	90%RH
E^*_{11} (MPa)	2026.40	1448.95	1516.75	1156.00
E^*_{22} (MPa)	992.11	668.04	561.57	499.23
G^*_{12} (MPa)	477.26	334.87	313.05	257.11
v^*_{12}	0.218	0.260	0.281	0.250

The flexural stiffnesses D_{11}, D_{22}, D_{12} and D_{66} in Table 4-4, and the overall paperboard thickness h, were used to calculate E^*_{11}, E^*_{22}, G^*_{12} and v^*_{12} based on orthotropic plate theory relations shown previously in Equations 2-8 to 2-12 of Chapter 2. The shear moduli, G^*_{13} (Pa) and G^*_{23} (Pa) were assumed to be the same as G^*_{12} because these are difficult to obtain experimentally and transverse shear is being neglected. There are alternative approximations given in Equation 1-23 and Equation 1-24.

These in-plane properties are different because corrugated paperboard material behaviour is not described well by orthotropic laminate theory. The flexural rigidity of corrugated paperboard is much greater than what

the in-plane properties would suggest because of the rigidity of the corrugated core.

4.2.2 Materials testing

The three test methods of edge compression, four-point bending and sonic vibration to obtain paperboard properties are described in this section. Edge compression and four-point bending tests were carried out according to TAPPI test standards T811 and T820 respectively (TAPPI, 2000, 2002), and sonic vibration tests using the method described in (Sato et al., 2008).

4.2.2.1 Specimen preparation

The paperboard specimens were prepared at Scion Research. The paperboard materials were cut into specimens using a knife cutter with guides in a conditioning room at 23 °C, 50 % relative humidity. The geometry of specimens used in the test methods are shown in Table 4-6.

Table 4-6: Materials tests specimen geometry.

Test Method	*Test orientation*	*MD dimension* (mm)	*CD dimension* (mm)
Edge compression	CD	50.8	38.1
Four-point bending	MD	250	30
	CD	30	250
Sonic Vibration		100	100

The test conditions considered were 23 °C, 50 % relative humidity and 23 °C, 90 % relative humidity. The number of specimens tested is shown in Table 4-7 along with the division of materials testing carried out at Scion Research and by the author at Waikato University.

Atmospheric control was necessary in sample preparation and testing, because changes in humidity have an influence on paperboard moisture content and thus its material properties. Also, the moisture hysteresis effect is evident in the absorption and desorption paths of the relation between paperboard moisture content and relative humidity (Markstrom, 2005).

Table 4-7: Number of specimens tested in materials tests at 23 °C.

Test Method	*Material*	*Relative Humidity*	*Test orientation*	*No. of specimens tested*	*Tested by*
Edge compression	Kraft	50%	CD	9	Kueh
		90%	CD	14	Scion
	Recycled	50%	CD	10	Kueh
		90%	CD	15	Scion
Four-point bending	Kraft	50%	MD - Top	8	Scion
			MD - Back	7	Scion
			CD - Top	8	Scion
			CD - Back	7	Scion
		90%	MD - Top	7	Scion
			MD - Back	7	Scion
			CD - Top	7	Scion
			CD - Back	8	Scion
	Recycled	50%	MD - Top	7	Scion
			MD - Back	7	Scion
			CD - Top	8	Scion
			CD - Back	7	Scion
		90%	MD - Top	6	Scion
			MD - Back	7	Scion
			CD - Top	7	Scion
			CD - Back	8	Scion
Sonic Vibration	Kraft	50%		5	Kueh
	Recycled	50%		5	Kueh

To achieve uniformity of paperboard moisture content in the tests, specimens were preconditioned and conditioned in accordance with the TAPPI T402. This involved preconditioning specimens in a dry atmosphere for 24 hours, before conditioning in the desired test atmosphere. Preconditioning ensures the correct equilibrium moisture content is reached by absorption, as internationally accepted.

For the room temperature test condition, the specimens were preconditioned at 34°C, 34 % relative humidity in a conditioning cabinet for 24 hours and then conditioned in a room at 23 °C, 50 % relative humidity for a minimum of three days before testing. For the high humidity test condition, the specimens were placed in the 23 °C, 90% relative humidity atmosphere for 48 hours, preconditioned at 23°C, 50% relative humidity for

24 hours, then conditioned at 23 °C, 90% relative humidity for five days before testing.

The tests were carried out in the conditioning atmosphere where possible. The moisture levels in some specimens were measured to verify that the desired test conditions and equilibrium moisture content had been achieved. Moisture content was obtained by measuring the mass of the specimens in a balance immediately before and after testing and after oven-drying at 105 °C overnight.

4.2.2.2 Edge compression

The edge compression tests were carried out according to TAPPI test standard T811, used to measure the compressive strength of corrugated paperboard in the cross-direction. The edge compression test is only done in the cross-direction because of the low compressive failure load in the machine-direction.

The specimens were cut as shown in Table 4-6 and additionally have paraffin wax reinforcement applied on the loading edges by dipping in molten paraffin at 60 to 70 °C to a 6 mm depth, before preconditioning and conditioning as detailed in the previous section on specimen preparation. The wax reinforcements help to avoid failure by crushing of loaded edge end surfaces. The sampling sizes for the edge compression tests are shown in Table 4-7.

The tests were carried out in the conditioning room. The specimen width, height and overall thickness were measured with Vernier callipers before testing. The compressive force was applied using rigidly supported and driven platens shown in Figure 4-2 (a) in a uniaxial test machine (Lloyd LR100K for tests carried out at Waikato University and Instron for tests carried out at Scion). The speed of the driven platen used in the test was 12.5 mm/min for both test conditions.

The specimens were supported at the start of testing by two metal guide blocks in the region above the bottom waxed edge, shown in Figure 4-2

(b), as specified in the T811 test standard. The blocks align the specimens vertically so that the applied force is parallel to the cross-direction, and are removed when the force is between 22 and 67 N to allow the sample to compress unhindered for the remainder of the test. The loading edges are ensured to be parallel by the use of guides for cutting the specimens and checking the loading platens are level during the test.

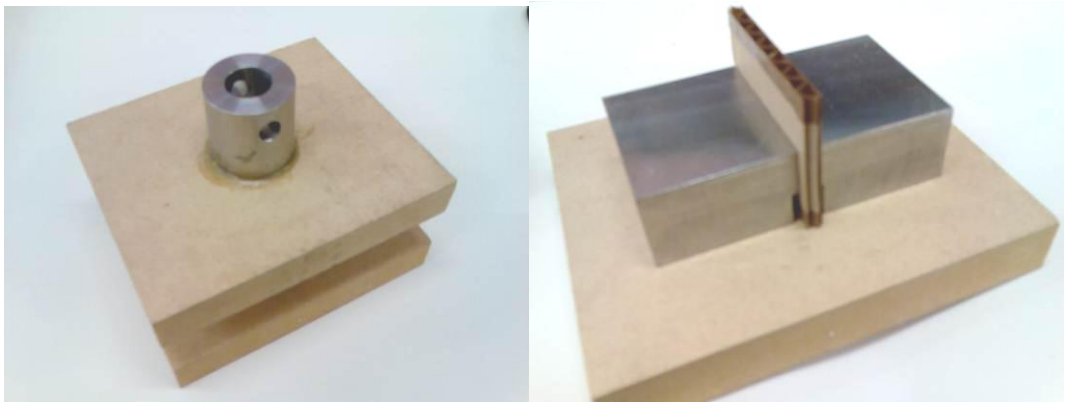

(a) (b)

Figure 4-2: (a) Edge compression test platens. (b) Specimen supported by metal blocks for vertical alignment at start of edge compression test

The tests recorded load and compressive displacement data which was converted to stress and strain as follows. Measurements of the thickness of paperboard layers and length of the corrugated layer with a micrometer and ruler were used to calculate the specimen's load-bearing cross-section. Stress values were obtained by division of the load data with the cross-section. Strain was obtained by division of the compressive displacement with the original height of the specimen.

Stress vs. strain plots were obtained for each specimen. The plots are typically non-linear at the start of the tests and prior to failure, refer to Figure 4-3 (a). The initial non-linearity found at the start of the test may have been caused by levelling of the waxed edges or imperfectly parallel cut edges and in-plane imperfections. The peak load in Figure 4-3 (a) represents the material failure load.

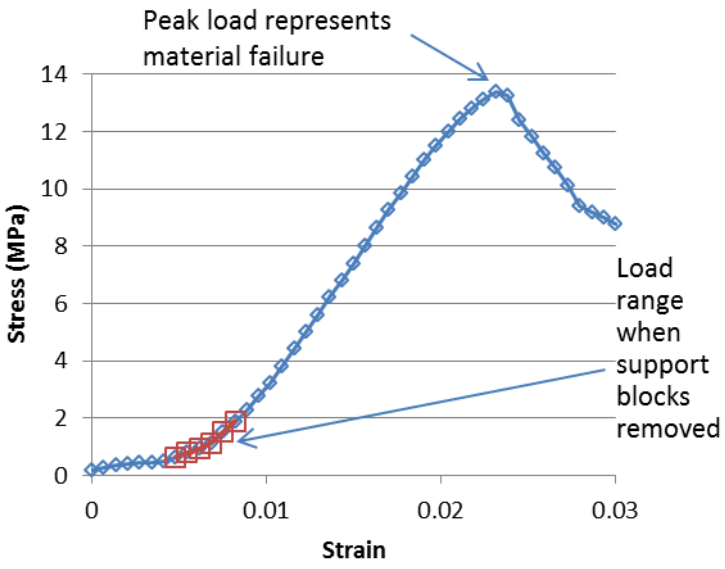

(a)

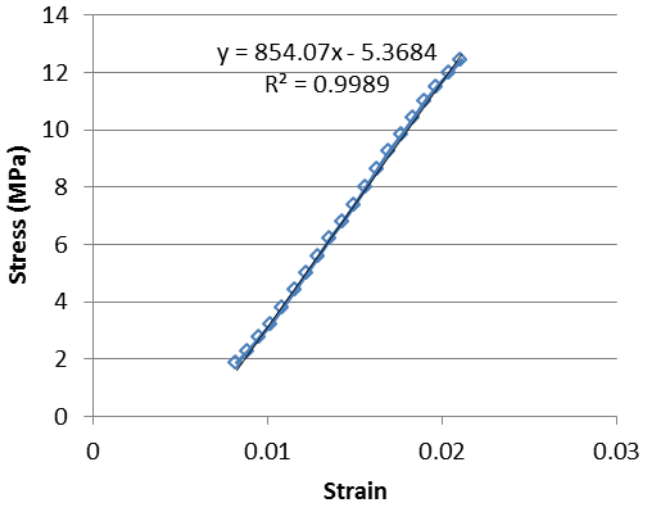

(b)

Figure 4-3: (a) Edge compression stress vs. strain plot. (b) Linear portion of the stress vs. strain plot after data at the start and end of test removed.

In analysis of the results, non-linearity at the start and end of the tests were removed, retaining only the linear portion of the stress vs. strain plots, refer to Figure 4-3 (b). An elastic modulus in the cross-direction E_{22} was determined from the gradient of a linear fit through the remaining stress vs. strain plots. The edge compression test results are shown in Appendix III, Figures III-8 to III-11.

A mean value of E_{22} and its uncertainty for a 95% confidence interval for the different tests were calculated using the following equations:

Sample mean $\bar{x} = \frac{\sum_{i=1}^{i=n} x_i}{n}$;

Equation 4-7

Sample mean uncertainty $x_{error} = \frac{s\, t_{n-1}}{\sqrt{n}}$;

Equation 4-8

where s is the sample standard deviation, n the number of specimens in the sample, and $t_{n\text{-}1}$ is the t-value of the student's t-distribution calculated using the inverse probability 0.05 and n-1 the degrees of freedom for the distribution.

4.2.2.3 Four-point bending

The four-point bending tests were carried out according to TAPPI test standard T820, used to measure flexural stiffness of corrugated paperboard in machine- and cross-directions.

The four-point bending method was used as shearing forces are absent in the middle segment of the bending specimen, giving a constant flexural stress and more accurate measure of flexural stiffness independent of the specimen length.

The specimens were cut to be longer along the tested direction (MD or CD) as shown in Table 4-6, then preconditioned and conditioned as detailed in the section above on specimen preparation. The sampling sizes for the bending tests are shown in Table 4-7, where in each test direction approximately half the specimens were tested with the single facer side up and half with the double backer side up.

The tests were carried out in the conditioning atmosphere using the four-point bending apparatus in Figure 4-4. The specimens were simply-supported on two cylindrical rods and loaded by another two cylindrical

rods connected to a uniaxial test machine (an IDM Instruments Pty. Ltd.), displacement driven at a speed of 10mm/min.

A diagram of the specimen in four-point bending is shown in Figure 4-5. where F (N) is the total load applied; δ (m) is the specimen deflection at mid-span; l_1 the distance between supporting and loading points is 50 mm; and l_2 distance between inner loading points is 100 mm.

The load applied F was measured using the test machine load cell and deflection at mid-span δ measured with a Linear Variable Differential Transformer linear potentiometer.

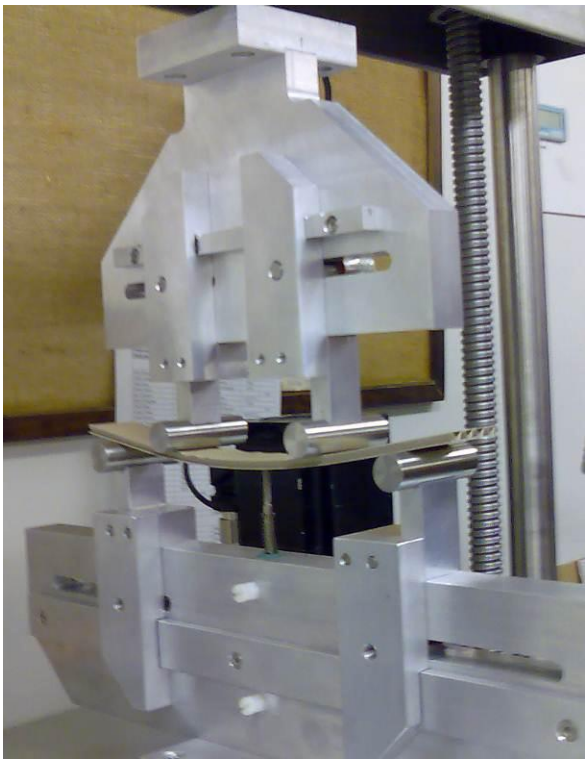

Figure 4-4: Four-point bending test apparatus.

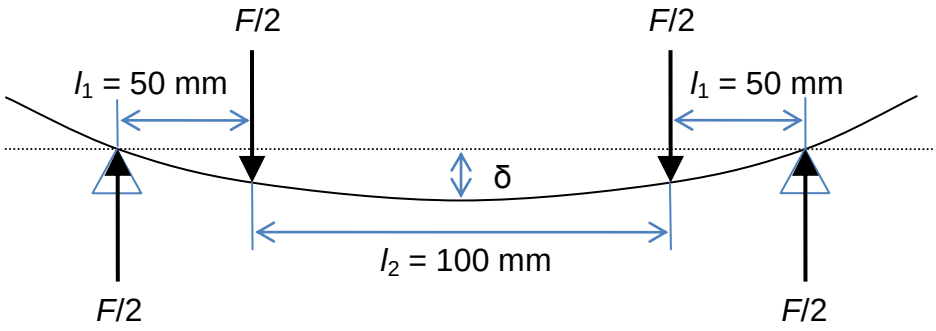

F = total load applied [N]

δ = deflection at mid span[m]

l_1 = distance between supporting and loading points [m]

l_2 = distance between inner loading points [m]

Figure 4-5: Four-point bending test diagram.

Load vs. deflection plots were obtained for each test. Then, the non-linear portions of each plot at the start and end of the test were removed and a gradient of a linear fit through the remaining data obtained. The results of the four-point bending experiments are shown in Appendix III, Figures III-17 to III-32.

The bending stiffness D (N m) for each test was then calculated using the following equation:

$$D = \frac{F}{\delta}\left(\frac{l_1 {l_2}^2}{16\, w}\right);$$

Equation 4-9

where F / δ is the gradient of the linear portion of the load vs. deflection plot and w is the width of the specimen.

The second moment of area for corrugated paperboard section I (m^4) was calculated for bending in the machine- and cross-directions (refer to Figure 4-6). The MD bending calculation of I only considers the contribution of the corrugated paperboard facings, while the CD bending calculation of I includes the contribution of the corrugated core profile.

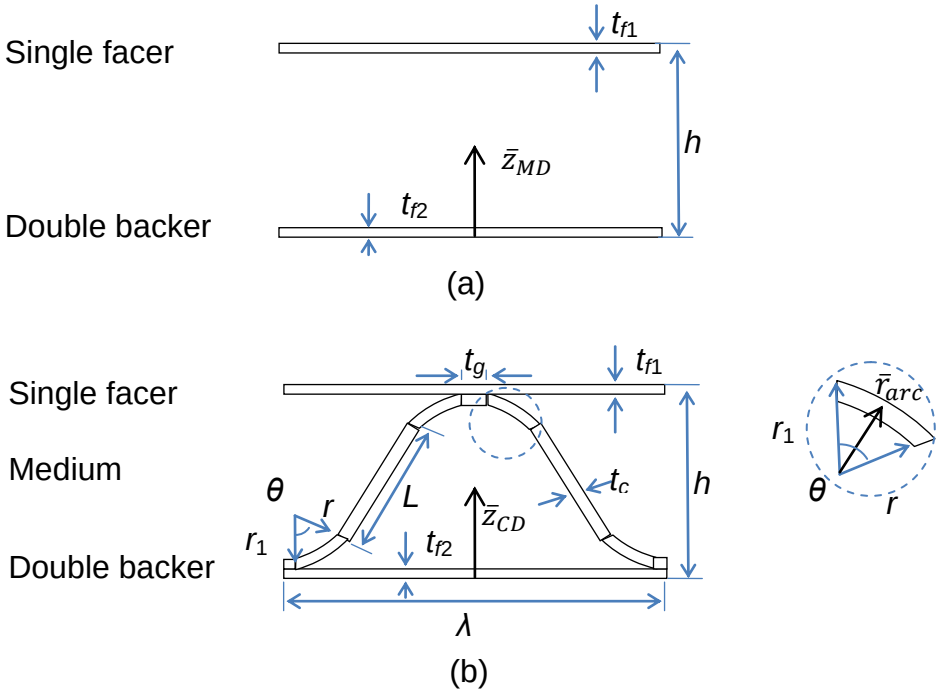

Figure 4-6: Corrugated paperboard sections for (a) bending in machine-direction neglecting the medium and (b) bending in cross-direction.

The centroid of a unit width corrugated paperboard section bending in MD $\bar{z}_{MD}$ is given below:

$$\bar{z}_{MD} = \frac{\left(h - \frac{t_{f\,1}}{2}\right) t_{f\,1} + \left(\frac{t_{f\,2}}{2}\right) t_{f\,2}}{t_{f\,1} + t_{f\,2}}$$

Equation 4-10

The second moment of area for the section bending in MD I_{MD} is given by:

$$I_{MD} = \frac{{t_{f\,1}}^3}{3} + t_{f\,1}\left(h - t_{f\,1} - \bar{z}_{MD}\right)^2 + \frac{{t_{f\,2}}^3}{3} + t_{f\,2}\left(\bar{z}_{MD} - t_{f\,2}\right)^2$$

Equation 4-11

The centroid of a corrugation wavelength wide corrugated paperboard section bending in CD $\bar{z}_{CD}$ is given below:

$$\bar{z}_{CD} = \frac{\sum \bar{z}A_{facings} + \sum \bar{z}A_{glue\ joints} + \sum zA_{angled\ sections} + \sum \bar{z}A_{arcs}}{(t_{f\,1} + t_{f\,2})\lambda + 2\,t_g\,t_c + 2\,(r_1{}^2 - r^2)\theta + 2\,L\,t_c} \quad \text{(i)}$$

$$\sum \bar{z}A_{facings} = \left(h - \frac{t_{f\,1}}{2}\right) t_{f\,1}\lambda + \frac{t_{f\,2}{}^2}{2}\lambda \quad \text{(ii)}$$

$$\sum \bar{z}A_{glue\ joints} = \left(h - t_{f\,1} - \frac{t_c}{2} + t_{f\,2} + \frac{t_c}{2}\right) t_c t_g \quad \text{(iii)}$$

$$\sum \bar{z}A_{angled\ sections} = 2\left(t_{f\,2} + r_1 - r\cos\theta + \frac{1}{2}(L - t_c\ \cot\theta)\sin\theta\right)\ t_c L \quad \text{(iv)}$$

$$\sum \bar{z}A_{arcs} = \left(t_{f\,2} + r_1 - \bar{r}_{arc}\cos\tfrac{\theta}{2} + h - t_{f\,1} - r_1 + \bar{r}_{arc}\cos\tfrac{\theta}{2}\right)(r_1{}^2 - r^2)\theta \quad \text{(v)}$$

$$\bar{r}_{arc} = \frac{2(r_1{}^3 - r^3)\sin\frac{\theta}{2}}{3(r_1{}^2 - r^2)\theta} \quad \text{(vi)}$$

Equation 4-12

The second moment of area for the corrugated paperboard section bending in CD I_{CD} is given by:

$$I_{CD} = I_{facings} + I_{glue\ joints} + I_{angled\ sections} + I_{arcs} \quad \text{(i)}$$

$$I_{facings} = \frac{\lambda t_{f\,1}{}^3}{3} + \lambda t_{f\,1}\left(h - t_{f\,1} - \bar{z}_{CD}\right)^2 + \frac{\lambda t_{f\,2}{}^3}{3} + \lambda t_{f\,2}\left(\bar{z}_{CD} - t_{f\,2}\right)^2 \quad \text{(ii)}$$

$$I_{glue\ joints} = \tfrac{2}{3} t_g\ t_c{}^3 + t_g\ t_c\left(\left(h - t_{f\,1} - t_c - \bar{z}_{CD}\right)^2 + \left(\bar{z}_{CD} - t_{f\,2}\right)^2\right) \quad \text{(iii)}$$

$$I_{angled\ sections} = 2\left(\tfrac{1}{3}\frac{t_c}{\sin\theta}\left((L - t_c\cot\theta)\sin\theta\right)^3 + t_c(L - t_c\cot\theta)\left(t_{f\,2} + r_1 - r\cos\theta - \bar{z}_{CD}\right)^2 + \tfrac{1}{6}\frac{t_c}{\sin\theta}(t_c\cos\theta)^3 + \tfrac{1}{2} t_c{}^2\cot\theta\left(\left(h - t_{f\,1} - r_1 + r\cos\theta - \bar{z}_{CD}\right)^2 + \left(\bar{z}_{CD} - t_{f\,2} - r_1 + r\cos\theta\right)^2\right)\right) \quad \text{(iv)}$$

$$I_{arcs} = 4\,I'_{arc} + (r_1{}^2 - r^2)\theta\left(\left(h - t_{f\,1} - \bar{z}_{CD}\right)^2 + \left(\bar{z}_{CD} - t_{f\,2}\right)^2\right) \quad \text{(v)}$$

$$I'_{arc} = \int\left(r_1 - \frac{(r_1 + r)}{2}\cos\theta\right)^2 \frac{(r_1{}^2 - r^2)}{2} d\theta = \left(\frac{r_1{}^2\theta}{2} - r_1\frac{(r_1 + r)}{2}\sin\theta + \frac{(r_1 + r)^2}{16}\left(\theta + \frac{\sin 2\theta}{2}\right)\right)(r_1{}^2 - r^2) \quad \text{(vi)}$$

Equation 4-13

The elastic modulus *E* (Pa) in each test direction was calculated using the following equation:

$$E = \frac{D\,w}{I},$$

Equation 4-14

where *w* is the width of the specimen, *D* is the flexural stiffness and *I* is the second moment of area of the section.

Mean values of *E* in the MD and CD directions and uncertainty for a 95% confidence interval were calculated using Equation 4-7 and Equation 4-8. Similar mean and uncertainty calculations were carried out for the bending stiffnesses in MD and CD.

4.2.2.4 Sonic Vibration

The sonic vibration tests were carried out using the method described in (Sato et al., 2008), to determine elastic properties of the corrugated paperboard from frequencies of free boundary condition vibration modes.

The specimens were cut square as shown in Table 4-6, then preconditioned and conditioned as detailed in the section on specimen preparation. This test method was only conducted at the 23°C, 50% relative humidity condition. A sampling size of five for each paperboard material was used for the sonic vibration tests.

The tests were carried out in a conditioned laboratory at room temperature and relative humidity. The overall thickness *h*, the MD dimension *a*, the CD dimension *b*, and mass of each specimen was measured with vernier callipers and a balance before testing, to calculate its density ρ.

The sonic vibration test apparatus shown in Figure 4-7 consists of a sine-wave function generator with a digital frequency counter and amplifier driving a loudspeaker attached with a panel which has a hole cut-out. The sound waves generated cause vibration of specimens which are placed over the speaker panel hole near the expected vibration mode anti-nodal

regions. Small, soft, and uniformly cut plastic foam supports are placed under specimens along the expected nodal lines to achieve the theoretical free edge boundary conditions. Fine tea leaves are sprinkled over the specimens to visualise the vibration modes, since nodal lines are shown where the tea leaves accumulate.

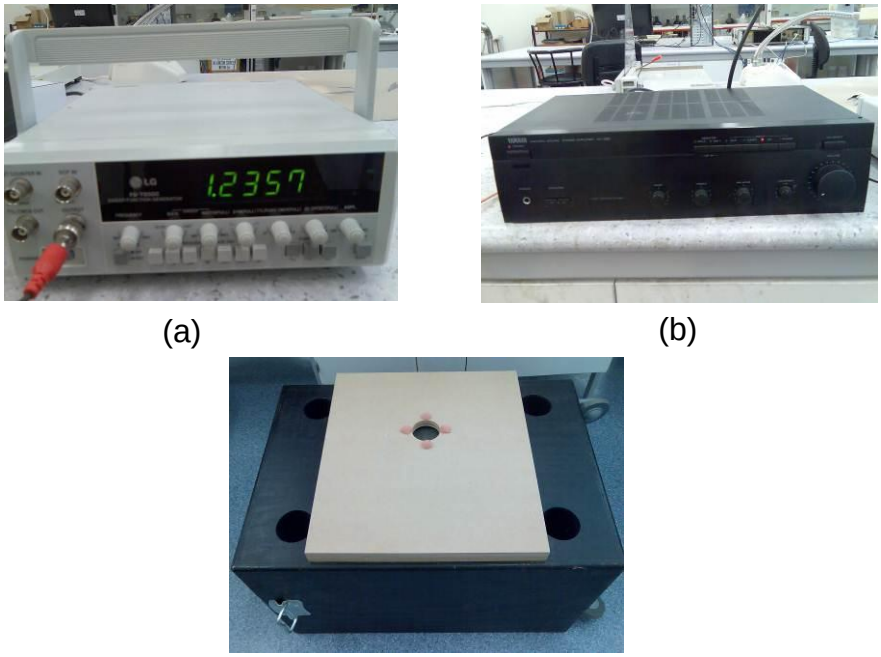

(a) (b)

(c)

Figure 4-7: Sonic vibration test apparatus: (a) sine-wave function generator, (b) amplifier, (c) loudspeaker and attached panel with hole cut-out.

The frequency of the function generator is adjusted to search for the three natural frequencies of the plate under free boundary conditions for the modes as shown in Figure 4-8. These are the anti-symmetric '+' mode f_{+}, CD bending mode $f_{b\,CD}$ and MD bending mode $f_{b\,MD}$ frequencies. The sonic vibration results are presented in Appendix III, Figures III-41 to III-46.

It is important that the sample is positioned so that the expected nodal lines of the vibration mode being searched for are not directly over the speaker hole. Otherwise, an anti-node will appear on the sample in the region over the speaker hole, which will prevent the desired vibration mode being found. For example, the vibration mode in Figure 4-8 (a) can only be found if the sample is placed with one corner over the speaker

hole. This is unlike the other vibration modes in Figure 4-8 (b) and (c) which have the samples centred directly over thespeaker hole.

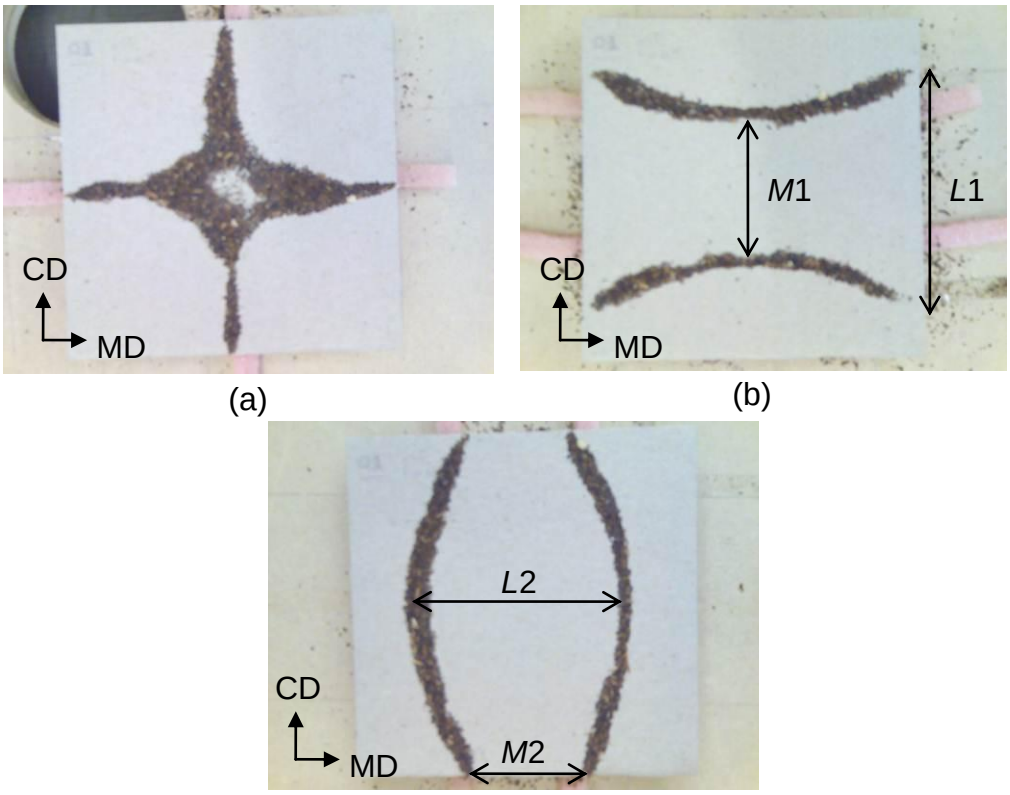

Figure 4-8: (a) Anti-symmetric '+', (b) bending CD and (c) bending MD, free boundary condition vibration modes.

From the three frequencies, initial values of flexural stiffnesses D_{11}, D_{22}, and D_{66} are calculated as follows (Sato et al., 2008):

$$D_{11} = 0.0789 {f_{b\,MD}}^2 \rho a^4 h \quad \text{(i)}$$

$$D_{22} = 0.0789 {f_{b\,CD}}^2 \rho b^4 h \quad \text{(ii)}$$

$$D_{66} = 0.274\, {f_{+}}^2 \rho a^2 b^2 h \quad \text{(iii)}$$

Equation 4-15

The flexural stiffness D_{12} is usually obtained by resizing the specimen dimensions to produce ring- and 'x'- modes of vibration. The new dimensions a_{ox} and b_{ox} would be calculated from the MD and CD bending mode frequencies:

$$\frac{a_{ox}}{b_{ox}} = \left(\frac{f_{b\,MD}}{f_{b\,CD}}\right)^{\frac{1}{2}}$$

Equation 4-16

The ring- f_o and 'x'- mode f_x frequencies measured for the resized specimen would be used to calculate an initial of D_{12}:

$$D_{12} = 0.114\left({f_o}^2 - {f_x}^2\right)\rho {a_{ox}}^2 {b_{ox}}^2 h$$

Equation 4-17

An alternative method of estimating D_{12} was used, where the ratio of distances $M1$, $M2$, $L1$, $L2$ between nodal lines of MD and CD bending modes shown in Figure 4-8 are measured to estimate the Poisson's ratios v_{12} and v_{21} and initial value of twisting stiffness D_{12}.

$$v_{12} = 1 - M1/L1 \quad \text{(i)}$$

$$v_{21} = 1 - M2/L2 \quad \text{(ii)}$$

$$D_{12} = v_{21}D_{11} = v_{12}D_{22} \quad \text{(iii)}$$

Equation 4-18

An iterative Rayleigh-Ritz vibration model (Sato et al., 2008) developed by Prof. Jim Woodhouse in MATLAB software was used to give final values of D_{11}, D_{22}, D_{12} and D_{66} which are used to calculated equivalent elastic moduli in MD and CD for the corrugated paperboard E_{11} and E_{22}:

$$E_{11} = \frac{12}{h^3}\left(D_{11} - \frac{{D_{12}}^2}{D_{22}}\right) \quad \text{(i)}$$

$$E_{22} = \frac{12}{h^3}\left(D_{22} - \frac{{D_{12}}^2}{D_{11}}\right) \quad \text{(ii)}$$

Equation 4-19

Mean and uncertainty values for a 95% confidence interval were calculated for the elastic moduli and flexural stiffnesses.

4.2.3 Finite Element materials test models

Finite Element models of the three materials tests presented in section 4.2.2 were created in *Abaqus* in order to compare the modelled material behaviour of paperboard with that in the experiments.

4.2.3.1 Material models of corrugated paperboard

The two types of corrugated paperboard models used in the Finite Element models were the equivalent single-layered and detailed geometric models. The equivalent single-layered model was assigned the equivalent material properties presented in Table 4-5, of section 4.2.1. The detailed geometric model has the facings and core layers modelled and assigned with material properties of the constituent layers presented in Table 4-2, of section 4.2.1. The detailed geometric model shown in Figure 4-9 has the core and facings layers bonded perfectly, since the model is created as one part by extruding the sketch of the mid-planes of the cross-section as a whole. Section assignments for the facings are applied offset from the model surfaces to account for the thickness of the layers.

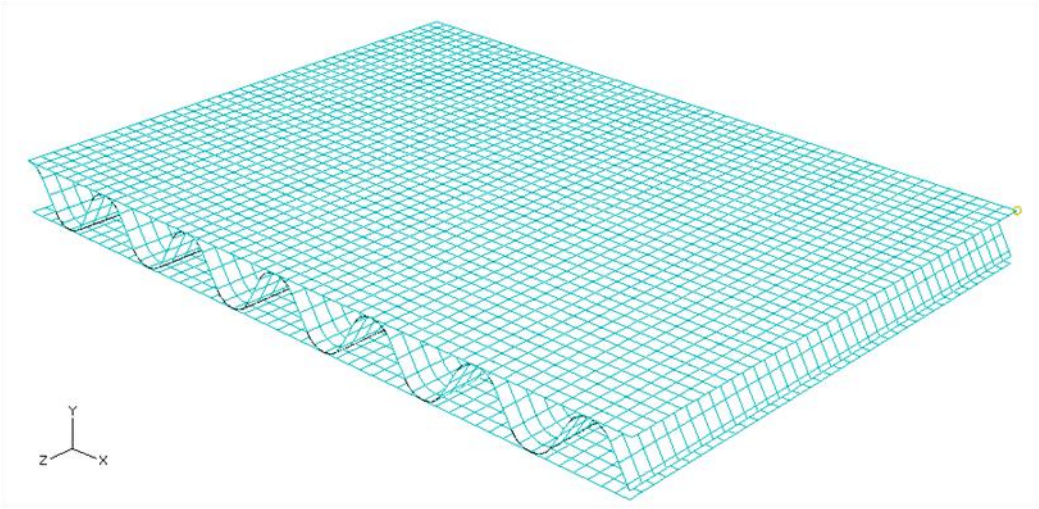

Figure 4-9: Detailed geometric Finite Element model of corrugated paperboard.

The corrugated paperboard FE models presented use 1 mm S8R5 quadratic quadrilateral thin shell elements with 8 nodes and five degrees of freedom (DOF) per node.

4.2.3.2 Analysis steps

A *Riks, General* step procedure was used for the edge compression and bending models, while a *Frequency* step procedure was used for the sonic vibration models. The *Riks* procedure controls the step by incrementing the arc length along the static equilibrium path of the load-displacement solution, allowing for unstable response, collapse and geometric nonlinearity. In the *Riks* analysis, the load magnitude is treated as unknown and is given in the solution as a proportion of the initial load value. The *Frequency* step obtains eigenvalues for the natural frequencies of the structure and corresponding vibration modes.

4.2.3.3 Loading, boundary conditions and calculation of elastic constants

Edge compression model

The edge compression models have clamped boundary conditions along the bottom edges, while the top edges have all rotational and translational DOF fixed except the y-direction translation, U2. A uniform displacement loading is enforced on the top edges of the model via a concentrated load at a reference point constraining their y-direction translational DOF, U2, by a kinematic coupling; refer to Figure 4-10. A concentrated load limit of 500 N, representative of the load range applied in the tests, was applied to the edge compression models.

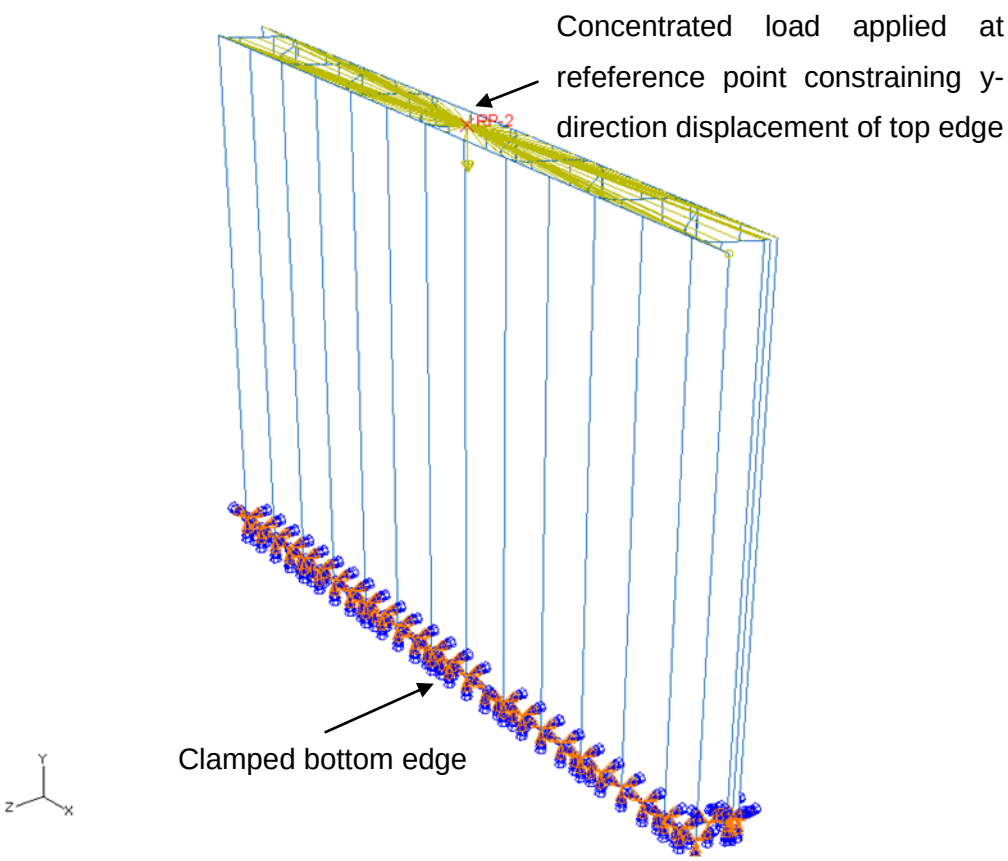

Figure 4-10: Edge compression FE model with fully clamped bottom edge and kinematic coupling constraining U2 displacement of the top loaded edge to a reference point.

Average stress due to loading vs. strain plots were determined from the load and edge displacement model results by division with the cross-section and original height of the paperboard model respectively. The equivalent Young's modulus in the cross-direction (CD) E^*_{22} is obtained from the gradient of the linear portion of the average stress vs. strain plots (Appendix III, Figures III-12 to III-16) as in the edge compression experimental method of section 4.2.2. E^*_{22} from the edge compression models and tests are compared.

Four-point bending model

The four-point bending FE models have loads applied at two inner lines across the model via a reference point which constrains their six DOF by a kinematic coupling, representative of the pair of upper loading anvils applied on the specimens in the four-point bending test; refer to Figure

4-11. Two other outer lines across the bending models are pin-supported, representative of the bottom supporting anvils in the four-point bending test.

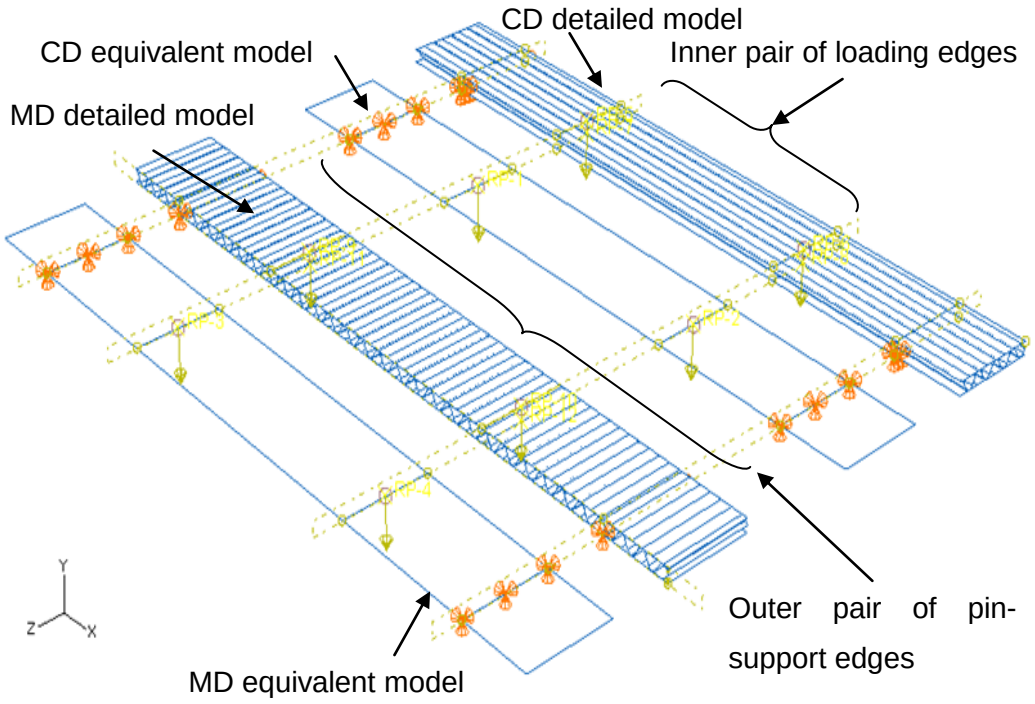

Figure 4-11: Four-point bending in MD and CD FE models.

The loads applied to the models are detailed in Table 4-8 and are representative of the load range achieved in the four-point bending tests for the materials and loading directions. The flexural stiffnesses D_{11} and D_{22}, and equivalent Young's moduli in the machine- (MD) and cross-directions (CD) E^*_{11} and E^*_{22} are determined from the load vs. mid-span deflection results (Appendix III, Figures III-33 to II-40) and compared between the bending models and tests. The calculations use the gradient of the linear portion of the load vs. deflection plots, sample geometry and second moment of area in the MD and CD directions as in the four-point bending experimental method of section 4.2.2.

Table 4-8: Load applied in four-point bending FE models.

Paperboard	Relative humidity	Test direction	Load limit (N)
Kraft	50%	MD	10
		CD	20
	90%	MD	6
		CD	10
Recycled	50%	MD	8
		CD	14
	90%	MD	5
		CD	7

Free vibration models

The free-vibration detailed FE models shown in Figure 4-12 are free of boundary conditions. Three vibration frequencies of the square models are obtained for the '+ mode', 'bending CD mode' and 'bending MD mode' shown in Figure 4-12.

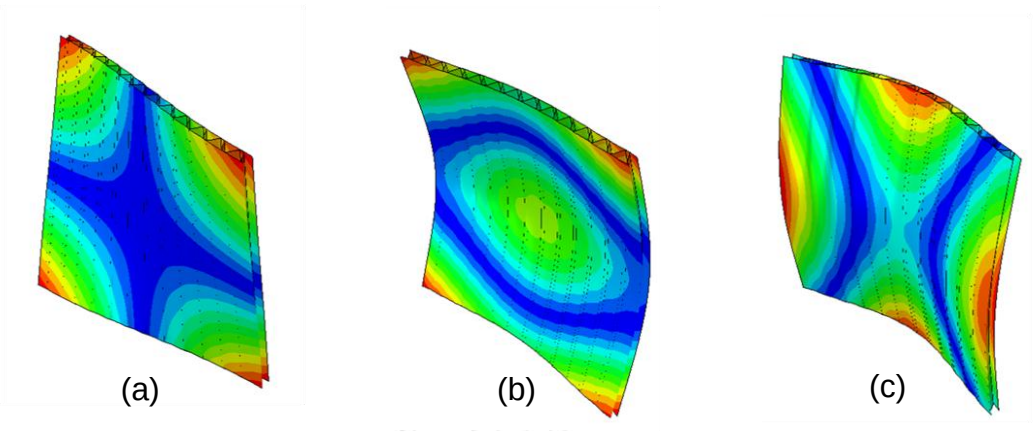

Figure 4-12: Free-vibration (a) '+ mode', (b) 'Bending CD mode' and (c) 'Bending MD mode' for corrugated paperboard FE model.

The models are then resized according to the ratio between the frequencies of the bending MD and CD modes; refer to Equation 4-16. The vibration frequencies of the resized models for the ring- and 'x'-modes shown in Figure 4-13 are then obtained.

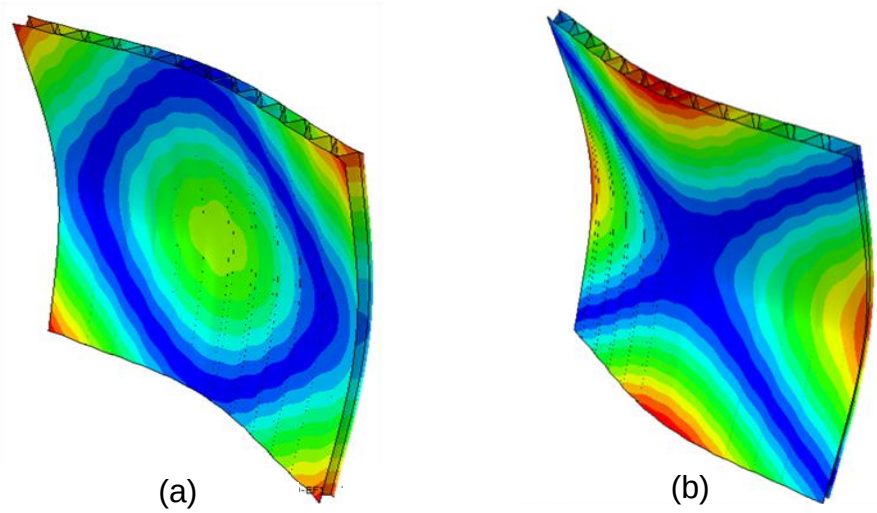

Figure 4-13: (a) Ring- and (b) 'x'- modes for the resized FE free-vibration model.

Similar free vibration equivalent single layer models were created. The free vibration model results are found in Appendix III, Figures III-47 to II-66.

The free-vibration frequencies along with the mass and dimensions of the paperboard are used to obtain initial values of the flexural stiffnesses D_{11}, D_{12}, D_{22}, D_{66}; refer to Equation 4-15 and Equation 4-17. The equivalent elastic moduli in the machine- (MD) and cross-directions (CD) E^*_{11} and E^*_{22} are found using the iterative Rayleigh-Ritz vibration model developed by Prof. Jim Woodhouse in MATLAB software, as in the sonic vibration experimental method of section 4.2.2.

4.3 Results and Discussion

The overall paperboard material properties from calculations, materials tests and FE models are compared in this section. A summary of the methods used to obtain effective properties for corrugated paperboard is given in Table 4-9.

The equivalent elastic moduli in MD and CD E^*_{11} and E^*_{22} of kraft and recycled corrugated paperboard at 50% and 90% relative humidity (RH) obtained by the different methods are shown in Figure 4-14 and Figure 4-15.

A summary of elastic properties of kraft and recycled paperboard obtained by the different methods, including the flexural stiffnesses D_{11}, D_{12}, D_{22}, D_{66}, shear modulus G^*_{12}, and Poisson's ratios ν^*_{12}, ν^*_{21} is given in Appendix III.

The experimental and Finite Element results for the edge compression, bending and free-vibration methods are also presented in Appendix III. For edge compression, the linear portions of average stress vs. strain plots are given. For four-point bending, the linear portions of applied load vs. centre deflection plots are shown. For free-vibration, three vibration modes and frequencies for the '+', MD- and CD-bending modes are presented. The FE results for free-vibration also include the 'x' and ring vibration modes.

Table 4-9: Methods used to obtain effective properties of corrugated paperboard.

Method	*Description*	*Equations used*
Equiv. analytical	In-plane and flexural properties calculated using the component layer properties and corrugation geometry.	In-plane properties: equations 2-1 to 2-7. Flexural properties: equations 4-3 to 4-6
Equiv. FE	Flexural properties calculated from component layer properties and corrugation geometry. In-plane properties calculated from flexural properties.	Flexural properties: equations 4-3 to 4-6. In-plane properties: equations 2-8 to 2-12.
4-pt bend test	Flexural stiffness in MD and CD from gradient of load vs. mid-span deflection plot of four-point bending experiment. In-plane stiffness in MD and CD calculated from flexural stiffness.	Flexural properties: equation 4-9. In-plane properties: equations 4-10 to 4-14.
4-pt bend equiv. FE	Flexural stiffness in MD and CD from gradient of load vs. mid-span deflection plot of four-point bending FE model given properties of 'Equiv. FE'. In-plane stiffness in MD and CD calculated from flexural stiffness.	Flexural properties: equation 4-9. In-plane properties: equations 4-10 to 4-14.
4-pt bend detailed FE	Flexural stiffness in MD and CD from gradient of load vs. mid-span deflection plot of four-point bending detailed geometric FE model given component layer properties. In-plane stiffness in MD and CD calculated from flexural stiffness.	Flexural properties: equation 4-9. In-plane properties: equations 4-10 to 4-14.
EC test	In-plane CD modulus from gradient of stress vs. strain plot of Edge Compression experiment.	
EC equiv. FE	In-plane CD modulus from gradient of stress vs. strain plot of Edge Compression FE model given properties of 'Equiv. FE'.	
EC detailed FE	In-plane CD modulus from gradient of stress vs. strain plot of Edge Compression detailed geometric FE model given component layer properties.	
Sonic vib. test	In-plane, shear and flexural stiffness and Poisson's ratio from iterative vibration model input with free-vibration frequencies of sonic vibration experiment.	Flexural properties: equation 4-15, 4-18. In-plane properties: equation 4-19.
Free-vib. equiv. FE	In-plane, shear and flexural stiffness and Poisson's ratio from iterative vibration model input with free-vibration frequencies of FE model given properties of 'Equiv. FE'.	Flexural properties: equation 4-15 to 4-17. In-plane properties: equation 4-19.
Free-vib. detailed FE	In-plane, shear and flexural stiffness and Poisson's ratio from iterative vibration model input with free-vibration frequencies of detailed geometric FE model given component layer properties.	Flexural properties: equation 4-15 to 4-17. In-plane properties: equation 4-19.

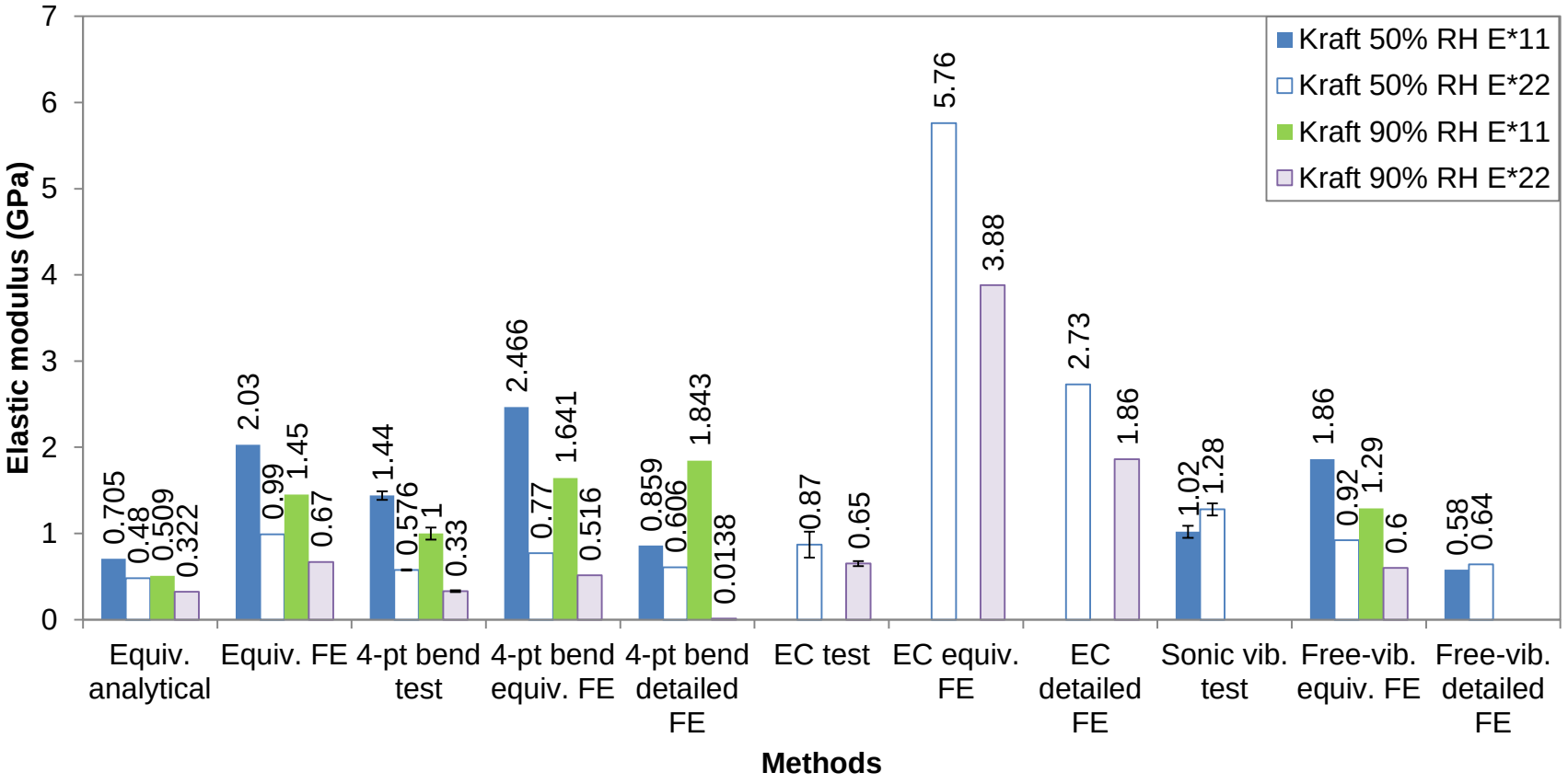

Figure 4-14: Elastic moduli E^*_{11} and E^*_{22} of kraft paperboard at 50% and 90% relative humidity, 23 °C, obtained by different methods.

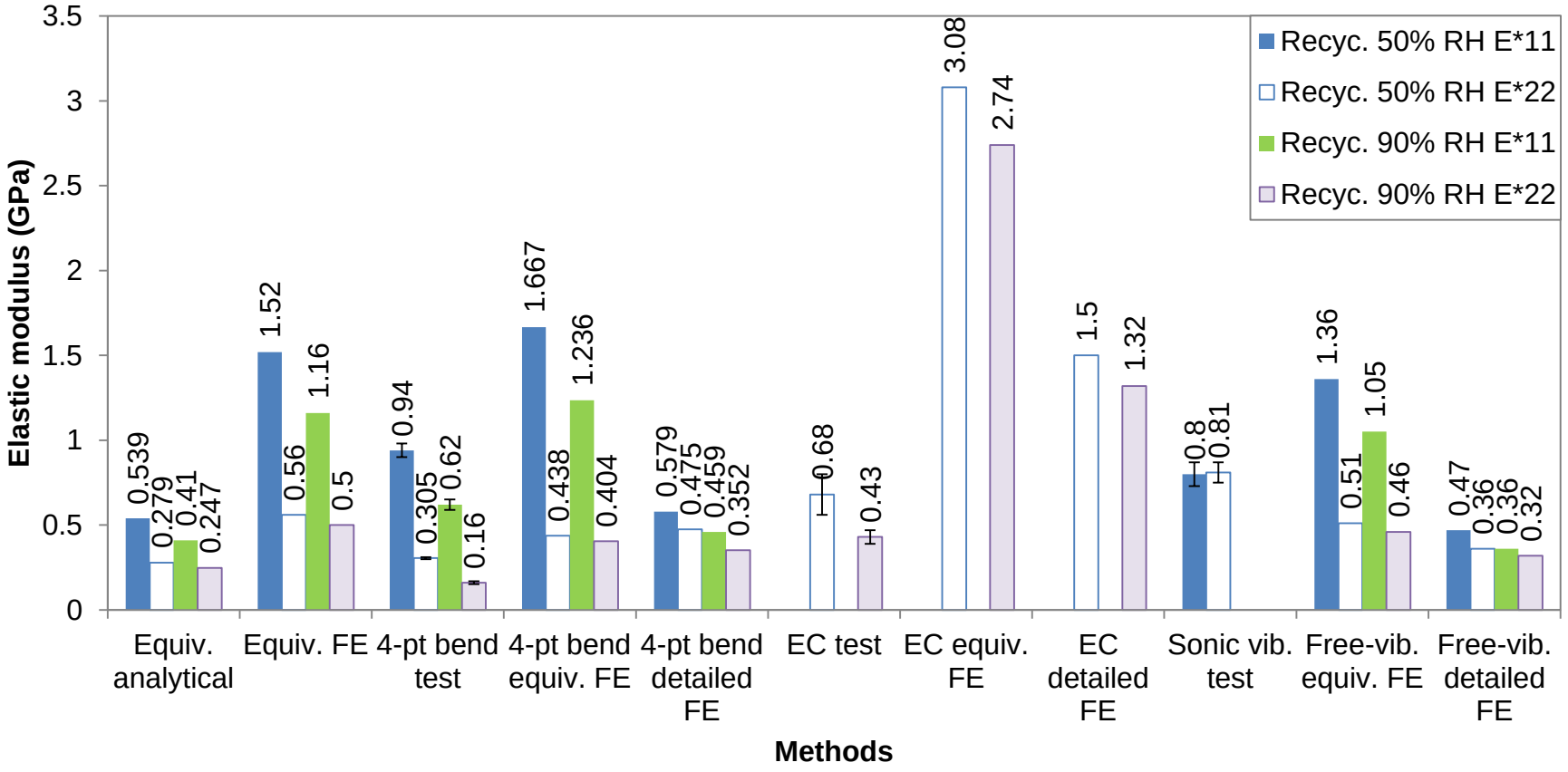

Figure 4-15: Elastic moduli E^*_{11} and E^*_{22} of recycled paperboard at 50% and 90% relative humidity, 23 °C, obtained by different methods.

The elastic moduli in MD and CD from the experiments are compared in the next section, followed by the comparisons of the experimental values to calculated and Finite Element results in the preceding sections.

4.3.1 Material properties from experiments

The elastic moduli of the experimental results are considered in the following. Firstly, the relative values of the MD and CD elastic moduli are discussed, followed by comparisons of elastic moduli among the experimental methods.

4.3.1.1 Comparing E^*_{11} with E^*_{22} in experiments

The ratio between the elastic moduli in MD and CD for the four-point bending and sonic vibration experiments are compared in this section. The four-bending and sonic vibration tests give one elastic modulus each in the MD and CD direction, though the results obtained are due to a combined effect of tensile and compressive properties of the material. This is because these tests involve bending and additionally twisting for the sonic vibration test and hence compressive and tensile behaviours of the material are incorporated. It is expected that the MD elastic modulus will be greater than the CD elastic modulus because in the paper layers, more fibres are aligned parallel to MD due to the manufacturing process. The differences in the MD and CD elastic moduli of corrugated paperboard could be due to the relative values of the elastic moduli in the MD and CD direction of the constituent paperboard layers (refer to Table 4-2). For the kraft corrugated paperboard at 50% relative humidity, the facing layers have slightly higher elastic moduli than the core. For recycled corrugated paperboard at 50% relative humidity, the core has slightly higher elastic moduli than the facings. For both corrugated paperboard materials at 90% relative humidity, the elastic moduli of the constituent layers are similar. The difference between the elastic moduli in MD and CD is more significant than the difference in the properties among the paperboard layers, with the MD elastic moduli being generally more than twice the CD elastic moduli for all the constituent paperboard materials.

For the four-point bending test results, it was found that the MD elastic modulus was higher than the CD elastic modulus. The ratio of E^*_{11} to E^*_{22} was 2.5 and 3 for kraft paperboard at 50% and 90% relative humidity respectively. For recycled paperboard at 50% and 90% relative humidity, the ratio E^*_{11} to E^*_{22} was 3.1 and 3.9 respectively.

In contrast, the sonic vibration test results gave more similar values of the MD and CD elastic moduli, with E^*_{22} being 26% and 1.25% higher than E^*_{11} for kraft and recycled paperboard at 50% relative humidity respectively. The differences in the trends of E^*_{11} and E^*_{22} for the bending tests and the sonic vibration tests remain unexplained. It could be that the sonic vibration results are obtained from bending and twisting vibration modes at differences vibration frequencies which does not permit fair comparison with the bending test properties obtained at one loading rate.

The four-point bending test results show the difference between the elastic moduli was greater for recycled paperboard than kraft paperboard and also increased with relative humidity. This shows that increasing relative humidity will cause a greater reduction of the CD elastic modulus than MD and weaken recycled paperboard more than kraft.

The contradictory trend given by the sonic vibration results with closer elastic moduli in MD and CD may be due to the method in which the flexural stiffnesses used to calculate the elastic moduli, are iteratively changed in the Rayleigh-Ritz vibration model to fit the free-vibration frequencies. The sonic vibration test also gave a different order in which the bending vibration modes appeared for the two paperboard materials. For kraft paperboard, the MD bending mode was the lower of the bending frequencies, but with recycled paperboard the CD bending mode was the lower bending frequency. Yet for both materials, the vibration model estimated a higher elastic modulus in CD than MD for the sonic vibration tests.

The dependency of the paperboard material behaviour on loading rate (Sato et al., 2008) may also explain the similarity of the MD and CD elastic moduli from the sonic vibration tests. The vibration model is unable to account for rate-dependent effects on material behaviour, and viscoelastic behaviour and damping have not been quantified in the tests.

4.3.1.2 Comparing E^*_{11} and E^*_{22} among experiments

Next, the values of the MD and CD elastic moduli are compared among the experimental results.

The results for the elastic modulus in MD E^*_{11} show that the four-point bending test values are 41% and 17.5% higher than the sonic vibration tests for kraft and recycled paperboard at 50% relative humidity respectively.

Conversely, the CD elastic modulus E^*_{22} results for both kraft and recycled paperboard show the four-point bending test has the lowest values, followed by the edge compression test and sonic vibration test in increasing order.

For kraft paperboard, the edge compression E^*_{22} result is 51% higher and nearly twice that of the four-point bending test at 50% and 90% relative humidity respectively. The sonic vibration test E^*_{22} result for kraft paperboard at 50% relative humidity is twice that of the four-point bending test value.

For recycled paperboard, the E^*_{22} results at 50% relative humidity show the edge compression and sonic vibration tests are 2.2 and 2.7 times higher than the four-point bending test respectively. At 90% relative humidity, the recycled paperboard E^*_{22} result for the edge compression test is 2.7 times the four-point bending result.

Some of the differences in elastic moduli among the experimental methods could be explained by the different loading rates in the methods. The edge compression test and bending tests have similar loading rates,

though the bending test has the lower rate of the two methods. The sonic vibration test gives dynamic material properties because the driving frequencies which cause comparatively faster movement in the specimen are changed to obtain different vibration modes. The CD elastic modulus for both paperboard materials at the 50% relative humidity condition are therefore highest in the sonic vibration test, followed by the edge compression and four-point bending tests. Since the edge compression and four-point bending tests were not attempted at other loading rates, the effect of loading rates on the elastic properties requires investigation in future work.

The higher MD elastic modulus for the four-point bending test in relation to the sonic vibration test could be due to the iterative vibration model predicting a lower than expected value.

The improved stiffness of paperboard attributed to its corrugated structure could mean the usual relations between flexural stiffnesses and elastic moduli for homogenous orthotropic plate sections are not applicable. The edge compression results will therefore differ from the four-point bending and sonic vibration results, which rely on the flexural stiffnesses to obtain the elastic moduli. Some tests such as the edge compression and four-point bending could also be affected by localised buckling or localised crushing failure in areas under compression. These tests with localised failure modes would be least representative of the elastic properties of the material. The sonic vibration test is non-destructive and does not show failure modes associated with the edge compression and four-point bending test.

4.3.2 Material properties from equivalent calculated analytical and FE models

The following section considers the elastic moduli obtained from calculations based on measured properties of constituent layers used for the analytical buckling analysis and equivalent single-layered Finite

Element paperboard models. The relative values of the MD and CD elastic moduli from the models are presented, followed by comparison of values among the equivalent models.

4.3.2.1 Comparing E^*_{11} with E^*_{22} in equivalent calculated models

The ratio between the MD and CD elastic moduli are now compared for the calculated equivalent analytical and equivalent single-layered Finite Element models.

The equivalent calculated material models show the MD elastic modulus E^*_{11} is higher than the CD elastic modulus E^*_{22} for both the kraft and recycled paperboard. The order of difference between the elastic moduli is larger for the equivalent Finite Element model than for the equivalent analytical model.

For kraft paperboard, the equivalent analytical E^*_{11} are 47% and 58% higher than E^*_{22} at 50% and 90% relative humidity respectively. For the equivalent Finite Element result, the ratio of E^*_{11} to E^*_{22} is 2.1 and 2.2 for kraft paperboard at 50% and 90% relative humidity respectively.

For recycled paperboard, the equivalent analytical model gives a value of E^*_{11} 93% and 66% higher than E^*_{22} at 50% and 90% relative humidity respectively. The equivalent Finite Element model for recycled paperboard at 50% and 90% relative humidity has ratios of E^*_{11} to E^*_{22} of 2.7 and 2.3 respectively.

As previously discussed, use of the relations between flexural stiffnesses and elastic moduli for homogenous orthotropic plate sections in the FE equivalent single-layered paperboard, may account for the larger difference in its elastic moduli.

4.3.2.2 Comparing E^*_{11} and E^*_{22} among equivalent calculated analytical and FE models

The equivalent calculated analytical material model was found to have lower elastic moduli than the equivalent Finite Element models in both MD and CD.

For kraft paperboard at 50% and 90% relative humidity, the equivalent Finite Element model result is 2.9 times higher for E^*_{11} and 2.1 times higher for E^*_{22}, in comparison to the equivalent analytical model.

Similarly, for recycled paperboard at 50% and 90% relative humidity, the equivalent Finite Element model results are 2.8 times higher for E^*_{11} and two times higher for E^*_{22}, than the equivalent analytical model.

The higher elastic moduli given by the equivalent FE model could also be due to the use of the relations between flexural stiffnesses and elastic moduli for homogenous orthotropic plate sections.

4.3.3 Materials testing and equivalent analytical model comparisons

The following section compares the elastic moduli of the equivalent calculated analytical material model with the experimental results for four-point bending, edge compression and sonic vibration.

At the 50% relative humidity condition, the disagreement between the equivalent analytical and sonic vibration test is least for the MD elastic modulus E^*_{11}, while for the CD elastic modulus E^*_{22} the equivalent analytical and four-point bending values are least different.

The differences in elastic moduli of the equivalent analytical model and materials tests could be due to problems associated with each experimental method discussed in the previous section on material properties from experiments.

4.3.3.1 Comparing E^*_{11} and E^*_{22} of equivalent analytical to four-point bending test

The elastic moduli in MD and CD of the equivalent analytical model compared to those of the four-point bending test are presented in the following. The agreement for the elastic modulus in CD E^*_{22} is generally better than the MD elastic modulus E^*_{11} for both the kraft and recycled paperboard. The four-point bending test elastic moduli results were also generally higher than the equivalent analytical results.

For kraft paperboard, the four-point bending test E^*_{11} result was twice that of the equivalent analytical model at 50% and 90% relative humidity. The E^*_{22} result for kraft paperboard from the four-point bending test was 20% higher at 50% relative humidity, and 2.5% higher at 90% relative humidity, compared to the equivalent analytical result.

The recycled paperboard comparisons between the equivalent analytical model and the four-point bending test elastic moduli results show less difference. The four-point bending E^*_{11} result for recycled paperboard is 74% higher at 50% relative humidity, and 51% higher at 90% relative humidity than the equivalent analytical result. The E^*_{22} result for recycled paperboard at 50% relative humidity for the four-bending test is 9% higher than the equivalent analytical value. An exception to the trends between the equivalent analytical and four-point bending test results was found for the E^*_{22} result of recycled paperboard at 90% relative humidity which shows a 54% higher value for the equivalent analytical model compared to the four-point bending test.

4.3.3.2 Comparing E^*_{22} of equivalent analytical to edge compression test

Next, the elastic modulus in CD E^*_{22} from the equivalent analytical model is compared with the edge compression test results. The edge compression test values are generally higher than those of the equivalent analytical model.

For kraft paperboard, the E^*_{22} edge compression test result is 81% higher at 50% relative humidity, and two times higher at 90% relative humidity, compared to the equivalent analytical results.

The recycled paperboard E^*_{22} result for the edge compression test is 2.4 times higher at 50% relative humidity, and 74% higher at 90% relative humidity, compared to the equivalent analytical values.

4.3.3.3 Comparing E^*_{11} and E^*_{22} of equivalent analytical to sonic vibration test

The elastic moduli in MD and CD at 50% relative humidity of the equivalent analytical model are now compared to the sonic vibration test results. The sonic vibration test results are generally higher than the equivalent analytical values, with better agreement for the MD elastic modulus than the CD elastic modulus.

For kraft paperboard, the sonic vibration test E^*_{11} result is 45% higher, while the E^*_{22} result is 2.7 times higher, compared to the equivalent analytical results. The differences between the sonic vibration test and equivalent analytical elastic moduli for recycled paperboard are similar to kraft paperboard, with the sonic vibration test being 48% higher for E^*_{11} and 2.9 times higher for E^*_{22}.

4.3.4 Material properties from Finite Element models

The following section considers the elastic moduli in MD and CD of the Finite Element equivalent single-layered and detailed models of four-point bending, edge compression, and free vibration. The elastic moduli ratios and values for the two FE models of the materials tests are compared.

4.3.4.1 Comparing E^*_{11} with E^*_{22} in equivalent and detailed geometric Finite Element models

The ratio between the elastic moduli in MD and CD are now presented for the equivalent single-layered and detailed geometric Finite Element

models of four-point bending and free vibration. The elastic modulus in MD E^*_{11} is generally higher than the CD elastic modulus E^*_{22}. The equivalent FE models generally have higher ratios of E^*_{11} to E^*_{22} than the detailed geometric FE models.

For kraft paperboard, E^*_{11} is 3.2 times higher than E^*_{22} for the equivalent FE four-point bending model results at both 50% and 90% relative humidity. The ratio E^*_{11}/E^*_{22} is 2 and 2.15 for the equivalent FE free vibration model results for kraft paperboard at 50% and 90% relative humidity respectively.

For the detailed FE model of kraft paperboard at 50% relative humidity results for four-point bending, E^*_{11} is 42% higher than E^*_{22}. The detailed FE four-point bending model results for kraft paperboard at 90% relative humidity has an unexpectedly low E^*_{22} value because errors stopped the FE analysis which meant there was insufficient data to obtain a reliable result. For the detailed FE free vibration model results of kraft paperboard at 50% relative humidity, the elastic moduli are more similar, with E^*_{22} being 10% higher than E^*_{11}.

For recycled paperboard, the equivalent FE four-point bending model values of E^*_{11} are 3.8 and 3.1 times higher than E^*_{22}, at 50% and 90% relative humidity respectively. The equivalent FE free vibration model of recycled paperboard has E^*_{11} values 2.7 and 2.3 times that of E^*_{22}, at 50% and 90% relative humidity respectively.

The detailed FE four-point bending models of recycled paperboard at 50% and 90% relative humidity have E^*_{11} values which are 22% and 31% higher than E^*_{22} respectively. The detailed FE free vibration model of recycled paperboard have values of E^*_{11} higher than E^*_{22} by 30% at 50% relative humidity, and by 12.5% at 90% relative humidity.

The larger difference between the MD and CD elastic moduli for the equivalent FE model compared to the detailed FE model is likely due to the same orthotropic relations for homogenous sections between flexural

stiffnesses and elastic moduli in the model input. The similarity between elastic moduli in the detailed FE free vibration results could be due to problems associated with the iterative vibration model.

4.3.4.2 Comparing E^*_{11} and E^*_{22} among equivalent and detailed geometric Finite Element models

The elastic moduli in MD and CD are now compared between the Finite Element equivalent single-layered and detailed geometric models of four-point bending, edge compression and free vibration. The equivalent FE models have generally higher elastic moduli than the detailed FE models of the tests.

For kraft paperboard at 50% relative humidity, the four-point bending models have E^*_{11} and E^*_{22} of the equivalent FE model being 2.9 times and 27% higher than the detailed FE model respectively. At 90% relative humidity, the kraft paperboard four-point bending FE models show more similar E^*_{11} values, with the detailed model being 10% higher than the equivalent model. The four-point bending E^*_{22} values of the detailed FE model of kraft paperboard at 90% relative humidity was not reliable as previously mentioned.

For recycled paperboard, the four-point bending FE models have E^*_{11} of the equivalent model being 2.9 and 2.7 times higher than the detailed model, at 50% and 90% relative humidity respectively. The E^*_{22} values of the recycled paperboard four-point bending FE models are more similar, with the detailed model value being 9% and15% higher than the equivalent model, at 50% and 90% relative humidity respectively.

The edge compression FE models of kraft and recycled paperboard at both 50% and 90% relative humidity show the equivalent model E^*_{22} result is 2.1 times that of the detailed model.

For kraft paperboard at 50% relative humidity, the E^*_{11} and E^*_{22} free vibration equivalent FE model results are 3.2 times and 44% higher than the detailed model respectively.

The free vibration FE models of recycled paperboard at 50% and 90% relative humidity show the E^*_{11} values of the equivalent model are 2.9 times higher than the detailed model. For the recycled paperboard E^*_{22} results from free vibration FE models, the equivalent models are 42% and 44% higher than the detailed model, at 50% and 90% relative humidity respectively.

The CD elastic modulus values have better agreement among the two FE model types than the MD elastic modulus for both paperboard materials in four-point bending and free vibration. The edge compression equivalent and detailed FE models give a much higher E^*_{22} than other test methods. The uncertainties in the four-point bending and edge compression results may possibly be due to errors with the non-linear FE model plots being fitted with linear equations.

4.3.5 Materials testing and Finite Element model comparisons

The elastic moduli in MD and CD of the Finite Element equivalent single-layered and detailed models of four-point bending, edge compression, and free vibration are now compared to the experimental results of the same materials test method.

4.3.5.1 Comparing E^*_{11} and E^*_{22} of equivalent and detailed geometric FE models to four-point bending tests

Firstly, the four-point bending FE model elastic moduli are compared with those of the four-point bending tests. The equivalent FE models of four-point bending generally gave higher elastic moduli compared to the experimental result, while the detailed FE models gave a mixture of higher and lower elastic moduli relative to the experiment.

For kraft paperboard at 50% relative humidity, the equivalent FE model of four-point bending gives a 71% higher value of E^*_{11} and 34% higher value of E^*_{22} compared to the experimental result. At 90% relative humidity, the kraft paperboard equivalent FE model of four-point bending is 64% and 56% higher compared to the experiment for E^*_{11} and E^*_{22} respectively.

The detailed FE model of kraft paperboard in four-point bending at 50% relative humidity gives a 68% lower E^*_{11} and a 5% higher E^*_{22} than the experiment, while at 90% relative humidity the detailed FE model is 84% and 56% higher than the experiment for values of E^*_{11} and E^*_{22} respectively.

For recycled paperboard at 50% relative humidity, the equivalent FE model of four-point bending gives a E^*_{11} value that is 77% higher and a E^*_{22} that is 44% higher than that of the experiment. At 90% relative humidity, the recycled paperboard equivalent FE four-point bending model gives a value of E^*_{11} that is 99% higher and a E^*_{22} that is 2.5 times higher compared to the experimental result.

The recycled paperboard detailed FE models of four-point bending at 50% relative humidity give a 62% lower E^*_{11} and a 56% higher E^*_{22} relative to the experimental value. For recycled paperboard at 90% relative humidity, the detailed FE models of four-point bending give a value of E^*_{11} that is 35% lower and E^*_{22} that is 2.2 times higher than that of the experiment.

4.3.5.2 Comparing E^*_{11} and E^*_{22} of equivalent and detailed geometric FE models to edge compression tests

Secondly, the edge compression FE model CD elastic modulus values are compared with the edge compression test results. The edge compression FE models in general give significantly higher CD elastic modulus than the experiment, with the equivalent FE model being the higher of the FE model results.

For kraft paperboard, the equivalent FE models of edge compression give values of E^*_{22} 6.6 and 6 times the experimental value at 50% and 90% relative humidity respectively. With the detailed FE models of edge compression for kraft paperboard, the difference is less, with values of E^*_{22} that are 3.1 and 2.9 times the experimental result, at 50% and 90% relative humidity respectively.

The recycled paperboard equivalent FE models of edge compression give values of E^*_{22} that are 4.5 and 6.4 times the experimental result, at 50% and 90% relative humidity respectively. With detailed FE models of recycled paperboard in edge compression, the values of E^*_{22} are 2.2 and 3.1 times the experimental result, at 50% and 90% relative humidity respectively.

4.3.5.3 Comparing E^*_{11} and E^*_{22} of equivalent and detailed geometric FE models to sonic vibration tests

Thirdly, the free-vibration FE models' elastic moduli are compared with the sonic vibration test results. The equivalent FE free vibration models' elastic moduli in MD are higher than the experimental value, but their CD elastic moduli are lower than the experimental value. Conversely, the detailed FE free vibration models give lower elastic moduli than the experimental results.

The equivalent FE free vibration models of kraft and recycled paperboard give E^*_{11} values that are 82% and 70% higher, while their E^*_{22} values are 39% and 59% lower than the experimental values respectively.

The detailed FE free vibration models of kraft and recycled paperboard give E^*_{11} values that are 76% and 70% lower, and E^*_{22} values 2 and 2.25 times lower than the experimental values respectively.

4.4 Concluding remarks

4.4.1 Materials testing methods

In four-point bending tests, the MD elastic modulus E^*_{11} is 2.5 to 3.9 times higher than the CD elastic modulus E^*_{22}, the difference being more for recycled than kraft material and for 90% relative humidity than 50% relative humidity. In sonic vibration tests, E^*_{22} is more similar, at 26% and 1.25% higher than E^*_{11} for kraft and recycled materials respectively at 50% relative humidity.

Between the different test methods, the four-point bending test gave 41% and 17.5% higher E^*_{11} than the sonic vibration test value for kraft and recycled materials respectively at 50% relative humidity. The sonic vibration test gave E^*_{22} values that were 2 to 2.7 times the four-point bending test value for kraft and recycled materials respectively at 50% relative humidity. The edge compression test E^*_{22} values were 51% to 2.7 times higher than the four-point bending test values, the difference being more for the recycled material and 90% relative humidity condition.

Difference in loading rates may account for some of the variation in results among the test methods. The relations between flexural stiffnesses and elastic moduli for homogenous orthotropic plate sections used to obtain the four-point bending and sonic vibration elastic moduli results from flexural stiffnesses may not be suitable for corrugated paperboard being treated as an equivalent orthotropic single layer plate.

The four-point bending and sonic vibration methods continue to be useful for obtaining flexural stiffness and Poisson's ratio properties, as well as edge compression measurements of the CD elastic modulus $E^*_{22.}$

4.4.2 Equivalent calculated model and materials testing

Between the equivalent single-layered analytical and FE material models, the elastic moduli of the equivalent FE models were 2 to 2.9 times higher than the equivalent analytical models. The E^*_{11} value is higher than E^*_{22}

by 47% to 93% in the equivalent analytical model, and 2.1 to 2.7 times higher in the equivalent FE model.

Comparing materials tests with equivalent analytical models, the four-point bending test gave E^*_{11} values 51% to 2 times higher and E^*_{22} values between 54% lower to 20% higher than the equivalent analytical model. The edge compression tests E^*_{22} were 74% to 2.4 times higher than the equivalent analytical model. The sonic vibration test gave E^*_{11} values 45% to 48% higher and E^*_{22} values 2.7 to 2.9 times higher compared to the equivalent analytical model.

It is difficult to verify whether the equivalent analytical material model is sufficient for modelling for corrugated paperboard, as there is only moderate agreement in elastic moduli with some of the four-point bending and sonic vibration test results. Alternative methods are needed to verify the material properties of the equivalent analytical model which presently appear to be conservative.

4.4.3 Materials testing and equivalent and detailed geometric Finite Element models

In the FE models of materials tests, the equivalent FE models gave a larger ratio between the MD and CD elastic moduli compared to the detailed FE models. The equivalent FE models gave E^*_{11} values that were 2 to 3.8 times higher than E^*_{22}, while the detailed FE models E^*_{11} values were between 10% lower to 42% higher than E^*_{22}.

There is better agreement between the equivalent FE models and detailed FE model types for the CD elastic modulus E^*_{22}. The E^*_{11} of the equivalent FE models are between 10% lower to 3.2 times higher and E^*_{22} between 15% lower to 44% higher compared to the detailed FE models.

The four-point bending test and FE model comparisons show that the equivalent FE model gave E^*_{11} values 64% to 99% higher and E^*_{22} values 34% to 2.5 times higher than the experiment. The four-point bending

detailed FE models gave E^*_{11} values 68% lower to 84% higher and E^*_{22} values 5% to 2.2 times higher compared to the experiment.

The edge compression FE models gave E^*_{22} values 4.5 to 4.6 times higher for the equivalent FE model and 2.2 to 3.1 times higher for the detailed FE model compared to the experiment.

The free-vibration equivalent FE models gave E^*_{11} and E^*_{22} values that were 70% to 82% higher and 39% to 59% lower respectively, compared to the sonic vibration experiment. The detailed FE models of free-vibration gave E^*_{11} and E^*_{22} values that were 70% to 76% lower and 2 to 2.25 times lower respectively, compared to the experiment.

The equivalent FE models appear less preferable than the detailed geometric FE models for modelling corrugated paperboard.

4.5 Summary

This chapter considered different methods of determining the overall effective material properties of corrugated paperboard. Its aim was the analysis of agreement between properties obtained by three materials testing methods, two equivalent calculated models and two Finite Element (FE) models of the materials tests.

Two corrugated paperboard materials – standard (kraft) and recycled were used in the tests at room temperature and high humidity conditions. The materials testing methods involved edge compression, four-point bending and sonic vibration. The equivalent calculated models considered were those used in the analytical buckling model in previous chapters and the equivalent FE models of corrugated paperboard. The FE models used were the equivalent single-layered and detailed geometric models of corrugated paperboard in four-point bending, edge compression and free vibration. The elastic moduli of corrugated paperboard in the machine- (MD) and cross-directions (CD) from different methods were compared.

In the experimental results, the sonic vibration results showed more similar elastic moduli in the two planar directions, while the four-point bending test gave a higher MD elastic modulus E^*_{11}. The edge compression test only gave the CD elastic modulus E^*_{22}.

For the MD elastic modulus, the four-point bending test gave values 41% and 17.5% higher than the sonic vibration test for kraft and recycled paperboard respectively at the room temperature condition. The CD elastic modulus E^*_{22} results for kraft and recycled paperboard show the four-point bending test has the lowest values, followed by the edge compression test and sonic vibration test in increasing order.

The difference in loading rates could account for some of the variation in results among the test methods. Also, the relations between flexural stiffnesses and elastic moduli for homogenous orthotropic plate sections which the four-point bending and sonic vibration results rely on to obtain elastic moduli from flexural stiffnesses may not be suitable for corrugated paperboard.

In comparisons of the four-point bending test results with the equivalent calculated analytical model, agreement was better for the CD elastic modulus E^*_{22} than the MD elastic modulus E^*_{11} for both kraft and recycled paperboard. In contrast, the agreement between the sonic vibration test and the equivalent calculated analytical model was better for the MD elastic modulus E^*_{11} than the CD elastic modulus E^*_{22}.

The edge compression, four-point bending and sonic vibration test elastic moduli results were generally higher than the equivalent calculated analytical results. At the room temperature condition, the disagreement between the analytical theory and sonic vibration test is least for the MD elastic modulus E^*_{11}, while for the CD elastic modulus E^*_{22} the analytical theory and four-point bending values are least different.

In comparisons of the test results with the FE models of the same test, the equivalent FE models gave generally higher elastic moduli than the

experimental results except for the free vibration model which were a combination of higher MD and lower CD elastic moduli relative to experimental values. The detailed FE models gave higher CD elastic moduli for edge compression, lower elastic modulus for free vibration and a combination of higher and lower elastic moduli in four-point bending relative to the experimental values. The equivalent FE models appear less preferable than the detailed geometric FE models for modelling corrugated paperboard.

In conclusion, the relations between flexural stiffness and elastic moduli for orthotropic homogenous plate sections used in the theoretical model implemented in the equivalent FE models of the materials test are not suitable for obtaining effective elastic properties for corrugated paperboard.

Alternative homogenisation models of corrugated paperboard such as analytical models based on sandwich and laminate plate theories could be used to improve the equivalent FE modelling results so that buckling of boxes are conveniently and accurately predicted.

5 Comparison of Predicted and Measured Results for Corrugated Board Panel

5.1 Introduction

The previous chapters have considered how post-buckling behaviour of a simply supported corrugated paperboard panel is affected by in-plane boundary conditions and multi-term shape functions in analytical Galerkin's method models. These were followed by a chapter comparing the effective properties of corrugated paperboard used in the post-buckling models with experimental values from materials testing.

In the initial part of the research, post-buckling models were created using the semi-analytical approach, with a sinusoidal out-of-plane displacement shape function instead of a polynomial as in the work of (Nordstrand, 2004a). There was agreement in the critical load but discrepancy in the post-buckling parameter compared with the analytical result of (Nordstrand, 2004a). The source of some of the material properties given to the paperboard could not be verified and this was suspected to be a cause of some of this discrepancy. This made a case for carrying out new panel buckling tests with paperboard materials that were available for study.

The current chapter is concerned with the post-buckling behaviour of panels in new experiments which reproduce the boundary conditions described in (Nordstrand, 2004a) as closely as possible. The experimental boundary conditions are assumed to be those modelled as case C in Chapter 2. The boundary conditions for the panel are: simply-supported along all edges, uniformly compressed along the loaded edges, with free in-plane normal movement along unloaded edges and in-plane free tangential movement (shear free) along all edges.

The following research questions are investigated:

- What boundary conditions most resemble the panel buckling experimental boundary conditions?
- Which panel out-of-plane displacement mode shapes are dominant in the test conditions?

To answer these questions, critical loads obtained using the Southwell plot and post-buckling results for the test panels are compared to those predicted by the Galerkin and Finite Element models for case C. The collocation method is used to fit out-of-plane displacements of the test panels into a double sine product Fourier series to obtain amplitudes of displacement modes.

The results show a significant discrepancy between experimental and predicted values, possible reasons for which are described in this chapter.

5.2 Methods of Study

This section details the corrugated paperboard materials tested, buckling experimental procedure, analysis of experimental data, and modelling methods used.

5.2.1 Materials

The materials used in the buckling tests were (kraft) standard and recycled fibre corrugated paperboards. The paperboard material was the same batch used in the work by (Ilmonen, 2007). Hence, the paperboard and constituent layers' geometry and property data from (Ilmonen, 2007) have been used. Effective material properties for the tested paperboards, used in the analytical and Finite Element models, have been presented in section 4.2.1 of the previous chapter.

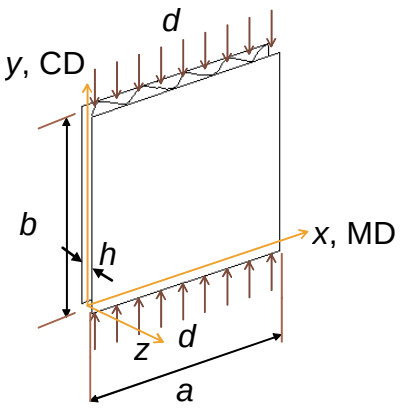

Figure 5-1: Corrugated paperboard panel with uniform in-plane compression, *d* (m)

The geometry of buckling test panels of width *a* and height *b*, between the simple supports, and thickness, *h*, are shown in Table 5-1 (refer to Figure 5-1).

Table 5-1: Dimensions of Scion buckling test panels.

Panel geometry	
Width[1], *a* (m)	0.330
Height[1], *b* (m)	0.281
Thickness, *h* (mm)	4.23

[1] Measurement between simple supports. Overall panel area 0.345 m x 0.295 m.

The number of specimens in the buckling tests at 23 °C, 50% relative humidity and 23 °C, 90% relative humidity are listed below in Table 5-2.

Table 5-2: Number of specimens tested in panel buckling experiment.

Material	Relative Humidity	No. of specimens tested
Kraft	50%	4
	90%	6
Recycled	50%	7
	90%	9

5.2.2 Buckling panel experiment

The buckling test procedure on corrugated paperboard panels carried out at Scion is described below. The preconditioning and conditioning of specimens to test conditions of 23 °C, and 50% or 90% relative humidity, were carried out in accordance with the TAPPI standard T402, detailed in the specimen preparation section of 4.2.2 of the previous chapter.

The experimental rig used, shown in Figure 5-2, has knife edge supports along the vertical unloaded edges and bevelled edge supports along the horizontal loaded edges to achieve the simply-supported edges boundary condition.

(a) Buckling test rig with panel specimen in axial load machine

(b) Buckling test rig without specimen

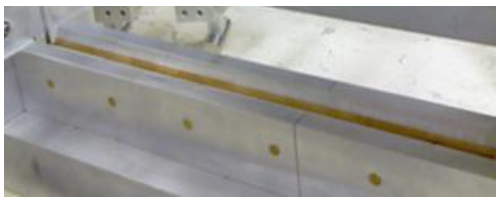

(c) Detailed view of horizontal bevelled edge support

(d) Detailed view of vertical knife edge support

Figure 5-2: Buckling test rig and panel edge support conditions.

These supports allow the panel to rotate about the knife edges or bevelled edges. The horizontal bevelled edges applied loading such that there is uniform in-plane normal movement. The vertical knife edge supports allow free in-plane movement on the unloaded edges. The out-of-plane movement along the edges are constrained, though freedom to move in-plane necessitates some tolerance in the gap between the supports compared to the panel thickness.

The corrugated paperboard panels are uniformly compressed between flat parallel compression test platens, at rates of 10 mm/min and 22 mm/min for the 50% relative humidity and 90% relative humidity tests respectively. The rate at which the 50% relative humidity test was conducted is within the limits specified for standard box compression test methods.

During testing, the applied load is measured with the test machine load cell, while the panel out-of-plane deflection is measured at four locations, shown in Figure 5-3, using Linear Variable Differential Transformer potentiometers, until buckling failure occurs (refer to Figure 5-4). The number of deflection measurement points were limited to four due to availability of equipment.

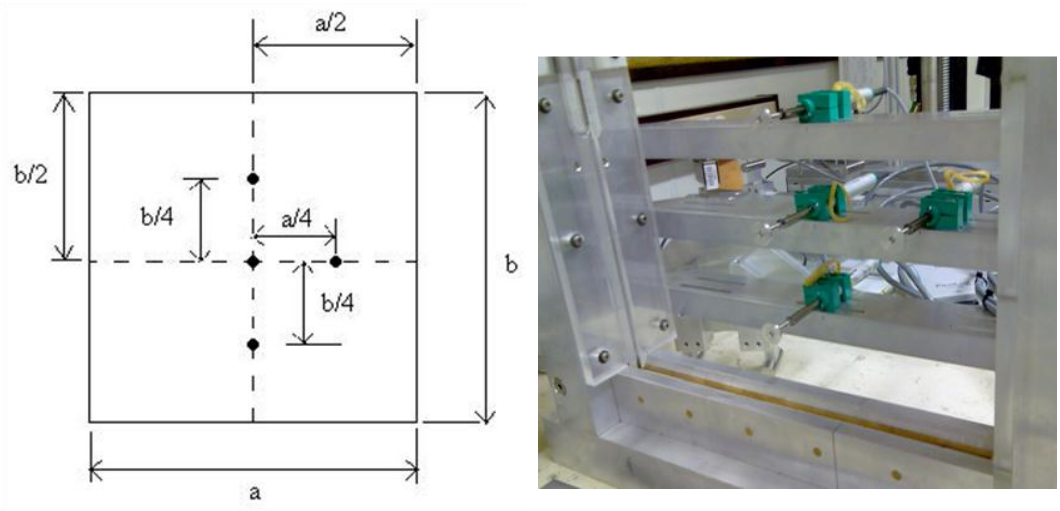

Figure 5-3: Four locations of panel deflection measurement using potentiometers.

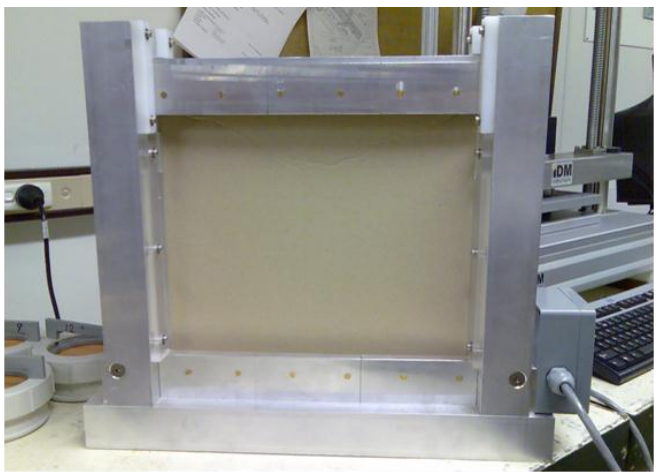

Figure 5-4: Buckled corrugated paperboard panel.

The four locations of deflection measurement were selected to optimise measurement of the out-of-plane displacement contour of the panel. The lowest displacement modes were expected to appear in the test and selection was based on finding the amplitudes of these modes. The panel centre measurement point was selected as the fundamental displacement mode *A*(1,1) was likely to be present. The two points, a quarter and three-quarters along a vertical line down the middle of the panel, were chosen to observe the presence of the anti-symmetric *A*(1,2) mode. The fourth available displacement measurement point was located at a quarter of the distance from one vertical edge along the horizontal line across the middle of the panel, to observe higher modes along the direction transverse to loading.

5.2.3 Analysis of experimental data

The out-of-plane panel displacements at four locations and applied load from the buckling tests are analysed for comparison with model results using the methods described below.

5.2.3.1 Obtaining panel displacement modes using the Collocation method

The buckling deflection of the panel is approximated by the following out-of-plane deflection function *w*, a Fourier series of sine products in the *x*- and *y*-directions.

$w(x,y) = \sum_i \sum_j A_{i,j}\, sin\left(\frac{i\pi x}{a}\right) sin\left(\frac{j\pi y}{b}\right)$, where *i, j* = 1, 2, 3, 4, 5

Equation 5-1

Using the collocation method, the deflection series amplitudes, $A_{i,j}$ for the experimental results are determined from the panel deflection measurements at four locations, $\overline{w}_r(\bar{x}_r, \bar{y}_r)$ where *r* = 1 … 4. The deflection series amplitudes, $A_{i,j}$ at a given load are obtained by matrix division of the following equation:

$$\begin{Bmatrix} \overline{w}_1(\bar{x}_1, \bar{y}_1) \\ \vdots \\ \overline{w}_4(\bar{x}_4, \bar{y}_4) \end{Bmatrix}$$

$$= \begin{bmatrix} \sin(i\pi\,\bar{x}_1/a)\sin(j\pi\bar{y}_1/b) & \cdots & \sin(i_{max}\pi\,\bar{x}_1/a)\sin(j_{max}\pi\,\bar{y}_1/b) \\ \vdots & \ddots & \vdots \\ \sin(i\pi\bar{x}_4/a)\sin(j\pi\bar{y}_4/b) & \cdots & \sin(i_{max}\pi\,\bar{x}_4/a)\sin(j_{max}\pi\bar{y}_4/b) \end{bmatrix} \begin{Bmatrix} A_{i,j} \\ \vdots \\ A_{i_{max},j_{max}} \end{Bmatrix}$$

Equation 5-2

Since there are only four locations where deflection *w* was measured, the solution to the equation above can only be used to obtain four non-zero deflection series amplitudes $A_{i,j}$.

The least squares method was also used to verify the deflection amplitudes obtained by the collocation method. The residual *S* or the sum of the squared differences between measured deflections and the value given by the Fourier series is:

$$S = \sum_{r=1}^{4} \left(\left(\sum_i \sum_j A_{i,j}\, sin\left(\frac{i\pi\bar{x}_r}{a}\right) sin\left(\frac{j\pi\bar{y}_r}{b}\right) \right) - \overline{w}_r \right)^2$$

Equation 5-3

S is minimised with respect to the deflection amplitudes $A_{i,j}$, which results in a series of equations:

$$\frac{\partial S}{\partial A_{i,j}} = \sum_{r=1}^{4} 2\left(sin\left(\frac{i\pi\bar{x}_r}{a}\right) sin\left(\frac{j\pi\bar{y}_r}{b}\right)\right)\left(\left(\sum_k \sum_l A_{k,l}\, sin\left(\frac{k\pi\bar{x}_r}{a}\right) sin\left(\frac{l\pi\bar{y}_r}{b}\right)\right) - \overline{w}_r\right) = 0 \quad ,$$

where $k = 1 \ldots i_{max}$, $l = 1 \ldots j_{max}$.

Equation 5-4

In using the least squares method, only four combinations of *i*, *j* could be included since there were only four locations of deflection measurement. The combination of four deflection series amplitudes found to be non-zero by the collocation method $A_{1,1}$, $A_{3,1}$, $A_{3,2}$, $A_{3,2}$ were solved for using the equation below:

$$\begin{Bmatrix} A_{1,1} \\ A_{3,1} \\ A_{3,2} \\ A_{3,3} \end{Bmatrix} = (X^T X)^{-1} X^T \begin{Bmatrix} \overline{w}_1(\bar{x}_1, \bar{y}_1) \\ \vdots \\ \overline{w}_4(\bar{x}_4, \bar{y}_4) \end{Bmatrix}$$

Equation 5-5

Where

$X =$

$$\begin{bmatrix} \sin\left(\frac{\pi \bar{x}_1}{a}\right)\sin\left(\frac{\pi \bar{y}_1}{b}\right) & \sin\left(\frac{3\pi \bar{x}_1}{a}\right)\sin\left(\frac{\pi \bar{y}_1}{b}\right) & \sin\left(\frac{3\pi \bar{x}_1}{a}\right)\sin\left(\frac{2\pi \bar{y}_1}{b}\right) & \sin\left(\frac{3\pi \bar{x}_1}{a}\right)\sin\left(\frac{3\pi \bar{y}_1}{b}\right) \\ \sin\left(\frac{\pi \bar{x}_2}{a}\right)\sin\left(\frac{\pi \bar{y}_2}{b}\right) & \sin\left(\frac{3\pi \bar{x}_2}{a}\right)\sin\left(\frac{\pi \bar{y}_2}{b}\right) & \sin\left(\frac{3\pi \bar{x}_2}{a}\right)\sin\left(\frac{2\pi \bar{y}_2}{b}\right) & \sin\left(\frac{3\pi \bar{x}_2}{a}\right)\sin\left(\frac{3\pi \bar{y}_2}{b}\right) \\ \sin\left(\frac{\pi \bar{x}_3}{a}\right)\sin\left(\frac{\pi \bar{y}_3}{b}\right) & \sin\left(\frac{3\pi \bar{x}_3}{a}\right)\sin\left(\frac{\pi \bar{y}_3}{b}\right) & \sin\left(\frac{3\pi \bar{x}_3}{a}\right)\sin\left(\frac{2\pi \bar{y}_3}{b}\right) & \sin\left(\frac{3\pi \bar{x}_3}{a}\right)\sin\left(\frac{3\pi \bar{y}_3}{b}\right) \\ \sin\left(\frac{\pi \bar{x}_4}{a}\right)\sin\left(\frac{\pi \bar{y}_4}{b}\right) & \sin\left(\frac{3\pi \bar{x}_4}{a}\right)\sin\left(\frac{\pi \bar{y}_4}{b}\right) & \sin\left(\frac{3\pi \bar{x}_4}{a}\right)\sin\left(\frac{2\pi \bar{y}_4}{b}\right) & \sin\left(\frac{3\pi \bar{x}_4}{a}\right)\sin\left(\frac{3\pi \bar{y}_4}{b}\right) \end{bmatrix}$$

Equation 5-6

The experimental deflection series amplitudes, $A_{i,j}$ are then compared to values from the modelling results.

5.2.3.2 Obtaining critical load and initial geometric imperfection of experimental panel post-buckling data

The presence of initial out-of-plane geometric imperfection in buckling test panels, which initiates panel deflection even below the critical load, makes it difficult to accurately determine the critical load. The Southwell plot (Southwell, 1932), commonly used for obtaining the critical load of beams, has been applied to the buckling panels to obtain experimental critical load and initial imperfection values.

The panel displacements relative to initial measurements at the start of the test ($w_r - w_{r\,initial}$) are plotted against the ratio of the same displacement divided by the applied load, ($w_r - w_{r\,initial}$) / P (refer to Figure 5-5). The linear portion of the plot is used to estimate the first critical load from the gradient and the initial imperfection from the displacement axis intercept, later referred to as the Southwell or ‘adjusted’ panel initial imperfection. The ‘unadjusted’ panel imperfections are the initial measured deflection measurement values.

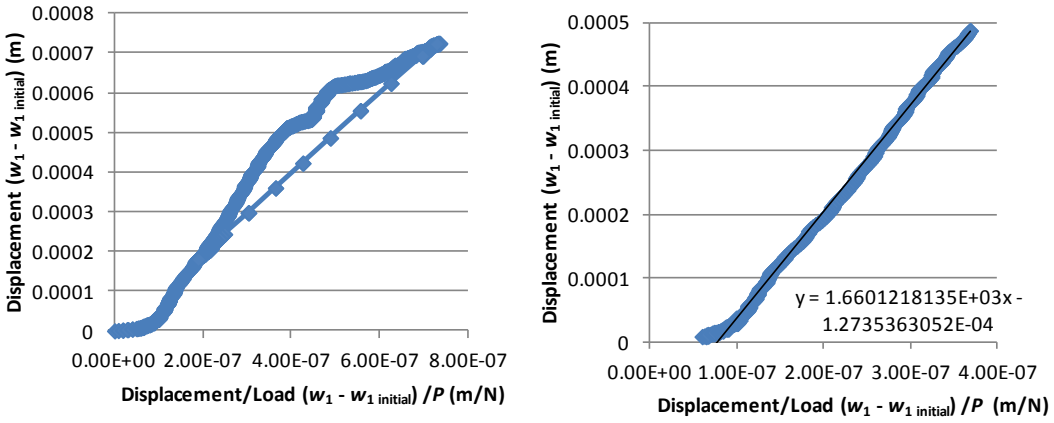

(a) (b)

Figure 5-5: (a) Southwell plot of panel centre displacement for buckling test and (b) linear portion of the same plot with gradient of critical load Pcrit.

Subsequent to using the Southwell method on the experimental results and finding a large uncertainty in the critical loads and imperfections, it was necessary to consider alternative methods such as numerical techniques for fitting the experimental data into a post-buckling function as in (Nordstrand, 2004a).

The post-buckling function is given below assuming a single term approximation for the out-of-plane displacement:

$$PA = P_{crit}(A - A_0) + \Psi A\left(A^2 - {A_0}^2\right)$$

Equation 5-7

Where A = absolute panel deflection amplitude relative to the plane of the panel edges; P = measured load; P_{crit} = critical load; A_0 = absolute panel imperfection amplitude relative to the plane of the panel edges; Ψ = post-buckling parameter.

Because of uncertainties in measurement of the initial imperfection the equation is rewritten in terms of A' the change in the panel deflection amplitude from the zero load value of A, obtainable from the measurements.

Since $A = A_0 + A'$,

$$P(A' + A_0) = P_{crit}A' + \Psi(A' + A_0)A'(A' + 2A_0)$$

Equation 5-8

The least squares method, where a residual *S* is minimised, was used to obtain values of the unknowns P_{crit}, Ψ, and A_0.

$$S = \sum_{r'}^{n} {R_{r'}}^2 = \sum_{r'}^{n} \left(P_{crit}\, {A'}_{r'} + \Psi(A'_{r'} + A_0)A'_{r'}(A'_{r'} + 2A_0) - P_{r'}(A'_{r'} + A_0) \right)^2,$$

Equation 5-9

where *r'* is the number of data points.

$$\frac{\partial S}{\partial P_{crit}} = 0 \rightarrow \sum_{r'}^{n} R_{r'} \frac{\partial R_{r'}}{\partial P_{crit}} = 0$$

$$\frac{\partial S}{\partial \Psi} = 0 \rightarrow \sum_{r'}^{n} R_{r'} \frac{\partial S}{\partial \Psi} = 0$$

$$\frac{\partial S}{\partial A_0} = 0 \rightarrow \sum_{r'}^{n} R_{r'} \frac{\partial S}{\partial A_0} = 0$$

Equation 5-10

The unknowns are given initial guess values, and then improved estimates are found by Newton-Raphson iteration.

$$\begin{bmatrix} \frac{\partial^2 \left(\sum_{r'}^{n} {R_{r'}}^2\right)}{\partial {P_{crit}}^2} & \frac{\partial^2 \left(\sum_{r'}^{n} {R_{r'}}^2\right)}{\partial P_{crit} \partial \Psi} & \frac{\partial^2 \left(\sum_{r'}^{n} {R_{r'}}^2\right)}{\partial P_{crit} \partial A_0} \\ \frac{\partial^2 \left(\sum_{r'}^{n} {R_{r'}}^2\right)}{\partial P_{crit} \partial \Psi} & \frac{\partial^2 \left(\sum_{r'}^{n} {R_{r'}}^2\right)}{\partial \Psi^2} & \frac{\partial^2 \left(\sum_{r'}^{n} {R_{r'}}^2\right)}{\partial \Psi \partial A_0} \\ \frac{\partial^2 \left(\sum_{r'}^{n} {R_{r'}}^2\right)}{\partial P_{crit} \partial A_0} & \frac{\partial^2 \left(\sum_{r'}^{n} {R_{r'}}^2\right)}{\partial \Psi \partial A_0} & \frac{\partial^2 \left(\sum_{r'}^{n} {R_{r'}}^2\right)}{\partial {A_0}^2} \end{bmatrix} \begin{Bmatrix} dP_{crit} \\ d\Psi \\ dA_0 \end{Bmatrix} = \begin{Bmatrix} \sum_{r'}^{n} \frac{\partial \left(\sum_{r'}^{n} {R_{r'}}^2\right)}{\partial P_{crit}} \\ \sum_{r'}^{n} \frac{\partial \left(\sum_{r'}^{n} {R_{r'}}^2\right)}{\partial \Psi} \\ \sum_{r'}^{n} \frac{\partial \left(\sum_{r'}^{n} {R_{r'}}^2\right)}{\partial A_0} \end{Bmatrix}$$

Equation 5-11

5.2.4 Buckling Panel Models

The methods used to model buckling of simply-supported kraft and recycled paperboard panels with out-of-plane geometric imperfection as in the Scion panel buckling experiments are described below. The model

results are used to verify the experimental boundary conditions are as in case C of Chapter 2, described in (Nordstrand, 2004a).

5.2.4.1 Analytical method

Post-buckling models of imperfect corrugated paperboard panels were created in *MATLAB* software using the analytical Galerkin method with multi-term shape functions, detailed in section 3.2 of Chapter 3.

In the analytical models, the material is modelled as an orthotropic lamina with equivalent material properties of the corrugated paperboard in directions MD and CD, based on first-order shear deformation laminated plate theory, assuming plane stress conditions (Nordstrand, 2004a) and (Carlsson et al., 2001). The material properties of kraft and recycled paperboard for the analytical method were presented in the analytical equivalent paperboard model section of 4.2.1 of Chapter 4. The material properties obtained from frequency tests described in Chapter 4 were also used in the analytical models of kraft and recycled paperboard at the 50% relative humidity.

The panel boundary conditions modelled include the simply-supported cases A and C, described in Chapter 2, with different in-plane boundary conditions. The post-buckling plots for these cases, presented in Chapter 2, were found to be closest to the experimental plot from (Nordstrand, 2004a).

The analytical models use two types of geometric out-of-plane imperfections values in the post-buckling analysis. One is the mean of ‘unadjusted’ initial out-of-plane deflection measurements from experiments. The other is the mean of Southwell imperfection values obtained from Southwell plots which have ‘adjusted’ displacements zeroed by the initial deflection measurements.

Subsequent to carrying out the post-buckling analyses, and finding panel imperfection estimates from the Southwell method to be inadequate, imperfection estimates from the least squares method were used in

additional post-buckling analyses for kraft and recycled paperboard at the 50% relative humidity condition.

As shown in chapter 4, there is difficulty in completely defining the material properties of corrugated paperboard. The frequency test properties were limited in their usefulness by their generally higher stiffness than from static tests. The effect of scaling the material properties from the frequency tests on corrugated paperboard on the analytical post-buckling load vs. centre displacement plot to replicate material behaviour in the buckling test was considered. The effective in-plane elastic properties E^*_{11}, E^*_{22}, G^*_{12} and v^*_{12} were multiplied by a correction factor $CF1$ and the flexural stiffness properties D_{11}, D_{22}, D_{12} and D_{66} multiplied by a correction factor $CF2$. The different scaling applied to the in-plane and flexural properties reflect the impact of the flexural properties on the critical load calculated and the in-plane properties on the post-buckling behaviour.

5.2.4.1 Finite Element method

Numerical Finite Element buckling and post-buckling models of the corrugated paperboard panels were created using *Abaqus* software.

In the *Abaqus* models, an elastic lamina material definition was also used for an equivalent single layer paperboard model. However, the bending stiffnesses D_{11}, D_{22}, D_{12} and D_{66} and the overall paperboard thickness h, were used to calculate $E^*_{11,}$ $E^*_{22,}$ G^*_{12} and v^*_{12}, based on orthotropic plate theory relations, presented in the FE equivalent paperboard model section of 4.2.1 of Chapter 4.

The equivalent layer panel models used shell elements of type S8R -an 8-node doubly curved thick shell element of quadratic order, using reduced integration. The convergence of the equivalent layer panel buckling load was checked by varying the number of elements on the edges from 1 to 128 and giving a total number of elements used from 1 to 16384 elements. The post-buckling analysis of the equivalent layer panel model without and

with the panel margins were carried out with a total of 3762 and 4060 S8R5 elements respectively.

The boundary conditions applied to the panel models of buckling and post-buckling includes those of simple-supports, and in-plane boundary condition case C from Chapter 2, as in the analytical model. The boundary conditions applied to the FE panel models were zero out-of-plane z-displacement U3 = 0 on all edges, zero y-displacement U2 = 0 on bottom edge, concentrated load at reference point constraining U2 of top edge to achieve uniform in-plane movement of top loaded edge.

Another boundary condition is modelled, case D, a slight modification of case C with free out-of-plane displacement U3 along the upper 38 mm of the unloaded edges (refer to Figure 5-6(b)). This modification of boundary condition case C is based on observation of the buckling test apparatus.

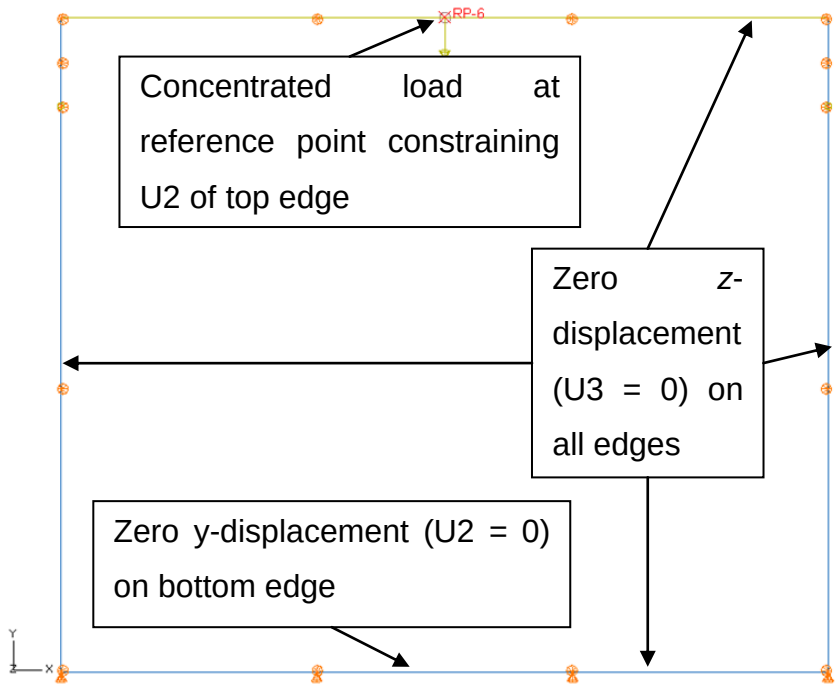

(a) Case C

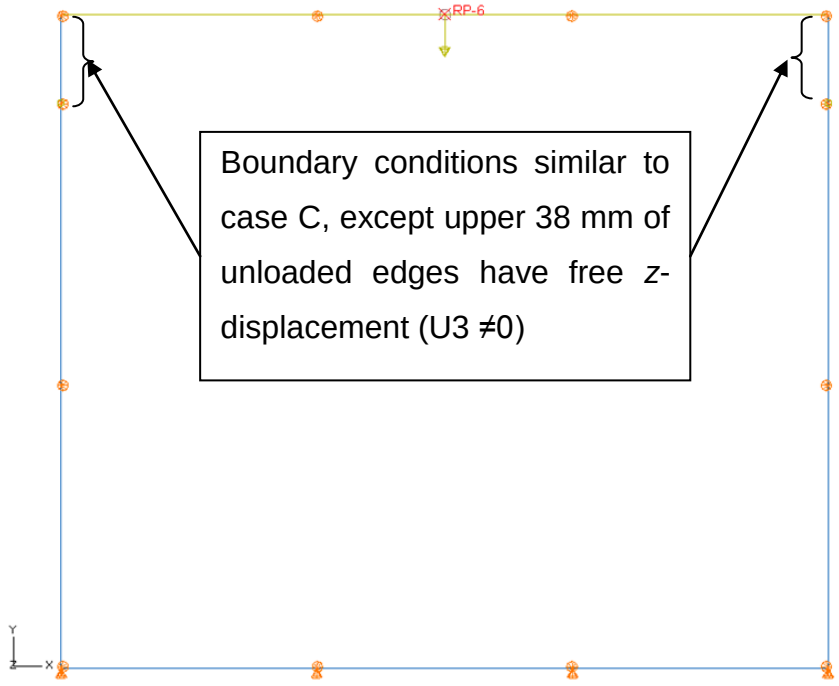

(b) Case D

Figure 5-6: FE panel models (a) Case C boundary conditions zero z-displacement U3 = 0 on all edges, zero y-displacement U2 = 0 on bottom edge, concentrated load at reference point constraining U2 of top edge, (b) Case D with boundary conditions as in case C except free z- displacement U3 ≠ 0 along upper 38 mm of unloaded edges.

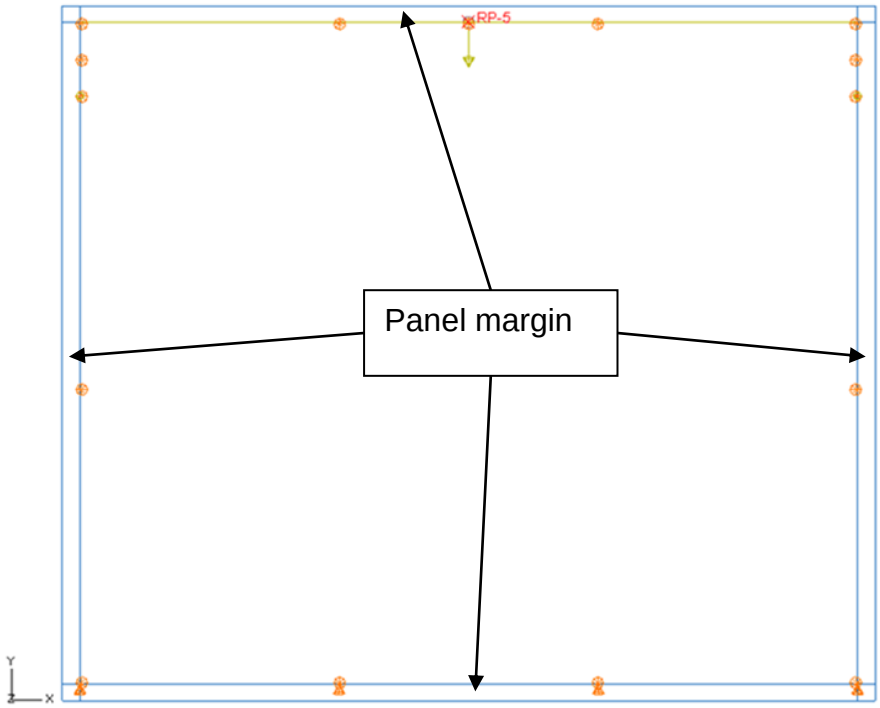

(a) Case C with panel margin

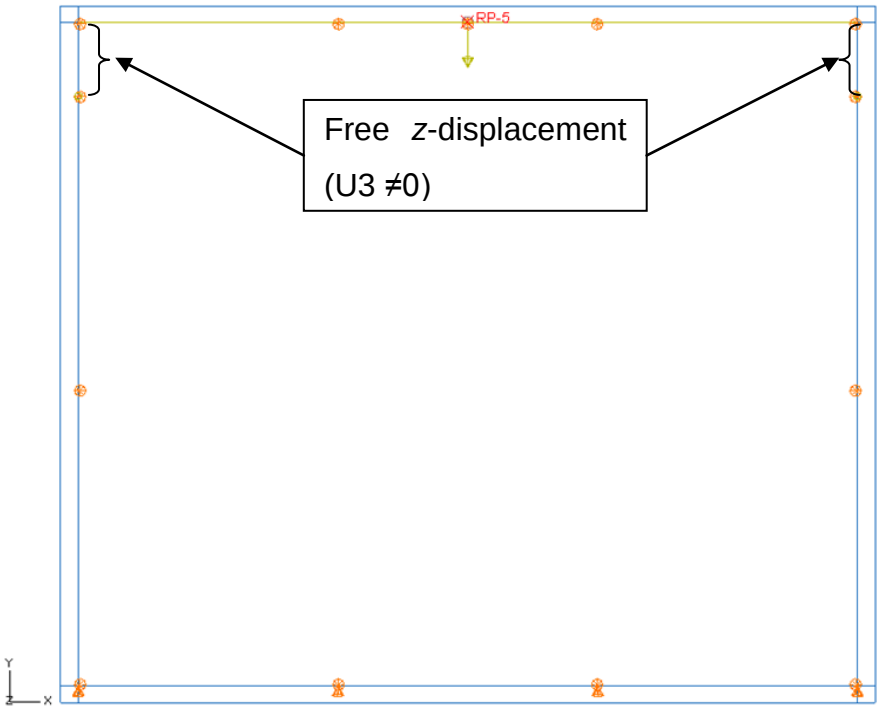

(b) Case D with panel margin

Figure 5-7: FE panel models (a) Case C with panel margin, (b) Case D with panel margin.

Buckling models of boundary condition cases C and D with panel margins to reflect the overall dimensions of the test samples were analysed (refer

to Figure 5-7 (b)). The actual panel dimensions (given in Table 5-1) are modelled and the boundary conditions as in case C (U3 = 0 along the edge supports, U2 = 0 along the bottom edge, uniform U2 along the top edge, and free in-plane movement on the unloaded edges) are applied along the lines where the supports act on the panel in the test, bordering the unsupported area of 0.33 m x 0.281 m.

In addition, a buckling model of test panel dimensions was created for boundary condition case C with detailed paperboard geometry and material properties assigned to the constituent layers, shown in Figure 5-8.

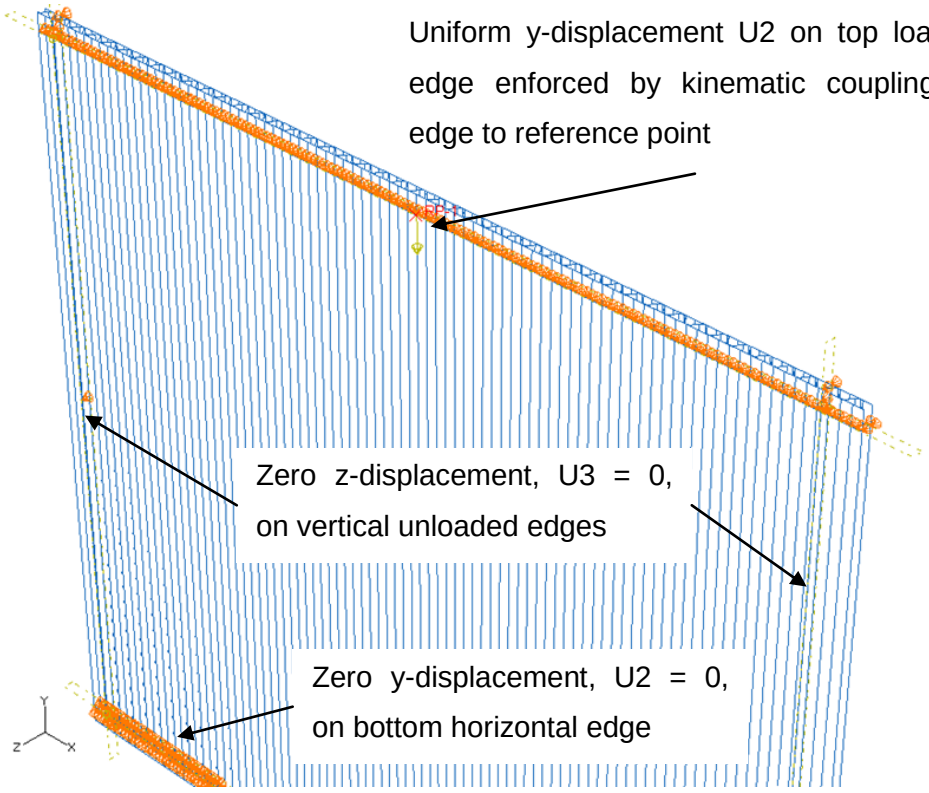

Figure 5-8: FE model of Case C boundary condition with detailed paperboard geometry and panel margins.

Another buckling model was subsequently added for boundary condition case C without panel margins where the corrugated paperboard is defined using a multi-layered composite shell section, that treats the core as an effective homogeneous layer. The effective material properties given to

the FE layered model are summarised below in Table 5-3 based on geometric parameters and component properties in Tables 4-1 and 4-2.

Table 5-3: Effective material properties of FE multi-layered plate model.

Effective properties	*Standard corrugated board*		*Recycled corrugated board*	
	50% RH	*90%RH*	*50% RH*	*90%RH*
Facing 1				
E_{11} (MPa)	6833	4779	4503	3424
E_{22} (MPa)	2811	1894	1444	1281
G_{12} (MPa) = 0.387$(E_{11}\,E_{22})^{1/2}$	1696	1164	987	810
E_{33} (MPa) = E_{11} / 200	34.17	23.90	22.52	17.12
G_{13} (MPa) = E_{11} / 55	124.24	86.89	81.87	62.25
G_{23} (MPa) = E_{22} / 35	80.31	54.11	41.26	36.60
v_{12}	0.308	0.319	0.325	0.289
v_{13}	0.01	0.01	0.01	0.01
v_{23}	0.01	0.01	0.01	0.01
Corrugated core				
$E^*_{11,\,c}$ (MPa)	5	5	5	5
$E^*_{22,\,c}$ (MPa) = $\alpha\, E_{22,c}\, t_c$ / (h - t_{f1} - t_{f2})	203.50	132.90	120.82	106.99
$G^*_{12,\,c}$ (MPa) =0.001 $E^*_{22,\,c}$	0.204	0.133	0.121	0.107
$G^*_{13,\,c}$ (MPa) = 0.00275 (h - t_{f1}/2 - t_{f2}/2) $E_{11,c}$ / (h (1-$v_{12,c}^2$))	14.24	11.12	16.21	13.22
$G^*_{23,\,c}$ (MPa) = 4*(h-t_{f1}/2-t_{f2}/2) t_c $G_{12,c}$ / ($\alpha\,\lambda^2$)	47.60	33.88	37.25	31.37
$v^*_{12,\,c}$	0.05	0.05	0.05	0.05
$v^*_{13,\,c}$	0.01	0.01	0.01	0.01
$v^*_{23,\,c}$	0.01	0.01	0.01	0.01
Facing 2				
E_{11} (MPa)	6398	4759	4503	3424
E_{22} (MPa)	2784	1927	1444	1281
G_{12} (MPa) = 0.387$(E_{11}\,E_{22})^{1/2}$	1633	1172	987	810
E_{33} (MPa) = E_{11} / 200	31.99	23.80	22.52	17.12
G_{13} (MPa) = E_{11} / 55	116.33	86.53	81.87	62.25
G_{23} (MPa) = E_{22} / 35	79.54	55.06	41.26	36.60
v_{12}	0.196	0.279	0.325	0.289
v_{13}	0.01	0.01	0.01	0.01
v_{23}	0.01	0.01	0.01	0.01

The element types used were S4 shell elements for the detailed geometric model and S8R5 shell elements for the multi-layered corrugated paperboard panel model. The S4 element is a four-node shell element.

The S8R5 is an eight-node doubly curved thick shell element of quadratic order, using reduced integration, with five degrees of freedom per node. The total number of elements for the multi-layered model and the detailed model was 3762 and 36018 elements respectively. The critical loads from the FE models are obtained using *Linear, Buckle step* on the panels without geometric imperfection and unit loading.

Reference results obtained by the exact strip method (DSM) and the Wittrick-Williams algorithm, using VICONOPT an industrial software in FORTRAN 77 for eigenvalue analysis of prismatic plate assemblies described in (Williams et al., 1991), have been included in the critical load comparison. These results for paperboard as an equivalent single layer and with detailed geometry (refer to Figure 5-9) were provided by a team of researchers at Cardiff University, School of Engineering for the panels used in this study. The boundary conditions applied to the models were that of case A from Chapter 2, simply-supported edges with uniformly distributed loading in the y-direction.

The number of strips used in the equivalent single layer DSM model was one strip of the same width as the panel. For the detailed geometry DSM model, 18 strips were used over the width of a corrugated paperboard wavelength, with 50 repeating wavelengths across the width of the panel along the MD direction across the panel.

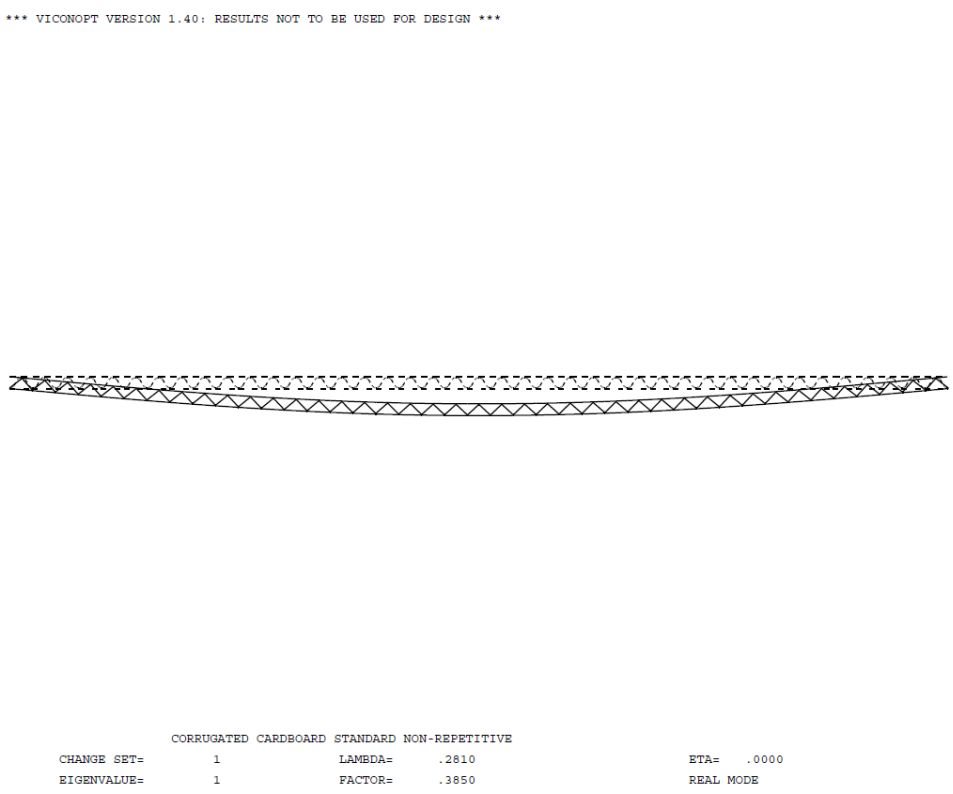

Figure 5-9: VICONOPT buckling analysis program output for model with detailed paperboard geometry.

Post-buckling load vs. displacement plots are obtained using the *General, Static step* the *general, static* post-buckling analysis as described in Chapter 2. Uniform displacement in the loading direction U2 was applied to the top edge of the panel in the post-buckling analysis (refer to Figure 5-10). The ‘unadjusted’ geometric out-of-plane initial imperfections modes averaged from the tests are introduced to the FE panels in the post-buckling analysis by the procedure detailed in Appendix I. The FE model out-of-plane displacement was obtained at four panel locations as in the experiment. The reaction forces in the loading direction RF2 along the top panel edge was summed to determine the total load applied in the post-buckling analysis.

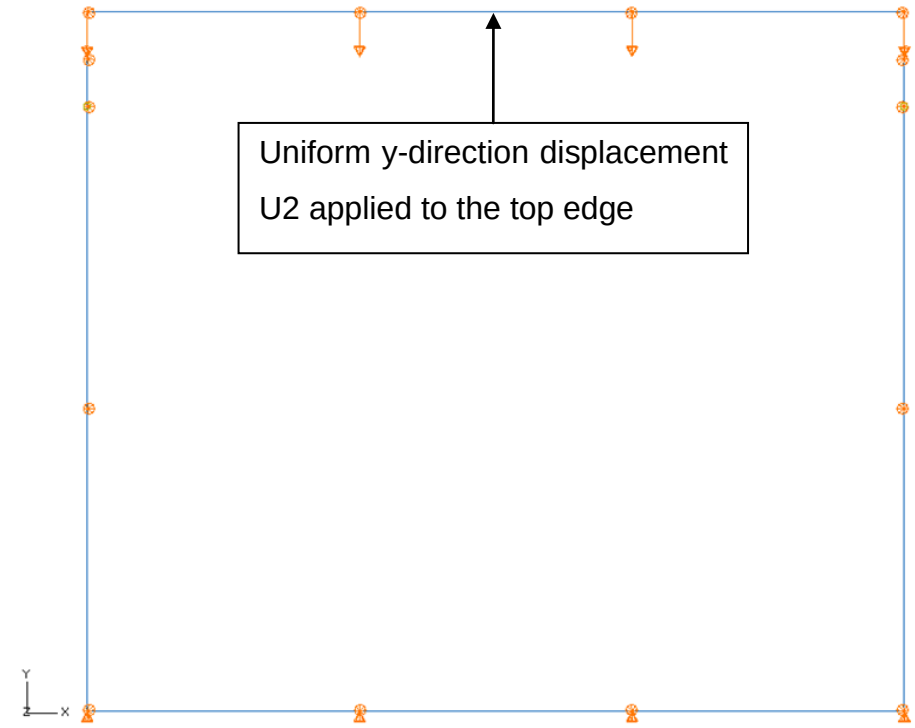

(a) Case C

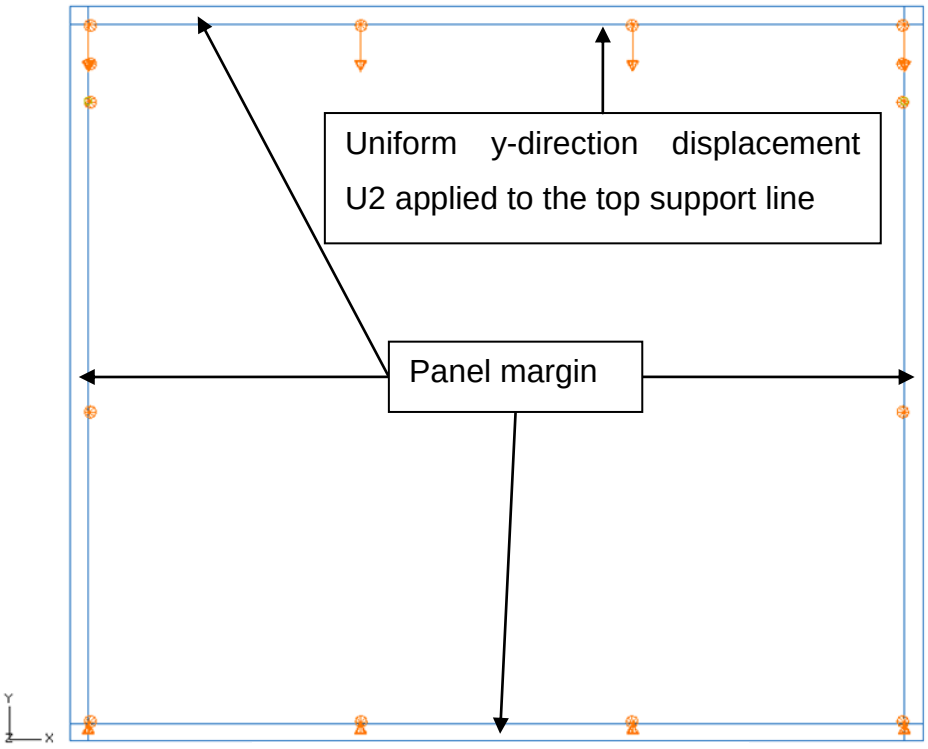

(b) Case C with panel margins

Figure 5-10: FE post-buckling model of boundary condition case C with uniform y-direction displacement U2 applied to the top edge, (a) without and (b) with panel margins.

FE post-buckling analyses with detailed and layered material definitions were also carried out at the 50% relative humidity condition for kraft and recycled paperboard, with panel imperfections estimated by the least squares method. The FE model results obtained were compared to the experimental and analytical results.

5.3 Results and Discussion

The following section compares critical loads obtained from analytical and FE models of paperboard panels with values from experiments estimated using the Southwell plot and least squares method and post-buckling plots from experiments with analytical and FE models.

5.3.1 Buckling critical load results

The critical load results from the analytical and FE models and Southwell plots of buckling experiments on Scion paperboard panels are presented in Table 5-4 and Table 5-5. The critical load of the case C analytical model with equivalent single layer material properties for each material and relative humidity is used as a reference value in the comparison.

Table 5-4: Critical load comparison of Scion kraft paperboard at 23 °C.

Material	Relative humidity	Method	Case	Critical load, P_{crit} (N)	% Δ P_{crit} relative to analytical P_{crit}
Kraft	50%	Analytical	A	991.46	-
			C	991.46	-
		Analytical (frequency test properties)	A	2283.91	130.36%
			C	2283.91	130.36%
		FE	C	979.17	-1.24%
			D	979.06	-1.25%
		FE (with panel margin)	C	1088.90	9.83%
			D	1088.60	9.80%
		FE (detailed geometry with panel margin)	C	1010.16	1.89%
		FE (layered plate)	C	902.45	-8.98%
		DSM (equivalent paperboard)	A	991.46	0.00%
		DSM (detailed geometry)	A	973.85	-1.78%
		Experiment (Southwell)		1406.38 ± 420.32	41.85% ± 42.4%
		Experiment (least squares three-point)		1128.82 ± 282.04	13.85% ± 28.45%
Kraft	90%	Analytical	A	704.18	-
			C	704.18	-
		FE	C	695.50	-1.23%
			D	695.43	-1.24%
		FE (with panel margin)	C	772.55	9.71%
			D	772.34	9.68%
		FE (detailed geometry with panel margin)	C	-	-
		FE (layered plate)	C	644.90	-8.42%
		DSM (equivalent paperboard)	A	704.18	0.00%
		DSM (detailed geometry)	A	696.75	-1.05%
		Experiment (Southwell)		1295.47 ± 274.01	83.97% ± 38.9%

Table 5-5: Critical load comparison of Scion recycled paperboard at 23 °C.

Material	Relative humidity	Method	Case	Critical load, P_{crit} (N)	% Δ P_{crit} relative to analytical P_{crit}
Recycled	50%	Analytical	A	661.83	-
			C	661.83	-
		Analytical (frequency test properties)	A	1605.46	142.58%
			C	1605.46	142.58%
		FE	C	653.75	-1.22%
			D	653.68	-1.23%
		FE (with panel margin)	C	726.07	9.71%
			D	725.85	9.67%
		FE (detailed geometry with panel margin)	C	654.19	-1.15%
		FE (layered plate)	C	556.45	-15.92%
		DSM (equivalent paperboard)	A	661.83	0.00%
		DSM (detailed geometry)	A	595.57	-10.01%
		Experiment (Southwell)		1275.60 ± 233.54	92.74% ± 35.3%
		Experiment (least squares three-point)		1260.40 ± 349.30	90.44% ± 52.78%
Recycled	90%	Analytical	A	538.48	-
			C	538.48	-
		FE	C	531.81	-1.24%
			D	531.75	-1.25%
		FE (with panel margin)	C	591.03	9.76%
			D	590.86	9.73%
		FE (detailed geometry with panel margin)	C	550.08	2.15%
		FE (layered plate)	C	452.94	-15.89%
		DSM (equivalent paperboard)	A	538.48	0.00%
		DSM (detailed geometry)	A	485.00	-9.93%
		Experiment (Southwell)		894.96 ± 424.22	66.20% ± 78.8%

The analytical models using equivalent single layer material properties and FEM models without panel margins have similar critical loads among the in- plane boundary condition cases A, C and D for all materials modelled.

The FE critical loads for models without panel margins are 1.22% to 1.25% lower than the analytical model results. The analytical models of case A and C, and FE models of case C and D have similar critical loads, the free out-of-plane edge segments in case D slightly lowering the critical load.

The analytical models which use the material properties obtained from frequency tests in Chapter 4 for kraft and recycled paperboard at 50% relative humidity show critical loads that are respectively 131% and 143% higher than the analytical models using equivalent single layer material properties. This is expected because the dynamic material properties of corrugated paperboard are stiffer than the static properties as viscoelastic behaviour is prevented.

The FE models with panel margins for kraft and recycled paperboard show critical loads 9.7% to 9.8% higher than the analytical models using equivalent single layer material properties. Therefore, including the margins of the panel that are positioned in the test fixture in the model has a stiffening effect on the panel.

The critical loads of FE models with detailed geometry of corrugated paperboard and panel margins are within 2% of the analytical values.

The critical load given by FE layered plate models with effective properties given to the core, are 9.0% and 8.4% lower than the analytical value for kraft corrugated paperboard at 50% and 90% relative humidity. The critical loads of the FE layered plate model given for recycled paperboard are 15.9% below the analytical values for 50% and 90% relative humidity. There is uncertainty in the definition of some of the effective core properties using the FE layered plate model and the properties used seem less suitable for the recycled paperboard.

The critical loads for the reference DSM equivalent single-layer paperboard model are identical to the analytical model results. The DSM detailed paperboard geometry model gives critical loads lower than the analytical value within 2% for kraft paperboard and 10% for recycled paperboard.

The mean Southwell plot critical loads from the experiments are above the analytical equivalent single layer model values by 42%, 84%, 93% and 66% for kraft paperboard at 50% and 90% relative humidity and recycled paperboard at 50% and 90% relative humidity respectively. It should be noted that the uncertainty in the mean Southwell plot critical loads based on a 95% confidence interval was high, 42%, 39%, 35%, 79% for kraft paperboard at 50% and 90% relative humidity and recycled paperboard at 50% and 90% relative humidity respectively.

The generally higher estimates of critical load values from the Southwell plot suggest the experimental boundary conditions are more constrained than modelled. However, the large uncertainties in the Southwell plot suggest that the Southwell method plot may not be reliable when applied to plate buckling.

According to (Mandal & Calladine, 2002) the method is useful for estimating the critical load in linearised beam flexural or lateral – torsional buckling problems but not for plate and shell buckling problems which would require non-linear governing equations in the eigenvalue analysis. The method also requires the testing to be at low loads within the material's elastic behaviour range with deflections or rotations remaining small. The panel buckling tests were conducted up to failure, though the Southwell plots created only include data prior to failure. There was however no measure of when the elastic limit may have been exceeded or whether deflections were excessive.

Other possible reasons include the presence of several imperfection modes apart from the fundamental mode and interactions between the plate displacement modes at higher load make clear and accurate prediction of the first critical load and imperfection problematic.

The least squares method to estimate of the experimental critical load, imperfection and post-buckling parameter by fitting the centre displacement data into a post-buckling function was only effective for the 50% relative humidity data, as there were problems in convergence to a

correct solution for the 90% relative humidity data. The problems in convergence when fitting the experimental data to the post-buckling equation at the 90% relative humidity levels could be due to material behaviour, such as plastic failure, not being adequately represented by the post-buckling equation.

The least squares estimates of the critical load for kraft corrugated paperboard at 50% relative humidity was slightly better than the Southwell estimate, with an average of 13.9% higher than the analytical value. However, the least squares critical load estimate for recycled corrugated paperboard at 50% relative humidity was not much better than the Southwell estimate at an average of 90.4% higher than the analytical value.

Although both the Southwell and least squares methods to obtain the experimental value of critical load gave much higher estimates than the models, the least squares method is the preferred of the two methods. This is because a post-buckling function is being fitted to the experimental data, allowing confirmation of the estimated parameters of the function by comparing with the experimental plot.

5.3.2 Post-buckling results

The post-buckling plots with dimensionless axes of load ratio relative to the analytical case C equivalent single layer properties model critical load P / P_{crit} and change in panel centre out-of-plane displacement relative to the panel thickness $\Delta w(0.5\,a, 0.5\,b)$ / h are presented in this section. The post-buckling plots for change in panel out-of-plane displacement at three other points Δw (0.5 a, 0.75 b), Δw (0.5 a, 0.25 b) and Δw (0.25 a, 0.5 b) can be found in Appendix IV.

Experimental post-buckling plots are presented together with analytical and FE model results.

The post-buckling models use mean values of panel imperfection modes obtained from Southwell plots of the experimental data denoted with ‘SW’

or ‘unadjusted’ initial displacement measurements, detailed in Appendix IV. The uncertainties in the mean values of panel imperfection given by the Southwell plots are larger than those of the ‘unadjusted’ panel deflection measurements. Therefore, the ‘unadjusted’ values are the preferred of the two panel imperfection types. However, the Southwell plot method imperfections were still considered because of the difficulty in measuring the initial panel imperfection. Additional post-buckling plots are also obtained using the panel imperfection from the least square method estimates shown in Appendix IV, only for the 50% relative humidity condition because of problems with convergence for the 90% relative humidity data.

The analytical results denoted with ‘freq. prop.’ have the material properties estimated from frequency tests, as opposed to equivalent single layered material properties.

The FE post-buckling model results only use panel imperfections from the ‘unadjusted’ displacement measurements.

5.3.2.1 Kraft paperboard at 50% RH

The post-buckling results for kraft paperboard at 50% relative humidity are shown in Figure 5-11. The experimental ‘unadjusted’ and Southwell post-buckling plots for the sample size of four, show smaller increase in displacements compared to the model results. These also show two values of peak load reached above the critical load and a load ratio of 1.3, possibly due to variation in the material. The initial stiffness in the experimental plots may be due to friction along the panel edges and the sharp decrease in load after buckling may be due to plasticity in the material.

The analytical plots using the ‘unadjusted’ panel imperfection have smaller increments of displacements than those using the Southwell obtained imperfection at low loads. However, the analytical plots for the same

boundary conditions case but different imperfection converge towards each other with increasing load.

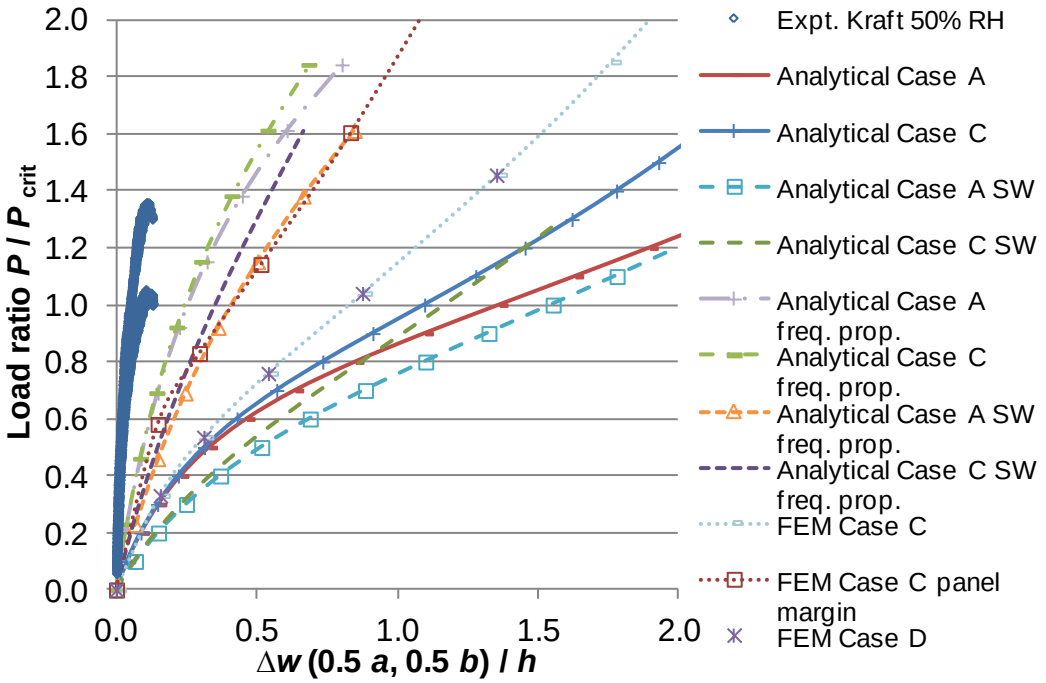

Figure 5-11: Dimensionless post-buckling plot of kraft paperboard panel centre displacement at 23 °C, 50% relative humidity.

The analytical plots for boundary condition cases A and C are similar, though case A has slightly larger displacements.

The analytical models which use equivalent single layer material properties of paperboard show larger displacements than those which use the material properties estimated from frequency tests.

The FE results of boundary condition cases C and D are similar to the analytical plot of case C but have smaller displacements above a load ratio of 0.4.

The inclusion of the panel margin in the FE model for case C reduces the panel out-of-plane displacements. The plot is similar to the analytical case C plot with frequency test material properties up to a load ratio of 0.6, with a greater increase in panel displacement above that load ratio.

The comparison of panel displacements at critical load below in Table 5-6 shows the results for the analytical model case C with 'unadjusted' panel

imperfection and frequency test material properties have the least disagreement with the mean 'unadjusted' experimental values.

Table 5-6: Panel displacements at analytical critical load for kraft paperboard at 23 °C, 50% relative humidity.

Kraft 50% RH Displacement at $P_{Critical}$	w (0.5 a, 0.5 b) / h	w (0.5 a, 0.75 b) / h	w (0.5 a, 0.25 b) / h	w (0.25 a, 0.5 b) / h
Expt. Average	0.430 ± 0.034	0.432 ± 0.021	1.564 ± 0.647	1.454 ± 0.407
Expt. SW Average	0.096 ± 0.036	0.095 ± 0.034	2.081 ± 0.742	2.116 ± 0.746
% Δ w to Expt.	-78%	-78%	33%	46%
Analy. Case A	1.723	1.361	1.073	1.252
% Δ w to Expt.	301%	215%	-31%	-14%
Analy. Case C	1.455	1.149	0.865	1.059
% Δ w to Expt.	239%	166%	-45%	-27%
Analy. Case A SW	1.578	1.213	1.691	2.062
% Δ w to Expt. SW	1539%	1179%	-19%	-3%
Analy. Case C SW	1.194	0.922	1.357	1.815
% Δ w to Expt. SW	1140%	871%	-35%	-14%
Analy. Case A freq. prop.	0.617	0.563	0.244	0.451
% Δ w to Expt.	44%	30%	-84%	-69%
Analy. Case C freq. prop.	0.604	0.553	0.236	0.442
% Δ w to Expt.	40%	28%	-85%	-70%
Analy. Case A SW freq. prop.	0.435	0.335	0.881	1.236
% Δ w to Expt. SW	352%	253%	-58%	-42%
Analy. Case C SW freq. prop.	0.379	0.302	0.818	1.205
% Δ w to Expt. SW	293%	218%	-61%	-43%
FE Case C	1.186	1.021	0.832	0.963
% Δ w to Expt.	176%	136%	-47%	-34%
FE Case C margin	0.773	0.664	0.360	0.562
% Δ w to Expt.	80%	54%	-77%	-61%
FE Case D	1.185	0.968	0.682	0.865
% Δ w to Expt.	176%	124%	-56%	-41%

5.3.2.2 Recycled paperboard at 50% RH

Post-buckling results for recycled paperboard at 50% relative humidity are shown in Figure 5-12.

The experimental post-buckling plots have comparatively smaller increase in displacement with load compared to the analytical and FE models as for

kraft paperboard. The peak load ratio reached in the experiments is about 1.7.

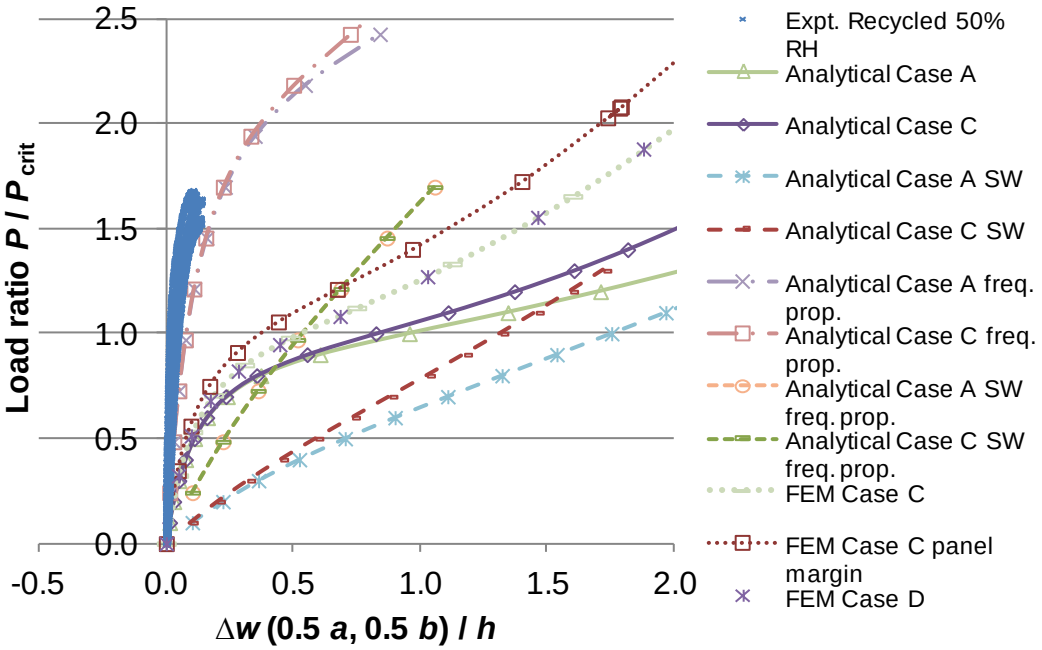

Figure 5-12: Dimensionless post-buckling plot of recycled paperboard panel centre displacement at 23 °C, 50% relative humidity.

The analytical results of boundary condition cases A and C are similar as for kraft paperboard, with case A having slightly larger displacements.

Analytical results with Southwell plot panel imperfection appear linear but may actually be curved at higher loads, approaching the curves of the cases with 'unadjusted' imperfection. This may be due to difference in panel imperfection amplitudes and the relative amplitudes among displacement mode shapes.

As with kraft paperboard, the analytical result with frequency test material properties of case C with 'unadjusted' panel imperfection appears to have the least discrepancy with the 'unadjusted' experimental plots.

The FE results of boundary condition cases C and D without the panel margins are similar to the analytical case C plot up to a load ratio of 0.5, with smaller displacements above that load ratio. The FE plot for boundary

condition case C with panel margins has smaller displacements than the other FE plots.

Table 5-7 below compares the panel displacements at critical load. The displacements from analytical cases A and C with 'unadjusted' imperfection and frequency test properties are least different to the mean 'unadjusted' experimental values.

Table 5-7: Panel displacements at analytical critical load for recycled paperboard at 23 °C, 50% relative humidity.

Recycled 50% RH Displacement at $P_{Critical}$	*w* (0.5 *a*, 0.5 *b*) / *h*	*w* (0.5 *a*, 0.75 *b*) / *h*	*w* (0.5 *a*, 0.25 *b*) / *h*	*w* (0.25 *a*, 0.5 *b*) / *h*
Expt. Average	0.367 ± 0.016	0.395 ± 0.009	0.252 ± 0.346	0.698 ± 0.186
Expt. SW Average	0.048 ± 0.036	0.091 ± 0.054	1.100 ± 0.863	2.197 ± 1.434
% Δ *w* to Expt.	-87%	-77%	336%	215%
Analy. Case A	1.302	1.027	0.443	0.569
% Δ *w* to Expt.	255%	160%	76%	-18%
Analy. Case C	1.170	0.939	0.341	0.473
% Δ *w* to Expt.	219%	137%	35%	-32%
Analy. Case A SW	1.779	1.389	1.830	2.656
% Δ *w* to Expt. SW	3634%	1422%	66%	21%
Analy. Case C SW	1.342	1.052	1.448	2.394
% Δ *w* to Expt. SW	2719%	1052%	32%	9%
Analy. Case A freq. prop.	0.425	0.420	-0.202	-0.047
% Δ *w* to Expt.	16%	6%	-180%	-107%
Analy. Case C freq. prop.	0.424	0.421	-0.203	-0.048
% Δ *w* to Expt.	15%	7%	-180%	-107%
Analy. Case A SW freq. prop.	0.563	0.435	0.980	1.790
% Δ *w* to Expt. SW	1083%	376%	-11%	-19%
Analy. Case C SW freq. prop.	0.563	0.435	0.980	1.790
% Δ *w* to Expt. SW	1083%	376%	-11%	-19%
FE Case C	0.879	0.693	0.129	0.272
% Δ *w* to Expt.	139%	75%	-49%	-61%
FE Case C margin	0.720	0.605	-0.001	0.158
% Δ *w* to Expt.	96%	53%	-101%	-77%
FE Case D	0.870	0.771	0.204	0.300
% Δ *w* to Expt.	137%	95%	-19%	-57%

5.3.2.3 Kraft paperboard at 90% RH

The post-buckling results for kraft paperboard at 90% relative humidity are given in Figure 5-13.

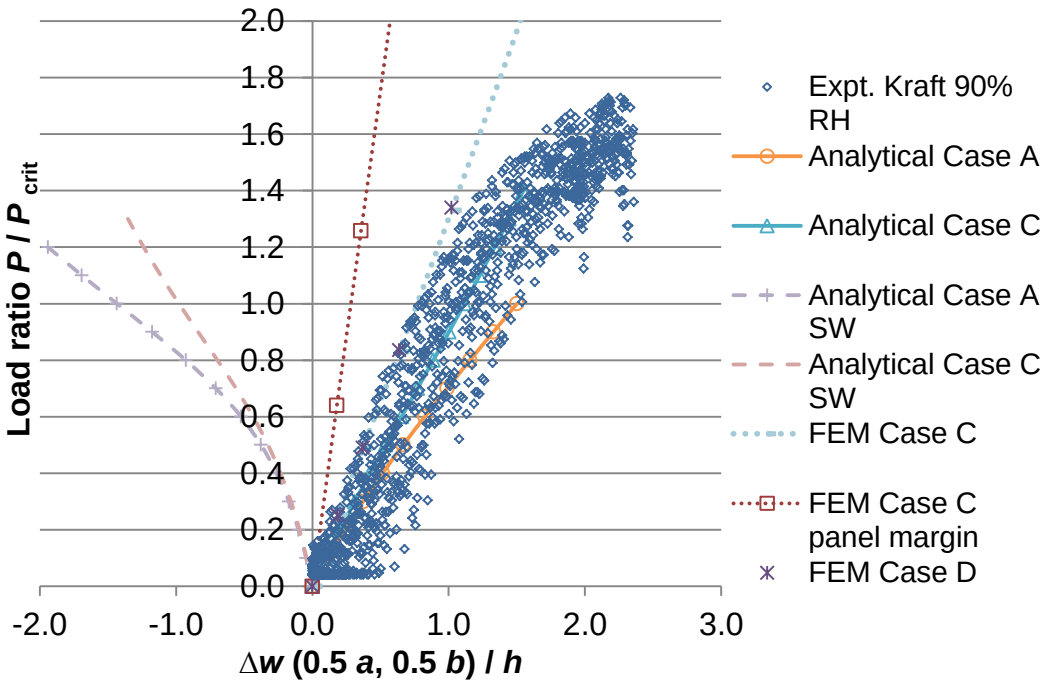

Figure 5-13: Dimensionless post-buckling plot of kraft paperboard panel centre displacement at 23 °C, 90% relative humidity.

The peak load ratios reached by the experimental plots are between 1.6 and 1.7. The 'unadjusted' experimental plots at this higher relative humidity show a greater range of panel centre imperfection than the 50% relative humidity results. The Southwell plots of the data also estimated opposing directions of the panel centre imperfection from tests of different specimens. However, the fact that the panel displacements become more positive with increasing load suggests that the panel imperfection should be in the positive direction.

This is confirmed by the contrast in panel displacement directions between analytical results which used the mean 'unadjusted' and Southwell plot imperfection values. The analytical and FE model results which use the 'unadjusted' imperfection values show better agreement with the experimental plots.

The analytical plot for boundary condition case C has closer agreement than that of case A. The FE results for boundary condition cases C and D without panel margins are identical as with previous materials and relative

humidity levels presented. The FE plot for case C with panel margins shows slightly smaller displacements than the other FE model results.

The comparison of the panel displacements at critical load below in Table 5-8 shows the results for FE models of cases C and D, and the analytical model of case C with 'unadjusted' imperfection are closest to the mean 'unadjusted' experimental values.

Table 5-8: Panel displacements at analytical critical load for kraft paperboard at 23 °C, 90% relative humidity.

Kraft 90% RH Displacement at $P_{Critical}$	w (0.5 a, 0.5 b) / h	w (0.5 a, 0.75 b) / h	w (0.5 a, 0.25 b) / h	w (0.25 a, 0.5 b) / h
Expt. Average	2.223 ± 0.422	1.702 ± 0.458	1.779 ± 0.308	1.772 ± 0.268
Expt. SW Average	0.850 ± 1.578	1.511 ± 0.867	-0.149 ± 1.106	0.080 ± 1.184
% Δ w to Expt.	-62%	-11%	-108%	-95%
Analy. Case A	2.823	2.086	2.276	2.246
% Δ w to Expt.	27%	23%	28%	27%
Analy. Case C	2.438	1.726	1.920	1.974
% Δ w to Expt.	10%	1%	8%	11%
Analy. Case A SW	-1.484	-0.398	-1.774	-1.613
% Δ w to Expt. SW	-274%	-126%	1094%	-2108%
Analy. Case C SW	-1.029	-0.138	-1.420	-1.301
% Δ w to Expt. SW	-221%	-109%	856%	-1720%
FE Case C	2.085	1.484	1.664	1.705
% Δ w to Expt.	-6%	-13%	-6%	-4%
FE Case C margin	1.608	1.101	1.297	1.318
% Δ w to Expt.	-28%	-35%	-27%	-26%
FE Case D	2.080	1.498	1.662	1.695
% Δ w to Expt.	-6%	-12%	-7%	-4%

5.3.2.4 Recycled paperboard at 90% RH

The post-buckling results for recycled paperboard at 90% relative humidity are presented in Figure 5-14.

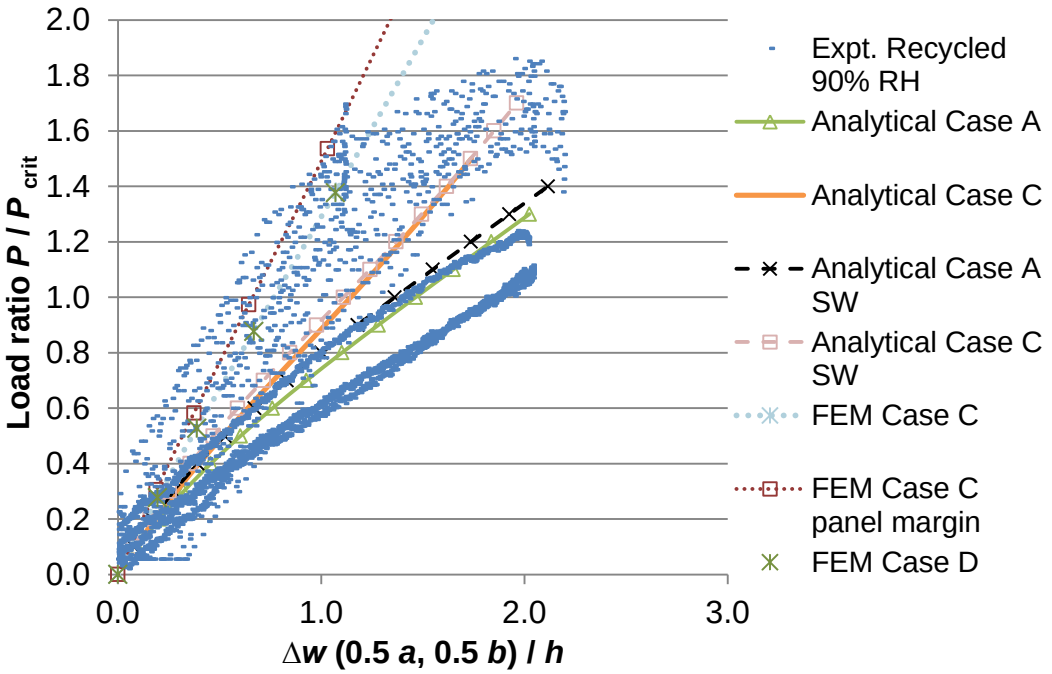

Figure 5-14: Dimensionless post-buckling plot of recycled paperboard panel centre displacement at 23 °C, 90% relative humidity.

The experimental plots show a variation of peak load ratios between 1.1 and 1.8. The Southwell plot estimates of the panel imperfection are also more scattered than the 50% relative humidity condition.

The analytical results for models with the 'unadjusted' and Southwell plot imperfections are fairly similar, with reasonable agreement with the experimental plots. The plots for boundary condition case C have slightly smaller displacements than for case A.

The FE results also have fair agreement with the experimental plots. The FE plots for boundary condition cases C and D are identical as with the previous results presented. The FE plot for case C with panel margins has slightly smaller displacements than the other FE plots shown.

The comparison of panel displacements at critical load below in Table 5-9 shows the results for analytical case C with 'unadjusted' imperfection are closest to the mean 'unadjusted' experimental values.

Table 5-9: Panel displacements at analytical critical load for recycled paperboard at 23 °C, 90% relative humidity.

Recycled 90% RH Displacement at $P_{Critical}$	w (0.5 a, 0.5 b) / h	w (0.5 a, 0.75 b) / h	w (0.5 a, 0.25 b) / h	w (0.25 a, 0.5 b) / h
Expt. Average	2.163 ± 0.691	1.848 ± 0.795	1.820 ± 0.429	1.629 ± 0.479
Expt. SW Average	2.113 ± 1.636	2.047 ± 1.340	1.736 ± 1.165	1.372 ± 1.122
% Δ w to Expt.	-2%	11%	-5%	-16%
Analy. Case A	2.469	1.936	1.995	1.926
% Δ w to Expt.	14%	5%	10%	18%
Analy. Case C	2.149	1.638	1.697	1.699
% Δ w to Expt.	-1%	-11%	-7%	4%
Analy. Case A SW	2.316	2.033	1.861	1.600
% Δ w to Expt. SW	10%	-1%	7%	17%
Analy. Case C SW	2.063	1.788	1.615	1.413
% Δ w to Expt. SW	-2%	-13%	-7%	3%
FE Case C	1.773	1.372	1.426	1.419
% Δ w to Expt.	-18%	-26%	-22%	-13%
FE Case C margin	1.668	1.289	1.333	1.331
% Δ w to Expt.	-23%	-30%	-27%	-18%
FE Case D	1.786	1.399	1.404	1.412
% Δ w to Expt.	-17%	-24%	-23%	-13%

In general, the comparison of post-buckling results for panel displacements at the measured points show that for the 50% relative humidity condition, the analytical results for case C with ‘unadjusted’ panel imperfection and frequency test material properties had least disagreement with the ‘unadjusted’ experimental results. For the 90% relative humidity condition, the analytical results for case C with ‘unadjusted’ panel imperfection for recycled paperboard and the FE results for case C for kraft paperboard are closest to the experimental results.

The post-buckling plots of data for the three other locations of panel deflection measurement in Appendix IV show the differences in the form of the experimental and modelling plots are like those of the panel centre plots for deflections at (0.5 a, 0.75 b), but not for deflections at (0.5 a, 0.25 b) and (0.25 a, 0.5 b). This difference is more obvious at the 50% relative humidity condition for both paperboard materials.

5.3.3 Post-buckling panel displacement modes

The post-buckling results are now reconsidered by comparing the amplitudes of panel out-of-plane displacement modes $A_{i,j}$. Using the collocation method, the experimental displacement measurements were found to be non-zero only for the modes $A_{1,1}$, $A_{3,1}$, $A_{3,2}$ and $A_{3,3}$. The analytical model displacement results however, show additional non-zero displacements amplitudes for modes $A_{1,2}$ and $A_{1,3}$.

The post-buckling plots of displacement modes $A_{1,1}$, $A_{3,1}$, $A_{3,2}$ and $A_{3,3}$ for kraft and recycled paperboard from the 'unadjusted' experimental and analytical model results are presented in Appendix IV. There is generally good agreement between the 'unadjusted' experimental displacement mode amplitudes and the analytical results for the 'unadjusted' panel imperfection for the fundamental mode $A_{1,1}$. The analytical results for other displacement modes $A_{3,1}$, $A_{3,2}$ and $A_{3,3}$ do not compare well to the experimental plots.

The relative amplitudes of the experimental displacement modes are next considered for the different paperboard materials and relative humidity levels. The displacement mode amplitudes at critical load from experimental and analytical results are also compared.

5.3.3.1 Kraft paperboard at 50% RH

The 'unadjusted' experimental post-buckling plot for kraft paperboard at 50% relative humidity for the non-zero displacement modes is shown in Figure 5-15.

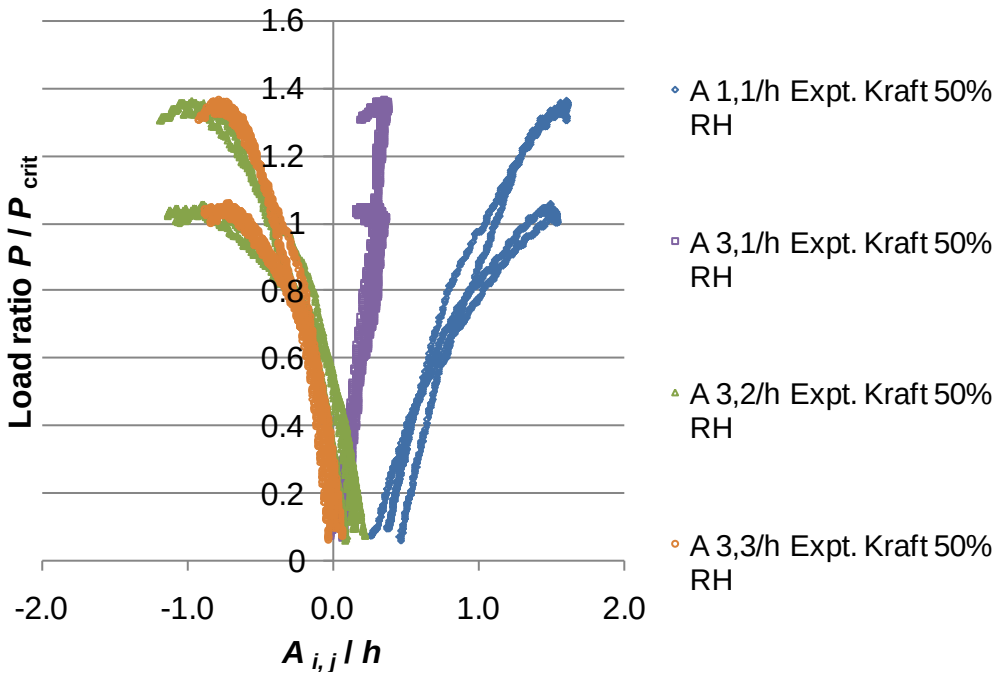

Figure 5-15: Dimensionless post-buckling plot of displacement modes for 'unadjusted' experimental results for kraft paperboard at 23 °C, 50% relative humidity.

The fundamental mode $A_{1,1}$ has the largest amplitude, while the amplitude of mode $A_{3,1}$ is about a third of $A_{1,1}$. The higher modes $A_{3,2}$ and $A_{3,3}$ have similar amplitudes to $A_{1,1}$ but are in the opposite direction, with the mode $A_{3,3}$ being the smaller of the two.

The table below Table 5-10 compares the displacement modes from the experiment and the analytical models at critical load. The analytical case C result for the 'unadjusted' panel imperfection shows least disagreement with the experimental result, with 20% difference for the fundamental mode.

The displacement amplitudes at critical load for the analytical models using Southwell plot imperfection and frequency test material properties are closest to the experimental values but this is because of the difference in initial panel imperfection. The post-buckling plots in Appendix IV show the form of the plots for these results differs from the experimental plot.

Table 5-10: Displacement mode amplitudes at analytical critical load for kraft paperboard at 23 °C, 50% relative humidity.

Kraft 50% RH Displacement amplitude at $P_{Critical}$	$A_{1,1}/h$	$A_{3,1}/h$	$A_{3,2}/h$	$A_{3,3}/h$
Expt. Average	1.243 ± 0.304	0.322 ± 0.052	-0.566 ± 0.313	-0.491 ± 0.220
Analy. Case A	1.775	0.053	0.170	0.029
% Δ $A_{i,j}$ to Expt.	43%	-84%	-130%	-106%
Analy. Case C	1.489	0.049	0.171	0.028
% Δ $A_{i,j}$ to Expt.	20%	-85%	-130%	-106%
Analy. Case A SW	2.267	0.451	-0.295	-0.217
% Δ $A_{i,j}$ to Expt.	82%	40%	-48%	-56%
Analy. Case C SW	1.865	0.462	-0.298	-0.224
% Δ $A_{i,j}$ to Expt.	50%	43%	-47%	-54%
Analy. Case A freq. prop.	0.630	0.003	0.002	0.000
% Δ $A_{i,j}$ to Expt.	-49%	-99%	-100%	-100%
Analy. Case C freq. prop.	0.617	0.036	0.163	0.025
% Δ $A_{i,j}$ to Expt.	-50%	-89%	-129%	-105%
Analy. Case A SW freq. prop.	1.090	0.442	-0.283	-0.214
% Δ $A_{i,j}$ to Expt.	-12%	37%	-50%	-56%
Analy. Case C SW freq. prop.	1.033	0.448	-0.283	-0.215
% Δ $A_{i,j}$ to Expt.	-17%	39%	-50%	-56%

5.3.3.2 Recycled paperboard at 50% RH

The experimental post-buckling plot for the non-zero displacement modes for recycled paperboard at 50% relative humdity is shown below.

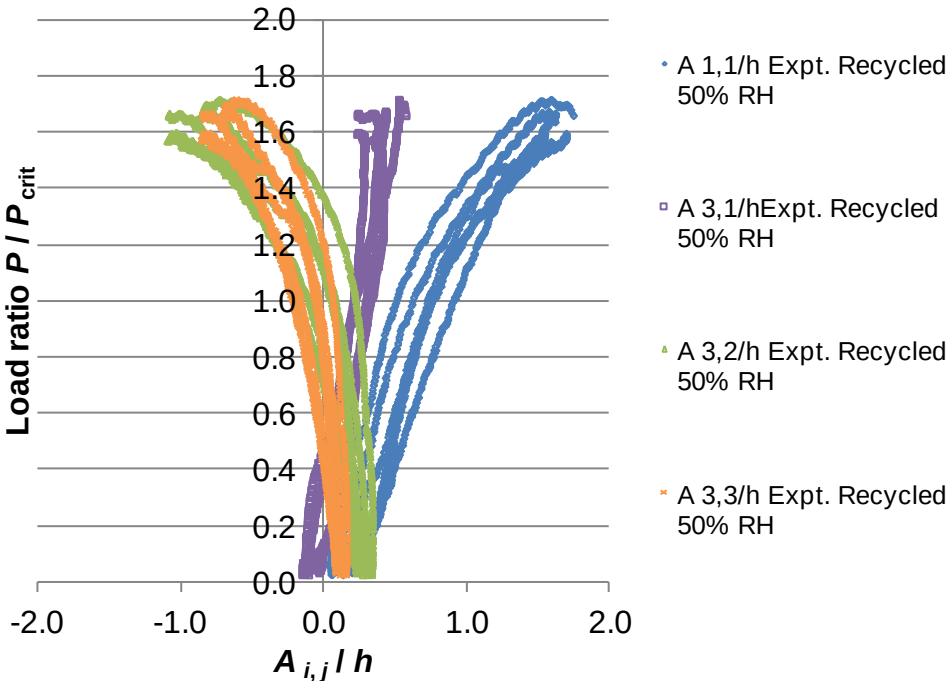

Figure 5-16: Dimensionless post-buckling plot of displacement modes for 'unadjusted' experimental results for recycled paperboard at 23 °C, 50% relative humidity.

The relative amplitudes of the displacement modes are similar to that of kraft paperboard at 50% relative humidity. The fundamental mode $A_{1,1}$ has the largest amplitude, followed by modes $A_{3,2}$ and $A_{3,3}$ which are in the opposite direction, and mode $A_{3,1}$ which has the smallest amplitude.

The comparison of displacement mode amplitudes at critical load for the experimental and analytical results in Table 5-11 shows the least disagreement is between the analytical case C results for 'unadjusted' panel imperfection and the experimental values, with 38% difference for the fundamental mode.

Table 5-11: Displacement mode amplitudes at analytical critical load for recycled paperboard at 23 °C, 50% relative humidity.

Recyc. 50% RH Displacement amplitude at $P_{Critical}$	$A_{1,1}/h$	$A_{3,1}/h$	$A_{3,2}/h$	$A_{3,3}/h$
Expt. Average	0.677 ± 0.139	0.265 ± 0.046	0.071 ± 0.169	-0.045 ± 0.117
Analy. Case A	1.067	-0.103	0.326	0.145
% Δ $A_{i,j}$ to Expt.	58%	-139%	356%	-420%
Analy. Case C	0.932	-0.106	0.326	0.145
% Δ $A_{i,j}$ to Expt.	38%	-140%	356%	-420%
Analy. Case A SW	2.796	0.769	-0.297	-0.220
% Δ $A_{i,j}$ to Expt.	313%	191%	-515%	384%
Analy. Case C SW	2.344	0.789	-0.300	-0.233
% Δ $A_{i,j}$ to Expt.	246%	198%	-520%	412%
Analy. Case A freq. prop.	0.180	-0.110	0.312	0.136
% Δ $A_{i,j}$ to Expt.	-73%	-142%	337%	-399%
Analy. Case C freq. prop.	0.179	-0.110	0.312	0.136
% Δ $A_{i,j}$ to Expt.	-74%	-142%	336%	-399%
Analy. Case A SW freq. prop.	1.540	0.758	-0.288	-0.226
% Δ $A_{i,j}$ to Expt.	127%	186%	-502%	397%
Analy. Case C SW freq. prop.	1.540	0.758	-0.288	-0.226
% Δ $A_{i,j}$ to Expt.	127%	186%	-502%	397%

5.3.3.3 Kraft paperboard at 90% RH

The experimental post-buckling plot of displacement modes for kraft paperboard at 90% relative humidity are shown below in Figure 5-17. The fundamental mode $A_{1,1}$ has the largest amplitude, followed by modes $A_{3,2}$, $A_{3,3}$ and $A_{3,1}$.

The comparison of displacement mode amplitudes at critical load for the analytical and experimental results in Table 5-12 shows that the least disagreement is between the analytical case C result for ‘unadjusted’ panel imperfection and the experimental values, with 12% difference for the fundamental mode.

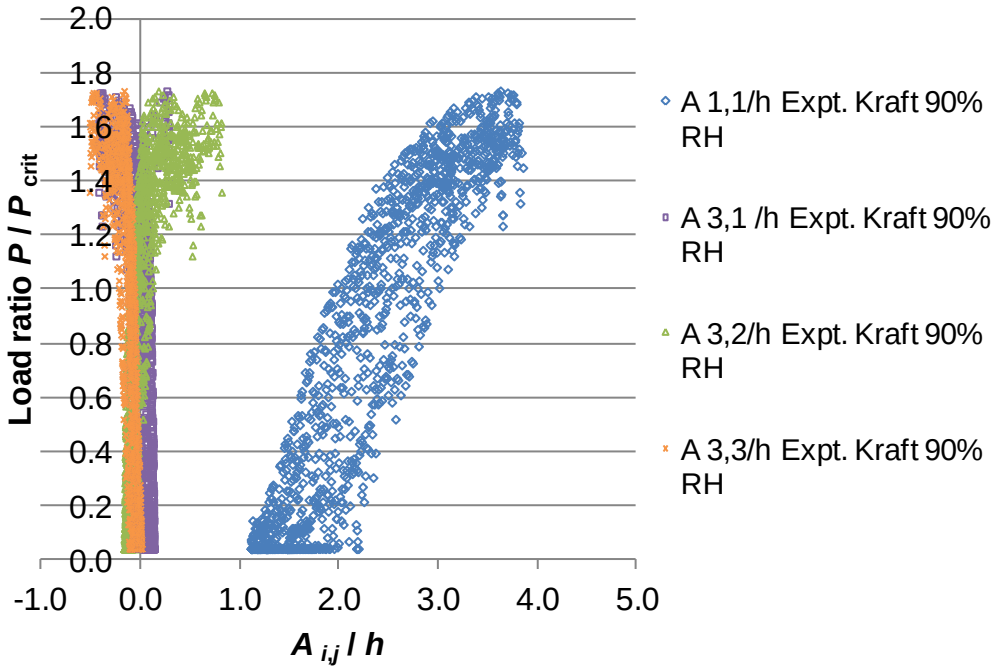

Figure 5-17: Dimensionless post-buckling plot of displacement modes for 'unadjusted' experimental results for kraft paperboard at 23 °C, 90% relative humidity.

Table 5-12: Displacement mode amplitudes at analytical critical load for kraft paperboard at 23 °C, 90% relative humidity.

Kraft 90% RH Displacement amplitude at $P_{Critical}$	$A_{1,1}/h$	$A_{3,1}/h$	$A_{3,2}/h$	$A_{3,3}/h$
Expt. Average	2.365 ± 0.400	0.022 ± 0.082	-0.038 ± 0.088	-0.119± 0.059
Analy. Case A	3.094	0.140	-0.123	-0.036
% Δ $A_{i,j}$ to Expt.	31%	525%	223%	-70%
Analy. Case C	2.642	0.134	-0.125	-0.043
% Δ $A_{i,j}$ to Expt.	12%	497%	227%	-64%
Analy. Case A SW	-1.892	-0.382	0.814	0.016
% Δ $A_{i,j}$ to Expt.	-180%	-1804%	-2236%	-114%
Analy. Case C SW	-1.448	-0.382	0.818	0.023
% Δ $A_{i,j}$ to Expt.	-161%	-1805%	-2247%	-119%

5.3.3.4 Recycled paperboard at 90% RH

The experimental post-buckling plot of displacement modes for recycled paperboard at 90% relative humidity is presented in Figure 5-18. The relative amplitudes of the displacement modes are similar to those of kraft paperboard at 90% relative humidity. The modes in decreasing amplitude are the fundamental mode $A_{1,1}$, followed by modes $A_{3,2}$, $A_{3,1}$ and $A_{3,3}$.

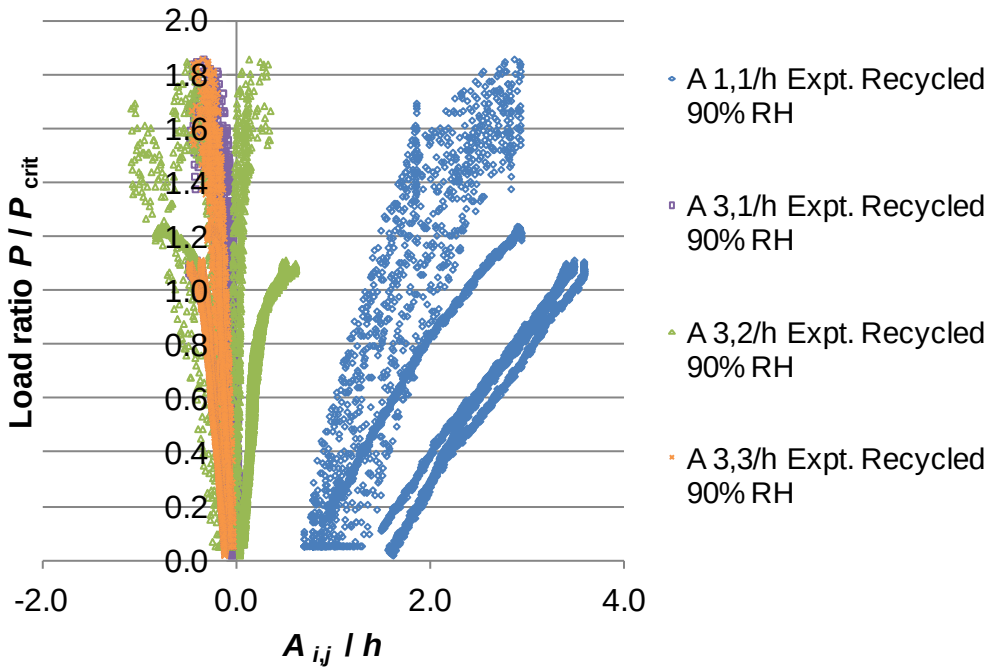

Figure 5-18: Dimensionless post-buckling plot of displacement modes for 'unadjusted' experimental results for recycled paperboard at 23 °C, 90% relative humidity.

Table 5-13: Displacement mode amplitudes at analytical critical load for recycled paperboard at 90% relative humidity.

Recycled 90% RH Displacement amplitude at $P_{Critical}$	$A_{1,1}/h$	$A_{3,1}/h$	$A_{3,2}/h$	$A_{3,3}/h$
Expt. Average	2.234 ± 0.683	-0.145 ± 0.098	0.014 ± 0.235	-0.215 ± 0.078
Analy. Case A	2.668	0.043	-0.039	-0.084
% Δ $A_{i,j}$ to Expt.	19%	-130%	-380%	-61%
Analy. Case C	2.292	0.038	-0.039	-0.088
% Δ $A_{i,j}$ to Expt.	3%	-126%	-383%	-59%
Analy. Case A SW	2.343	-0.192	0.116	-0.165
% Δ $A_{i,j}$ to Expt.	5%	32%	739%	-23%
Analy. Case C SW	2.037	-0.198	0.117	-0.166
% Δ $A_{i,j}$ to Expt.	-9%	37%	745%	-23%

Table 5-13 above compares the displacement mode amplitudes of the analytical and experimental results at critical load. The analytical case C result shows closest agreement with the experimental values, with 3% difference for the fundamental mode.

The experimental displacement amplitudes for the higher modes $A_{3,1}$, $A_{3,2}$ and $A_{3,3}$ are generally larger than the analytical model results for all the paperboard materials and humidity levels considered.

This may be due to the additional non-zero $A_{1,2}$ and $A_{1,3}$ modes present for the analytical results changing the distribution of the displacement mode amplitudes. The uncertainty in the initial panel imperfection values applied to the models also could result in some differences between the experimental and modelling results.

The experimental results show that the fundamental mode is dominant for all the paperboard materials and relative humidity levels. Therefore, the comparison of results for this mode is most important. Based on the comparison of the fundamental displacement mode results, the analytical results of case C with the 'unadjusted' panel imperfection are closest to the experimental post-buckling results.

The experimental boundary conditions are likely to be similar to the boundary condition case C. However, the comparison of displacements at the measurement points in section 5.3.2 show the modelling displacements at the panel centre and at (0.5 *a*, 0.75 *b*) are generally larger than the experimental values for the 50% relative humidity level. For these results, using the frequency test material properties improves the agreement between the analytical model and experimental results.

However, the analytical models using frequency test material properties have the unfavourable disadvantage of overestimating the critical load. Even so, the large uncertainty in the critical load values predicted by Southwell plots of experimental panel centre displacement also means difficulty in verifying the critical load results. Variability in the materials may contribute to some of the uncertainty in test results.

The experimental in-plane boundary conditions are likely to be similar to the case C boundary condition, although the higher post-buckling out-of-

plane displacement modes $A_{3,1}$, $A_{3,2}$ and $A_{3,3}$ from the experimental results might suggest the boundary conditions are less restrained.

The higher estimated experimental critical loads relative to the analytical values could also be due to differences in the modelling of the out-of-plane boundary condition that would increase the critical load, seen in the FE models with panel margins. In the experiment, the panel regions on the periphery of the supports may provide some resistance against rotation along the edges.

5.3.4 Panel imperfection and material properties

5.3.4.1 Least squares method panel imperfection

The post-buckling results for kraft paperboard at 50% relative humidity are reconsidered by using the panel centre imperfection estimated by the least squares method. The case C boundary conditions are applied in the analytical and FE models with the least squares imperfection.

As reference, the post-buckling plots for kraft paperboard at 50% relative humidity using the 'unadjusted' initial displacement measurements as imperfections, from analytical equivalent single layered and frequency test properties models and FE single layered models with and without panel margins, are shown in Figure 5-19. It shows that the result from the analytical frequency test properties model was the least different to the experimental plot.

The post-buckling plots using the least squares method estimates of panel centre imperfection are given in Figure 5-20, showing results from analytical equivalent single layered and frequency test properties with and without scaling, and FE detailed geometric and effective multi-layered models.

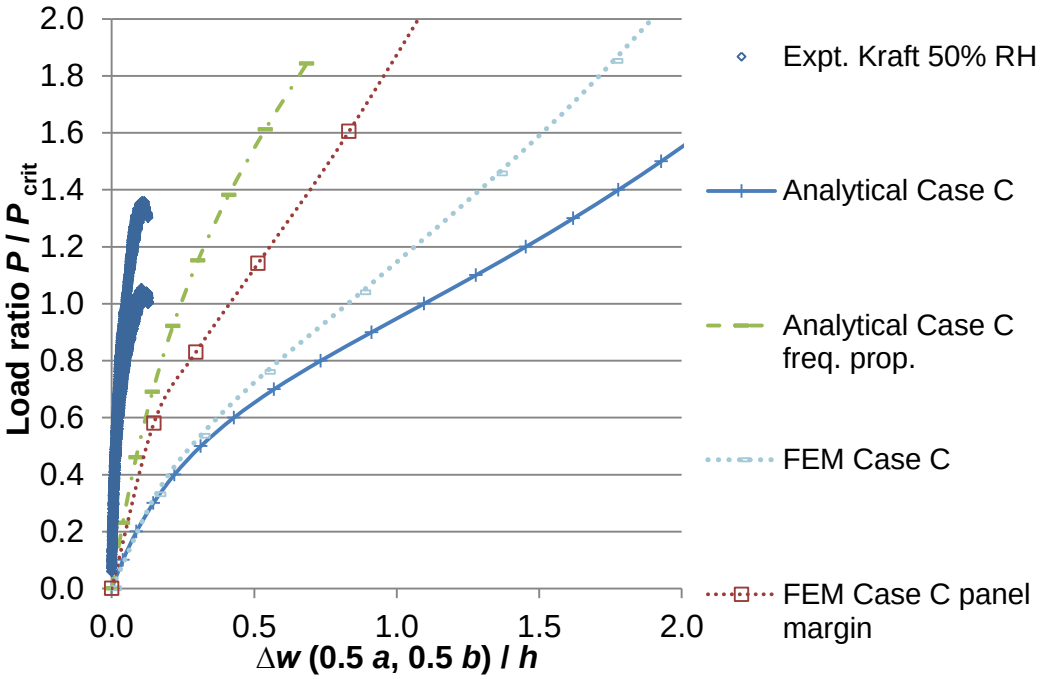

Figure 5-19: Post-buckling results for kraft paperboard at 50% RH using unadjusted initial displacement measurements as imperfections, from analytical equivalent single layered and frequency test properties, and FE single layered models.

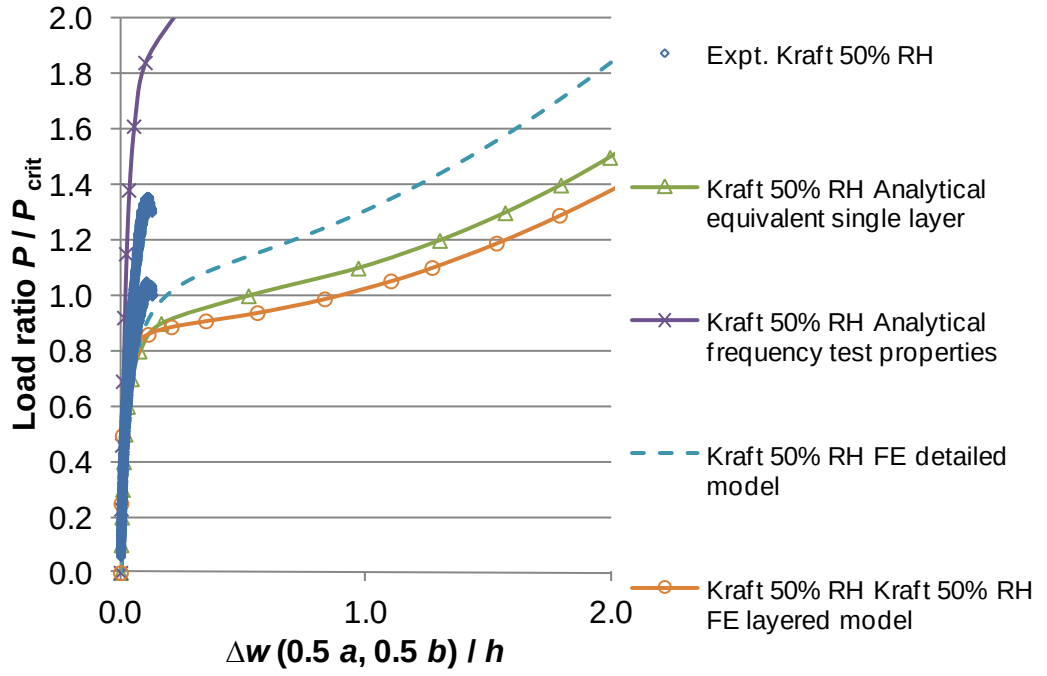

Figure 5-20: Post-buckling results for kraft paperboard at 50% RH using least squares method estimates of panel centre imperfection, from analytical equivalent single layered and frequency test properties, and FE detailed and multi-layered models.

Since the average panel centre imperfection obtained by the least squares method was smaller than the unadjusted panel displacement measurement, the post-buckling plots in Figure 5-20 have lower out-of-plane displacements prior to buckling, improving model agreement with the experiment.

The FE detailed geometric model has better agreement with the experimental result than the analytical equivalent single layered and FE multi-layered models, with higher load onset of buckling and smaller displacements. This shows that there are inadequacies in the FE multi-layered material definition and the equivalent single layered material model. The analytical frequency test properties model gives displacements that are smaller than those found in the experiment and a much higher buckling load, due to the higher stiffness of the frequency test material properties.

Similarly, the post-buckling results of recycled paperboard at 50% relative humidity are reconsidered by using the imperfection estimated by the least squares method.

The reference post-buckling results using the unadjusted panel displacement measurements as imperfection for recycled paperboard at 50% relative humidity is given in Figure 5-21. The analytical frequency test properties model results in this plot are nearest to the experimental plot.

Figure 5-22 shows post-buckling results for recycled paperboard at 50% relative humidity that use least squares method estimates of panel centre imperfection. The agreement between the analytical frequency test properties model and the experiment has worsened because of the smaller imperfection estimated by the least squares method.

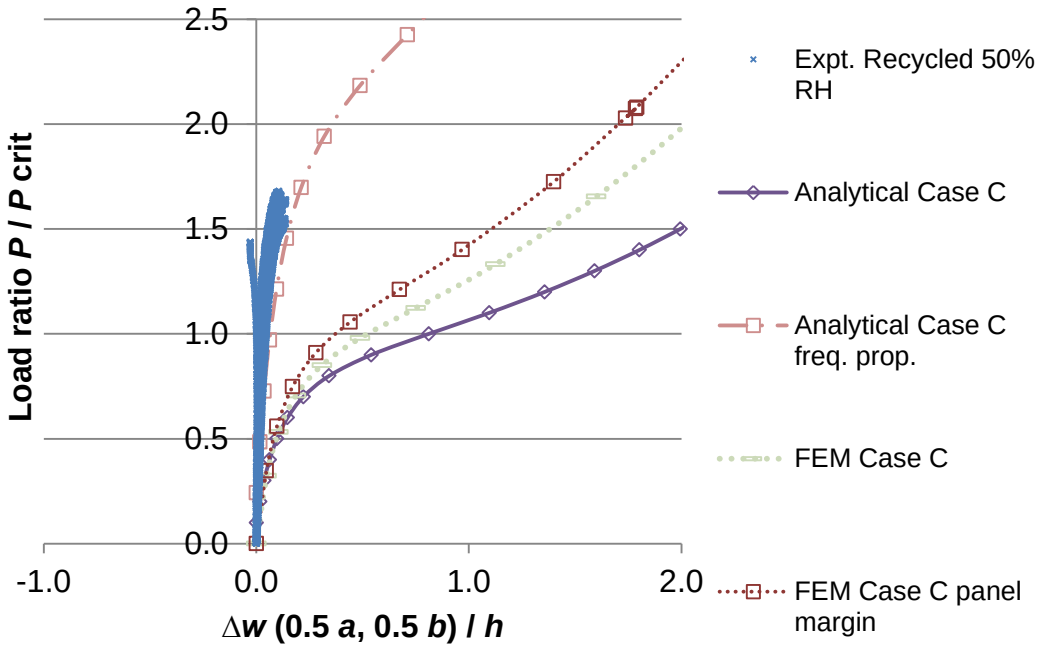

Figure 5-21: Post-buckling results for recycled paperboard at 50% RH using unadjusted initial displacement measurements as imperfections, from analytical equivalent single layered and frequency test properties, and FE single layered models.

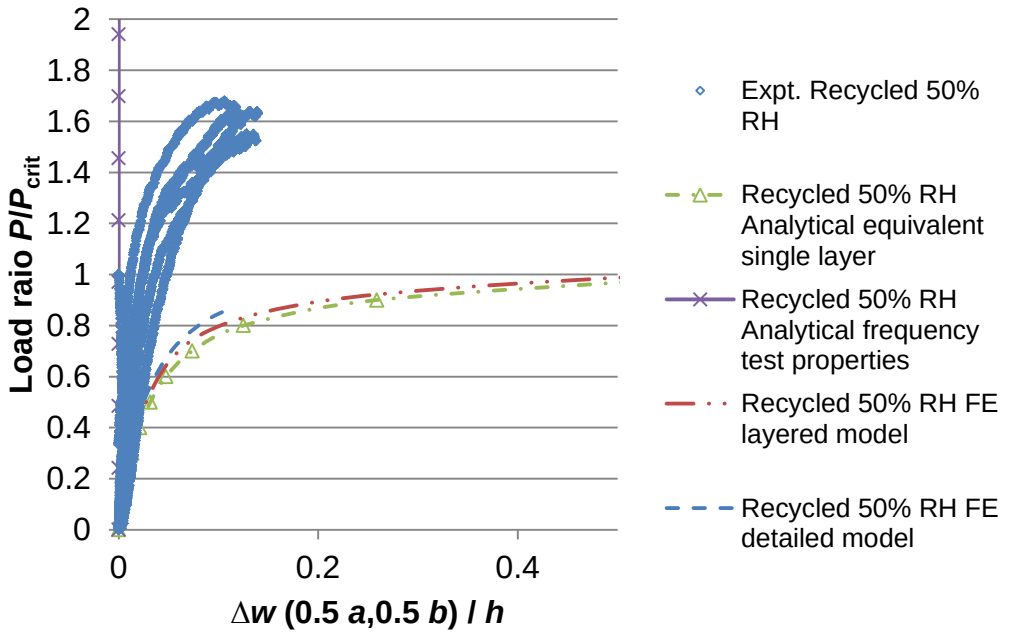

Figure 5-22: Post-buckling results for recycled paperboard at 50% RH using least squares method estimates of panel centre imperfection, from analytical equivalent single layered and frequency test properties, and FE detailed and multi-layered models.

The analytical equivalent single layered and FE detailed geometric and multi-layered models give similar post-buckling plots which have larger displacements than the experiment and lower loads for the onset of buckling. These results show the imperfection values given to the models have some influence on the post-buckling agreement with the experiments.

There was some uncertainty in obtaining the panel imperfection. Hence, different methods to estimate the imperfection were explored. From the results of the study, the least squares method is preferable over Southwell's method. However, problems with convergence to a correct solution were encountered which raised questions on the reliability of the Newton-Raphson method used in solving the non-linear equations from the application of the least squares method.

Some support can be given to the general trends in the post-buckling results though. This is because the imperfection amplitudes will affect the post-buckling plot displacements up to buckling but the discrepancy between plots of different imperfection should reduce at higher loads. This assumes the same imperfection modes are considered, for instance the fundamental mode. The relative amplitudes and interactions between imperfection modes is a different issue that was considered in chapter 3.

The next section considers the impact of scaling the frequency test material properties on the analytical post-buckling result of kraft paperboard at 50% relative humidity.

5.3.4.2 Scaled frequency test material properties

The previous section showed the post-buckling results from analytical frequency test properties models for the 50% relative humidity condition were generally the least different to the experiment, though the panel imperfection had some influence on the level of agreement.

This section now considers the post-buckling results of the analytical model using scaled frequency test material properties for kraft paperboard

at 50% relative humidity. The in-plane elastic properties are scaled by the factor *CF*1 and the flexural properties are scaled by the factor *CF*2. Two scaling constants were chosen because it was known that the in-plane and flexural properties of corrugated paperboard should to be independently scaled. This is because orthotropic plate relations between in-plane and flexural properties do not apply to corrugated paperboard since it has higher flexural stiffness than what would be predicted from its in-plane elastic properties.

The post-buckling results in Figure 5-23 have scaling values of *CF*1 as 0.2, 0.5, 1.5 and 3 and *CF*2 as unity. Figure 5-24 shows post-buckling results with scaling values of *CF*1 as 1, 4, 5, 10, 15 and 20 and *CF*2 as 0.5.

The reference analytical frequency test properties model result is also shown, along with the analytical equivalent single layered and experimental result, using the least squares imperfection estimate.

The results show that setting the scaling factor *CF*2 as 0.5 lowers the critical load of the plot closer to the experimental plot. The value of *CF*1 influences the steepness of the post-buckling plot at loads above critical. The higher the value of *CF*1, the steeper the post-buckling plot. The combination of scaling factors for the frequency test material properties which had good agreement with the experiment was *CF*1 = 20, *CF*2 = 0.5.

The results show that it may be possible to use the frequency test material properties by establishing scaling factors that account for the difference in material behaviour in static and dynamic loading as well as in-plane and flexural properties for corrugated paperboard. The scaling factors could be assumed to be constants for a given material at a specific temperature and humidity condition. The material behaviour in frequency tests and post-buckling tests could be used to determine the scaling factors which need to be verified by experiments on various sample geometry of the same corrugated paperboard geometry.

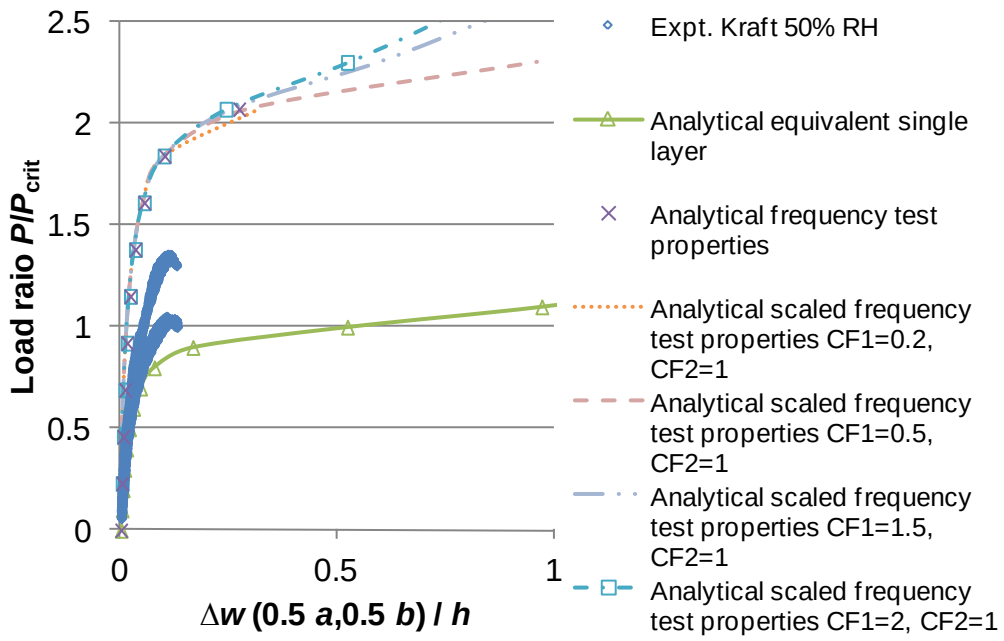

Figure 5-23: Post-buckling results for kraft paperboard at 50% RH using least squares method estimates of panel centre imperfection, from analytical equivalent single layered and scaled frequency test properties models with *CF*2 = 1.

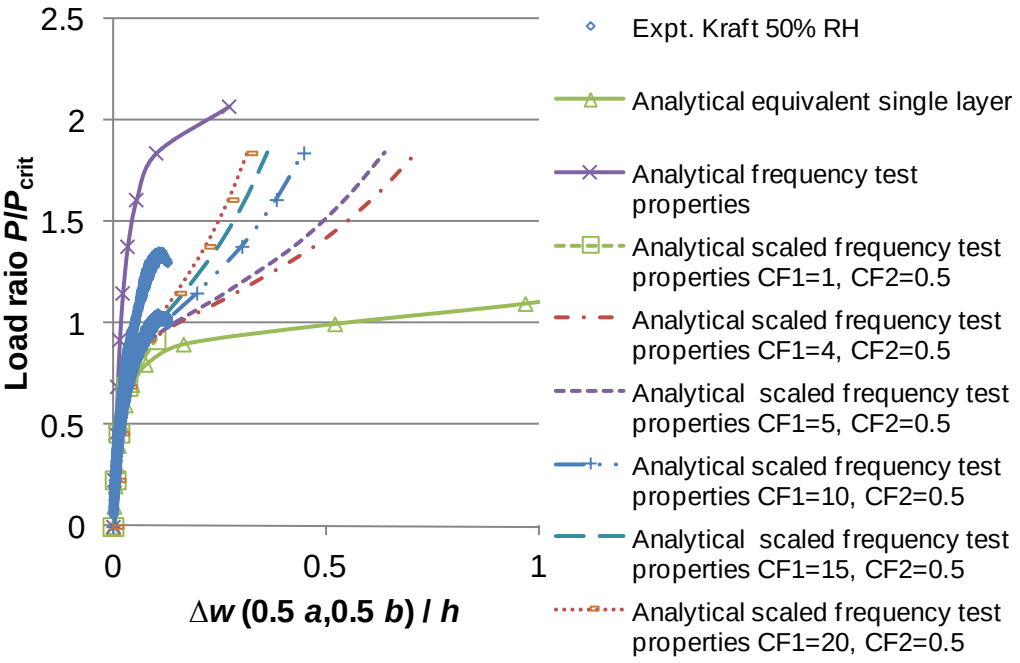

Figure 5-24: Post-buckling results for kraft paperboard at 50% RH using least squares method estimates of panel centre imperfection, from analytical equivalent single layered and scaled frequency test properties models with *CF*2 = 0.5.

5.4 Concluding remarks

5.4.1 Critical loads

The Southwell method is not precise when used to obtain the critical load for the panel buckling experiments. Material variability could be another contributor to the uncertainty in test results.

The least squares method also gave higher critical load estimates compared to the models. There could be problems with convergence to a correct solution but where it gives a converging solution, the method is preferred to the Southwell method.

The material properties obtained from frequency tests resulted in the highest critical loads. Including modelling details relevant to the out-of-plane boundary condition such as the panel margins could increase the critical load of the model by about 8.5%.

5.4.2 Post-buckling plots of panel displacement

The analytical models for case C have the least discrepancy with the experimental post-buckling plots of panel displacement. The panel imperfections predicted form the Southwell method plots are not reliable as the plots show a large variation. The unadjusted initial panel deflection measurements are the preferred of the two types of imperfection values.

5.4.3 Post-buckling plots of displacement modes

As to be expected, the fundamental displacement mode $A_{1,1}$ is most dominant in the experimental buckling results, based on comparison of displacement mode amplitudes obtained using the collocation method.

5.3.4 Panel imperfection and material properties

The least squares method panel imperfection estimates improved the agreement of post-buckling model results with the experiment for kraft paperboard but worsened the agreement for recycled paperboard at 50%

relative humidity compared to using the unadjusted displacement measurements.

The material properties given to the models have a more significant role on the post-buckling results. The in-plane and flexural material properties from the frequency test for kraft paperboard at 50% relative humidity were scaled by two factors to adjust the critical load and steepness of the post-buckling plot. This improved the analytical frequency test properties model agreement with the experimental plot. This was done only to show that the material properties from frequency tests without scaling are insufficient to accurately model the post-buckling behaviour of the panels. Further work is needed to verify the use of such scaling and in general to investigate the best possible way to determine material properties for the purpose of modelling corrugated paperboard.

5.5 Summary

This chapter compared the experimental buckling and post-buckling results of kraft and recycled paperboard panels to those obtained from the Galerkin and FE models. The research questions were the investigation of what boundary conditions most resemble the panel buckling test boundary conditions and which displacement mode shapes were dominant in the test conditions.

Several cases of in-plane boundary condition cases A and C were modelled using the analytical method, while cases C and D were modelled using an FE software package. The paperboard material models used were the equivalent single layer properties from Chapter 4, for the analytical models and equivalent sinlge layer FE and DSM models, since there was less certainty in the experimental results from that chapter estimating effective material properties. The detailed geometric FE and DSM models referenced used material properties of the constituent paperboard layers. There was also a multi-layered FE model treating the core as one layer with effective properties. For the analytical models,

additional results were also obtained using frequency test material properties for the paperboard materials at 50% relative humidity from Chapter 4. The FE results also consider the effect of including of panel margins in the models to represent the unsupported regions near the panel edges. The Southwell method was used to estimate critical loads and initial geometric imperfections from the experimental data. The panel out-of-plane displacement measurements were fitted into double sine product Fourier series using the collocation method. The least squares fitting of the panel centre displacement data into a post-buckling function to estimate critical load, a post-buckling parameter and initial imperfection was also carried out.

The critical load comparisons were agreeable among analytical models. The frequency test material properties increase the analytical model critical load by 131% to 143%. The critical loads for FE models without the unsupported panel margins are within 1.25% below the analytical value, while the FE models with the panel margins give critical loads about 10% higher than the analytical value. The experimental critical loads predicted by the Southwell method were generally higher than the analytical value by 42% to 93%, with large uncertainties. The least squares estimates of critical load were also higher than the analytical values by 14% and 90% for the kraft and recycled paperboard at 50% relative humidity.

The post-buckling plots of panel displacement show the analytical model results for case C with ‘unadjusted’ panel imperfection were least different to the experimental plots. The analytical models using frequency test material properties had better agreement with the experimental plot for the 50% relative humidity condition for panel centre displacement and $w(0.75\,a, 0.5\,b)$. For all other post-buckling plots, the analytical models of case C with equivalent single layer material properties were the least different to the experimental results.

The experimental out-of-plane displacement measurements yielded only four displacement modes since there were only four locations of

measurement. The most suitable lowest displacement modes were given from the measurements by the collocation method. The fundamental mode $A_{1,1}$ was dominant for the test condition. Modes $A_{3,1}$, $A_{3,2}$, and $A_{3,3}$ were significant for the 50% relative humidity condition and less so for the 90% relative humidity condition. The comparison of analytical model and experimental post-buckling results was agreeable only for the fundamental mode.

In further post-buckling analyses using panel imperfection values estimated by the least squares method instead of the initial displacement measurement, the agreement between model and experimental plots improved for kraft paperboard at 50% relative humidity but worsened for recycled paperboard at 50% relative humidity. The difference in results could be due to the imperfection estimates being less accurate for recycled paperboard.

There is still uncertainty in the accuracy of the effective material models of corrugated paperboard. The frequency test material properties were previously found to be much stiffer than static test properties. The application of frequency test material properties in the analytical post-buckling models overestimate the stiffness of the panel, with high critical load and small displacements.

The frequency test material properties for kraft paperboard at 50% RH were scaled in order to replicate the material behaviour in the buckling test by multiplying the in-plane and flexural properties by two factors. A combination of the factors was found which improved agreement of the critical load and post-buckling plot for the analytical model using scaled frequency test properties with the experimental result. However, further studies are needed to justify the use of such scaling.

Overall, the post-buckling displacement results showed significant discrepancy between experimental values and predicted values. It is thought that the lack of a reliable procedure to obtain material properties,

inaccuracies in the measurements of initial imperfection, and deficiencies in the single layer equivalent orthotropic model are the main causes of these discrepancies.

6 Conclusions and Recommendations

6.1 Conclusions

The work presented was aimed at understanding the buckling and post-buckling behaviour of corrugated paperboard structures. Finding the reasons for the discrepancy between predicted and measured behaviour for paperboard panels in a published paper was one of the initial motivations. The following conclusions were drawn from the study themes of in-plane boundary conditions, multi-term analytical models, effective material properties of corrugated paperboard, and experimental verification of panel buckling behaviour.

6.1.1 In-plane boundary conditions for corrugated paperboard panel

The study of different in-plane boundary conditions and loading on simply supported corrugated paperboard panels, considered their effect on the critical buckling load and on post-buckling plot for analytical and Finite Element (FE) models.

6.1.1.1 Critical loads

There was discrepancy between the critical loads of the analytical and Finite Element models and reference experimental values. The predicted critical loads are very similar among the three in-plane boundary conditions cases considered in the analytical and FE models, as well to the reference analytical value in (Nordstrand, 2004a). The difference in critical load among the two methods is about 1.2%. The comparatively lower experimental reference value by 16.4% to 17.6% showed the critical load discrepancy was not due to in-plane boundary conditions.

Instead, shortcomings in the material models of corrugated paperboard were the likely to be the major cause of the discrepancy in the critical

loads. However, inaccuracies in the modelling of the experimental out-of-plane boundary conditions may have contributed, but to a lesser degree.

6.1.1.2 Post-buckling plots

The difference between the reference experimental plot and the modelled post-buckling plots could be due in part to variation of in-plane boundary conditions, but the material models used for corrugated paperboard have a more significant influence on the results. This was evident in the differences between the analytical and FE post-buckling results.

The three in-plane-boundary condition cases gave post-buckling plots that were consistent with published results for composite plates (Banks et al., 1978). Case B with uniformly compressed loaded edges and straight unloaded edges showed the least panel deflection; Case C, with the assumed experimental boundary conditions corresponding to uniformly compressed loaded edges and in-plane free unloaded edges was less restrained, while Case A with uniform load intensity on loaded edges and in-plane free unloading edges had the largest panel deflection as to be expected due to its lower overall stiffness.

The reference post-buckling plots for case C in (Nordstrand, 2004) show discrepancy, with the experimental plot having larger diplacements than the present analytical plot.

Post-buckling plots for the current analytical models show Case A had closest agreement with the experimental plot, followed by Case C. The analytical plot for Case B showed smaller panel deflections and was more similar to the reference analytical plot.

The FE post-buckling plots had lower deflection compared to the analytical models, but the same order of deflection among the cases, cases A, C, and B varying from largest to smallest deflection.

Among the FE cases, the plot for Case A was closest to the reference experimental plot of (Nordstrand, 2004a), the plot for Case C was similar

to the reference analytical plot of (Nordstrand, 2004a), while Case B had the lowest panel deflections.

However, the discrepancy in the published result is not being attributed to in-plane boundary conditions, as there are other more significant factors.

6.1.2 Multi-term analytical Galerkin's model

The study on multi-term analytical Galerkin's buckling models for simply supported corrugated paperboard panels investigated the influence of higher mode displacement functions and symmetric and / or anti-symmetric imperfection modes on the post-buckling behaviour.

6.1.2.1 Single-term and multi-term displacement modes

A single-term solution is inadequate at loads above the critical load as central deflection values changed by as much as 16% at a load of 1.8 times the critical load for a symmetric displacement mode nine-term case (three modes in each planar direction) compared to a single-term result.

The study showed that generally as more modes are included in the out-of-plane displacement function, particularly in the loading *y*-direction, the greater the difference in panel deflection relative to the single-term result.

For the case with (1, 1) symmetric imperfection of amplitude 0.2 *h*, there was convergence in the centre deflection in including up to the third symmetric term in both planar directions, with a 5.31% increase in centre deflection at a load ratio of 1.8 times the critical load compared to including up to the second symmetric term in both planar directions.

For the case with (1, 2) anti-symmetric imperfection of amplitude 0.2 *h*, there was a 6.71% increase at a load ratio of 1.8, in including four symmetric and anti-symmetric terms compared to three symmetric and anti-symmetric terms in both planar directions.

For the case with (1, 1) symmetric imperfection with an amplitude of 0.2 *h* and (1, 2) anti-symmetric imperfection with an amplitude of 0.1 *h*, there

was a 5.49% increase at a load ratio 1.8, in including five symmetric and anti-symmetric terms compared to four symmetric and anti-symmetric terms in both planar directions.

For the case with (1, 1) symmetric and (1, 2) anti-symmetric imperfection both with an amplitude of 0.2 *h*, there was a 15% increase at a load ratio 1.7, in including five symmetric and anti-symmetric terms compared to four symmetric and anti-symmetric terms in both planar directions.

This difference between single-term and multi-term post-buckling plots appears and increases at loads above a threshold load determined by the initial imperfection value. The smaller the imperfection, the higher the threshold load will be up to the first critical load. However, the effect of initial imperfection as a proportion of total displacement decreases with load and the results for imperfect plates are similar to perfect plates at very high loads.

6.1.2.2 Symmetric and/or anti-symmetric imperfection

The models with symmetric and / or anti-symmetric displacement modes showed if either a symmetric or anti-symmetric panel imperfection was present, only higher modes of the same type as the imperfection contribute to the panel displacement. However, if both symmetric and anti-symmetric panel imperfections were present, the symmetric and anti-symmetric displacement modes influence each other's relative amplitudes noticeably.

Thus, interactions between symmetric and anti-symmetric displacement modes were observed in the presence of both symmetric and anti-symmetric panel imperfections and these may be attributed to changes to the in-plane stress distribution, which in turn affects the overall stiffness of the plate. The relative imperfection magnitudes also determine the dominance of displacement mode types.

The direction of higher imperfection modes relative to the fundamental mode and the magnitude of the fundamental mode affect the apparent

panel stiffness below the critical load, observed as higher or lower out-of-plane panel centre displacements compared to a panel with only a fundamental imperfection mode. A small fundamental imperfection mode with additive higher imperfection modes causes the panel to have lower out-of-plane displacements, while a larger fundamental imperfection mode with opposing higher imperfection modes results in higher out-of-plane displacements.

6.1.3 Effective material properties of corrugated paperboard

In the study on different material testing methods, effective material properties were compared among test methods. The effective material properties from the tests were also compared to those obtained from equivalent analytical and FE models with equivalent single-layered or detailed geometry.

6.1.3.1 Materials testing methods

For the four-point bending test, the MD elastic modulus E^*_{11} is 2.5 to 3.9 times higher than the CD elastic modulus E^*_{22}, the difference being more for recycled than kraft material and for 90% relative humidity than 50% relative humidity. The sonic vibration tests gave more similar relative values of the planar direction elastic moduli, E^*_{22} is 26% and 1.25% higher than E^*_{11} for kraft and recycled materials respectively at 50% relative humidity.

Between test methods, the four-point bending test gave MD elastic modulus E^*_{11} values that were 41% and 17.5% higher than the sonic vibration test for kraft and recycled paperboard respectively at the room temperature condition. The sonic vibration test gives the highest CD elastic modulus E^*_{22} for kraft and recycled paperboard at the room temperature condition, followed by the results for edge compression and the four-point bending tests. The CD elastic modulus E^*_{22} of the edge

compression and sonic vibration tests are between 51% to 2.7 times higher than the four-point bending test E^*_{22} values.

Difference in loading rates could account for some of the variation in results among the test methods. Also, the theoretical relations between flexural stiffnesses and elastic moduli for homogenous orthotropic plate sections used to obtain elastic moduli results from flexural stiffnesses may not be suitable for corrugated paperboard being treated as an equivalent orthotropic single layer plate. Both bending and membrane action contribute to post-buckling behaviour and an equivalent single layer plate model may be unable to represent both these correctly. The four-point bending and sonic vibration methods can still be used for obtaining flexural stiffness and Poisson's ratio properties, and edge compression for finding the CD elastic modulus E^*_{22}.

6.1.3.2 Equivalent properties based on analytical models and materials testing

Between the equivalent single-layered analytical and FE material models, the elastic moduli of the equivalent FE models were 2 to 2.9 times higher than the equivalent analytical models. The E^*_{11} value is higher than E^*_{22} by 47% to 93% in the equivalent analytical model, and 2.1 to 2.7 times higher in the equivalent FE model.

The comparisons of the elastic moduli of the equivalent calculated analytical model to those measured from materials testing showed the measured results were generally higher than the equivalent calculated analytical results. Comparing materials tests with equivalent analytical models, the four-point bending test gave E^*_{11} values 51% to 2 times higher and E^*_{22} values between 54% lower to 20% higher than the equivalent analytical model. The edge compression tests E^*_{22} were 74% to 2.4 times higher than the equivalent analytical model. The sonic vibration test gave E^*_{11} values 45% to 48% higher and E^*_{22} values 2.7 to 2.9 times higher compared to the equivalent analytical model.

It is difficult to justify the equivalent analytical material model as sufficient for modelling corrugated paperboard, as there is only moderate agreement in elastic moduli with some of the four-point bending and sonic vibration tests results. Alternative methods are needed to verify the material properties of the equivalent analytical model.

6.1.3.3 Materials testing, and equivalent and detailed geometry Finite Element models

In the FE models of materials tests, the equivalent FE models gave a larger ratio between the MD and CD elastic moduli compared to the detailed FE models. The equivalent FE models gave E^*_{11} values that were 2 to 3.8 times higher than E^*_{22}, while the detailed FE models E^*_{11} values were between 10% lower to 42% higher than E^*_{22}.

There is better agreement between the equivalent FE models and detailed FE model types for the CD elastic modulus E^*_{22}. The E^*_{11} of the equivalent FE models are between 10% lower to 3.2 times higher and E^*_{22} between 15% lower to 44% higher compared to the detailed FE models.

Comparison with experimental results suggest that the equivalent FE models are less suitable than the FE models based on the detailed geometry of corrugation for modelling corrugated paperboard.

The equivalent FE material testing models gave generally higher elastic moduli than the experimental values except for the free vibration model which were a combination of higher MD and lower CD elastic moduli relative to experimental values. The equivalent FE material testing models gave E^*_{11} values 64% to 99% higher and E^*_{22} values 34% to 2.5 times higher than the experiment for four-point bending, E^*_{22} values 4.5 to 4.6 times higher for edge compression, and E^*_{11} and E^*_{22} values that were 70% to 82% higher and 39% to 59% lower respectively for free-vibration.

The detailed FE material testing models gave higher CD elastic moduli for edge compression, lower elastic modulus for free vibration and a

combination of higher and lower elastic moduli in four-point bending relative to the experimental values. The detailed FE material testing models gave E^*_{11} values 68% lower to 84% higher and E^*_{22} values 5% to 2.2 times higher than the experiment for four-point bending, E^*_{22} values 2.2 to 3.1 times higher for edge compression, and E^*_{11} and E^*_{22} values that were 70% to 76% and 2 to 2.25 times lower respectively for free-vibration.

6.1.4 Predicted and measured results for corrugated paperboard panel

In the study with experiments for corrugated paperboard panel buckling, equivalent analytical and FE models with different boundary conditions were compared to experimental buckling and post-buckling results.

6.1.4.1 Critical loads

Determining the critical load through experiments proved to be very challenging, as there is always some imperfection and the change in deflection is rather gradual. Southwell plot method was employed to determine the experimental critical load, but unlike its success with beams, it is difficult to determine the critical loads in panel buckling tests, due to the lack of straightness of the plot as evident in the large uncertainties in the experimental critical load estimates. The experimental critical loads predicted by the Southwell method were generally higher than the analytical value by 42% to 93%, with large uncertainties.

The least squares method also gave higher critical load estimates compared to the models. There could be problems with convergence to a correct solution but the method is preferred over the Southwell method when a correctly converged solution is obtained. In the case of paperboard plates, material variability could be another contributor to the high degree of uncertainty in the results.

The critical loads were in agreement among analytical models and with the reference exact strip method (DSM) values. The frequency test material properties caused a significant increase in the analytical model critical load in the range of 131% to 143%.

The FE models show that the variation in critical load due to not accounting for modelling details relevant to the out-of-plane boundary condition, such as the unsupported regions near the panel edges, may be significant. The critical loads for equivalent single-layered FE models without the unsupported panel margins are within 1.25% below the analytical value, while the FE models with the panel margins give critical loads about 9.7% higher than the analytical value.

6.1.4.2 Post-buckling plots of panel displacement

It was found that the analytical models for Case C had the least discrepancy with the experimental post-buckling plots of panel centre out-of-plane displacement. As mentioned earlier, the presence of geometric imperfection makes it difficult to generate analytical or numerical results to compare with experimental plots. As stated earlier, initial imperfections predicted from the Southwell method plots were not reliable due to the uncertainties and lack of straightness of the plot. The unadjusted initial panel deflection measurements were the preferred of the two types of imperfection values.

The analytical models using material properties based on frequency test measurements had improved agreement with the experimental plot for the 50% relative humidity condition for panel centre displacement and $w(0.75\,a, 0.5\,b)$. For all other post-buckling plots, the analytical models of Case C with theoretical material properties had least discrepancy with the experimental results.

6.1.4.3 Post-buckling plots of displacement modes

The fundamental displacement mode $A_{1,1}$ was found to be most dominant in the experimental buckling results, based on comparison of displacement

mode amplitudes obtained using the collocation method. The experimental out-of-plane displacement measurements yielded four non-zero displacement modes since there were only four locations of measurement.

Modes $A_{3,1}$, $A_{3,2}$, and $A_{3,3}$ were also significant for the 50% relative humidity condition but less so for the 90% relative humidity condition experimental results. The comparison of analytical model and experimental post-buckling results showed agreement only for the fundamental mode.

6.1.4.4 Panel imperfection and material properties

Panel imperfection estimates were also obtained by the least squares method, which improved the agreement of post-buckling model results with the experiment for kraft paperboard but worsened the agreement for recycled paperboard at 50% relative humidity, compared to using the unadjusted displacement measurements.

Since the material properties given to models have a significant role in their post-buckling results, the in-plane and flexural material properties from the frequency test for kraft paperboard at 50% relative humidity were scaled by two factors to show their effect on the critical load and steepness of the post-buckling plot. The material properties from frequency tests without scaling are insufficient to accurately model the post-buckling behaviour of the panels and agreement with the experimental results could be improved by scaling the frequency test material properties.

It should be emphasises that the scaling was only done to investigate and demonstrate the shortcoming of the use of the properties based on frequency tests for post-buckling predictions. Further work is needed to justify the use of such scaling and establish their values, from frequency tests and post-buckling tests on various sample geometry, for a given corrugated paperboard material at a specific temperature and humidity condition. Also, there could be more investigations on how best to

determine material properties for the purpose of modelling corrugated paperboard.

6.2 Recommendations

The findings of this study show further work in the areas of determination of material properties and development of a simplified mathematical model of a corrugated paperboard is needed to gain a better understanding of the post buckling behaviour of paperboard structures. The basic problems of post-buckling at the 50% relative humidity condition associated with the material modelling of corrugated paperboard need to be resolved before considering more complex problems of high or changing relative humidity and creep.

6.2.1 Buckling and post-buckling models

Further work could be done in the analytical models by employing improved corrugated paperboard material homogenisation models or material models with detailed geometry such as in (Biancolini, 2005).

There are prospects in the use of other analytical methods such as the exact strip method for buckling and post-buckling models of corrugated paperboard. The work could be extended to models of boxes and used in conjunction with FE methods where non-prismatic regions such as box hole details.

The Finite Element (FE) buckling models presented used equivalent orthotropic plate and detailed geometry models of corrugated paperboard. The post-buckling models used only equivalent orthotropic plate models of the material, since the computational cost for detailed geometry FE models would be high. It is recommended that future work modelling corrugated paperboard post-buckling be done using material models with detailed geometry or homogenisation models such as those in the analytical models.

The material behaviour used in the analytical and FE models was elastic and for constant humidity. Corrugated paperboard packaging is likely to encounter changes in humidity in use. Paper materials also exhibit creep and viscoelastic behaviour.

Future buckling and post-buckling models of corrugated paperboard should allow the material properties to change with humidity and factor time in the loading application. Non-linear elastic and plastic stress vs. strain behaviour could be used in the future work. The effect of including transverse shear deformation in the models may also need to be investigated as in (Nordstrand, 2004b). Failure models could also be incorporated.

The problem would need to be solved as a dynamic analysis. This would allow creep and cyclic loading behaviour associated with long-term buckling failure in corrugated paperboard packaging to be studied.

6.2.2 Materials Testing

There could be further study on the effective properties of corrugated paperboard from testing methods. This could include the impact of loading rate on results from different test methods and using viscoelastic behaviour in models of the tests to account for the difference between static and dynamic test material properties.

The sonic vibration test could be useful if the material properties could be scaled such that they were appropriate for the buckling problem which may be in static loading. Whether such constant scaling factors can be utilised to predict the post-buckling behaviour of corrugated panels needs careful studies involving large number of samples of different size. The variations in the directions of the bending vibration mode among kraft and recycled corrugated paperboard may also pose opportunities for future research into the relative importance of the constituent layer properties and overall structural geometric stiffness in determining the vibration characteristics of corrugated paperboard.

6.2.3 Buckling Tests

The work on buckling tests presented involved panels, which could be considered as a side wall of a box. However, there are differences in the boundary conditions specified for the panel test and those of boxes due to the stiffness provided by the box corners. Further work could be added to the panel buckling models by addition of rotational springs, effectively changing the simply supported boundary condition. The work could investigate the box boundary conditions by comparison of box compression tests with panel model post-buckling results.

For future buckling tests, it is recommended that more locations of displacement measurement be included to gain a broader picture of the deflection response and initial imperfection. The estimation of the critical load in the panel buckling test presented could be improved by using function fitting methods such as non-linear regression analysis.

Other methods such as the Digital Image Stereocorrelation technique have been used to obtain three-dimensional displacement and strain fields in the outer facing of corrugated paperboard boxes in compression tests (Viguié et al., 2011). Employing this or similar techniques may be useful, if detailed stress analysis need to be carried out on the post-buckled boards.

6.2.4 Packaging design

As a part of this study, some preliminary work was done, though not presented in the thesis, on modelling open empty corrugated paperboard box structures with and without handholds in FE software, using the equivalent orthotropic plate material model. Stress results with the application of static loads were obtained from the model. There was a difference between the stress results of the model and experiments using lock-in infrared thermography by (Navaranjan & Jones, 2010), that could be due to the overly simplified material model of corrugated paperboard.

This work could be further extended by use of a more reliable material model of corrugated paperboard. Also, further investigation into methods

of analysing box structures using methods such as the exact strip method may be useful in the design of packaging.

The information about stress distribution would be used to study failure mechanisms in the packaging which may initiate at design features such as holes. There would be possibility of studying how the packaging performance is altered when the box has contents. These would be useful for improving and optimising packaging design.

6.3 Summary

The overall conclusions and recommendations from the study were presented in this chapter. The shortcomings of the corrugated paperboard material models, rather than difference in-plane boundary conditions, likely caused discrepancy between modelled and reference experimental critical loads and post-buckling behaviour from (Nordstrand, 2004a). Further work in using alternative homogenisation or detailed geometric material models for corrugated paperboard in the buckling and post-buckling models was recommended. Material models that account for changes in humidity, viscoelastic and elastic-plastic behaviour and transverse shear deformation could be considered in future work.

The difference between analytical single-term and multi-term post-buckling plots appears and increases at loads above a threshold load determined by the initial imperfection value. The difference increases as more displacement modes are included particularly in the loading direction. The central deflection values changed by as much as 16% at a load of 1.8 times the critical load for a symmetric displacement mode nine-term case compared to a single-term result. A single term solution is therefore not adequate for post-buckling analysis.

For panels with both symmetric and anti-symmetric panel imperfections present, interactions between symmetric and anti-symmetric displacement modes were observed and attributed to changes to the in-plane stress distribution. The relative imperfection magnitudes determine the

dominance of displacement mode types. The direction of higher imperfection modes relative to the fundamental mode and the magnitude of the fundamental mode affect the apparent panel stiffness below the critical load.

Variation in effective material properties of corrugated paperboard determined through different testing methods may be due to different loading rates. Homogenous orthotropic plate theory used to obtain elastic moduli from flexural stiffnesses may not suit corrugated paperboard because of its distinctive bending and in-plane membrane behaviour, both of which contribute to post-buckling behaviour. The equivalent analytical material model for corrugated paperboard could not be verified as there is only moderate agreement in elastic moduli with some of the four-point bending and sonic vibration tests results. The FE models of materials tests suggest that the equivalent FE models are less suitable than the detailed geometric FE models based for modelling corrugated paperboard.

There was difficulty in applying the Southwell method to the panel buckling test for finding critical load, due to the lack of straightness of the Southwell plot. The least squares method also gave high critical load estimates compared to the models but is preferred over the Southwell method when a correctly converged solution is obtained. Material variability could be another contributor to the test result uncertainty.

The frequency test material properties significantly reduced panel deflection and increased the critical load prediction of the analytical model compared to those generated from material properties derived from other methods. Including modelling details relevant to the boundary condition such as the panel margins could influence the model critical load. Further work could be done to relate boundary conditions specified for the panel test and those of box structures.

The analytical models for boundary condition Case C had least discrepancy with the experimental post-buckling panel displacements. The

unadjusted initial panel deflection measurements were preferred over Southwell method imperfection predictions. Panel imperfection estimates were also obtained by the least squares method which improved the agreement of post-buckling model results with the experiment for kraft paperboard at 50% relative humidity, compared to using the unadjusted displacement measurements.

The fundamental displacement mode $A_{1,1}$ is most dominant in the experimental buckling results, based on displacement mode amplitudes obtained using the collocation method. In future buckling tests, it is recommended that more locations of displacement measurement be included or three-dimensional displacement and strain fields imaging techniques be used to gain a broader picture of the deflection response and initial imperfection.

The material properties from frequency tests without some form of calibration are insufficient to accurately model the post-buckling behaviour of the panels and agreement with the experimental results could be improved by scaling the frequency test material properties. Further work is needed to justify such scaling and how best to determine material properties for modelling corrugated paperboard.

References

Abbès, B., & Guo, Y. Q. (2010). Analytic homogenization for torsion of orthotropic sandwich plates: Application to corrugated cardboard. *Composite Structures, 92*(3), 699-706.

Aboura, Z., Talbi, N., Allaoui, S., & Benzeggagh, M. L. (2004). Elastic behavior of corrugated cardboard: Experiments and modeling. *Composite Structures, 63*(1), 53-62.

Allansson, A., & Svärd, B. (2001). *Stability and collapse of corrugated board; numerical and experimental analysis.* Lund University, Lund.

Allaoui, S., Aboura, Z., & Benzeggagh, M. L. (2009). Effects of the environmental conditions on the mechanical behaviour of the corrugated cardboard. *Composites Science and Technology, 69*(1), 104-110.

Armentani, E., Caputo, F., & Esposito, R. (2006). *Fe analyses of stability of single and double corrugated boards.* Paper presented at the ICAD2006 4th International Conference on Axiomatic Design, Firenze, Italy.

Åslund, P., & Isaksson, P. (2010, May 16-21, 2010). *Analysis of in-plane fibre buckling influence on macroscopic stiffness of paper.* Paper presented at the ECCM 2010 IV European Conference on Computational Mechanics, Palais des Congrès, Paris, France.

Assaee, H., & Ovesy, H. R. (2007). A multi-term semi-energy finite strip method for post-buckling analysis of composite plates. *International Journal for Numerical Methods in Engineering, 70*(11), 1303-1323.

Banks, W. M., Harvey, J. M., & Rhodes, J. (1978). Non-linear behaviour of composite panels with alternative membrane boundary conditions on the unloaded edges. *Proceedings of the Annual Meeting and Technical Conference - Numerical Control Society*, 316-336.

Bassily, S. F., & Dickinson, S. M. (1977). The plane stress problem for rectangular regions treated using functions related to beam flexure. *International Journal of Mechanical Sciences, 19*(11), 639-650.

Baum, G. A., Brennan, D. C., & Habeger, C. C. (1981). Orthotropic elastic constants of paper. *Tappi, 64*(8), 97-101.

Beldie, L., Sandberg, G., & Sandberg, L. (2001). Paperboard packages exposed to static loads-finite element modelling and experiments. *Packaging Technology and Science, 14*(4), 171-178.

Bennett, K. A. (1977). Elastic stability of corrugated fiberboard containers. 177-186.

Bernad, C., Laspalas, A., González, D., Liarte, E., & Jiménez, M. A. (2010). Dynamic study of stacked packaging units by operational modal analysis. *Packaging Technology and Science, 23*(3), 121-133.

Biancolini, M. E. (2005). Evaluation of equivalent stiffness properties of corrugated board. *Composite Structures, 69*(3), 322-328.

Biancolini, M. E., & Brutti, C. (2003). Numerical and experimental investigation of the strength of corrugated board packages. *Packaging Technology and Science, 16*(2), 47-60.

Biancolini, M. E., Brutti, C., Mottola, E., & Porziani, S. (2005). *Numerical evaluation of buckling and post-buckling behaviour of corrugated board containers*. Paper presented at the XXXIV Convegno Nazionale Associazione Italiana per l'Analisi delle Sollecitazioni.

Biancolini, M. E., Brutti, C., & Porziani, S. (2009a). Analysis of corrugated board panels under compression load. *Steel and Composite Structures, 9*(1), 1-17.

Biancolini, M. E., Brutti, C., & Porziani, S. (2009b). *Experimental characterisation of paper for corrugated board*.

Biancolini, M. E., Brutti, C., & Porziani, S. (2010). Corrugated board containers design methods. *International Journal of Computational Materials Science and Surface Engineering, 3*(2-3), 143-163.

Blevins, R. D. (1979). *Formulas for natural frequency and mode shape.* Malabar, FL: Krieger Publishing Company.

Bronkhorst, C. A., & Riedemann, J. R. (1994, December 5-7, 1994). *The creep deformation behavior of corrugated containers in a cyclic moisture environment.* Paper presented at the Symposium on Moisture Induced Creep Behavior of Paper and Board, Stockholm, Sweden.

Buannic, N., Cartraud, P., & Quesnel, T. (2003). Homogenization of corrugated core sandwich panels. *Composite Structures, 59*(3), 299-312.

Carlsson, L. A., Nordstrand, T., & Westerlind, B. (2001). On the elastic stiffnesses of corrugated core sandwich. *Journal of Sandwich Structures and Materials, 3*(4), 253-267.

Chalmers, I. Vca 1000 vaccum compression apparatus. In P. G. P. N. P. a. P. D. o. FRI (Ed.).

Daxner, T., Flatscher, T., & Rammerstorfer, F. G. (2007, 21 May - 25 May 2007,). *Optimum design of corrugated board under buckling constraints.* Paper presented at the 7th World Congress on Structural and Multidisciplinary Optimization COEX Seoul, Korea.

Daxner, T., Pahr, D. H., & Rammerstorfer, F. G. (2008). Micro- and meso-instabilities in structured materials and sandwich structures. In B. G. Falzon & F. M. H. Aliabadi (Eds.), *Buckling and postbuckling structures: Experimental, analytical and numerical studies* (Vol. 1, pp. 453-495). London: Imperial College Press.

Fellers, C., & Carlsson, L. (2002). Bending stiffness. In R. E. Mark, C. C. Habeger Jr, J. Borch & M. B. Lyne (Eds.), *Handbook of physical testing of paper* (Second ed., Vol. 1, pp. 234-256). New York: Marcel Dekker Inc.

Flatscher, T., Daxner, T., Pahr, D. H., & Rammerstorfer, F. G. (2011). Optimization of corrugated paperboard under local and global buckling constraints. In E. Ramm & R. de Borst (Eds.), *Multiscale methods in computational mechanics* (Vol. 55, pp. 329-346): Springer Science+Business Media B.V.

Fok, W.-C. (1984). Evaluation of experimental data of plate buckling. *Journal of Engineering Mechanics, 110*(4), 577-588.

Gilchrist, A. C., Suhling, J. C., & Urbanik, T. J. (1999). Nonlinear finite element modeling of corrugated board. *American Society of Mechanical Engineers, Applied Mechanics Division, AMD, 231*, 101-106.

Hahn, E. K., Carlsson, L. A., & Westerlind, B. S. (1992). Edge-compression fixture for buckling studies of corrugated board panels. *Experimental Mechanics, 32*(3), 252-258.

Hahn, E. K., de Ruvo, A., Westerlind, B. S., & Carlsson, L. A. (1992). Compressive strength of edge-loaded corrugated board panels. *Experimental Mechanics, 32*(3), 259-265.

Haj-Ali, R., Choi, J., Wei, B.-S., Popil, R., & Schaepe, M. (2009). Refined nonlinear finite element models for corrugated fiberboards. *Composite Structures, 87*(4), 321-333.

Han, J., & Park, J. M. (2007). Finite element analysis of vent/hand hole designs for corrugated fibreboard boxes. *Packaging Technology and Science, 20*(1), 39-47.

Hohe, J., & Becker, W. (2002). Effective stress-strain relations for two-dimensional cellular sandwich cores: Homogenization, material models, and properties. *Applied Mechanics Reviews, 55*(1), 61-87.

Hui, D. (1984). Effects of mode interaction on collapse of short, imperfect, thin-walled columns. *Transactions of the ASME. Journal of Applied Mechanics, 51*(3), 566-573.

Hui, D. (1986). Design of beneficial geometric imperfections for elastic collapse of thin-walled box columns. *International Journal of Mechanical Sciences, 28*(3), 163-172.

Hui, D., & Leissa, A. W. (1983). Effects of geometric imperfections on vibrations of biaxially compressed rectangular flat plates. *Transactions of the ASME. Journal of Applied Mechanics, 50*(4A), 750-756.

Ilanko, S. (2002). Vibration and post-buckling of in-plane loaded rectangular plates using a multiterm galerkin's method. *Journal of Applied Mechanics, Transactions ASME, 69*(5), 589-592.

Ilanko, S., & Dickinson, S. M. (1991). On natural frequencies of geometrically imperfect, simple-supported rectangular-plates under uniaxial compressive loading. *Journal of Applied Mechanics, Transactions ASME, 58*(4), 1082-1086.

Ilmonen, K. (2007). *Measuring and modelling of corrugated board creep behaviour.* Helsinki University of Technology, Espoo.

Isaksson, P., Krusper, A., & Gradin, P. A. (2007). Shear correction factors for corrugated core structures. *Composite Structures, 80*(1), 123-130.

Jiménez-Caballero, M. A., Conde, I., García, B., & Liarte, E. (2009). *Design of different types of corrugated board packages using finite element tools*. Paper presented at the 2009 SIMULIA Customer Conference.

Johnson, M. W., Jr., & Urbanik, T. J. (1984). Nonlinear theory for elastic plates with application to characterizing paper properties. *Journal of Applied Mechanics, Transactions ASME, 51*(1), 146-152.

Johnson, M. W., Jr., & Urbanik, T. J. (1989). Analysis of the localized buckling in composite plate structures with application to determining the strength of corrugated fiberboard. *Journal of Composites Technology & Research, 11*(4), 121-128.

Johnson, M. W. j., & Urbanik, T. J. (1987). Buckling of axially loaded, long rectangular paperboard plates. *Wood and Fiber Science, 19*(2), 135-146.

Jones, R. M. (1975). *Mechanics of composite materials* (International Student ed.). Washington, D.C.: Scripta Book Company.

Kennedy, D., Fischer, M., & Featherston, C. A. (2007). Recent developments in exact strip analysis and optimum design of aerospace structures. *Proceedings of the Institution of Mechanical Engineers, Part C: Journal of Mechanical Engineering Science, 221*(4), 399-413.

Koning, J. W., Jr. (1986). New rapid method for determining edgewise compressive strength of corrugated fiberboard. *Tappi Journal, 69*(1), 74-76.

Lu, T. J., Chen, C., & Zhu, G. (2001). Compressive behaviour of corrugated board panels. *Journal of Composite Materials, 35*(23), 2098-2126.

Lu, T. J., & Zhu, G. (2001). The elastic constants of corrugated board panels. *Journal of Composite Materials, 35*(20), 1868-1887.

Luo, S., Suhling, J. C., Considine, J. M., & Laufenberg, T. L. (1992). The bending stiffnesses of corrugated board. *Mechanics of Cellulosic Materials, AMD-Vol. 145 / MD-Vol. 36*.

Mandal, P., & Calladine, C. R. (2002). Lateral-torsional buckling of beams and the southwell plot. *International Journal of Mechanical Sciences, 44*(12), 2557-2571.

Mann, R. W., Baum, G. A., & Habeger, C. C. (1980). Determination of all nine orthotropic elastic constants for machine-made paper. *Tappi 63*(2), 163-166.

Marguerre, K. (1937). *The apparent width of the plate in compression* (NACA Technical Memorandum No. NACA-TM-833). Washington: NATIONAL ADVISORY COMMITTEE FOR AERONAUTICS

Marguerre, K. (1947). *On the application of the energy method to stability problems*

(NACA Technical Memorandum (TM) No. NACA-TM-1138). Washington: NATIONAL ADVISORY COMMITTEE FOR AERONAUTICS. (DVL Document Number|)

Mark, R. E., Borch, J., & Habeger, C. (2001). *Handbook of physical testing of paper*: Marcel Dekker.

Markstrom, H. (2005). *Testing methods and instruments for corrugated board*. KISTA, Sweden: AB Lorentzen & Wettre.

McIntyre, M. E., & Woodhouse, J. (1988). On measuring the elastic and damping constants of orthotropic sheet materials. *Acta Metallurgica, 36*(6), 1397-1416.

McKee, R. C., Gander, J. W., & Wachuta, J. R. (1963). Compression strength formula for corrugated boxes. *Paperboard Packaging, 43*(3), 149-159.

Navaranjan, N., Dickson, A., Paltakari, J., & Ilmonen, K. (2012). Humidity effect on compressive deformation and failure of recycled and virgin layered corrugated paperboard structures. *Composites Part B: Engineering, In Press*.

Navaranjan, N., & Johnson, B. (2006). *Modelling and experimental study of creep behaviour of corrugated paperboard*. Paper presented at the Appita Annual Conference.

Navaranjan, N., & Jones, R. (2010). Lock-in infrared thermography for the evaluation of the structural performance of corrugated paperboard structures. *Composite Structures, 92*(10), 2525-2531.

Navaranjan, N., Paltakari, J., & Ilmonen, K. (2008). *Measuring, modelling and microscopic analsis of hygroscopic viscoelastic behaviour of virgin and recycled fibre paperboard*. Paper presented at the Progress in Paper Physics Seminar 2008.

Nordstrand, T. (1995). Parametric study of the post-buckling strength of structural core sandwich panels. *Composite Structures, 30*(4), 441-451.

Nordstrand, T. (2004a). Analysis and testing of corrugated board panels into the post-buckling regime. *Composite Structures, 63*(2), 189-199.

Nordstrand, T. (2004b). On buckling loads for edge-loaded orthotropic plates including transverse shear. *Composite Structures, 65*(1), 1-6.

Nordstrand, T., Blackenfeldt, M., & Renman, M. (2003). *A strength prediction method for corrugated board containers*. Lund, Sweden: Lund University

Nordstrand, T., & Carlsson, L. A. (1997). Evaluation of transverse shear stiffness of structural core sandwich plates. *Composite Structures, 37*(2), 145-153.

Nordstrand, T., Carlsson, L. A., & Allen, H. G. (1994). Transverse shear stiffness of structural core sandwich. *Composite Structures, 27*(3), 317-329.

Nyman, U., & Gustafsson, P. J. (1999). *Local buckling of corrugated board facings*. Paper presented at the European Conference on Computational Mechanics.

Nyman, U., & Gustafsson, P. J. (2000a). Buckling of long orthotropic plates including higher-order transverse shear. *Journal of Engineering Mechanics, 126*(12), 1209-1215.

Nyman, U., & Gustafsson, P. J. (2000b). Material and structural failure criterion of corrugated board facings. *Composite Structures, 50*(1), 79-83.

Paetow, R., & Göttsching, L. (1990). Poisson's ratio of paper. *Das Papier, 6*, 229-237.

Pahr, D. H., & Rammerstorfer, F. G. (2006). Buckling of honeycomb sandwiches: Periodic finite element considerations. *Cmes-Computer Modeling in Engineering & Sciences, 12*(3), 229-241.

Patel, P., Nordstrand, T., & Carlsson, L. A. (1997a). Instability and failure of corrugated core sandwich cylinders under combined stress. *SAE Special Publications*(1280), 264-289.

Patel, P., Nordstrand, T., & Carlsson, L. A. (1997b). Local buckling and collapse of corrugated board under biaxial stress. *Composite Structures, 39*(1-2), 93-110.

Persson, K. (1991). *Material model for paper: Experimental and theoretical aspects* (Diploma Report). Lund, Sweden: Lund University

Peterson, W. S. (1980). Minimum-cost design for corrugated containers under top-to-bottom compression. *Tappi, 63*(2), 143-146.

Peterson, W. S. (1983). Flute/liner interaction for bending of combined board beams. *Paperboard Packaging, 68*(8), 37-41.

Peterson, W. S., & Schimmelpfenning, W. J. (1982). *Panel edge boundary conditions and compressive strengths of tubes and boxes*.

Pommier, J. C., & Poustis, J. (1989). *Box stacking strength prediction: Today mckee, tomorrow?* Paper presented at the American Society of Mechanical Engineers, Applied Mechanics Division, AMD, San Diego, CA, USA.

Pommier, J. C., & Poustis, J. (1990). Bending stiffness of corrugated board prediction using the finite element method. *Mechanics of Wood and Paper Materials, 112*, 67-70.

Pommier, J. C., Poustis, J., Fourcade, E., & Morlier, P. (1991). *Determination of the critical load of a corrugated box subjected to vertical compression by finite element methods* Paper presented at the International Paper Physics Conference, Kona, HI.

Popil, R. E., Schaepe, M. K., Haj-Ali, R., Wei, B. S., & Choi, J. (2006). *Adhesive level effect on corrugated board strength–experiment and fe modeling.* Paper presented at the 2007 International Progress in Paper Physics Seminar

Rahman, A. A., & Abubakr, S. (2004). A finite element investigation of the role of adhesive in the buckling failure of corrugated fiberboard. *Wood and Fiber Science, 36*(2), 260-268.

Rahman, A. A., Urbanik, T. J., & Mahamid, M. (2002, September 8-13). *Moisture diffusion through a corrugated fiberboard under compressive loading : Its deformation and stiffness response.* Paper presented at the 2002 Progress in Paper Physics Seminar, Syracuse, NY.

Rahman, A. A., Urbanik, T. J., & Mahamid, M. (2003). *Response of corrugated fiberboard to moisture flow: A 3d finite element transient nonlinear analysis*, Montreal, Que., Canada.

Rhodes, J., & Harvey, J. M. (1975). Local instability of thin-walled sections under combined compression and bending. *American Society of Mechanical Engineers (Paper)*, 51-84.

Rhodes, J., & Harvey, J. M. (1977). Examination of plate post-buckling behaviour. *103*(3), 461-478.

Rhodes, J., Harvey, J. M., & Fok, W. C. (1975). The load-carrying capacity of initially imperfect eccentrically loaded plates. *International Journal of Mechanical Sciences, 17*(3), 161-175.

Sandstrom, J., & Titus, M. (1995). Field experience in prediction of corrugated board strength with ultrasonic testing. *Tappi Journal, 78*(10), 240-219.

Sato, J., Hutchings, I. M., & Woodhouse, J. (2008). Determination of the dynamic elastic properties of paper and paperboard from the low-frequency vibration modes of rectangular plates. *Appita Journal, 61*(4), 291-296.

Schaepe, M. (2000). *The influence of pin adhesion strength on edge crush and box compression strength*. Altanta, Georgia: Institute of Paper Science and Technology. (I. o. P. S. a. Technology Document Number|)

SIMULIA. (2009a). Defining a concentrated force. In *Abaqus/cae user's manual*. Providence, RI, USA: Dassault Systèmes.

SIMULIA. (2009b). Defining a displacement/rotation boundary condition. In *Abaqus/cae user's manual*. Providence, RI, USA: Dassault Systèmes.

SIMULIA. (2009c). Defining a shell edge load. In *Abaqus/cae user's manual*. Providence, RI, USA: Dassault Systèmes.

SIMULIA. (2009d). Defining coupling constraints. In *Abaqus/cae user's manual*. Providence, RI, USA: Dassault Systèmes.

SIMULIA. (2009e). Defining elasticity. In *Abaqus/cae user's manual.* Providence, RI, USA: Dassault Systèmes.

SIMULIA. (2009f). Defining orthotropic elasticity in plane stress. In *Abaqus analysis user's manual*. Providence, RI, USA.: Dassault Systèmes.

SIMULIA. (2009g). Defining stress-based failure measures for an elastic model. In *Abaqus/cae user's manual*. Providence, RI, USA: Dassault Systèmes.

SIMULIA. (2009h). Eigenvalue buckling prediction. In *Abaqus analysis user's manual*. Providence, RI, USA: Dassault Systèmes.

SIMULIA. (2009i). Introducing a geometric imperfection into a model. In *Abaqus analysis user's manual*. Providence, RI, USA: Dassault Systèmes.

SIMULIA. (2009j). Plane stress orthotropic failure measures. In *Abaqus analysis user's manual*. Providence, RI, USA: Dassault Systèmes.

SIMULIA. (2009k). Static stress analysis. In *Abaqus analysis user's manual*. Providence, RI, USA: Dassault Systèmes.

SIMULIA. (2009l). Three-dimensional conventional shell element library. In *Abaqus analysis user's manual*. Providence, RI, USA: Dassault Systèmes.

SIMULIA. (2009m). Unstable collapse and postbuckling analysis. In *Abaqus analysis user's manual*. Providence, RI, USA: Dassault Systèmes.

Southwell, R. V. (1932). On the analysis of experimental observations in problems of elastic stability. *Proceedings of the Royal Society of London. Series A, Containing Papers of a Mathematical and Physical Character, 135*(828), 601-616.

Spencer, H. H., & Walker, A. C. (1975). Critique of southwell plots with proposals for alternative methods [in elastic analysis of thin-walled structural elements]. *Experimental Mechanics, 15*(8), 303-310.

Steadman, R. (2002). Corrugated board. In R. E. Mark, C. C. Habeger Jr, J. Borch & M. B. Lyne (Eds.), *Handbook of physical testing of paper* (Second ed., Vol. 1). New York: Marcel Dekker Inc.

Talbi, N., Batti, A., Ayad, R., & Guo, Y. Q. (2009). An analytical homogenization model for finite element modelling of corrugated cardboard. *Composite Structures, 88*(2), 280-289.

TAPPI. (2000). Flexural stiffness of corrugated board t 820.

TAPPI. (2002). Edgewise compressive strength of corrugated fiberboard (short column test) t 811.

Tsai, S. W., & Wu, E. M. (1971). A general theory of strength for anisotropic materials. *Journal of Composite Materials, 5*(1), 58-80.

Urbanik, T. J. (1982). Method analyzes analogue plots of paperboard stress-strain data. *Tappi Journal, 65*(4), 104-133.

Urbanik, T. J. (1996a). Machine direction strength theory of corrugated fiberboard. *Journal of Composites Technology & Research, 18*(2), 80-88.

Urbanik, T. J. (1996b). *Review of buckling mode and geometry effects on postbuckling strength of corrugated containers*, Atlanta, GA, USA.

Urbanik, T. J. (2001). Effect of corrugated flute shape on fibreboard edgewise crush strength and bending stiffness. *Journal of Pulp and Paper Science, 27*(10), 330-335.

Urbanik, T. J., & Frank, B. (2006). Box compression analysis of world-wide data spanning 46 years. *Wood and Fiber Science, 38*(3), 399-416.

Urbanik, T. J., & Saliklis, E. P. (2002, 2002 September 8-13). *Comparison of postbuckling model and finite element model with compression strength of corrugated boxes.* Paper presented at the 2002 Progress in Paper Physics Seminar Syracuse, NY. Rochester, NY: Rochester Institute of Technology.

Urbanik, T. J., & Saliklis, E. P. (2003). Finite element corroboration of buckling phenomena observed in corrugated boxes. *Wood and Fiber Science, 35*(3), 322-333.

Viguié, J., Dumont, P. J. J., Orgéas, L., Vacher, P., Desloges, I., & Mauret, E. (2011). Surface stress and strain fields on compressed panels of corrugated board boxes. An experimental analysis by using digital image stereocorrelation. *Composite Structures, 93*(11), 2861-2873.

Viguie, J., Dumont, P. J. J., Vacher, P., Orgeas, L., Desloges, I., & Mauret, E. (2010). *Analysis of the strain and stress fields of cardboard box during compression by 3d digital image correlation*, Liverpool, United kingdom.

Weaver, P. M. (2008). Anisotropic elastic tailoring in laminated composite plates and shells. In B. G. Falzon & F. M. H. Aliabadi (Eds.), *Buckling and postbuckling structures: Experimental, analytical and numerical studies* (Vol. 1, pp. 177-224). London: Imperial College Press.

Williams, F. W., Kennedy, D., Butler, R., & Anderson, M. S. (1991). Viconopt: Program for exact vibration and buckling analysis or design of prismatic plate assemblies. *AIAA Journal, 29*(11), 1927-1928.

Williams, F. W., & Wittrick, W. H. (1969). Computational procedures for a matrix analysis of the stability and vibration of thin flat-walled structures in compression. *International Journal of Mechanical Sciences, 11*(12), 979-998.

Wittrick, W. H. (1968). A unified approach to the initial buckling of stiffened panels in compression (initial buckling stresses of stiffened panels under uniform longitudinal compression analyzed using stiffness matrix method)

AERONAUTICAL QUARTERLY, 19, 265-283.

Wittrick, W. H., & Williams, F. W. (1971). A general algorithm for computing natural frequencies of elastic structures. *Quarterly Journal of Mechanics and Applied Mathematics, 24*, 263-284.

Wittrick, W. H., & Williams, F. W. (1973). An algorithm for computing critical buckling loads of elastic structures. *Journal of Structural Mechanics, 1*(4), 497-518.

Zirakian, T. (2010). On the application of the extrapolation techniques in elastic buckling. *Journal of Constructional Steel Research, 66*(3), 335-341.

Appendices

Appendix I

I.1 Geometric imperfection in panel FE model

The buckle modes of the panel model are first obtained in a *linear perturbation, buckle* eigenvalue analysis prior to carrying out the post-buckling analysis. The buckle modes of interest corresponding to the mode of geometric imperfection to be introduced to the post-buckle analysis, are written to a *results* (`.fil`) file of the same name as the buckle analysis job. This is achieved by adding the lines in Figure I-1 to the buckle step lines in the *input* (`.inp`) file of the *linear perturbation, buckle* job, to request nodal displacement output `U` for specified buckle modes (*m* = first mode requested, *n* = last mode requested).

```
*NODE OUTPUT
U,
*NODE FILE, GLOBAL=YES, MODE=m, LAST MODE=n
U,
```

Figure I-1: Lines in an eigenvalue buckle analysis input (`.inp`) file to write nodal displacement output `U` for buckle modes numbered *m* to *n* to a results (`.fil`) file.

The modes of imperfection were then introduced to the perfect geometry of the same panel model for the post-buckling analysis by adding the lines in Figure I-2 before the post-buckling step lines in the *input* (`.inp`) file of the *general, static* post-buckling job. The *results* (`.fil`) file and step number from the previous buckle analysis job containing the nodal displacements of the buckle modes are referenced. The second line in Figure I-2 defines the imperfection mode (*mode_number*) and amplitude (*scaling_factor*), and can be repeated for other imperfection modes as needed .The imperfection is a linear superposition of the scaled buckling eigenmodes.

```
*IMPERFECTION, FILE=results_file_name, STEP=step_number
mode_number, scaling_factor
```

Figure I-2: Lines in a post-buckle analysis input (`.inp`) file to introduce geometric imperfection based on eigenmode data in results file *results_file_name*`.fil`.

Appendix II

II.1 Post-buckling panel multi-term analytical model results

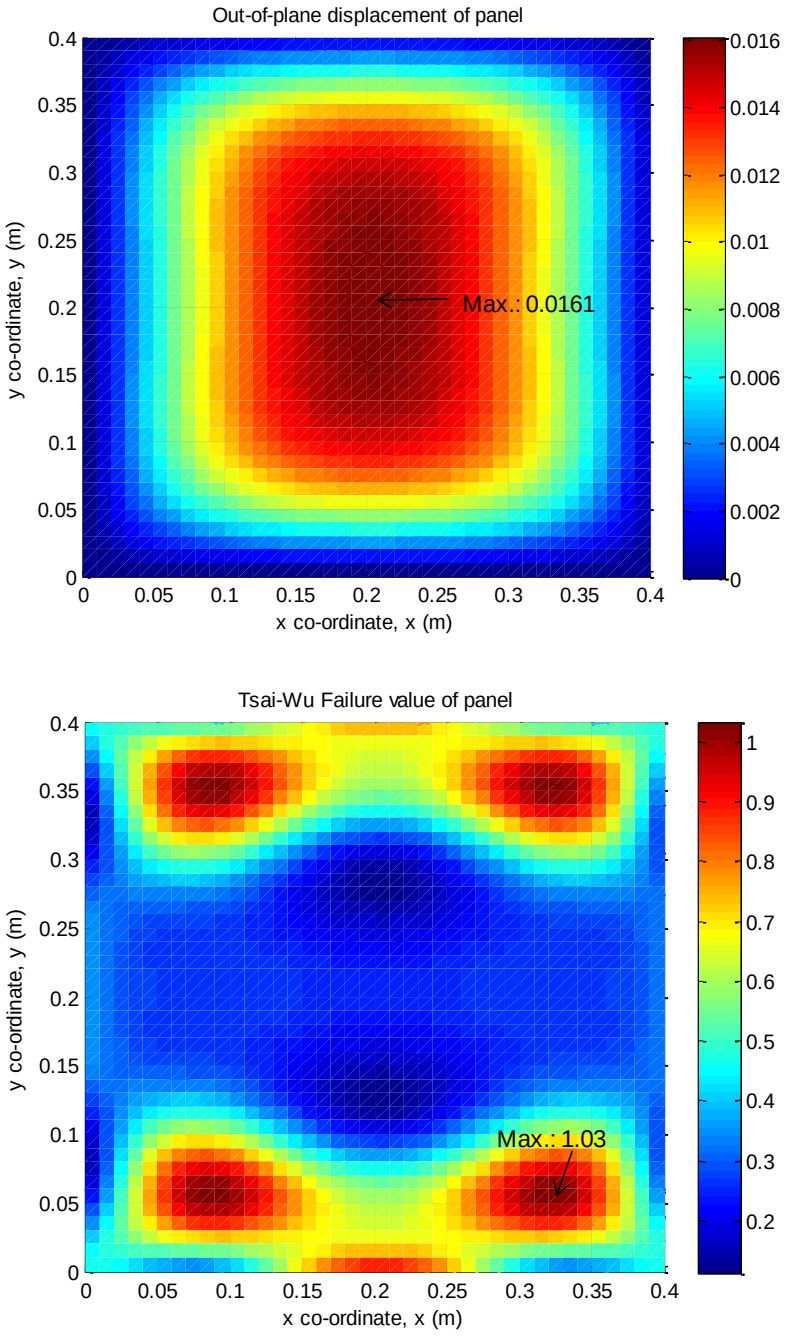

Figure II-1: Out-of-plane displacement and Tsai-Wu Failure index contour plots at the failure load ratio 1.8 or load 1724 N, for analytical symmetric multi-term model Case 2(ix), for paperboard panel from (Nordstrand, 2004a) with imperfection $A_{0\,1,1}$ = 0.02 *h*.

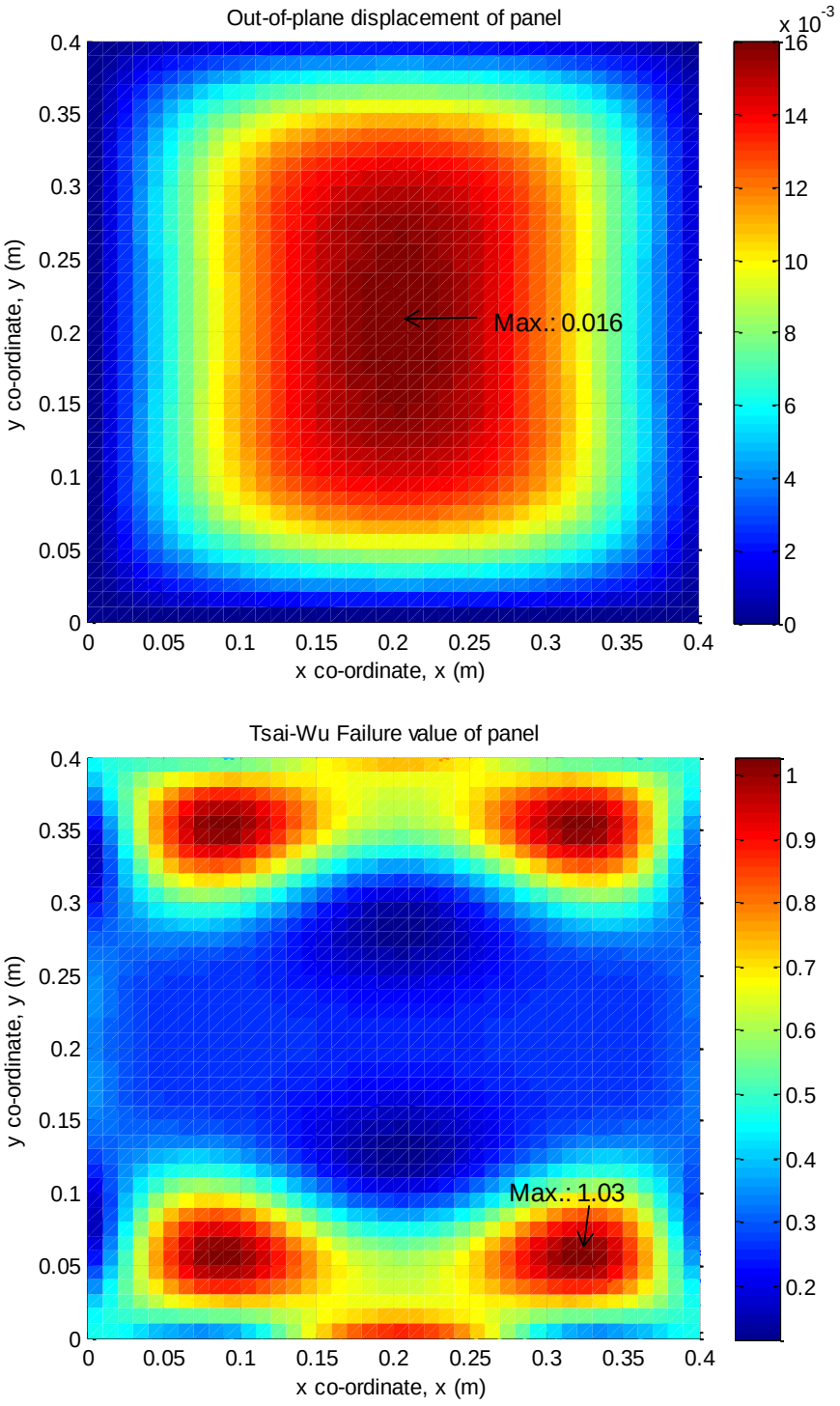

Figure II-2: Out-of-plane displacement and Tsai-Wu Failure index contour plots at the failure load ratio 1.8 or load 1724 N, for analytical symmetric multi-term model Case 3(ix), for paperboard panel from (Nordstrand, 2004a) with imperfection $A_{0\,1,1}$ = 0.000025 *h*.

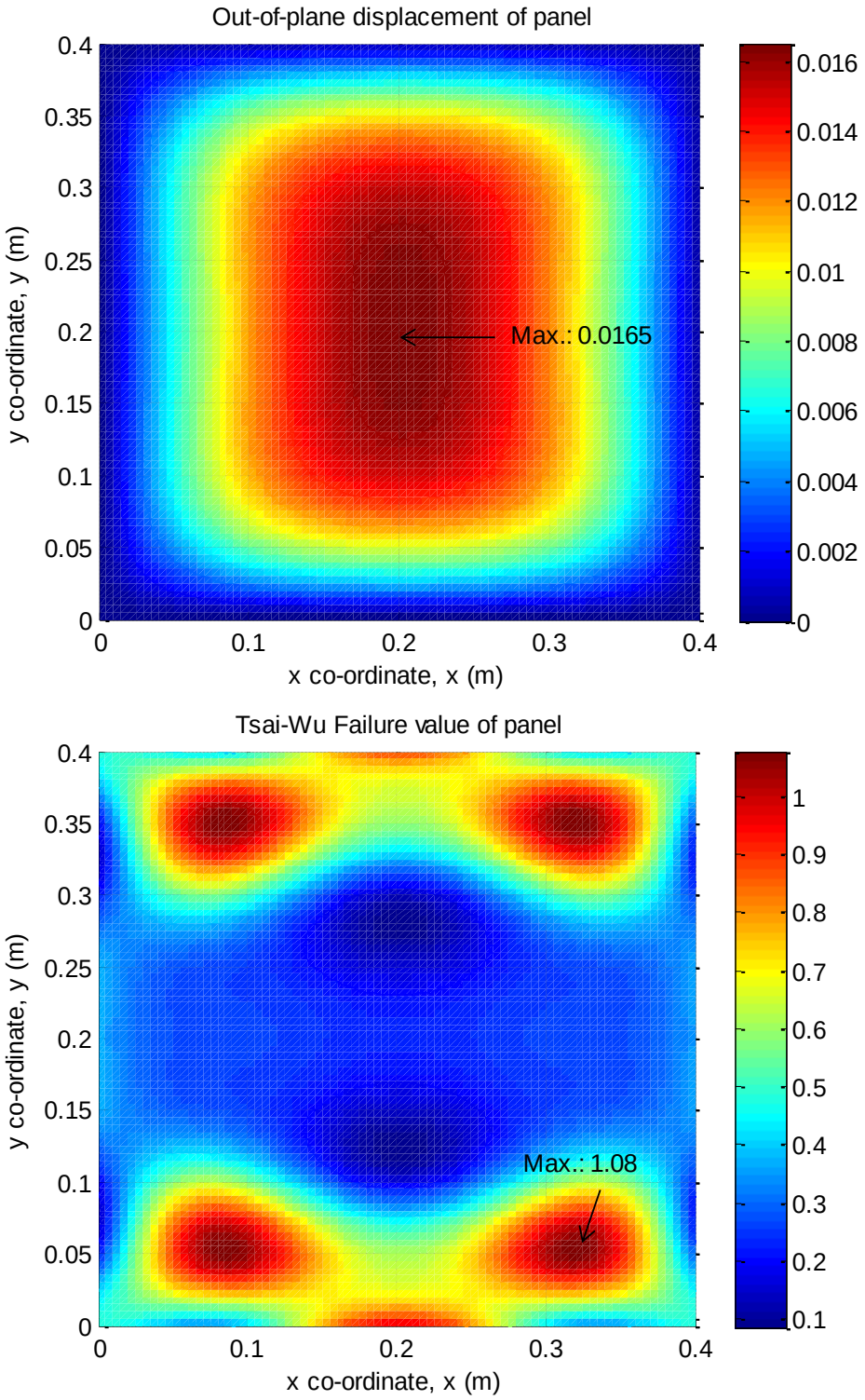

Figure II-3: Out-of-plane displacement and Tsai-Wu failure index contour plot at the failure load ratio 1.8 or load 1724 N, for analytical symmetric and anti-symmetric multi-term model Case 4(viii), for paperboard panel from (Nordstrand, 2004a) with imperfection $A_{0\,1,1} = 0.2\,h$.

Table II-1: Comparison of centre displacements for symmetric multi-term cases relative to the single-term symmetric Case 1(i) for paperboard panel from (Nordstrand, 2004a) with imperfection $A_{0\,1,1} = 0.2\,h$.

Load ratio $P/P_{\text{crit }1,1}$	% Δw_{centre} relative to w_{centre} of Case 1(i): i=1, j=1							
	Case 1(ii): i=1, 3, j=1	Case 1(iii): i=1, j=1, 3	Case 1(iv): i=1, 3, j=1, 3	Case 1(v): i=1, 3, 5, j=1	Case 1(vi): i=1, j=1, 3, 5	Case 1(vii): i=1, 3, 5, j=1, 3	Case 1(viii): i=1, 3, j=1, 3, 5	Case 1(ix): i=1, 3, 5, j=1, 3, 5
0.2	-0.01%	-0.01%	-0.02%	-0.01%	-0.01%	-0.02%	-0.02%	-0.02%
0.4	-0.02%	-0.05%	-0.07%	-0.02%	-0.05%	-0.07%	-0.07%	-0.06%
0.5	-0.03%	-0.08%	-0.11%	-0.03%	-0.08%	-0.11%	-0.11%	-0.11%
0.6	-0.05%	-0.14%	-0.19%	-0.05%	-0.14%	-0.19%	-0.19%	-0.19%
0.7	-0.08%	-0.23%	-0.30%	-0.08%	-0.23%	-0.30%	-0.30%	-0.30%
0.8	-0.14%	-0.29%	-0.41%	-0.14%	-0.28%	-0.40%	-0.40%	-0.39%
0.9	-0.22%	-0.03%	-0.21%	-0.22%	-0.01%	-0.20%	-0.19%	-0.18%
1	-0.31%	0.85%	0.63%	-0.30%	0.92%	0.64%	0.70%	0.71%
1.1	-0.42%	2.25%	2.04%	-0.40%	2.44%	2.05%	2.22%	2.23%
1.2	-0.53%	3.83%	3.69%	-0.51%	4.28%	3.71%	4.11%	4.12%
1.3	-0.66%	5.32%	5.34%	-0.63%	6.20%	5.35%	6.15%	6.17%
1.4	-0.80%	6.53%	6.80%	-0.75%	8.05%	6.82%	8.21%	8.22%
1.5	-0.94%	7.39%	7.99%	-0.89%	9.73%	8.00%	10.19%	10.19%
1.6	-1.10%	7.90%	8.90%	-1.02%	11.22%	8.90%	12.03%	12.03%
1.7	-1.26%	8.12%	9.55%	-1.17%	12.50%	9.53%	13.74%	13.72%
1.8	-1.42%	8.11%	9.98%	-1.32%	13.61%	9.94%	15.32%	15.29%
1.9	-1.59%	7.91%	10.23%	-1.47%	14.57%	10.17%		
2	-1.77%	7.59%		-1.62%				

Table II-2: Comparison of centre displacements for symmetric multi-term cases relative to the single-term symmetric Case 2(i) for paperboard panel from (Nordstrand, 2004a) with imperfection $A_{0\,1,1} = 0.02\,h$.

Load ratio $P / P_{\text{crit } 1,1}$	% Δw_{centre} relative to w_{centre} of Case 2(i): i=1, j=1							
	Case 2(ii): i=1, 3, j=1	Case 2(iii): i=1, j=1, 3	Case 2(iv): i=1, 3, j=1, 3	Case 2(v): i=1, 3, 5, j=1	Case 2(vi): i=1, j=1, 3, 5	Case 2(vii): i=1, 3, 5, j=1, 3	Case 2(viii): i=1, 3, j=1, 3, 5	Case 2(ix): i=1, 3, 5, j=1, 3, 5
0.8	0.00%	-0.01%	-0.01%	0.00%	-0.01%	-0.01%	-0.01%	-0.01%
0.9	-0.01%	-0.04%	-0.05%	-0.01%	-0.04%	-0.05%	-0.05%	-0.05%
1	-0.07%	0.22%	0.17%	-0.07%	0.23%	0.17%	0.17%	0.18%
1.1	-0.18%	2.15%	2.05%	-0.17%	2.22%	2.06%	2.12%	2.13%
1.2	-0.32%	4.20%	4.12%	-0.30%	4.48%	4.13%	4.38%	4.39%
1.3	-0.46%	5.99%	6.04%	-0.43%	6.68%	6.05%	6.68%	6.69%
1.4	-0.61%	7.37%	7.64%	-0.58%	8.70%	7.66%	8.89%	8.90%
1.5	-0.77%	8.27%	8.88%	-0.72%	10.46%	8.89%	10.94%	10.95%
1.6	-0.94%	8.75%	9.75%	-0.87%	11.95%	9.75%	12.79%	12.79%
1.7	-1.11%	8.90%	10.32%	-1.02%	13.20%	10.31%	14.47%	14.45%
1.8	-1.28%	8.79%	10.66%	-1.18%	14.26%	10.63%	15.99%	15.96%
1.9	-1.45%	8.50%	10.81%	-1.34%	15.16%	10.76%		
2	-1.63%	8.08%		-1.50%				

Table II-3: Comparison of centre displacements for symmetric multi-term cases relative to the single-term symmetric Case 3(i) for paperboard panel from (Nordstrand, 2004a) with imperfection $A_{0\ 1,1} = 0.000025\ h$

Load ratio $P / P_{\text{crit } 1,1}$	% Δw_{centre} relative to w_{centre} of Case 3(i): i=1, j=1							
	Case 3(ii): i=1, 3, j=1	Case 3(iii): i=1, j=1, 3	Case 3(iv): i=1, 3, j=1, 3	Case 3(v): i=1, 3, 5, j=1	Case 3(vi): i=1, j=1, 3, 5	Case 3(vii): i=1, 3, 5, j=1, 3	Case 3(viii): i=1, 3, j=1, 3, 5	Case 3(ix): i=1, 3, 5, j=1, 3, 5
1.1	-0.14%	2.17%	2.10%	-0.13%	2.23%	2.11%	2.16%	2.16%
1.2	-0.28%	4.28%	4.21%	-0.27%	4.53%	4.22%	4.45%	4.46%
1.3	-0.44%	6.10%	6.15%	-0.41%	6.76%	6.16%	6.77%	6.78%
1.4	-0.59%	7.49%	7.76%	-0.55%	8.80%	7.78%	8.99%	9.00%
1.5	-0.75%	8.39%	8.99%	-0.70%	10.56%	9.01%	11.04%	11.05%
1.6	-0.92%	8.86%	9.86%	-0.85%	12.05%	9.86%	12.89%	12.89%
1.7	-1.09%	8.99%	10.42%	-1.01%	13.29%	10.41%	14.56%	14.54%
1.8	-1.26%	8.87%	10.74%	-1.16%	14.34%	10.71%	16.07%	16.04%
1.9	-1.44%	8.57%	10.88%	-1.32%	15.23%	10.82%		
2	-1.62%	8.14%		-1.49%				
2.1	-1.80%			-1.65%				
2.2	-1.99%			-1.81%				
2.3	-2.18%			-1.98%				
2.4	-2.37%			-2.15%				
2.5	-2.56%			-2.32%				

Table II-4: Comparison of centre displacements for multi-term cases with symmetric or symmetric and anti-symmetric modes of *w*, *i* = 1 and j_{max} up to 5, relative to the single-term symmetric Case 1(i) paperboard panel from (Nordstrand, 2004a) with panel imperfection $A_{0\,1,1} = 0.2\,h$.

Load ratio $P/P_{crit\,1,1}$	% Δw_{centre} relative to w_{centre} of Case 1(i): i=1, j=1						
	Case 4(i): i=1, j=1, 2	Case 1(iii): i=1, j=1, 3	Case 4(ii): i=1, j=1, 2, 3	Case 4(iii): i=1, j=1, 2, 3, 4	Case 1(vi): i=1, j=1, 3, 5	Case 4(iv): i=1, j=1, 2, 3, 4, 5	FEM Case A
0.2	0.00%	-0.01%	-0.01%	-0.01%	-0.01%	-0.01%	-0.12%
0.3	0.00%	-0.03%	-0.03%	-0.03%	-0.03%	-0.03%	-0.20%
0.4	0.00%	-0.05%	-0.05%	-0.05%	-0.05%	-0.05%	-0.46%
0.5	0.00%	-0.08%	-0.08%	-0.08%	-0.08%	-0.08%	-1.05%
0.6	0.00%	-0.14%	-0.14%	-0.14%	-0.14%	-0.14%	-2.49%
0.7	0.00%	-0.23%	-0.23%	-0.23%	-0.23%	-0.23%	-5.71%
0.8	0.00%	-0.29%	-0.29%	-0.29%	-0.28%	-0.28%	-11.35%
0.9	0.00%	-0.03%	-0.03%	-0.03%	-0.01%	-0.01%	-17.45%
1	0.00%	0.85%	0.85%	0.85%	0.92%	0.92%	-21.94%
1.1	0.00%	2.25%	2.25%	2.25%	2.44%	2.44%	-24.15%
1.2	0.00%	3.83%	3.83%	3.83%	4.28%	4.28%	-24.74%
1.3	0.00%	5.32%	5.32%	5.32%	6.20%	6.20%	-24.41%
1.4	0.00%	6.53%	6.53%	6.53%	8.05%	8.05%	-23.59%
1.5	0.00%	7.39%	7.39%	7.39%	9.73%	9.73%	-22.51%
1.6	0.00%	7.90%	7.90%	7.90%	11.22%	11.22%	-21.30%
1.7	0.00%	8.12%	8.12%	8.12%	12.50%	12.50%	-20.00%
1.8	0.00%	8.11%	8.11%	8.11%	13.61%	13.61%	-18.67%
1.9	0.00%	7.91%	7.91%	7.91%	14.57%	14.57%	-17.30%

Table II-5: Comparison of centre displacements for multi-term cases with symmetric or symmetric and anti-symmetric modes of w, i_{max} and j_{max} up to 5, relative to the single-term symmetric Case 1(i) paperboard panel from (Nordstrand, 2004a) with panel imperfection $A_{0\,1,1} = 0.2\,h$,.

Load ratio $P/P_{crit\,1,1}$	% Δw_{centre} relative to w_{centre} of Case 1(i): i=1, j=1					
	Case 4(v): i=1, 2, j=1, 2	Case 1(iv): i=1, 3, j=1, 3	Case 4(vi): i=1, 2, 3, j=1, 2, 3	Case 4(vii): i=1, 2, 3, 4, j=1, 2, 3, 4	Case 1(ix): i=1, 3, 5, j=1, 3, 5	Case 4(viii): i=1, 2, 3, 4, 5, j=1, 2, 3, 4, 5
0.1	0.00%	-0.01%	-0.01%	-0.01%	-0.01%	-0.01%
0.2	0.00%	-0.02%	-0.02%	-0.02%	-0.02%	-0.02%
0.3	0.00%	-0.04%	-0.04%	-0.04%	-0.04%	-0.04%
0.4	0.00%	-0.07%	-0.07%	-0.07%	-0.06%	-0.06%
0.5	0.00%	-0.11%	-0.11%	-0.11%	-0.11%	-0.11%
0.6	0.00%	-0.19%	-0.19%	-0.19%	-0.19%	-0.19%
0.7	0.00%	-0.30%	-0.30%	-0.30%	-0.30%	-0.30%
0.8	0.00%	-0.41%	-0.41%	-0.41%	-0.39%	-0.39%
0.9	0.00%	-0.21%	-0.21%	-0.21%	-0.18%	-0.18%
1	0.00%	0.63%	0.63%	0.63%	0.71%	0.71%
1.1	0.00%	2.04%	2.04%	2.04%	2.23%	2.23%
1.2	0.00%	3.69%	3.69%	3.69%	4.12%	4.12%
1.3	0.00%	5.34%	5.34%	5.34%	6.17%	6.17%
1.4	0.00%	6.80%	6.80%	6.80%	8.22%	8.22%
1.5	0.00%	7.99%	7.99%	7.99%	10.19%	10.19%
1.6	0.00%	8.90%	8.90%	8.90%	12.03%	12.03%
1.7	0.00%	9.55%	9.55%	9.55%	13.72%	13.72%
1.8	0.00%	9.98%	9.98%	9.98%	15.29%	15.29%

Table II-6: Dimensionless post-buckling results of cases with symmetric only or symmetric and anti-symmetric displacement modes, i=1 and j_{max} up to 4, for paperboard panel from (Nordstrand, 2004a) with symmetric geometric imperfection $A_{0\,1,1} = 0.2\,h$.

Load ratio P / $P_{crit\ 1,1}$	Case 1(i): i =1, j=1	Case 4(i): i=1, j=1, 2		Case 1(iii): i=1, j=1, 3		Case 4(ii): i=1, j=1, 2, 3			Case 4(iii): i=1, j=1, 2, 3, 4			
	$A_{1,1}$ / h	$A_{1,1}$ / h	$A_{1,2}$ / h	$A_{1,1}$ / h	$A_{1,3}$ / h	$A_{1,1}$ / h	$A_{1,2}$ / h	$A_{1,3}$ / h	$A_{1,1}$ / h	$A_{1,2}$ / h	$A_{1,3}$ / h	$A_{1,4}$ / h
0	0.199	0.199	0	0.199	0	0.199	0	0	0.199	0	0	0
0.2	0.248	0.248	0.000	0.248	0.000	0.248	0.000	0.000	0.248	0.000	0.000	0.000
0.4	0.329	0.329	0.000	0.329	0.000	0.329	0.000	0.000	0.329	0.000	0.000	0.000
0.6	0.482	0.482	0.000	0.482	0.001	0.482	0.000	0.001	0.482	0.000	0.001	0.000
0.8	0.820	0.820	0.000	0.823	0.005	0.823	0.000	0.005	0.823	0.000	0.005	0.000
0.9	1.106	1.106	0.000	1.119	0.014	1.119	0.000	0.014	1.119	0.000	0.014	0.000
1	1.442	1.442	0.000	1.489	0.035	1.489	0.000	0.035	1.489	0.000	0.035	0.000
1.1	1.781	1.781	0.000	1.892	0.071	1.892	0.000	0.071	1.892	0.000	0.071	0.000
1.2	2.097	2.097	0.000	2.303	0.125	2.303	0.000	0.125	2.303	0.000	0.125	0.000
1.3	2.389	2.389	0.000	2.710	0.194	2.710	0.000	0.194	2.710	0.000	0.194	0.000
1.4	2.657	2.657	0.000	3.105	0.275	3.105	0.000	0.275	3.105	0.000	0.275	0.000
1.5	2.906	2.906	0.000	3.484	0.363	3.484	0.000	0.363	3.484	0.000	0.363	0.000
1.6	3.138	3.138	0.000	3.842	0.456	3.842	0.000	0.456	3.842	0.000	0.456	0.000
1.7	3.356	3.356	0.000	4.179	0.550	4.179	0.000	0.550	4.179	0.000	0.550	0.000
1.8	3.563	3.563	0.000	4.495	0.643	4.495	0.000	0.643	4.495	0.000	0.643	0.000
1.9	3.759	3.759	0.000	4.791	0.735	4.791	0.000	0.735	4.791	0.000	0.735	0.000
2	3.946	3.946	0.000	5.070	0.825	5.070	0.000	0.825	5.070	0.000	0.825	0.000

Table II-7: Dimensionless post-buckling results of multi-term cases with symmetric only or symmetric and anti-symmetric displacement modes, *i*=1 and j_{max}=5, for paperboard panel from (Nordstrand, 2004a) with symmetric geometric imperfection $A_{0\,1,1} = 0.2\,h$.

Load ratio $P / P_{crit\ 1,1}$	Case 1(vi): *i*=1, *j*=1, 3, 5			Case 4(iv): *i*=1, *j*=1, 2, 3, 4, 5				
	$A_{1,1} / h$	$A_{1,3} / h$	$A_{1,5} / h$	$A_{1,1} / h$	$A_{1,2} / h$	$A_{1,3} / h$	$A_{1,4} / h$	$A_{1,5} / h$
0	0.199	0	0	0.199	0	0	0	0
0.2	0.248	0.000	0.000	0.248	0.000	0.000	0.000	0.000
0.4	0.329	0.000	0.000	0.329	0.000	0.000	0.000	0.000
0.6	0.482	0.001	0.000	0.482	0.000	0.001	0.000	0.000
0.8	0.823	0.005	0.000	0.823	0.000	0.005	0.000	0.000
0.9	1.120	0.014	0.000	1.120	0.000	0.014	0.000	0.000
1	1.490	0.035	0.001	1.490	0.000	0.035	0.000	0.001
1.1	1.894	0.072	0.002	1.894	0.000	0.072	0.000	0.002
1.2	2.309	0.127	0.005	2.309	0.000	0.127	0.000	0.005
1.3	2.726	0.200	0.011	2.726	0.000	0.200	0.000	0.011
1.4	3.141	0.289	0.019	3.141	0.000	0.289	0.000	0.019
1.5	3.548	0.390	0.031	3.548	0.000	0.390	0.000	0.031
1.6	3.943	0.500	0.047	3.943	0.000	0.500	0.000	0.047
1.7	4.324	0.614	0.066	4.324	0.000	0.614	0.000	0.066
1.8	4.691	0.731	0.088	4.691	0.000	0.731	0.000	0.088
1.9	5.042	0.849	0.113	5.042	0.000	0.849	0.000	0.113

Table II-8: Dimensionless post-buckling results of cases with symmetric only or symmetric and anti-symmetric displacement modes, i_{max} and j_{max} up to 2, for paperboard panel from (Nordstrand, 2004a) with symmetric geometric imperfection $A_{0\,1,1} = 0.2\,h$.

Load ratio $P / P_{crit\ 1,1}$	Case 1(i): i =1, j=1	Case 4(v): i =1, 2, j=1, 2			
	$A_{1,1} / h$	$A_{1,1} / h$	$A_{1,2} / h$	$A_{2,1} / h$	$A_{2,2} / h$
0	0.199	0.199	0	0	0
0.1	0.221	0.221	0.000	0.000	0.000
0.2	0.248	0.248	0.000	0.000	0.000
0.3	0.283	0.283	0.000	0.000	0.000
0.4	0.329	0.329	0.000	0.000	0.000
0.5	0.392	0.392	0.000	0.000	0.000
0.6	0.482	0.482	0.000	0.000	0.000
0.7	0.616	0.616	0.000	0.000	0.000
0.8	0.820	0.820	0.000	0.000	0.000
0.9	1.106	1.106	0.000	0.000	0.000
1	1.442	1.442	0.000	0.000	0.000
1.1	1.781	1.781	0.000	0.000	0.000
1.2	2.097	2.097	0.000	0.000	0.000
1.3	2.389	2.389	0.000	0.000	0.000
1.4	2.657	2.657	0.000	0.000	0.000
1.5	2.906	2.906	0.000	0.000	0.000
1.6	3.138	3.138	0.000	0.000	0.000
1.7	3.356	3.356	0.000	0.000	0.000
1.8	3.563	3.563	0.000	0.000	0.000
1.9	3.759	3.759	0.000	0.000	0.000
2	3.946	3.946	0.000	0.000	0.000

Table II-9: Dimensionless post-buckling results of cases with symmetric only or symmetric and anti-symmetric displacement modes, i_{max} and j_{max} = 3, for paperboard panel from (Nordstrand, 2004a) with symmetric geometric imperfection $A_{0\,1,1} = 0.2\,h$.

Load ratio	Case 1(iv): i =1, 3 j=1, 3				Case 4(vi): i =1, 2, 3, j=1, 2, 3								
$P / P_{crit\ 1,1}$	$A_{1,1} / h$	$A_{1,3} / h$	$A_{3,1} / h$	$A_{3,3} / h$	$A_{1,1} / h$	$A_{1,2} / h$	$A_{1,3} / h$	$A_{2,1} / h$	$A_{2,2} / h$	$A_{2,3} / h$	$A_{3,1} / h$	$A_{3,2} / h$	$A_{3,3} / h$
0	0.199	0	0	0	0.199	0	0	0	0	0	0	0	0
0.1	0.221	0.000	0.000	0.000	0.221	0.000	0.000	0.000	0.000	0.000	0.000	0.000	0.000
0.2	0.248	0.000	0.000	0.000	0.248	0.000	0.000	0.000	0.000	0.000	0.000	0.000	0.000
0.3	0.283	0.000	0.000	0.000	0.283	0.000	0.000	0.000	0.000	0.000	0.000	0.000	0.000
0.4	0.329	0.000	0.000	0.000	0.329	0.000	0.000	0.000	0.000	0.000	0.000	0.000	0.000
0.5	0.392	0.000	0.000	0.000	0.392	0.000	0.000	0.000	0.000	0.000	0.000	0.000	0.000
0.6	0.482	0.001	0.000	0.000	0.482	0.000	0.001	0.000	0.000	0.000	0.000	0.000	0.000
0.7	0.617	0.002	0.001	0.000	0.617	0.000	0.002	0.000	0.000	0.000	0.001	0.000	0.000
0.8	0.823	0.005	0.001	0.000	0.823	0.000	0.005	0.000	0.000	0.000	0.001	0.000	0.000
0.9	1.121	0.014	0.003	0.000	1.121	0.000	0.014	0.000	0.000	0.000	0.003	0.000	0.000
1	1.493	0.035	0.008	0.001	1.493	0.000	0.035	0.000	0.000	0.000	0.008	0.000	0.001
1.1	1.900	0.071	0.015	0.003	1.900	0.000	0.071	0.000	0.000	0.000	0.015	0.000	0.003
1.2	2.319	0.126	0.025	0.006	2.319	0.000	0.126	0.000	0.000	0.000	0.025	0.000	0.006
1.3	2.738	0.196	0.038	0.013	2.738	0.000	0.196	0.000	0.000	0.000	0.038	0.000	0.013
1.4	3.151	0.281	0.054	0.022	3.151	0.000	0.281	0.000	0.000	0.000	0.054	0.000	0.022
1.5	3.551	0.376	0.072	0.035	3.551	0.000	0.376	0.000	0.000	0.000	0.072	0.000	0.035
1.6	3.935	0.477	0.092	0.052	3.935	0.000	0.477	0.000	0.000	0.000	0.092	0.000	0.052
1.7	4.301	0.583	0.114	0.073	4.301	0.000	0.583	0.000	0.000	0.000	0.114	0.000	0.073
1.8	4.647	0.690	0.138	0.098	4.647	0.000	0.690	0.000	0.000	0.000	0.138	0.000	0.098
1.9	4.976	0.797	0.162	0.127	4.976	0.000	0.797	0.000	0.000	0.000	0.162	0.000	0.127

Table II-10: Dimensionless post-buckling results of cases with symmetric and anti-symmetric displacement modes, i_{max} and j_{max} = 4, for paperboard panel from (Nordstrand, 2004a) with symmetric geometric imperfection $A_{0\,1,1} = 0.2\,h$.

Load ratio $P / P_{crit\ 1,1}$	Case 4(vii): i =1, 2, 3, 4, j=1, 2, 3, 4															
	$A_{1,1}/h$	$A_{1,2}/h$	$A_{1,3}/h$	$A_{1,4}/h$	$A_{2,1}/h$	$A_{2,2}/h$	$A_{2,3}/h$	$A_{2,4}/h$	$A_{3,1}/h$	$A_{3,2}/h$	$A_{3,3}/h$	$A_{3,4}/h$	$A_{4,1}/h$	$A_{4,2}/h$	$A_{4,3}/h$	$A_{4,4}/h$
0	0.199	0	0	0	0	0	0	0	0	0	0	0	0	0	0	0
0.2	0.248	0.000	0.000	0.000	0.000	0.000	0.000	0.000	0.000	0.000	0.000	0.000	0.000	0.000	0.000	0.000
0.3	0.283	0.000	0.000	0.000	0.000	0.000	0.000	0.000	0.000	0.000	0.000	0.000	0.000	0.000	0.000	0.000
0.4	0.329	0.000	0.000	0.000	0.000	0.000	0.000	0.000	0.000	0.000	0.000	0.000	0.000	0.000	0.000	0.000
0.5	0.392	0.000	0.000	0.000	0.000	0.000	0.000	0.000	0.000	0.000	0.000	0.000	0.000	0.000	0.000	0.000
0.6	0.482	0.000	0.001	0.000	0.000	0.000	0.000	0.000	0.000	0.000	0.000	0.000	0.000	0.000	0.000	0.000
0.7	0.617	0.000	0.002	0.000	0.000	0.000	0.000	0.000	0.001	0.000	0.000	0.000	0.000	0.000	0.000	0.000
0.8	0.823	0.000	0.005	0.000	0.000	0.000	0.000	0.000	0.001	0.000	0.000	0.000	0.000	0.000	0.000	0.000
0.9	1.121	0.000	0.014	0.000	0.000	0.000	0.000	0.000	0.003	0.000	0.000	0.000	0.000	0.000	0.000	0.000
1	1.493	0.000	0.035	0.000	0.000	0.000	0.000	0.000	0.008	0.000	0.001	0.000	0.000	0.000	0.000	0.000
1.1	1.900	0.000	0.071	0.000	0.000	0.000	0.000	0.000	0.015	0.000	0.003	0.000	0.000	0.000	0.000	0.000
1.2	2.319	0.000	0.126	0.000	0.000	0.000	0.000	0.000	0.025	0.000	0.006	0.000	0.000	0.000	0.000	0.000
1.3	2.738	0.000	0.196	0.000	0.000	0.000	0.000	0.000	0.038	0.000	0.013	0.000	0.000	0.000	0.000	0.000
1.4	3.151	0.000	0.281	0.000	0.000	0.000	0.000	0.000	0.054	0.000	0.022	0.000	0.000	0.000	0.000	0.000
1.5	3.551	0.000	0.376	0.000	0.000	0.000	0.000	0.000	0.072	0.000	0.035	0.000	0.000	0.000	0.000	0.000
1.6	3.935	0.000	0.477	0.000	0.000	0.000	0.000	0.000	0.092	0.000	0.052	0.000	0.000	0.000	0.000	0.000
1.7	4.301	0.000	0.583	0.000	0.000	0.000	0.000	0.000	0.114	0.000	0.073	0.000	0.000	0.000	0.000	0.000
1.8	4.647	0.000	0.690	0.000	0.000	0.000	0.000	0.000	0.138	0.000	0.098	0.000	0.000	0.000	0.000	0.000
1.9	4.976	0.000	0.797	0.000	0.000	0.000	0.000	0.000	0.162	0.000	0.127	0.000	0.000	0.000	0.000	0.000

Table II-11: Dimensionless post-buckling results of cases with symmetric only displacement modes, i_{max} and j_{max} = 5, for paperboard panel from (Nordstrand, 2004a) with symmetric geometric imperfection $A_{0\ 1,1} = 0.2\ h$.

Load ratio	Case 1(ix): i =1, 3, 5, j=1, 3, 5								
$P / P_{crit\ 1,1}$	$A_{1,1} / h$	$A_{1,3} / h$	$A_{1,5} / h$	$A_{3,1} / h$	$A_{3,3} / h$	$A_{3,5} / h$	$A_{5,1} / h$	$A_{5,3} / h$	$A_{5,5} / h$
0	0.199	0	0	0	0	0	0	0	0
0.1	0.221	0.000	0.000	0.000	0.000	0.000	0.000	0.000	0.000
0.2	0.248	0.000	0.000	0.000	0.000	0.000	0.000	0.000	0.000
0.3	0.283	0.000	0.000	0.000	0.000	0.000	0.000	0.000	0.000
0.4	0.329	0.000	0.000	0.000	0.000	0.000	0.000	0.000	0.000
0.5	0.392	0.000	0.000	0.000	0.000	0.000	0.000	0.000	0.000
0.6	0.482	0.001	0.000	0.000	0.000	0.000	0.000	0.000	0.000
0.7	0.617	0.002	0.000	0.001	0.000	0.000	0.000	0.000	0.000
0.8	0.823	0.005	0.000	0.001	0.000	0.000	0.000	0.000	0.000
0.9	1.121	0.014	0.000	0.003	0.000	0.000	0.000	0.000	0.000
1	1.493	0.035	0.001	0.008	0.001	0.000	0.000	0.000	0.000
1.1	1.902	0.072	0.002	0.015	0.003	0.000	0.000	0.000	0.000
1.2	2.325	0.128	0.005	0.025	0.006	0.000	0.000	0.000	0.000
1.3	2.754	0.203	0.010	0.038	0.012	0.001	0.001	0.000	0.000
1.4	3.185	0.295	0.019	0.054	0.021	0.001	0.001	0.000	0.000
1.5	3.614	0.402	0.030	0.072	0.035	0.003	0.001	0.001	0.000
1.6	4.037	0.520	0.046	0.094	0.053	0.005	0.001	0.001	0.000
1.7	4.450	0.647	0.065	0.117	0.075	0.009	0.002	0.002	0.000
1.8	4.854	0.778	0.087	0.143	0.103	0.014	0.002	0.003	0.000

Table II-12: Dimensionless post-buckling results of cases with symmetric and anti-symmetric displacement modes, i_{max} and j_{max} = 5, for paperboard panel from (Nordstrand, 2004a) with symmetric geometric imperfection $A_{0\,1,1} = 0.2\,h$.[5]

Load ratio	Case 4(viii): i =1, 2, 3, 4, 5, j=1, 2, 3, 4, 5												
$P / P_{crit\ 1,1}$	$A_{1,1} / h$	$A_{1,2} / h$	$A_{1,3} / h$	$A_{1,4} / h$	$A_{1,5} / h$	$A_{2,1} / h$	$A_{2,2} / h$	$A_{2,3} / h$	$A_{2,4} / h$	$A_{2,5} / h$	$A_{3,1} / h$	$A_{3,2} / h$	$A_{3,3} / h$
0	0.199	0	0	0	0	0	0	0	0	0	0	0	0
0.2	0.248	0.000	0.000	0.000	0.000	0.000	0.000	0.000	0.000	0.000	0.000	0.000	0.000
0.4	0.329	0.000	0.000	0.000	0.000	0.000	0.000	0.000	0.000	0.000	0.000	0.000	0.000
0.5	0.392	0.000	0.000	0.000	0.000	0.000	0.000	0.000	0.000	0.000	0.000	0.000	0.000
0.6	0.482	0.000	0.001	0.000	0.000	0.000	0.000	0.000	0.000	0.000	0.000	0.000	0.000
0.7	0.617	0.000	0.002	0.000	0.000	0.000	0.000	0.000	0.000	0.000	0.001	0.000	0.000
0.8	0.823	0.000	0.005	0.000	0.000	0.000	0.000	0.000	0.000	0.000	0.001	0.000	0.000
0.9	1.121	0.000	0.014	0.000	0.000	0.000	0.000	0.000	0.000	0.000	0.003	0.000	0.000
1	1.493	0.000	0.035	0.000	0.001	0.000	0.000	0.000	0.000	0.000	0.008	0.000	0.001
1.1	1.902	0.000	0.072	0.000	0.002	0.000	0.000	0.000	0.000	0.000	0.015	0.000	0.003
1.2	2.325	0.000	0.128	0.000	0.005	0.000	0.000	0.000	0.000	0.000	0.025	0.000	0.006
1.3	2.754	0.000	0.203	0.000	0.010	0.000	0.000	0.000	0.000	0.000	0.038	0.000	0.012
1.4	3.185	0.000	0.295	0.000	0.019	0.000	0.000	0.000	0.000	0.000	0.054	0.000	0.021
1.5	3.614	0.000	0.402	0.000	0.030	0.000	0.000	0.000	0.000	0.000	0.072	0.000	0.035
1.6	4.037	0.000	0.520	0.000	0.046	0.000	0.000	0.000	0.000	0.000	0.094	0.000	0.053
1.7	4.450	0.000	0.647	0.000	0.065	0.000	0.000	0.000	0.000	0.000	0.117	0.000	0.075
1.8	4.854	0.000	0.778	0.000	0.087	0.000	0.000	0.000	0.000	0.000	0.143	0.000	0.103

[5] Continued in Table II-13.

Table II-13: Dimensionless post-buckling results of cases with symmetric and anti-symmetric displacement modes, i_{max} and j_{max} = 5, for paperboard panel from (Nordstrand, 2004a) with symmetric geometric imperfection $A_{0\,1,1} = 0.2\,h$.[6]

Load ratio	Case 4(viii): i =1, 2, 3, 4, 5, j=1, 2, 3, 4, 5											
$P / P_{crit\ 1,1}$	$A_{3,4} / h$	$A_{3,5} / h$	$A_{4,1} / h$	$A_{4,2} / h$	$A_{4,3} / h$	$A_{4,4} / h$	$A_{4,5} / h$	$A_{5,1} / h$	$A_{5,2} / h$	$A_{5,3} / h$	$A_{5,4} / h$	$A_{5,5} / h$
0	0	0	0	0	0	0	0	0	0	0	0	0
0.2	0.000	0.000	0.000	0.000	0.000	0.000	0.000	0.000	0.000	0.000	0.000	0.000
0.4	0.000	0.000	0.000	0.000	0.000	0.000	0.000	0.000	0.000	0.000	0.000	0.000
0.5	0.000	0.000	0.000	0.000	0.000	0.000	0.000	0.000	0.000	0.000	0.000	0.000
0.6	0.000	0.000	0.000	0.000	0.000	0.000	0.000	0.000	0.000	0.000	0.000	0.000
0.7	0.000	0.000	0.000	0.000	0.000	0.000	0.000	0.000	0.000	0.000	0.000	0.000
0.8	0.000	0.000	0.000	0.000	0.000	0.000	0.000	0.000	0.000	0.000	0.000	0.000
0.9	0.000	0.000	0.000	0.000	0.000	0.000	0.000	0.000	0.000	0.000	0.000	0.000
1	0.000	0.000	0.000	0.000	0.000	0.000	0.000	0.000	0.000	0.000	0.000	0.000
1.1	0.000	0.000	0.000	0.000	0.000	0.000	0.000	0.000	0.000	0.000	0.000	0.000
1.2	0.000	0.000	0.000	0.000	0.000	0.000	0.000	0.000	0.000	0.000	0.000	0.000
1.3	0.000	0.001	0.000	0.000	0.000	0.000	0.000	0.001	0.000	0.000	0.000	0.000
1.4	0.000	0.001	0.000	0.000	0.000	0.000	0.000	0.001	0.000	0.000	0.000	0.000
1.5	0.000	0.003	0.000	0.000	0.000	0.000	0.000	0.001	0.000	0.001	0.000	0.000
1.6	0.000	0.005	0.000	0.000	0.000	0.000	0.000	0.001	0.000	0.001	0.000	0.000
1.7	0.000	0.009	0.000	0.000	0.000	0.000	0.000	0.002	0.000	0.002	0.000	0.000
1.8	0.000	0.014	0.000	0.000	0.000	0.000	0.000	0.002	0.000	0.003	0.000	0.000

[6] Continued from Table II-12.

Table II-14: Comparison of displacement *w* (0.5 *a*,0.25 *b*) relative to the two-term Case 5(i) paperboard panel from (Nordstrand, 2004a) with panel imperfection $A_{0\ 1,2}$ 0.2 *h*, for multi-term cases with symmetric and anti-symmetric modes of displacement function *w*, i_{max} and j_{max} up to 5.

Load ratio $P/P_{crit\ 1,1}$	% Δ*w* (0.5 *a*,0.25 *b*) relative to *w* (0.5 *a*, 0.25 *b*) Case 5(i): *i*=1, *j*=1, 2							
	Case 5(v): *i*=1, 2, *j*=1, 2	Case 5(ii): *i*=1, *j*=1, 2, 3	Case 5(vi): *i*=1, 2, 3, *j*=1, 2, 3	Case 5(iii): *i*=1, *j*=1, 2, 3, 4	Case 5(vii): *i*=1, 2, 3, 4, *j*=1, 2, 3, 4	Case 5(iv): *i*=1, *j*=1, 2, 3, 4, 5	Case 5(viii): *i*=1, 2, 3, 4, 5, *j*=1, 2, 3, 4, 5	FEM Case A
0	0.00%	0.00%	0.00%	0.00%	0.00%	0.00%	0.00%	0.00%
0.2	0.00%	0.00%	-0.02%	0.00%	-0.02%	0.00%	-0.02%	-0.21%
0.4	0.00%	0.00%	-0.05%	0.00%	-0.05%	0.00%	-0.05%	-0.58%
0.6	0.00%	0.00%	-0.13%	0.01%	-0.12%	0.01%	-0.12%	-2.84%
0.8	0.00%	0.00%	-0.33%	0.05%	-0.28%	0.05%	-0.27%	-6.96%
1	0.00%	0.00%	-0.84%	0.42%	-0.41%	0.42%	-0.40%	-17.07%
1.1	0.00%	0.00%	-1.25%	0.92%	-0.32%	0.92%	-0.30%	-21.11%
1.2	0.00%	0.00%	-1.77%	1.61%	-0.13%	1.61%	-0.10%	-23.76%
1.3	0.00%	0.00%	-2.35%	2.42%	0.09%	2.42%	0.15%	-25.15%
1.4	0.00%	0.00%	-3.00%	3.27%	0.32%	3.27%	0.41%	-25.70%
1.5	0.00%	0.00%	-3.69%	4.12%	0.50%	4.12%	0.63%	-25.75%
1.6	0.00%	0.00%	-4.41%	4.95%	0.65%	4.95%	0.82%	-25.50%
1.7	0.00%	0.00%	-5.15%	5.74%	0.75%	5.74%	0.97%	-25.06%
1.8	0.00%	0.00%	-5.91%	6.49%	0.80%	6.49%	1.08%	-24.52%

Table II-15: Dimensionless post-buckling results of cases with symmetric and anti-symmetric modes, i=1 and j_{max} up to 5, for paperboard panel from (Nordstrand, 2004a) with anti-symmetric geometric imperfection $A_{0\,1,2} = 0.2\,h$.

Load ratio $P / P_{crit\ 1,1}$	Case 5(i): i=1, j=1, 2		Case 5(ii): i=1, j=1, 2, 3			Case 5(iii): i=1, j=1, 2, 3, 4				Case 5(iv): i=1, j=1, 2, 3, 4, 5				
	$A_{1,1}/h$	$A_{1,2}/h$	$A_{1,1}/h$	$A_{1,2}/h$	$A_{1,3}/h$	$A_{1,1}/h$	$A_{1,2}/h$	$A_{1,3}/h$	$A_{1,4}/h$	$A_{1,1}/h$	$A_{1,2}/h$	$A_{1,3}/h$	$A_{1,4}/h$	$A_{1,5}/h$
0	0	0.199	0	0.199	0	0	0.199	0	0	0	0.199	0	0	0
0.1	0.000	0.218	0.000	0.218	0.000	0.000	0.218	0.000	0.000	0.000	0.218	0.000	0.000	0.000
0.2	0.000	0.241	0.000	0.241	0.000	0.000	0.241	0.000	0.000	0.000	0.241	0.000	0.000	0.000
0.3	0.000	0.269	0.000	0.269	0.000	0.000	0.269	0.000	0.000	0.000	0.269	0.000	0.000	0.000
0.4	0.000	0.305	0.000	0.305	0.000	0.000	0.305	0.000	0.000	0.000	0.305	0.000	0.000	0.000
0.5	0.000	0.350	0.000	0.350	0.000	0.000	0.350	0.000	0.000	0.000	0.350	0.000	0.000	0.000
0.6	0.000	0.411	0.000	0.411	0.000	0.000	0.411	0.000	0.000	0.000	0.411	0.000	0.000	0.000
0.7	0.000	0.494	0.000	0.494	0.000	0.000	0.494	0.000	0.001	0.000	0.494	0.000	0.001	0.000
0.8	0.000	0.609	0.000	0.609	0.000	0.000	0.609	0.000	0.002	0.000	0.609	0.000	0.002	0.000
0.9	0.000	0.768	0.000	0.768	0.000	0.000	0.770	0.000	0.004	0.000	0.770	0.000	0.004	0.000
1	0.000	0.976	0.000	0.976	0.000	0.000	0.980	0.000	0.009	0.000	0.980	0.000	0.009	0.000
1.1	0.000	1.215	0.000	1.215	0.000	0.000	1.226	0.000	0.018	0.000	1.226	0.000	0.018	0.000
1.2	0.000	1.462	0.000	1.462	0.000	0.000	1.486	0.000	0.033	0.000	1.486	0.000	0.033	0.000
1.3	0.000	1.701	0.000	1.701	0.000	0.000	1.743	0.000	0.053	0.000	1.743	0.000	0.053	0.000
1.4	0.000	1.926	0.000	1.926	0.000	0.000	1.989	0.000	0.078	0.000	1.989	0.000	0.078	0.000
1.5	0.000	2.137	0.000	2.137	0.000	0.000	2.225	0.000	0.107	0.000	2.225	0.000	0.107	0.000
1.6	0.000	2.333	0.000	2.333	0.000	0.000	2.449	0.000	0.141	0.000	2.449	0.000	0.141	0.000
1.7	0.000	2.518	0.000	2.518	0.000	0.000	2.663	0.000	0.178	0.000	2.663	0.000	0.178	0.000
1.8	0.000	2.693	0.000	2.693	0.000	0.000	2.868	0.000	0.218	0.000	2.868	0.000	0.218	0.000

Table II-16: Dimensionless post-buckling results of cases with symmetric and anti-symmetric modes, i_{max} and j_{max} up to 3, for paperboard panel from (Nordstrand, 2004a) with anti-symmetric geometric imperfection $A_{0\,1,2} = 0.2\,h$.

Load ratio $P / P_{crit\ 1,1}$	Case 5(v): i =1, 2, j=1, 2				Case 5(vi): i =1, 2, 3, j=1, 2, 3								
	$A_{1,1} / h$	$A_{1,2} / h$	$A_{2,1} / h$	$A_{2,2} / h$	$A_{1,1} / h$	$A_{1,2} / h$	$A_{1,3} / h$	$A_{2,1} / h$	$A_{2,2} / h$	$A_{2,3} / h$	$A_{3,1} / h$	$A_{3,2} / h$	$A_{3,3} / h$
0	0	0.199	0	0	0	0.199	0	0	0	0	0	0	0
0.1	0.000	0.218	0.000	0.000	0.000	0.218	0.000	0.000	0.000	0.000	0.000	0.000	0.000
0.2	0.000	0.241	0.000	0.000	0.000	0.241	0.000	0.000	0.000	0.000	0.000	0.000	0.000
0.3	0.000	0.269	0.000	0.000	0.000	0.269	0.000	0.000	0.000	0.000	0.000	0.000	0.000
0.4	0.000	0.305	0.000	0.000	0.000	0.305	0.000	0.000	0.000	0.000	0.000	0.000	0.000
0.5	0.000	0.350	0.000	0.000	0.000	0.350	0.000	0.000	0.000	0.000	0.000	0.000	0.000
0.6	0.000	0.411	0.000	0.000	0.000	0.411	0.000	0.000	0.000	0.000	0.000	0.001	0.000
0.7	0.000	0.494	0.000	0.000	0.000	0.494	0.000	0.000	0.000	0.000	0.000	0.001	0.000
0.8	0.000	0.609	0.000	0.000	0.000	0.609	0.000	0.000	0.000	0.000	0.000	0.002	0.000
0.9	0.000	0.768	0.000	0.000	0.000	0.769	0.000	0.000	0.000	0.000	0.000	0.004	0.000
1	0.000	0.976	0.000	0.000	0.000	0.977	0.000	0.000	0.000	0.000	0.000	0.009	0.000
1.1	0.000	1.215	0.000	0.000	0.000	1.218	0.000	0.000	0.000	0.000	0.000	0.018	0.000
1.2	0.000	1.462	0.000	0.000	0.000	1.469	0.000	0.000	0.000	0.000	0.000	0.032	0.000
1.3	0.000	1.701	0.000	0.000	0.000	1.713	0.000	0.000	0.000	0.000	0.000	0.051	0.000
1.4	0.000	1.926	0.000	0.000	0.000	1.943	0.000	0.000	0.000	0.000	0.000	0.075	0.000
1.5	0.000	2.137	0.000	0.000	0.000	2.160	0.000	0.000	0.000	0.000	0.000	0.102	0.000
1.6	0.000	2.333	0.000	0.000	0.000	2.364	0.000	0.000	0.000	0.000	0.000	0.133	0.000
1.7	0.000	2.518	0.000	0.000	0.000	2.556	0.000	0.000	0.000	0.000	0.000	0.168	0.000
1.8	0.000	2.693	0.000	0.000	0.000	2.738	0.000	0.000	0.000	0.000	0.000	0.205	0.000

Table II-17: Dimensionless post-buckling results of cases with symmetric and anti-symmetric modes, i_{max} and j_{max} = 4, for paperboard panel from (Nordstrand, 2004a) with anti-symmetric geometric imperfection $A_{0\,1,2} = 0.2\,h$.

Load ratio $P / P_{crit\ 1,1}$	Case 5(vii): i =1, 2, 3, 4, j=1, 2, 3, 4															
	$A_{1,1}/h$	$A_{1,2}/h$	$A_{1,3}/h$	$A_{1,4}/h$	$A_{2,1}/h$	$A_{2,2}/h$	$A_{2,3}/h$	$A_{2,4}/h$	$A_{3,1}/h$	$A_{3,2}/h$	$A_{3,3}/h$	$A_{3,4}/h$	$A_{4,1}/h$	$A_{4,2}/h$	$A_{4,3}/h$	$A_{4,4}/h$
0	0	0.199	0	0	0	0	0	0	0	0	0	0	0	0	0	0
0.1	0.000	0.218	0.000	0.000	0.000	0.000	0.000	0.000	0.000	0.000	0.000	0.000	0.000	0.000	0.000	0.000
0.2	0.000	0.241	0.000	0.000	0.000	0.000	0.000	0.000	0.000	0.000	0.000	0.000	0.000	0.000	0.000	0.000
0.3	0.000	0.269	0.000	0.000	0.000	0.000	0.000	0.000	0.000	0.000	0.000	0.000	0.000	0.000	0.000	0.000
0.4	0.000	0.305	0.000	0.000	0.000	0.000	0.000	0.000	0.000	0.000	0.000	0.000	0.000	0.000	0.000	0.000
0.5	0.000	0.350	0.000	0.000	0.000	0.000	0.000	0.000	0.000	0.000	0.000	0.000	0.000	0.000	0.000	0.000
0.6	0.000	0.411	0.000	0.000	0.000	0.000	0.000	0.000	0.000	0.001	0.000	0.000	0.000	0.000	0.000	0.000
0.7	0.000	0.494	0.000	0.001	0.000	0.000	0.000	0.000	0.000	0.001	0.000	0.000	0.000	0.000	0.000	0.000
0.8	0.000	0.609	0.000	0.002	0.000	0.000	0.000	0.000	0.000	0.002	0.000	0.000	0.000	0.000	0.000	0.000
0.9	0.000	0.770	0.000	0.004	0.000	0.000	0.000	0.000	0.000	0.004	0.000	0.000	0.000	0.000	0.000	0.000
1	0.000	0.981	0.000	0.009	0.000	0.000	0.000	0.000	0.000	0.009	0.000	0.000	0.000	0.000	0.000	0.000
1.1	0.000	1.229	0.000	0.018	0.000	0.000	0.000	0.000	0.000	0.018	0.000	0.000	0.000	0.000	0.000	0.000
1.2	0.000	1.493	0.000	0.032	0.000	0.000	0.000	0.000	0.000	0.032	0.000	0.001	0.000	0.000	0.000	0.000
1.3	0.000	1.755	0.000	0.052	0.000	0.000	0.000	0.000	0.000	0.052	0.000	0.002	0.000	0.000	0.000	0.000
1.4	0.000	2.008	0.000	0.077	0.000	0.000	0.000	0.000	0.000	0.076	0.000	0.004	0.000	0.000	0.000	0.000
1.5	0.000	2.252	0.000	0.106	0.000	0.000	0.000	0.000	0.000	0.104	0.000	0.007	0.000	0.000	0.000	0.000
1.6	0.000	2.485	0.000	0.139	0.000	0.000	0.000	0.000	0.000	0.137	0.000	0.012	0.000	0.000	0.000	0.000
1.7	0.000	2.710	0.000	0.175	0.000	0.000	0.000	0.000	0.000	0.173	0.000	0.018	0.000	0.000	0.000	0.000
1.8	0.000	2.926	0.000	0.214	0.000	0.000	0.000	0.000	0.000	0.212	0.000	0.025	0.000	0.000	0.000	0.000

Table II-18: Dimensionless post-buckling results of cases with symmetric and anti-symmetric modes, i_{max} and j_{max} = 5, for paperboard panel from (Nordstrand, 2004a) with anti-symmetric geometric imperfection $A_{0\,1,2} = 0.2\,h$.[7]

Load ratio $P / P_{crit\ 1,1}$	Case 5(viii): i =1, 2, 3, 4, 5, j=1, 2, 3, 4, 5												
	$A_{1,1} / h$	$A_{1,2} / h$	$A_{1,3} / h$	$A_{1,4} / h$	$A_{1,5} / h$	$A_{2,1} / h$	$A_{2,2} / h$	$A_{2,3} / h$	$A_{2,4} / h$	$A_{2,5} / h$	$A_{3,1} / h$	$A_{3,2} / h$	$A_{3,3} / h$
0	0	0.199	0	0	0	0	0	0	0	0	0	0	0
0.2	0.000	0.241	0.000	0.000	0.000	0.000	0.000	0.000	0.000	0.000	0.000	0.000	0.000
0.4	0.000	0.305	0.000	0.000	0.000	0.000	0.000	0.000	0.000	0.000	0.000	0.000	0.000
0.5	0.000	0.350	0.000	0.000	0.000	0.000	0.000	0.000	0.000	0.000	0.000	0.000	0.000
0.6	0.000	0.411	0.000	0.000	0.000	0.000	0.000	0.000	0.000	0.000	0.000	0.001	0.000
0.7	0.000	0.494	0.000	0.001	0.000	0.000	0.000	0.000	0.000	0.000	0.000	0.001	0.000
0.8	0.000	0.609	0.000	0.002	0.000	0.000	0.000	0.000	0.000	0.000	0.000	0.002	0.000
0.9	0.000	0.770	0.000	0.004	0.000	0.000	0.000	0.000	0.000	0.000	0.000	0.004	0.000
1	0.000	0.981	0.000	0.009	0.000	0.000	0.000	0.000	0.000	0.000	0.000	0.009	0.000
1.1	0.000	1.229	0.000	0.018	0.000	0.000	0.000	0.000	0.000	0.000	0.000	0.018	0.000
1.2	0.000	1.493	0.000	0.032	0.000	0.000	0.000	0.000	0.000	0.000	0.000	0.032	0.000
1.3	0.000	1.755	0.000	0.052	0.000	0.000	0.000	0.000	0.000	0.000	0.000	0.052	0.000
1.4	0.000	2.008	0.000	0.077	0.000	0.000	0.000	0.000	0.000	0.000	0.000	0.076	0.000
1.5	0.000	2.252	0.000	0.106	0.000	0.000	0.000	0.000	0.000	0.000	0.000	0.105	0.000
1.6	0.000	2.485	0.000	0.138	0.000	0.000	0.000	0.000	0.000	0.000	0.000	0.137	0.000
1.7	0.000	2.710	0.000	0.175	0.000	0.000	0.000	0.000	0.000	0.000	0.000	0.173	0.000
1.8	0.000	2.927	0.000	0.214	0.000	0.000	0.000	0.000	0.000	0.000	0.000	0.213	0.000

[7] Continued in Table II-19.

Table II-19: Dimensionless post-buckling results of cases with symmetric and anti-symmetric modes, i_{max} and j_{max} = 5, for paperboard panel from (Nordstrand, 2004a) with anti-symmetric geometric imperfection $A_{0\,1,2} = 0.2\,h$.[8]

Load ratio	Case 5(viii): i =1, 2, 3, 4, 5, j=1, 2, 3, 4, 5											
$P / P_{crit\ 1,1}$	$A_{3,4} / h$	$A_{3,5} / h$	$A_{4,1} / h$	$A_{4,2} / h$	$A_{4,3} / h$	$A_{4,4} / h$	$A_{4,5} / h$	$A_{5,1} / h$	$A_{5,2} / h$	$A_{5,3} / h$	$A_{5,4} / h$	$A_{5,5} / h$
0	0	0	0	0	0	0	0	0	0	0	0	0
0.2	0.000	0.000	0.000	0.000	0.000	0.000	0.000	0.000	0.000	0.000	0.000	0.000
0.4	0.000	0.000	0.000	0.000	0.000	0.000	0.000	0.000	0.000	0.000	0.000	0.000
0.5	0.000	0.000	0.000	0.000	0.000	0.000	0.000	0.000	0.000	0.000	0.000	0.000
0.6	0.000	0.000	0.000	0.000	0.000	0.000	0.000	0.000	0.000	0.000	0.000	0.000
0.7	0.000	0.000	0.000	0.000	0.000	0.000	0.000	0.000	0.000	0.000	0.000	0.000
0.8	0.000	0.000	0.000	0.000	0.000	0.000	0.000	0.000	0.000	0.000	0.000	0.000
0.9	0.000	0.000	0.000	0.000	0.000	0.000	0.000	0.000	0.000	0.000	0.000	0.000
1	0.000	0.000	0.000	0.000	0.000	0.000	0.000	0.000	0.000	0.000	0.000	0.000
1.1	0.000	0.000	0.000	0.000	0.000	0.000	0.000	0.000	0.000	0.000	0.000	0.000
1.2	0.001	0.000	0.000	0.000	0.000	0.000	0.000	0.000	0.001	0.000	0.000	0.000
1.3	0.002	0.000	0.000	0.000	0.000	0.000	0.000	0.000	0.001	0.000	0.000	0.000
1.4	0.004	0.000	0.000	0.000	0.000	0.000	0.000	0.000	0.002	0.000	0.000	0.000
1.5	0.007	0.000	0.000	0.000	0.000	0.000	0.000	0.000	0.003	0.000	0.000	0.000
1.6	0.011	0.000	0.000	0.000	0.000	0.000	0.000	0.000	0.004	0.000	0.000	0.000
1.7	0.017	0.000	0.000	0.000	0.000	0.000	0.000	0.000	0.006	0.000	0.000	0.000
1.8	0.025	0.000	0.000	0.000	0.000	0.000	0.000	0.000	0.008	0.000	0.001	0.000

[8] Continued from Table II-18.

Table II-20: Comparison of displacement *w* (0.5 *a*,0.5 *b*) relative to the two-term Case 6(i) paperboard panel from (Nordstrand, 2004a) with panel imperfection $A_{0\,1,1}$ = 0.2 *h*, $A_{0\,1,2}$ = 0.1 *h,* for multi-term cases with symmetric and anti-symmetric modes of *w,* i_{max} and j_{max} up to 5.

Load ratio $P/P_{crit\,1,1}$	% Δ*w* (0.5 *a*,0.5 *b*) relative to *w* (0.5 *a*, 0.5 *b*) Case 6(i): *i*=1, *j*=1, 2							
	Case 6(v): *i*=1, 2, *j*=1, 2	Case 6(ii): *i*=1, *j*=1, 2, 3	Case 6(vi): *i*=1, 2, 3, *j*=1, 2, 3	Case 6(iii): *i*=1, *j*=1, 2, 3, 4	Case 6(vii): *i*=1, 2, 3, 4, *j*=1, 2, 3, 4	Case 6(iv): *i*=1, *j*=1, 2, 3, 4, 5	Case 6(viii): *i*=1, 2, 3, 4, 5, *j*=1, 2, 3, 4, 5	FEM Case A
0	0.00%	0.00%	0.00%	0.00%	0.00%	0.00%	0.00%	0.00%
0.2	0.00%	-0.01%	-0.02%	-0.01%	-0.02%	-0.01%	-0.02%	-0.43%
0.4	0.00%	-0.04%	-0.07%	-0.03%	-0.07%	-0.03%	-0.06%	-1.48%
0.6	0.00%	-0.11%	-0.20%	-0.09%	-0.18%	-0.07%	-0.16%	-5.38%
0.8	0.00%	-0.24%	-0.44%	-0.11%	-0.31%	-0.05%	-0.25%	-14.40%
1	0.00%	0.91%	0.54%	1.35%	1.00%	1.51%	1.15%	-24.26%
1.1	0.00%	4.07%	3.57%	4.17%	3.70%	4.40%	3.92%	-24.49%
1.2	0.00%	9.21%	8.72%	8.58%	8.11%	9.06%	8.55%	-21.83%
1.3	0.00%	12.48%	12.27%	11.81%	11.58%	12.77%	12.48%	-19.93%
1.4	0.00%	13.30%	13.45%	12.85%	12.99%	14.51%	14.54%	-19.14%
1.5	0.00%	13.04%	13.60%	12.77%	13.33%	15.29%	15.69%	-18.70%
1.6	0.00%	12.46%	13.46%	12.30%	13.30%	15.80%	16.61%	-18.13%
1.7	0.00%	11.79%	13.23%	11.69%	13.13%	16.25%	17.50%	-17.39%
1.8	0.00%	11.07%	12.97%	11.01%	12.92%	16.69%	18.41%	-16.50%

Table II-21: Dimensionless post-buckling results of cases with symmetric and anti-symmetric modes, i=1 and j_{max} up to 5, for paperboard panel from (Nordstrand, 2004a) with symmetric and anti-symmetric geometric imperfection $A_{0\ 1,1} = 0.2\ h$, $A_{0\ 1,2} = 0.1\ h$.

Load ratio $P / P_{crit\ 1,1}$	Case 6(i): i=1, j=1, 2		Case 6(ii): i=1, j=1, 2, 3			Case 6(iii): i=1, j=1, 2, 3, 4				Case 6(iv): i=1, j=1, 2, 3, 4, 5				
	$A_{1,1} / h$	$A_{1,2} / h$	$A_{1,1} / h$	$A_{1,2} / h$	$A_{1,3} / h$	$A_{1,1} / h$	$A_{1,2} / h$	$A_{1,3} / h$	$A_{1,4} / h$	$A_{1,1} / h$	$A_{1,2} / h$	$A_{1,3} / h$	$A_{1,4} / h$	$A_{1,5} / h$
0.0	0.199	0.0995	0.199	0.0995	0.000	0.199	0.0995	0.000	0.000	0.199	0.0995	0.000	0.000	0.000
0.2	0.248	0.1205	0.248	0.1205	0.000	0.248	0.1205	0.000	0.000	0.248	0.1205	0.000	0.000	0.000
0.3	0.282	0.1345	0.282	0.1345	0.000	0.282	0.1345	0.000	0.000	0.282	0.1345	0.000	0.000	0.000
0.4	0.327	0.1521	0.327	0.1521	0.000	0.327	0.1521	0.000	0.000	0.327	0.1521	0.000	0.000	0.000
0.5	0.387	0.1746	0.387	0.1746	0.000	0.387	0.1746	0.000	0.000	0.387	0.1746	0.000	0.000	0.000
0.6	0.471	0.2040	0.471	0.2040	0.001	0.471	0.2040	0.001	0.000	0.471	0.2040	0.001	0.000	0.000
0.7	0.591	0.2426	0.592	0.2426	0.001	0.592	0.2427	0.001	0.001	0.592	0.2427	0.001	0.001	0.000
0.8	0.763	0.2923	0.765	0.2921	0.004	0.766	0.2924	0.003	0.002	0.766	0.2925	0.004	0.002	0.000
0.9	0.995	0.3507	1.003	0.3491	0.009	1.005	0.3505	0.009	0.005	1.006	0.3507	0.009	0.005	0.001
1.0	1.271	0.4100	1.304	0.4001	0.021	1.309	0.4051	0.021	0.009	1.310	0.4058	0.021	0.009	0.002
1.1	1.566	0.4606	1.678	0.4145	0.048	1.678	0.4315	0.047	0.015	1.679	0.4331	0.048	0.015	0.003
1.2	1.865	0.4944	2.138	0.3633	0.101	2.121	0.4019	0.096	0.022	2.127	0.4036	0.098	0.022	0.006
1.3	2.165	0.5054	2.611	0.2872	0.176	2.590	0.3369	0.170	0.025	2.607	0.3367	0.176	0.025	0.011
1.4	2.459	0.4949	3.050	0.2246	0.263	3.033	0.2749	0.257	0.026	3.069	0.2717	0.272	0.025	0.019
1.5	2.739	0.4731	3.452	0.1788	0.356	3.440	0.2259	0.351	0.026	3.505	0.2196	0.378	0.024	0.031
1.6	2.998	0.4483	3.824	0.1459	0.451	3.815	0.1888	0.448	0.024	3.918	0.1797	0.492	0.022	0.046
1.7	3.239	0.4243	4.168	0.1218	0.547	4.162	0.1607	0.544	0.023	4.309	0.1493	0.609	0.020	0.065
1.8	3.463	0.4022	4.488	0.1039	0.641	4.484	0.1391	0.639	0.022	4.682	0.1260	0.728	0.018	0.088
1.9	3.674	0.3821	4.787	0.0902	0.734	4.784	0.1222	0.732	0.021	5.037	0.1079	0.847	0.016	0.113

Table II-22: Dimensionless post-buckling results of cases with symmetric and anti-symmetric modes, i_{max} and j_{max} up to 3, for paperboard panel from (Nordstrand, 2004a) with symmetric and anti-symmetric geometric imperfection $A_{0\ 1,1} = 0.2\ h$, $A_{0\ 1,2} = 0.1\ h$.

Load ratio $P / P_{crit\ 1,1}$	Case 6(v): i =1, 2, j=1, 2				Case 6(vi): i =1, 2, 3, j=1, 2, 3								
	$A_{1,1} / h$	$A_{1,2} / h$	$A_{2,1} / h$	$A_{2,2} / h$	$A_{1,1} / h$	$A_{1,2} / h$	$A_{1,3} / h$	$A_{2,1} / h$	$A_{2,2} / h$	$A_{2,3} / h$	$A_{3,1} / h$	$A_{3,2} / h$	$A_{3,3} / h$
0	0.199	0.0995	0.000	0.000	0.199	0.100	0.000	0.000	0.000	0.000	0.000	0.000	0.000
0.2	0.248	0.1205	0.000	0.000	0.248	0.120	0.000	0.000	0.000	0.000	0.000	0.000	0.000
0.3	0.282	0.1345	0.000	0.000	0.282	0.135	0.000	0.000	0.000	0.000	0.000	0.000	0.000
0.4	0.327	0.1521	0.000	0.000	0.327	0.152	0.000	0.000	0.000	0.000	0.000	0.000	0.000
0.5	0.387	0.1746	0.000	0.000	0.387	0.175	0.000	0.000	0.000	0.000	0.000	0.000	0.000
0.6	0.471	0.2040	0.000	0.000	0.471	0.204	0.001	0.000	0.000	0.000	0.000	0.000	0.000
0.7	0.591	0.2426	0.000	0.000	0.592	0.243	0.001	0.000	0.000	0.000	0.001	0.001	0.000
0.8	0.763	0.2923	0.000	0.000	0.765	0.292	0.004	0.000	0.000	0.000	0.002	0.001	0.000
0.9	0.995	0.3507	0.000	0.000	1.004	0.350	0.009	0.000	0.000	0.000	0.004	0.002	0.000
1	1.271	0.4100	0.000	0.000	1.307	0.402	0.021	0.000	0.000	0.000	0.009	0.004	0.001
1.1	1.566	0.4606	0.000	0.000	1.683	0.419	0.048	0.000	0.000	0.000	0.015	0.007	0.002
1.2	1.865	0.4944	0.000	0.000	2.148	0.371	0.101	0.000	0.000	0.000	0.025	0.010	0.006
1.3	2.165	0.5054	0.000	0.000	2.634	0.295	0.178	0.000	0.000	0.000	0.038	0.012	0.011
1.4	2.459	0.4949	0.000	0.000	3.092	0.231	0.269	0.000	0.000	0.000	0.053	0.013	0.021
1.5	2.739	0.4731	0.000	0.000	3.517	0.184	0.368	0.000	0.000	0.000	0.072	0.014	0.034
1.6	2.998	0.4483	0.000	0.000	3.915	0.150	0.472	0.000	0.000	0.000	0.092	0.014	0.051
1.7	3.239	0.4243	0.000	0.000	4.289	0.124	0.579	0.000	0.000	0.000	0.114	0.014	0.072
1.8	3.463	0.4022	0.000	0.000	4.640	0.105	0.688	0.000	0.000	0.000	0.138	0.013	0.098
1.9	3.674	0.3821	0.000	0.000	4.972	0.091	0.796	0.000	0.000	0.000	0.162	0.013	0.127

Table II-23: Dimensionless post-buckling results of cases with symmetric and anti-symmetric modes, i_{max} and j_{max} = 4, for paperboard panel from (Nordstrand, 2004a) with symmetric and anti-symmetric geometric imperfection $A_{0\ 1,1} = 0.2\ h$, $A_{0\ 1,2} = 0.1\ h$.

Load ratio $P / P_{crit\ 1,1}$	Case 6(vii): i =1, 2, 3, 4, j=1, 2, 3, 4															
	$A_{1,1}/h$	$A_{1,2}/h$	$A_{1,3}/h$	$A_{1,4}/h$	$A_{2,1}/h$	$A_{2,2}/h$	$A_{2,3}/h$	$A_{2,4}/h$	$A_{3,1}/h$	$A_{3,2}/h$	$A_{3,3}/h$	$A_{3,4}/h$	$A_{4,1}/h$	$A_{4,2}/h$	$A_{4,3}/h$	$A_{4,4}/h$
0	0.199	0.0995	0.000	0.000	0.000	0.000	0.000	0.000	0.000	0.000	0.000	0.000	0.000	0.000	0.000	0.000
0.2	0.248	0.1205	0.000	0.000	0.000	0.000	0.000	0.000	0.000	0.000	0.000	0.000	0.000	0.000	0.000	0.000
0.3	0.282	0.1345	0.000	0.000	0.000	0.000	0.000	0.000	0.000	0.000	0.000	0.000	0.000	0.000	0.000	0.000
0.4	0.327	0.1521	0.000	0.000	0.000	0.000	0.000	0.000	0.000	0.000	0.000	0.000	0.000	0.000	0.000	0.000
0.5	0.387	0.1746	0.000	0.000	0.000	0.000	0.000	0.000	0.000	0.000	0.000	0.000	0.000	0.000	0.000	0.000
0.6	0.471	0.2040	0.001	0.000	0.000	0.000	0.000	0.000	0.000	0.000	0.000	0.000	0.000	0.000	0.000	0.000
0.7	0.592	0.2427	0.001	0.001	0.000	0.000	0.000	0.000	0.001	0.001	0.000	0.000	0.000	0.000	0.000	0.000
0.8	0.766	0.2926	0.003	0.002	0.000	0.000	0.000	0.000	0.002	0.001	0.000	0.000	0.000	0.000	0.000	0.000
0.9	1.007	0.3510	0.009	0.005	0.000	0.000	0.000	0.000	0.004	0.002	0.001	0.000	0.000	0.000	0.000	0.000
1	1.312	0.4067	0.021	0.009	0.000	0.000	0.000	0.000	0.009	0.004	0.001	0.000	0.000	0.000	0.000	0.000
1.1	1.683	0.4357	0.047	0.015	0.000	0.000	0.000	0.000	0.015	0.007	0.003	0.001	0.000	0.000	0.000	0.000
1.2	2.132	0.4094	0.096	0.022	0.000	0.000	0.000	0.000	0.025	0.010	0.006	0.002	0.000	0.000	0.000	0.000
1.3	2.613	0.3453	0.172	0.025	0.000	0.000	0.000	0.000	0.038	0.012	0.011	0.002	0.000	0.000	0.000	0.000
1.4	3.075	0.2824	0.263	0.026	0.000	0.000	0.000	0.000	0.053	0.014	0.021	0.003	0.000	0.000	0.000	0.000
1.5	3.505	0.2320	0.363	0.026	0.000	0.000	0.000	0.000	0.071	0.015	0.034	0.004	0.000	0.000	0.000	0.000
1.6	3.907	0.1932	0.469	0.025	0.000	0.000	0.000	0.000	0.092	0.015	0.051	0.004	0.000	0.000	0.000	0.000
1.7	4.283	0.1635	0.577	0.023	0.000	0.000	0.000	0.000	0.114	0.015	0.072	0.005	0.000	0.000	0.000	0.000
1.8	4.636	0.1403	0.685	0.022	0.000	0.000	0.000	0.000	0.138	0.015	0.098	0.005	0.000	0.000	0.000	0.000
1.9	4.969	0.1220	0.794	0.021	0.000	0.000	0.000	0.000	0.162	0.014	0.127	0.005	0.000	0.000	0.000	0.000

Table II-24: Dimensionless post-buckling results of cases with symmetric and anti-symmetric modes, i_{max} and j_{max} = 5, for paperboard panel from (Nordstrand, 2004a) with symmetric and anti-symmetric geometric imperfection $A_{0\ 1,1} = 0.2\ h$, $A_{0\ 1,2} = 0.1\ h$.[9]

Load ratio $P / P_{crit\ 1,1}$	Case 6(viii): i =1, 2, 3, 4, 5, j=1, 2, 3, 4, 5												
	$A_{1,1} / h$	$A_{1,2} / h$	$A_{1,3} / h$	$A_{1,4} / h$	$A_{1,5} / h$	$A_{2,1} / h$	$A_{2,2} / h$	$A_{2,3} / h$	$A_{2,4} / h$	$A_{2,5} / h$	$A_{3,1} / h$	$A_{3,2} / h$	$A_{3,3} / h$
0	0.199	0.0995	0.000	0.000	0.000	0.000	0.000	0.000	0.000	0.000	0.000	0.000	0.000
0.2	0.248	0.1205	0.000	0.000	0.000	0.000	0.000	0.000	0.000	0.000	0.000	0.000	0.000
0.4	0.327	0.1521	0.000	0.000	0.000	0.000	0.000	0.000	0.000	0.000	0.000	0.000	0.000
0.5	0.387	0.1747	0.000	0.000	0.000	0.000	0.000	0.000	0.000	0.000	0.000	0.000	0.000
0.6	0.471	0.2040	0.001	0.000	0.000	0.000	0.000	0.000	0.000	0.000	0.000	0.000	0.000
0.7	0.592	0.2428	0.001	0.001	0.000	0.000	0.000	0.000	0.000	0.000	0.001	0.001	0.000
0.8	0.766	0.2926	0.003	0.002	0.000	0.000	0.000	0.000	0.000	0.000	0.002	0.001	0.000
0.9	1.007	0.3512	0.009	0.005	0.001	0.000	0.000	0.000	0.000	0.000	0.004	0.002	0.000
1	1.312	0.4074	0.021	0.009	0.002	0.000	0.000	0.000	0.000	0.000	0.009	0.004	0.001
1.1	1.684	0.4373	0.048	0.015	0.003	0.000	0.000	0.000	0.000	0.000	0.015	0.007	0.003
1.2	2.137	0.4112	0.098	0.022	0.006	0.000	0.000	0.000	0.000	0.000	0.025	0.010	0.005
1.3	2.629	0.3453	0.178	0.025	0.010	0.000	0.000	0.000	0.000	0.000	0.038	0.012	0.011
1.4	3.110	0.2796	0.277	0.026	0.018	0.000	0.000	0.000	0.000	0.000	0.054	0.014	0.020
1.5	3.570	0.2261	0.390	0.024	0.030	0.000	0.000	0.000	0.000	0.000	0.072	0.014	0.034
1.6	4.011	0.1846	0.512	0.023	0.045	0.000	0.000	0.000	0.000	0.000	0.093	0.015	0.052
1.7	4.435	0.1527	0.641	0.021	0.064	0.000	0.000	0.000	0.000	0.000	0.117	0.015	0.074
1.8	4.844	0.1280	0.775	0.019	0.086	0.000	0.000	0.000	0.000	0.000	0.142	0.014	0.102

[9] Continued in Table II-25.

Table II-25: Post-buckling results showing out-of-plane displacement amplitudes of cases with symmetric and anti-symmetric modes, i_{max} and j_{max} = 5, for paperboard panel from (Nordstrand, 2004a) with symmetric and anti-symmetric geometric imperfection $A_{0\ 1,1} = 0.2\ h$, $A_{0\ 1,2} = 0.1\ h$.[10]

Load ratio	Case 6(viii): i =1, 2, 3, 4, 5, j=1, 2, 3, 4, 5											
$P / P_{crit\ 1,1}$	$A_{3,4} / h$	$A_{3,5} / h$	$A_{4,1} / h$	$A_{4,2} / h$	$A_{4,3} / h$	$A_{4,4} / h$	$A_{4,5} / h$	$A_{5,1} / h$	$A_{5,2} / h$	$A_{5,3} / h$	$A_{5,4} / h$	$A_{5,5} / h$
0	0.000	0.000	0.000	0.000	0.000	0.000	0.000	0.000	0.000	0.000	0.000	0.000
0.2	0.000	0.000	0.000	0.000	0.000	0.000	0.000	0.000	0.000	0.000	0.000	0.000
0.4	0.000	0.000	0.000	0.000	0.000	0.000	0.000	0.000	0.000	0.000	0.000	0.000
0.5	0.000	0.000	0.000	0.000	0.000	0.000	0.000	0.000	0.000	0.000	0.000	0.000
0.6	0.000	0.000	0.000	0.000	0.000	0.000	0.000	0.000	0.000	0.000	0.000	0.000
0.7	0.000	0.000	0.000	0.000	0.000	0.000	0.000	0.000	0.000	0.000	0.000	0.000
0.8	0.000	0.000	0.000	0.000	0.000	0.000	0.000	0.000	0.000	0.000	0.000	0.000
0.9	0.000	0.000	0.000	0.000	0.000	0.000	0.000	0.000	0.000	0.000	0.000	0.000
1	0.000	0.000	0.000	0.000	0.000	0.000	0.000	0.000	0.000	0.000	0.000	0.000
1.1	0.001	0.000	0.000	0.000	0.000	0.000	0.000	0.000	0.000	0.000	0.000	0.000
1.2	0.002	0.000	0.000	0.000	0.000	0.000	0.000	0.000	0.000	0.000	0.000	0.000
1.3	0.003	0.001	0.000	0.000	0.000	0.000	0.000	0.001	0.000	0.000	0.000	0.000
1.4	0.003	0.001	0.000	0.000	0.000	0.000	0.000	0.001	0.000	0.000	0.000	0.000
1.5	0.004	0.003	0.000	0.000	0.000	0.000	0.000	0.001	0.000	0.001	0.000	0.000
1.6	0.004	0.005	0.000	0.000	0.000	0.000	0.000	0.001	0.001	0.001	0.000	0.000
1.7	0.005	0.009	0.000	0.000	0.000	0.000	0.000	0.002	0.001	0.002	0.000	0.000
1.8	0.005	0.014	0.000	0.000	0.000	0.000	0.000	0.002	0.001	0.003	0.000	0.000

[10] Continued from Table II-24.

Table II-26: Comparison of nonzero symmetric displacement modes of case 6(viii) with case 4(viii)[11].

Load ratio	Difference in displacement mode amplitudes of Case 6(viii) relative to case 4(viii)							
$P/P_{crit\ 1,1}$	$A_{1,1}/h$	$A_{1,3}/h$	$A_{1,5}/h$	$A_{3,1}/h$	$A_{3,3}/h$	$A_{3,5}/h$	$A_{5,1}/h$	$A_{5,3}/h$
0	0.00%							
0.1	-0.07%	-26.22%	1441.30%	137.32%	195.04%	-1136.35%	138.00%	-26.12%
0.2	-0.18%	-25.80%	1388.76%	132.83%	188.54%	-1109.09%	133.69%	-26.87%
0.3	-0.37%	-25.43%	1321.10%	127.06%	180.13%	-1075.71%	128.25%	-27.91%
0.4	-0.68%	-25.19%	1231.98%	119.47%	168.96%	-1034.27%	121.17%	-29.43%
0.5	-1.23%	-25.31%	1112.10%	109.19%	153.72%	-982.38%	111.68%	-31.80%
0.6	-2.22%	-26.20%	949.30%	94.95%	132.43%	-917.88%	98.62%	-35.64%
0.7	-4.01%	-28.60%	734.34%	75.35%	102.85%	-842.95%	80.63%	-41.88%
0.8	-6.87%	-32.95%	483.30%	50.82%	65.17%	-779.88%	58.05%	-51.29%
0.9	-10.15%	-37.52%	260.16%	27.08%	27.40%	-822.83%	36.45%	-63.42%
1	-12.09%	-38.67%	118.12%	11.07%	0.69%	-1766.63%	23.07%	-80.39%
1.1	-11.43%	-33.90%	43.46%	2.98%	-12.31%	640.13%	17.81%	-142.29%
1.2	-8.09%	-23.01%	9.03%	-0.08%	-13.69%	111.84%	15.50%	77.92%
1.3	-4.54%	-12.39%	-1.34%	-0.67%	-9.45%	24.60%	12.48%	8.41%
1.4	-2.37%	-6.15%	-2.50%	-0.58%	-5.50%	5.10%	9.22%	1.34%
1.5	-1.23%	-3.05%	-1.80%	-0.39%	-3.07%	0.70%	6.51%	0.09%
1.6	-0.65%	-1.56%	-1.09%	-0.25%	-1.71%	-0.19%	4.47%	-0.13%
1.7	-0.35%	-0.82%	-0.64%	-0.15%	-0.98%	-0.29%	3.01%	-0.14%
1.8	-0.19%	-0.45%	-0.37%	-0.09%	-0.58%	-0.23%	1.99%	-0.12%

[11] The grey background indicates that for one or both cases the dimensionless displacement was zero within three decimal places.

Table II-27: Comparison of nonzero anti-symmetric displacement modes of case 6(viii) with case 5(viii)[12].

Load ratio	Difference in displacement mode amplitudes of Case 6(viii) relative to case 5(viii) normalised by initial values					
$P/P_{crit\,1,1}$	$A_{1,2}/h$	$A_{1,4}/h$	$A_{3,2}/h$	$A_{3,4}/h$	$A_{5,2}/h$	$A_{5,4}/h$
0	0.00%					
0.1	-0.01%	-15.06%	-57.44%	-317.02%	-42.63%	-91.91%
0.2	-0.02%	-13.23%	-56.70%	-327.47%	-41.52%	-92.11%
0.3	-0.06%	-10.90%	-55.77%	-342.10%	-40.14%	-92.37%
0.4	-0.13%	-7.89%	-54.56%	-363.57%	-38.40%	-92.75%
0.5	-0.30%	-3.99%	-53.02%	-397.19%	-36.19%	-93.32%
0.6	-0.69%	0.95%	-51.09%	-454.77%	-33.48%	-94.23%
0.7	-1.65%	6.60%	-48.99%	-568.00%	-30.59%	-95.81%
0.8	-3.94%	10.92%	-47.65%	-861.64%	-29.04%	-98.61%
0.9	-8.77%	9.42%	-49.03%	-3197.17%	-32.00%	-103.26%
1	-16.95%	-0.34%	-54.01%	960.57%	-41.00%	-110.02%
1.1	-28.86%	-15.25%	-60.93%	286.11%	-52.76%	-119.22%
1.2	-44.91%	-33.47%	-68.61%	111.20%	-64.08%	-131.08%
1.3	-60.64%	-52.15%	-76.04%	27.79%	-73.33%	-144.89%
1.4	-72.16%	-66.76%	-81.94%	-18.76%	-79.81%	-165.08%
1.5	-79.92%	-76.85%	-86.25%	-45.97%	-84.15%	-213.28%
1.6	-85.14%	-83.63%	-89.36%	-62.63%	-87.13%	-659.64%
1.7	-88.73%	-88.20%	-91.62%	-73.29%	-89.29%	63.01%
1.8	-91.25%	-91.33%	-93.30%	-80.39%	-90.92%	-34.17%

[12] The grey background indicates that for one or both cases the dimensionless displacement was zero within three decimal places.

Table II-28: Comparison of displacement *w* (0.5 *a*,0.5 *b*) for multi-term cases with symmetric and anti-symmetric modes of *w*, i_{max} and j_{max} up to 5, relative to the four-term Case 7(i) paperboard panel from (Nordstrand, 2004a) with panel imperfection $A_{0\,1,1} = 0.2\,h$, $A_{0\,1,2} = 0.2\,h$.

Load ratio $P/P_{crit\,1,1}$	% Δ*w* (0.5 *a*,0.5 *b*) relative to *w* (0.5 *a*, 0.5 *b*) Case 7(i): *i*=1, 2, *j*=1, 2			
	Case 7(ii): *i*=1, 2, 3, *j*=1, 2, 3	Case 7(iii): *i*=1, 2, 3, 4, *j*=1, 2, 3, 4	Case 7(iv): *i*=1, 2, 3, 4, 5, *j*=1, 2, 3, 4, 5	FEM Case A
0	0.00%	0.00%	0.00%	0.00%
0.1	-0.01%	-0.01%	-0.01%	-0.51%
0.2	-0.03%	-0.03%	-0.02%	-1.27%
0.3	-0.06%	-0.05%	-0.03%	-2.36%
0.4	-0.09%	-0.08%	-0.05%	-4.17%
0.5	-0.15%	-0.12%	-0.06%	-7.15%
0.6	-0.22%	-0.14%	-0.06%	-11.26%
0.7	-0.32%	-0.13%	0.01%	-17.58%
0.8	-0.43%	0.03%	0.28%	-23.98%
0.9	-0.52%	0.54%	0.99%	-34.22%
1	-0.50%	1.78%	2.75%	-37.44%
1.1	0.19%	4.09%	6.48%	-35.52%
1.2	1.49%	6.98%	11.42%	-26.28%
1.3	2.51%	10.06%	16.58%	-16.95%
1.4	3.19%	13.46%	22.02%	-8.85%
1.5	3.63%	17.30%	27.89%	-0.09%
1.6	3.89%	21.67%	34.38%	7.71%
1.7	4.03%	26.68%	41.65%	15.04%
1.8	4.09%			23.08%

Table II-29: Dimensionless post-buckling results of cases with symmetric and anti-symmetric modes, i_{max} and j_{max} up to 3, for paperboard panel from (Nordstrand, 2004a) with symmetric and anti-symmetric geometric imperfection $A_{0\ 1,1} = 0.2\ h$, $A_{0\ 1,2} = 0.2\ h$.

Load ratio $P / P_{crit\ 1,1}$	Case 7(i): i =1, 2, j=1, 2				Case 7(ii): i =1, 2, 3, j=1, 2, 3								
	$A_{1,1} / h$	$A_{1,2} / h$	$A_{2,1} / h$	$A_{2,2} / h$	$A_{1,1} / h$	$A_{1,2} / h$	$A_{1,3} / h$	$A_{2,1} / h$	$A_{2,2} / h$	$A_{2,3} / h$	$A_{3,1} / h$	$A_{3,2} / h$	$A_{3,3} / h$
0	0.199	0.199	0.000	0.000	0.199	0.199	0.000	0.000	0.000	0.000	0.000	0.000	0.000
0.1	0.220	0.218	0.000	0.000	0.220	0.218	0.000	0.000	0.000	0.000	0.000	0.000	0.000
0.2	0.247	0.241	0.000	0.000	0.247	0.241	0.000	0.000	0.000	0.000	0.000	0.000	0.000
0.3	0.279	0.268	0.000	0.000	0.279	0.268	0.000	0.000	0.000	0.000	0.000	0.000	0.000
0.4	0.321	0.303	0.000	0.000	0.321	0.303	0.000	0.000	0.000	0.000	0.000	0.000	0.000
0.5	0.374	0.346	0.000	0.000	0.374	0.346	0.000	0.000	0.000	0.000	0.001	0.000	0.000
0.6	0.443	0.403	0.000	0.000	0.443	0.403	0.000	0.000	0.000	0.000	0.001	0.001	0.000
0.7	0.530	0.476	0.000	0.000	0.530	0.476	0.000	0.000	0.000	0.000	0.002	0.002	0.000
0.8	0.632	0.573	0.000	0.000	0.633	0.573	0.000	0.000	0.000	0.000	0.004	0.003	0.000
0.9	0.724	0.702	0.000	0.000	0.726	0.703	0.000	0.000	0.000	0.000	0.006	0.005	0.001
1	0.746	0.886	0.000	0.000	0.749	0.888	-0.002	0.000	0.000	0.000	0.010	0.009	0.001
1.1	0.631	1.144	0.000	0.000	0.637	1.148	-0.007	0.000	0.000	0.000	0.013	0.018	0.001
1.2	0.474	1.424	0.000	0.000	0.485	1.430	-0.010	0.000	0.000	0.000	0.015	0.031	0.001
1.3	0.361	1.682	0.000	0.000	0.372	1.693	-0.012	0.000	0.000	0.000	0.016	0.050	0.001
1.4	0.285	1.916	0.000	0.000	0.297	1.933	-0.012	0.000	0.000	0.000	0.016	0.074	0.001
1.5	0.234	2.131	0.000	0.000	0.245	2.154	-0.012	0.000	0.000	0.000	0.015	0.102	0.001
1.6	0.197	2.331	0.000	0.000	0.207	2.361	-0.012	0.000	0.000	0.000	0.015	0.133	0.001
1.7	0.170	2.517	0.000	0.000	0.179	2.555	-0.012	0.000	0.000	0.000	0.015	0.167	0.000
1.8	0.149	2.693	0.000	0.000	0.157	2.738	-0.012	0.000	0.000	0.000	0.015	0.204	0.000

Table II-30: Dimensionless post-buckling results of cases with symmetric and anti-symmetric modes, i_{max} and j_{max} = 5, for paperboard panel from (Nordstrand, 2004a) with symmetric and anti-symmetric geometric imperfection $A_{0\ 1,1} = 0.2\ h$, $A_{0\ 1,2} = 0.01\ h$.

Load ratio $P / P_{crit\ 1,1}$	Case 7(iii): i =1, 2, 3, 4, j=1, 2, 3, 4															
	$A_{1,1}/h$	$A_{1,2}/h$	$A_{1,3}/h$	$A_{1,4}/h$	$A_{2,1}/h$	$A_{2,2}/h$	$A_{2,3}/h$	$A_{2,4}/h$	$A_{3,1}/h$	$A_{3,2}/h$	$A_{3,3}/h$	$A_{3,4}/h$	$A_{4,1}/h$	$A_{4,2}/h$	$A_{4,3}/h$	$A_{4,4}/h$
0	0.199	0.199	0.000	0.000	0.000	0.000	0.000	0.000	0.000	0.000	0.000	0.000	0.000	0.000	0.000	0.000
0.1	0.220	0.218	0.000	0.000	0.000	0.000	0.000	0.000	0.000	0.000	0.000	0.000	0.000	0.000	0.000	0.000
0.2	0.247	0.241	0.000	0.000	0.000	0.000	0.000	0.000	0.000	0.000	0.000	0.000	0.000	0.000	0.000	0.000
0.3	0.279	0.268	0.000	0.000	0.000	0.000	0.000	0.000	0.000	0.000	0.000	0.000	0.000	0.000	0.000	0.000
0.4	0.321	0.303	0.000	0.000	0.000	0.000	0.000	0.000	0.000	0.000	0.000	0.000	0.000	0.000	0.000	0.000
0.5	0.374	0.346	0.000	0.001	0.000	0.000	0.000	0.000	0.001	0.000	0.000	0.000	0.000	0.000	0.000	0.000
0.6	0.443	0.403	0.000	0.001	0.000	0.000	0.000	0.000	0.001	0.001	0.000	0.000	0.000	0.000	0.000	0.000
0.7	0.531	0.476	0.000	0.002	0.000	0.000	0.000	0.000	0.002	0.002	0.000	0.000	0.000	0.000	0.000	0.000
0.8	0.635	0.574	0.000	0.004	0.000	0.000	0.000	0.000	0.004	0.003	0.000	0.000	0.000	0.000	0.000	0.000
0.9	0.734	0.705	0.000	0.007	0.000	0.000	0.000	0.000	0.006	0.005	0.001	0.000	0.000	0.000	0.000	0.000
1	0.766	0.891	-0.003	0.013	0.000	0.000	0.000	0.000	0.010	0.009	0.001	0.000	0.000	0.000	0.000	0.000
1.1	0.660	1.157	-0.008	0.021	0.000	0.000	0.000	0.000	0.013	0.017	0.002	0.001	0.000	0.000	0.000	0.000
1.2	0.508	1.453	-0.013	0.034	0.000	0.000	0.000	0.000	0.015	0.031	0.002	0.001	0.000	0.000	0.000	0.000
1.3	0.395	1.734	-0.016	0.053	0.000	0.000	0.000	0.000	0.016	0.051	0.001	0.002	0.000	0.000	0.000	0.000
1.4	0.320	1.997	-0.018	0.078	0.000	0.000	0.000	0.000	0.016	0.075	0.001	0.004	0.000	0.000	0.000	0.000
1.5	0.270	2.245	-0.020	0.106	0.000	0.000	0.000	0.000	0.016	0.104	0.001	0.007	0.000	0.000	0.000	0.000
1.6	0.234	2.482	-0.021	0.139	0.000	0.000	0.000	0.000	0.016	0.136	0.001	0.012	0.000	0.000	0.000	0.000
1.7	0.209	2.708	-0.022	0.175	0.000	0.000	0.000	0.000	0.016	0.172	0.000	0.018	0.000	0.000	0.000	0.000

Table II-31: Dimensionless post-buckling results of cases with symmetric and anti-symmetric modes, i_{max} and j_{max} = 5, for paperboard panel from (Nordstrand, 2004a) with symmetric and anti-symmetric geometric imperfection $A_{0\ 1,1} = 0.2\ h$, $A_{0\ 1,2} = 0.2\ h$.[13]

Load ratio $P / P_{crit\ 1,1}$	Case 7(iv): i =1, 2, 3, 4, 5, j=1, 2, 3, 4, 5												
	$A_{1,1} / h$	$A_{1,2} / h$	$A_{1,3} / h$	$A_{1,4} / h$	$A_{1,5} / h$	$A_{2,1} / h$	$A_{2,2} / h$	$A_{2,3} / h$	$A_{2,4} / h$	$A_{2,5} / h$	$A_{3,1} / h$	$A_{3,2} / h$	$A_{3,3} / h$
0	0.199	0.199	0.000	0.000	0.000	0.000	0.000	0.000	0.000	0.000	0.000	0.000	0.000
0.2	0.247	0.241	0.000	0.000	0.000	0.000	0.000	0.000	0.000	0.000	0.000	0.000	0.000
0.4	0.321	0.303	0.000	0.000	0.000	0.000	0.000	0.000	0.000	0.000	0.000	0.000	0.000
0.5	0.374	0.346	0.000	0.001	0.000	0.000	0.000	0.000	0.000	0.000	0.001	0.000	0.000
0.6	0.443	0.403	0.000	0.001	0.000	0.000	0.000	0.000	0.000	0.000	0.001	0.001	0.000
0.7	0.531	0.476	0.000	0.002	0.001	0.000	0.000	0.000	0.000	0.000	0.002	0.002	0.000
0.8	0.636	0.574	0.000	0.004	0.001	0.000	0.000	0.000	0.000	0.000	0.004	0.003	0.000
0.9	0.735	0.705	0.000	0.007	0.002	0.000	0.000	0.000	0.000	0.000	0.006	0.005	0.001
1	0.770	0.892	-0.002	0.013	0.004	0.000	0.000	0.000	0.000	0.000	0.010	0.009	0.001
1.1	0.671	1.157	-0.008	0.021	0.005	0.000	0.000	0.000	0.000	0.000	0.014	0.017	0.001
1.2	0.524	1.452	-0.012	0.034	0.006	0.000	0.000	0.000	0.000	0.000	0.015	0.031	0.001
1.3	0.415	1.733	-0.015	0.053	0.006	0.000	0.000	0.000	0.000	0.000	0.016	0.051	0.001
1.4	0.341	1.996	-0.016	0.078	0.007	0.000	0.000	0.000	0.000	0.000	0.016	0.075	0.001
1.5	0.291	2.245	-0.018	0.107	0.007	0.000	0.000	0.000	0.000	0.000	0.017	0.104	0.001
1.6	0.257	2.481	-0.019	0.139	0.007	0.000	0.000	0.000	0.000	0.000	0.017	0.137	0.000
1.7	0.232	2.707	-0.020	0.175	0.007	0.000	0.000	0.000	0.000	0.000	0.017	0.173	0.000

[13] Continued in Table II-32.

Table II-32: Dimensionless post-buckling results of cases with symmetric and anti-symmetric modes, i_{max} and j_{max} = 5, for paperboard panel from (Nordstrand, 2004a) with symmetric and anti-symmetric geometric imperfection $A_{0\ 1,1} = 0.2\ h$, $A_{0\ 1,2} = 0.2\ h$.[14]

Load ratio	Case 7(iv): i =1, 2, 3, 4, 5, j=1, 2, 3, 4, 5											
$P / P_{crit\ 1,1}$	$A_{3,4} / h$	$A_{3,5} / h$	$A_{4,1} / h$	$A_{4,2} / h$	$A_{4,3} / h$	$A_{4,4} / h$	$A_{4,5} / h$	$A_{5,1} / h$	$A_{5,2} / h$	$A_{5,3} / h$	$A_{5,4} / h$	$A_{5,5} / h$
0	0.000	0.000	0.000	0.000	0.000	0.000	0.000	0.000	0.000	0.000	0.000	0.000
0.2	0.000	0.000	0.000	0.000	0.000	0.000	0.000	0.000	0.000	0.000	0.000	0.000
0.4	0.000	0.000	0.000	0.000	0.000	0.000	0.000	0.000	0.000	0.000	0.000	0.000
0.5	0.000	0.000	0.000	0.000	0.000	0.000	0.000	0.000	0.000	0.000	0.000	0.000
0.6	0.000	0.000	0.000	0.000	0.000	0.000	0.000	0.000	0.000	0.000	0.000	0.000
0.7	0.000	0.000	0.000	0.000	0.000	0.000	0.000	0.000	0.000	0.000	0.000	0.000
0.8	0.000	0.000	0.000	0.000	0.000	0.000	0.000	0.000	0.000	0.000	0.000	0.000
0.9	0.000	0.000	0.000	0.000	0.000	0.000	0.000	0.000	0.000	0.000	0.000	0.000
1	0.000	0.000	0.000	0.000	0.000	0.000	0.000	0.000	0.000	0.000	0.000	0.000
1.1	0.001	0.001	0.000	0.000	0.000	0.000	0.000	0.000	0.000	0.000	0.000	0.000
1.2	0.001	0.001	0.000	0.000	0.000	0.000	0.000	0.000	0.001	0.000	0.000	0.000
1.3	0.002	0.001	0.000	0.000	0.000	0.000	0.000	0.000	0.001	0.000	0.000	0.000
1.4	0.004	0.001	0.000	0.000	0.000	0.000	0.000	0.001	0.002	0.000	0.000	0.000
1.5	0.007	0.002	0.000	0.000	0.000	0.000	0.000	0.001	0.003	0.000	0.000	0.000
1.6	0.012	0.002	0.000	0.000	0.000	0.000	0.000	0.001	0.004	0.000	0.000	0.000
1.7	0.017	0.002	0.000	0.000	0.000	0.000	0.000	0.001	0.006	0.000	0.000	0.000

[14] Continued from Table II-31.

Table II-33: Comparison of nonzero symmetric displacement modes of case 7(iv) with case 4(viii)[15].

Load ratio	Difference in displacement mode amplitudes of Case 7(iv) relative to case 4(viii)						
$P/P_{crit\ 1,1}$	$A_{1,1}/h$	$A_{1,3}/h$	$A_{1,5}/h$	$A_{3,1}/h$	$A_{3,3}/h$	$A_{3,5}/h$	$A_{5,1}/h$
0	0.00%						
0.1	-0.28%	-102.67%	5679.51%	541.29%	770.20%	-4496.07%	544.71%
0.2	-0.72%	-100.30%	5435.66%	520.15%	739.41%	-4375.67%	525.75%
0.3	-1.43%	-97.73%	5118.50%	492.69%	699.09%	-4222.93%	501.26%
0.4	-2.61%	-95.10%	4698.52%	456.29%	645.20%	-4024.76%	468.81%
0.5	-4.60%	-92.74%	4136.59%	407.24%	572.03%	-3762.95%	424.77%
0.6	-8.04%	-91.32%	3393.32%	341.32%	472.97%	-3417.32%	364.59%
0.7	-13.83%	-91.84%	2471.46%	257.01%	345.29%	-2988.00%	285.46%
0.8	-22.74%	-95.00%	1506.90%	163.57%	202.71%	-2569.89%	194.66%
0.9	-34.40%	-100.31%	764.02%	83.66%	80.47%	-2517.09%	115.05%
1	-48.43%	-106.71%	347.76%	29.59%	-0.15%	-5268.58%	62.24%
1.1	-64.70%	-110.64%	131.43%	-9.38%	-49.50%	1994.63%	26.45%
1.2	-77.45%	-109.50%	16.90%	-38.69%	-76.37%	401.63%	-0.60%
1.3	-84.95%	-107.27%	-38.09%	-57.66%	-88.92%	101.90%	-19.03%
1.4	-89.29%	-105.57%	-64.42%	-69.50%	-94.75%	0.75%	-31.38%
1.5	-91.94%	-104.44%	-77.81%	-77.08%	-97.60%	-42.26%	-40.32%
1.6	-93.64%	-103.68%	-85.10%	-82.11%	-99.10%	-63.35%	-47.71%
1.7	-94.79%	-103.17%	-89.35%	-85.54%	-99.94%	-74.81%	-54.57%

[15] The grey background indicates that for one or both cases the dimensionless displacement was zero within three decimal places.

Table II-34: Comparison of nonzero anti-symmetric displacement modes of case 7(iv) with case 5(viii)[16].

Load ratio	Difference in displacement mode amplitudes of Case 7(iv) relative to case 5(viii)				
$P/P_{crit\ 1,1}$	$A_{1,2}/h$	$A_{1,4}/h$	$A_{3,2}/h$	$A_{3,4}/h$	$A_{5,2}/h$
0	0.00%				
0.1	-0.06%	140.97%	57.94%	-454.63%	88.48%
0.2	-0.17%	142.76%	58.39%	-474.65%	90.30%
0.3	-0.34%	144.50%	58.67%	-501.70%	92.25%
0.4	-0.62%	145.80%	58.52%	-539.48%	94.12%
0.5	-1.12%	145.77%	57.40%	-594.42%	95.32%
0.6	-1.99%	142.49%	54.24%	-678.97%	94.44%
0.7	-3.49%	132.47%	47.20%	-823.64%	88.54%
0.8	-5.81%	111.35%	34.31%	-1152.80%	73.34%
0.9	-8.44%	78.61%	16.34%	-3656.75%	47.33%
1	-9.08%	42.70%	0.27%	833.23%	18.81%
1.1	-5.92%	16.89%	-5.27%	154.36%	2.15%
1.2	-2.76%	6.10%	-3.79%	38.57%	-1.66%
1.3	-1.26%	2.60%	-2.09%	12.47%	-1.61%
1.4	-0.61%	1.33%	-1.15%	5.08%	-1.13%
1.5	-0.32%	0.79%	-0.67%	2.48%	-0.77%
1.6	-0.18%	0.52%	-0.41%	1.40%	-0.53%
1.7	-0.10%	0.37%	-0.26%	0.88%	-0.38%

[16] The grey background indicates that for one or both cases the dimensionless displacement was zero within three decimal places.

Appendix III

III.1 Equivalent elastic properties of paperboard obtained by different methods

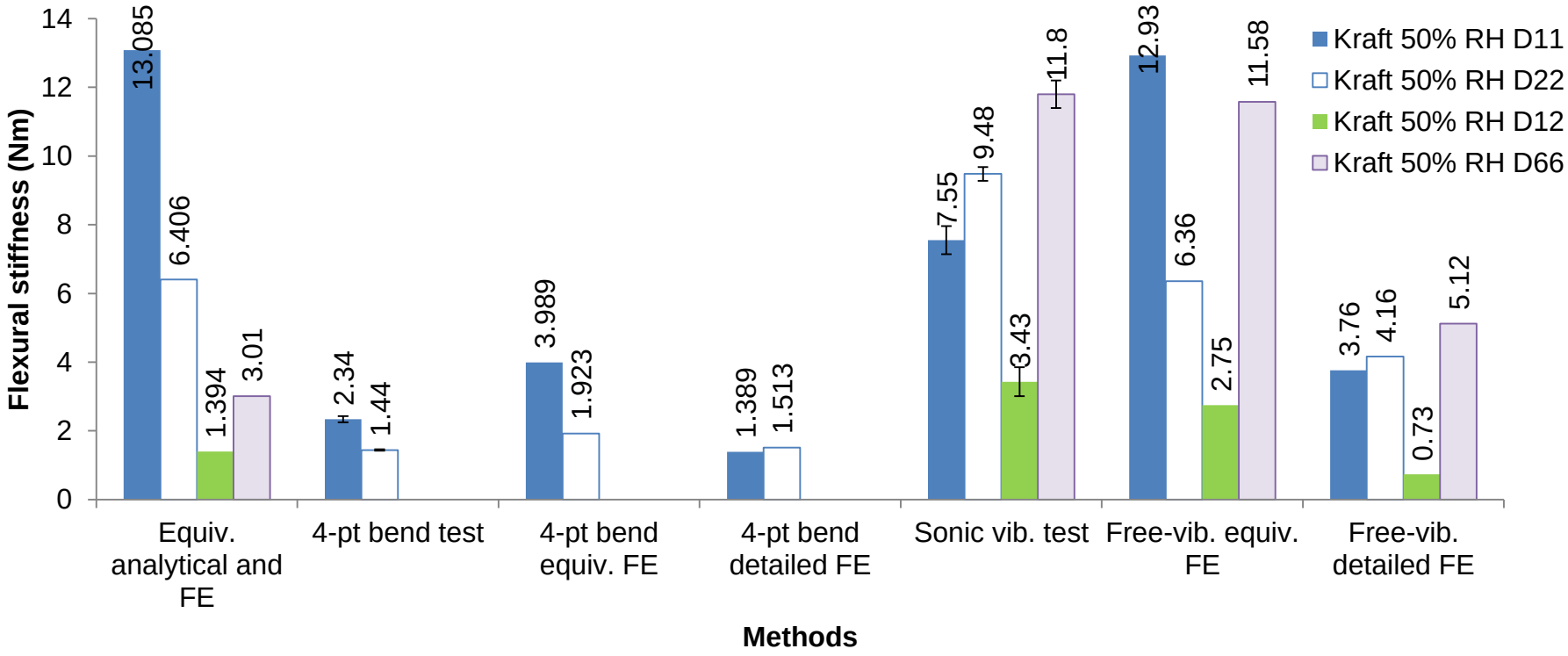

Figure III-1: Flexural stiffnesses D_{11}, D_{22}, D_{12}, *and* D_{66} of kraft paperboard at 50% relative humidity, 23 °C, obtained by different methods.

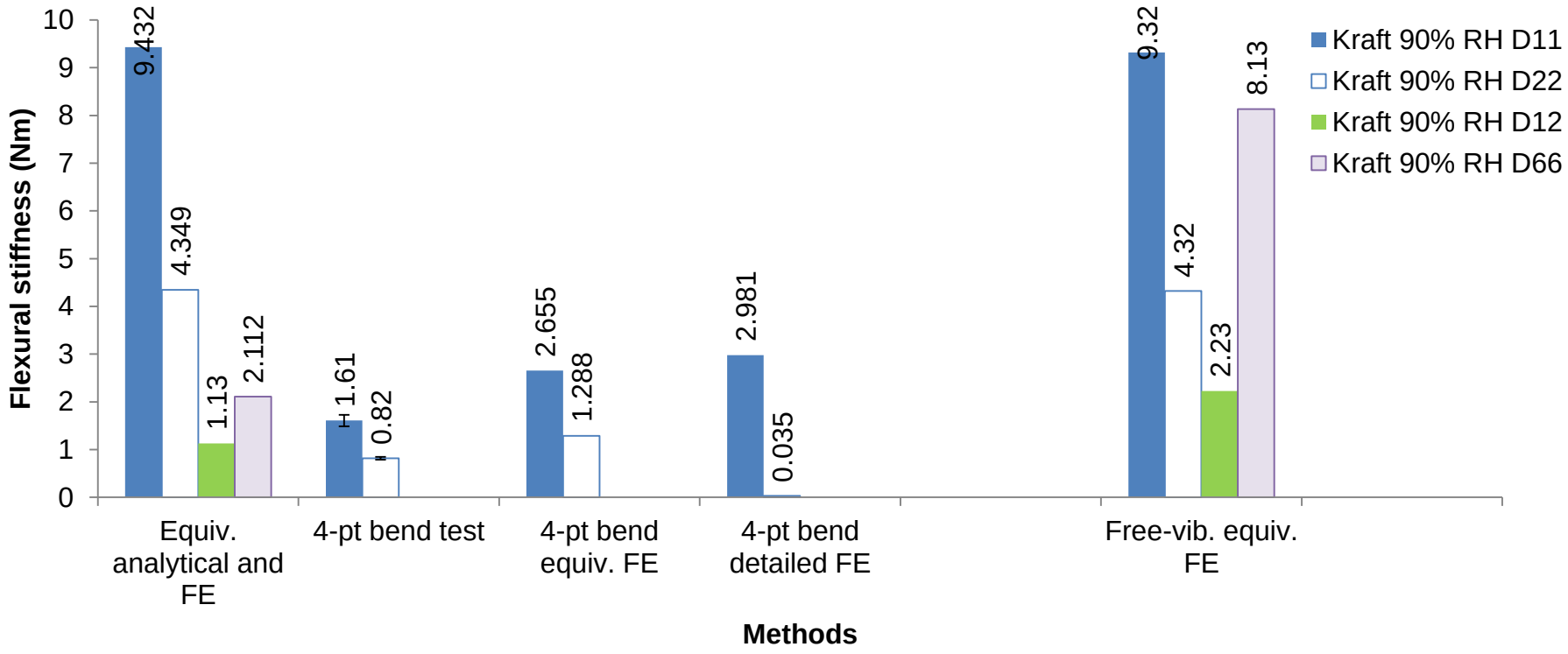

Figure III-2: Flexural stiffnesses D_{11}, D_{22}, D_{12}, *and* D_{66} of kraft paperboard at 90% relative humidity, 23 °C, obtained by different methods.

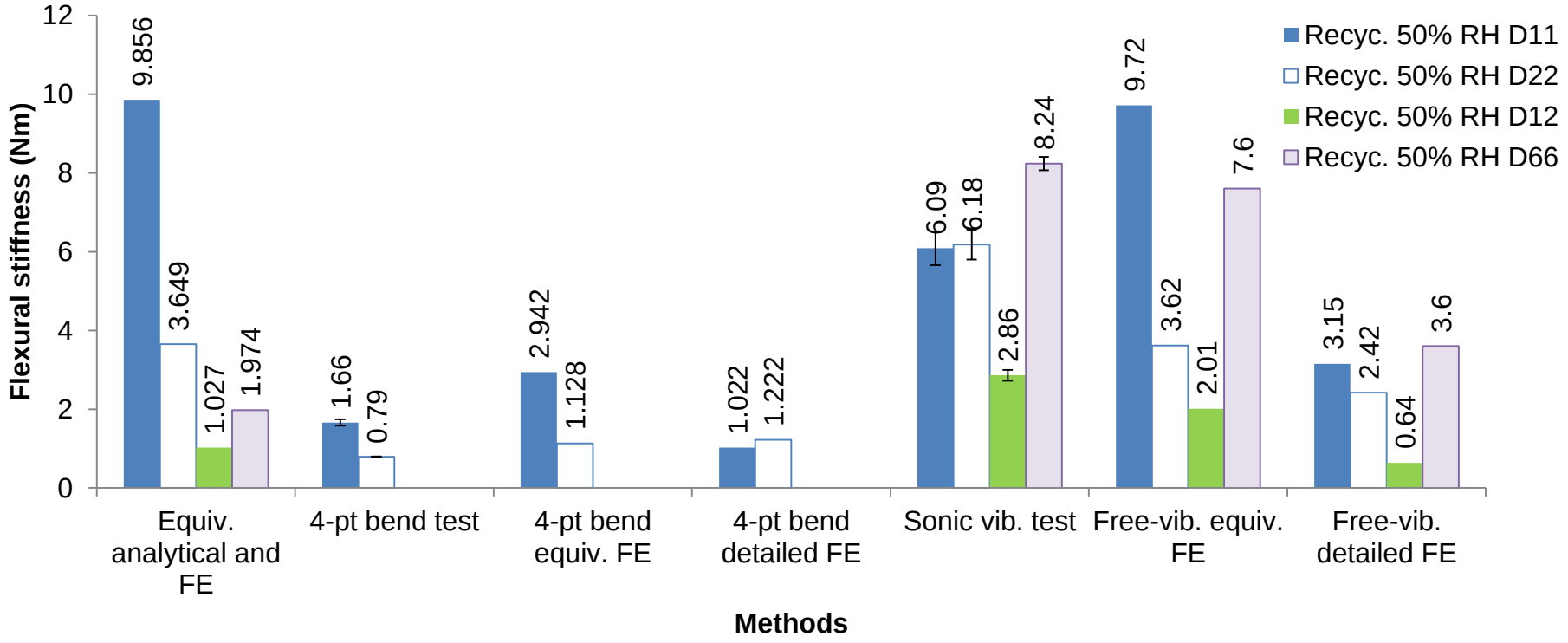

Figure III-3: Flexural stiffnesses D_{11}, D_{22}, D_{12}, *and* D_{66} of recycled paperboard at 50% relative humidity, 23 °C, obtained by different methods.

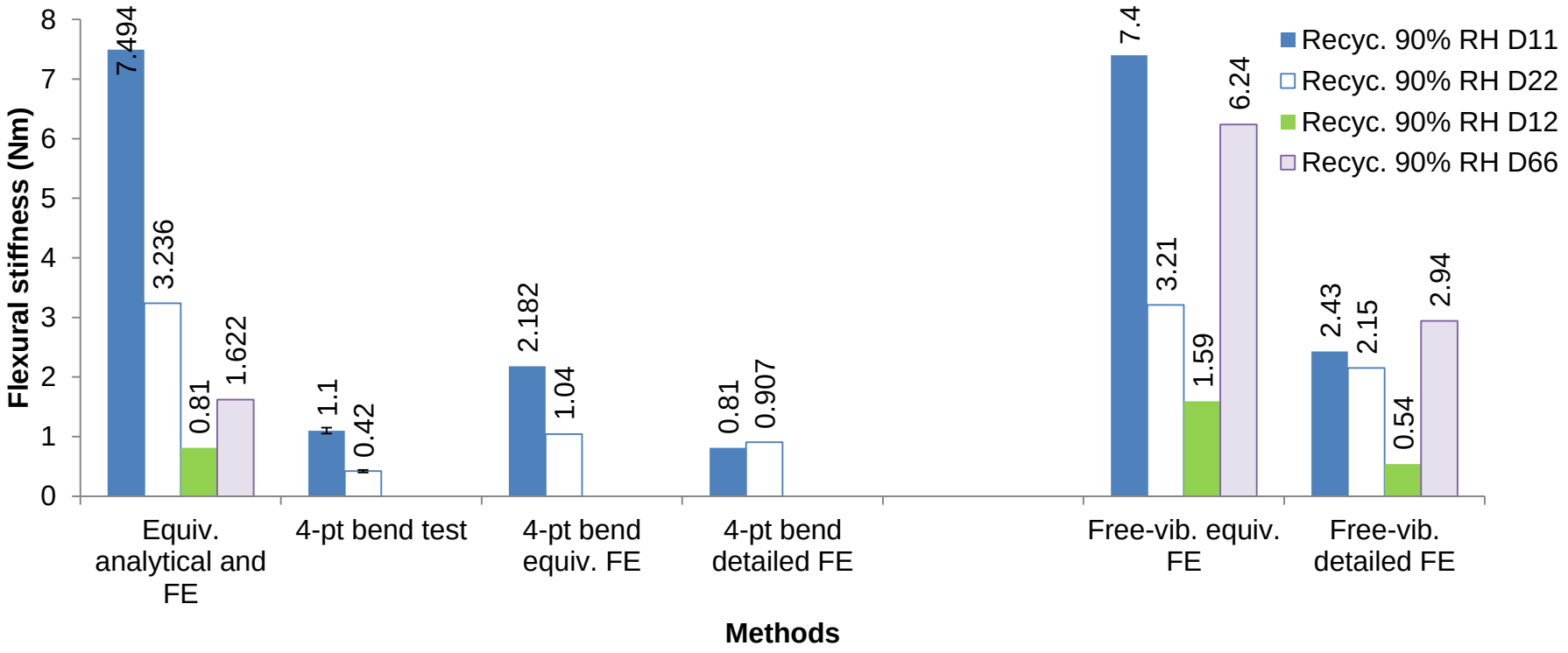

Figure III-4: Flexural stiffnesses D_{11}, D_{22}, D_{12}, *and* D_{66} of recycled paperboard at 90% relative humidity, 23 °C, obtained by different methods.

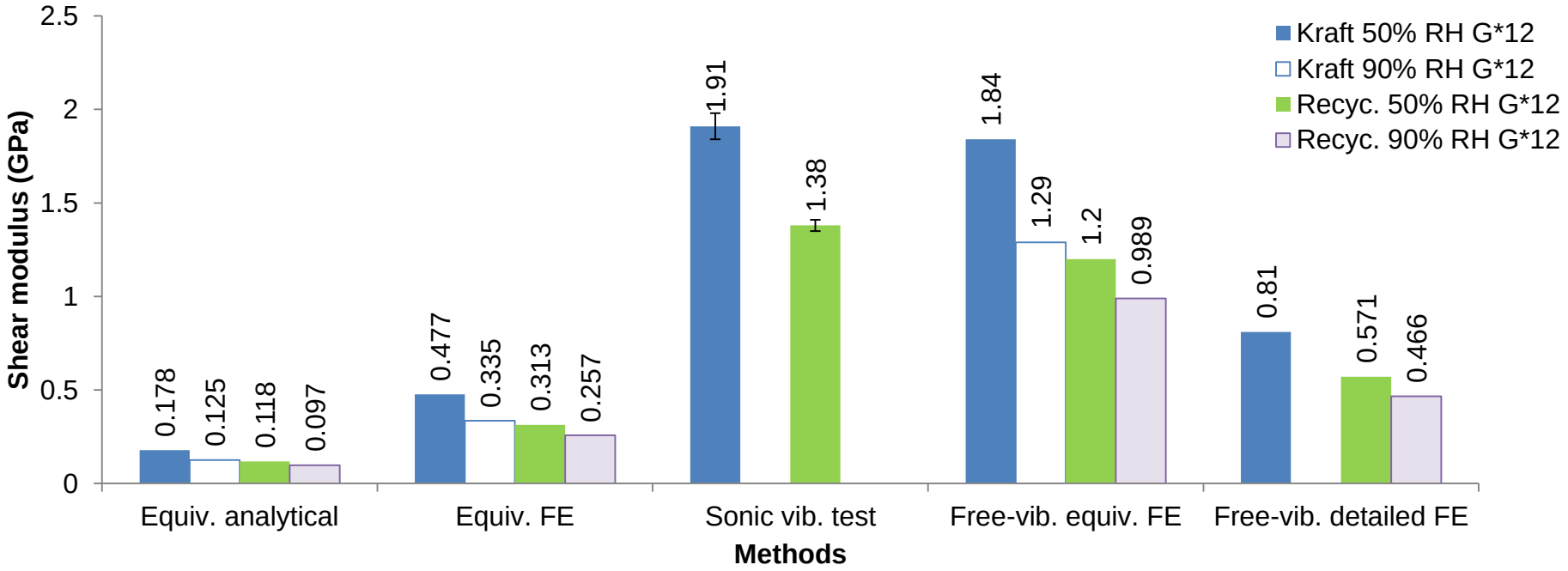

Figure III-5: Shear modulus G^*_{12} of kraft and recycled paperboards at 50% and 90% relative humidity, 23 °C, obtained by different methods.

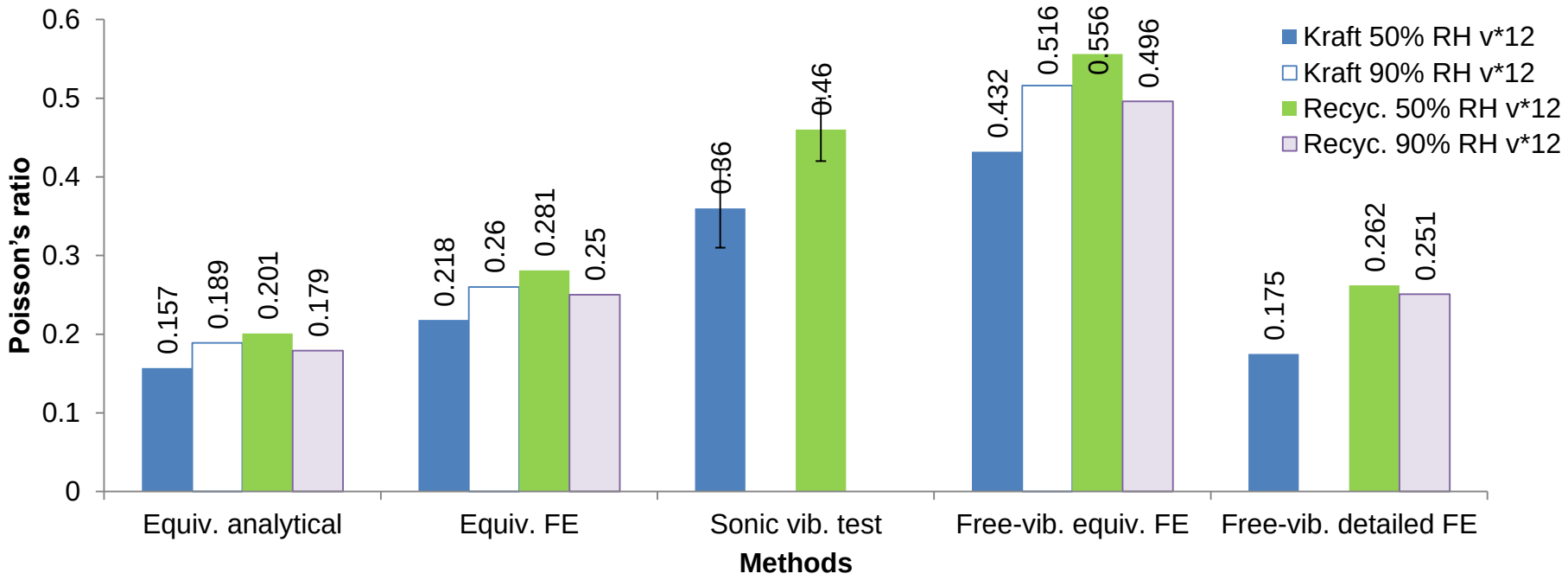

Figure III-6: Poisson's ratio v^*_{12} of kraft and recycled paperboards at 50% and 90% relative humidity, 23 °C, obtained by different methods.

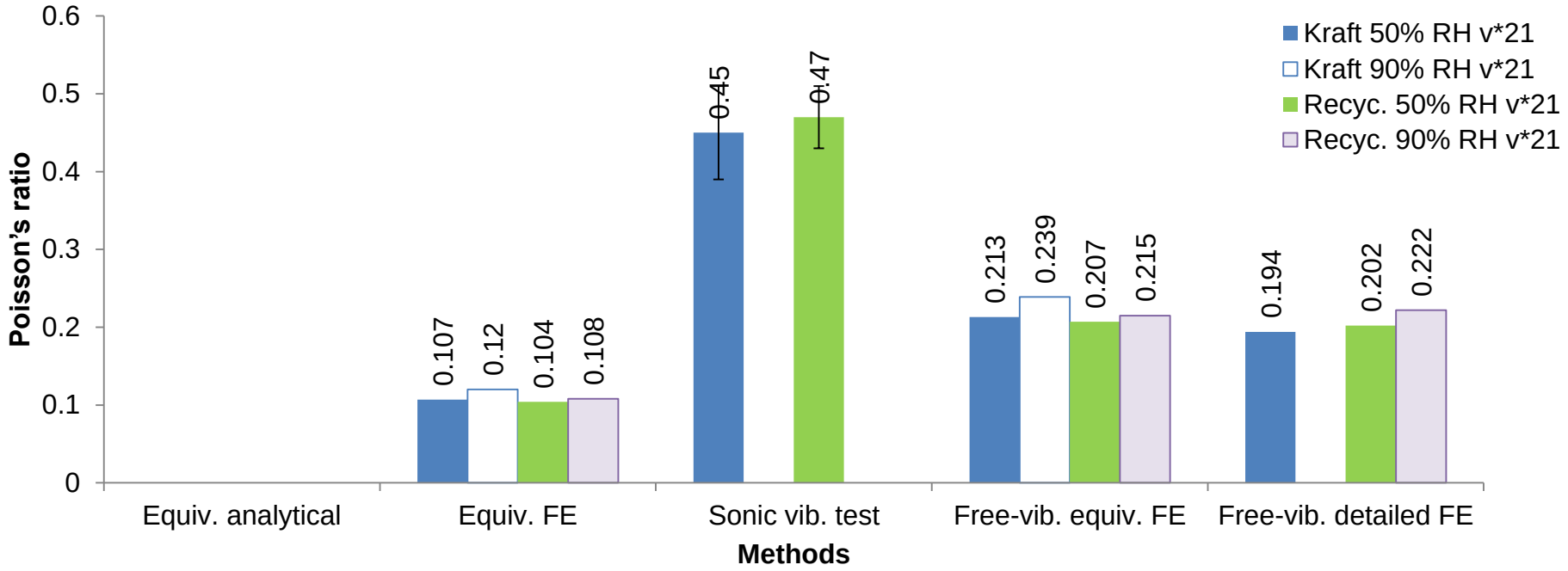

Figure III-7: Poisson's ratio v^*_{21} of kraft and recycled paperboards at 50% and 90% relative humidity, 23 °C, obtained by different methods.

Table III-1: Equivalent elastic moduli for Kraft 205/160/205 standard corrugated paperboard at 50% and 90% relative humidity, 23 °C obtained by different methods.

	Kraft 50% relative humidity		Kraft 90% relative humidity	
Methods to obtain equivalent paperboard properties	**MD Young's modulus E^*_{11} (GPa)**	**CD Young's modulus E^*_{22} (GPa)**	**MD Young's modulus E^*_{11} (GPa)**	**CD Young's modulus E^*_{22} (GPa)**
Equivalent orthotropic plate theory for analytical	0.705	0.480	0.509	0.322
Equivalent orthotropic plate theory for FE	2.03	0.99	1.45	0.67
Four-point bending experiment [c]	1.44±0.05	0.576±0.008	1.00±0.07	0.33±0.01
Four-point bending equivalent FE model	2.466	0.770	1.641	0.516
Four-point bending detailed FE model	0.859	0.606	1.843	0.0138
Edge compression experiment [c]	-	0.87±0.15	-	0.65±0.03
Edge compression equivalent FE model	-	5.76	-	3.88
Edge compression detailed FE model	-	2.73	-	1.86
Sonic vibration experiment [c]	1.02±0.07	1.28±0.07	-	-
Free-vibration equivalent FE model	1.86	0.92	1.29	0.60
Free-vibration detailed FE model	0.58	0.64	-	-

[c] Uncertainty limits based on 95% confidence interval.

Table III-2: Flexural stiffnesses for Kraft 205/160/205 standard corrugated paperboard at 50% relative humidity, 23 °C obtained by different methods.

	Kraft 50% relative humidity			
Methods to obtain equivalent paperboard properties	**MD Bending stiffness D_{11} (Nm)**	**CD Bending stiffness D_{22} (Nm)**	**Bending stiffness D_{12} (Nm)**	**Bending stiffness D_{66} (Nm)**
Equivalent orthotropic plate theory for analytical and FE	13.085	6.406	1.394	3.010
Four-point bending experiment [c]	2.34±0.09	1.44±0.02	-	-
Four-point bending equivalent FE model	3.989	1.923	-	-
Four-point bending detailed FE model	1.389	1.513	-	-
Sonic vibration experiment [c]	7.55±0.41	9.48±0.20	3.43±0.42	11.80±0.40
Free-vibration equivalent FE model	12.93	6.36	2.75	11.58
Free-vibration detailed FE model	3.76	4.16	0.73	5.12

Table III-3: Flexural stiffnesses for Kraft 205/160/205 standard corrugated paperboard at 90% relative humidity, 23 °C obtained by different methods.

	Kraft 90% relative humidity			
Methods to obtain equivalent paperboard properties	**MD Bending stiffness D_{11} (Nm)**	**CD Bending stiffness D_{22} (Nm)**	**Bending stiffness D_{12} (Nm)**	**Bending stiffness D_{66} (Nm)**
Equivalent orthotropic plate theory for analytical and FE	9.432	4.349	1.130	2.112
Four-point bending experiment [c]	1.61±0.12	0.82±0.03	-	-
Four-point bending equivalent FE model	2.655	1.288	-	-
Four-point bending detailed FE model	2.981	0.035	-	-
Sonic vibration experiment [c]	-	-	-	-
Free-vibration equivalent FE model	9.32	4.32	2.23	8.13
Free-vibration detailed FE model	-	-	-	-

Table III-4: Equivalent shear modulus and Poisson's ratios for Kraft 205/160/205 standard corrugated paperboard at 50% and 90% relative humidity, 23 °C obtained by different methods.

	Kraft 50% relative humidity			Kraft 90% relative humidity		
Methods to obtain equivalent paperboard properties	**Shear modulus G^*_{12} (GPa)**	**Poisson's ratio v^*_{12}**	**Poisson's ratio v^*_{21}**	**Shear modulus G^*_{12} (GPa)**	**Poisson's ratio v^*_{12}**	**Poisson's ratio v^*_{21}**
Equivalent orthotropic plate theory for analytical	0.178	0.157		0.125	0.189	
Equivalent orthotropic plate theory for FE	0.477	0.218	0.107	0.335	0.260	0.120
Sonic vibration experiment [c]	1.91±0.07	0.36±0.05	0.45±0.06	-	-	-
Free-vibration equivalent FE model	1.84	0.432	0.213	1.29	0.516	0.239
Free-vibration detailed FE model	0.81	0.175	0.194	-	-	-

Table III-5: Equivalent elastic moduli for Recycled 190/140/190 corrugated paperboard at 50% and 90% relative humidity, 23 °C obtained by different methods.

	Recycled 50% relative humidity		Recycled 90% relative humidity	
Methods to obtain equivalent paperboard properties	**MD Young's modulus E^*_{11} (GPa)**	**CD Young's modulus E^*_{22} (GPa)**	**MD Young's modulus E^*_{11} (GPa)**	**CD Young's modulus E^*_{22} (GPa)**
Equivalent orthotropic plate theory for analytical	0.539	0.279	0.410	0.247
Equivalent orthotropic plate theory for FE	1.52	0.56	1.16	0.50
Four-point bending experiment [c]	0.94±0.04	0.305±0.006	0.62±0.03	0.16±0.008
Four-point bending equivalent FE model	1.667	0.438	1.236	0.404
Four-point bending detailed FE model	0.579	0.475	0.459	0.352
Edge compression experiment [b]	-	0.68±0.12	-	0.43±0.04
Edge compression equivalent FE model	-	3.08	-	2.74
Edge compression detailed FE model	-	1.50	-	1.32
Sonic vibration experiment [b]	0.80±0.07	0.81±0.06	-	-
Free-vibration equivalent FE model	1.36	0.51	1.05	0.46
Free-vibration detailed FE model	0.47	0.36	0.36	0.32

[c] Uncertainty limits based on 95% confidence interval.

Table III-6: Flexural stiffnesses for Recycled 190/140/190 standard corrugated paperboard at 50% relative humidity, 23 °C obtained by different methods.

	Recycled 50% relative humidity			
Methods to obtain equivalent paperboard properties	**MD Bending stiffness D_{11} (Nm)**	**CD Bending stiffness D_{22} (Nm)**	**Bending stiffness D_{12} (Nm)**	**Bending stiffness D_{66} (Nm)**
Equivalent orthotropic plate theory for analytical and FE	9.856	3.649	1.027	1.974
Four-point bending experiment [c]	1.66±0.08	0.79±0.01	-	-
Four-point bending equivalent FE model	2.942	1.128	-	-
Four-point bending detailed FE model	1.022	1.222	-	-
Sonic vibration experiment [c]	6.09±0.43	6.18±0.38	2.86±0.14	8.24±0.17
Free-vibration equivalent FE model	9.72	3.62	2.01	7.60
Free-vibration detailed FE model	3.15	2.42	0.64	3.60

Table III-7: Flexural stiffnesses for Recycled 190/140/190 standard corrugated paperboard at 90% relative humidity, 23 °C obtained by different methods.

	Recycled 90% relative humidity			
Methods to obtain equivalent paperboard properties	**MD Bending stiffness D_{11} (Nm)**	**CD Bending stiffness D_{22} (Nm)**	**Bending stiffness D_{12} (Nm)**	**Bending stiffness D_{66} (Nm)**
Equivalent orthotropic plate theory for analytical and FE	7.494	3.236	0.810	1.622
Four-point bending experiment [c]	1.10±0.05	0.42±0.02	-	-
Four-point bending equivalent FE model	2.182	1.040	-	-
Four-point bending detailed FE model	0.810	0.907	-	-
Sonic vibration experiment [c]	-	-	-	-
Free-vibration equivalent FE model	7.40	3.21	1.59	6.24
Free-vibration detailed FE model	2.43	2.15	0.54	2.94

Table III-8: Equivalent shear modulus and Poisson's ratios for Recycled 190/140/190 standard corrugated paperboard at 50% and 90% relative humidity, 23 °C obtained by different methods.

	Recycled 50% relative humidity			Recycled 90% relative humidity		
Methods to obtain equivalent paperboard properties	**Shear modulus G^*_{12} (GPa)**	**Poisson's ratio v^*_{12}**	**Poisson's ratio v^*_{21}**	**Shear modulus G^*_{12} (GPa)**	**Poisson's ratio v^*_{12}**	**Poisson's ratio v^*_{21}**
Equivalent orthotropic plate theory for analytical	0.118	0.201		0.097	0.179	
Equivalent orthotropic plate theory for FE	0.313	0.281	0.104	0.257	0.250	0.108
Sonic vibration experiment [c]	1.38±0.03	0.46±0.04	0.47±0.04	-	-	-
Free-vibration equivalent FE model	1.20	0.556	0.207	0.989	0.496	0.215
Free-vibration detailed FE model	0.571	0.262	0.202	0.466	0.251	0.222

III.1 Edge compression test plots

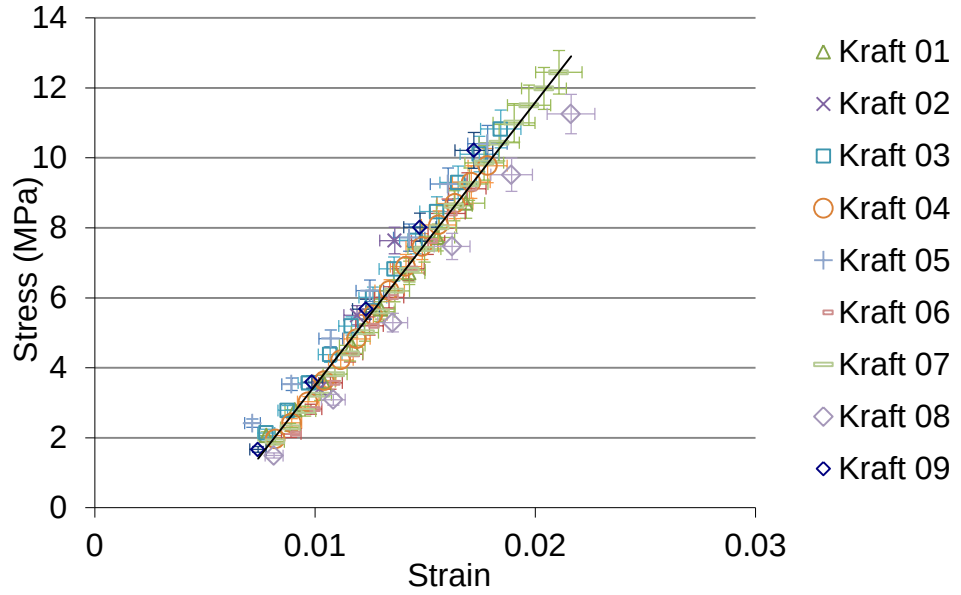

Figure III-8: Kraft paperboard 50% relative humidity, 23 °C edge compression test.

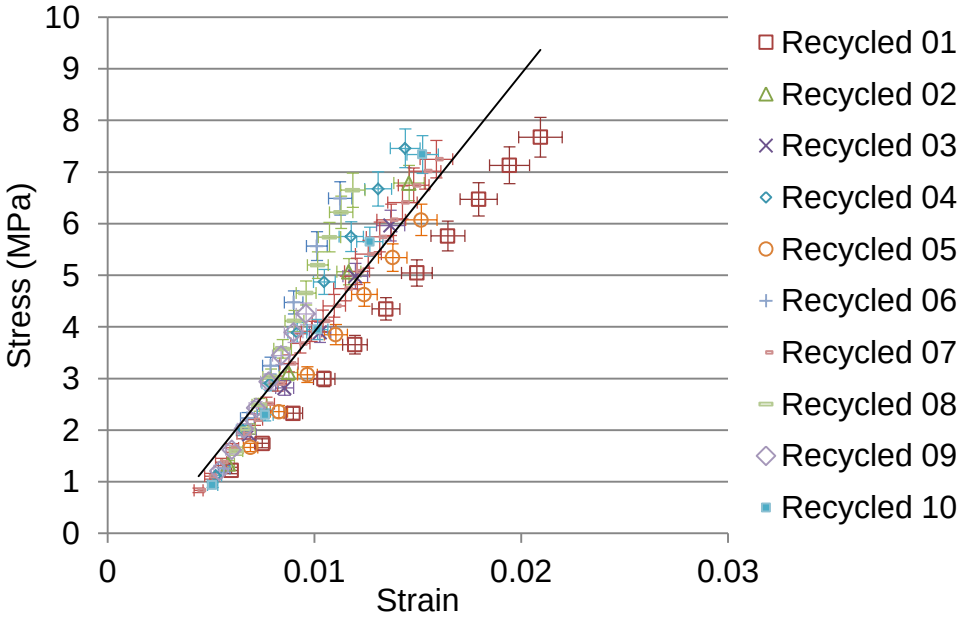

Figure III-9: Recycled paperboard 50% relative humidity, 23 °C edge compression test.

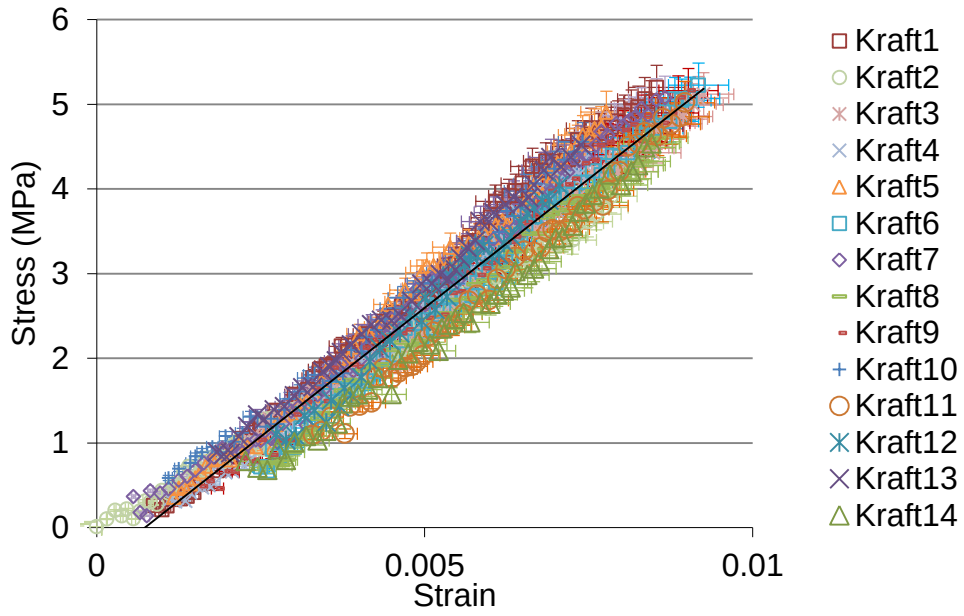

Figure III-10: Kraft paperboard 90% relative humidity, 23 °C edge compression test.

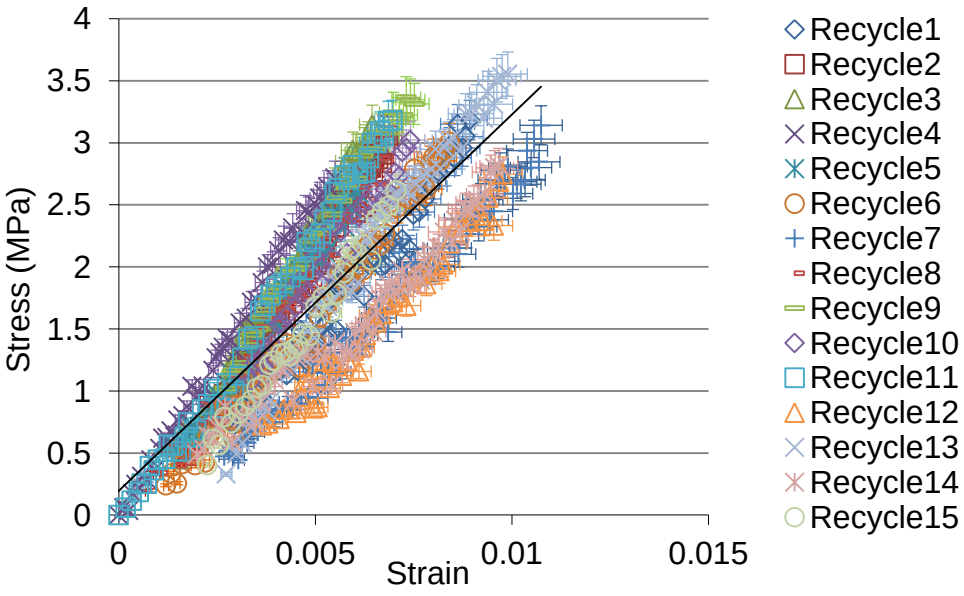

Figure III-11: Recycled paperboard 90% relative humidity, 23 °C edge compression test.

III.2 Edge compression FE model plots

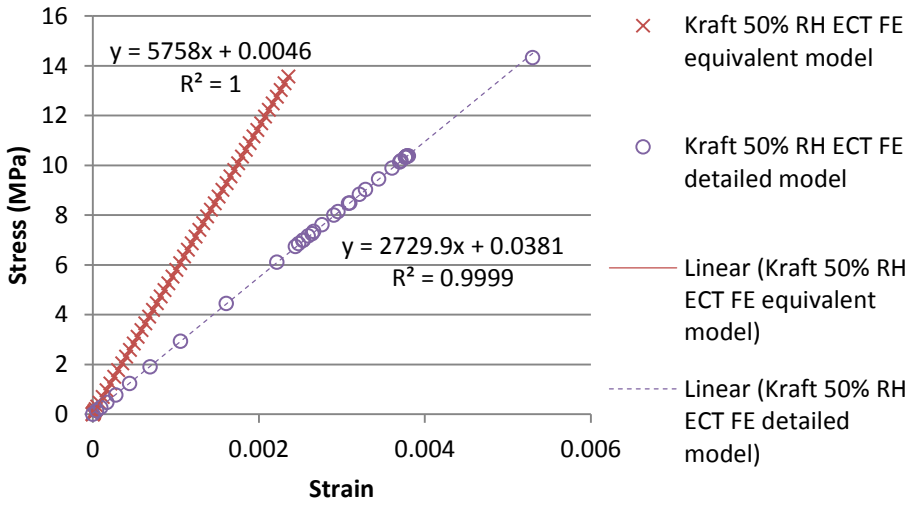

Figure III-12: FEM equivalent and detailed kraft paperboard at 50% RH, 23 °C, edge compression linear portion of stress vs. strain plot.

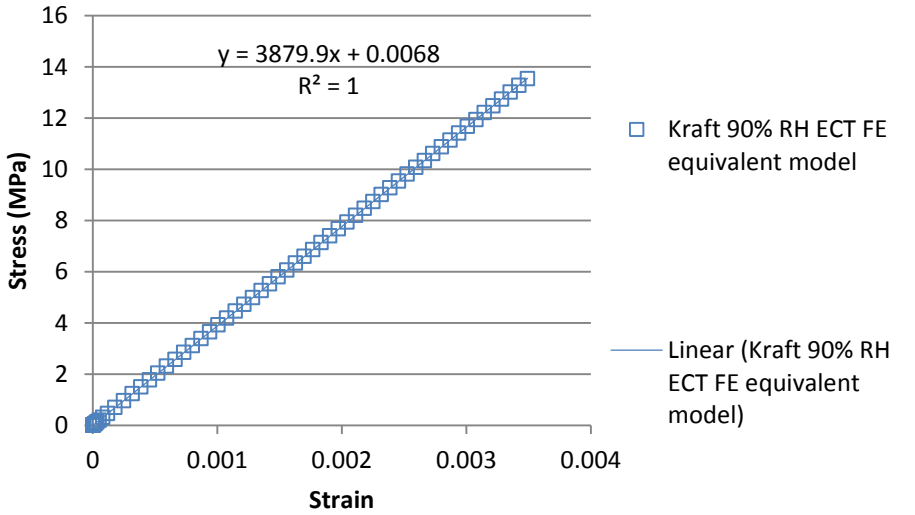

Figure III-13: FEM equivalent kraft paperboard at 90% RH, 23 °C, edge compression linear portion of stress vs. strain plot.

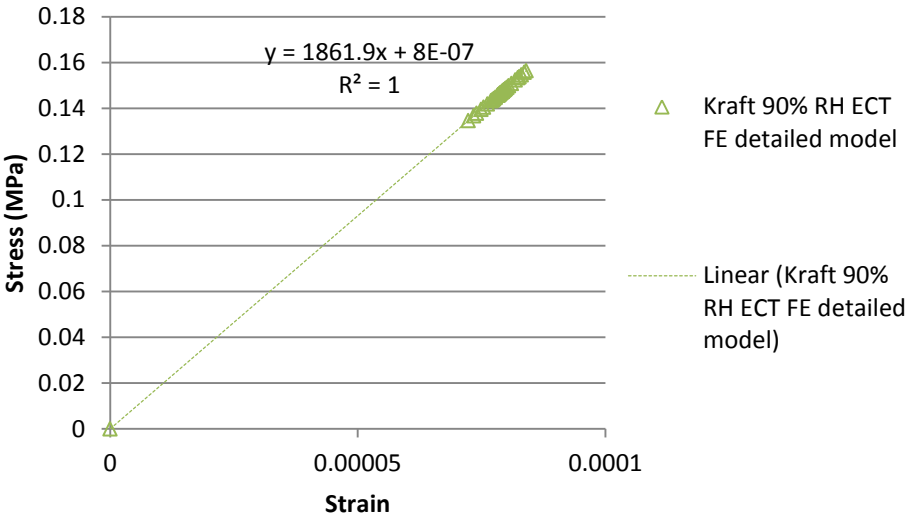

Figure III-14: FEM detailed kraft paperboard at 90% RH, 23 °C, edge compression linear portion of stress vs. strain plot.

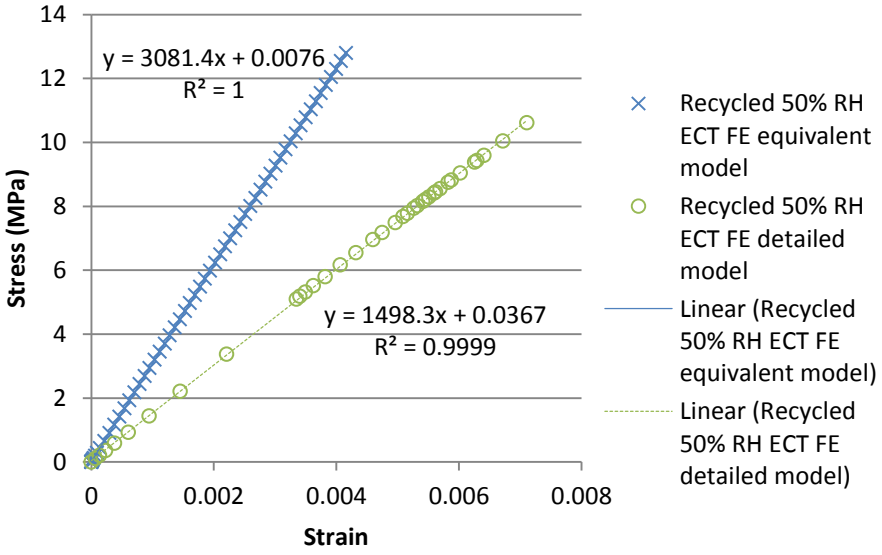

Figure III-15: FEM equivalent and detailed recycled paperboard at 50% RH, 23 °C, edge compression linear portion of stress vs. strain plot.

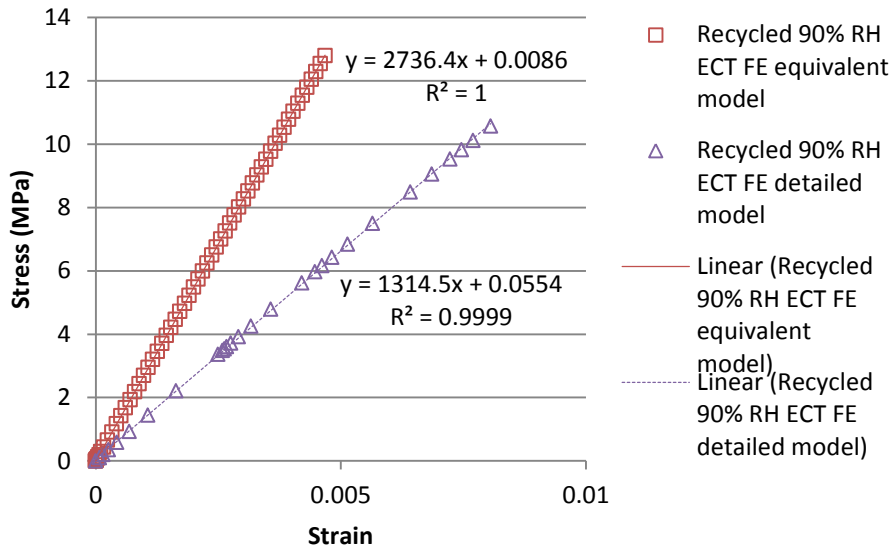

Figure III-16: FEM equivalent and detailed recycled paperboard at 90% RH, 23 °C, edge compression linear portion of stress vs. strain plot.

III.3 Four-point bending test plots

III.3.1 Kraft 50% RH MD-bending test plots

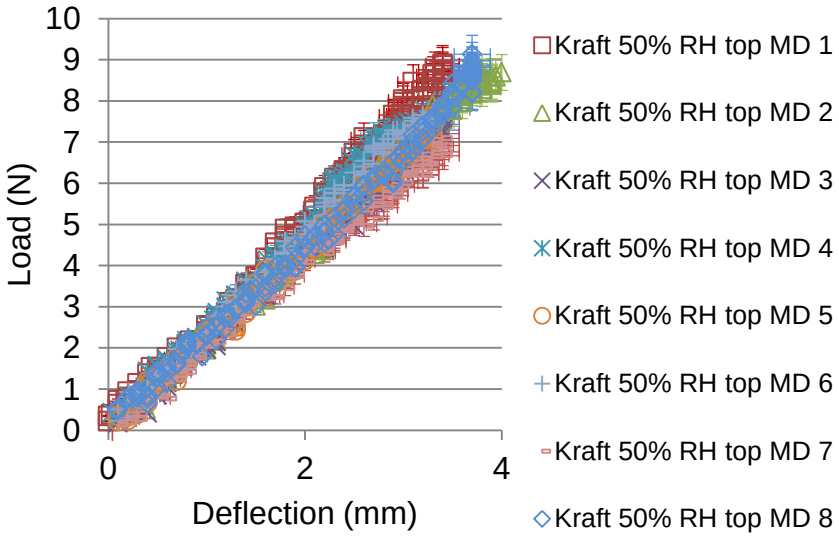

Figure III-17: Kraft paperboard at 50% RH, 23 °C, MD-bending with single facer side up, linear portion of load vs. deflection plot.

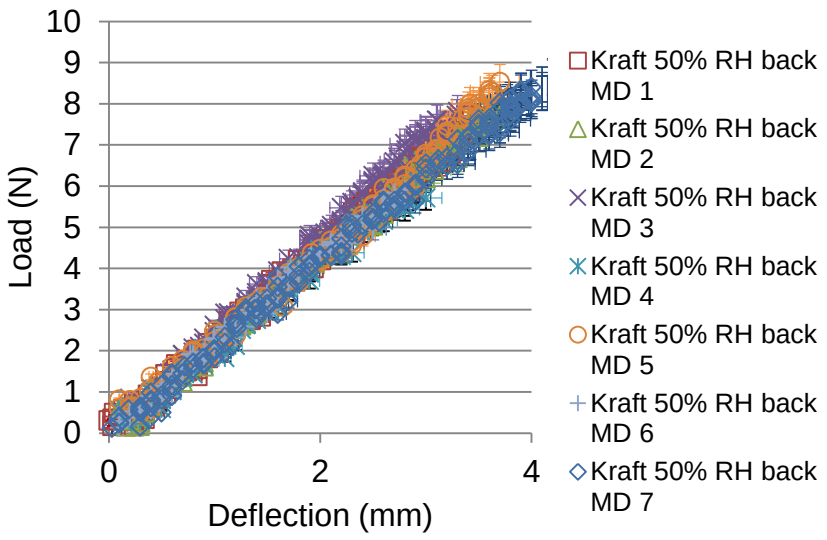

Figure III-18: Kraft paperboard at 50% RH, 23 °C, MD-bending with double backer side up, linear portion of load vs. deflection plot.

III.3.2 Kraft 50% RH CD-bending test plots

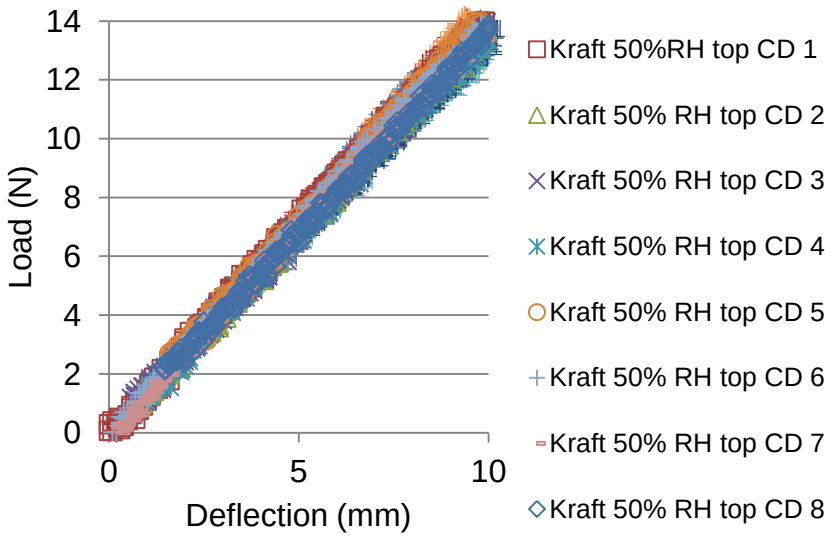

Figure III-19: Kraft paperboard at 50% RH, 23 °C, CD-bending with single facer side up, linear portion of load vs. deflection plot.

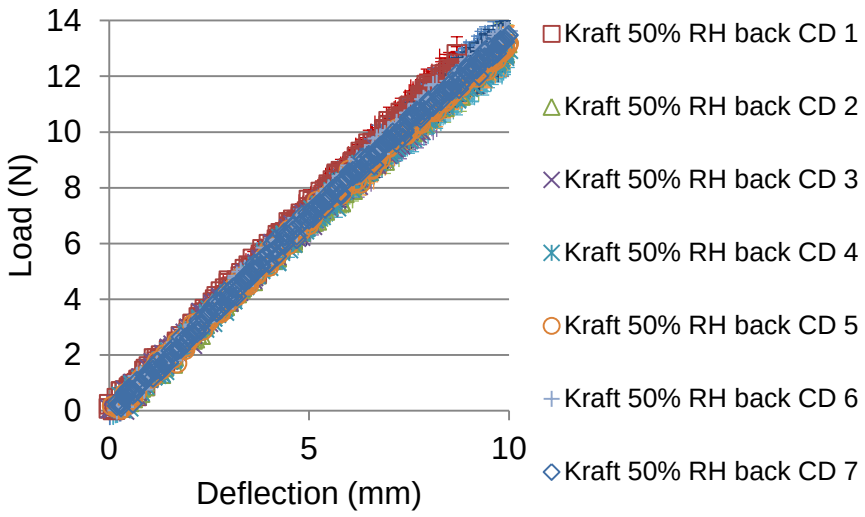

Figure III-20: Kraft paperboard at 50% RH, 23 °C, CD-bending with double backer side up, linear portion of load vs. deflection plot.

III.3.3 Recycled 50% RH MD-bending test plots

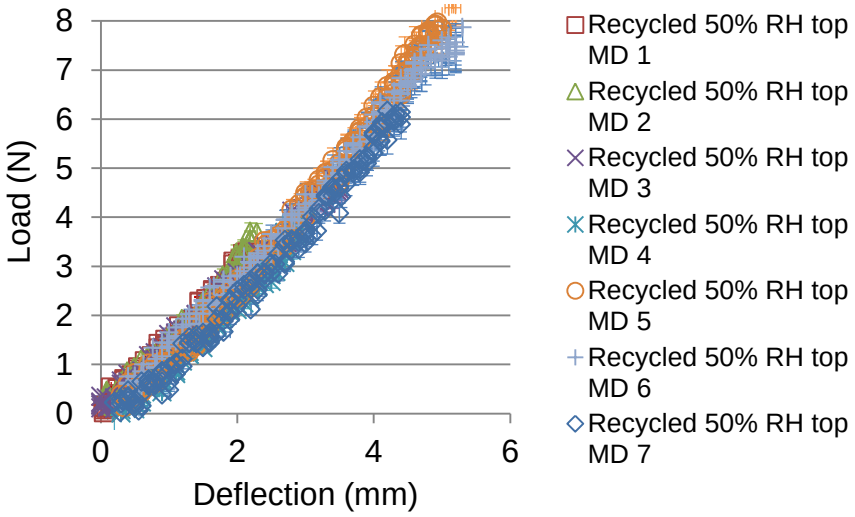

Figure III-21: Recycled paperboard at 50% RH, 23 °C, MD-bending with single facer side up, linear portion of load vs. deflection plot.

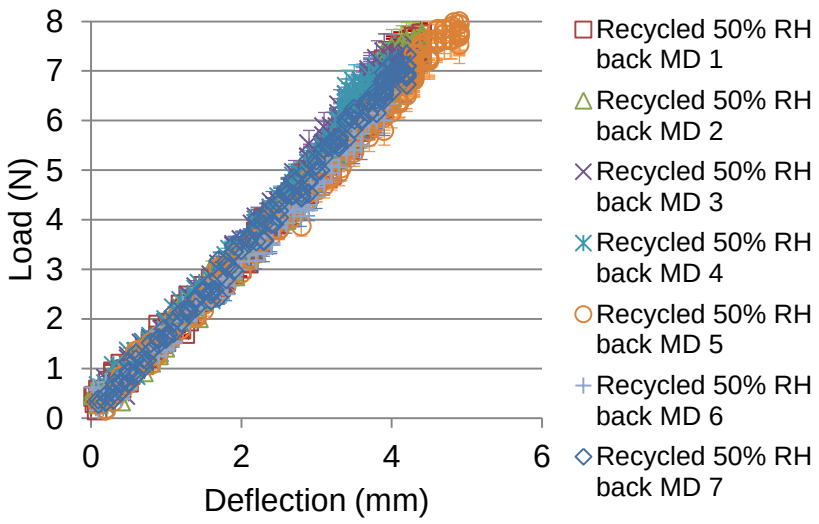

Figure III-22: Recycled paperboard at 50% RH, 23 °C, MD-bending with double backer side up, linear portion of load vs. deflection plot.

III.3.4 Recycled 50% RH CD-bending test plots

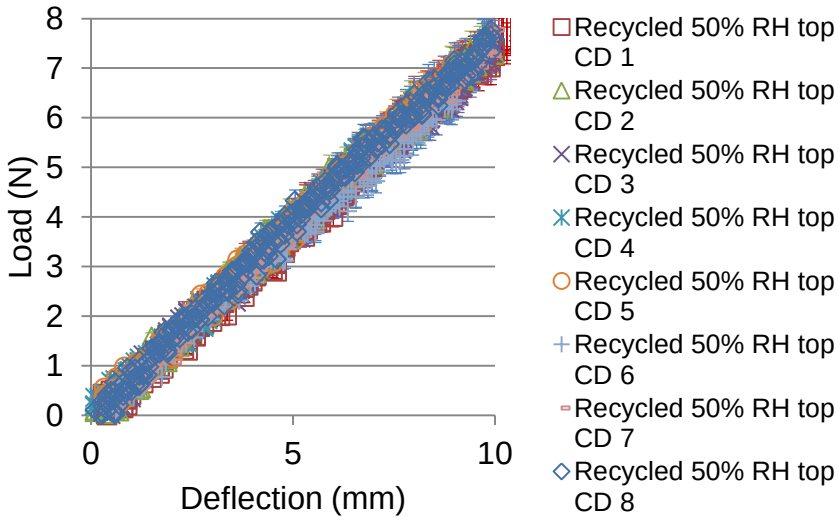

Figure III-23: Recycled paperboard at 50% RH, 23 °C, CD-bending with single facer side up, linear portion of load vs. deflection plot.

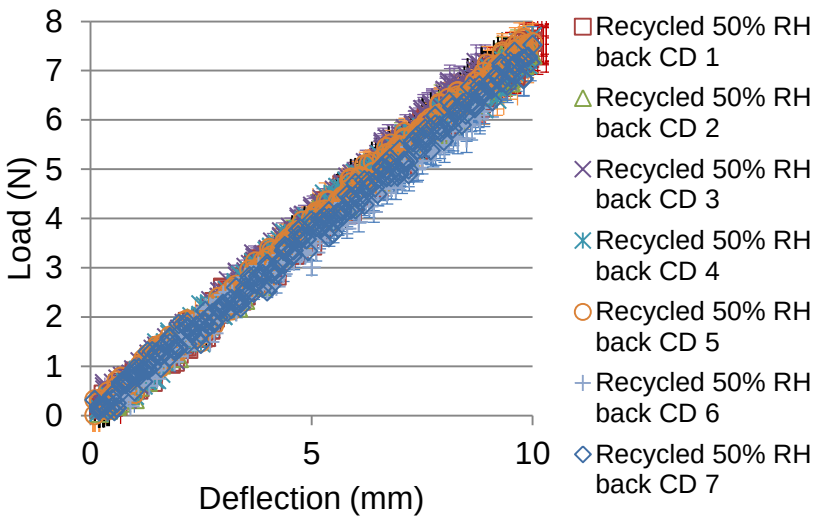

Figure III-24: Recycled paperboard at 50% RH, 23 °C, CD-bending with double backer side up, linear portion of load vs. deflection plot.

III.3.5 Kraft 90% RH MD-bending test plots

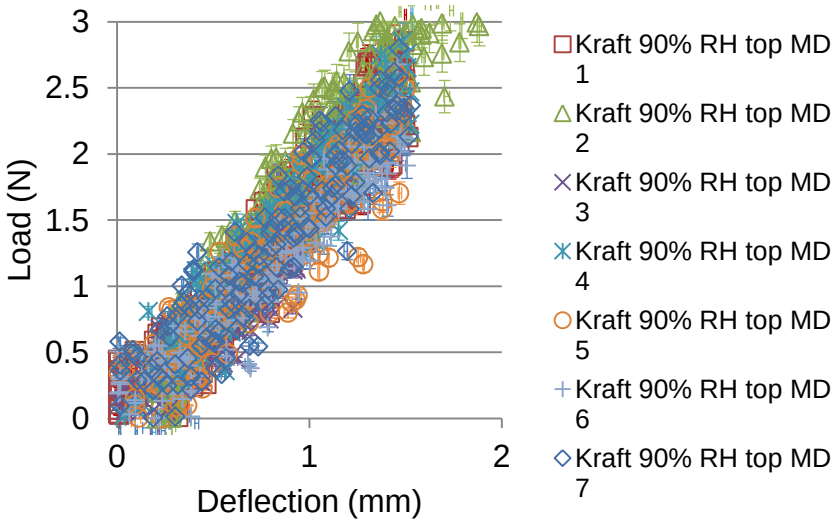

Figure III-25: Kraft paperboard at 90% RH, 23 °C, MD-bending with single facer side up, linear portion of load vs. deflection plot.

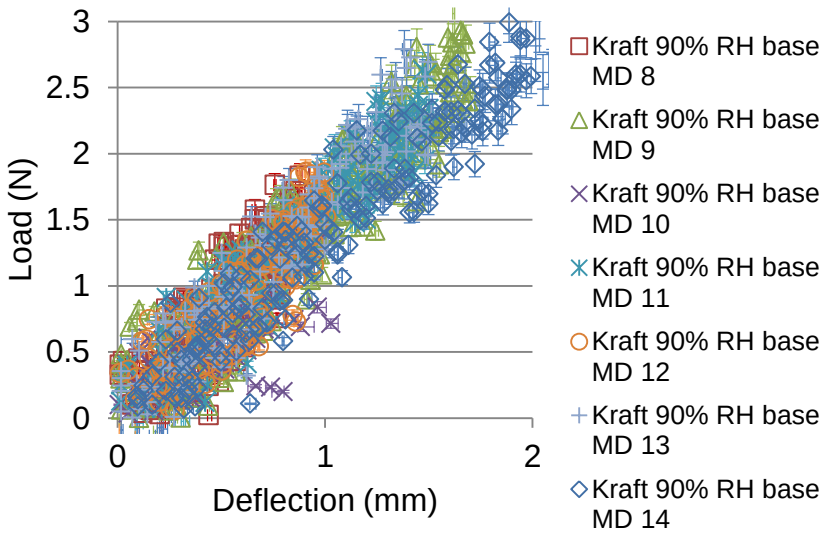

Figure III-26: Kraft paperboard at 90% RH, 23 °C, MD-bending with double backer side up, linear portion of load vs. deflection plot.

III.3.6 Kraft 90% RH CD-bending test plots

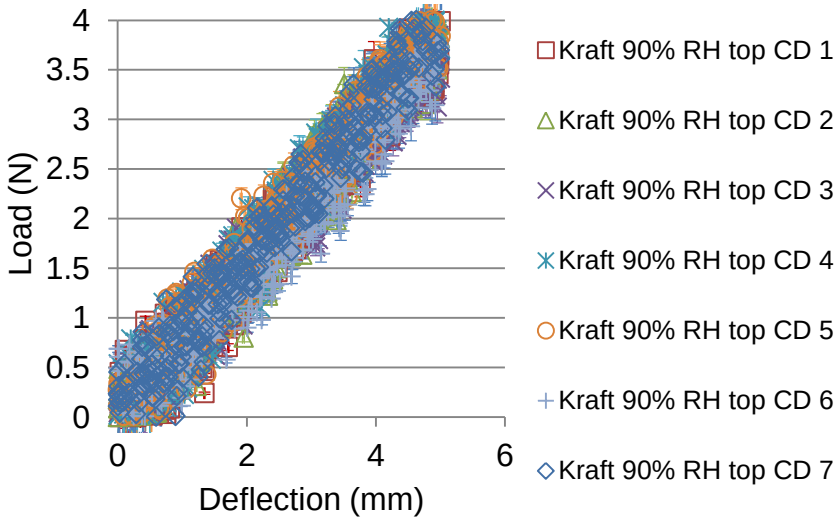

Figure III-27: Kraft paperboard at 90% RH, 23 °C, CD-bending with single facer side up, linear portion of load vs. deflection plot.

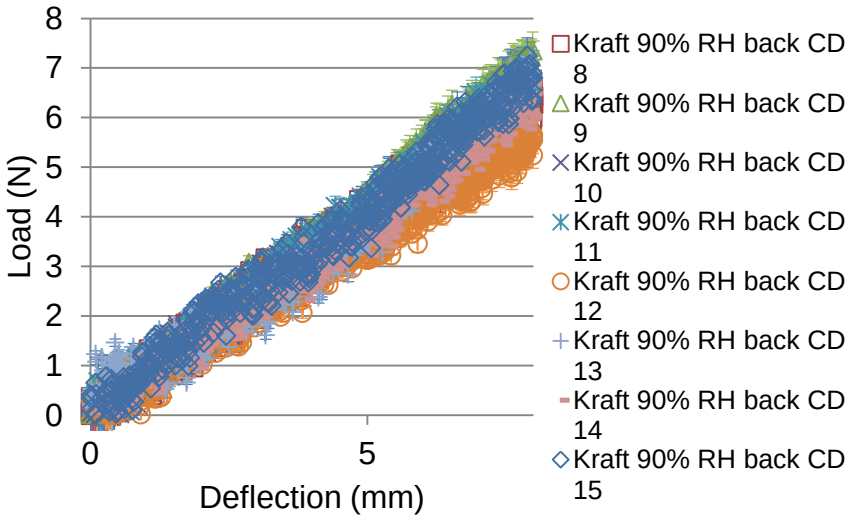

Figure III-28: Kraft paperboard at 90% RH, 23 °C, CD-bending with double backer side up, linear portion of load vs. deflection plot.

III.3.7 Recycled 90% RH MD-bending test plots

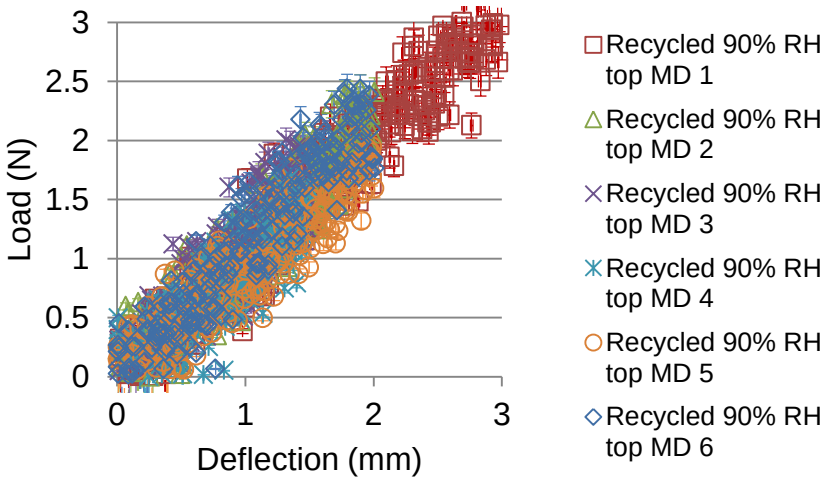

Figure III-29: Recycled paperboard at 90% RH, 23 °C, MD-bending with single facer side up, linear portion of load vs. deflection plot.

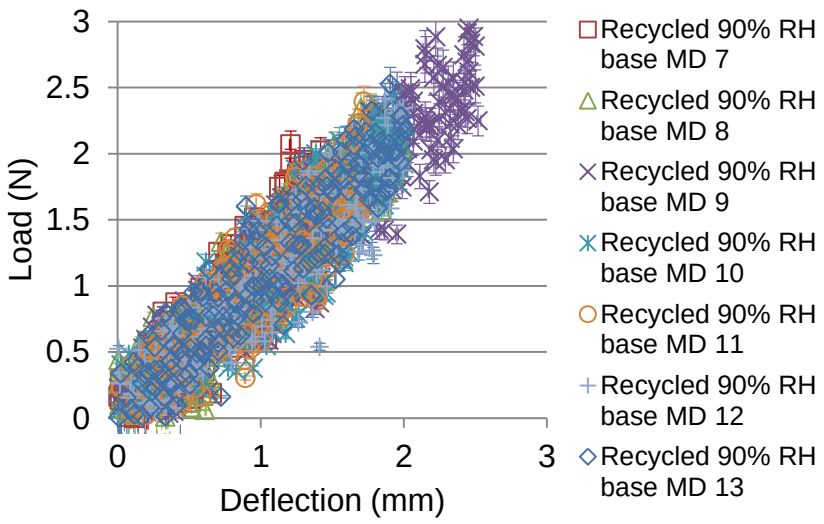

Figure III-30: Recycled paperboard at 90% RH, 23 °C, MD-bending with double backer side up, linear portion of load vs. deflection plot.

III.3.8 Recycled 90% RH CD-bending test plots

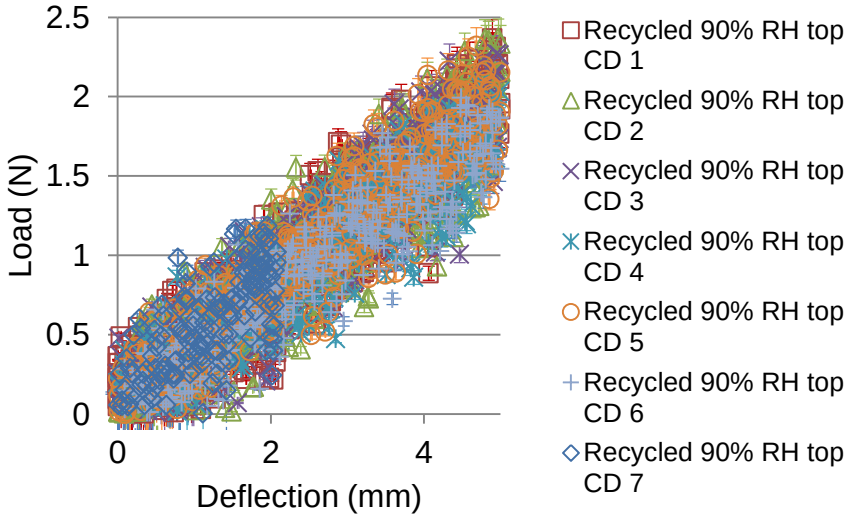

Figure III-31: Recycled paperboard at 90% RH, 23 °C, CD-bending with single facer side up, linear portion of load vs. deflection plot.

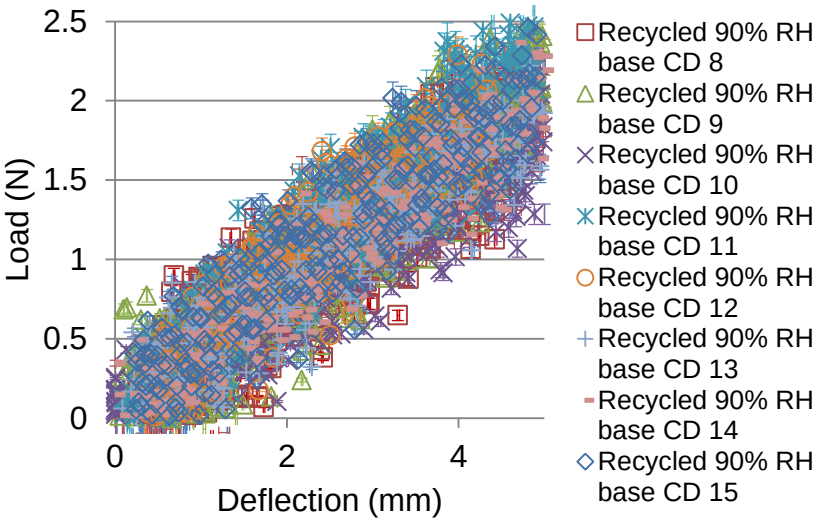

Figure III-32: Recycled paperboard at 90% RH, 23 °C, CD-bending with double backer side up, linear portion of load vs. deflection plot.

III.4 Four-point Bending FE model plots

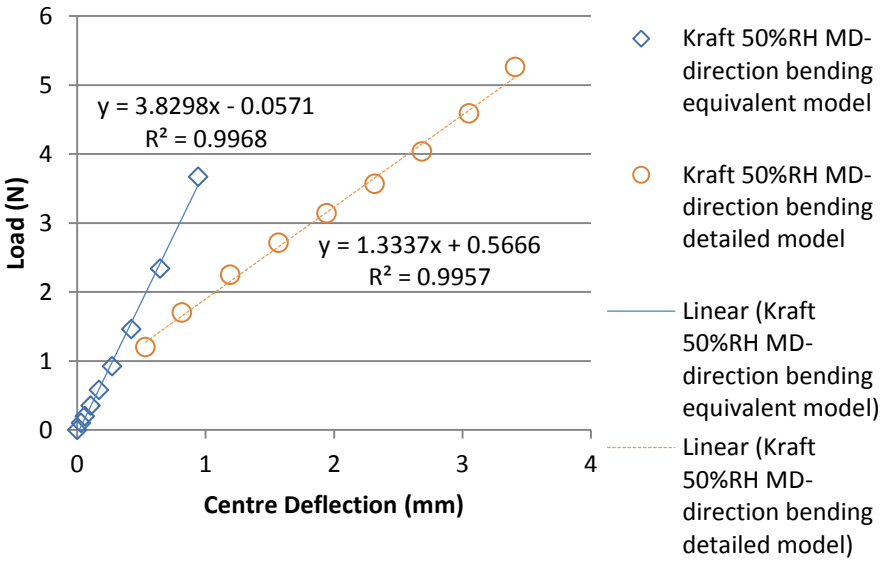

Figure III-33: FEM equivalent and detailed kraft paperboard at 50% RH, 23 °C, MD-bending linear portion of load vs. deflection plot.

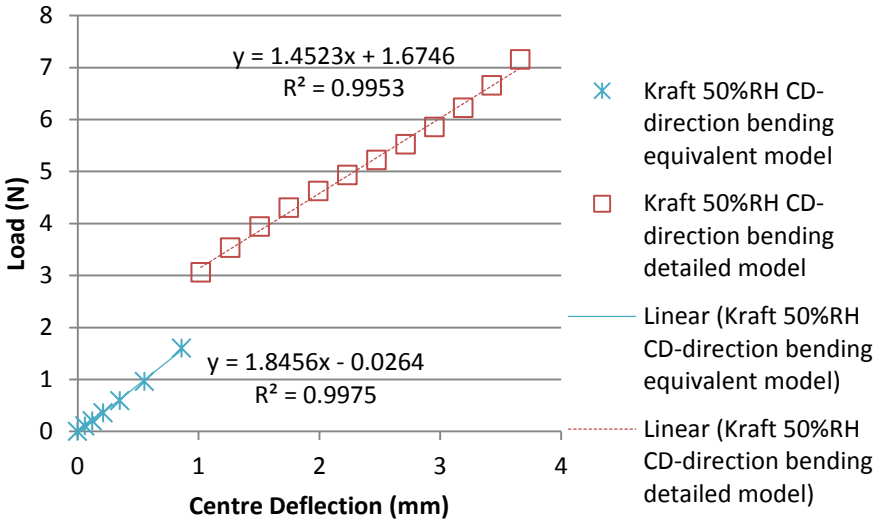

Figure III-34: FEM equivalent and detailed kraft paperboard at 50% RH, 23 °C, CD-bending linear portion of load vs. deflection plot.

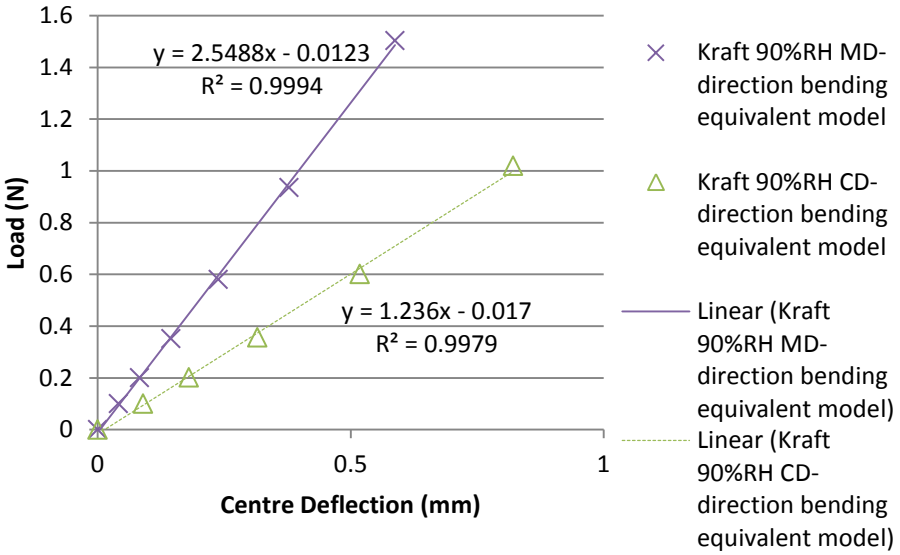

Figure III-35: FEM equivalent kraft paperboard at 90% RH, 23 °C, MD- and CD-bending linear portion of load vs. deflection plot.

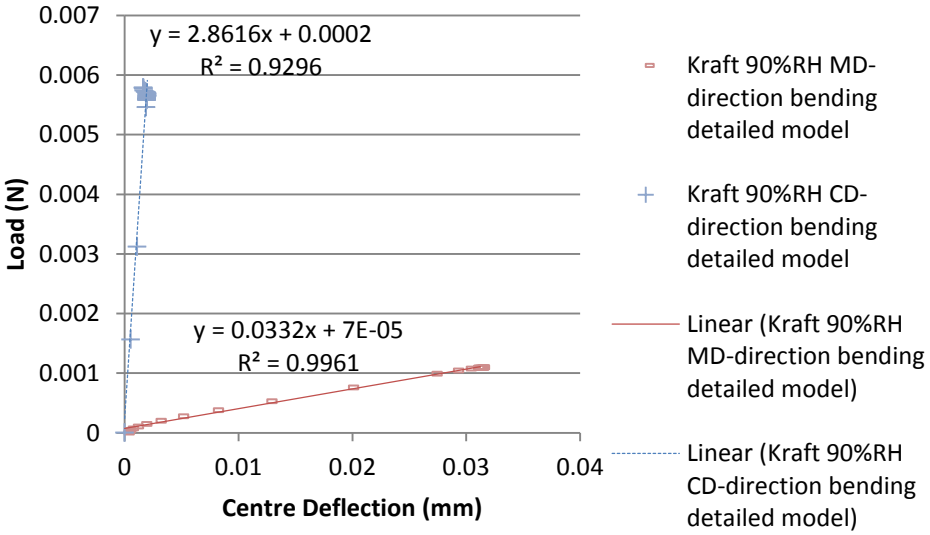

Figure III-36: FEM detailed kraft paperboard at 90% RH, 23 °C, MD- and CD-bending linear portion of load vs. deflection plot.

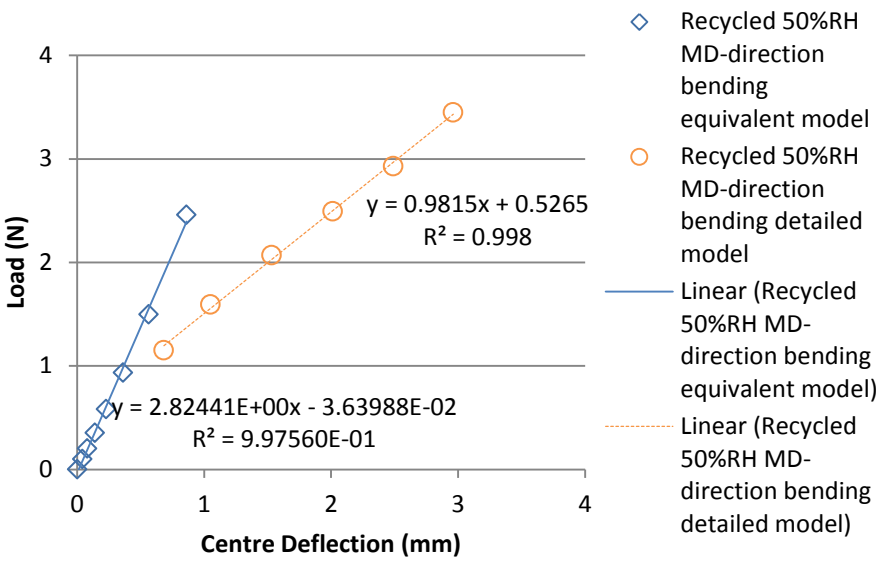

Figure III-37: FEM equivalent and detailed recycled paperboard at 50% RH, 23 °C, MD-bending linear portion of load vs. deflection plot.

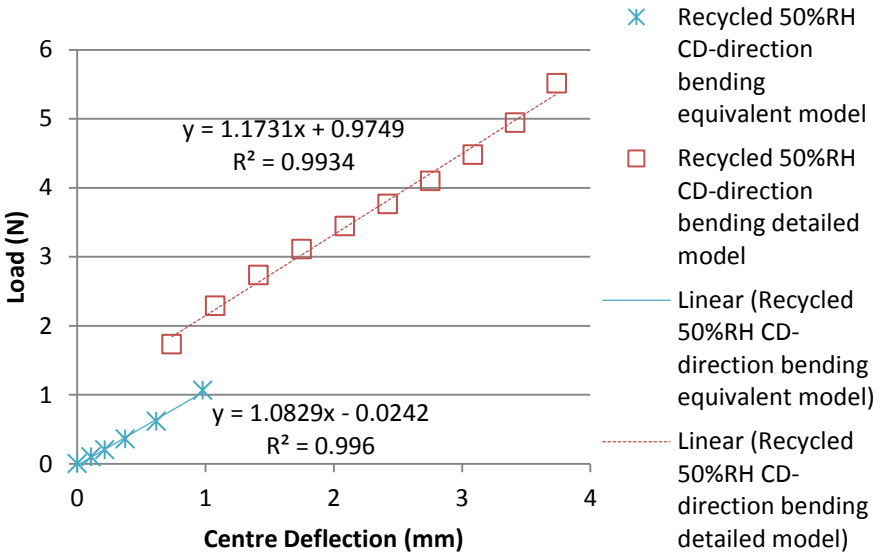

Figure III-38: FEM equivalent and detailed recycled paperboard at 50% RH, 23 °C, CD-bending linear portion of load vs. deflection plot.

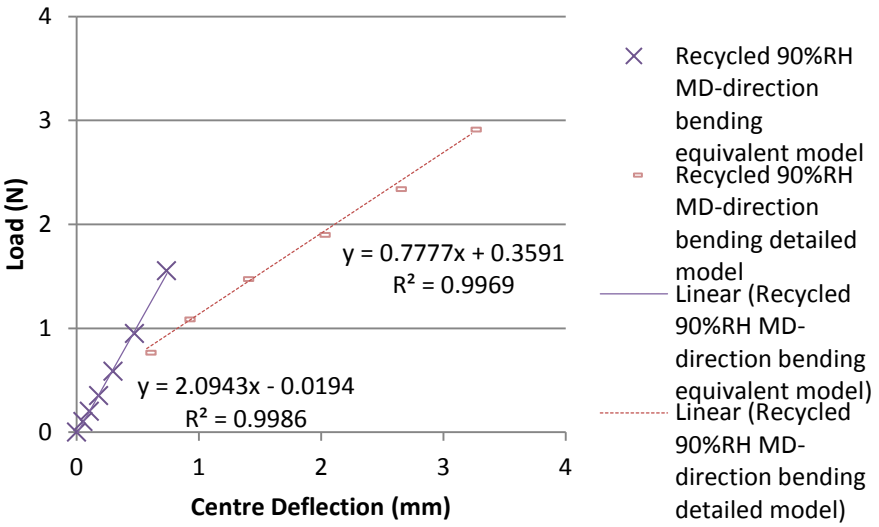

Figure III-39: FEM equivalent and detailed recycled paperboard at 90% RH, 23 °C, MD-bending linear portion of load vs. deflection plot.

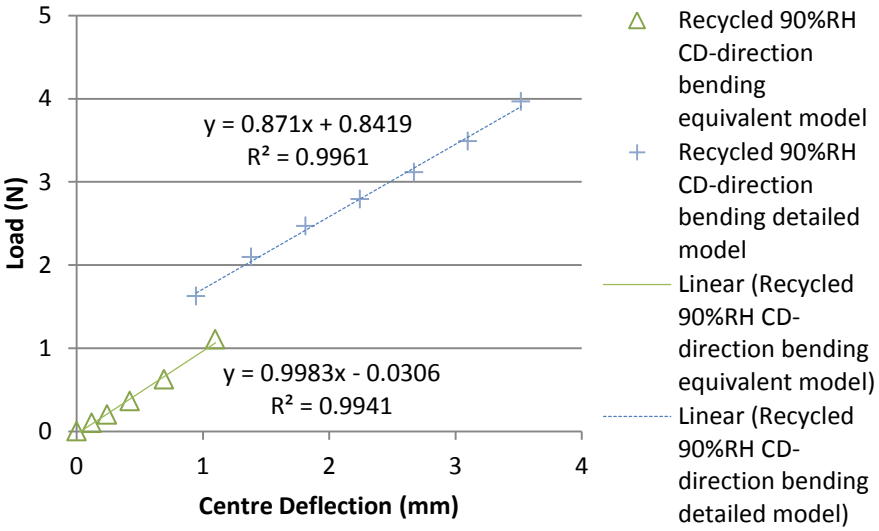

Figure III-40: FEM equivalent and detailed recycled paperboard at 90% RH, 23 °C, CD-bending linear portion of load vs. deflection plot.

III.5 Sonic vibration test images

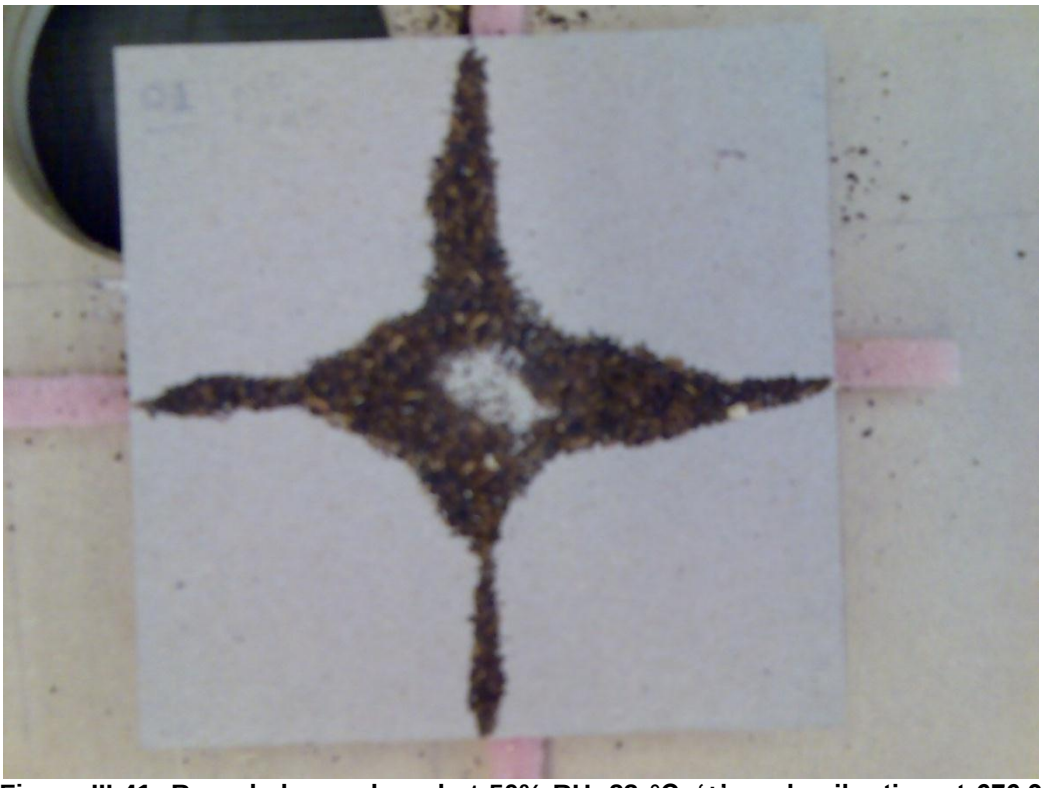

Figure III-41: Recycled paperboard at 50% RH, 23 °C, '+' mode vibration at 676.92 Hz.

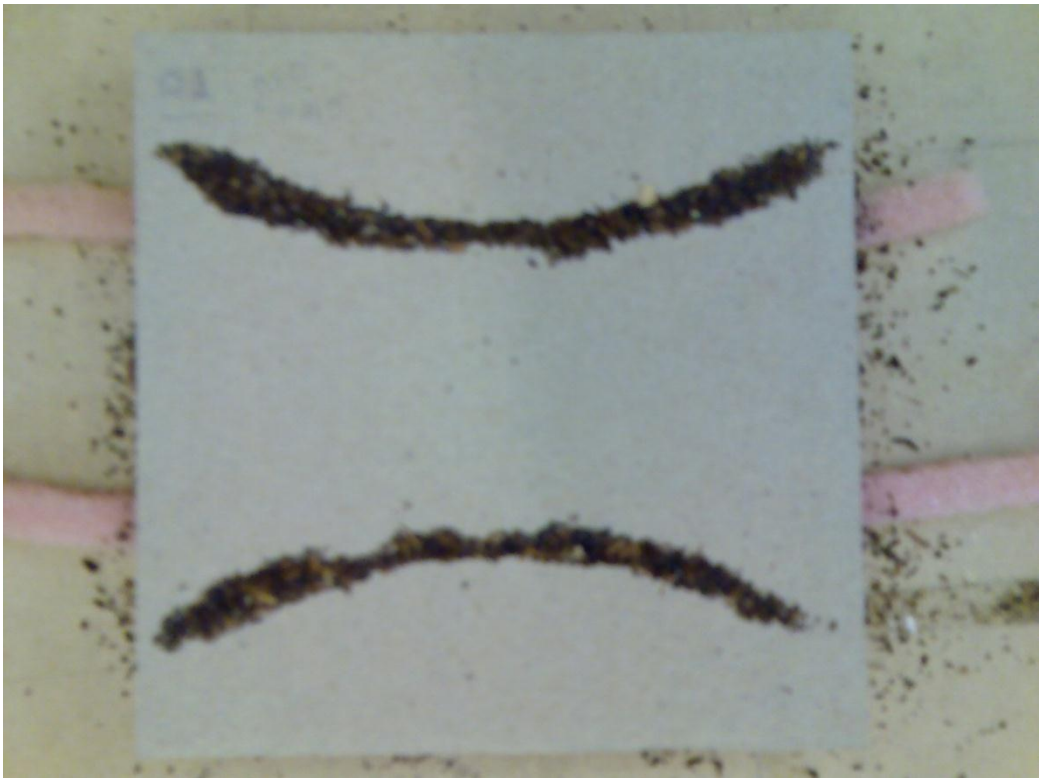

Figure III-42: Recycled paperboard at 50% RH, 23 °C, CD-bending mode vibration at 1056.4 Hz.

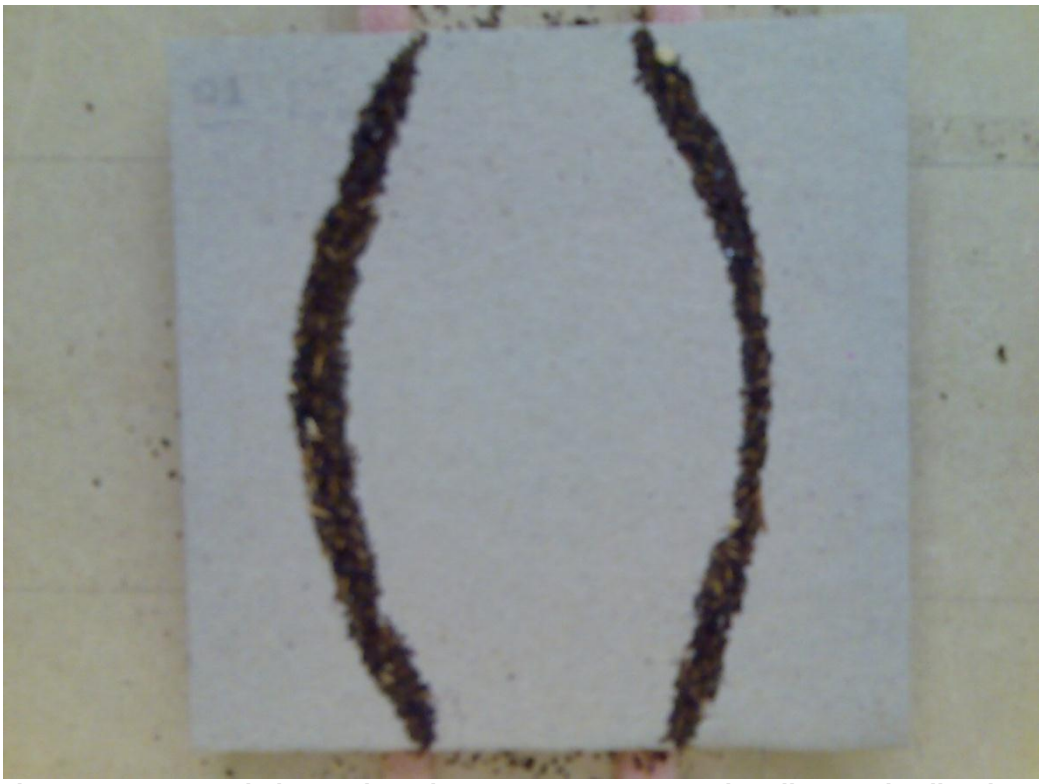

Figure III-43: Recycled paperboard at 50% RH, 23 °C, MD-bending mode vibration at 1200.5 Hz.

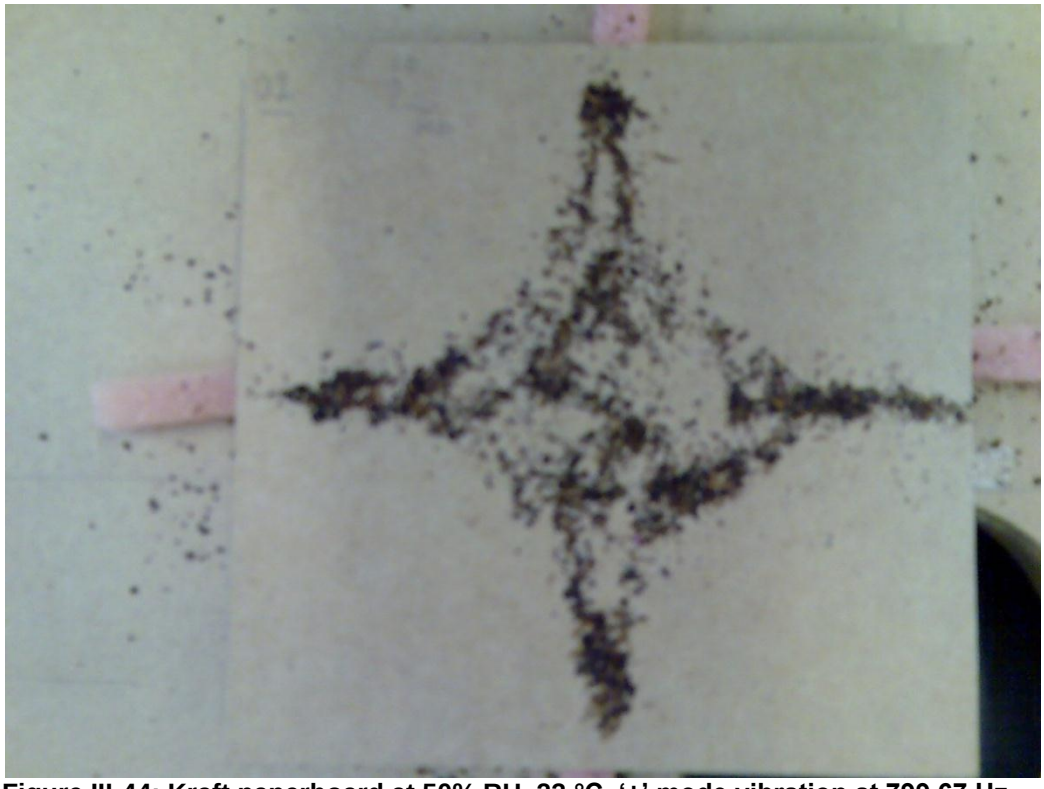

Figure III-44: Kraft paperboard at 50% RH, 23 °C, '+' mode vibration at 799.67 Hz.

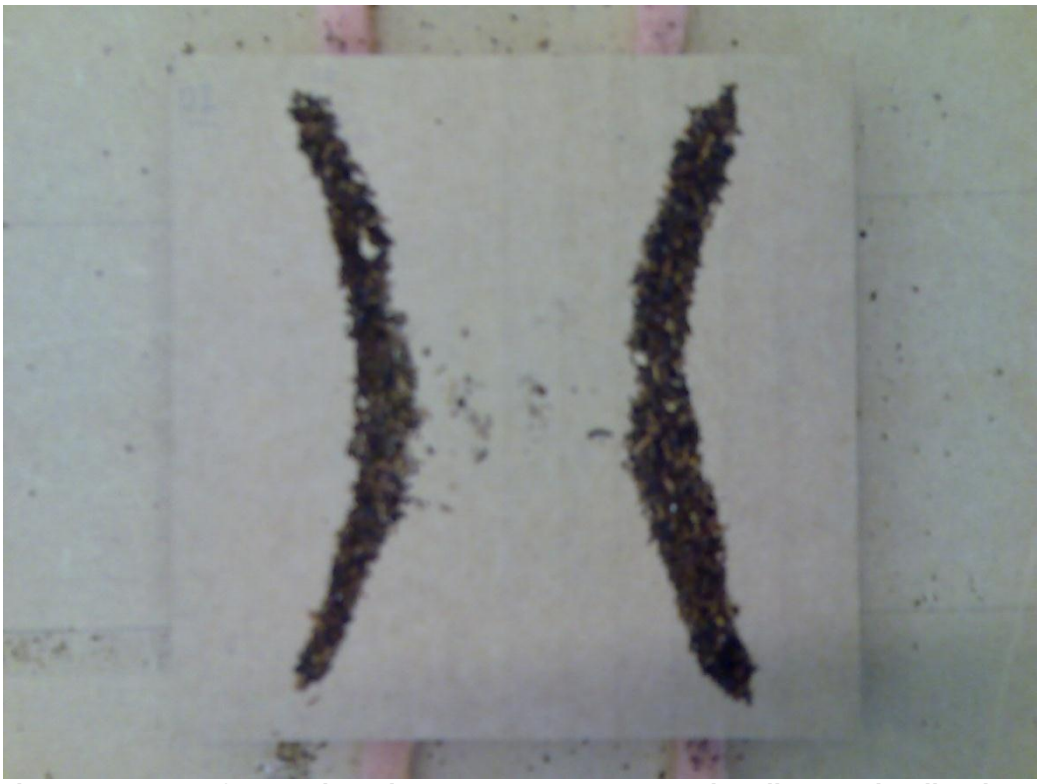

Figure III-45: Kraft paperboard at 50% RH, 23 °C, MD-bending mode vibration at 1220.6 Hz.

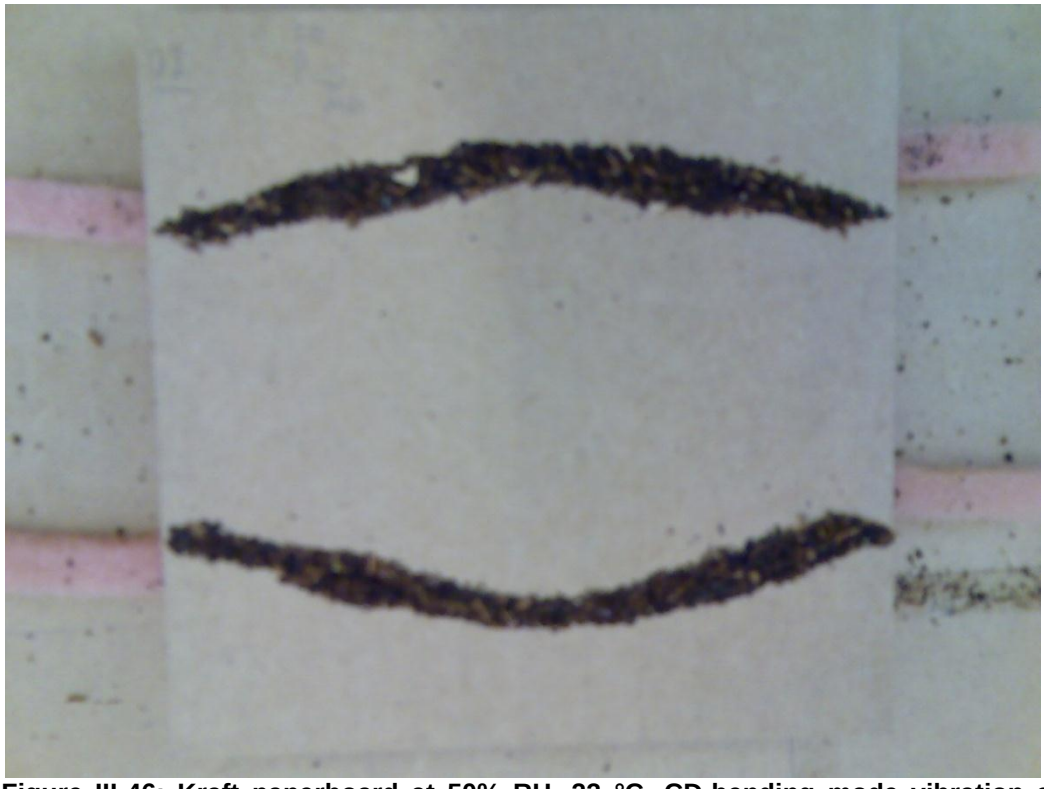

Figure III-46: Kraft paperboard at 50% RH, 23 °C, CD-bending mode vibration at 1432.1 Hz.

III.6 Free-vibration FE model plots

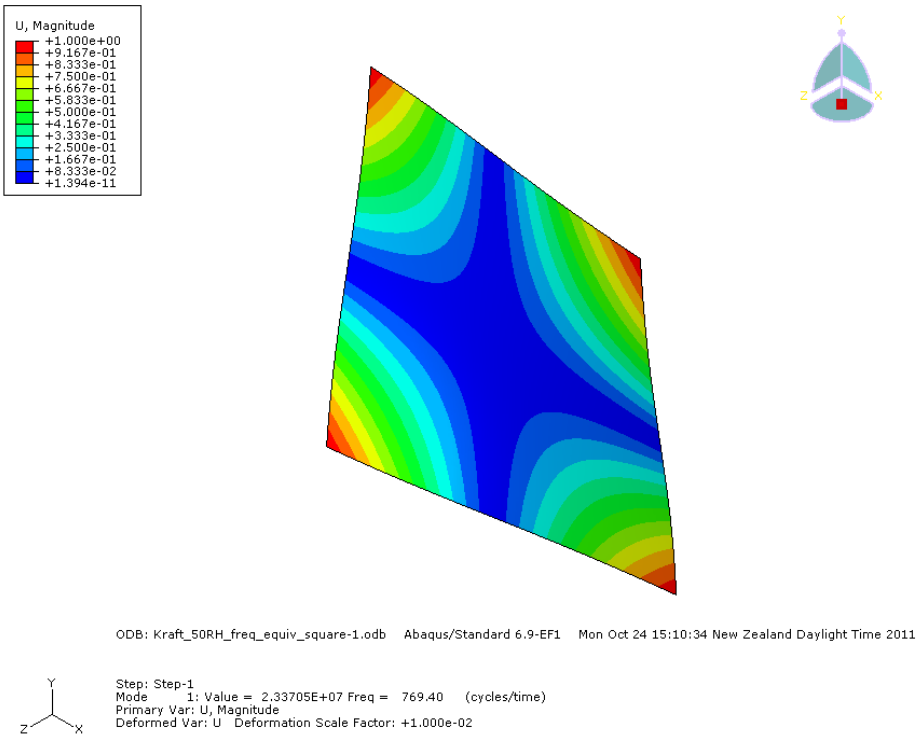

Figure III-47: FEM equivalent kraft paperboard at 50% RH, 23 °C, '+' mode vibration.

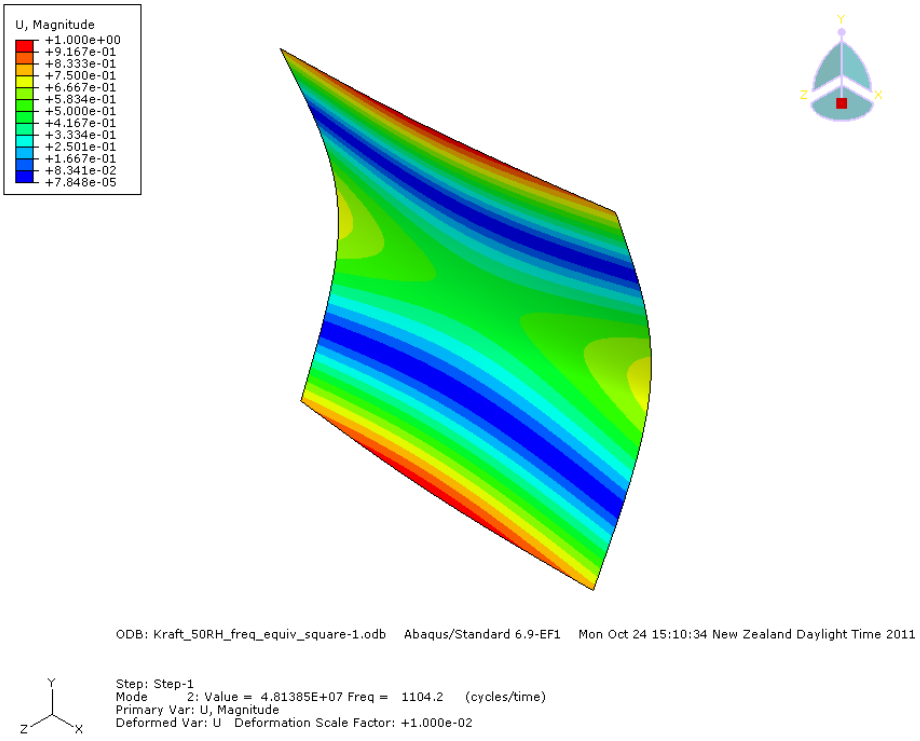

Figure III-48: FEM equivalent kraft paperboard at 50% RH, 23 °C, CD-bending mode vibration.

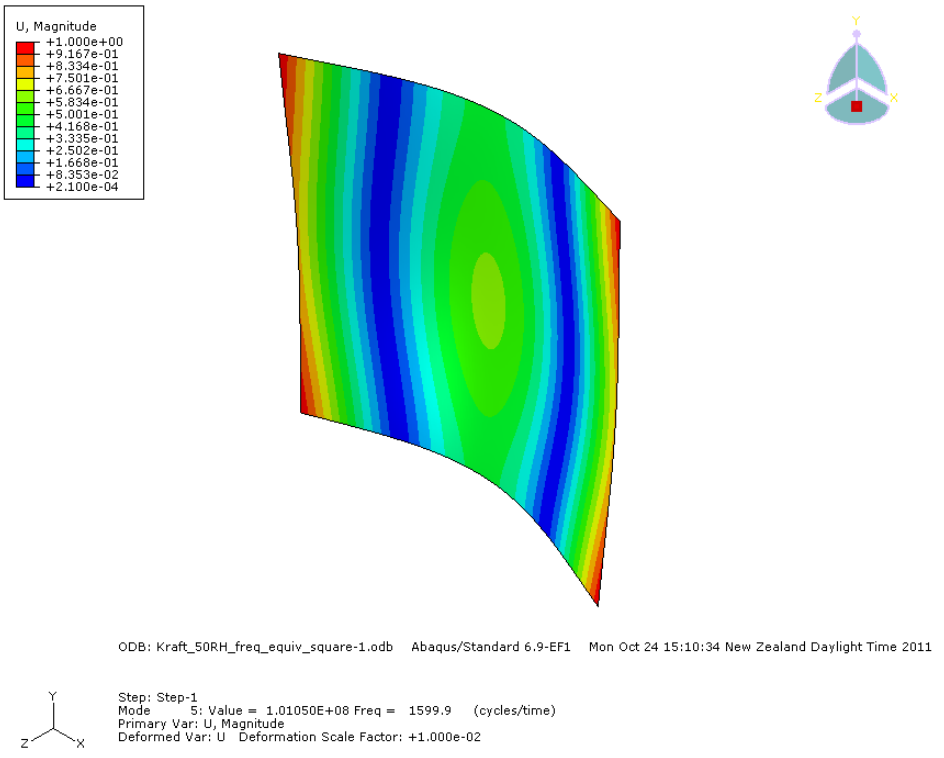

Figure III-49: FEM equivalent kraft paperboard at 50% RH, 23 °C, MD-bending mode vibration.

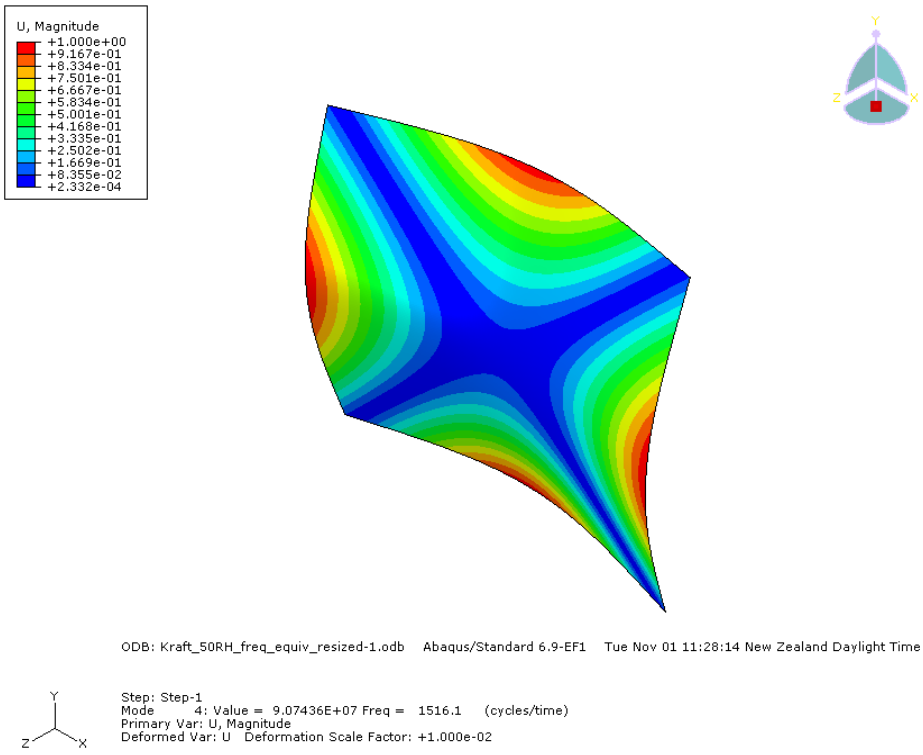

Figure III-50: FEM equivalent kraft paperboard at 50% RH, 23 °C, 'x' mode vibration.

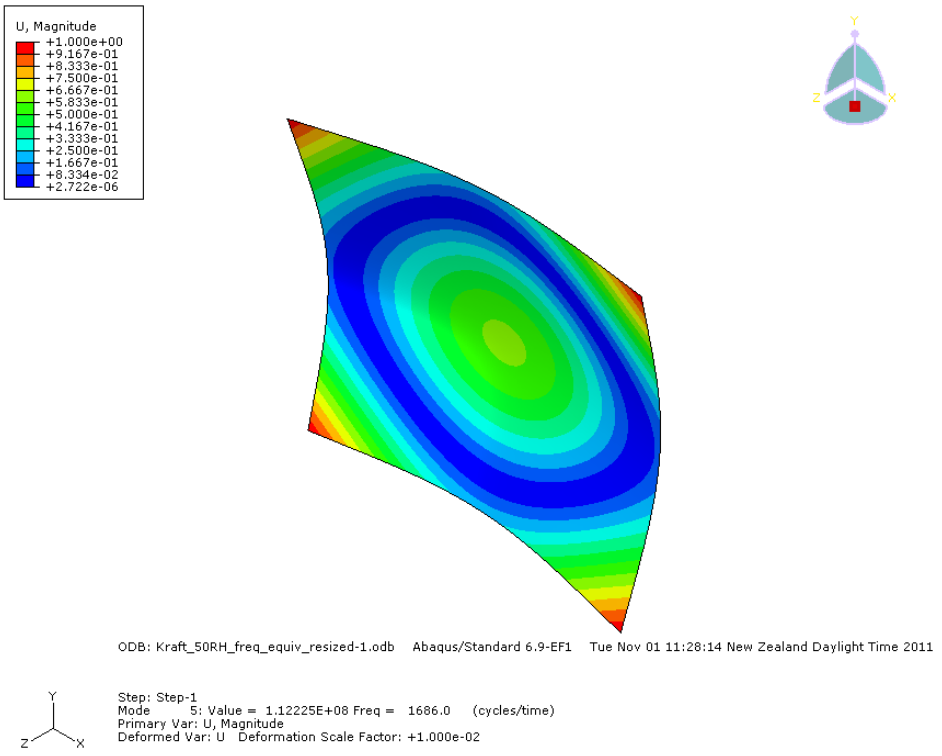

Figure III-51: FEM equivalent kraft paperboard at 50% RH, 23 °C, ring mode vibration.

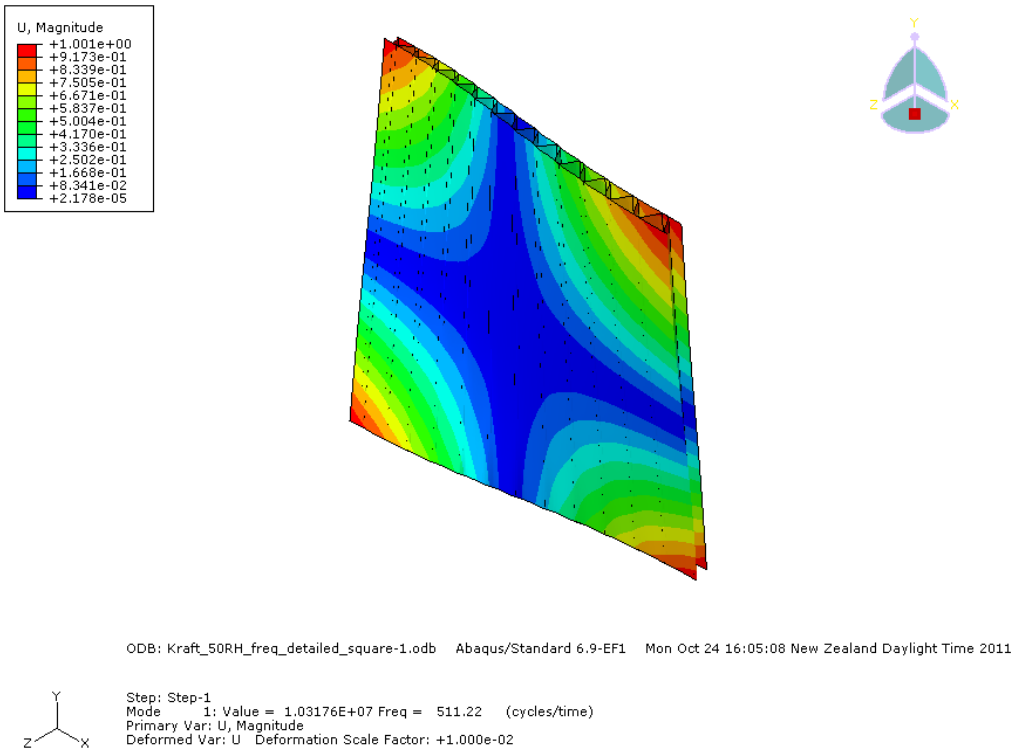

Figure III-52: FEM detailed kraft paperboard at 50% RH, 23 °C, '+' mode vibration.

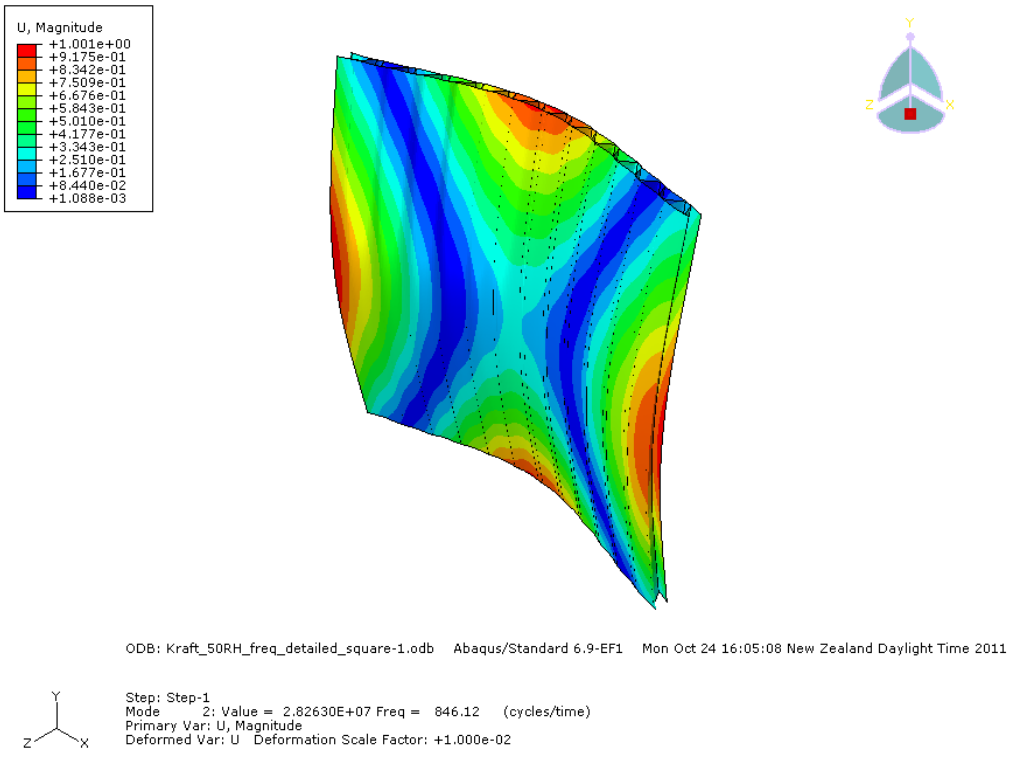

Figure III-53: FEM detailed kraft paperboard at 50% RH, 23 °C, MD-bending mode vibration.

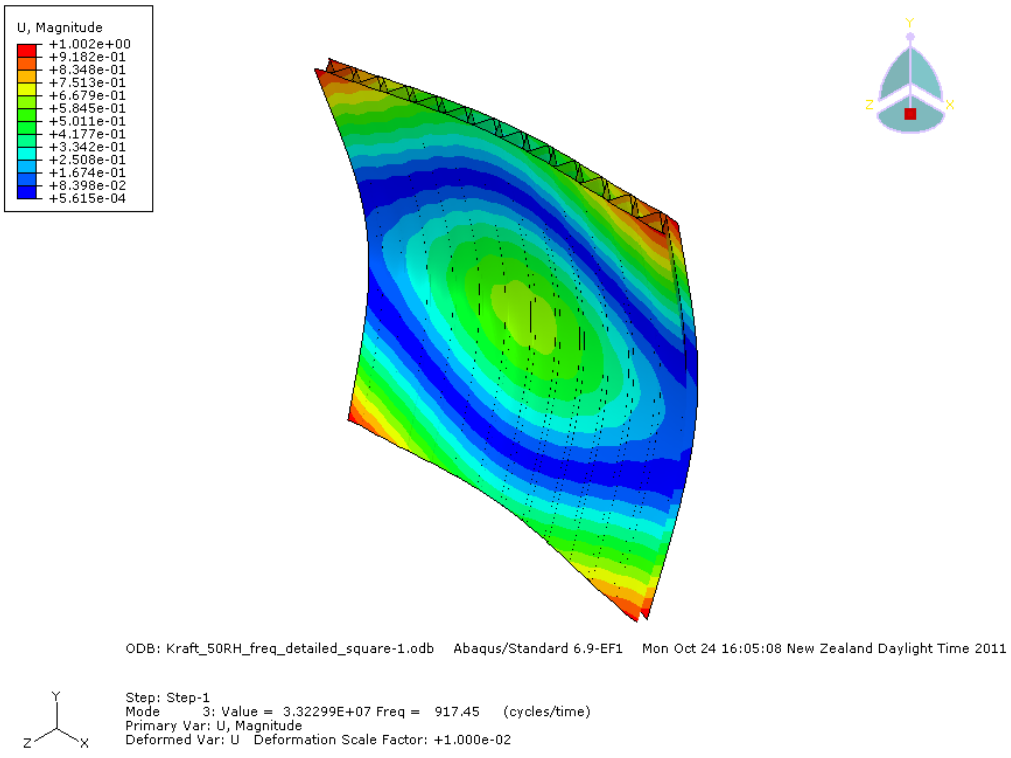

Figure III-54: FEM detailed kraft paperboard at 50% RH, 23 °C, CD-bending mode vibration.

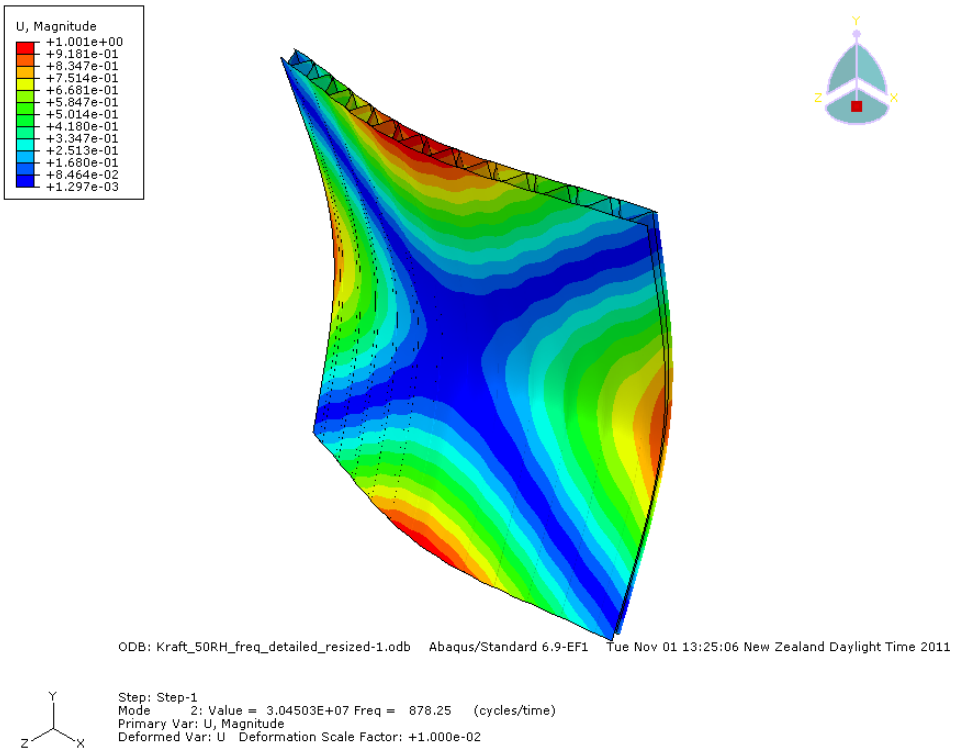

Figure III-55: FEM detailed kraft paperboard at 50% RH, 23 °C, ‘x’ mode vibration.

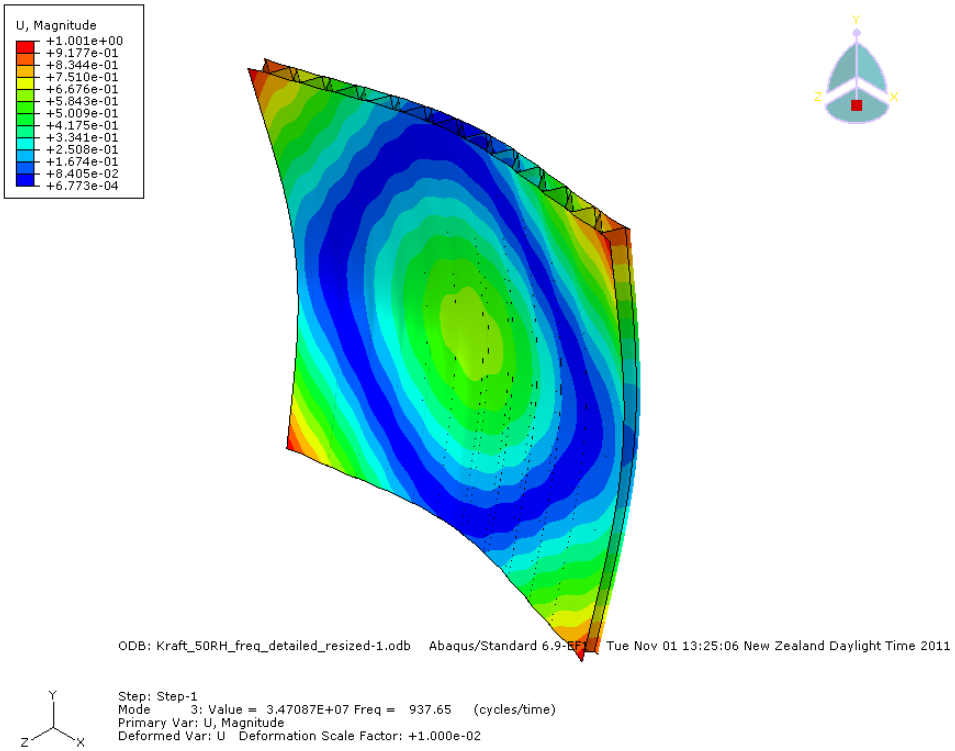

Figure III-56: FEM detailed kraft paperboard at 50% RH, 23 °C, ring mode vibration.

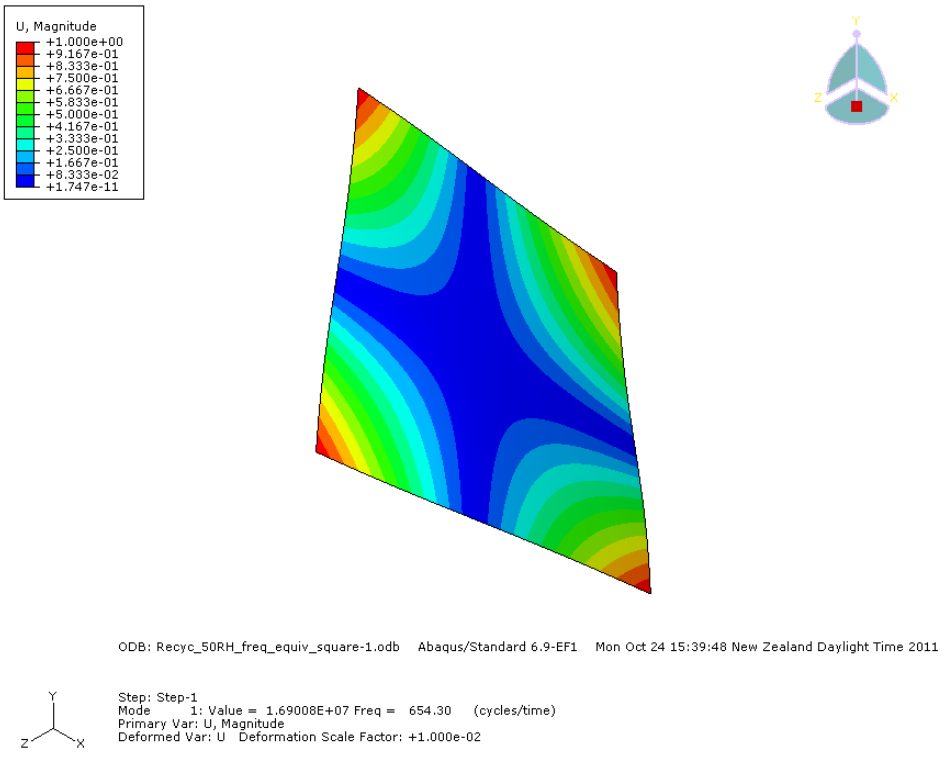

Figure III-57: FEM equivalent recycled paperboard at 50% RH, 23 °C, '+' mode vibration.

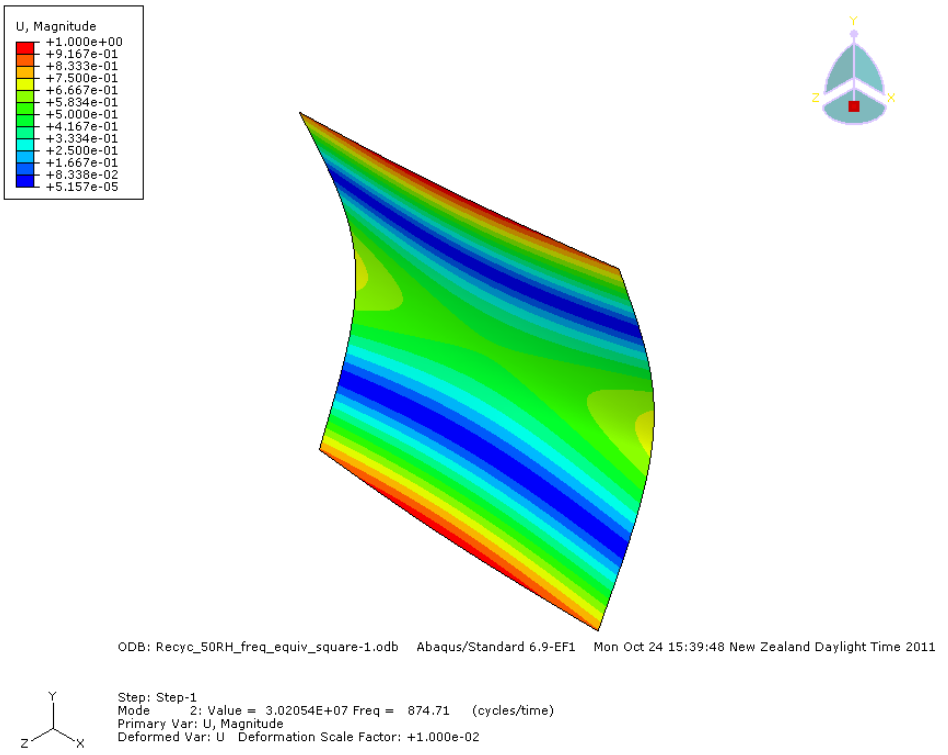

Figure III-58: FEM equivalent recycled paperboard at 50% RH, 23 °C, CD-bending mode vibration.

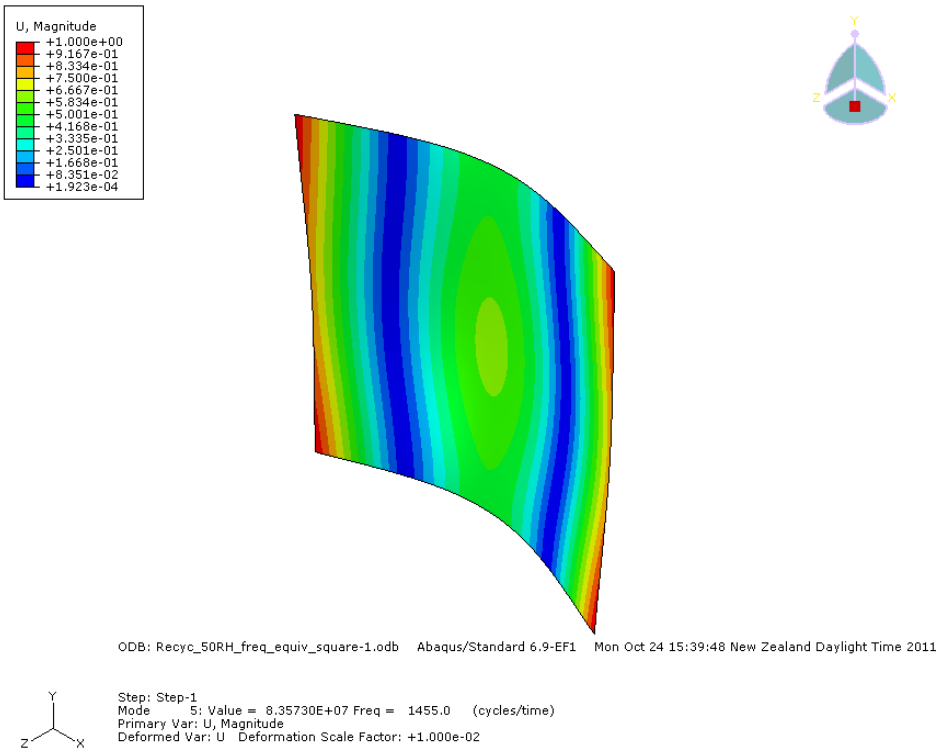

Figure III-59: FEM equivalent recycled paperboard at 50% RH, 23 °C, MD-bending mode vibration.

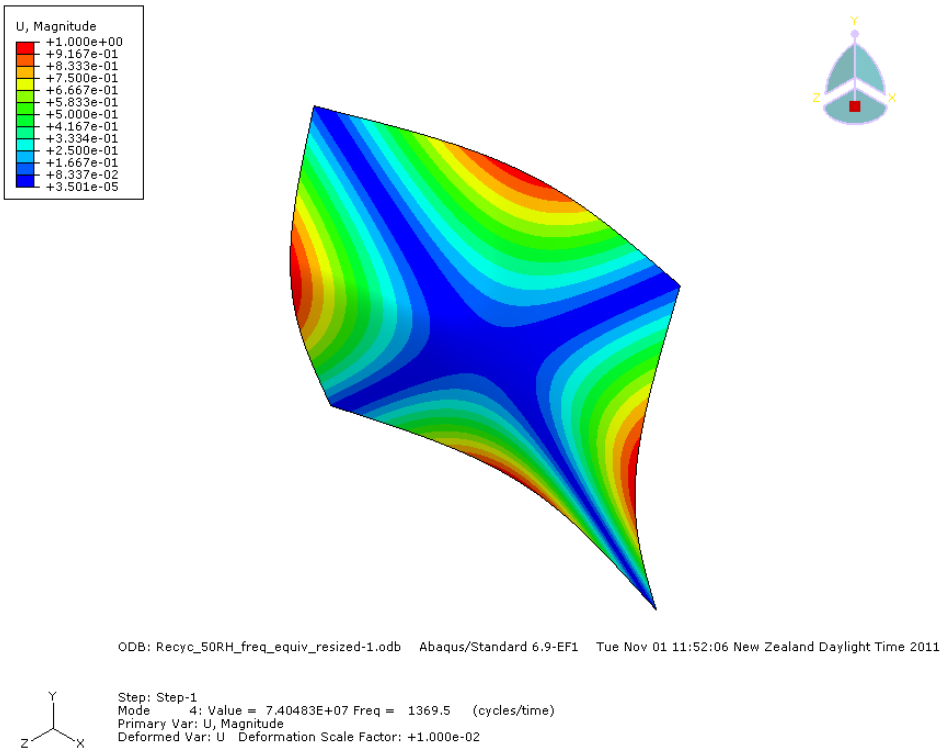

Figure III-60: FEM equivalent recycled paperboard at 50% RH, 23 °C, 'x' mode vibration.

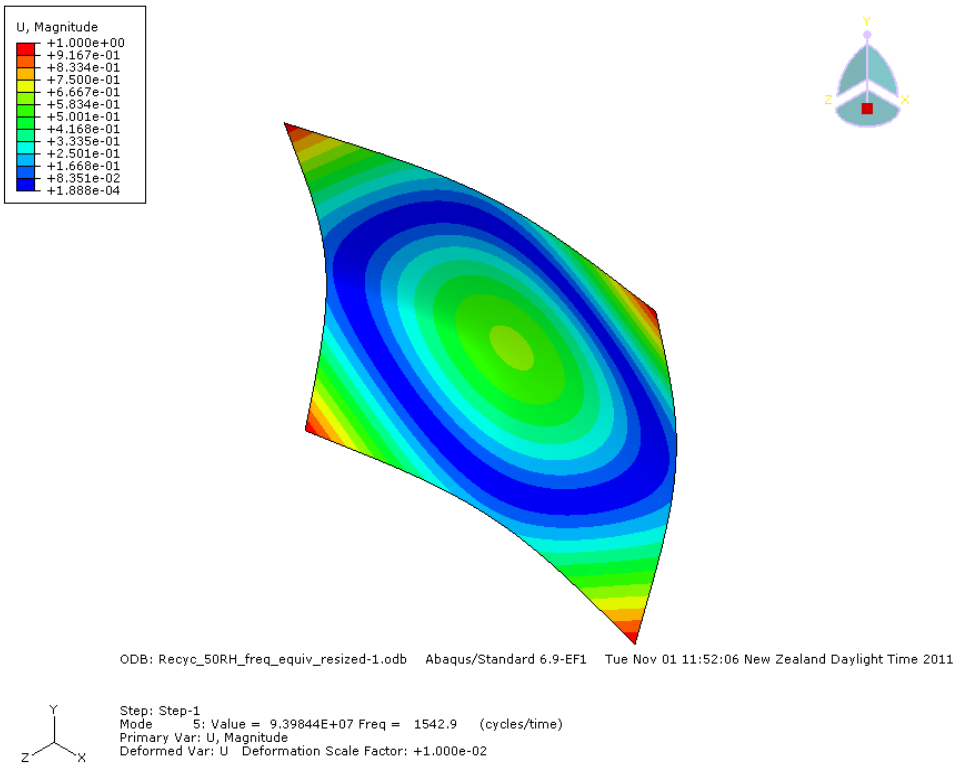

Figure III-61: FEM equivalent recycled paperboard at 50% RH, 23 °C, ring mode vibration.

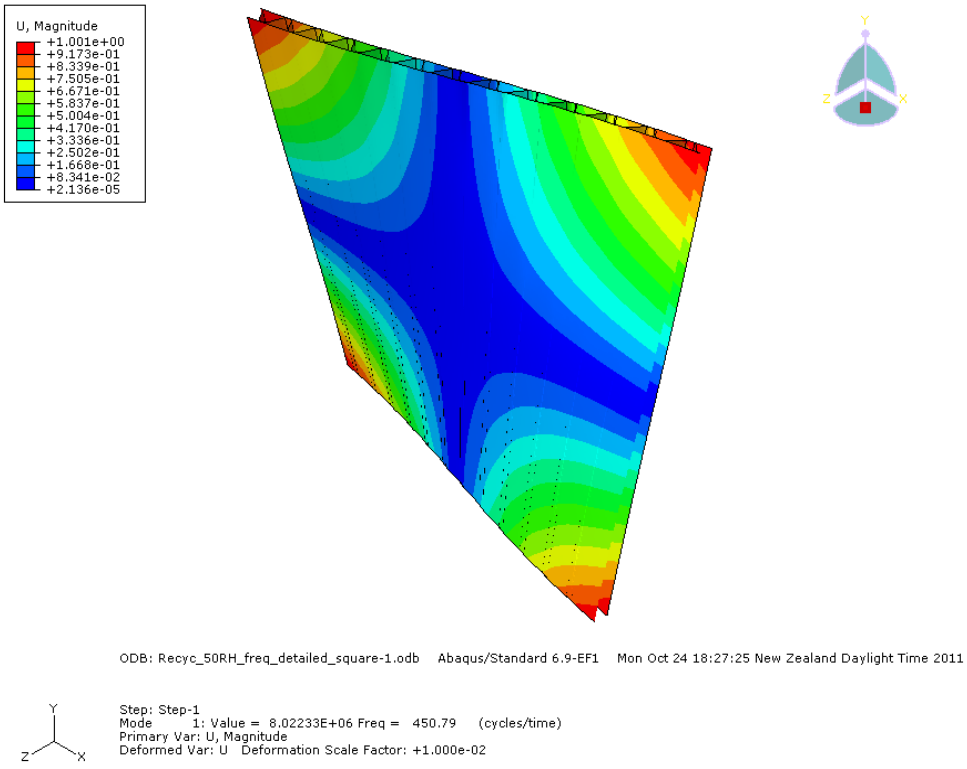

Figure III-62: FEM detailed recycled paperboard at 50% RH, 23 °C, '+' mode vibration.

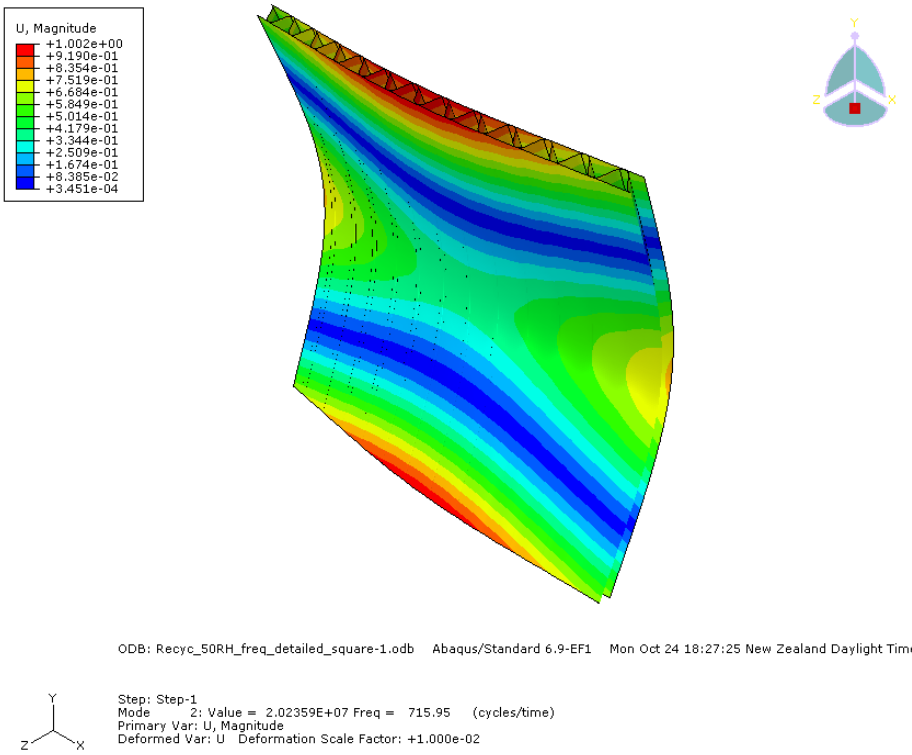

Figure III-63: FEM detailed recycled paperboard at 50% RH, 23 °C, CD-bending mode vibration.

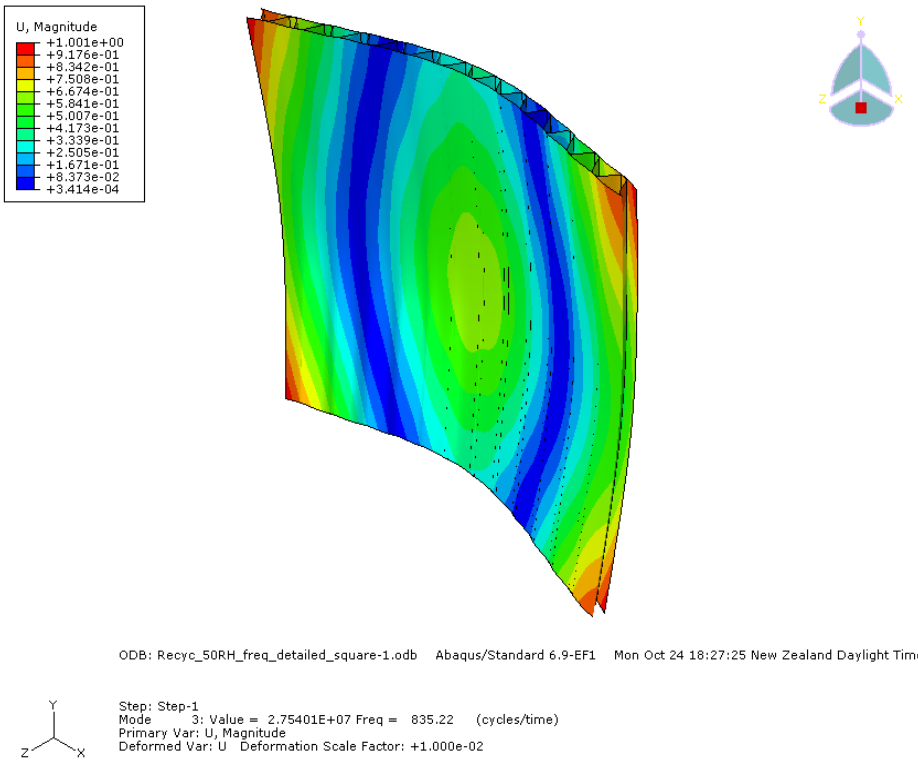

Figure III-64: FEM detailed recycled paperboard at 50% RH, 23 °C, MD-bending mode vibration.

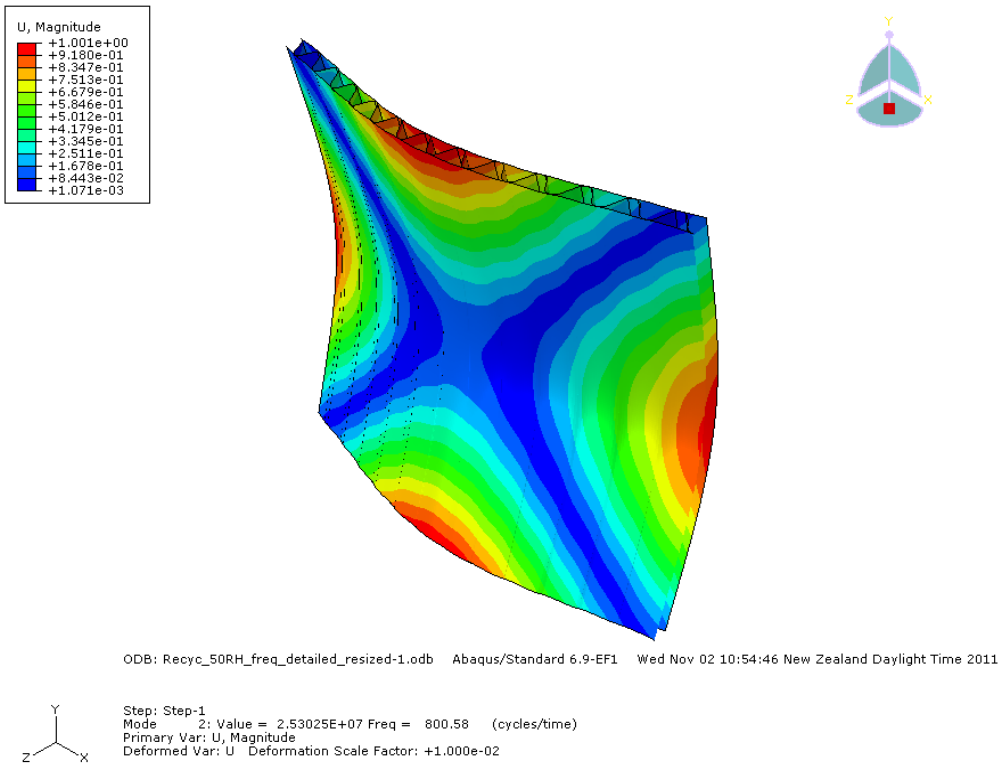

Figure III-65: FEM detailed recycled paperboard at 50% RH, 23 °C, 'x' mode vibration.

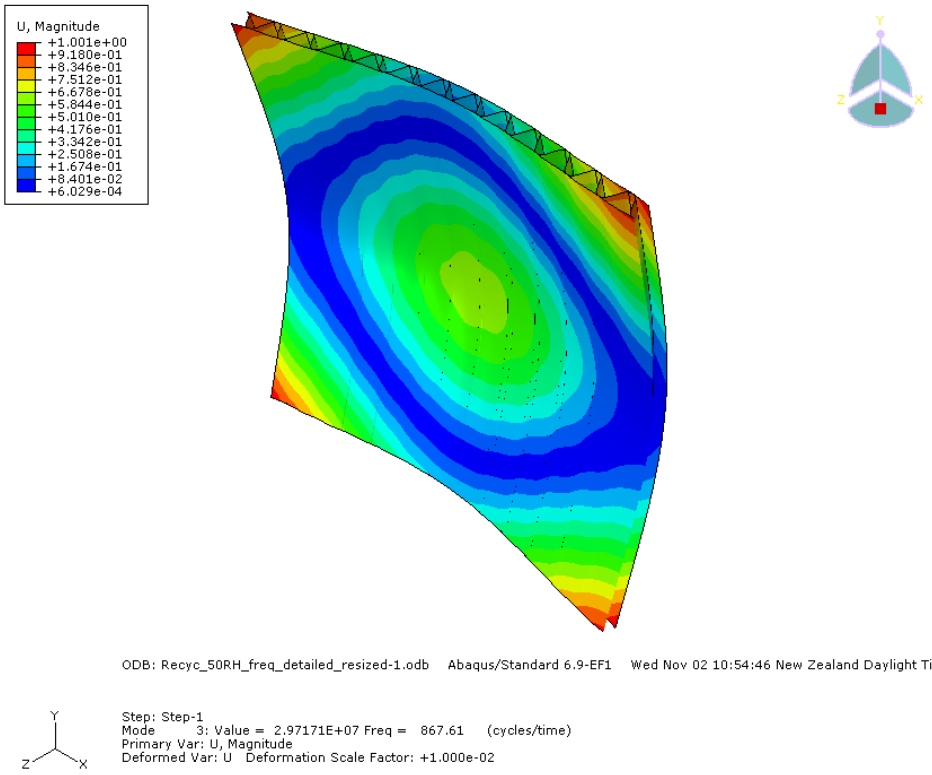

Figure III-66: FEM detailed recycled paperboard at 50% RH, 23 °C, ring mode vibration.

Appendix IV

Table IV-1: Mean values of out-of-plane geometric imperfection w_0 of buckling panel samples obtained by Southwell plots and unadjusted initial measurements.

Material	R.H.	Method	w_0(0.5 a, 0.5 b) / h	w_0(0.5 a, 0.75 b) / h	w_0(0.5 a, 0.25 b) / h	w_0(0.25 a, 0.75 b) / h
Kraft	50%	Southwell	0.026±0.014	0.039±0.022	0.581±0.323	0.929±0.557
		Unadjusted	0.359±0.008	0.376±0.008	0.065±0.175	0.267±0.178
	90%	Southwell	-0.050±1.787	0.693±0.408	-0.816±1.330	-0.584±1.372
		Unadjusted	1.322±0.397	0.884±0.366	1.111±0.293	1.108±0.295
Recycled	50%	Southwell	0.025±0.023	0.055±0.046	0.609±0.581	1.407±1.264
		Unadjusted	0.345±0.003	0.359±0.003	-0.239±0.073	-0.091±0.071
	90%	Southwell	0.954±1.285	0.990±0.881	0.778±0.967	0.569±0.916
		Unadjusted	1.004±0.263	0.790±0.274	0.862±0.167	0.826±0.216

Table IV-2: : Least square method estimates of critical load P_{crit}, post-buckling parameter Ψ and imperfection A_0 from panel post-buckling experiment for recycled paperboard at 23 °C, 50% relative humidity.

Kraft 50% RH sample no.	P_{crit} (N)	Ψ (Pa)	A_0 (m)
1	1.30E+03	9.56E+08	8.36E-05
2	1.25E+03	1.82E+09	1.06E-04
3	1.04E+03	7.50E+08	9.35E-05
4	9.25E+02	1.23E+09	4.22E-05
Average	1.13E+03	1.19E+09	8.13E-05
Standard deviation	1.77E+02	4.62E+08	2.76E-05
95% confidence interval uncertainty	2.82E+02	7.36E+08	4.39E-05

Table IV-3: Least square method estimates of critical load P_{crit}, post-buckling parameter Ψ and imperfection A_0 from panel post-buckling experimental data for recycled paperboard at 23 °C, 50% relative humidity.

Recycled 50% RH sample no.	P_{crit} (N)	Ψ (Pa)	A_0 (m)
1	1.07E+03	5.61E+08	5.36E-05
2	1.64E+03	1.00E+08	3.00E-0
3	1.72E+03	-2.45E+08	2.46E-04
4	1.10E+03	1.81E+08	6.67E-05
6	9.22E+02	3.02E+09	5.43E-05
7	1.11E+03	5.61E+07	3.22E-05
Average	1.26E+03	6.12E+08	1.26E-04
Standard deviation	3.33E+02	1.21E+09	1.16E-04
95% confidence interval uncertainty	3.49E+02	1.27E+09	1.22E-04

IV.1 Post-buckling plots of panel displacement at measurement points

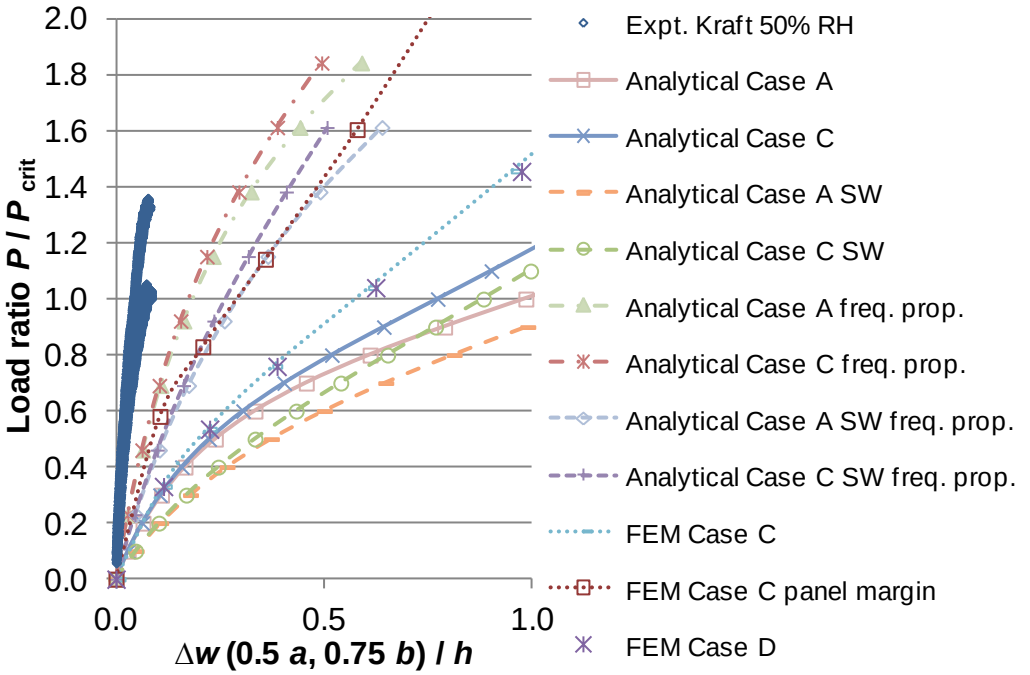

Figure IV-1: Dimensionless post-buckling plot of kraft paperboard panel displacement *w* (0.5 *a*, 0.75 *b*) at 23 °C, 50% relative humidity.

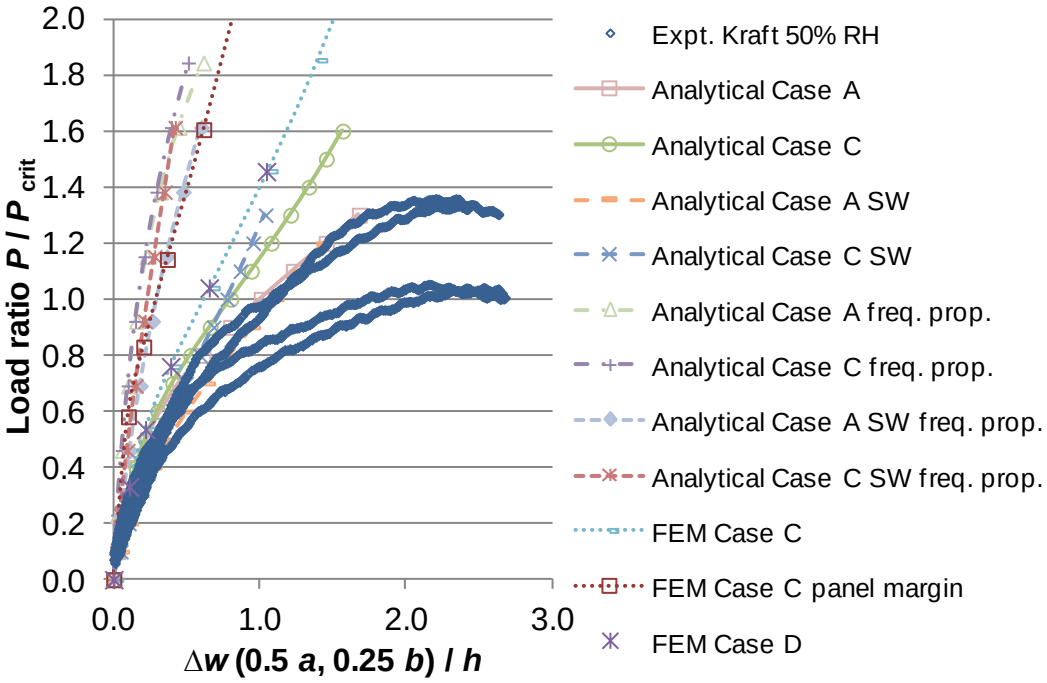

Figure IV-2: Dimensionless post-buckling plot of kraft paperboard panel displacement *w* (0.5 *a*, 0.25 *b*) at 23 °C, 50% relative humidity.

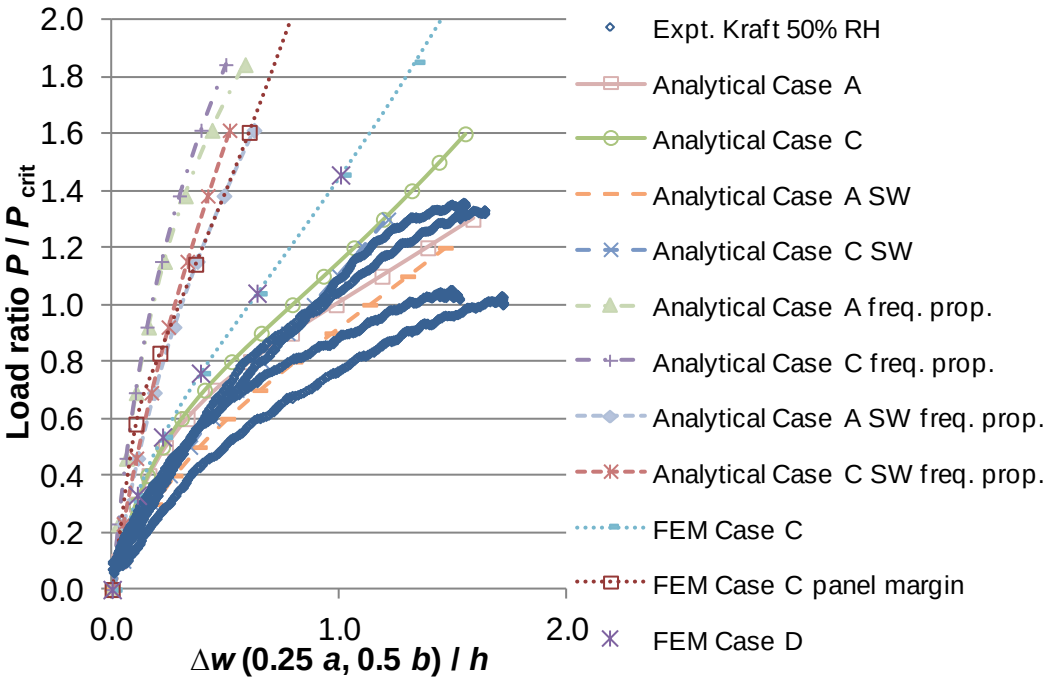

Figure IV-3: Dimensionless post-buckling plot of kraft paperboard panel displacement *w* (0.25 *a*, 0. 5 *b*) at 23 °C, 50% relative humidity.

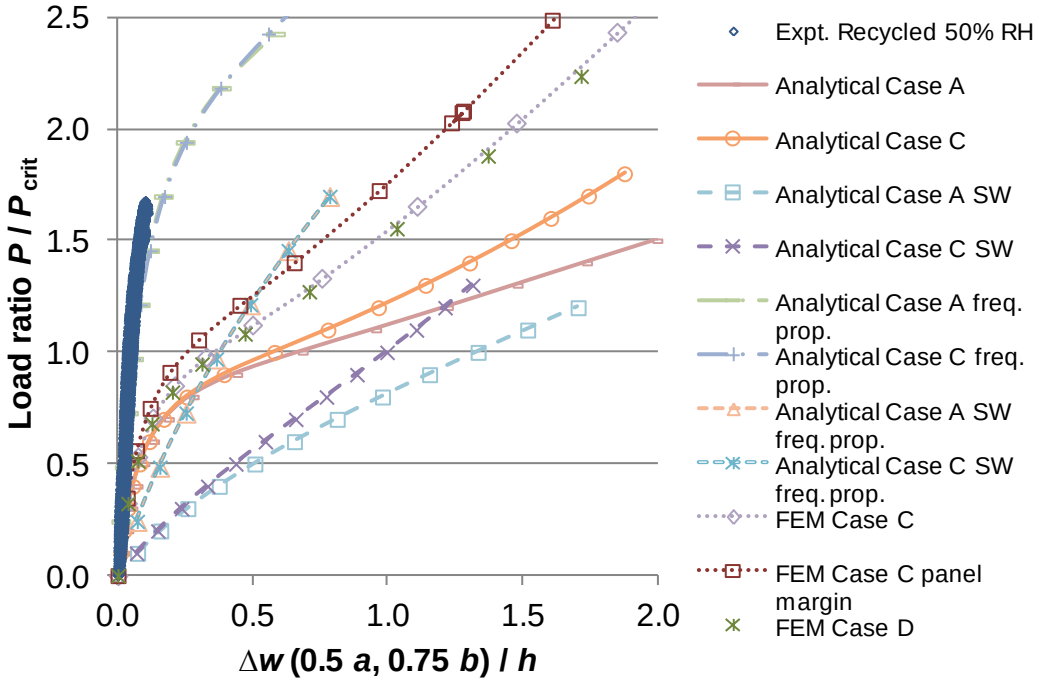

Figure IV-4: Dimensionless post-buckling plot of recycled paperboard panel displacement *w* (0.5 *a*, 0.75 *b*) at 23 °C, 50% relative humidity.

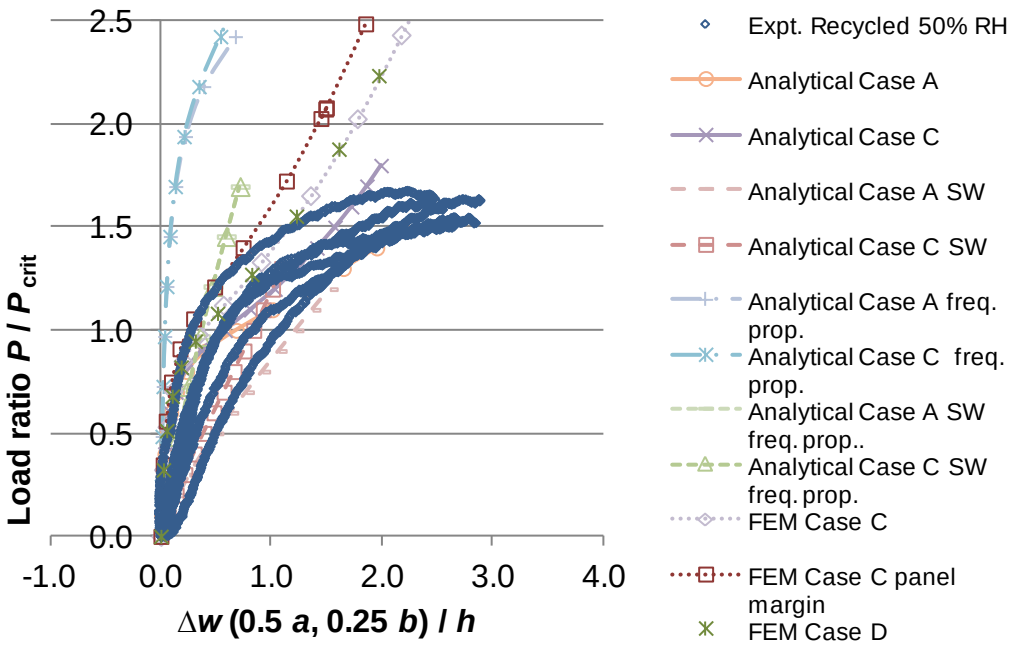

Figure IV-5: Dimensionless post-buckling plot of recycled paperboard panel displacement *w* (0.5 *a*, 0.25 *b*) at 23 °C, 50% relative humidity.

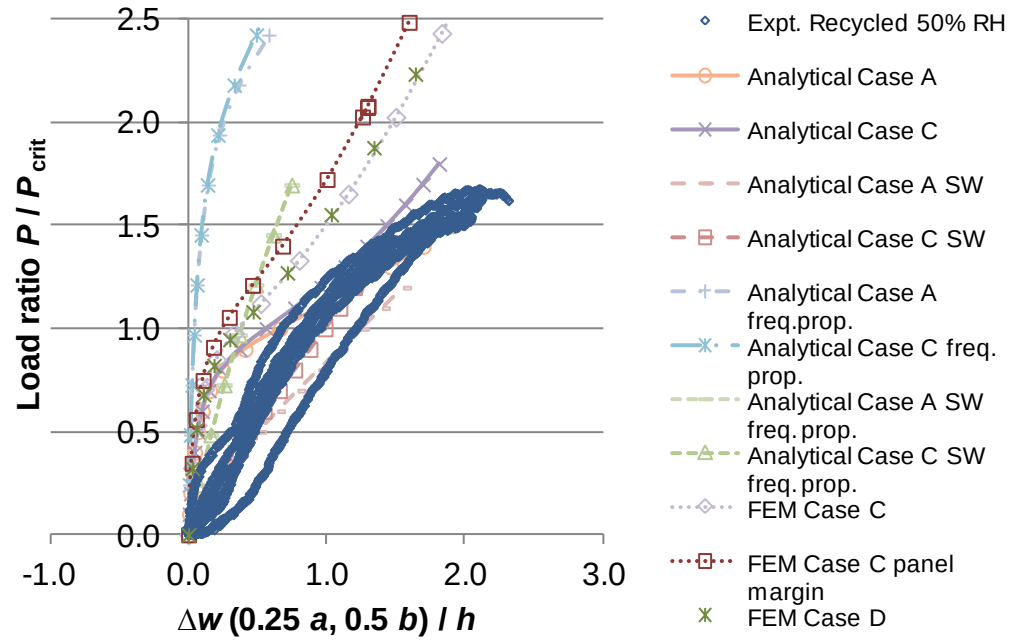

Figure IV-6: Dimensionless post-buckling plot of recycled paperboard panel displacement w (0.25 a, 0.5 b) at 23 °C, 50% relative humidity.

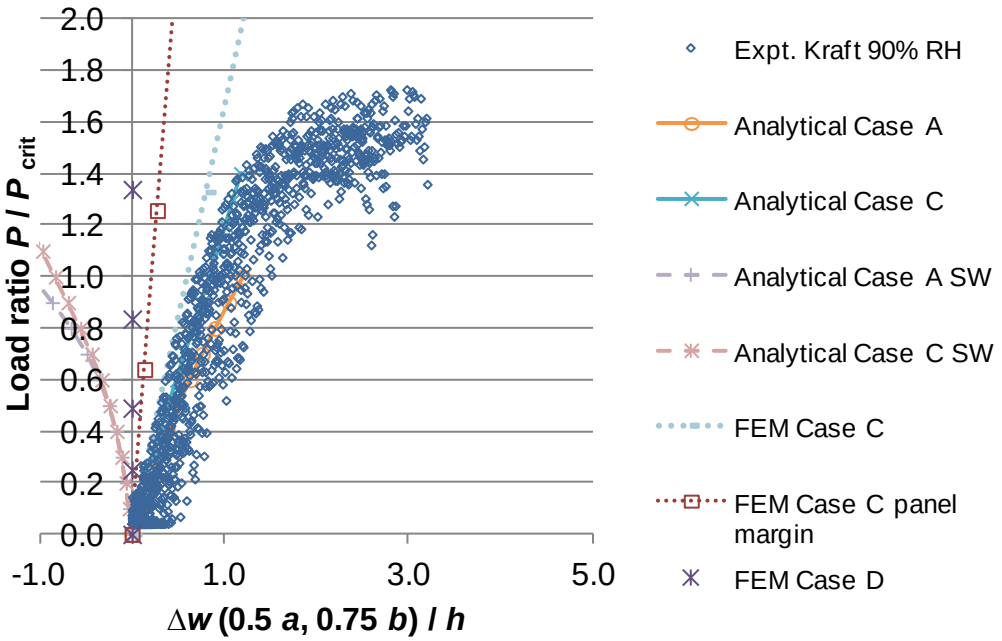

Figure IV-7: Dimensionless post-buckling plot of kraft paperboard panel displacement *w* (0.5 *a*, 0.75 *b*) at 23 °C, 90% relative humidity.

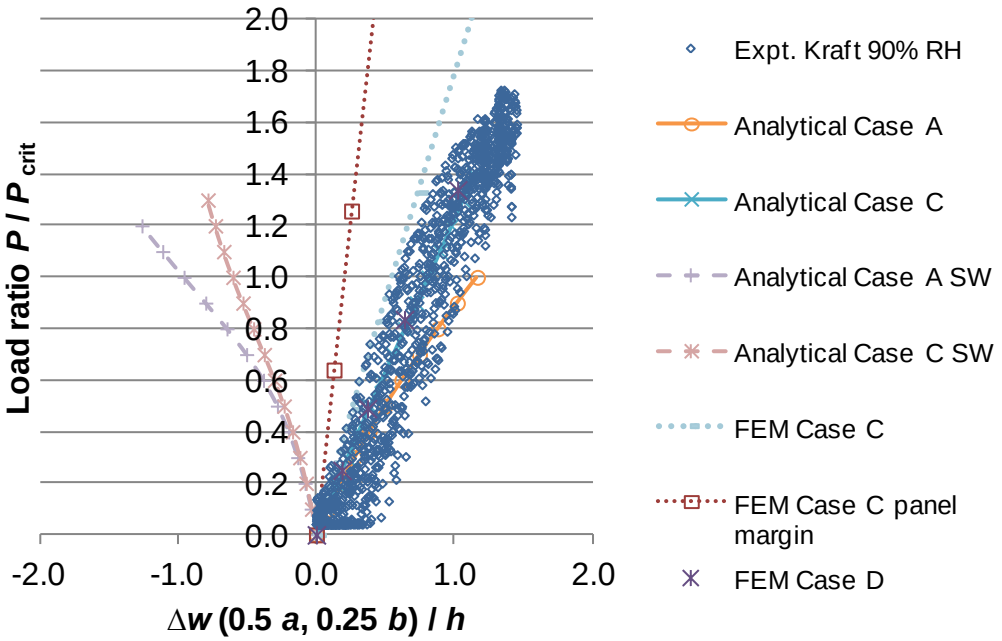

Figure IV-8: Dimensionless post-buckling plot of kraft paperboard panel displacement *w* (0.5 *a*, 0.25 *b*) at 23 °C, 90% relative humidity.

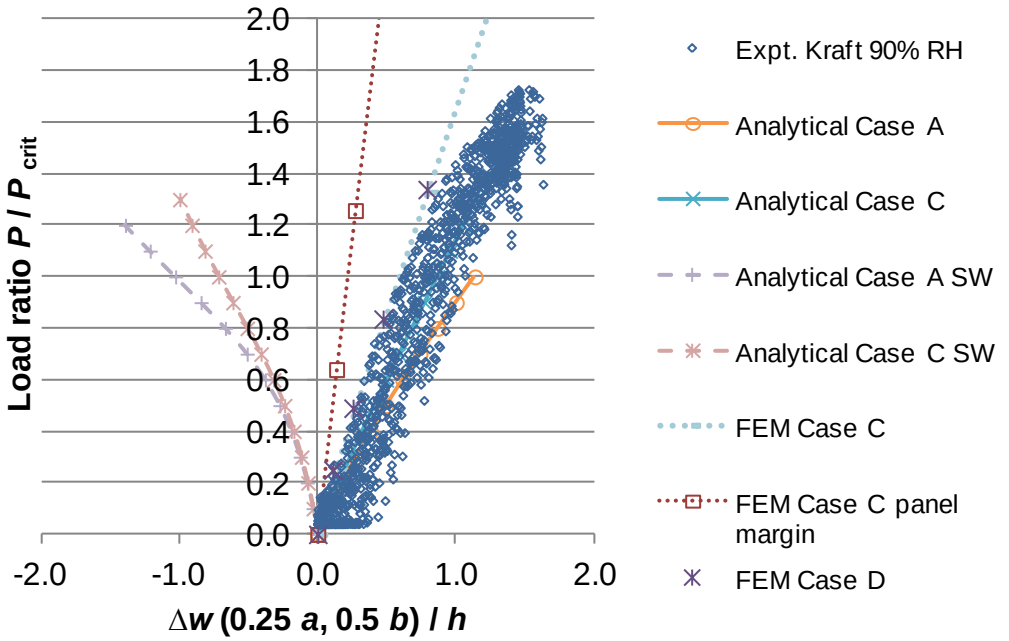

Figure IV-9: Dimensionless post-buckling plot of kraft paperboard panel displacement *w* (0.25 *a*, 0.5 *b*) at 23 °C, 90% relative humidity.

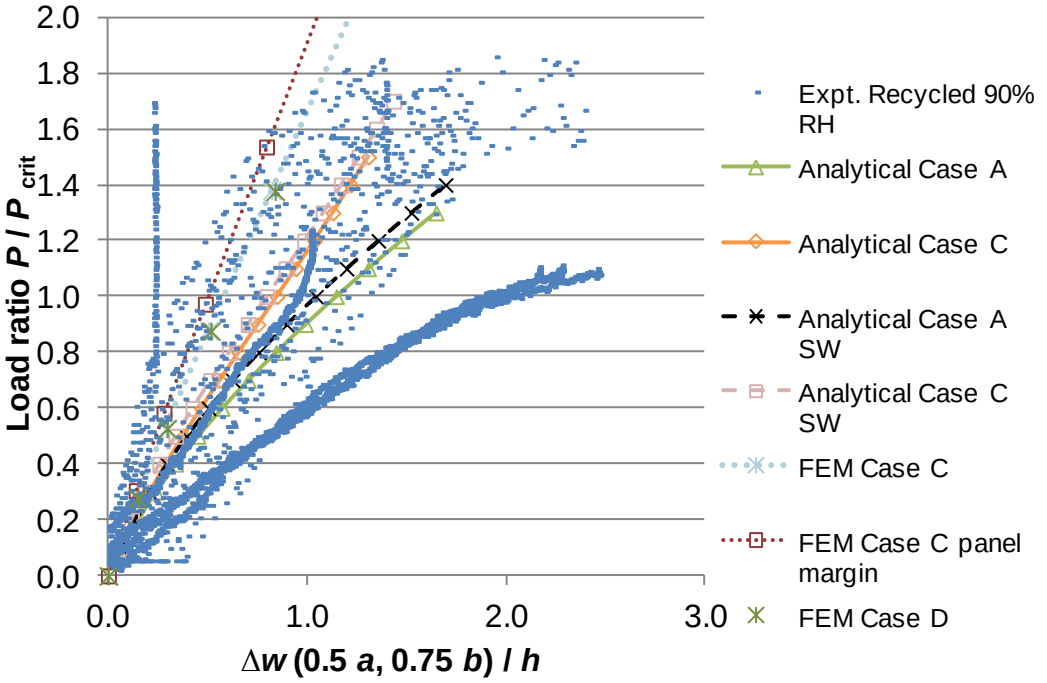

Figure IV-10: Dimensionless post-buckling plot of recycled paperboard panel displacement *w* (0.5 *a*, 0.75 *b*) at 23 °C, 90% relative humidity.

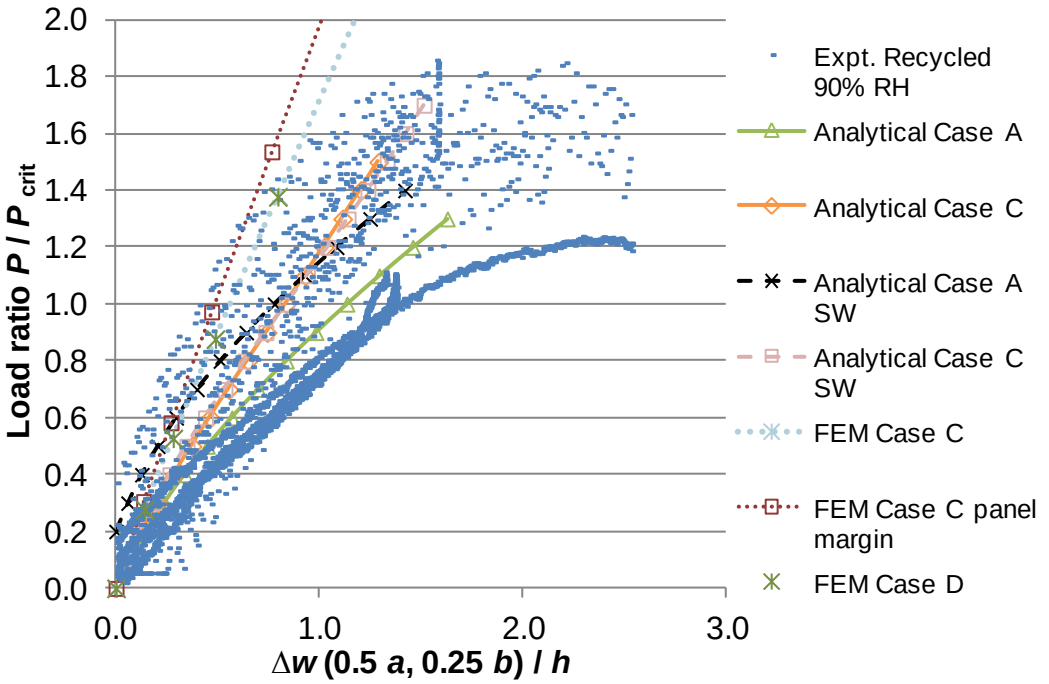

Figure IV-11: Dimensionless post-buckling plot of recycled paperboard panel displacement *w* (0.5 *a*, 0.25 *b*) at 23 °C, 90% relative humidity.

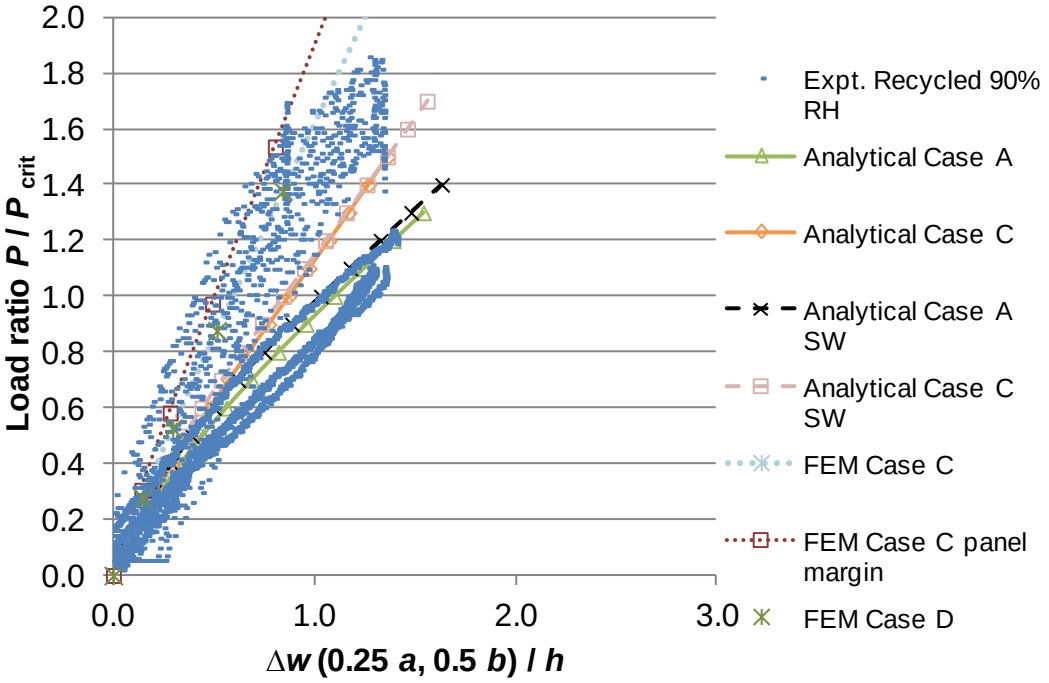

Figure IV-12: Dimensionless post-buckling plot of recycled paperboard panel displacement *w* (0.25 *a*, 0.5 *b*) at 23 °C, 90% relative humidity.

IV.2 Post-buckling plots of panel displacement modes

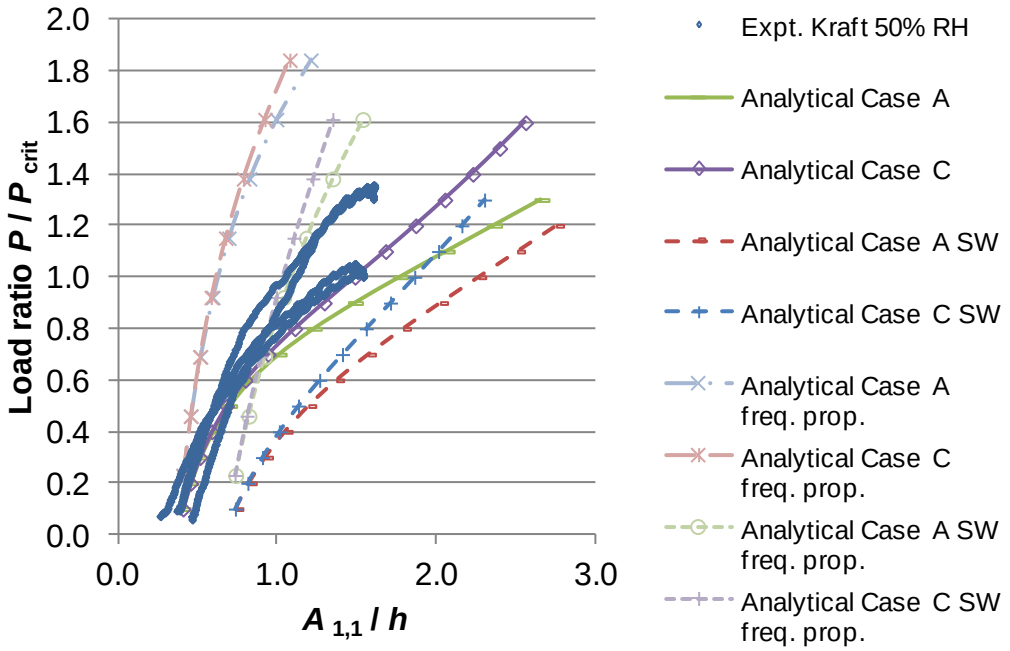

Figure IV-13: Dimensionless post-buckling plot of $A_{1,1}$ displacement modes for kraft paperboard at 23 °C, 50% relative humidity.

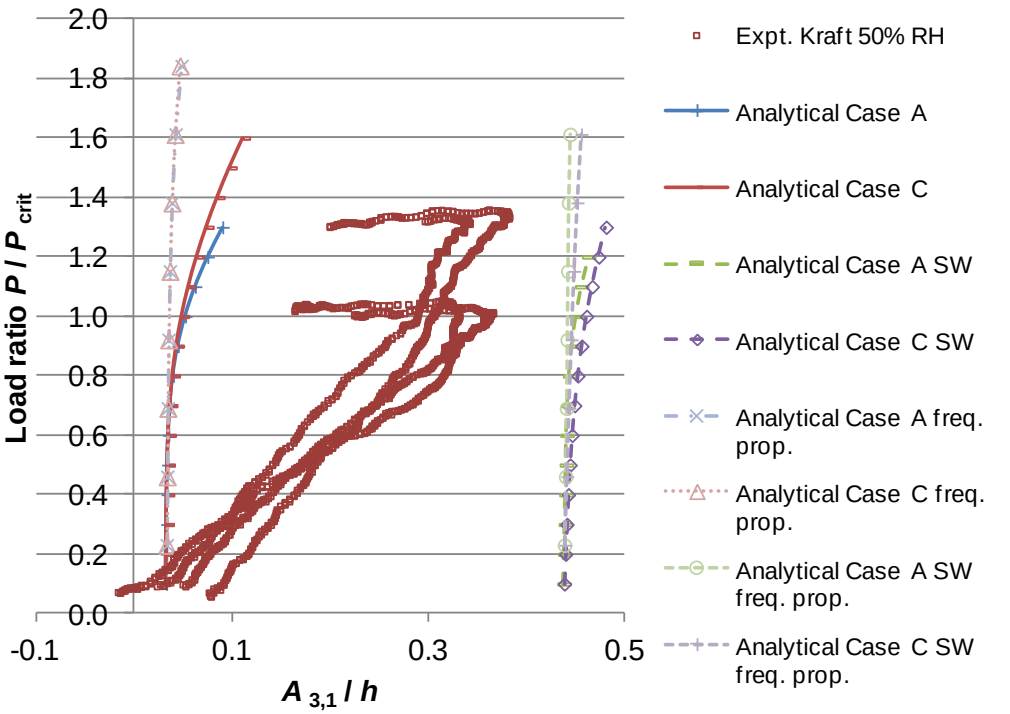

Figure IV-14: Dimensionless post-buckling plot of $A_{3,1}$ displacement modes for kraft paperboard at 23 °C, 50% relative humidity.

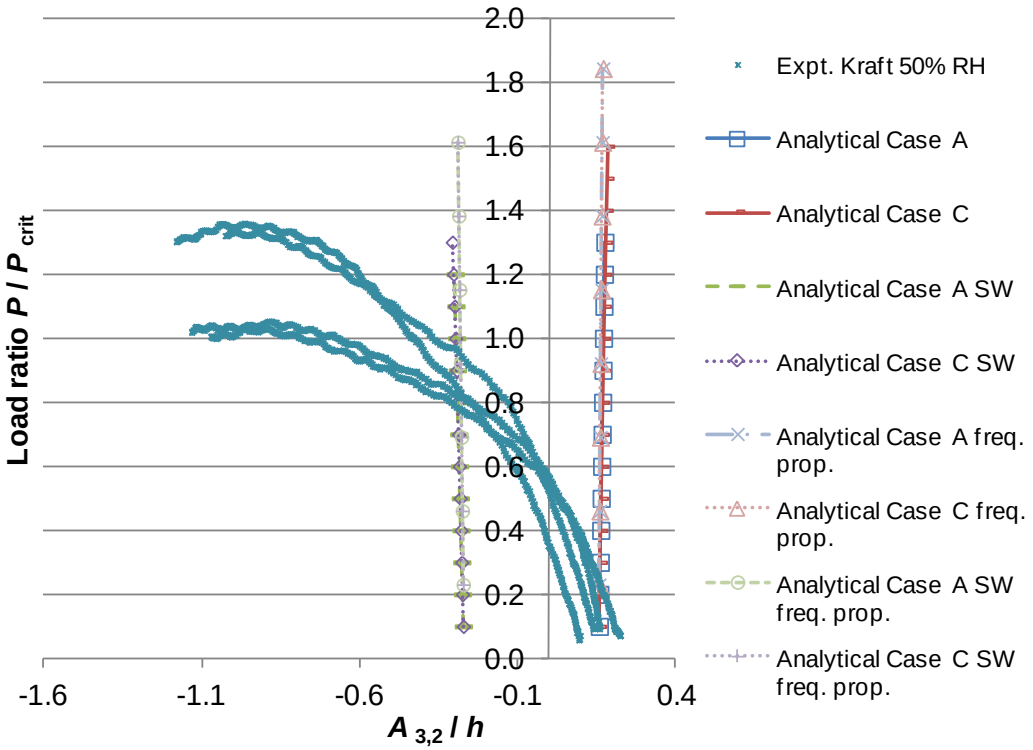

Figure IV-15: Dimensionless post-buckling plot of $A_{3,2}$ displacement modes for kraft paperboard at 23 °C, 50% relative humidity.

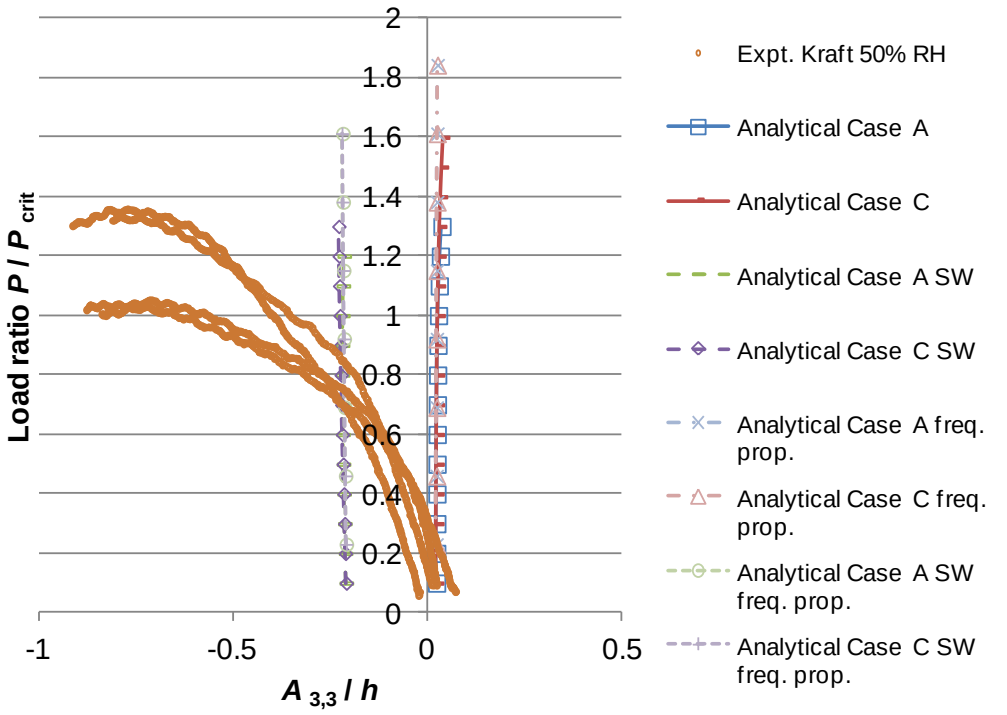

Figure IV-16: Dimensionless post-buckling plot of $A_{3,3}$ displacement modes for kraft paperboard at 23 °C, 50% relative humidity.

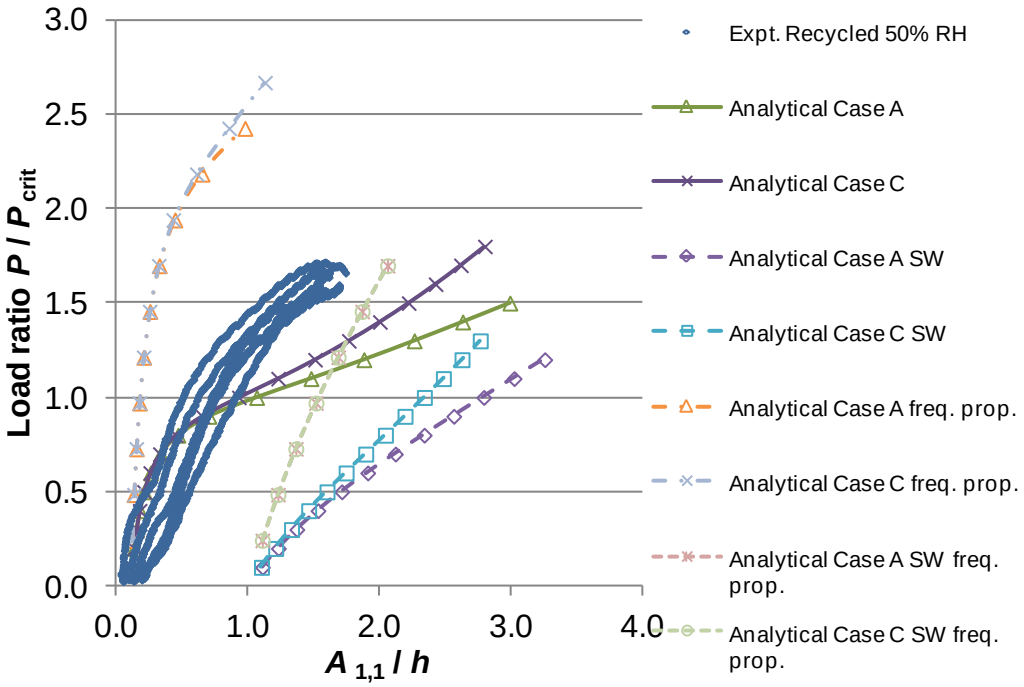

Figure IV-17: Dimensionless post-buckling plot of $A_{1,1}$ displacement modes for recycled paperboard at 23 °C, 50% relative humidity.

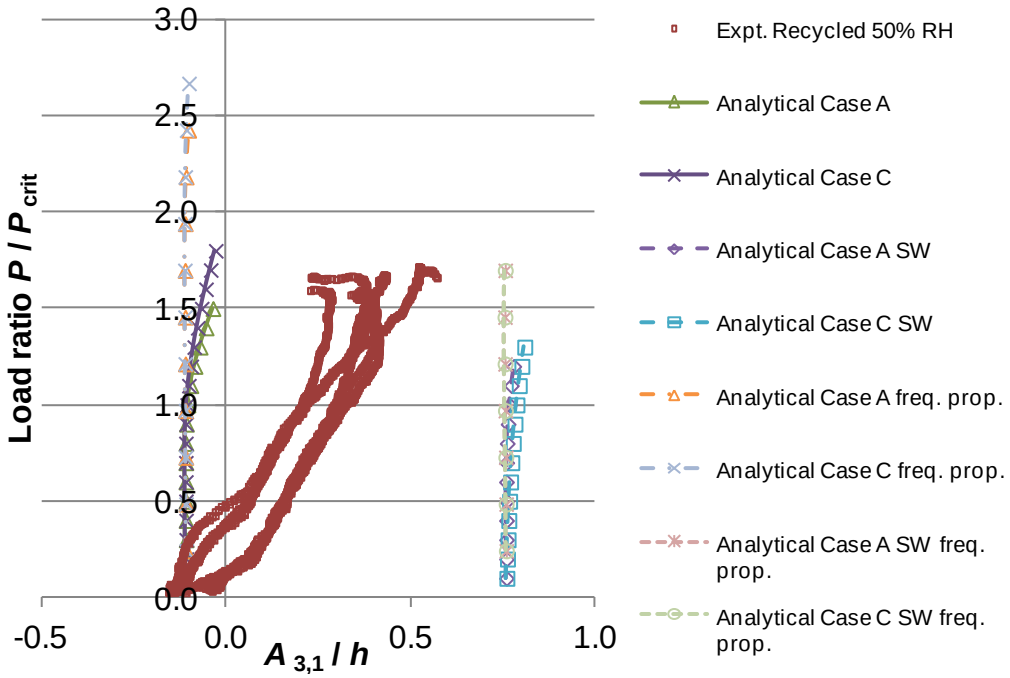

Figure IV-18: Dimensionless post-buckling plot of $A_{3,1}$ displacement modes for recycled paperboard at 23 °C, 50% relative humidity.

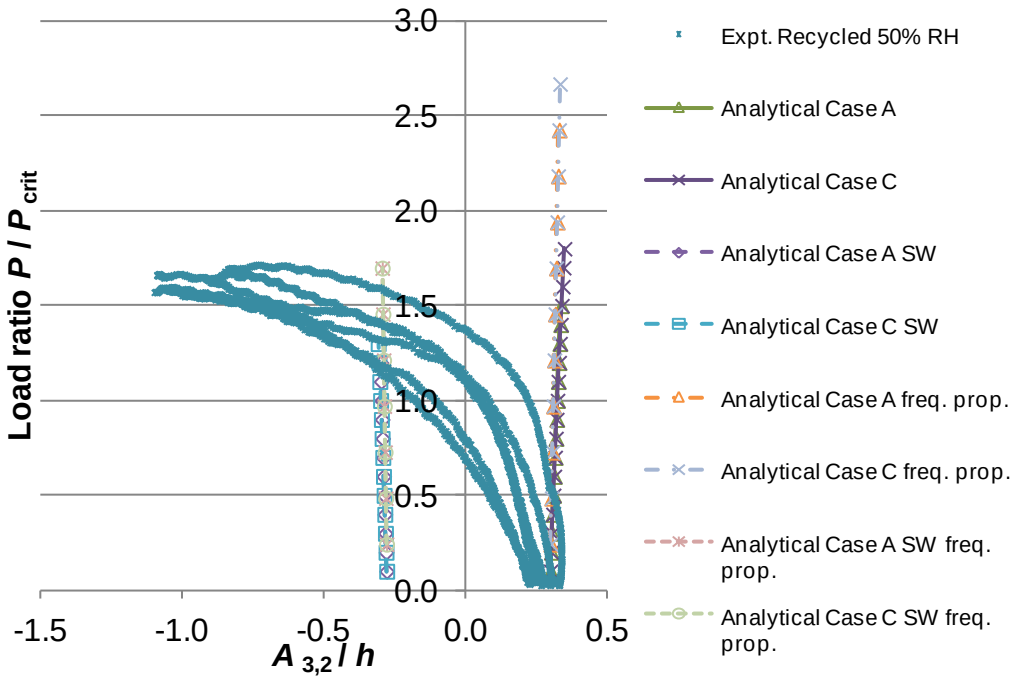

Figure IV-19: Dimensionless post-buckling plot of $A_{3,2}$ displacement modes for recycled paperboard at 23 °C, 50% relative humidity.

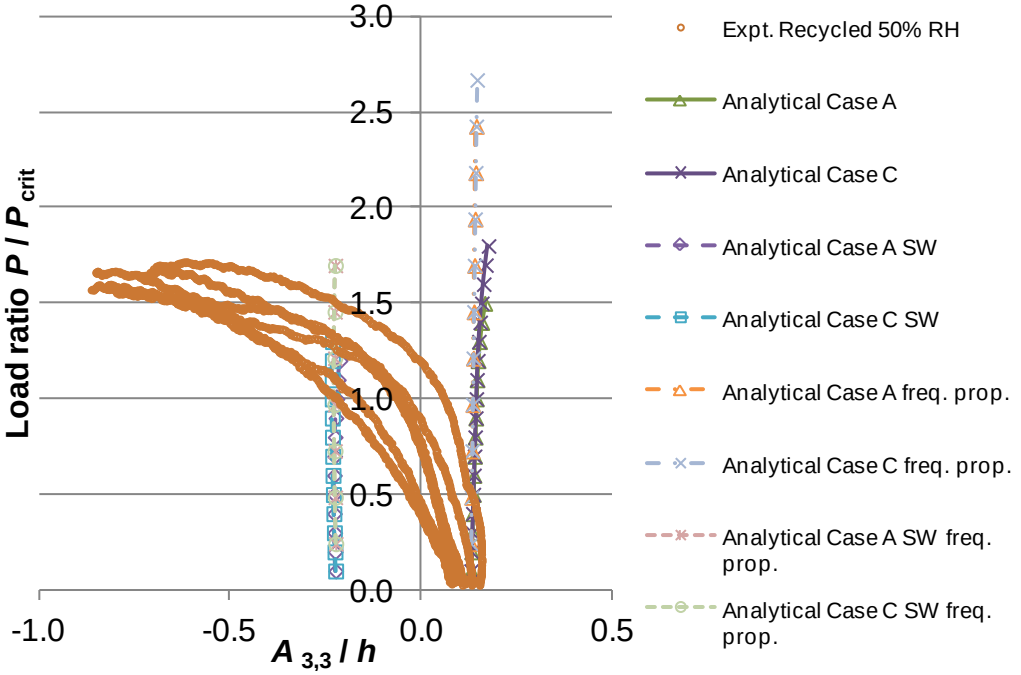

Figure IV-20: Dimensionless post-buckling plot of $A_{3,3}$ displacement modes for recycled paperboard at 23 °C, 50% relative humidity.

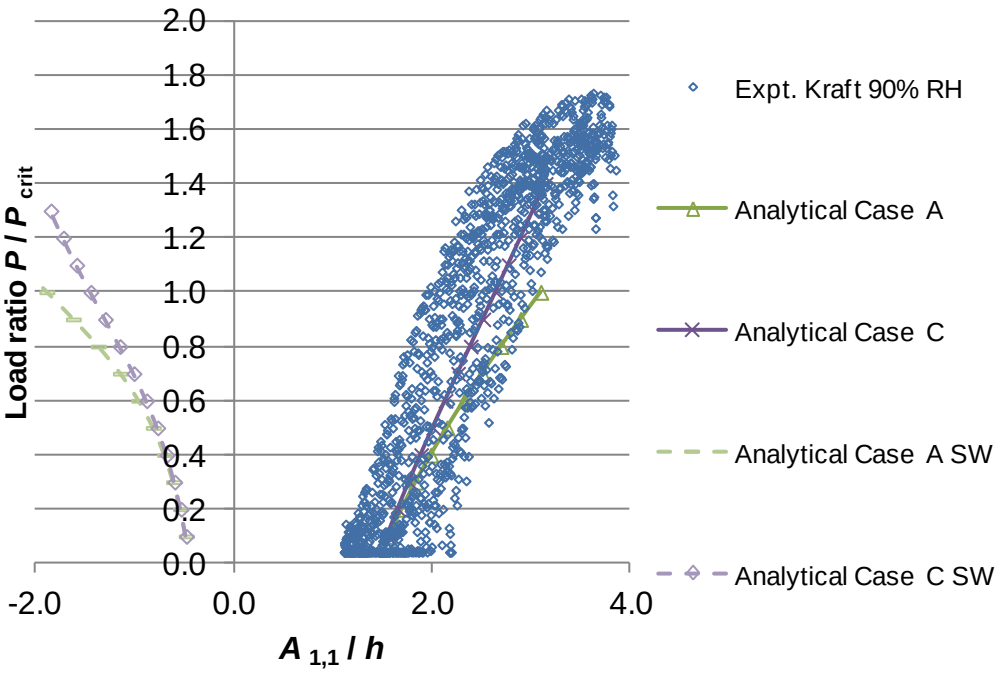

Figure IV-21: Dimensionless post-buckling plot of $A_{1,1}$ displacement modes for kraft paperboard at 23 °C, 90% relative humidity.

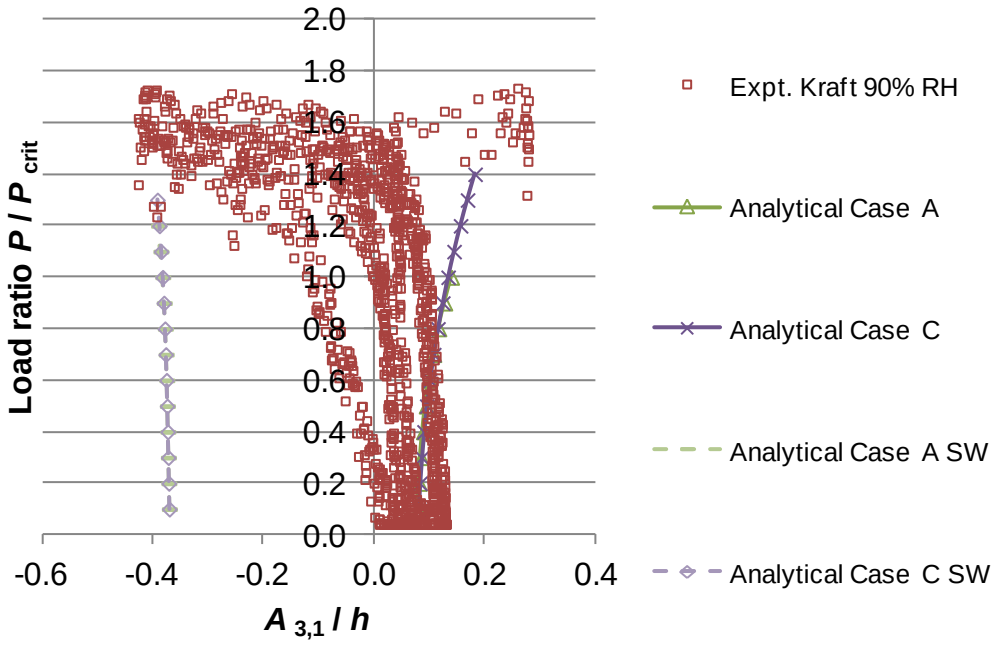

Figure IV-22: Dimensionless post-buckling plot of $A_{3,1}$ displacement modes for kraft paperboard at 23 °C, 90% relative humidity.

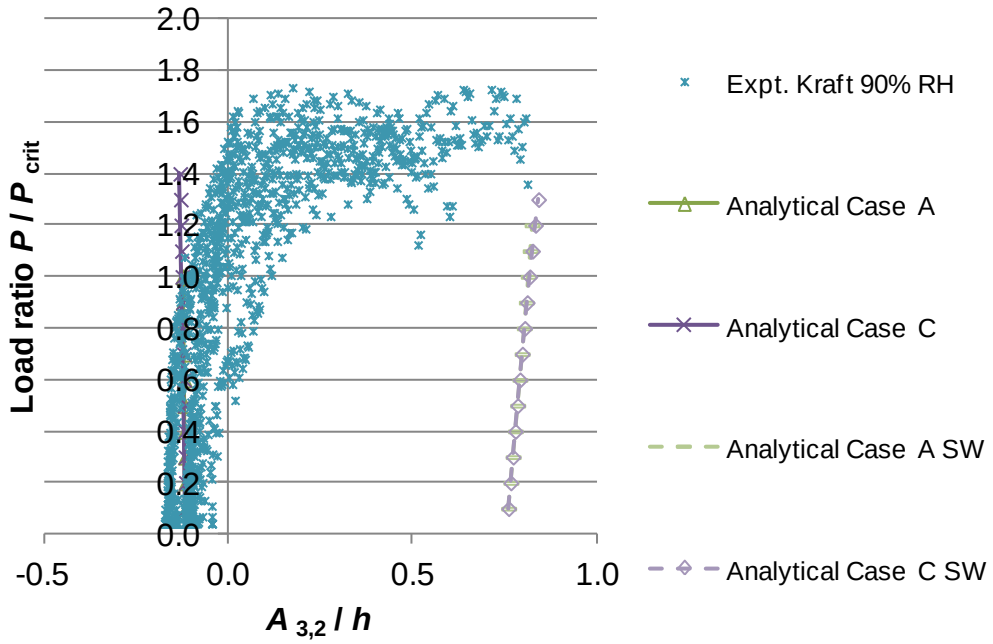

Figure IV-23: Dimensionless post-buckling plot of $A_{3,2}$ displacement modes for kraft paperboard at 23 °C, 90% relative humidity.

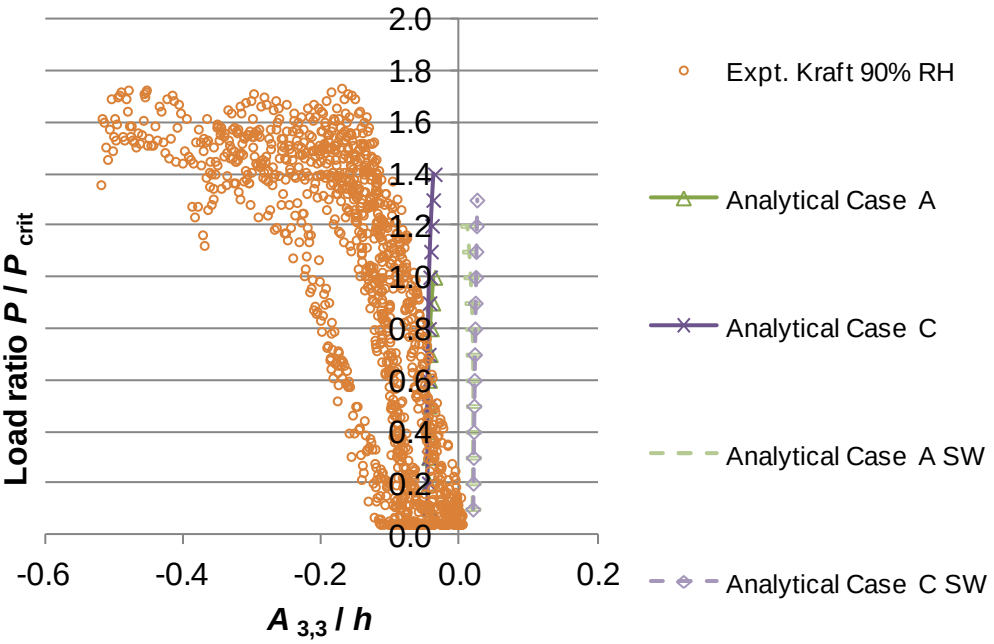

Figure IV-24: Dimensionless post-buckling plot of $A_{3,3}$ displacement modes for kraft paperboard at 23 °C, 90% relative humidity.

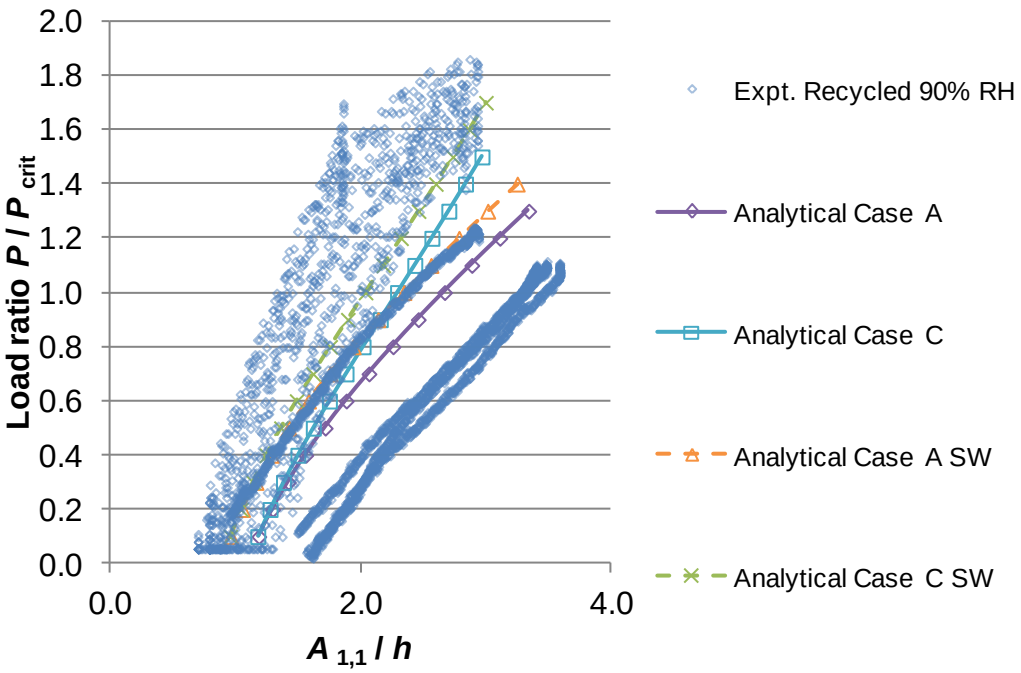

Figure IV-25: Dimensionless post-buckling plot of $A_{1,1}$ displacement modes for recycled paperboard at 23 °C, 90% relative humidity.

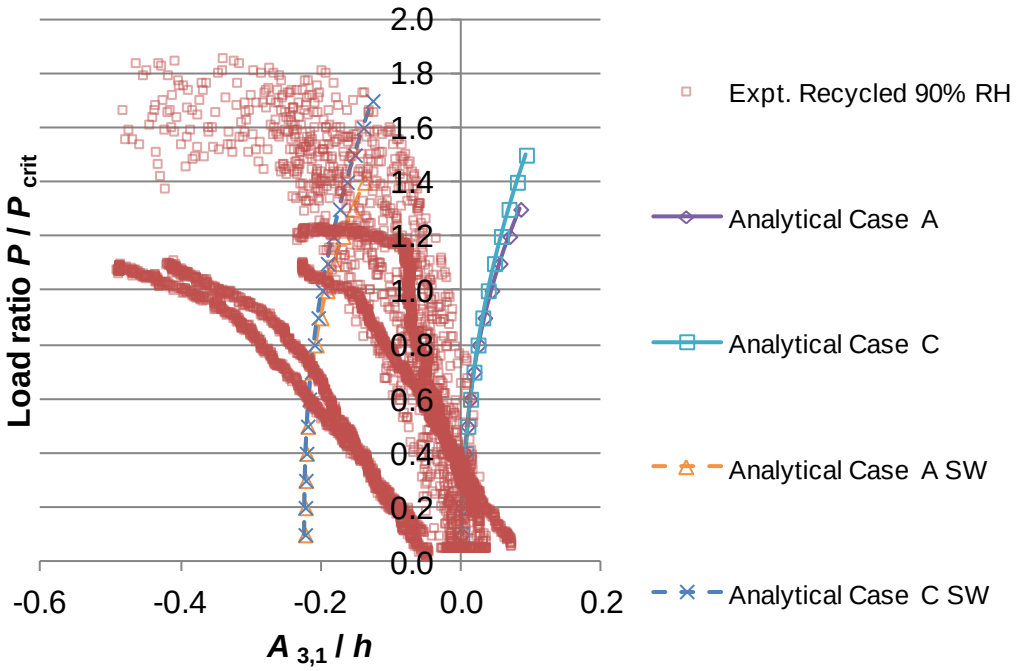

Figure IV-26: Dimensionless post-buckling plot of $A_{3,1}$ displacement modes for recycled paperboard at 23 °C, 90% relative humidity.

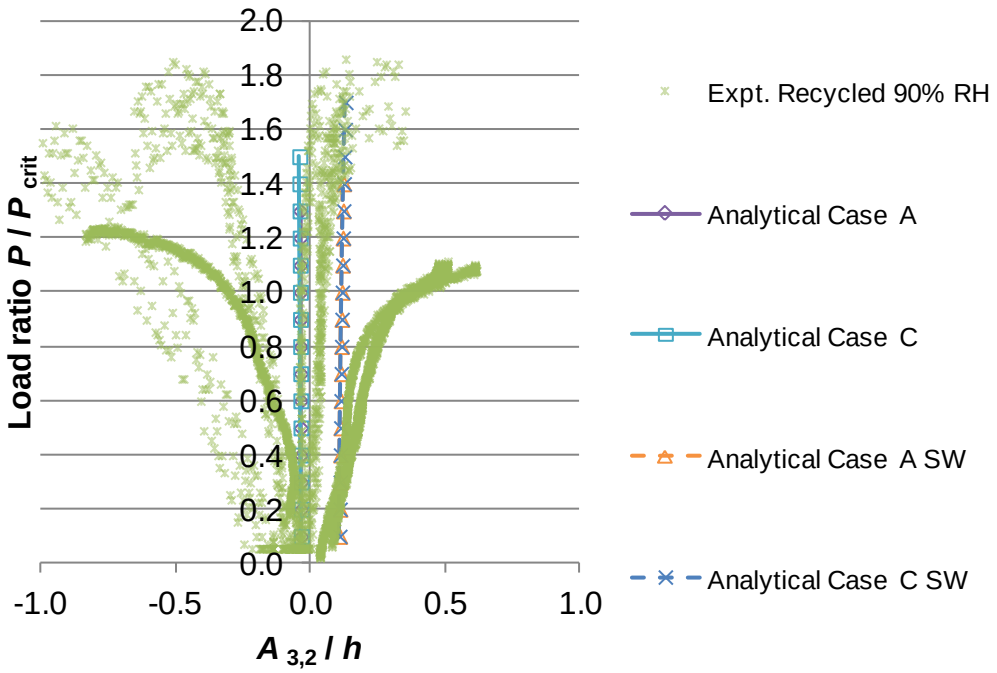

Figure IV-27: Dimensionless post-buckling plot of $A_{3,2}$ displacement modes for recycled paperboard at 23 °C, 90% relative humidity.

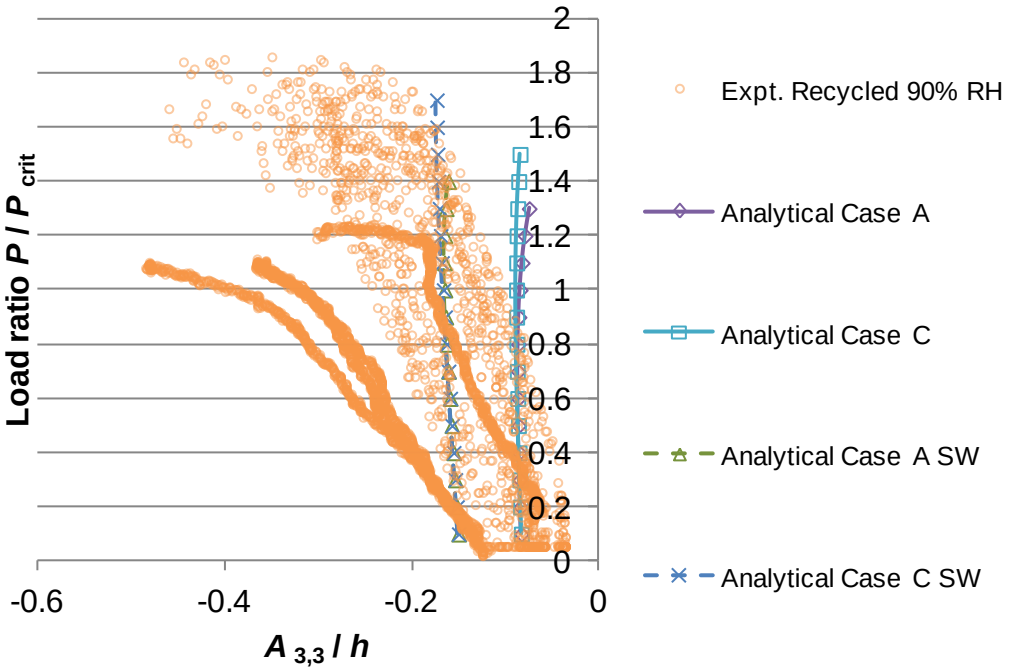

Figure IV-28: Dimensionless post-buckling plot of $A_{3,3}$ displacement modes for recycled paperboard at 23 °C, 90% relative humidity.